

Metal Fatigue:
Effects of Small Defects
and Nonmetallic Inclusions

Yukitaka Murakami

Elsevier

**Metal Fatigue:
Effects of Small Defects
and Nonmetallic Inclusions**

Elsevier Science Internet Homepage – <http://www.elsevier.com>

Consult the Elsevier homepage for full catalogue information on all books, journals and electronic products and services.

Elsevier Titles of Related Interest

CARPINTERI

Minimum Reinforcement in Concrete Members.
ISBN: 008-043022-8

FUENTES *ET AL.*

Fracture Mechanics: Applications and Challenges.
ISBN: 008-043699-4

JONES

Failure Analysis Case Studies II.
ISBN: 008-043959-4

KISHI *ET AL.*

Acoustic Emission. Beyond the Millennium.
ISBN: 008-043851-2

MACHA *ET AL.*

Multiaxial Fatigue and Fracture.
ISBN: 008-043336-7

MARQUIS & SOLIN

Fatigue Design of Components.
ISBN: 008-043318-9

MARQUIS & SOLIN

Fatigue Design and Reliability.
ISBN: 008-043329-4

MOORE *ET AL.*

Fracture Mechanics Testing Methods for Polymers,
Adhesives and Composites.
ISBN: 008-043689-7

RAVICHANDRAN *ET AL.*

Small Fatigue Cracks: Mechanics, Mechanisms &
Applications.
ISBN: 008-043011-2

RÉMY & PETIT

Temperature-Fatigue Interaction.
ISBN: 008-043982-9

TANAKA & DULIKRAVICH

Inverse Problems in Engineering Mechanics III.
ISBN: 008-043951-9

UOMOTO

Non-Destructive Testing in Civil Engineering.
ISBN: 008-043717-6

VOYIADJIS *ET AL.*

Damage Mechanics in Engineering Materials.
ISBN: 008-043322-7

VOYIADJIS & KATTAN

Advances in Damage Mechanics: Metals and Metal
Matrix Composites.
ISBN: 008-043601-3

WILLIAMS & PAVAN

Fracture of Polymers, Composites and Adhesives.
ISBN: 008-043710-9

Related Journals

Free specimen copy gladly sent on request. Elsevier Science Ltd, The Boulevard, Langford Lane, Kidlington, Oxford, OX5 1GB, UK

Acta Metallurgica et Materialia
Cement and Concrete Research
Composite Structures
Computers and Structures
Corrosion Science
Engineering Failure Analysis
Engineering Fracture Mechanics
European Journal of Mechanics A & B
International Journal of Fatigue
International Journal of Impact Engineering
International Journal of Mechanical Sciences
International Journal of Non-Linear Mechanics
International Journal of Plasticity

International Journal of Pressure Vessels & Piping
International Journal of Solids and Structures
Journal of Applied Mathematics and Mechanics
Journal of Construction Steel Research
Journal of the Mechanics and Physics of Solids
Materials Research Bulletin
Mechanics of Materials
Mechanics Research Communications
NDT&E International
Scripta Metallurgica et Materialia
Theoretical and Applied Fracture Mechanics
Tribology International
Wear

To Contact the Publisher

Elsevier Science welcomes enquiries concerning publishing proposals: books, journal special issues, conference proceedings, etc. All formats and media can be considered. Should you have a publishing proposal you wish to discuss, please contact, without obligation, the publisher responsible for Elsevier's mechanics and structural integrity publishing programme:

Dean Eastbury

Senior Publishing Editor, Materials Science & Engineering

Elsevier Science Ltd

The Boulevard, Langford Lane

Kidlington, Oxford

OX5 1GB, UK

Phone: +44 1865 843580

Fax: +44 1865 843920

E.mail: deastbury@elsevier.co.uk

General enquiries, including placing orders, should be directed to Elsevier's Regional Sales Offices – please access the Elsevier homepage for full contact details (homepage details at the top of this page).

Metal Fatigue: Effects of Small Defects and Nonmetallic Inclusions

Yukitaka Murakami

Kyushu University, Japan



2002
ELSEVIER

AMSTERDAM – BOSTON – LONDON – NEW YORK – OXFORD – PARIS
SAN DIEGO – SAN FRANCISCO – SINGAPORE – SYDNEY – TOKYO

ELSEVIER SCIENCE Ltd
The Boulevard, Langford Lane
Kidlington, Oxford OX5 1GB, UK

© 2002 Elsevier Science Ltd. All rights reserved.

This work is protected under copyright by Elsevier Science, and the following terms and conditions apply to its use:

Photocopying

Single photocopies of single chapters may be made for personal use as allowed by national copyright laws. Permission of the Publisher and payment of a fee is required for all other photocopying, including multiple or systematic copying, copying for advertising or promotional purposes, resale, and all forms of document delivery. Special rates are available for educational institutions that wish to make photocopies for non-profit educational classroom use.

Permissions may be sought directly from Elsevier Science Global Rights Department, PO Box 800, Oxford OX5 1DX, UK; phone: (+44) 1865 843830, fax: (+44) 1865 853333, e-mail: permissions@elsevier.co.uk. You may also contact Global Rights directly through Elsevier's home page (<http://www.elsevier.com>), by selecting 'Obtaining Permissions'.

In the USA, users may clear permissions and make payments through the Copyright Clearance Center, Inc., 222 Rosewood Drive, Danvers, MA 01923, USA; phone: (+1) (978) 7508400, fax: (+1) (978) 7504744, and in the UK through the Copyright Licensing Agency Rapid Clearance Service (CLARCS), 90 Tottenham Court Road, London W1P 0LP, UK; phone: (+44) 207 631 5555, fax: (+44) 207 631 5500. Other countries may have a local reprographic rights agency for payments.

Derivative Works

Tables of contents may be reproduced for internal circulation, but permission of Elsevier Science is required for external resale or distribution of such material.

Permission of the Publisher is required for all other derivative works, including compilations and translations.

Electronic Storage or Usage

Permission of the Publisher is required to store or use electronically any material contained in this work, including any chapter or part of a chapter.

Except as outlined above, no part of this work may be reproduced, stored in a retrieval system or transmitted in any form or by any means, electronic, mechanical, photocopying, recording or otherwise, without prior written permission of the Publisher.

Address permissions requests to: Elsevier Science Global Rights Department, at the mail, fax and e-mail addresses noted above.

Notice

No responsibility is assumed by the Publisher for any injury and/or damage to persons or property as a matter of products liability, negligence or otherwise, or from any use or operation of any methods, products, instructions or ideas contained in the material herein. Because of rapid advances in the medical sciences, in particular, independent verification of diagnoses and drugs dosages should be made.

First edition 2002

Library of Congress Cataloging in Publication Data

A catalog record from the Library of Congress has been applied for.

British Library Cataloguing in Publication Data

A catalogue record from the British Library has been applied for.

ISBN: 0-08-044064-9

Ⓢ The paper used in this publication meets the requirements of ANSI/NISO Z39.48-1992 (Permanence of Paper).
Printed in The Netherlands.

Preface

This book has two objectives. One is to present a new way of understanding through the phenomena of metal fatigue the effect of small defects. The other is to set out a practical method for engineers and researchers working on fatigue design and structural integrity to use when assessing the influence of small defects and nonmetallic inclusions on fatigue strength. It goes without saying that the method presented here is based on a rational interpretation of fatigue phenomena. Consequently, this book takes the form of a specialist work for practical use rather than a textbook or comprehensive introduction. The second half mainly addresses problems related to the influence of nonmetallic inclusions. This includes the introduction of an inclusion rating method based on the statistics of extremes, which will be useful not only for fatigue strength evaluation but also for making improvements in steel processing and material quality control.

For design engineers taking metal fatigue into account for the first time, the related phenomena may seem like an extremely complex and incomprehensible subject. I had the same impression myself when I initially approached the field of metal fatigue, for it takes years of experience to really understand the various relationships between the numerous phenomena involved. This is also why existing works for design engineers tend to adopt simple formulae or codes for strength design rather than explain concepts for understanding the details of the phenomena themselves.

The first part of this book includes a concise explanation of metal fatigue. The topics presented are limited in scope and by no means comprehensive, as they consist mainly of themes that I myself have experienced over the last 20 years. As such, some readers may feel that their own particular questions have not been adequately addressed. Nevertheless, since the methodology I have employed is based on important and reliable experimental results, I believe it may be usefully applied to other fatigue problems that have not been treated directly here. Some readers may also have expected to find complicated mathematical formulae designed to develop fatigue theories, but I have avoided using these. Similarly, I have avoided discussing the influence of various microstructures from a metallurgical point of view because, as far as any microstructure's intrinsic fatigue strength is concerned, systematic experimental results have clearly demonstrated the critical factor to be its average deformation resistance. Material scientists and engineers involved in developing new materials may find this approach dissatisfactory, but viewed from another angle, it actually has some advantages for metallurgical material design. Finally, even though some of the questions treated have not been entirely resolved here, I would be delighted if engineers and researchers involved in the study of metal fatigue find this work useful for solving practical problems in industry and developing new laboratory research.

I would like to dedicate this book to the memory of the late Professor Tatsuo Endo of Kyushu Institute of Technology. He played an instrumental role in the experiments

conducted from 1975 onwards on the effect of small defects, the results of which feature in the first part of this volume. Without his warm encouragement and cooperation, in fact, this study may never have come to fruition. I would also like to thank all the students who devoted so much time and energy in my laboratories over the last twenty years to the problems of metal fatigue. In particular, thanks are due to Professor Masahiro Endo of Fukuoka University for his kind collaboration in the early days of my research on small defects at a time when he was still a student, and for all his support and advice right up to the present day.

I am also indebted to the following students for all their assistance in the course of my research: to Yoshihiro Fukushima, Shiro Fukuda, Yoshiyuki Tazunoki, Hiroyuki Kawano and Hiroshi Oba for their help in the early stages of my study on small defects; to Hisakazu Morinaga, Masajiro Abe and Kenji Matsuda for their help during the transition period from the study on small defects to the study on inclusions; to Naoshi Usuki, Yujiro Uemura, Katsumi Kawakami, Taizo Makino, Yuuki Matsuo, Yoshihiro Ohkomori, Toshiyuki Toriyama, Emanuelle Coudert, Akio Yamashita, Masayuki Takada, Tetsushi Nomoto, Toru Ueda, Hiroshi Konishi and Junji Nagata for their help on inclusion problems; to Masatoshi Yatsuda, Yukihiko Uchiyama and Mitsutoshi Uchida for their help with the analysis of stress concentration of inclusions; and to Tetsuya Takafuji, Hirokazu Kobayashi, Hideyuki Fujii and Hisao Matsunaga for their help with inhomogeneity problems; and to Akio Yamashita, Kazuya Tsutsumi and Koji Takahashi for their help with surface roughness problems; and to Koji Takahashi for his help with biaxial problems.

In addition, I am grateful to Professor Shotaro Kodama of Tokyo Metropolitan University and Dr. Shizuyo Konuma of Niigata University for kindly offering me their valuable experimental data on nonmetallic inclusions, which enabled me to extend the theory of small defects to inclusion problems. I have also received numerous valuable suggestions, comments, advice and support from the following researchers and engineers based at other academic institutions, research institutes and companies: Jin-ichi Takamura (the late Emeritus Professor of Kyoto University), W.E. Duckworth, Toru Araki, Kyozauro Furumura, Yasuo Murakami, Kazu-ichi Tsubota, Kazuo Toyama, Shin-ichi Nishida, Yoshitaka Natsume, Makoto Saito, Kimio Mine, Shozo Nakayama, Hayato Ikeda, Motokazu Kobayashi, Yoshiro Koyasu, Kazuo Hoshino, Masao Shimizu, Tatsumi Kimura, Jun Eguchi, Ryuichiro Ebara, Ken-ichi Takai, Bengt Johannesson, Gill Baudry, Saburo Matsuoka, Setsuo Takaki, Yoshiyuki Kondo and Tatsuhiko Yoshimura.

Furthermore, I am indebted to the following for their encouraging comments and advice: Keith J. Miller (University of Sheffield, UK), Darrell Socie (University of Illinois, USA), Robert O. Ritchie (University of California, Berkeley, USA), Stefano Beretta (Politecnico di Milano, Italy), Arthur J. McEvily (University of Connecticut, USA), Toshio Mura (Northwestern University, USA), Ronald Landgraf (formerly Virginia Polytechnic, USA), Arne Melander (Swedish Institute of Metallic Research, Sweden), Gary Marquis (Lappeenranta University of Technology, Finland), Jacques de Mare (Chalmers University, Sweden) and Clive Anderson (University of Sheffield, UK).

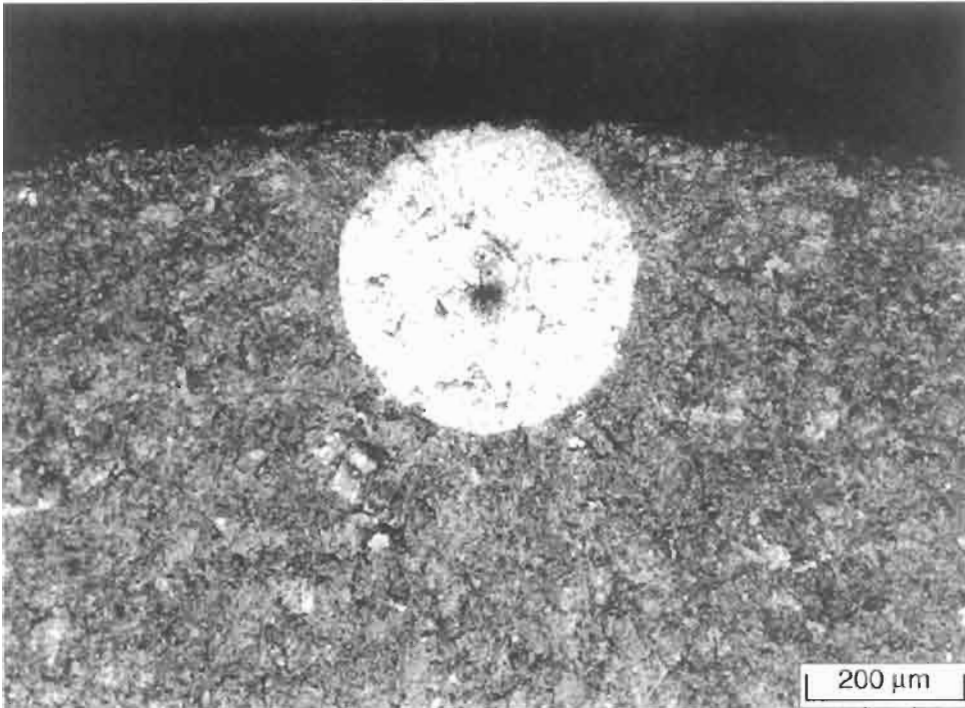
I wish to thank my laboratory staff, Shigeru Shinozaki, Masahiro Fujishima, Yoshihiro Fukushima and Masaki Kobayashi, for all their invaluable help with preparing specimens, experimental equipment and drawing figures. I am indebted, moreover,

to Kiyoshi Oikawa, the President of Yokendo Publishing Co. Ltd. for publishing the original Japanese version of this book and kindly approving the publication of this English edition. Les Pook revised the English translation. I thank Dr. Les Pook and Prof. Andrew Cobbing for their help with correcting and revising the original English manuscript.

Finally, I would like to express my sincere thanks to my secretary, Tamiko Terai (current name Tamiko Kojima), for all her help in preparing the final arrangement of the manuscript for this English version.

Yukitaka Murakami

Frontispiece



Material: Roll steel,
Loading type: Rotating bending fatigue,
Vickers hardness $H_V = 561$,
Number of cycles to failure $N_f = 1.030 \times 10^7$,
Inclusion size $\sqrt{area} = 16.7 \mu\text{m}$,
Distance from specimen surface = $212 \mu\text{m}$,
Nominal stress at the inclusion = 772 MPa

A fisheye pattern appeared on fatigue fracture surface

Contents

1. Mechanism of Fatigue in the Absence of Defects and Inclusions	1
1.1 What is a Fatigue Limit?	1
1.1.1 Steels	1
1.1.2 Nonferrous Metals	4
1.2 Relationship between Static Strength and Fatigue Strength	5
1.3 References	8
2. Stress Concentration	11
2.1 Stress Concentrations at Holes and Notches	11
2.2 Stress Concentration at a Crack	15
2.2.1 'area' as a New Geometrical Parameter	16
2.2.2 Effective 'area' for Particular Cases	17
2.2.3 Cracks at Stress Concentrations	21
2.2.4 Interaction between Two Cracks	21
2.2.5 Interaction between a Crack and a Free Surface	22
2.3 References	24
3. Notch Effect and Size Effect	25
3.1 Notch Effect	25
3.1.1 Effect of Stress Distribution at Notch Roots	25
3.1.2 Non-Propagating Cracks at Notch Roots	28
3.2 Size Effect	31
3.3 References	32
4. Effect of Size and Geometry of Small Defects on the Fatigue Limit	35
4.1 Introduction	35
4.2 Influence of Extremely Shallow Notches or Extremely Short Cracks ...	35
4.3 Fatigue Tests on Specimens Containing Small Artificial Defects	37
4.3.1 Effect of Small Artificial Holes Having the Diameter d Equal to the Depth h	37
4.3.2 Effect of Small Artificial Holes Having Different Diameters and Depths	42
4.4 Critical Stress for Fatigue Crack Initiation from a Small Crack	47
4.5 References	54

5. Effect of Hardness H_V on Fatigue Limits of Materials Containing Defects, and Fatigue Limit Prediction Equations	57
5.1 Relationship between ΔK_{th} and the Geometrical Parameter, \sqrt{area}	57
5.2 Material Parameter H_V which Controls Fatigue Limits	60
5.3 Application of the Prediction Equations	62
5.4 Limits of Applicability of the Prediction Equations: Eqs. 5.4 and 5.5 ...	66
5.5 The Importance of the Finding that Specimens with an Identical Value of \sqrt{area} for Small Holes or Small Cracks Have Identical Fatigue Limits: When the Values of \sqrt{area} for a Small Hole and a Small Crack are Identical, are the Fatigue Limits for Specimens Containing these Two Defect Types Really Identical?	66
5.6 References	71
6. Effects of Nonmetallic Inclusions on Fatigue Strength	75
6.1 Review of Existing Studies and Current Problems	75
6.1.1 Correlation of Material Cleanliness and Inclusion Rating with Fatigue Strength.....	75
6.1.2 Size and Location of Inclusions and Fatigue Strength.....	77
6.1.3 Mechanical Properties of Microstructure and Fatigue Strength ..	78
6.1.4 Influence of Nonmetallic Inclusions Related to the Direction and Mode of Loading	81
6.1.5 Inclusion Problem Factors	82
6.2 Similarity of Effects of Nonmetallic Inclusions and Small Defects and a Unifying Interpretation	85
6.3 Quantitative Evaluation of Effects of Nonmetallic Inclusions: Strength Prediction Equations and their Application.....	88
6.4 Causes of Fatigue Strength Scatter for High Strength Steels and Scatter Band Prediction	94
6.5 Effect of Mean Stress	99
6.5.1 Quantitative Evaluation of the Mean Stress Effect on Fatigue of Materials Containing Small Defects	100
6.5.2 Effects of Both Nonmetallic Inclusions and Mean Stress in Hard Steels	104
6.5.3 Prediction of the Lower Bound of Scatter and its Application ...	108
6.6 Estimation of Maximum Inclusion Size \sqrt{area}_{max} by Microscopic Examination of a Microstructure	110
6.6.1 Measurement of \sqrt{area}_{max} for Largest Inclusions by Optical Microscopy	112
6.6.2 True and Apparent Maximum Sizes of Inclusions	114
6.6.3 Two-dimensional (2D) Prediction Method for Largest Inclusion Size and Evaluation by Numerical Simulation	118
6.7 References	122

7. Bearing Steels	129
7.1 Influence of Steel Processing	130
7.2 Inclusions at Fatigue Fracture Origins	130
7.3 Cleanliness and Fatigue Properties	133
7.3.1 Total Oxygen (O) Content	136
7.3.2 Ti Content	136
7.3.3 Ca Content	136
7.3.4 Sulphur (S) Content	137
7.4 Fatigue Strength of Super Clean Bearing Steels and the Role of Nonmetallic Inclusions	139
7.5 Tessellated Stresses Associated with Inclusions: Thermal Residual Stresses around Inclusions	142
7.6 What Happens to the Fatigue Limit of Bearing Steels without Nonmetallic Inclusions? — Fatigue Strength of Electron Beam Remelted Super Clean Bearing Steel	148
7.6.1 Material and Experimental Procedure	148
7.6.2 Inclusion Rating Based on the Statistics of Extremes	152
7.6.3 Fatigue Test Results	153
7.6.4 The True Character of Small Inhomogeneities at Fracture Origins	154
7.7 References	159
8. Spring Steels	163
8.1 Spring Steels (SUP12) for Automotive Components	163
8.2 Explicit Analysis of Nonmetallic Inclusions, Shot Peening, Decarburised Layers, Surface Roughness, and Corrosion Pits in Automobile Suspension Spring Steels	168
8.2.1 Materials and Experimental Procedure	169
8.2.2 Interaction of Factors Influencing Fatigue Strength	172
8.2.2.1 Effect of Shot Peening	173
8.2.2.2 Effects of Nonmetallic Inclusions and Corrosion Pits .	178
8.2.2.3 Prediction of Scatter in Fatigue Strength using the Statistics of Extreme	180
8.3 References	182
9. Tool Steels: Effect of Carbides	185
9.1 Low Temperature Forging and Microstructure	185
9.2 Static Strength and Fatigue Strength	187
9.3 Relationship Between Carbide Size and Fatigue Strength	190
9.4 References	192

10. Effects of Shape and Size of Artificially Introduced Alumina Particles on 1.5Ni–Cr–Mo (En24) Steel	193
10.1 Artificially Introduced Alumina Particles with Controlled Sizes and Shapes, Specimens, and Test Stress	193
10.2 Rotating Bending Fatigue Tests without Shot Peening	195
10.3 Rotating Bending Fatigue Tests on Shot-Peened Specimens	199
10.4 Tension Compression Fatigue Tests	202
10.5 References	203
11. Nodular Cast Iron	205
11.1 Introduction	205
11.2 Fatigue Strength Prediction of Nodular Cast Irons by Considering Graphite Nodules to be Equivalent to Small Defects	206
11.3 References	215
12. Influence of Si-Phase on Fatigue Properties of Aluminium Alloys	217
12.1 Materials, Specimens and Experimental Procedure	217
12.2 Fatigue Mechanism	217
12.2.1 Continuously Cast Material	220
12.2.2 Extruded Material	221
12.2.3 Fatigue Behaviour of Specimens Containing an Artificial Hole ..	225
12.3 Mechanisms of Ultralong Fatigue Life	227
12.4 Low-Cycle Fatigue	231
12.4.1 Fatigue Mechanism	231
12.4.2 Continuously Cast Material	232
12.4.3 Extruded Material	232
12.4.4 Comparison with High-Cycle Fatigue	232
12.4.5 Cyclic Property Characterisation	235
12.5 Summary	238
12.6 References	239
13. Ti Alloys	241
13.1 References	244
14. Torsional Fatigue	247
14.1 Introduction	247
14.2 Effect of Small Artificial Defects on Torsional Fatigue Strength	248
14.2.1 Ratio of Torsional Fatigue Strength to Bending Fatigue Strength	248
14.2.2 The State of Non-Propagating Cracks at the Torsional Fatigue Limit	253

14.2.3 Torsional Fatigue of High Carbon Cr Bearing Steel	256
14.3 Effects of Small Cracks	258
14.3.1 Material and Test Procedures	261
14.3.2 Fatigue Test Results	262
14.3.3 Crack Initiation and Propagation from Precracks	263
14.3.4 Fracture Mechanics Evaluation of the Effect of Small Cracks on Torsional Fatigue	266
14.3.5 Prediction of Torsional Fatigue Limit by the \sqrt{area} Parameter Model	268
14.4 References	270
15. The Mechanism of Fatigue Failure of Steels in the Ultralong Life Regime of $N > 10^7$ Cycles	273
15.1 Mechanism of Elimination of Conventional Fatigue Limit: Influence of Hydrogen Trapped by Inclusions	273
15.1.1 Method of Data Analysis	274
15.1.2 Material, Specimens and Experimental Method	275
15.1.3 Distribution of Residual Stress and Hardness	276
15.1.4 Fracture Origins	277
15.1.5 $S-N$ Curves	277
15.1.6 Details of Fracture Surface Morphology and Influence of Hydrogen	279
15.2 Fractographic Investigation	291
15.2.1 Measurement of Surface Roughness	292
15.2.2 The Outer Border of a Fish Eye	292
15.2.3 Crack Growth Rate and Fatigue Life	298
15.3 Current Conclusions	299
15.4 References	302
16. Effect of Surface Roughness on Fatigue Strength	305
16.1 Introduction	305
16.2 Material and Experimental Procedure	306
16.2.1 Material	306
16.2.2 Introduction of Artificial Surface Roughness and of a Single Notch	306
16.2.3 Measurement of Hardness and Surface Roughness	308
16.3 Results and Discussion	312
16.3.1 Results of Fatigue Tests	312
16.3.2 Quantitative Evaluation by the \sqrt{area} Parameter Model	312
16.3.2.1 Geometrical Parameter to Evaluate the Effect of Surface Roughness on Fatigue Strength	312
16.3.2.2 Evaluation of Equivalent Defect Size for Roughness $\sqrt{area_R}$	315

16.4	Guidance for Fatigue Design Engineers	319
16.5	References	319
Appendix A. Instructions for a New Method of Inclusion Rating and Correlations with the Fatigue Limit		321
A1	Background of Extreme Value Theory and Data Analysis	323
A2	Simple Procedure for Extreme Value Inclusion Rating	325
A3	Prediction of the Maximum Inclusion	329
A4	Prediction of \sqrt{area}_{max} of Inclusions Expected to be Contained in a Volume	331
A5	Method for Estimating the Prediction Volume (or Control Volume)	333
A6	Prediction of the Lower Limit (Lower Bound) of the Fatigue Strength ..	337
A7	The Comparison of Predicted Lower Bound of the Scatter in Fatigue Strength of a Medium Carbon Steel with Rotating Bending Fatigue Test Results	339
A8	Optimisation of Extreme Value Inclusion Rating (EVIR)	345
A9	Recent Developments in Statistical Analysis and its Perspectives	347
A10	References	349
Appendix B. Database of Statistics of Extreme Values of Inclusion Size \sqrt{area}_{max}		351
Appendix C. Probability Sheets of Statistics of Extremes		357
Index		359

Chapter 1

Mechanism of Fatigue in the Absence of Defects and Inclusions

In order to evaluate quantitatively the effects of defects and inclusions we must first understand the basic mechanism of fatigue. Researchers who are mainly interested in the mechanism of fatigue on a microscopic scale may study the behaviour of dislocations during the fatigue process. In fact, active research in this field, including many experiments and theories on persistent slip bands and various dislocation structures [1–19], has led to understanding of some aspects of the fatigue phenomenon. However, study from the viewpoint of dislocation structure is somewhat qualitative, and has not so far been developed to a level that permits the quantitative solution of practical engineering problems. In this chapter, discussion of the fatigue mechanism is based on more macroscopic phenomena such as those observed with an optical microscope. The phenomena observed with an optical microscope are those which may be detected within one grain, in commercial materials, ranging in size from a few μm to several tens of μm . Thus, the process of initiation and propagation of so-called small cracks is perhaps the most important phenomenon discussed in this book. Although several theories of small cracks have been proposed, this chapter is restricted to the presentation of experimental evidence during the fatigue of unnotched specimens, and to the derivation of practically useful conclusions.

1.1 What is a Fatigue Limit?

1.1.1 Steels

Fig. 1.1 shows a typical relationship between the applied stress, σ , and the number of cycles to failure, N_f , for unnotched steel specimens tested either in rotating bending or in tension-compression. This relationship is called an $S-N$ curve, and the abrupt change in slope is called the 'knee point'. Most steels show a clear knee point. The stress amplitude at the knee point is called the 'fatigue limit' since there is no sign of failure, even after the application of more than 10^7 stress cycles. In this book the fatigue limit of unnotched specimens is denoted σ_{w0} . Fig. 1.1 consists of two simple straight lines. If we predict, without prior knowledge, data for stresses lower than point B, then

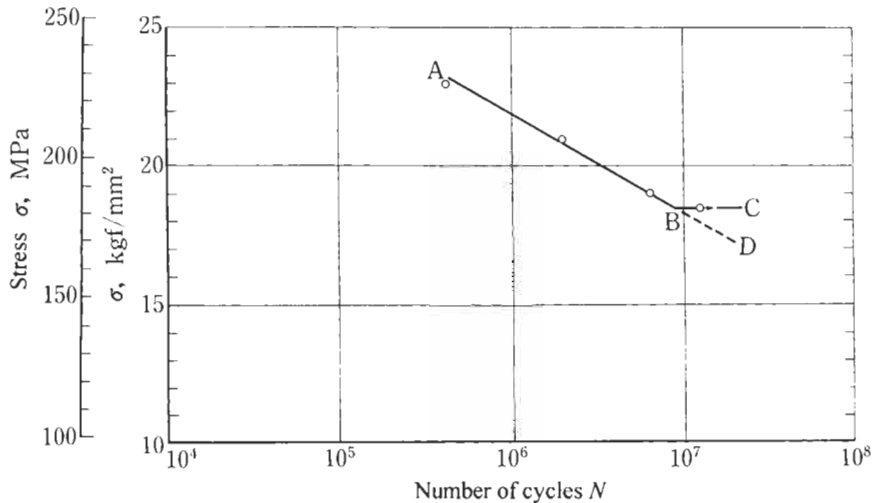


Figure 1.1 $S-N$ curve for a low carbon steel.

extrapolation of the line AB leads to the predicted line $A \rightarrow B \rightarrow D$. However, the observed result is $B \rightarrow C$ and not $B \rightarrow D$. Therefore, we anticipate that something unexpected might be happening at $\sigma = \sigma_{w0}$. The interpretation of ‘fatigue limit’ which had been made in the era before the precise observation of fatigue phenomena on a specimen surface became possible, was the ‘limit of crack initiation under cyclic stress’ [20–22]. In its historical context this interpretation was natural, and is still correct for some metals. However, this interpretation is inexact for most steels.

Fig. 1.2 shows the change in the surface appearance of an electropolished 0.13% C steel during a fatigue test at the fatigue limit stress, σ_{w0} . Slip bands appear at a very early stage, prior to crack initiation, and some of them become cracks. Some cracks remain within a grain, but others propagate through grain boundaries and then stop propagating. These cracks are called non-propagating cracks in unnotched specimens. The maximum size of a non-propagating crack in an annealed 0.13% C steel is of the order of 100 μm , which is much larger than the 34 μm average ferrite grain size. This experimental

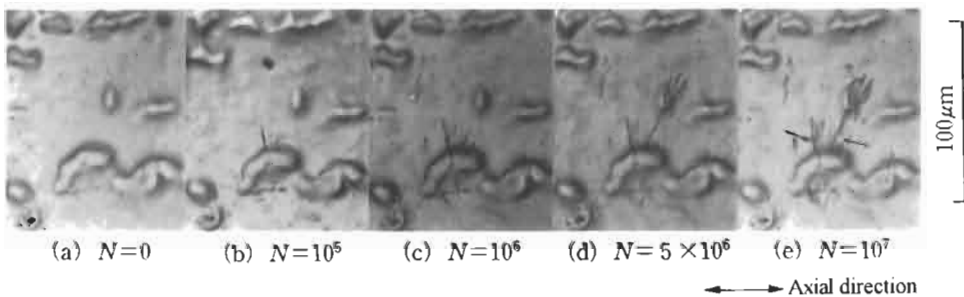


Figure 1.2 Sequence of development of a non-propagating crack observed at the fatigue limit ($\sigma_{w0} = 181$ MPa) of an annealed 0.13% carbon steel.

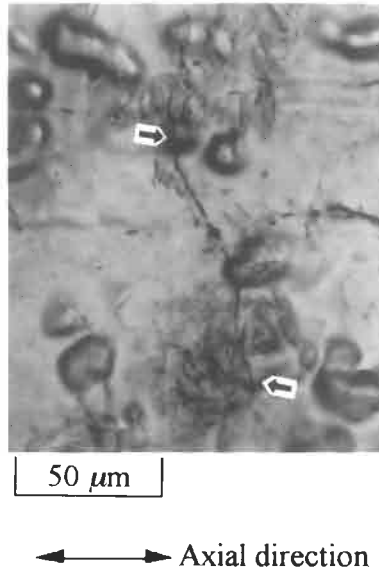


Figure 1.3 Largest non-propagating crack observed at the fatigue limit ($\sigma_{w0} = 181$ MPa) of an annealed 0.13% carbon steel. $H_V = 120$, crack length, $l_0 \cong 100$ μm .

fact suggests that the fatigue limit is controlled by the average strength properties of the microstructure, and not directly by the grain size itself.¹ The relationship between non-propagating cracks of this kind and microstructures has been examined in detail [26–28]. The abrupt change (knee) at point B on the $S-N$ curve in Fig. 1.1 is caused by the existence of non-propagating cracks, such as those shown in Figs. 1.2 and 1.3. If the fatigue limit were correlated with crack initiation, this would imply that an $S-N$ curve would not show a clear knee point (point B). This is because crack initiation would be determined by the condition of some individual grain out of the huge number of grains contained within one specimen. Accordingly, the crack initiation limit for individual grains varies almost continuously with the variation of test stress.

Thus, if the condition for crack initiation determined a fatigue limit, then the $S-N$ curve would be expected to decrease continuously and gradually from a high stress level to a low stress level up to numbers of cycles larger than 10^7 . However, what we actually observe in fatigue tests on low and medium carbon steels is a clear and sudden change in an $S-N$ curve, and we can determine a fatigue limit to within a narrow band of ± 5 MPa.

¹ The author does not insist that grain size has no influence on fatigue limits. Rather, it should be said that grain size has an indirect influence on fatigue limits. Regarding this issue, studies on the relationship between non-propagating cracks and grain size by Tamura et al. [24], and by Kawachi et al. [25], provide further information on the point. Furthermore, when we discuss this issue, it should be taken into consideration that fatigue limits have a strong correlation with Vickers hardness (one of the most important average mechanical properties of a microstructure).

Summarising the available experimental data, and the facts derived from their analysis, the correct definition of a fatigue limit is 'a fatigue limit is the threshold stress for crack propagation and not the critical stress for crack initiation' [23–27]. The non-propagating behaviour of fatigue cracks (including short cracks) is really a very strange phenomenon, which had not been correctly interpreted for a long time in the history of metal fatigue. There have been many theories to explain this strange phenomenon. A detailed discussion is given in a later chapter. In this chapter, the reader must note that the phenomenon of non-propagation of cracks, after crack initiation, is not just an experimental fact which we cannot deny, but is also a very important issue related to the fatigue behaviour of small defects and inclusions.

Thus the fatigue limit, σ_{w0} , for carbon steels is the threshold stress for non-propagation of cracks. The critical stress, σ_{wi} , for crack initiation is 2–3% lower than σ_{w0} , and no slip bands can be observed at a stress 5–10% lower than σ_{w0} (these values naturally depend on the materials). The results of fatigue tests, using many specimens, at a stress level close to σ_{w0} show that the maximum size of non-propagating cracks at the stress level σ_{w0} is always larger than one grain size, though of course there is some scatter in size.

At a stress 2–3% higher than σ_{w0} , these maximum size cracks exceed the threshold condition for non-propagation, and all specimens fail. On the other hand, at a stress 2–3% lower than σ_{w0} , not even crack initiation is detected. Therefore, it must be noted that the condition for a fatigue limit based on the condition of non-propagation of a crack is satisfied only within a narrow band of stress level. In other words, individual specimens tested at the fatigue limit stress have non-propagating cracks with different maximum sizes. At the same time, each specimen contains many grains which show different states such as crack initiation, slip bands, and no change from the initial condition. There are big differences from location to location on the surface of a specimen, even though the stress level is the same. Changing the stress amplitude on these specimens by ± 2 –3% results in more substantial changes, such as specimen failure or no crack initiation.

1.1.2 Nonferrous Metals

Nonferrous metals such as copper, aluminum alloys, and brass do not have a clearly defined fatigue limit. Fig. 1.4 shows examples of S – N curves for these metals. Once a crack initiates in these metals it is thought that the crack continues to grow gradually, even under very low stress, and the crack eventually leads to specimen failure. However, there are some exceptions which do show non-propagation of cracks on the surface of unnotched specimens [29], as do steels. Fig. 1.5a shows the crack initiation and growth behaviour of 70/30 brass, which does not show a coaxing effect. On the other hand, Fig. 1.5b shows crack initiation and growth for 2017-T4 aluminum alloy, which shows a distinct coaxing effect, even though the material is nonferrous. Determination of fatigue life, N_f , is time consuming, so the stress for a life $N_f = 10^7$ or 10^8 cycles is conventionally defined as the fatigue limit. Thus, at present it is difficult to reach a definite conclusion on the existence of fatigue limits for unnotched specimens of nonferrous metals. On the other hand, it has been reported that sharply notched specimens of nonferrous metals do have clearly defined fatigue limits [29,30].

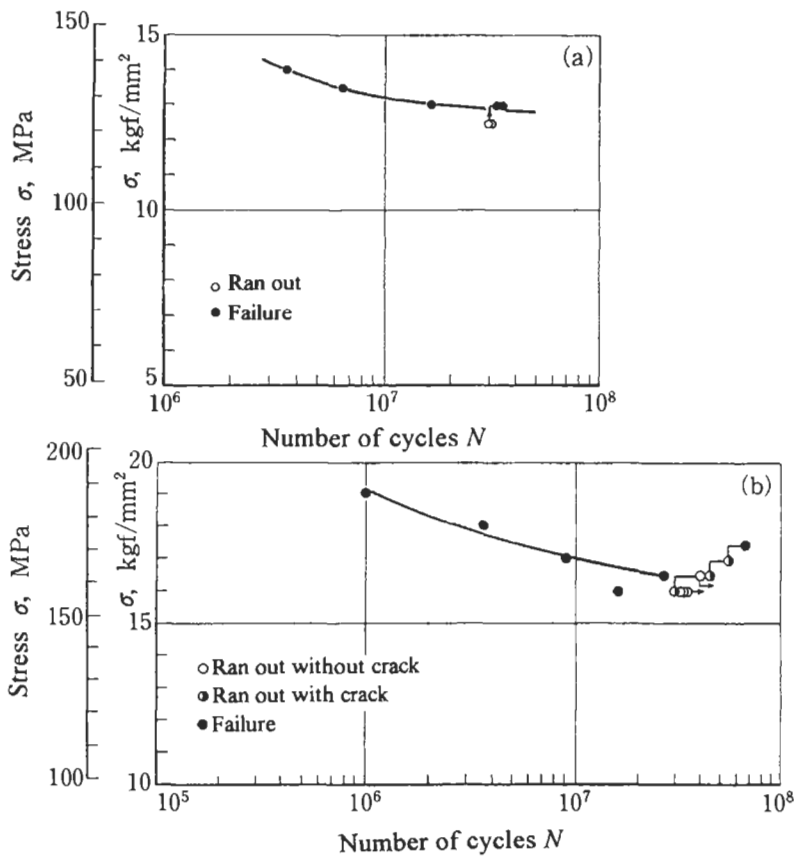


Figure 1.4 (a) S - N curve for 70/30 brass. (b) S - N curve for 2017-T4 aluminum alloy and investigation of coaxing effect.

Therefore, the mechanism of the fatigue limit for notched specimens may be used in the understanding of the fatigue limit behaviour of unnotched specimens of nonferrous metals.

1.2 Relationship between Static Strength and Fatigue Strength

The relationships between fatigue strength and yield stress, σ_Y , ultimate tensile strength, σ_U , and hardness, H_B or H_V , have been of interest for a long time in the history of metal fatigue. Because fatigue crack initiation is mainly caused by slip within grains, the yield stress, which has a relationship with the start of slip in grains, has been thought to have the strongest correlation with the fatigue limit. However, this is not correct, and better correlations have been obtained among ultimate tensile strength, σ_U , hardness (H_B or H_V), and fatigue limits [31–34]. The following empirical equations have been

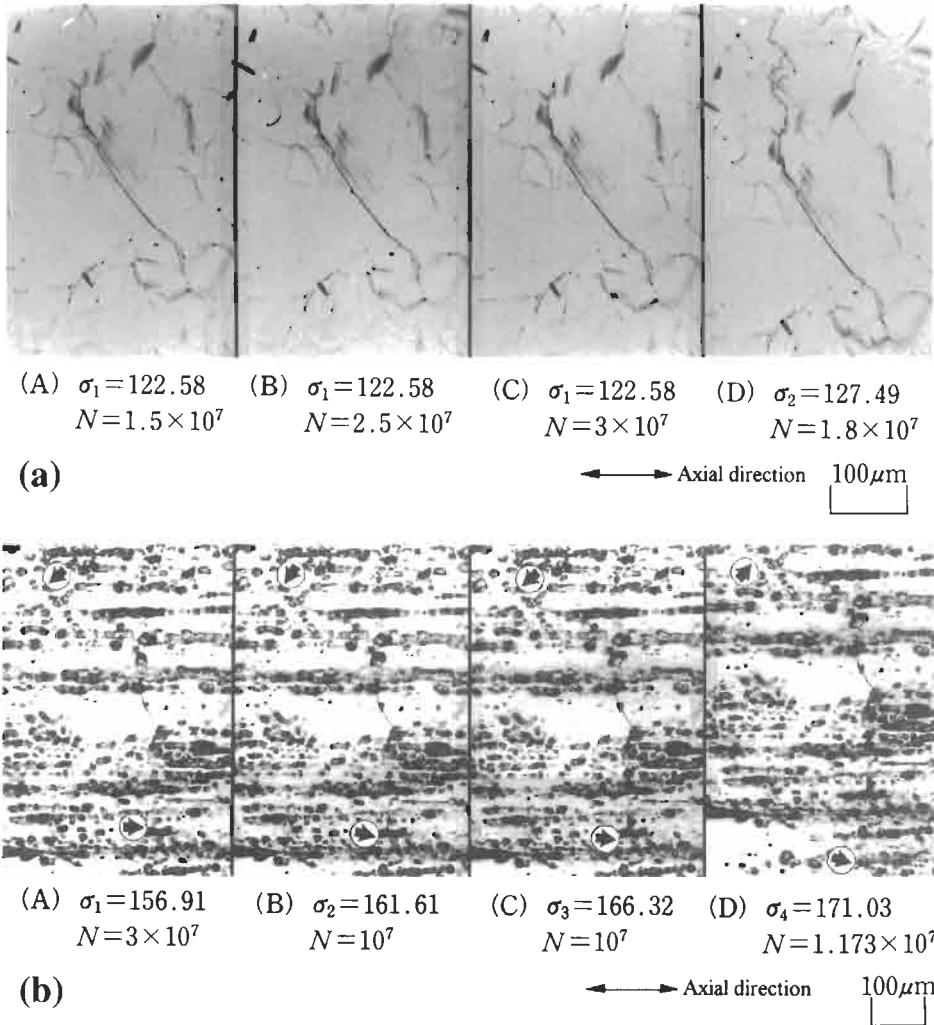


Figure 1.5 Process of fatigue crack initiation in nonferrous metallic materials. (a) Crack initiation and propagation in 70/30 brass. A crack initiated at the stress σ_1 needs $N = 10^8$ or 10^9 additional stress cycles to cause failure. However, at the slightly increased stress level, σ_2 , crack growth starts immediately, and leads to specimen failure without coaxing effects. (b) Non-propagating crack in 2017-T4 aluminum alloy. A crack initiated at the stress σ_1 , and then cycled for an additional $N = 10^7$ cycles at an increased stress, either does not grow, or tends to stop propagating after a small amount of growth. This is a very rare example of a coaxing effect in nonferrous materials.

used previously:

$$\sigma_{w0} \cong 0.5\sigma_U \quad (1.1)$$

$$\sigma_{w0} \cong 1.6H_V \pm 0.1H_V \quad (1.2)$$

(σ_{w0} in MPa; H_V , Vickers hardness, in kgf/mm^2)

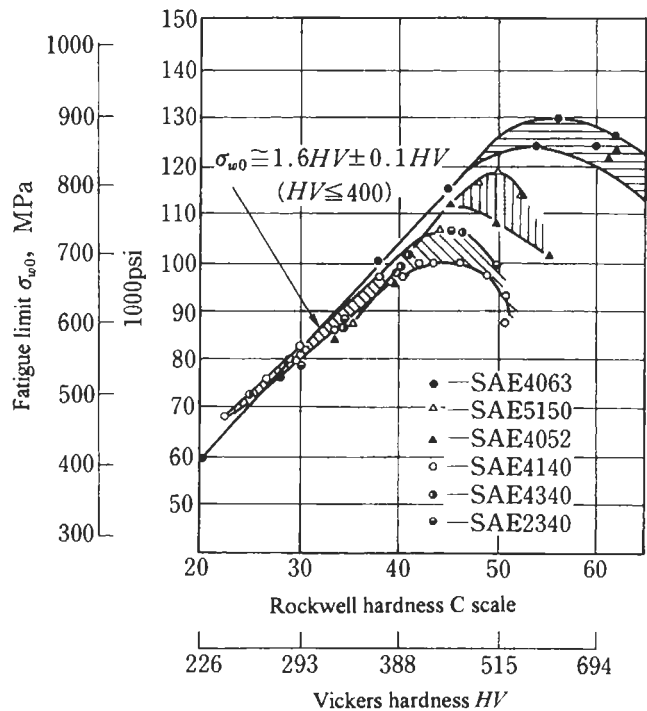


Figure 1.6 Relationship between hardness and fatigue limit (Garwood et al. [31]).

Eq. 1.2 is valid for $H_V \leq 400$, but unconservative (overestimation) for $H_V > 400$. Since there is little difference between H_V and H_B values when these are less than 450 [35] H_B may substituted for H_V , without significant loss of accuracy, in practical evaluations.

Aoyama et al. [33] reported a more detailed investigation on the relationship between H_B or H_V and σ_U , and proposed an empirical formula more precise than Eq. 1.2. Their study also indicates that their empirical equation is valid for $H_B < 400$. Fig. 1.6 [31] and Fig. 1.7 [34] show relationships between σ_{w0} and H_V ; σ_{w0} increases with H_V for $H_V \leq 400$. However, for $H_V > 400$ σ_{w0} has no definite correlation with H_V , and there is a large amount of scatter, which is material-dependent. The difficulty of predicting the fatigue strength of hard steels from their static strength has been recognised since Garwood et al. [31] reported the relationship between σ_{w0} and H_V for a wide range of hardness values (Fig. 1.6). One objective of this book is to give a solution to this problem. This will be described after Chapter 3. The fact that σ_{w0} can be approximated by Eq. 1.2 for steels with $H_V \leq 400$, and that this approximation does not depend on microstructure such as ferrite, pearlite, or martensite [36], or on steel type, means that a material property showing the average resistance to plastic deformation determines the fatigue limit. This is a simple but very important conclusion for practical applications. It means that changing microstructures by metallurgical processes, or by various heat treatments, contributes to fatigue strength only through the hardness [36].

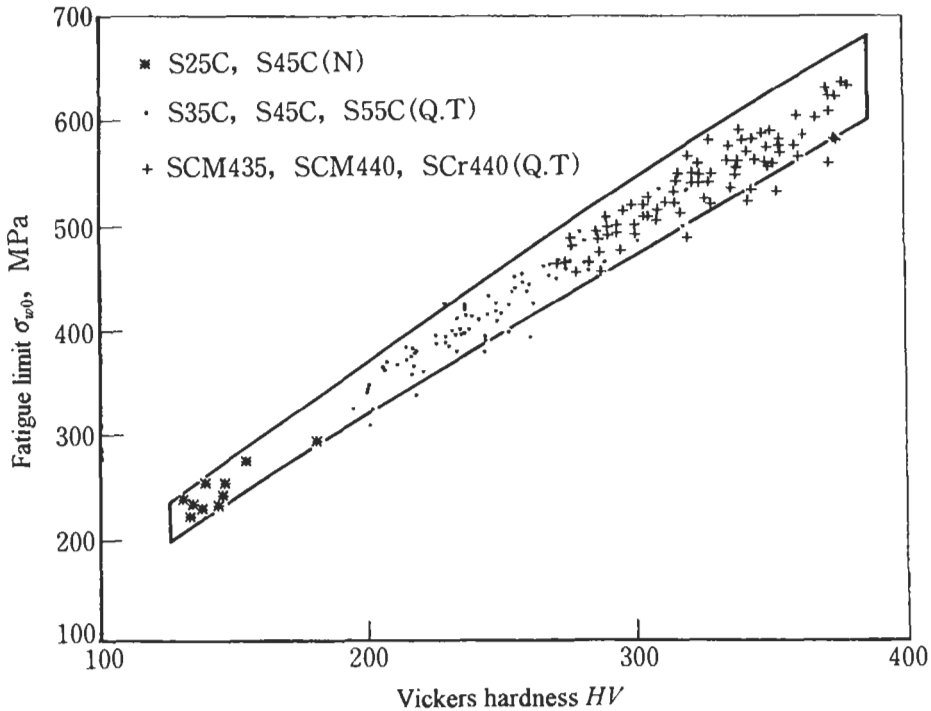


Figure 1.7 Relationship between hardness and fatigue limit (Nishijima [34]) (N = normalised; Q.T = quenched and tempered).

On the other hand, it had been said that the accuracy of Eq. 1.2 for nonferrous metals is not as good as for steels, although there have been no detailed studies on this problem. The accuracy of Eq. 1.2 for 2017S-T4 aluminum alloy [29] and 70/30 brass is quite good when the fatigue limit is defined by $N_f = 10^7$ (the error is less than $\pm 12\%$). It can at least be concluded that the correlation of σ_{w0} with H_V for nonferrous metals is much better than with yield stress. Thus, the hardness of microstructures may be considered the crucial factor which controls fatigue strength for nonferrous metals, as well as for steels.

1.3 References

1. E.E. Laufer and W.N. Roberts: Dislocation Structures in Fatigued Copper Single Crystals, *Philos. Mag.*, **10** (1964), 883–885.
2. M. Klesnil and P.J. Lukas: Dislocation Arrangement in the Surface Layer of Iron Grains during Cyclic Loading, *J. Iron Steel Inst.*, **203** (1965), 1043–1048.
3. C.E. Felner: A debris mechanism of cyclic strain hardening for F.C.C. metals, *Philos. Mag. Ser. A*, **12** (1965), 1229–1248.
4. P. Neumann: Bildung und Ausbreitung von Rissen bei Wechselverformung, *Z. Metalkd.*, **58** (1967), 780–789.
5. J.M. Finney and C. Laird: Strain Localization in Cyclic Deformation of Copper Single Crystals, *Philos.*

- Mag., **31** (1975), 339–366.
6. J.G. Antonopoulos, L.M. Brown and A.T. Winter: Vacancy Dipoles in Fatigued Copper, *Philos. Mag.*, **34** (1976), 549–563.
 7. C. Laird: Mechanisms and Theories of Fatigue, in *Fatigue and Microstructure*, 1978 ASM Material Science Seminar, St. Louis, ASTM, 1979, pp. 149–203.
 8. K. Katagiri, A. Omura, K. Koyanagi, J. Awatani, T. Shiraishi and H. Kaneshiro: Early Stage Crack Tip Dislocation Morphology in Fatigued Copper, *Metall. Trans. A*, **8** (1977), 1769–1773.
 9. H. Mughrabi, F. Acherman and K. Herz: Persistent Slipbands in Fatigued Face-Centered and Body Centered Cubic Metals, In: J.T. Fong (Ed): *Fatigue Mechanisms*, ASTM STP 675, Philadelphia, PA, 1979, pp. 69–105.
 10. H. Mughrabi, R. Wang, K. Differt and U. Essmann: Fatigue Crack Initiation by Cyclic Slip Irreversibilities in High-Cycle Fatigue, In: J. Lankford, D.L. Davidson, W.L. Morris and R.P. Wei (Eds): *Fatigue Mechanisms*, ASTM STP 811, Philadelphia, PA, 1983, pp. 5–45.
 11. T. Tabata, H. Fujita, M. Hiraoka and K. Onishi: Dislocation Behaviour and the Formation of Persistent Slip Bands in Fatigued Copper Single Crystals Observed in High-Voltage Electron Microscopy, *Philos. Mag. Ser. A*, **47** (1983), 841–857.
 12. P.J.E. Forsyth and C.A. Stubbington: The Slip-Band Extrusion Effect Observed in Some Aluminum Alloys Subjected to Cyclic Stresses, *J. Inst. Metals*, **83** (1954–1955) 395–401.
 13. A.H. Cottrell and D. Hull: Extrusion and Intrusion by Cyclic Slip in Copper, *Proc. R. Soc. London Ser. A*, **242** (1957), 211–213.
 14. D. Kuhlmann-Wilsdorf and C. Laird: Dislocation Behavior in Fatigue, *Mater. Sci. Eng.*, **27** (1977), 137–156.
 15. K. Tanaka and T. Mura: A Dislocation Model for Fatigue Crack Initiation, *Trans., ASME, J. Appl. Mech.*, **103** (1981), 97–103.
 16. U. Essmann, U. Gosele and H. Mughrabi: A Model of Extrusions in Fatigued Metals: I. Point-Defect Production and the Growth of Extrusions, *Philos. Mag. Ser. A*, **44** (1981), 405–428.
 17. K. Tanaka and T. Mura: A Theory of Fatigue Crack Initiation at Inclusions, *Metall. Trans. A*, **13** (1982), 117–123.
 18. H. Kaneshiro, K. Katagiri, H. Mori, C. Makabe and T. Yafuso: Dislocation Structures in the Strain Localized Region in Fatigued 85/15 Brass, *Metall. Trans. A*, **19** (1988), 1257–1262.
 19. Y. Murakami, T. Mura and M. Kobayashi: Change of Dislocation Structures and Macroscopic Conditions from Initial State to Fatigue Crack Nucleation, *ASTM STP 924*, **1** (1998) 39–63.
 20. J.A. Ewing and J.W.C. Humfrey: The Fracture of Metals under Repeated Alternations of Stress, *Philos. Trans. R. Soc.*, **200** (1903), 241–253.
 21. H.J. Gough, *Fatigue of Metals*, Scott Greenwood, London, 1924.
 22. T. Isibasi: *Prevention of Fatigue and Fracture of Metals* (in Japanese), Yokendo Ltd., Tokyo, 1967.
 23. For example, Watanabe and Kumada: Preliminary Proc. JSME, No. **37** (1956) 67–70; N.J. Wadsworth: *Philos. Mag.*, **6**(8) (1961) 397–401; H. Ohkubo and T. Sakai: *Trans. Jpn. Soc. Mech. Eng.*, **33**(248) (1967) 495–502; H. Nisitani and Y. Murakami: *Trans. Jpn. Soc. Mech. Eng.*, **35**(275) (1969) 1389–1396; H. Nisitani and S. Nishida: *Trans. Jpn. Soc. Mech. Eng.*, **35**(280) (1969) 2310–2315; T. Kunio, M. Shimizu and K. Yamada: *Proc. 2nd Int. Cont. Frac.*, Chapman and Hall, London, 1969, p. 630; H. Kobayashi and H. Nakazawa: *J. Soc. Mater. Sci., Jpn.*, **21**(223) (1972) 267; H. Nisitani and K. Takao: *Trans. Jpn. Soc. Mech. Eng.*, **40**(340) (1974) 3254–3266; Y. Murakami, S. Fukuda and T. Endo: *Trans. Jpn. Soc. Mech. Eng.*, **44**(388) (1978) 4003–4013.
 24. M. Tamura, K. Yamada, M. Shimizu and T. Kuio: On the Relationship between Threshold Behavior of Micro-Crack and Endurance Limit of Pearlitic-Ferritic Steel, *Trans. Jpn. Soc. Mech. Eng. A*, **49**(447) (1983), 1378–1387.
 25. S. Kawachi, K. Yamada and T. Kunio: Characteristics of Small Crack Propagation near the Endurance Limit of Low Carbon Steel, *Trans. Jpn. Soc. Mech. Eng. A*, **55**(511) (1989), 424–429.
 26. T. Kunio, M. Shimizu and K. Yamada: Microstructural Aspects of the Fatigue Behavior of Rapid Heat-Treated Steel, *Proc. 2nd Int. Conf. Fract.*, Chapman and Hall, London, 1969, pp. 630–642.
 27. T. Kunio and K. Yamada: Microstructural Aspects of the Threshold Condition for the Non-Propagating Fatigue Cracks in Martensitic and Ferritic Steel, *ASTM STP*, **675** (1979), 342–370.

28. K. Tokaji, T. Ogawa and S. Osako: The Growth Behaviour of Microstructurally Small Fatigue Cracks in a Ferritic-Pearlitic Steel, *Trans. Jpn. Soc. Mech. Eng. A*, **54(501)** (1988), 884–891.
29. Y. Murakami, Y. Tazunoki and T. Endo: Existence of Coaxing Effect and Effect of Small Artificial Holes of 40–200 μm Diameter on Fatigue Strength in 2017S-T4 Al Alloy and 7 : 3 Brass, *Trans. Jpn. Soc. Mech. Eng. A*, **47(424)** (1981) 1293–1300; *ibid*, *Metall. Trans. A*, **15** (1984) 2029–2038.
30. H. Nisitani and A. Yamaguchi: Coaxing Effect of Specimens with a Hole and Behavior of Their Cracks, *Trans. Jpn. Soc. Mech. Eng. A*, **45(391)** (1979), 260–266.
31. M.F. Garwood, H.H. Zurburg and M.A. Erickson: Correlation of Laboratory Tests and Service Performance, Interpretation of Tests and Correlation with Service, ASM, Philadelphia, PA, 1951, pp. 1–77.
32. JoDean Morrow, G.R. Halford and J.F. Millan: Optimum Hardness for Maximum Fatigue Strength of Steel, *Proc. 1st Int. Conf. Fract.*, Sendai, 2, 1966, pp. 1611–1635.
33. S. Aoyama: Strength of Hardened and Tempered Steels for Machine Structural Use (Part 1), *Review of TOYOTA RD CENTER*, **5(2)** (1968) 1–30; (Part 2), *ibid*, **5(4)** (1968) 1–35.
34. S. Nishijima: Statistical Analysis of Fatigue Test Data, *J. Soc. Mater. Sci., Jpn.*, **29(316)** (1980), 24–29.
35. T. Isibasi: Strength of Metals for Design Engineers (in Japanese), Yokendo Ltd., Tokyo, 1965, 16 pp.
36. G. Chalant and B.M. Suyitno: Effects of Microstructure on Low and High Cycle Fatigue Behaviour of a Micro-Alloyed Steel, *Proc. 6th Int. Conf. Mech. Behav. Mater.*, Kyoto, VI, 1991, pp. 511–516.

Chapter 2

Stress Concentration

The stress at the edge of a hole, or at a notch root, has a higher value than the remote stress. This phenomenon is called 'stress concentration'. Fatigue cracks mostly initiate at the sites of stress concentrations. Once a crack initiates, we have to consider the stress concentration of the crack. However, it must be noted that the characteristics of stress concentration at a crack tip are quite different from those at holes and notches. An understanding of the basic features of stress concentration is needed to understand the main topic of this book, which develops a new idea for the quantitative evaluation of the effect on fatigue strength of small defects, small cracks, and nonmetallic inclusions.

2.1 Stress Concentrations at Holes and Notches

Fig. 2.1 shows a circular hole in an infinite plate under a uniaxial remote tensile stress, σ_{x0} , in the x -direction. The tangential normal stress, σ_θ , at points A and C is three

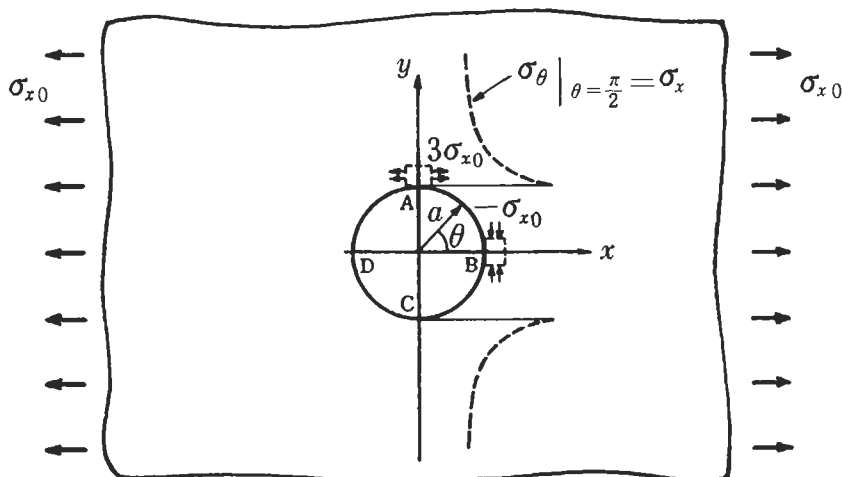


Figure 2.1 Stress concentrations at a circular hole ($\sigma_{xA} = 3\sigma_{x0}$, $\sigma_{yB} = -\sigma_{x0}$).

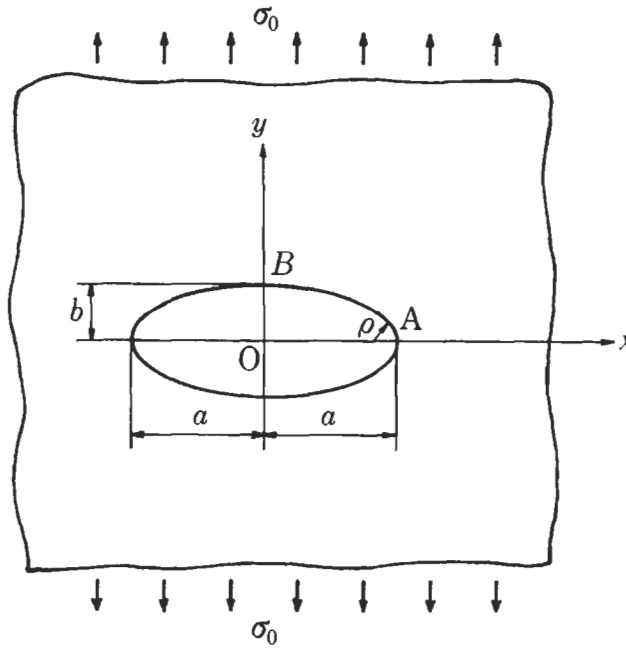


Figure 2.2 Stress concentrations at an elliptical hole ($\sigma_{yA} = (1 + 2a/b)\sigma_0$, $\sigma_{xB} = -\sigma_0$).

times larger than σ_{x0} , that is $\sigma_\theta = 3\sigma_{x0}$. We write the stress concentration factor, K_t , as:

$$K_t = 3 \quad (2.1)$$

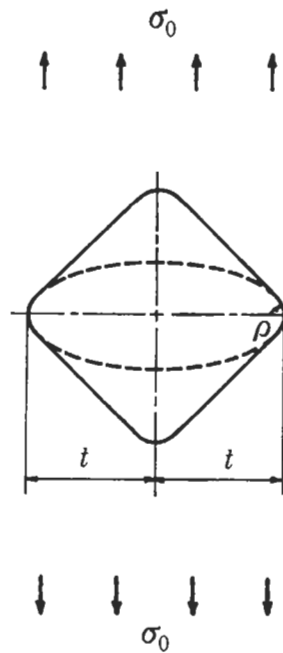
The value of σ_θ at points B and D is $\sigma_\theta = -\sigma_{x0}$. The importance of this negative value is often overlooked. This is because σ_θ is compressive and arithmetically smaller than at points A and C. However, the value $\sigma_\theta = -\sigma_{x0}$ at B and D is important for many practical applications [1]. For example, if in addition to the stress σ_{x0} applied to the plate shown in Fig. 2.1, we also have a remote stress, σ_{y0} , in the y-direction, then the stress σ_θ becomes $3\sigma_{x0} - \sigma_{y0}$ at points A and C, and $3\sigma_{y0} - \sigma_{x0}$ at points B and D. Thus, the combination of the magnitudes σ_{x0} and σ_{y0} changes both the maximum stress at the hole edge and its location.

Fig. 2.2 shows an elliptical hole in a wide plate under uniaxial tension in the y-direction. In this case the stress concentration factor, K_t , is:

$$K_t = 1 + \frac{2a}{b} \quad (2.2)$$

The stress at point B is the same as for a circular hole, that is $\sigma_{xB} = -\sigma_0$. Therefore, if the plate is also subject to a remote stress, σ_{x0} , in the x-direction then the stress concentrations for a biaxial stress condition can be calculated with the aid of Eq. 2.2.

It is possible to extend the application of Eq. 2.2 to the estimation of stress concentration factors for holes and notches, such as those shown in Figs. 2.3 and 2.4. This extended application is called 'the concept of equivalent ellipse' [2]. The



$$K_t \cong 1 + 2\sqrt{\frac{t}{\rho}}$$

Figure 2.3 Approximation of the stress concentration at a hole by the equivalent ellipse concept.

approximate equation for K_t is written as:

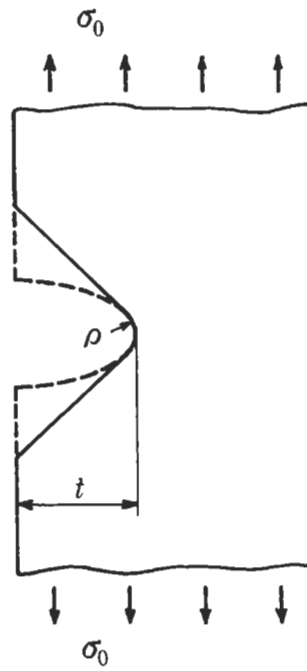
$$K_t \cong 1 + 2\sqrt{\frac{t}{\rho}} \quad (2.3)$$

where t is the half length of the hole (Fig. 2.3), or the depth of the notch (Fig. 2.4), and ρ is the notch root radius, or the hole edge radius. When we have a spherical cavity in an infinite solid under uniaxial tension in the z -direction (Fig. 2.5) the maximum stress, σ_z , is in the z -direction at the equator. The value of K_t in this case is [3]:

$$K_t = \frac{27 - 15\nu}{2(7 - 5\nu)} \quad (2.4)$$

where ν is Poisson's ratio.

When we have a spherical inclusion, as shown in Fig. 2.6, the value and location of the maximum stress depend on the values both of Young's modulus E and of Poisson's ratio ν , for the inclusion and for the matrix. There have been many studies on stress concentrations, and solutions for various notches under various boundary conditions have been collected in handbooks [4–7].



$$K_t \cong 1 + 2 \sqrt{\frac{t}{\rho}}$$

Figure 2.4 Approximation of the stress concentration at a notch by the equivalent ellipse concept.

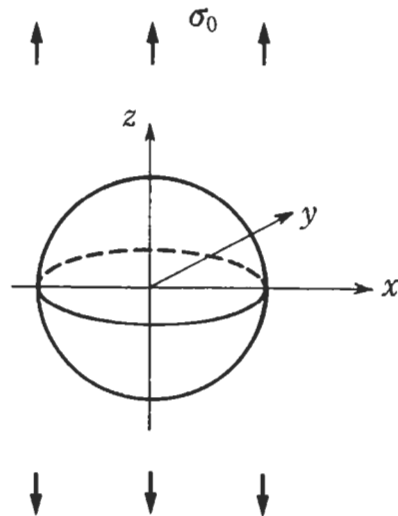


Figure 2.5 Stress concentration at a spherical cavity.

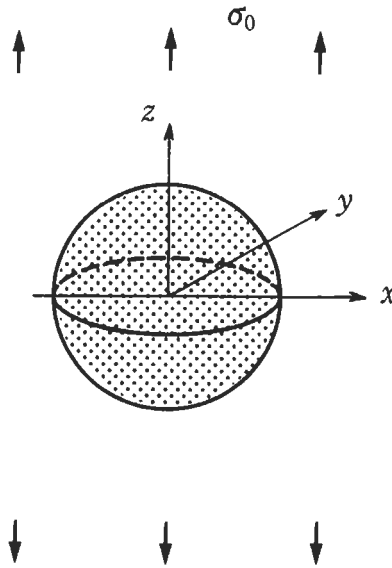


Figure 2.6 Stress concentration at a spherical inclusion.

Notches having a geometrically similar shape have the same value of stress concentration factor regardless of the difference in size. Most fatigue cracks initiate at the sites of stress concentrations. However, it is known that the maximum stress at a stress concentration is not the only factor controlling the crack initiation condition. This phenomenon has been studied by many researchers as the problem of the 'fatigue notch effect' (Chapter 3).

2.2 Stress Concentration at a Crack

Unlike holes and notches, a crack has a sharp tip whose root radius ρ is zero. The definition of a crack, in elastic analysis, is the limiting shape of an extremely slender ellipse. As an extremely slender elliptical hole is reduced towards the limiting shape, then the stress concentration ahead of the elliptical hole, that is at the tip of the crack, becomes unbounded regardless of the length of the crack. Therefore, it is not appropriate to compare the maximum stresses at the tips of various cracks as a measure of their stress concentration. The idea needed to solve the difficulty of treating unbounded stresses at crack tips was proposed by G.R. Irwin at the end of the 1950s [8,9]. From the theory of his idea, the stresses in the vicinity of a crack tip have a singularity of $r^{-1/2}$, where r is the distance from the crack tip [10]. The stress intensity factor is defined as the parameter describing the intensity of the singular stress field in the vicinity of a crack tip [8,9].

As shown in Fig. 2.7, when we have a crack of length $2a$ in the x -direction in a wide plate, which is under a uniaxial tensile stress, σ_0 , in the y -direction, the stress intensity

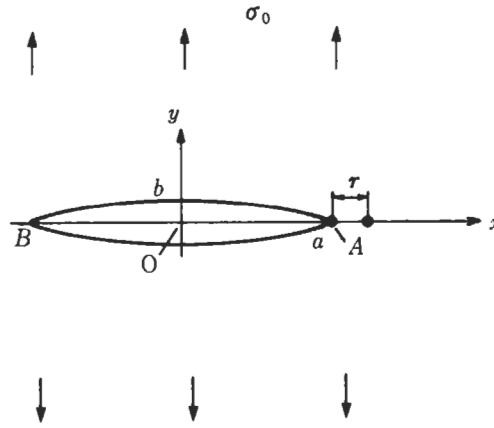


Figure 2.7 Two dimensional crack, length $2a$.

factor, which describes the singular stress distribution in the vicinity of the crack tip, is written as:

$$K_I = \sigma_0 \sqrt{\pi a} \quad (2.5)$$

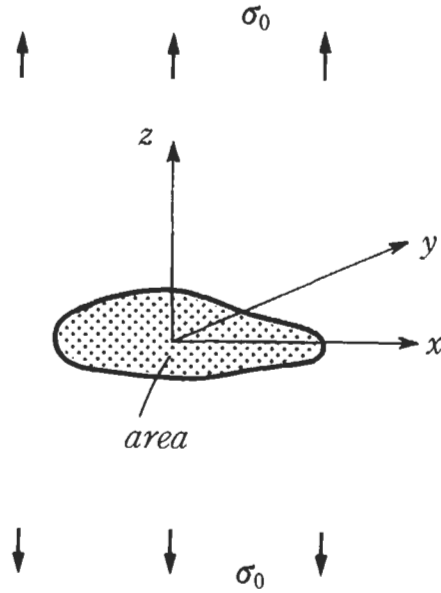
Using K_I , the normal stress, σ_y , near the crack tip on the x -axis can be expressed approximately by:

$$\sigma_y = \frac{K_I}{\sqrt{2\pi r}} \quad (2.6)$$

The crack shown in Fig. 2.7 is open in the direction of the tensile stress, σ_0 . This is called an opening mode, or Mode I, crack, and the associated stress intensity factor is K_I . When the crack shown in Fig. 2.7 is under a remote shear stress, τ_{xy0} , it is an in-plane shear, or Mode II, crack, and the stress intensity factor is K_{II} . Similarly for out-of-plane shear it is an out-of-plane shear, or Mode III, crack. Once a crack emanates from a stress concentration site, the problem must be treated from the viewpoint of the mechanics of the crack, rather than as a problem of stress concentration at a hole or a notch. Therefore, stress intensity factors for various crack geometries under various boundary conditions are essential for strength evaluations. Nowadays, many stress intensity factor solutions have been collected in handbooks [11]. In this book, the equations below are used frequently. They were proposed in order to approximate the maximum stress intensity factor, $K_{I_{max}}$, for three-dimensional cracks of indefinite shape [12,13].

2.2.1 'area' as a New Geometrical Parameter

Fig. 2.8 shows an internal crack on the x - y plane of an infinite solid which is under a uniform remote tensile stress, σ_0 , in the z -direction. If the area of this crack is denoted by 'area', then the maximum value, $K_{I_{max}}$, of the stress intensity factor along its crack



$$K_{\perp} \cong 0.5 \sigma_0 \sqrt{\pi \sqrt{\text{area}}}$$

Figure 2.8 Stress intensity factor for an arbitrarily shaped 3D internal crack ('area' = area of crack).

front is given approximately by [12]:

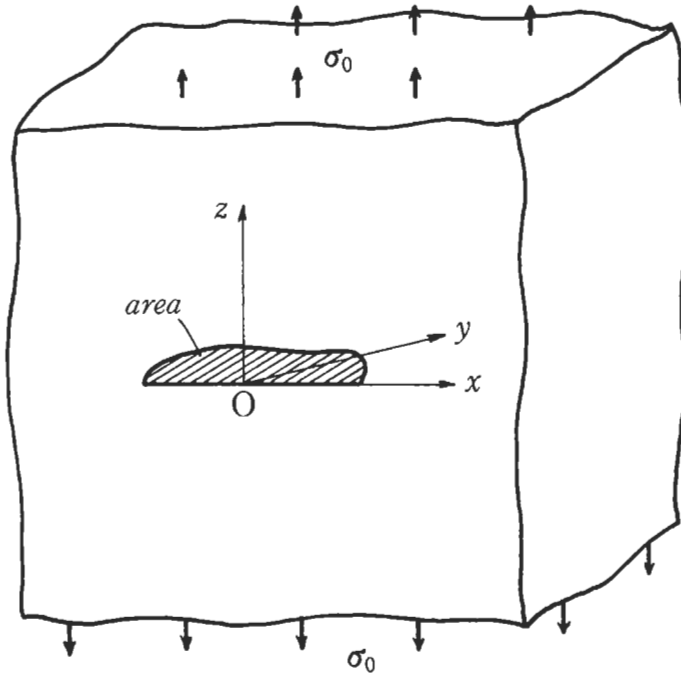
$$K_{I_{\max}} = 0.5 \sigma_0 \sqrt{\pi \sqrt{\text{area}}} \quad (2.7)$$

Similarly, for a surface crack as shown in Fig. 2.9, $K_{I_{\max}}$ is given approximately by:

$$K_{I_{\max}} = 0.65 \sigma_0 \sqrt{\pi \sqrt{\text{area}}} \quad (2.8)$$

2.2.2 Effective 'area' for Particular Cases

As shown in Fig. 2.10, the actual area is not used for irregularly shaped cracks. An effective area is estimated by considering a smooth contour which envelopes the original irregular shape. This effective area is substituted as 'area' into Eqs. 2.7 and 2.8 [14]. The effective area, to be substituted in Eqs. 2.7 and 2.8, is defined differently for certain crack types. For very slender cracks, as shown in Fig. 2.11, the effective area is evaluated by truncating the slender shape to a limiting length. This is because the stress intensity factor tends to a constant value as the crack length increases, even though the area increases without limit. Eq. 2.9 is used to estimate effective area for the very shallow crack ($l/c \geq 10$) shown in Fig. 2.11a, and for the very deep crack ($l/c \geq 5$)



$$K_I \cong 0.65 \sigma_0 \sqrt{\pi \sqrt{\text{area}}}$$

Figure 2.9 Stress intensity factor for an arbitrarily shaped 3D surface crack ('area' = area of crack).



Figure 2.10 Irregularly shaped crack, and estimation method for effective area.

shown in Fig. 2.11b [14].

$$\sqrt{\text{area}} = \sqrt{10}c \quad (2.9)$$

This equation estimates the size of a 2D crack as an equivalent 3D crack, and is useful, in conjunction with Eqs. 2.7 and 2.8, for estimating stress intensity factors for a very shallow circumferential crack, and for surface roughness.

Fig. 2.12 shows a crack inclined to a free surface and to the x - y plane. It is under a remote tension, σ_0 , in the z -direction. The projected area, 'area_p', obtained by projecting

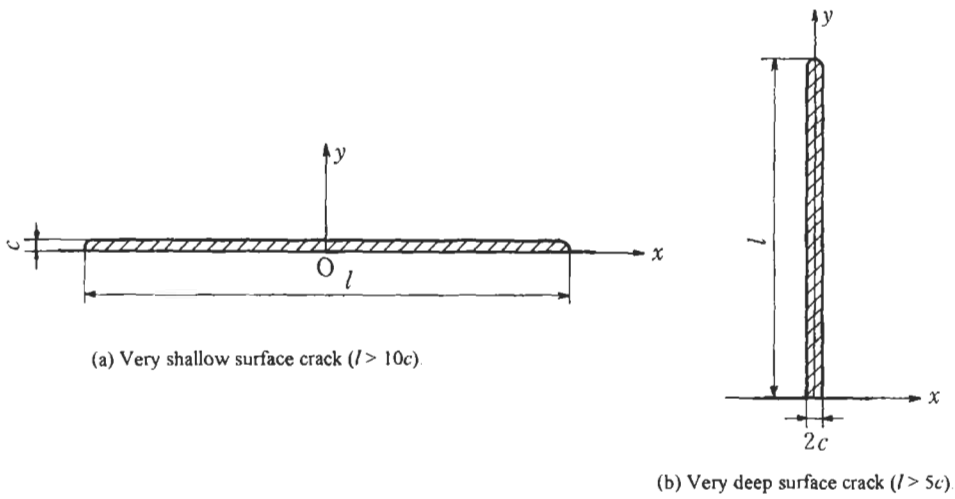


Figure 2.11 (a) Very shallow surface crack ($l > 10c$). (b) Very deep surface crack ($l > 5c$).

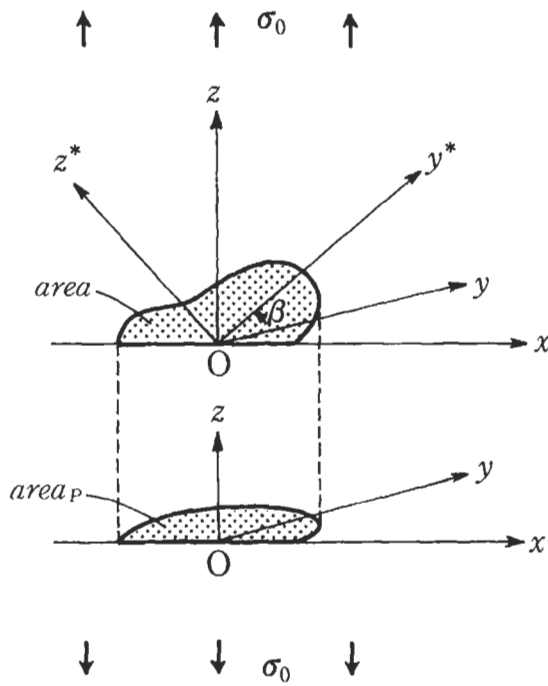
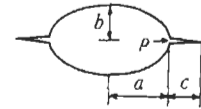


Figure 2.12 Equivalent crack area ('area_p') for an oblique surface crack of arbitrary shape.

the original inclined crack onto the x - y plane, is substituted for 'area' in Eqs. 2.7 and 2.8 [15].

Table 2.1 Stress intensity factors K_I for cracks emanating from an elliptical hole
 The values in the table are dimensionless stress intensity factors F_I defined by: $K_I = F_I \sigma_\infty \sqrt{\pi(a+c)}$



$\frac{c}{a}$	b/a											
	0	0.01	0.02	0.05	0.1	0.2	0.3	0.5	1.0	2.0	4.0	∞
0.001	1.0000	0.9996	0.9911	0.8760	0.6259	0.3714	0.2658	0.1758	0.1061	0.0709	0.0532	0.0354
0.01	1.0000	1.0003	1.0010	1.0020	0.9799	0.8471	0.7040	0.5157	0.3277	0.2219	0.1671	0.1116
0.02	1.0000	1.0002	1.0008	1.0035	1.0030	0.9504	0.8541	0.6764	0.4517	0.3106	0.2349	0.1570
0.05	1.0000	1.0001	1.0004	1.0026	1.0080	1.0100	0.9856	0.8860	0.6637	0.4760	0.3644	0.2447
0.1	1.0000	1.0001	1.0003	1.0016	1.0058	1.0169	1.0214	0.9939	0.8401	0.6403	0.4998	0.3381
0.2	1.0000	1.0001	1.0002	1.0008	1.0033	1.0121	1.0229	1.0356	0.9851	0.8241	0.6671	0.4579
0.3	1.0000	1.0001	1.0002	1.0005	1.0021	1.0085	1.0177	1.0365	1.0358	0.9255	0.7739	0.5388
0.4	1.0000	1.0001	1.0001	1.0004	1.0015	1.0062	1.0135	1.0317	1.0536	0.9866	0.8494	0.5995
0.5	1.0000	1.0000	1.0001	1.0003	1.0011	1.0047	1.0105	1.0266	1.0581	1.0245	0.9052	0.6475
0.6	1.0000	1.0000	1.0001	1.0002	1.0008	1.0036	1.0084	1.0222	1.0570	1.0482	0.9477	0.6868
0.8	1.0000	1.0000	1.0001	1.0002	1.0005	1.0024	1.0056	1.0158	1.0494	1.0713	1.0062	0.7477
1.0	1.0000	1.0000	1.0000	1.0001	1.0004	1.0016	1.0039	1.0116	1.0409	1.0777	1.0424	0.7930
2.0	1.0000	1.0000	1.0000	1.0000	1.0001	1.0004	1.0011	1.0035	1.0161	1.0548	1.0927	0.9157
3.0	1.0000	1.0000	1.0000	1.0000	1.0000	1.0002	1.0004	1.0015	1.0076	1.0328	1.0826	0.9713
5.0	1.0000	1.0000	1.0000	1.0000	1.0000	1.0000	1.0001	1.0004	1.0025	1.0133	1.0506	1.0238

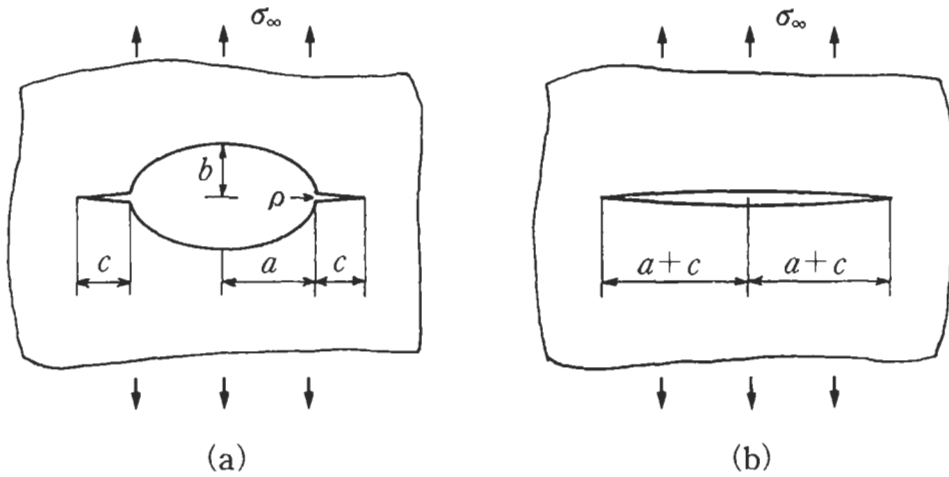


Figure 2.13 Cracks emanating from an elliptical hole and its equivalent crack.

2.2.3 Cracks at Stress Concentrations

Investigation of stress intensity factors for cracks emanating from holes and notches is important in the discussion of the influence of notches and small defects on fatigue strength. Fig. 2.13a shows cracks emanating from both ends of an elliptical hole. Table 2.1 shows stress intensity factors for such cracks, length c , emanating from an elliptical hole, major axis $2a$ [16]. The values of F_1 are dimensionless stress intensity factors in which K_1 is normalised by the stress intensity factor for a crack of length $2(a+c)$ (see Fig. 2.13b). F_1 is called either the dimensionless stress intensity factor or the correction factor for the stress intensity factor. If the overall crack length for cracks emanating from an elliptical hole, as shown in Fig. 2.13a, is defined as $2(a+c)$, and its value is equal to the crack length $2(a+c)$ shown in Fig. 2.13b, then the stress intensity factors for both problems are approximately equal. They are within $\pm 10\%$ error for $b/a < 1$ and $c/a > 0.2$ (Table 2.1). A similar approximation is also applicable to the relationship, shown in Fig. 2.14, between stress intensity factors for a crack emanating from an ellipsoidal cavity and those for a penny-shaped crack [11,17]. The error for the approximation is less than $\pm 10\%$ for $b/a < 1$ and $\lambda/a > 0.15$ as shown in Fig. 2.15 [17]. Because of the above evidence, a notch with a small crack at its tip may be regarded as a crack.

2.2.4 Interaction between Two Cracks

If a crack is close to another crack or near a cavity, or an internal crack is close to a free surface, then the interaction between the crack and another crack, a cavity, or a free surface causes an increase in the value of the stress intensity factor compared with that for the isolated crack case. Although this interaction effect cannot be expressed by a simple equation, it may be said that the interaction effect for 3D cracks is always

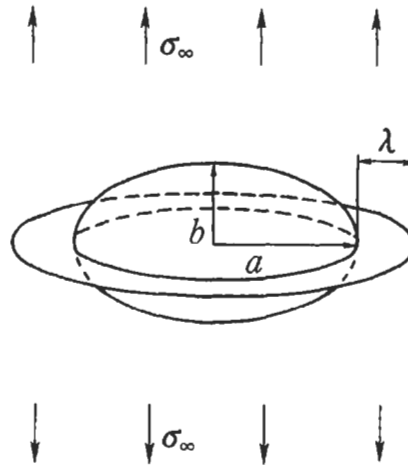


Figure 2.14 Crack emanating from an ellipsoidal cavity.

smaller than for 2D cracks. Two examples which are important in practice are explained below.

Fig. 2.16 shows two adjacent semi-circular cracks of different sizes. If a remote tensile stress is applied in the direction perpendicular to the crack surfaces then the maximum stress intensity factor, $K_{I\max}$, is at point A on the larger crack. Accurate numerical analysis [18] shows that the interaction effect between these two cracks can be estimated using the following rule of thumb. If there is enough space between the two cracks to insert an additional crack of the same size as the smaller crack, then $K_{I\max}$ is approximately equal to that for the larger crack in isolation. That is, the interaction effect is negligibly small.

However, if these cracks are closer to each other than in the case described above, then K_I at point A increases significantly, and cracks so near to each other are likely to coalesce by fatigue crack growth in a small number of cycles. *Therefore, in this case we must estimate the effective area as the sum of the areas of these two cracks, together with the space between these cracks, which is done by taking the area of the three semi-circles shown in Fig. 2.16.*

2.2.5 Interaction between a Crack and a Free Surface

Fig. 2.17 shows stress intensity factors for an internal circular crack close to a free surface. In this case $K_{I\max}$ is at the point closest to the free surface. However, if the ratio of the crack radius, a , to the depth to the centre of the crack, h , that is a/h , is less than 0.8, then K_I at point A may be regarded as approximately equal to the value for an isolated internal penny shaped crack [19]. That is, the interaction between the crack and the free surface is negligible. For $a/h = 0.8$, $K_{I\max}$ is only 11% larger than for a penny-shaped crack in an infinite solid, and only 8% larger than at the deepest point B. These numerical results are consistent with the observation that fish-eye patterns

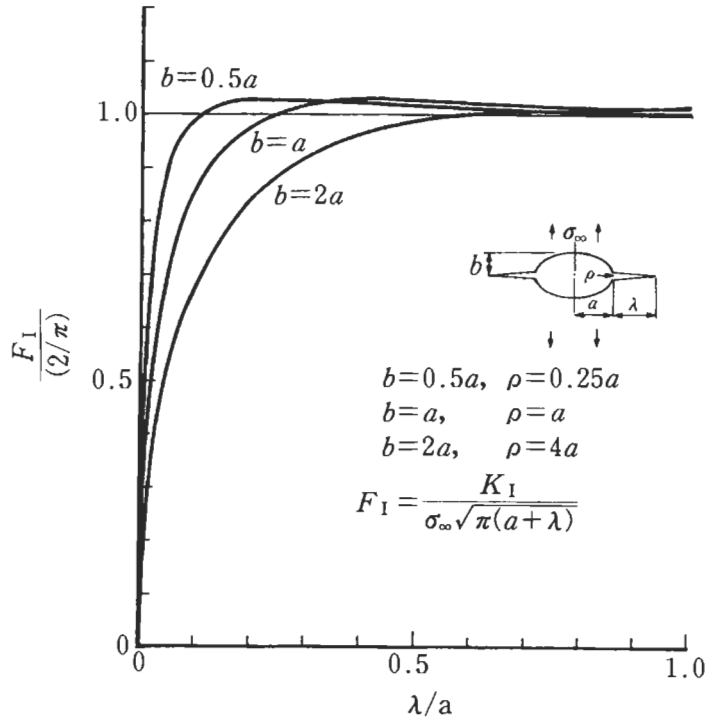


Figure 2.15 Crack emanating from an ellipsoidal cavity.

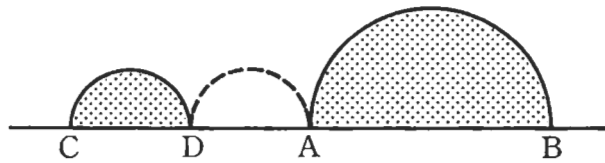


Figure 2.16 Interaction effect between adjacent cracks.

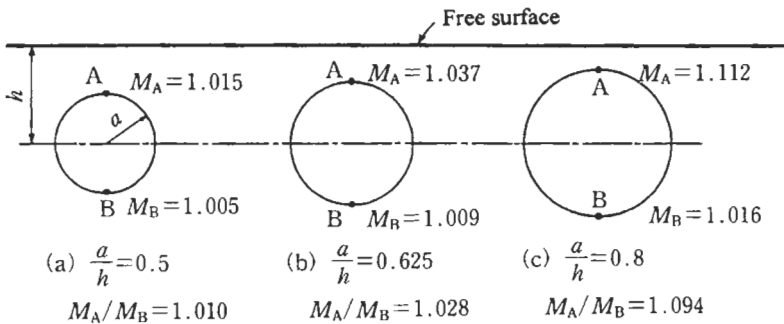


Figure 2.17 Stress intensity factors for a circular crack close to a free surface ($K_I = M(2/\pi)\sigma_0\sqrt{\pi a}$).

observed on fatigue fracture surfaces, and close to a free surface, are almost always of a completely circular shape (see the frontispiece photograph and Chapter 6).

2.3 References

1. Y. Murakami: Theory of Elasticity (in Japanese), 3rd ed., Yokendo Ltd., Tokyo, 1989.
2. F. Hirano: Research on Stress Concentration Factors for Two-dimensional Elastic Bodies (Report No. 2), *Trans. Jpn. Soc. Mech. Eng.*, **16**(55) (1950) 52–58; Research on Stress Concentration Factors for Two-dimensional Elastic Bodies (Report No. 3), *ibid*, **17**(61) (1951) 12–16.
3. S.P. Timoshenko and J.N. Goodier: Theory of Elasticity, 3rd ed., McGraw-Hill, New York, 1982.
4. R.E. Peterson: Stress Concentration Factors, John Wiley, New York, 1974.
5. H. Neuber: Kerbspannungslehre, Springer, Berlin, 1957.
6. M. Nishida: Stress Concentration (in Japanese), Morikita Shuppan Ltd., Tokyo, 1973.
7. Handbook of Mechanical Engineering, Vol. 4, Strength of Materials, Japanese Society of Mechanical Engineers, 1984.
8. G.R. Irwin: Analysis of Stresses and Strains Near the End of a Crack Traversing a Plate, *Trans. ASME, J. Appl. Mech.*, **24** (1957), 361–364.
9. G.R. Irwin: Fracture. In: *Handbuch der Physik VI*, Springer, Berlin, 1958, pp. 551–590.
10. I.N. Sneddon: The Distribution of Stress in the Neighbourhood of a Crack in an Elastic Solid. *Proc. R. Soc. London A*, **187** (1946), 229–260.
11. Y. Murakami, Editor-in-Chief: Stress Intensity Factors Handbook, Vols. 1 and 2, Pergamon Press, Oxford, 1987; Vol. 3, Soc. Materials Science, Japan and Pergamon Press, Kyoto, 1992; Vols. 4 and 5, Soc. Materials Science, Japan, Kyoto, 2001.
12. Y. Murakami, S. Kodama and S. Konuma: Quantitative Evaluation of Effects of Nonmetallic Inclusions on Fatigue Strength of High Strength Steel, *Trans. Jpn. Soc. Mech. Eng. A*, **54**(500) (1988), 688–696.
13. Y. Murakami and M. Ishida: Analysis of an Arbitrarily Shaped Surface Crack and Stress Field at Crack Front near Surface, *Trans. Jpn. Soc. Mech. Eng. A*, **51**(464) (1985), 1050–1056.
14. Y. Murakami and M. Endo: Effects of Hardness and Crack Geometry of ΔK_{th} of Small Cracks, *J. Soc. Mater. Sci., Jpn.*, **35**(395) (1986), 911–917.
15. Y. Murakami and M. Isida: Analysis of Mixed Mode Stress Intensity Factors for Arbitrarily Shaped Inclined Surface Cracks, *Trans. Jpn. Soc. Mech. Eng. A*, **50**(455) (1984) 1359–1366; also see Y. Murakami: Analysis of Stress Intensity Factors of Modes I, II and III for Inclined Surface Cracks of Arbitrary Shape, *Eng. Fract. Mech.*, **22**(1) (1985) 101–114.
16. H. Nisitani and M. Isida: Simple Procedure for Calculating K_I of Notch with a Crack of Arbitrary Size and Its Application to Non-propagating Fatigue Crack, *Proc. Joint JSME–SESA Conf. Experimental Mechanics*, 1982, Part I, pp. 150–155.
17. Y. Murakami and M. Uchida: Effects of Thermal Residual Stress and External Stress on Stress Intensity Factors for a Penny-Shaped Crack Emanating from an Ellipsoidal Nonmetallic Inclusion, *Proc. JSME Meeting*, No. 920-78, Vol. B, 1992, pp. 239–241.
18. Y. Murakami and S. Nemat-Nasser: Interacting Dissimilar Semi-Elliptical Surface Flaws under Tension and Bending, *Eng. Fract. Mech.*, **16**(3) (1982), 373–386.
19. H. Nisitani and Y. Murakami: Stress Intensity Factors of Semi-Elliptical Crack and Elliptical Crack (Tension), *Trans. Jpn. Soc. Mech. Eng.*, **40**(329) (1974), 31–40.

Chapter 3

Notch Effect and Size Effect

3.1 Notch Effect

3.1.1 Effect of Stress Distribution at Notch Roots

It has been said that 80–90% of fracture accidents are caused by fatigue. Investigation indicates that almost 100% of these fractures start from the sites of stress concentrations at structural discontinuities such as holes, notches, shoulders, cracks, defects, and scratches [1]. Stresses at structural discontinuities are higher than at other places on structures because of stress concentration, as described in Chapter 2. The phenomenon of decrease in fatigue strength, due to stress concentration, is called the ‘notch effect’. The fatigue notch effect has not always been understood correctly despite numerous studies over many years. The relationship between stress concentration, and the size and shape of holes and notches must be correctly understood for correct understanding of the notch effect phenomenon.

In the fatigue design of machine components and structures which are intended to be used for an indefinitely long life, that is in design for high cycle fatigue, the nominal stress is usually set to a much lower level than the yield stress. However, even in such cases the stress at stress concentrations sometimes exceeds the yield stress, and accordingly local plastic strain is induced. *Plastic strain in such cases is smaller than the elastic strain which preceded it, and materials are assumed to behave elastically.* Thus, the shape effect due to the shape and size of structures is evaluated in such cases using elastic stress analysis. In this chapter the effects of holes, notches and cracks which are relatively large compared with so-called small defects are described. The effects of small defects, of the order of grain size or inclusion size, are different from those due to large or deep notches, and are discussed separately in later chapters.

If the fatigue strength of components and structures containing notches were determined only by the maximum stress, σ_{\max} , fatigue design would be very simple. In fact, fatigue strength cannot be determined solely by σ_{\max} at stress concentrations [2].

Not only σ_{\max} , but also the variation of stress from the notch root into the interior of the material (stress distribution) are important factors which need to be considered. A gradually decreasing stress distribution from a notch root has a different effect on

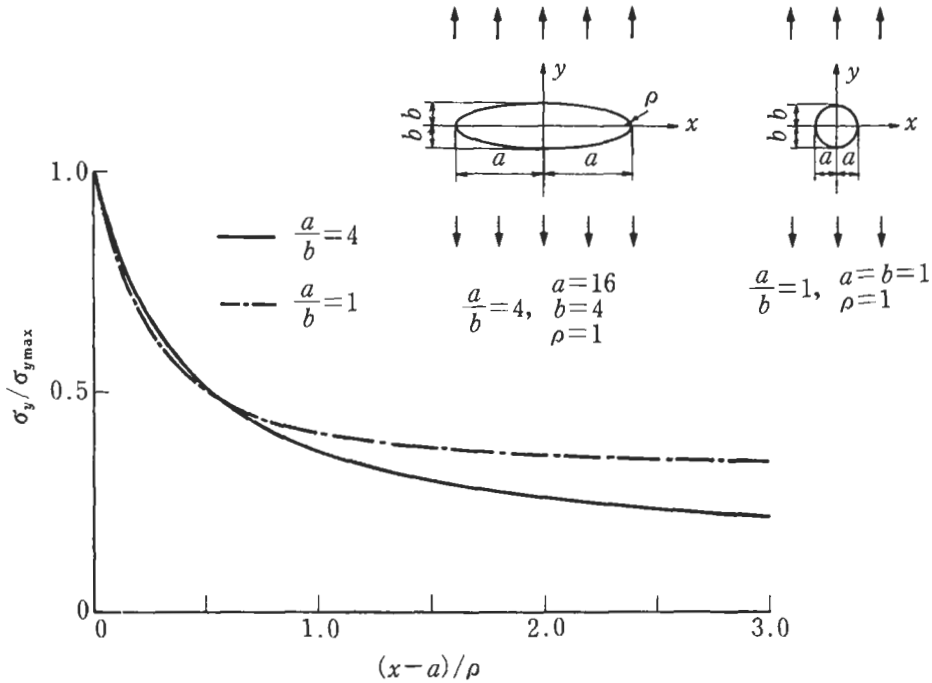


Figure 3.1 Stress distribution near an elliptical hole under uniaxial tension.

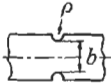
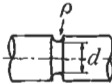
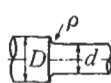
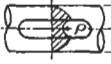
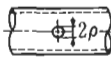
material damage, due to fatigue, at a notch root than does a steep decrease in stress. It is obvious that the former is more damaging.

In order to investigate the effect on the fatigue strength of various materials which is due to differences in stress distribution, it is convenient to define a quantity which reflects these differences. Isibasi [2] proposed the concept that a notched specimen reaches its fatigue limit when the stress at a distance ε_0 from the notch root is equal to the fatigue limit, σ_{w0} , of an unnotched specimen, where ε_0 is a material constant. Siebel and Stieler [3] proposed a method which uses the stress gradient at a notch root for the evaluation of the notch effect. Siebel and Stieler's method is explained in the following. As an example, the stress distribution in the vicinity of the end of the major axis of an elliptical hole is shown in Fig. 3.1. Since it is thought that only the stress distribution very close to the hole influences the fatigue strength, the stress distribution is approximated by a straight line and its gradient is used as the factor representing the stress distribution.

The absolute value of the stress gradient is not convenient for assessing fatigue notch effect data, because it depends on the applied stress even for identical notches. That is, the absolute value of the stress gradient cannot be correlated with the pure effect of notch shape.

For this reason, Siebel and Stieler [3] proposed using the nondimensional stress gradient, χ , which is calculated from the stress distribution normalised by the maximum

Table 3.1 Gradients of nondimensional stress distributions at notch roots [3]

Tension		$\frac{2}{\rho}$		$\frac{2}{\rho}$		$\frac{2}{\rho}$
Bending		$\frac{2}{\rho} + \frac{2}{b}$		$\frac{2}{\rho} + \frac{2}{d}$		$\frac{2}{\rho} + \frac{4}{D+d}$
Torsion		$\frac{1}{\rho} + \frac{2}{d}$		$\frac{1}{\rho} + \frac{2}{d}$		$\frac{3}{\rho}$

stress, σ_{\max} , at a notch root. That is, χ is given by the following equation:

$$\chi = \left| \frac{d\sigma^*}{dx} \right|_{x=0} \tag{3.1}$$

where

$$\sigma^* = \frac{\sigma_y}{\sigma_{\max}} \tag{3.2}$$

Table 3.1 shows approximate expressions for χ proposed by Siebel and Stieler. The table shows that the notch root radius, ρ , has the major influence on χ , regardless of notch depth. Nisitani [4] extended the concept of Siebel and Stieler, and made it clear that the root radius, ρ , controls not only the stress gradient, χ , but also the nondimensional stress distribution. In his more detailed investigation of the notch effect Nisitani discussed two separate threshold conditions in terms of χ . These are the critical stress for crack initiation, and the threshold stress for crack propagation. Thus, one approach to the notch effect is to investigate the relationship between σ_{\max} at a notch root, and the stress gradient χ , for two conditions. These are the threshold for non-propagation of a crack emanating from a notch, and the critical condition for crack initiation at a notch root [3,4].

By using these ideas [2–4] it has been shown that for various situations the fatigue strength of commercial materials cannot be determined from the maximum stress at a single, local point on a notch root. Fig. 3.2 shows fatigue strength data for notched specimens, as presented in terms of σ_{\max} and χ by Siebel and Stieler [3].

The general characteristics of the notch effect may be summarised as follows.

(a) A sharp notch \rightarrow small root radius $\rho \rightarrow$ large stress gradient $\chi \rightarrow$ high permissible maximum elastic stress, σ_{\max} , at notch root.

(b) A blunt notch \rightarrow large root radius $\rho \rightarrow$ small stress gradient $\chi \rightarrow$ low permissible maximum elastic stress, σ_{\max} , at notch root.

However, it should be noted that a high permissible maximum elastic stress, σ_{\max} , at a notch root does not necessarily mean a high permissible nominal stress, σ_n . This is because $\sigma_{\max} = K_t \sigma_n$, and K_t is a function of root radius, ρ , and especially notch depth t .

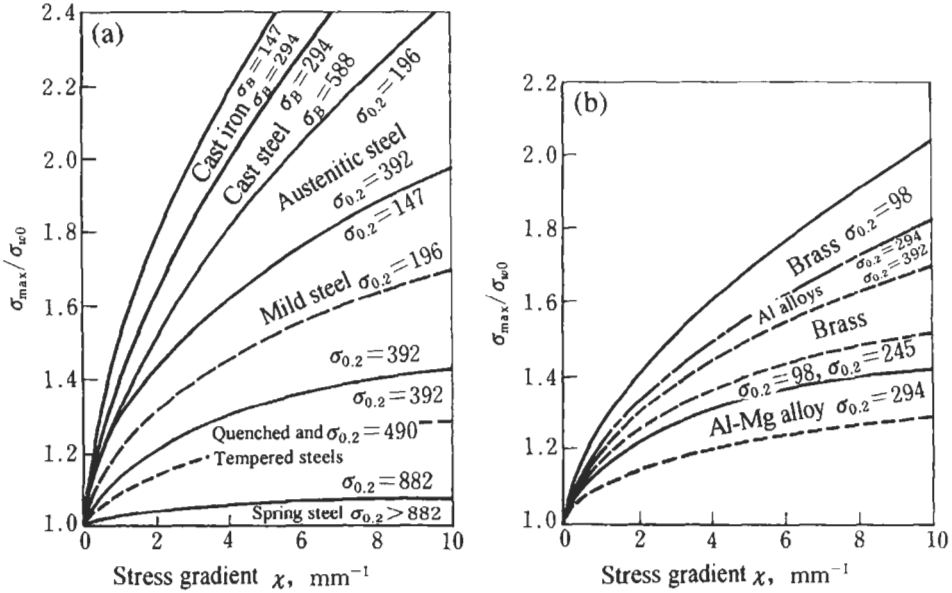


Figure 3.2 Relationship between the stress gradient and the maximum elastic stress at a notch root [3]: (a) ferrous materials, (b) nonferrous materials.

3.1.2 Non-Propagating Cracks at Notch Roots

From the early days of metal fatigue study it was believed for a long time that the fatigue limit was the critical condition for crack initiation at a notch root. However, when the distinct difference between the fatigue behaviour of blunt notch and sharp notch specimens became appreciated, it was found that, at the fatigue limit, sharp notch specimens contain peculiar cracks, around the circumference of the notch root, which stop propagating even after high cycle fatigue [2]. These cracks are called ‘non-propagating cracks’. This phenomenon was believed to occur for notches having K_t above a critical value. However, this idea was disproved by Nisitani’s experiments, in which geometrically similar specimens were used. He showed that larger specimens did not have non-propagating cracks at a value of K_t for which smaller specimens did have non-propagating cracks [4].

According to Nisitani’s interpretation, the critical condition for which fatigue strength does not decrease, even with increasing stress concentration factor, K_t , is determined by a specific value of notch root radius, ρ_0 , which is material-dependent. Fig. 3.3 illustrates schematically typical results for fatigue tests on notched carbon steel specimens. Point A in Fig. 3.3 shows the fatigue limit for unnotched specimens. Point A is not the critical condition for fatigue crack initiation, because in most steels microscopic non-propagating cracks exist, as previously mentioned in Chapter 1, although the stress at point A is not much higher than the critical stress for crack initiation. Therefore, the surface fatigue damage condition on curve A–B–C may be considered fairly similar to

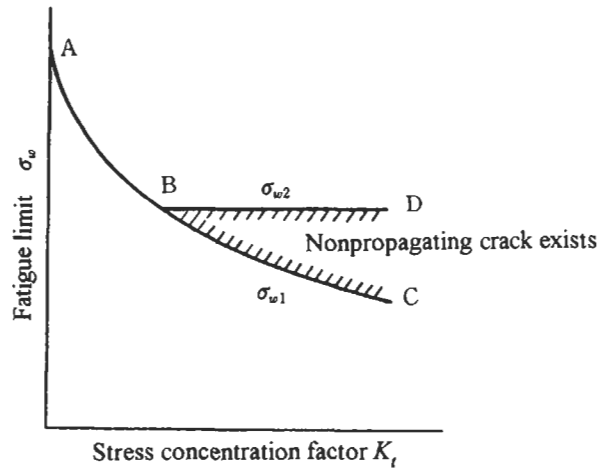


Figure 3.3 Relationship between stress concentration factor, K_t , and the fatigue limit. As the notch becomes sharper two fatigue limits may be defined. One is the fatigue limit σ_{w1} , as the critical stress for microscopic crack initiation and non-propagation at the notch root. The other is the fatigue limit σ_{w2} , as the threshold stress for non-propagation of the crack around the circumference of the notch root.

that for the fatigue limit of unnotched specimens. The stress on the curve is called 'the fatigue strength with microscopic non-propagating cracks', and is denoted by σ_{w1} [2]. On the other hand, when the notch root radius, ρ , is smaller than the critical value, ρ_0 , a fatigue crack initiates at the notch root, propagates into the interior of the material around the whole circumference of the notch root, but the specimen survives without failure. The upper bound stress for this condition is called 'the fatigue strength with macroscopic non-propagating cracks', and is denoted by σ_{w2} [2], which is shown by the straight line B–D. On the line B–D cracks stop propagating as shown in Fig. 3.4, after initiating at notch roots and then growing into specimen interiors. Thus, it is very difficult to attribute the reason for non-propagation of these cracks to strong or hard microstructures which cracks encounter during propagation. Furthermore, if we consider this phenomenon from the viewpoint of elastic stress concentration, the stress concentration after crack initiation is much higher than that for the initial notch. Thus, non-propagation of cracks must be regarded as a very strange phenomenon.

Several theories have been proposed to explain the phenomenon of non-propagating cracks. The most crucial and rational theory was based on a very strange aspect of crack behaviour, that is plasticity-induced crack closure, as found by Elber [5].

The mechanics of this phenomenon is explained as follows. As a crack grows in a material, a small region at the tip of the crack is stretched plastically and fractured. The plastically stretched material is at the surface of the wake of the crack, and prevents opening of the crack even under as much as 50% of the maximum tensile applied load.

The mechanism of this surprising phenomenon is usually explained by a figure such as Fig. 3.5. This phenomenon is called 'plasticity-induced crack closure'. Two other possible mechanisms of crack closure have also been reported, they are 'oxide-induced crack closure' [6,7], and 'roughness-induced crack closure' [8,9]. If a crack

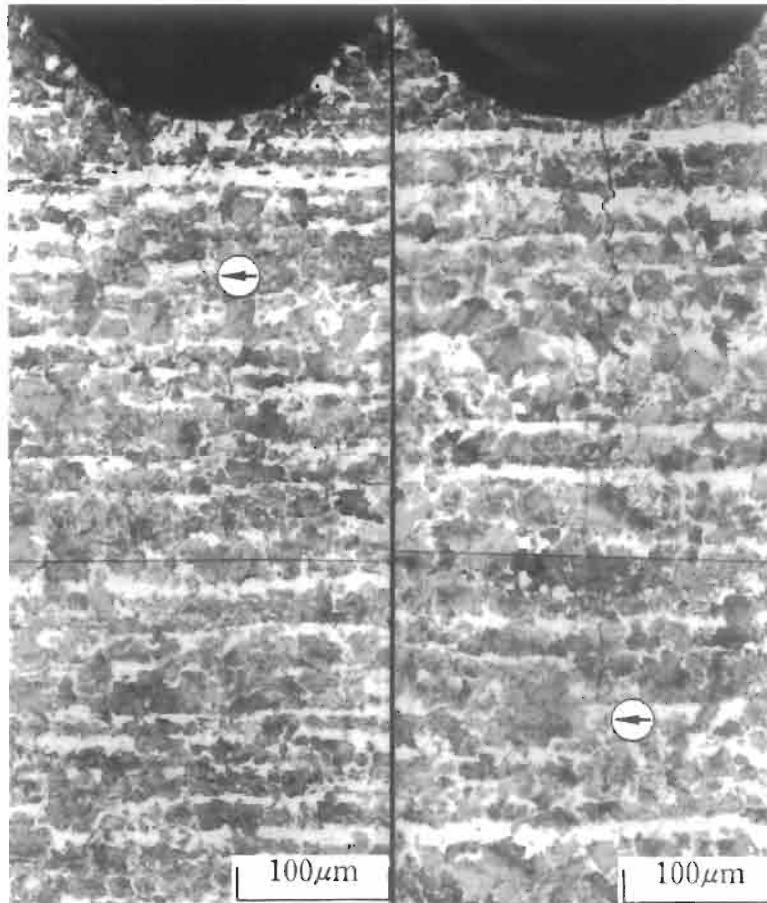


Figure 3.4 Non-propagating cracks at the roots of sharp notches (annealed medium carbon steel). (a) Notch depth $t = 3$ mm, notch root radius $\rho = 0.1$ mm, $\sigma_w = 83.3$ MPa, diameter of the minimum section $D = 10$ mm. (b) Notch depth $t = 5$ mm, notch root radius $\rho = 0.1$ mm, $\sigma_w = 83.3$ MPa, diameter of the minimum section $D = 10$ mm.

grows and crack closure develops, then the crack growth rate decreases, and in some particular cases the crack stops propagating. In such a case the stress concentration at the crack tip is not as high as the value estimated using elastic analysis, and the stress concentration becomes negligible. However, it must be noted that a suitable history of plastic deformation at the crack tip, that is a suitable variation of the K value with increase in crack length, which leads to sufficient crack closure, is necessary for the occurrence of a non-propagating crack.

As previously described, one possible approach to the investigation of the fatigue notch effect is to find the correlation between σ_{\max} and χ (stress gradient) at a notch root. However, the fatigue limit of sharply notched specimens is determined by the threshold condition for non-propagation of circumferential cracks. Thus, the threshold

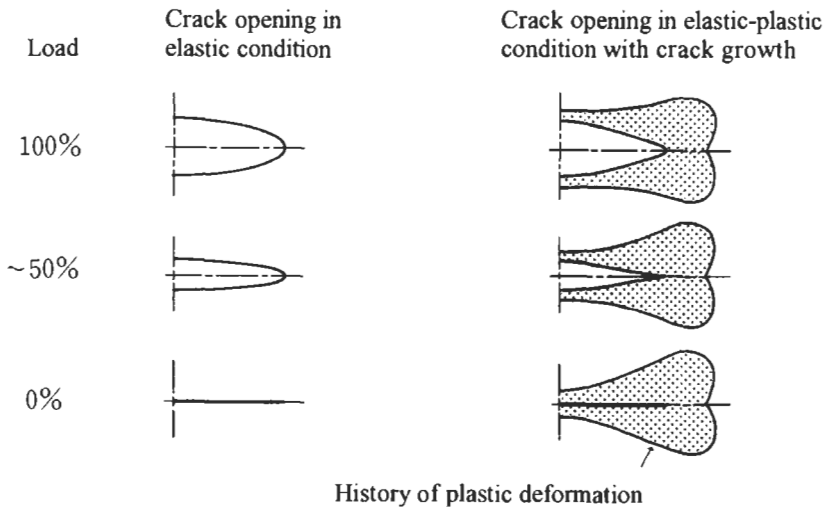


Figure 3.5 Schematic illustration of plasticity-induced crack closure mechanism [5].

condition has also been studied and interpreted using a fracture mechanics approach [10–13], which is perhaps more direct and easier to understand than the approach using σ_{\max} and χ . In particular, the Smith and Miller interpretation of the fatigue threshold for notched components [12,13] has been accepted as the most rational.

3.2 Size Effect

In general, the sizes of real structures and components are larger than those of specimens for laboratory fatigue tests. Design engineers do not use directly the values of fatigue limits obtained in laboratory tests for their allowable stresses. In extreme cases, they do not trust the values obtained by laboratory tests. The reason is that they frequently experience fracture accidents at stresses much lower than the fatigue limits determined by laboratory tests.

One cause of this kind of fracture accident at stresses much lower than those for laboratory tests is the ‘size effect’. Let us take two geometrically similar specimens, A and B. We assume that A is larger than B. The fatigue limit for A, σ_{wA} , under tension–compression, cyclic bending, and cyclic torsion is in general lower than that for B.

There are two reasons for these results: (1) differences in stress distribution for different sizes, and (2) statistical scatter of strength and microstructure at the critical part under cyclic loading.

Structures having larger sizes have both larger critical volumes and larger scatter bands for strength.

The fatigue strength of an individual structure is determined by the weakest value in the critical volume.

Factor (1) is essentially the same as the notch effect. Since the stress concentration factors, K_t , for the two geometrically similar specimens A and B, under the same nominal stress are the same, the values of the maximum elastic stresses at the notch roots of the two specimens are also the same. However, the stress gradient, χ , for the larger specimen, A, is smaller, and accordingly the critical condition for A is more severe than for B. When we compare two specimens which are not geometrically similar, we can apply the same evaluation method so long as the factor (2) is neglected. Qualitatively, the factor (2) phenomenon is caused by statistical scatter. A quantitative evaluation is thought to be difficult, and has not previously been accomplished. In fact, factor (2) is not particularly important for low and medium carbon steels of low static strength, and of the cleanliness specified in standards [14].

However, for hard and high strength steels the influence of factor (2) is not negligible, and is of practical importance. The effect of factor (2) must also be considered in the fatigue of low strength materials containing various types of defects. For example, cast iron contains graphite, which in fatigue can be regarded as equivalent to defects.

The size effect with regard to factor (2) has not previously been sufficiently studied because of the complicated phenomena and complicated data. However, a quantitative solution to this problem is very much needed, both because the loads applied to components and structures are being raised year by year, and because new materials of higher strength are being developed. This problem is a very difficult fatigue problem, and is not easily solved. The main objective of this book is to provide a quantitative and practical solution to the problem, and this is explained in detail in the following chapters. As a preliminary, a reader must at least understand clearly the differences and similarities between notch effect and size effect, as described in this chapter.

3.3 References

1. For example, A.J. McEvily: *Metal Failures: Mechanisms, Analysis, Prevention*, John Wiley, New York, 2002 and S. Nishida: *Failure Analysis in Engineering Applications*, Butterworth Heinemann, London, 1992.
2. T. Isibasi: *Prevention of Fatigue and Fracture of Metals* (in Japanese), Yokendo, Tokyo, 1967.
3. E. Siebel and M. Stieler: Ungleichformige Spannungsverteilung bei Schwingender Beanspruchung, *VDI Z.*, **97**(5) (1955), 121–126.
4. H. Nisitani: Size Effects of Branch Point and Fatigue Limit of Carbon Steel in Rotary Bending Tests, *Trans. Jpn. Soc. Mech. Eng.*, **34**(259) (1968), 371–382.
5. W. Elber: The Significance of Fatigue Crack Closure. *Damage Tolerance in Aircraft Structures*, ASTM STP, **486** (1971), 230–242.
6. K. Endo, K. Komai and K. Ohnishi: Effects of Stress History and Corrosive Environment on Fatigue Crack Propagation, *Mem. Fac. Eng. Kyoto Univ.*, **31**(1) (1969), 25–46.
7. R.O. Ritchie, S. Suresh and C.M. Moss: Near-Threshold Fatigue Crack Growth in a 2 1/4 Cr–Mo Pressure Vessel Steel in Air and Hydrogen, *J. Eng. Mater. Technol., Trans. ASME, Ser. H*, **102** (1980), 293–299.
8. N. Walker and C.J. Beevers: A Fatigue Crack Closure Mechanism in Titanium, *Fatigue Eng. Mater. Struct.*, **1** (1979), 135–148.
9. K. Minakawa and A.J. McEvily: On Crack Closure in the Near-Threshold Region, *Scr. Metall.*, **15** (1981), 633–636.
10. Y. Akiniwa and K. Tanaka: Notch-Size Effect on Propagation Threshold of Short Fatigue Cracks,

- Trans. Jpn. Soc. Mech. Eng. A, **53(492)** (1987), 1474–1481.
11. Y. Nakai, K. Tanaka and R. Kawashima: Propagation and Non-Propagation of Fatigue Cracks in Notched Plates of Low-Carbon Steel, *J. Soc. Mater. Sci., Jpn.*, **32(356)** (1983), 535–541.
 12. R.A. Smith and K.J. Miller: Fatigue Cracks at Notches, *Int. J. Mech. Sci.*, **19** (1977), 11–22.
 13. R.A. Smith and K.J. Miller: Prediction of Fatigue Regimes in Notched Components, *Int. J. Mech. Sci.*, **20** (1978), 201–206.
 14. Japanese Industrial Standard G0555: Lattice Points Counting Method, Optical Method of Nonmetallic Inclusion Rating for Steels, 1977.

Chapter 4

Effect of Size and Geometry of Small Defects on the Fatigue Limit

4.1 Introduction

Traditional theories of notch effect evaluation, based on stress concentration factors, and stress distribution or gradient, are applicable to notches which may be seen by the naked eye, that is notches larger than ~ 1 mm. However, as notch size decreases, these theories become invalid. As well as artificial notches, and notch effects due to surface defects and scratches, both natural defects and nonmetallic inclusions, are of practical importance. Since so-called traditional or conventional theories cannot be applied to these very small defects, the problem needs substantial reconsideration. There are too many factors which may influence fatigue strength to permit the establishment of a unifying theory. These factors include matters such as the size and shape of surface defects, natural defects and nonmetallic inclusions, chemical composition, etc. There have been numerous investigations on effects of these factors, and there are many review papers. In this chapter there is first an overview of previous investigations in order to identify the key points of the problem, and then a unifying and quantitative evaluation method for the effects of small defects on fatigue strength is described.

Previous studies on small defects may be divided into those which mainly considered small notches and small cracks, and those which investigated the influence of nonmetallic inclusions as equivalent notches or voids. There has been no consensus on the idea that inclusions may be regarded as equivalent to stress-free defects. Rather, this concept has been used to treat inclusion problems from a simplified viewpoint, because of the difficulty of rigorous analysis of complex inclusion-related conditions. The factors which need consideration are: inclusion shape, inclusion adhesion to the matrix, elastic constants of inclusions and matrix, inclusion chemical composition, and inclusion size. As a simplification, only the problems of small holes and notches are treated in this chapter. Inclusion problems are discussed in later chapters.

4.2 Influence of Extremely Shallow Notches or Extremely Short Cracks

As described in Section 3.1, if the size of notches is relatively large, and visible to the naked eye, then the maximum permissible stress, σ_{\max} , at a notch root has a one-to-one

correspondence with the stress gradient, χ , at the notch root [1,2]. Therefore, if a master curve for the relationship between σ_{\max} at the fatigue limit and χ , is determined from laboratory tests, then the maximum elastic stress, σ_{\max} , at the notch roots of components and structures can be predicted. However, as notches become extremely small, then σ_{\max} deviates from the master curve [3]. This is because the size (depth) of notches becomes of the same order as the size of the fatigue damage domain at a notch root.

A phenomenon similar to that for extremely shallow notches occurs, in the threshold region, for the growth of small cracks. Values of the threshold stress intensity factor range, ΔK_{th} , for cracks larger than a few mm, in common structural steels and at a constant R ratio, are a material constant [4]. However, as crack lengths become smaller, values of ΔK_{th} decrease, and this decrease cannot be ignored in practical applications. This decrease was originally pointed out by Frost et al. [5], Kitagawa and Takahashi [4], and Kobayashi and Nakazawa [6].¹ El Haddad et al. [7] compensated for the difference, between ΔK_{th} values for small cracks and those for long cracks, by adding a fictitious crack length to the physical crack length, and proposed the use of this method to predict small crack thresholds. Usami and Shida [8] proposed a threshold criterion in which the cyclic crack tip plastic zone size, calculated using the Dugdale model, is a material constant for the small crack threshold. Tanaka et al. [9] proposed prediction of threshold conditions ranging from small cracks to long cracks by using ΔK_{th} for long cracks, and the fatigue limit, σ_{w0} , for unnotched specimens. The latter was taken as the condition for non-propagation of a small crack.

The study of Isibasi and Uryu [10], Frost's early study [11] using the model $\sigma_w^3 l = C$, and the similar study of Kobayashi and Nakazawa [12], all indicate indirectly that ΔK_{th} is not a material constant, but is dependent on crack length, l . In order to evaluate quantitatively the influence of very shallow notches and very small cracks on fatigue strength, we need to investigate transitions of long crack laws to the small crack region. That is, the size of the transition region for which a new law is needed must be determined. Previous experimental data for small cracks were not adequate for analysis leading to the determination of any new law. Furthermore, the influence of not only two-dimensional (2D) dimensions such as notch depth and crack length, but also three-dimensional (3D) dimensions such as those of blind holes, defects, and surface cracks, need evaluation in a unified manner. Therefore, in this book, we treat both 2D defects and 3D defects as a single category.

¹ Satisfaction of the conditions for the appearance of non-propagating cracks, and for the crack growth threshold, means that a new crack always emanates from the initial crack, grows for a small distance, and then stops growing. Therefore, some researchers consider that if they add the small distance of new crack growth to the initial crack length, and then calculate ΔK_{th} this compensates for the difference between long cracks and small cracks, and ΔK_{th} becomes constant. However, experimental data have shown that the small amount of crack growth, which takes place, is insufficient for the modification to compensate for the difference between long cracks and small cracks. The phenomenon is actually caused by the distinct difference, for the same value of ΔK , between stress distributions in the vicinity of the crack tip for long cracks and for small cracks.

4.3 Fatigue Tests on Specimens Containing Small Artificial Defects

4.3.1 Effect of Small Artificial Holes Having the Diameter d Equal to the Depth h

In order to simulate small natural defects Murakami and Endo introduced small artificial holes, with diameters ranging from 40 μm to 200 μm , into the surfaces of specimens [13]. Fig. 4.1 shows the hole geometry. Fig. 4.2 shows photographs of small artificial holes introduced into the surfaces of 0.13% C and 0.46% C steel specimens.

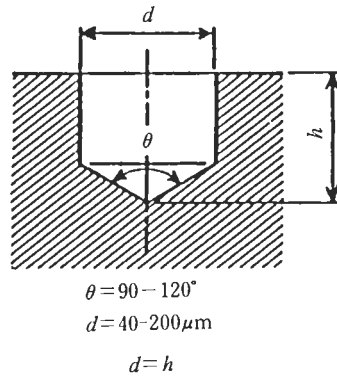


Figure 4.1 Artificial hole geometry.

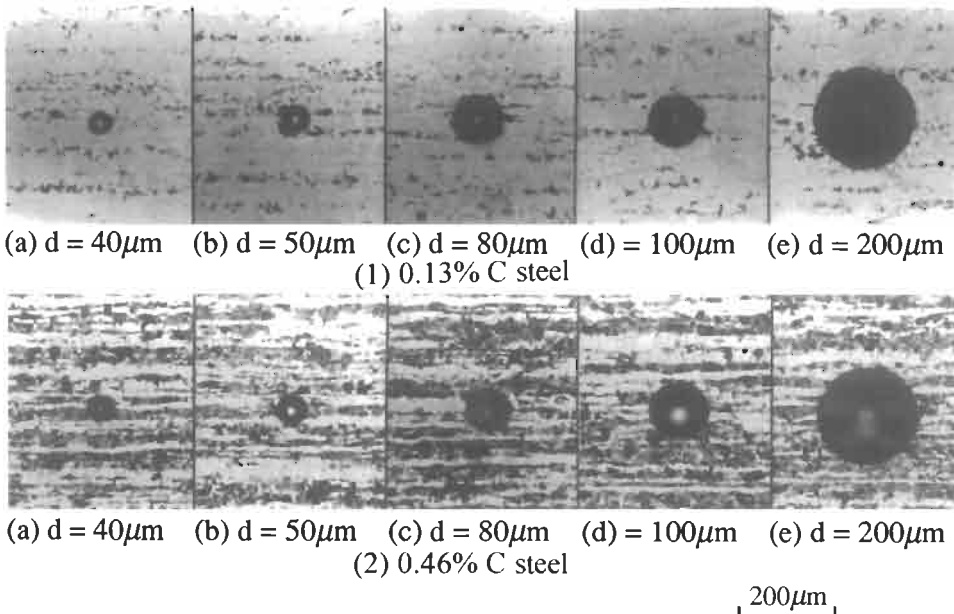


Figure 4.2 Comparison between the sizes of artificial holes and microstructural features.

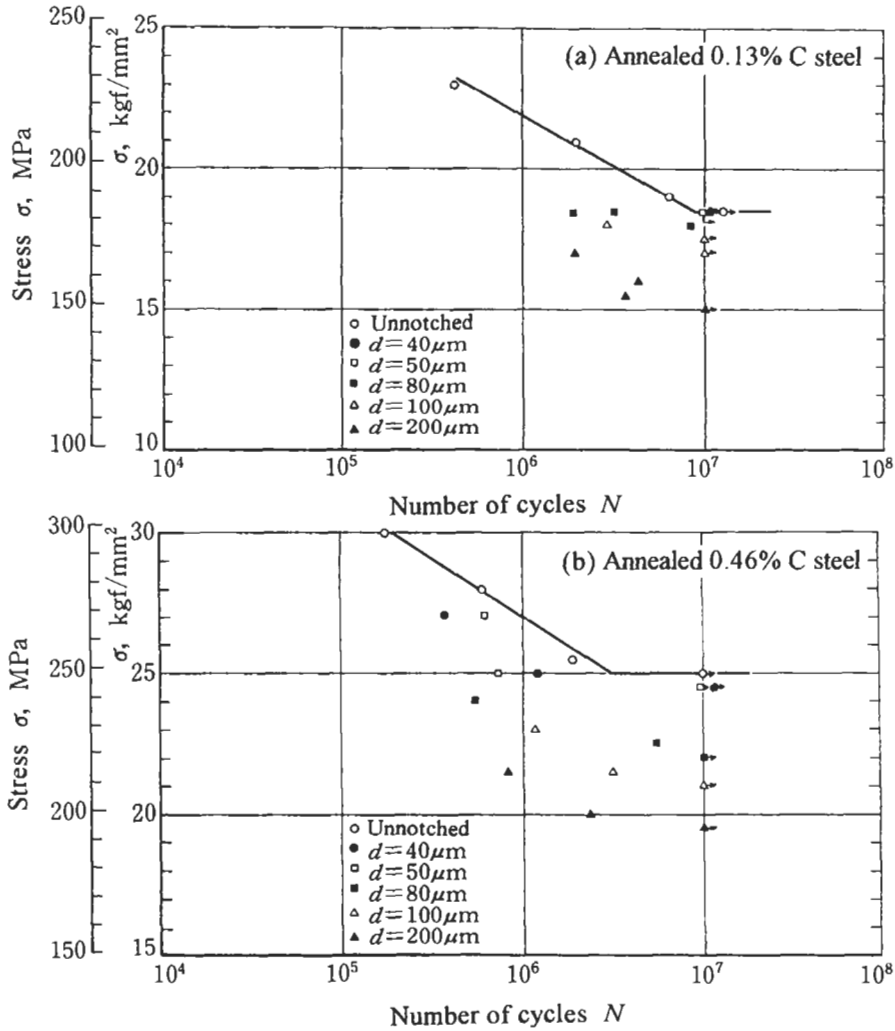
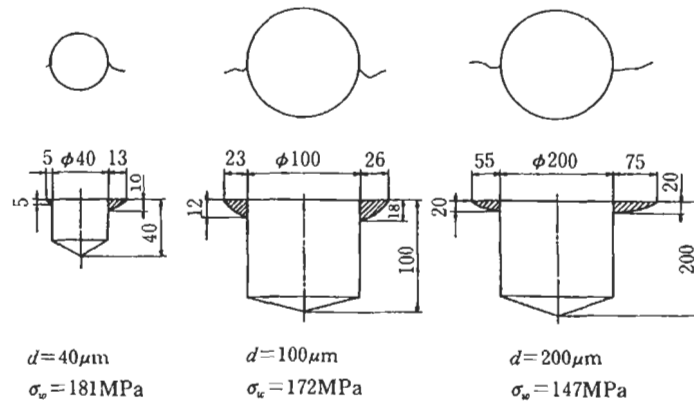


Figure 4.3 $S-N$ data for specimens containing artificial holes (rotating bending). (a) Low carbon steel. (b) Medium carbon steel.

A $40 \mu\text{m}$ hole in the 0.13% C steel is the same order of size ($\sim 37 \mu\text{m}$) as the ferrite grains. Fig. 4.3 shows $S-N$ data for rotating bending fatigue tests on 0.13% C steel, and 0.46% C steel, specimens containing these small artificial holes. Several important results are summarised below.

At fatigue limits, defined as the maximum nominal stress for a life of at least 10^7 cycles, non-propagating cracks were observed in all specimens. Fig. 4.4 shows sketches of such non-propagating cracks. Thus, the fatigue limit for specimens containing small artificial defects is not the critical condition for crack initiation at the corner

(a) Annealed 0.13% C steel



(b) Annealed 0.46% C steel

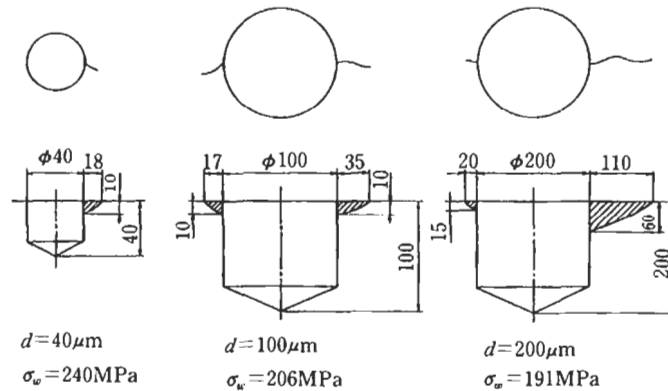


Figure 4.4 Configuration of non-propagating cracks emanating from artificial holes. (a) Low carbon steel. (b) Medium carbon steel.

of a hole where it intersects the specimen surface, but is the threshold condition for non-propagation of cracks emanating from holes. Understanding this phenomenon is very important, not only for understanding the problem of small defects, but also for understanding the problem of nonmetallic inclusions, which is discussed in later chapters.

On one type of specimen 12 small artificial holes, either $40 \mu\text{m}$ or $50 \mu\text{m}$ in diameter, were drilled into the surface at four equally divided points on three circumferences, which were equally spaced in the axial direction. Non-propagating cracks were not always observed. There were some holes without cracks, and some with either one non-propagating crack or with two non-propagating cracks, at hole corners. Some examples are shown in Fig. 4.4. No non-propagating cracks were observed in 0.13% C steel specimens tested at a stress 4.9 MPa lower than the fatigue limit. The fatigue limit for

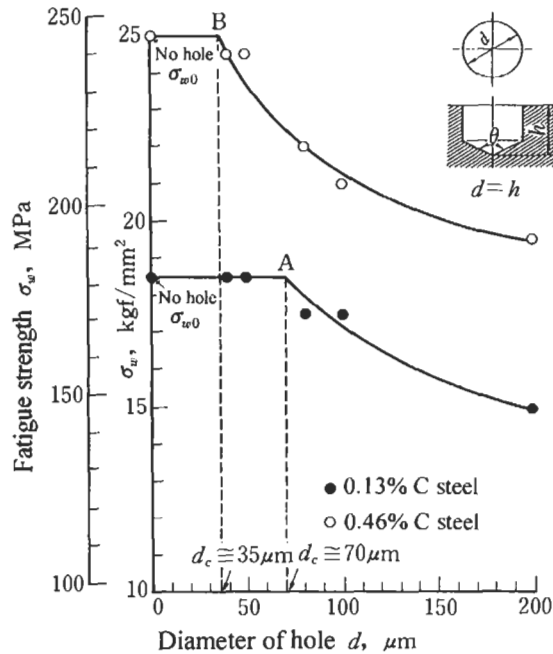


Figure 4.5 Relationship between the size of an artificial hole and the fatigue limit.

0.13% C steel specimens, containing 12 holes of either 40 μm or 50 μm diameter, was equal to that for unnotched specimens.

On the other hand, holes of 40 μm or 50 μm diameter lowered the fatigue limit of 0.46% C steel slightly compared to that for unnotched specimen. The decrease was about 2%.

Although these experimental results may appear strange to inexperienced engineers, the mechanism is related to the phenomenon that the fatigue limit for unnotched specimens is not a critical stress for crack initiation, but is a threshold condition for the non-propagation of cracks (see pages 1–4). As previously mentioned, non-propagating cracks approximately 100 μm in maximum size exist, at the fatigue limit, on the surface of an unnotched 0.13% C steel specimen without causing specimen fracture. Therefore, cracks emanating from initial defects, which are a little smaller than 100 μm , become non-propagating cracks because of a mechanism similar to that which causes non-propagation of small cracks which have initiated from slip bands and grain boundaries, and are growing towards neighbouring grains. In the case of 0.46% C steel, the maximum non-propagating crack size, at the fatigue limit, is approximately 50 μm . Accordingly, defects a little smaller than 50 μm would not be expected to be detrimental to fatigue strength. Thus, we can understand the reason why a hole of 40 μm or 50 μm diameter lowers the fatigue strength of 0.46% C steel by only 2%.

Fig. 4.5 shows the decrease of fatigue strength with the increase of hole diameter, d (in μm). Two important conclusions may be drawn from this figure. The first is that

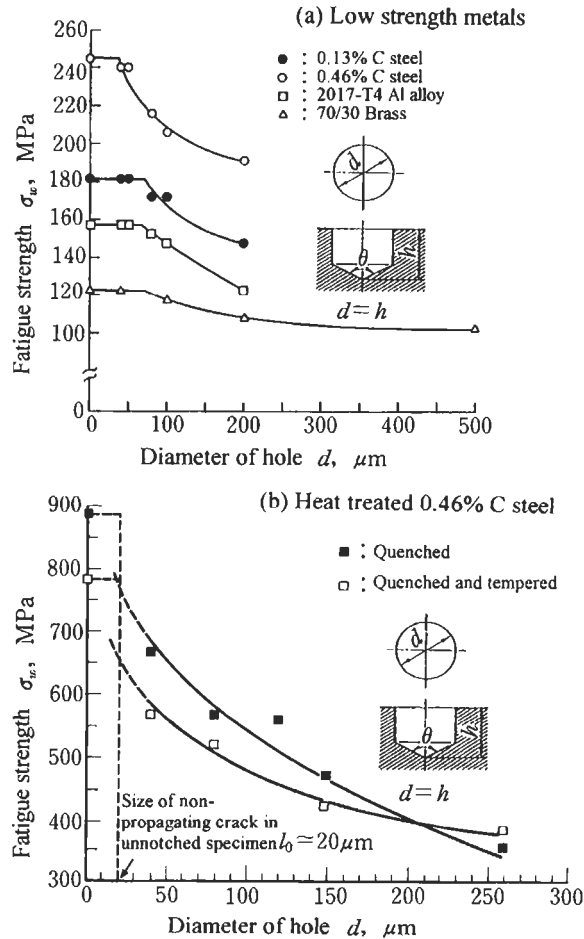


Figure 4.6 Relationship between the size of an artificial hole and the rotating bending fatigue limit. (a) Low strength materials. (b) Heat-treated medium carbon steel.

there are non-damaging defects which do not lower the fatigue strength. The second is that the size of defects is more crucial for fatigue strength than is the stress concentration factor, K_t , for defects. This is because the value of K_t for all the defects in Fig. 4.5 (geometrically similar drilled holes) are approximately the same, regardless of their size. In other words, K_t is not the crucial factor which controls fatigue strength. In the case of holes with equal diameter and depth, cracks always emanated from hole corners, as shown in Fig. 4.4. However, as the depths of holes become smaller than their diameters, cracks are likely to initiate at the bottoms of holes [14].

Fig. 4.6 shows experimental data for some similar fatigue tests on various materials [15,16]. The general trend, due to the existence of small defects, is a larger decrease in fatigue strength for materials of higher static strength. Fig. 4.6a shows that holes of 40

μm diameter are not detrimental to soft materials, such as 0.13% C steel [13] and 70/30 brass [15]. On the other hand, even a very small defect of 40 μm is very detrimental to the fatigue strength of hard steels, such as quenched steels (see Fig. 4.6b) [16] and maraging steel [17]. This phenomenon corresponds to the well known fact that 'hard steels are sensitive to notches and defects'. This fact may be expressed more precisely, using the unequivocal data obtained for specimens containing small holes, as: 'Defects smaller than a critical size are non-damaging (not detrimental) to fatigue strength, and the critical size is smaller for materials having a higher static strength, so that a defect of a given size is more detrimental to high strength steels than to low strength metals'.

4.3.2 Effect of Small Artificial Holes Having Different Diameters and Depths

The influence of geometrically similar holes with $d = h$ was described in the previous section.

The influence of holes with $d \neq h$ is discussed in this section.

Table 4.1 Relationship between the geometry of artificial holes and the fatigue limit (annealed medium carbon steel)

	Hole dia d , μm	Hole depth h , μm	h/d	Fatigue limit, MPa {kgf/mm ² }
Unnotched	—	—	—	240 {24.5 }
Specimens with small holes	40	40	1.0	235 {24.0 }
	50	50	1.0	226 {23.0 }
		100	2.0	226 {23.0 }
	80	40	0.5	230 {23.5 }
		80	1.0	211 {21.5 }
	100	160	2.0	201 {20.5 }
		50	0.5	226 {23.0 }
		50*	0.5*	226* {23.0* }
		100	1.0	201 {20.5 }
	200	100*	1.0*	196* {20.0* }
		200	2.0	191 {19.5 }
		400	2.0	201 {20.5 }
	500	100	0.5	201 {20.5 }
		200	1.0	181 {18.5 }
400		2.0	172 {17.5 }	
500	250	0.5	181 {18.5 }	
	500	1.0	157 {16.0 }	
	1000	2.0	147 {15.0 }	

* Electropolished after drilling

Table 4.2 Relationship between the geometry of artificial holes and the fatigue limit (annealed low carbon steel)

	Hole dia d , μm	Hole depth h , μm	h/d	Fatigue limit, MPa {kgf/mm ² }
Unnotched	—	—	—	181{18.5}
Specimens with small holes	100	50	0.5	181{18.5}
		100	1.0	172{17.5}
		200	2.0	157{16.0}
	200	100	0.5	157{16.0}
		200	1.0	147{15.0}
		400	2.0	137{14.0}
	500	250	0.5	142{14.5}
		500	1.0	128{13.0}
		1000	2.0	118{12.0}

Tables 4.1 and 4.2 show fatigue test results for 0.46% C steel and 0.13% C steel, obtained using specimens containing holes with various combinations of diameter, d , and depth, h . All the data show values of the fatigue limit for which there are non-propagating cracks, either at a hole corner, or at the bottom of a hole. Data marked * in Table 4.1 are results for specimens which were electropolished again after the holes were drilled. These holes were introduced by first drilling holes of 80 μm diameter, and then electropolishing until the diameters became 100 μm . The fatigue limits for these specimens is either the same as, or is 4.9 MPa (0.5 kgf/mm²) lower than, fatigue limits for specimens where holes were not electropolished after drilling. These data show that the effect of work hardening due to drilling is small.

Fig. 4.7 shows a photograph of a specimen, containing a deep hole, at the fatigue limit. The fatigue limit is determined, not by the condition for crack initiation, but by the condition for crack propagation. Shallow holes, unlike deep holes, tend to have non-propagating cracks at the bottoms of holes. As shown by the results in Fig. 4.5, it is not only very difficult, but also not very helpful, to summarise these data from the viewpoint of the stress concentration factor, K_t . If we consider that the condition for the fatigue limits for all these data is the condition for the non-propagating crack threshold, then we must recognise that the problem of small defects is essentially a small crack problem. We need to solve this problem using stress intensity factors rather than stress concentration factors. On page 17 the maximum stress intensity factor, $K_{I\text{max}}$, along the crack front of a three-dimensional crack has a strong correlation with the square root of crack area, $\sqrt{\text{area}}$. Therefore, $\sqrt{\text{area}}$ appears to be a promising parameter for use as

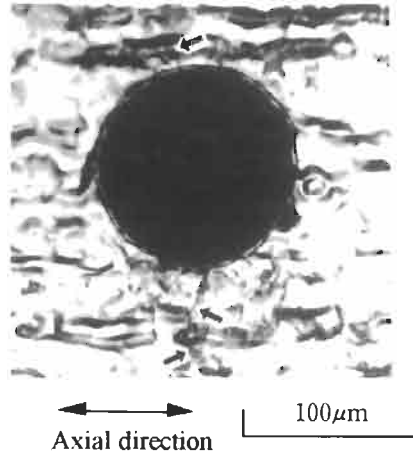


Figure 4.7 Non-propagating cracks at an artificial hole (annealed medium carbon steel, diameter of hole, $d = 100 \mu\text{m}$, depth of hole, $h = 200 \mu\text{m}$, $\sigma_w = 191 \text{ MPa}$).

the characteristic dimension for the evaluation of the effects of defects of various sizes and shapes on fatigue strength, as in Tables 4.1 and 4.2. The author wishes to reaffirm here the point that this approach is based on two important findings. These are that the fatigue limit of materials containing defects is essentially a crack problem, and that there is a very strong correlation between $\sqrt{\text{area}}$ and K_{Imax} . This concept is illustrated in Fig. 4.8. The data shown in Tables 4.1 and 4.2 are discussed below from this point of view.

Figs. 4.9 and 4.10 show the relationships between the rotating bending fatigue limits of 0.46% C steel and 0.13% C steel, and the square root of defect projected area, $\sqrt{\text{area}}$. The value of $\sqrt{\text{area}}$ for the holes is calculated using $\sqrt{dh - d^2/4\sqrt{3}}$. This assumes that the flank angle at the bottom of a hole is 120° , which is approximately true. As can be seen in Figs. 4.9 and 4.10, $\sqrt{\text{area}}$ seems to be a relevant controlling parameter over a wide range of dimensions; $h/d = 0.5-2$, $d = 40-500 \mu\text{m}$.

Therefore, we can anticipate that $\sqrt{\text{area}}$ will also be useful for the prediction of fatigue strength, σ_w , in the presence of natural defects.²

² Here, it must be noted that the value of $\sqrt{\text{area}}$ is defined as the square root of the initial defect projected area. The area of a newly produced crack at the initial defect is not added. As was pointed out on page 39, in rotating bending tests on 0.13% C steel specimens, containing 12 artificial small holes either $40 \mu\text{m}$ or $50 \mu\text{m}$ in diameter, various crack behaviours were observed at the fatigue limit. At some holes there were non-propagating cracks on opposite sides of a hole corner, some holes had a crack on one side only, and other holes had no cracks. Thus, if we were to add in the area of newly initiated cracks when calculating $\sqrt{\text{area}}$, then several different values of $\sqrt{\text{area}}$ would be defined for one specimen, and it would not be possible to obtain a satisfactory relationship, such as that given by Eq. 4.1, between σ_w and $\sqrt{\text{area}}$. This is also true when the initial defect is a crack, because at the fatigue limit new cracks emanate from the initial main crack, and eventually stop propagating. If we consider the nominal applied stress, then the fatigue limit stress, σ_w , remains within a very narrow band. A specimen fails at a stress 5 MPa higher than σ_w , and there are no non-propagating cracks at a stress 5 MPa lower than σ_w . Within this very narrow band, three distinct

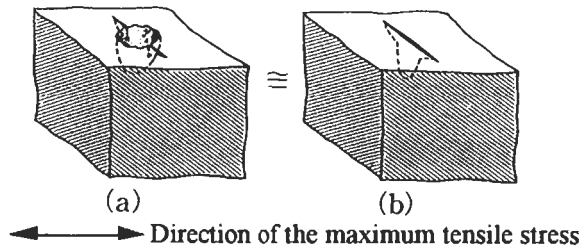


Figure 4.8 A small defect having cracks is equivalent to a crack having a shape identical to the projected shape of the small defect plus cracks.

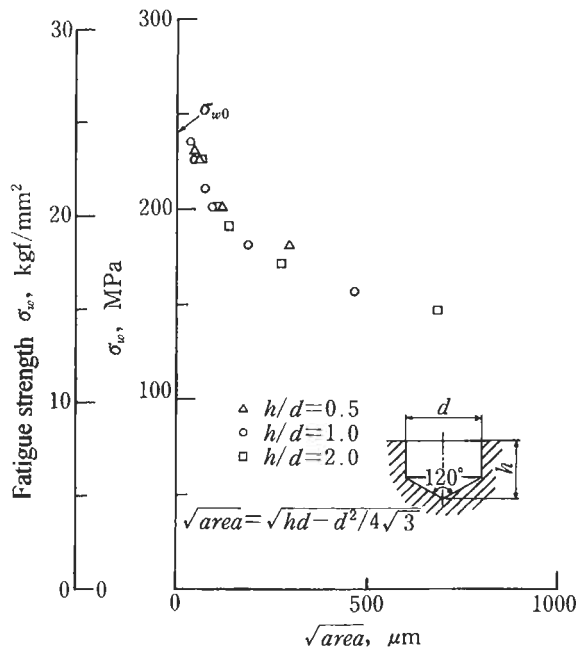


Figure 4.9 Relationship between the rotating bending fatigue limit and the square root of the projected area of small defects (annealed medium carbon steel).

Figs. 4.11 and 4.12 are redrawn versions of Figs. 4.9 and 4.10, using logarithmic scales. They show that, for both 0.13% C steel and 0.46% C steel, the relationships

different states are possible on a specimen surface. The areas of newly initiated cracks show a large amount of scatter, so adding these to initial areas leads to a large amount of scatter for σ_w when this is predicted using ΔK . Furthermore, predictions based on crack sizes, including newly initiated cracks, are not useful in practice because the size of newly initiated cracks can only be determined after fatigue tests have been completed.

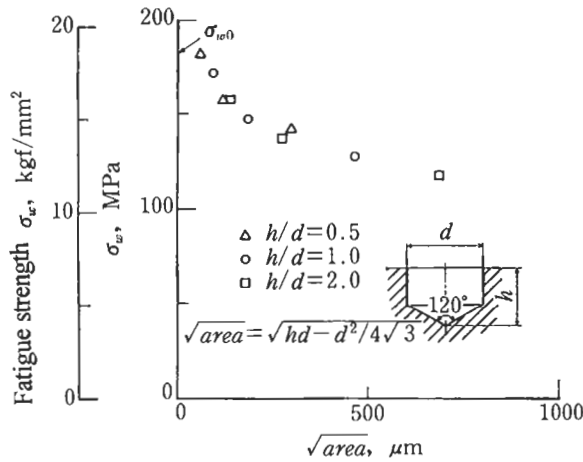


Figure 4.10 Relationship between the rotating bending fatigue limit and the square root of the projected area of small defects (annealed low carbon steel).

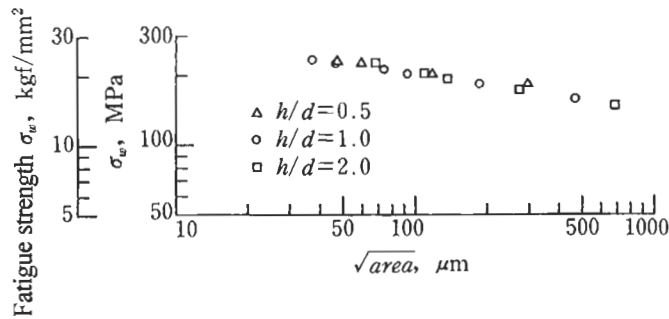


Figure 4.11 Relationship, on logarithmic scales, between the rotating bending fatigue limit and the square root of the projected area of small defects (annealed medium carbon steel).

between σ_w and \sqrt{area} have a slope of $-1/6$. Thus, we have the relationship:

$$\sigma_w^n \sqrt{area} = C \tag{4.1}$$

Eq. 4.1 indicates that $n = 6$, and not $n = 2$ which is usual for large cracks. Recent research has made it clear that the so-called threshold stress intensity factor range, ΔK_{th} , depends both on crack size and on loading history, and accordingly does not have a constant value. That is, the rule $\Delta K_{th} = \text{const.}$ (which means $n = 2$) does not hold. Rather, the recently accepted viewpoint is that the effective threshold stress intensity factor range, $\Delta K_{eff,th}$, which is defined using the range of crack opening and the cyclic loading, does have a constant value regardless of crack size [18,19]. Unfortunately, it is very difficult to measure the value of ΔK_{eff} for service loadings, as experienced by components and structures, so the prediction of fatigue strength using ΔK_{eff} for various defects is not easy.

On the other hand, if we could obtain prediction equations, in the form of Eq. 4.1,

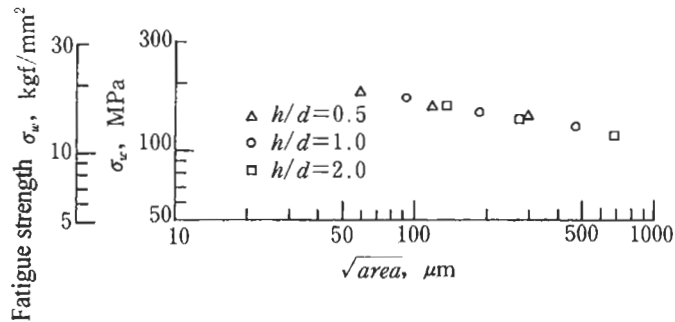


Figure 4.12 Relationship, on logarithmic scales, between the rotating bending fatigue limit and the square root of the projected area of small defects (annealed low carbon steel).

for various materials containing small defects, then application would be very easy and practical. In fact, Frost [11], and Kobayashi and Nakazawa [12], previously proposed the equation, in the form $\sigma_w^n l = \text{const.}$, for 2D cracks of length l . According to Frost $n = 3$, and according to Kobayashi and Nakazawa $n = 4$. These values ($n = 3-4$) are smaller than $n = 6$, as obtained from Figs. 4.11 and 4.12. Murakami and Endo [20], and Murakami and Matsuda [21] investigated in detail the reasons for this difference in the value of n . They found that the difference is not caused by differences in materials, but is due to the sizes of cracks or defects introduced into specimens. The essence of their investigations is explained in the following. If we compare the influence of 2D cracks and 3D cracks using for both the same geometric parameter, \sqrt{area} , which was introduced on page 19 of Chapter 2, then it may be seen that even very shallow 2D cracks have a large equivalent value of \sqrt{area} . For example, a 2D crack 0.1 mm (100 μm) deep is equivalent to a 3D crack of $\sqrt{area} = 316 \mu\text{m}$. Therefore, as long as we continue to use specimens containing 2D cracks, it is difficult to reveal the true nature of very small defects. Fig. 4.13 shows how ΔK_{Ih} depends on defect size in the range from a few μm to ~ 10 mm. The figure indicates that Frost's experimental data are in the transition zone between the nature of small cracks and the nature of large cracks.

4.4 Critical Stress for Fatigue Crack Initiation from a Small Crack

As previously described, at the fatigue limit (σ_w) cracks emanate from small initial defects and cracks, and then stop propagating. In addition to this value σ_w , we can define another critical stress, σ_{wi} , under which no cracks initiate from the original cracks. These two critical stresses play an important role in life prediction for fatigue under variable amplitude loading. This is because the two quantities provide the measures needed to evaluate the contribution of variable amplitude stresses to fatigue damage at applied stresses higher than σ_{wi} .

The objectives of this section are to show how σ_{wi} is measured, and to describe the small amount of crack propagation at stresses between σ_{wi} and σ_w , together with non-propagation following propagation.

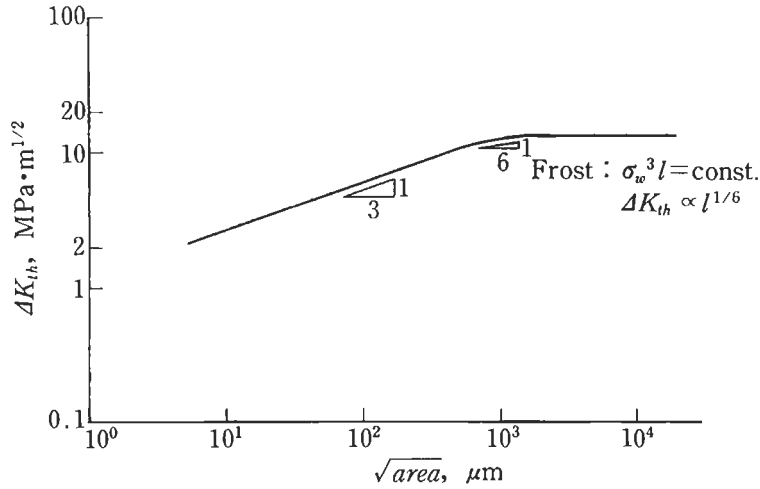


Figure 4.13 Dependence of ΔK_{th} on crack size (defect size).

A very simple experimental method was used. Specimens containing small cracks, which had emanated from small artificial holes, were prepared. These specimens were then annealed in order to relieve the residual stresses produced during the introduction of the initial fatigue cracks. Therefore, these specimens should contain so-called ideal cracks before the subsequent fatigue testing, during which the critical stress for fatigue crack initiation, σ_{wi} , is measured. The method may also be used for the determination of the effective threshold stress intensity factor range, $\Delta K_{eff,th}$. This method is called the annealing method using \sqrt{area} of cracks [22].

Fig. 4.14 illustrates the procedure used to determine σ_{wi} . If an annealed crack does not propagate it can be assumed that neither plastically induced crack closure [23], nor surface roughness induced crack closure [24,25], nor oxide induced crack closure [26,27], will occur. Therefore, if we can estimate the crack opening stress under constant amplitude loading, the value of $\Delta K_{eff,th}$ is easily determined.

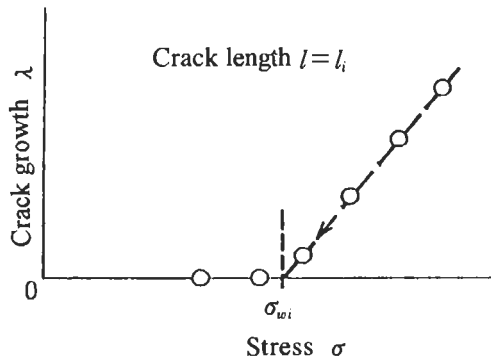


Figure 4.14 Determination of the critical stress, σ_{wi} , from an initial crack.

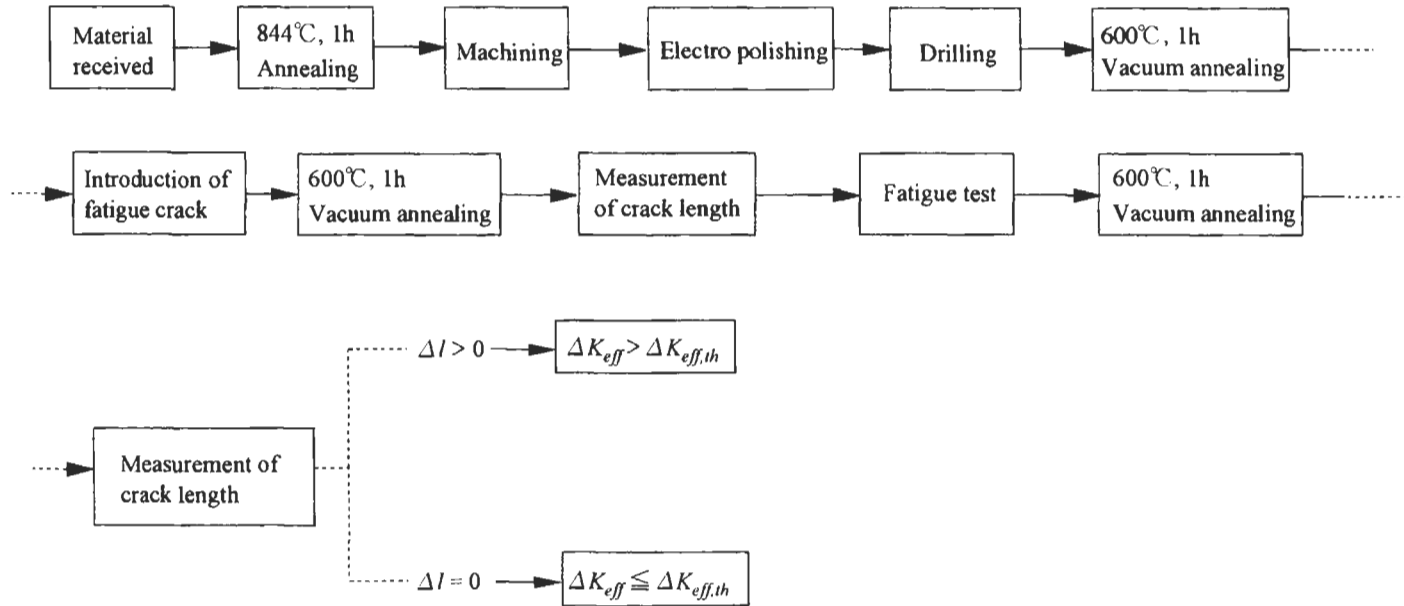


Figure 4.15 Experimental procedure for the determination of the critical stress, σ_{wi} , from an initial crack.

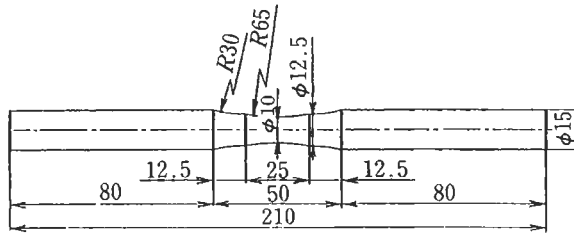


Figure 4.16 Specimen geometry for preparation of initially cracked specimens.

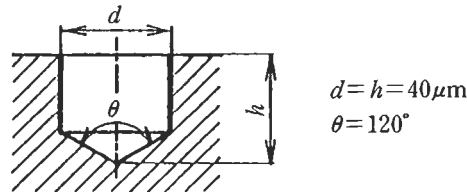


Figure 4.17 Geometry of artificial hole.

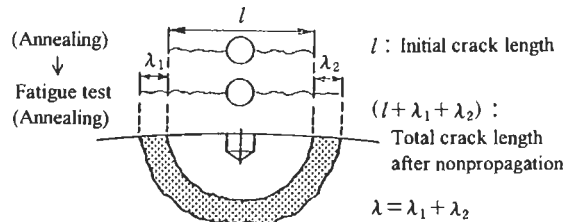


Figure 4.18 Determination of crack growth length, λ .

Fig. 4.15 shows the experimental procedure. The material used was a rolled 0.46% C steel, which was annealed before machining the specimens. Fig. 4.16 shows the specimen geometry. After machining a surface layer ($40\ \mu\text{m}$ per diameter) was removed by electropolishing. Four holes of $40\ \mu\text{m}$ diameter (Fig. 4.17) were then drilled into the specimen surface. Finally, specimens were annealed, in a vacuum, for 1 h at 600°C to relieve residual stresses. The specimens were loaded under rotating bending at a stress of $284.2\ \text{MPa}$ in order to introduce initial cracks, and were then again annealed at 600°C in a vacuum to relieve the residual stresses due to fatigue. All specimens were annealed after every test, if they survived 10^7 cycles, and the crack length was then measured, either by a replica method, or with an optical microscope.

The amount of crack growth, λ , was defined, as shown in Fig. 4.18, as the sum ($\lambda_1 + \lambda_2$) of the lengths, λ_1 and λ_2 , of the two new cracks which initiated at the end of the initial crack.

Fig. 4.19 shows an initial crack, and the behaviour of cracks after testing. One specimen was used for the test series, in order to avoid the preparation of many specimens. It should be noted that the specimen was annealed, after every test to 10^7 cycles, before the next test was carried out.

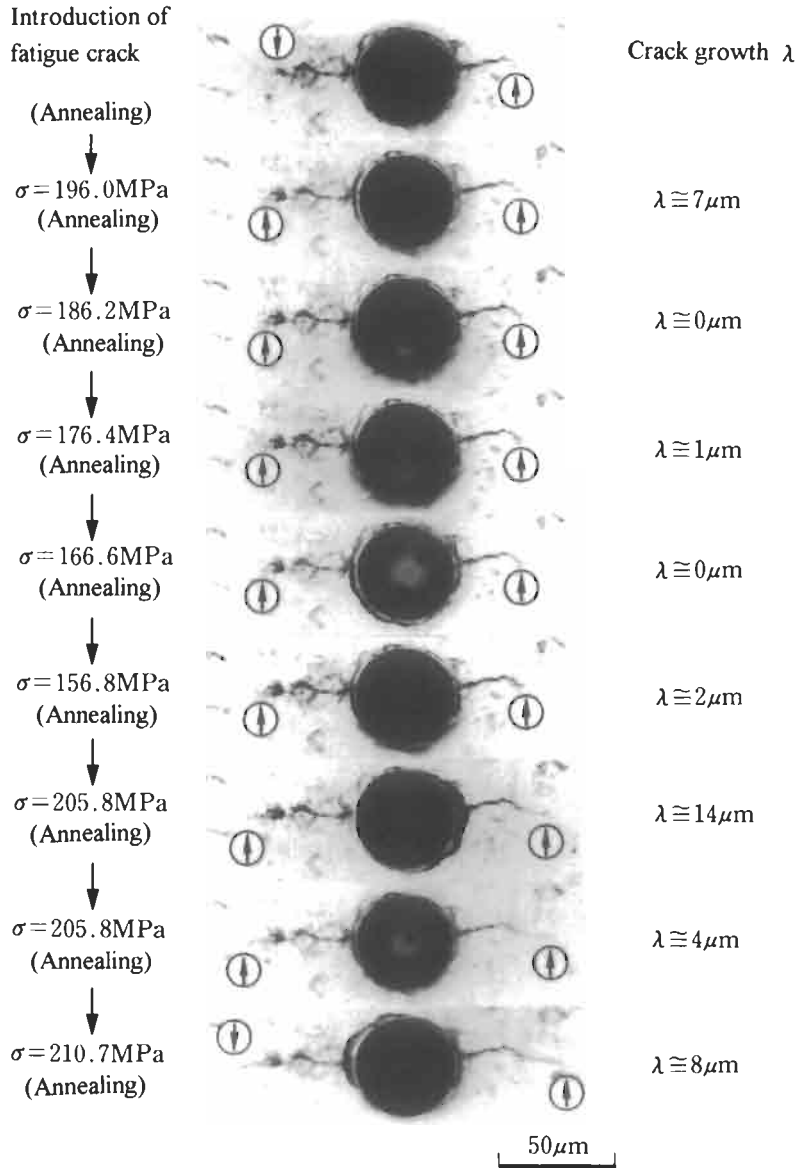


Figure 4.19 Crack initiation from an initial fatigue crack, and non-propagation behaviour (initial crack length, $l = 100 \mu\text{m}$).

Fig. 4.20 shows the relationships between the initial crack length, l , the stress amplitude, σ , and the amount of crack propagation, λ . Despite the data scatter, it is evident that λ increases approximately linearly with increasing stress. The intersection of a straight line with an abscissa, that is at $\lambda = 0$, defines the critical stress, σ_{wi} , under

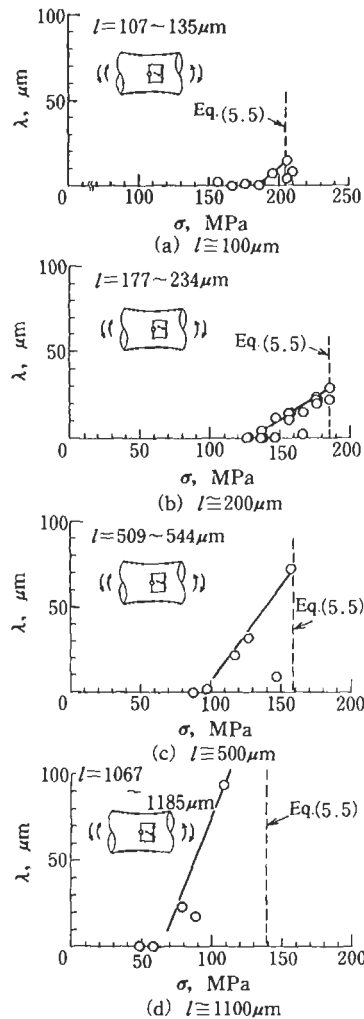


Figure 4.20 Relationship between applied stress, σ , and crack growth length, λ , at initial crack length, l .

which no cracks initiate from the initial ideal crack. Values of σ_{wi} , estimated from Fig. 4.20 are $\sigma_{wi} = 180$ MPa for $l = 100 \mu\text{m}$, $\sigma_{wi} = 130$ MPa for $l = 200 \mu\text{m}$, $\sigma_{wi} = 90$ MPa for $l = 500 \mu\text{m}$, and $\sigma_{wi} = 60$ MPa for $l = 1100 \mu\text{m}$.

Fig. 4.20 also shows predictions of values of σ_w (fatigue limit). These were estimated using Eq. 5.5 (see Chapter 5), assuming that cracks were semicircular. The intersection of the straight line defining λ with the vertical line, obtained from Eq. 5.5, predicts the maximum length of non-propagating cracks, λ_{\max} , as $\lambda_{\max} \cong 0.15l$. Fig. 4.21 was plotted using the same data as was used in Fig. 4.20. Fig. 4.21 shows the relationship between K_{\max} and the length, λ , of a non-propagating crack from an initial crack. K_{\max}

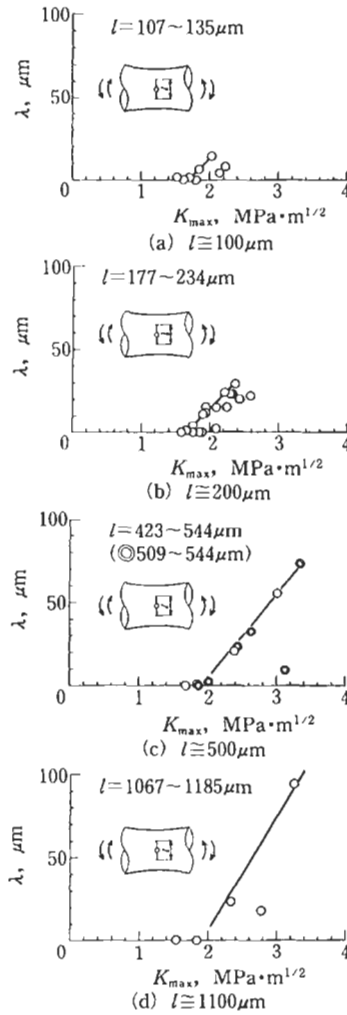


Figure 4.21 Relationship between K_{\max} and crack growth length, λ , at initial crack length, l ($R = -1$).

was calculated using Eq. 2.8. Following the procedure used for the determination of σ_{wi} , we can determine the critical value, $K_{\max,th}$, under which no cracks initiate from initial cracks. Consequently, we have $K_{\max,th} \cong 1.8 \text{ MPa}\cdot\text{m}^{1/2}$, regardless of crack size.

If an initial crack shows no growth, then it can be regarded as an ideal crack, and the value of K_{op} can be estimated using the Dugdale model [28]. Using a numerical calculation based on the Dugdale model, we estimated $\Delta K_{eff} = 2.0K_{\max}$ under our experimental conditions ($R = -1.0$) [21]. This means that a crack is open during a complete cycle. This conclusion is in agreement with the experimental result that K_{\max} has a constant value at $\sigma = \sigma_{wi}$. This phenomenon is not observed for large cracks. The values of ΔK_{th} for long or large cracks do not increase monotonically, for

various materials, with increasing tensile strength. This is because the crack closure phenomenon [23], caused by small-scale yielding at a crack tip, always affects the value of the effective stress intensity factor range.

As described above, it has been made clear that there are two important critical stresses for structures containing initial cracks. One is the maximum critical stress (fatigue limit), σ_w , under which fatigue cracks emanating from an initial crack stop propagating. The other is the critical stress, σ_{wi} , under which no cracks initiate from initial cracks. It must be noted that if defects occupying three-dimensional space (volume) are contained in a material, then the fatigue limit stress, σ_w , is determined only by the square root of the projected area, \sqrt{area} . The value is then identical to that for a 3D crack having the same \sqrt{area} , even though the corresponding values of σ_{wi} for the defect and the crack are completely different.

4.5 References

1. E. Siebel and M. Stieler: Ungleichformige Spannungsverteilung bei Schwingender Beanspruchung, VDI Z., **97(5)** (1955), 121–126.
2. H. Nisitani: Size Effects of Branch Point and Fatigue Limit of Carbon Steel in Rotary Bending Tests, Trans. Jpn. Soc. Mech. Eng., **34(259)** (1968), 371–382.
3. H. Nisitani and M. Endo: Unifying Treatment of Notch Effects in Fatigue, Trans. Jpn. Soc. Mech. Eng. A, **51(463)** (1985), 784–789.
4. H. Kitagawa and S. Takahashi: Fracture Mechanics Approach to Very Small Fatigue Crack Growth and to the Threshold Condition, Trans. Jpn. Soc. Mech. Eng. A, **45(399)** (1979), 1289–1303.
5. N.E. Frost, L.P. Pook and K. Denton: A Fracture Mechanics Analysis of Fatigue Crack Growth Data for Various Materials, Eng. Fract. Mech., **3** (1971), 109–126.
6. H. Kobayashi and H. Nakazawa: A Stress Criterion for Fatigue Crack Propagation in Metals, Proc. 1st Int. Conf. Mech. Behav. Mater., Kyoto, II, 1972, pp. 199–208.
7. M.H. El Haddad, K.N. Smith and T.H. Topper: Fatigue Crack Propagation of Short Crack, J. Eng. Mater. Technol, Trans. ASME, **101** (1979), 42–46.
8. S. Usami and S. Shida: Elastic–Plastic Analysis of the Fatigue Limit for a Material with Small Flaws, Fatigue Eng. Mater. Struct., **1** (1979), 471–481.
9. K. Tanaka, Y. Nakai and M. Yamashita: Fatigue Growth Threshold of Small Cracks, Int. J. Fract., **17(5)** (1981), 519–533.
10. T. Isibasi and T. Uryu: Fatigue Strength of Carbon Steel Bars with Round-Crack, Rep. Res. Inst. Appl. Mech., Kyushu Univ., **II(6)** (1953) 65–74.
11. N.E. Frost: A Relation between the Critical Alternating Propagation Stress and Crack Length for Mild Steel, Proc. Int. Mech. Eng., **173(35)** (1959), 811–827.
12. H. Kobayashi and H. Nakazawa: The Effects of Notch Depth on the Initiation Propagation and Non-propagation of Fatigue Cracks, Trans. Jpn. Soc. Mech. Eng. Ser. I, **35(277)** (1969), 1856–1863.
13. Y. Murakami, S. Fukuda and T. Endo: Effect of Micro-hole on Fatigue Strength [1st Report, Effect of Micro-hole (Dia.: 40, 50, 80, 100 and 200 μm) on the Fatigue Strength of 0.13% and 0.46% Carbon Steels], Trans. Jpn. Soc. Mech. Eng. Ser. I, **44(388)** (1978), 4003–4013.
14. Y. Murakami and M. Endo: A Geometrical Parameter for the Quantitative Estimation of the Effects of Small Defects on Fatigue Strength of Metals, Trans. Jpn. Soc. Mech. Eng. A, **49(438)** (1983), 127–136.
15. Y. Murakami, Y. Tazunoki and T. Endo: Existence of Coaxing Effect and Effect of Small Artificial Holes of 40–200 μm Diameter on Fatigue Strength in 2017S-T4 Al Alloy and 7 : 3 Brass, Trans. Jpn. Soc. Mech. Eng. A, **47(424)** (1981), 1293–1300.
16. Y. Murakami, H. Kawano and T. Endo: Effect of Micro-Hole on Fatigue Strength (2nd Report, Effect of Micro-Hole of 40 μm –200 μm in Diameter on the Fatigue Strength of Quenched or Quenched and Tempered 0.46% Carbon Steel), Trans. Jpn. Soc. Mech. Eng. A, **45(400)** (1979), 1479–1486.

17. Y. Murakami, M. Abe and T. Kiyota: Effects of Small Defects and Inclusions on Fatigue Strength of Maraging Steel, *Trans. Jpn. Soc. Mech. Eng. A*, **53(492)** (1987), 1482–1491.
18. M. Kikukawa, M. Jono, K. Tanaka and M. Takatani: Measurement of Fatigue Crack Propagation and Crack Closure at Low Stress Intensity Level by Unloading Elastic Compliance Method, *J. Soc. Mater. Sci., Jpn.*, **25(276)** (1976), 899–903.
19. M. Kikukawa, M. Jono and Y. Kondo: An Estimation Method of Fatigue Crack Propagation Rate under Varying Loading Conditions of Low Stress Intensity Level, *Trans. Jpn. Soc. Mech. Eng. A*, **47(417)** (1981), 468–482.
20. Y. Murakami and M. Endo: Effects of Hardness and Crack Geometry on ΔK_{th} of Small Cracks, *J. Soc. Mater. Sci., Jpn.*, **35(395)** (1986), 911–917.
21. Y. Murakami and K. Matsuda: Dependence of Threshold Stress Intensity Factor Range ΔK_{th} on Crack Size and Geometry, and Material Properties, *Trans. Jpn. Soc. Mech. Eng. A*, **52(478)** (1986), 1492–1499.
22. Y. Murakami and K. Matsuda: Threshold Stress for Fatigue Crack Initiation from a Small Crack, *Trans. Jpn. Soc. Mech. Eng. A*, **53(489)** (1987), 871–877.
23. W. Elber: The Significance of Fatigue Crack Closure. *Damage Tolerance in Aircraft Structures*, ASTM STP, **486** (1971), 230–242.
24. N. Walker and C.J. Beevers: A Fatigue Crack Closure Mechanism in Titanium, *Fatigue Eng. Mater. Struct.*, **1** (1979), 135–148.
25. K. Minakawa and A.J. McEvily: On Crack Closure in the Near-Threshold Region, *Scr. Metall.*, **15** (1981), 633–636.
26. K. Endo, K. Komai and K. Ohnishi: Effects of Stress History and Corrosive Environment on Fatigue Crack Propagation, *Mem. Fac. Eng. Kyoto Univ.*, **31(1)** (1969), 25–46.
27. R.O. Ritchie, S. Suresh and C.M. Moss: Near-Threshold Fatigue Crack Growth in a 1 1/2 Cr–Mo Pressure Vessel Steel in Air and Hydrogen, *J. Eng. Mater. Technol., Trans. ASME, Ser. H.*, **102** (1980), 293–299.
28. D.S. Dugdale: Yielding of Steel Sheets Containing Slits, *J. Mech. Phys. Solids*, **8** (1960), 100–104.

Chapter 5

Effect of Hardness H_V on Fatigue Limits of Materials Containing Defects, and Fatigue Limit Prediction Equations

Methods for the prediction of the fatigue limit, σ_w , and also ΔK_{th} , from limited information are a long-standing request from engineers involved in the structural integrity assessment of machine components and structures. In response to this difficult request, many investigations have been conducted both to clarify fatigue mechanisms, and to identify the crucial controlling factors. However, as fatigue research expanded, the complicated nature of fatigue phenomena became apparent. Until recently, it was thought that there was so much diverse information on metal fatigue that the prediction of fatigue strength, from limited information, was almost impossible. This situation was worrying structural integrity engineers.

With the above situation as background, this chapter presents a simple and useful method, based on only two basic quantities, for the prediction of both ΔK_{th} and σ_w for materials containing small defects and cracks [1]. These two basic quantities are the Vickers hardness as the representative material parameter, and \sqrt{area} as the representative geometrical parameter for defects and cracks. \sqrt{area} is defined as the square root of the area obtained by projecting a small defect or crack onto a plane perpendicular to the maximum principal stress.

5.1 Relationship between ΔK_{th} and the Geometrical Parameter, \sqrt{area}

The possibility of using \sqrt{area} as the geometrical parameter was suggested in Chapter 4. As described in that chapter, if we accept that the fatigue limit of a material containing small defects or cracks is the threshold condition for non-propagating cracks, then it is rational to first consider ΔK_{th} , rather than immediately considering the fatigue limit stress, σ_w . If an explicit formulation for ΔK_{th} is available, then quantitative evaluation of σ_w is routine.

It is now well known that, in general, ΔK_{th} depends on crack size, and decreases with decreasing crack size [2–4].

Values of ΔK_{th} for various materials were compared in many previous studies, but the dependence of ΔK_{th} on crack size and geometry was not considered. Such incomplete comparisons are likely to lead to erroneous conclusions. One objective of

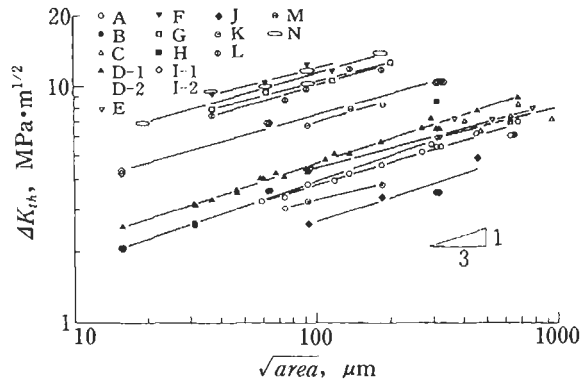


Figure 5.1 Relationship between ΔK_{th} and \sqrt{area} for various small defects and cracks. Letters correspond to those used in Table 5.1.

this chapter is to elucidate the dependence of ΔK_{th} on the shape and size of cracks, with special emphasis on small cracks. A large amount of available rotating bending fatigue data for various materials is analysed. The geometrical parameter \sqrt{area} , which is defined as the square root of the projected area of a defect or a crack onto a plane perpendicular to the maximum tensile stress, is proposed in order to unify the effects of various notches, holes, and cracks. An explicit relationship between ΔK_{th} and \sqrt{area} is confirmed for more than ten materials.

Another objective is to find the most appropriate material parameter for the characterisation of threshold behaviour. It should be noted that the dependence of ΔK_{th} on material parameters can only be made clear after finding the most appropriate geometrical parameter. Although various material parameters such as yield stress (σ_Y) [5], ultimate tensile stress (σ_U), and hardness (H_V or H_B) [6], may be correlated with ΔK_{th} , the Vickers hardness number, H_V , is chosen after observing the trend of many data, and also for the sake of simplicity in measurement and availability of data.

Finally, a simple formula is derived for the prediction of ΔK_{th} , in terms of one material parameter, H_V , and one geometrical parameter, \sqrt{area} .

Fig. 5.1 shows the results of rotating bending and tension-compression tests on various materials plotted in terms of the geometrical parameter \sqrt{area} [1]. The values of ΔK_{th} were calculated by substituting the stress range at the fatigue limit, $2\sigma_w$, for σ_0 in Eq. 2.8. Letters identifying materials correspond to those used in Table 5.1. Some of these data were obtained by the author's group, and some by other researchers.

The artificial defects investigated in this analysis are: very small drilled holes with diameters ranging from 40 to 500 μm and depths greater than 40 μm [7–14], very small and shallow notches with depths ranging from 5 to 300 μm [8,15–25], very shallow circumferential cracks with depths ranging from 30 to 260 μm [26], and Vickers hardness indentations of 72 μm surface length [8]. The geometries of the defects and cracks considered are shown in Fig. 5.2. The effects of work hardening and residual stresses, due to drilling the holes, were investigated and shown to be small [7]. In these tests almost all the notched specimens were electropolished after introducing the

Table 5.1 Vickers hardness, H_V , for various materials, and the type of defects evaluated using \sqrt{area}

Materials	H_V	Defects	Materials	H_V	Defects
A S10C (A)	120	Notch Hole	H: S50C (T)	319	Notch
B S30C (A)	153	Notch	I-1 S50C (T)	378	Notch
C S35C (A)	160	Notch Hole	I-2 S50C (T)	375	Notch
D-1. S45C (A)	180	Notch	J: 7/3 Brass	70	Notch Hole
D-2 S45C (A)	170	Hole	K: Al alloy (2017-T4)	114	Hole
E. S50C (A)	177	Notch Crack	L Stainless Steel (SUS603)	355	Hole
F S45C (Q)	650	Hole	M: Stainless Steel (YUS170)	244	Hole
G S45C (T)	520	Hole	N Maraging Steel	720	Vickers Indentation, Hole, Notch

Letters correspond to those used in Figs. 5.1, 5.3 and 5.4: A = annealed, Q = quenched, T = quenched and tempered. S10C, etc. mean structural carbon steels and the number indicates the nominal carbon content such as 0.10%.

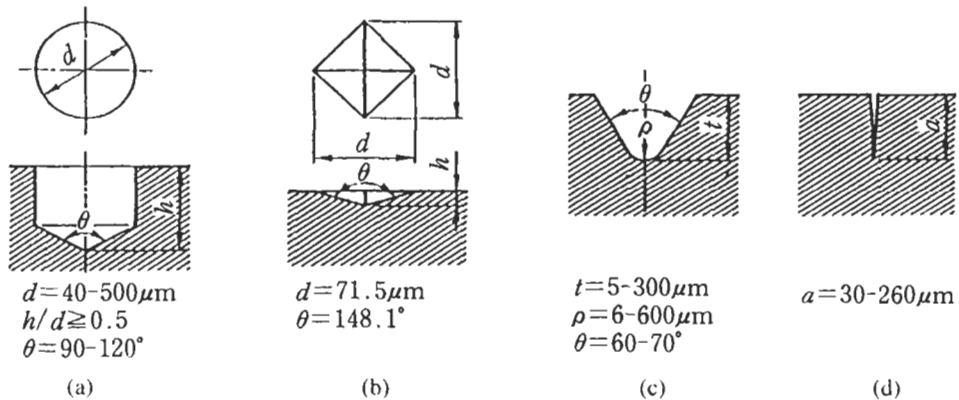


Figure 5.2 Geometries of artificial defects. (a) Hole. (b) Vickers indentation. (c) Notch. (d) Circumferential crack.

notches,¹ and the cracked specimens were annealed after introducing the fatigue cracks.¹ Accordingly, the effects of work hardening would be expected to be negligible.

It must be noted [8], that an apparently very shallow circumferential notch or crack with a depth of 0.3 mm and which may be regarded as a 2D crack, is equivalent to a 3D surface defect of $\sqrt{area} = 950 \mu\text{m}$, and also that an apparently large Vickers hardness indentation of $72 \mu\text{m}$ in surface length has a small \sqrt{area} of less than $20 \mu\text{m}$.

From Fig. 5.1 it can be seen that adoption of the new parameter \sqrt{area} characterises threshold behaviour for the data on very small cracks.

For $\sqrt{area} < 1000 \mu\text{m}$, a relationship between ΔK_{th} and \sqrt{area} , on logarithmic

¹ With regard to the detail, see Refs. [35-47].

scales is approximately linear, and has a slope of 1/3. Hence the following expression holds regardless of material:

$$\Delta K_{th} \propto (\sqrt{area})^{1/3} \quad (5.1)$$

5.2 Material Parameter H_V which Controls Fatigue Limits

Fig. 5.1 shows data for an aluminum alloy and 70/30 brass, as well as data for various steels.² The Vickers hardness, H_V , for these materials is shown in Table 5.1. The H_V range, from 70 to 720, is of an order of magnitude.

From the trends of ΔK_{th} in Fig. 5.1, it may be seen that materials having higher Vickers hardness show higher values of ΔK_{th} , and concomitant higher fatigue strengths. However, the trends cannot be expressed in a simple form, such as $\Delta K_{th} \propto H_V$. It has been observed empirically that the fatigue limit of a specimen, containing a notch or a defect, is not directly proportional to the Vickers hardness. This is presumably because the occurrence of non-propagating cracks follows a different relationship. In other words, a crack is likely to show non-propagating behaviour in soft materials, whereas for hard steels it is difficult to find non-propagating cracks at the fatigue limit. With increasing hardness, non-propagating cracks occur only within a narrow range of stress amplitude, and in this case are usually very short [8,10,11,27]. Therefore, it may be concluded that ΔK_{th} does not follow a function of the form $\Delta K_{th} \propto H_V$, or $\Delta K_{th} \propto H_V^q$. Rather, for a wide range of H_V , the difference in the threshold behaviour between soft and hard materials may be expressed by:

$$\Delta K_{th} \propto (H_V + C) \quad (5.2)$$

where C is a material-independent constant. In order to check the validity of this expression Eq. 5.1 was considered, and values of $\Delta K_{th}/(\sqrt{area})^{1/3}$ were plotted against H_V for many data. Apart from a few exceptional data for stainless steels, the validity of Eq. 5.2 was confirmed. Combining Eqs. 5.1 and 5.2 leads to the following equation, which may be expected to hold for a wide range of materials:

$$\Delta K_{th} = C_1(H_V + C_2)(\sqrt{area})^{1/3} \quad (5.3)$$

where C_1 and C_2 are material independent constants.

The constants C_1 and C_2 in Eq. 5.3 can be determined by applying the least squares method to the data in Fig. 5.1, and this leads to:

² Thus, ΔK_{th} for short or small cracks increases with H_V , and has a correlation with static strength. As described in Chapter 4 (page 53), this is because at the threshold region the applied stress for small cracks is high, accordingly cracks are likely to be open for most of a load cycle regardless of material, so materials having intrinsically strong microstructures also have higher values of ΔK_{th} . On the other hand, in the case of long cracks, low strength materials have large crack tip plastic zones. This induces a strong crack closure phenomenon, which reduces the effective stress intensity factor range, ΔK_{eff} , with a concomitant decrease in effective load. Therefore, the values of ΔK_{th} for low strength materials are not necessarily small, so we have the impression that values of ΔK_{th} for high strength materials are unexpectedly low.

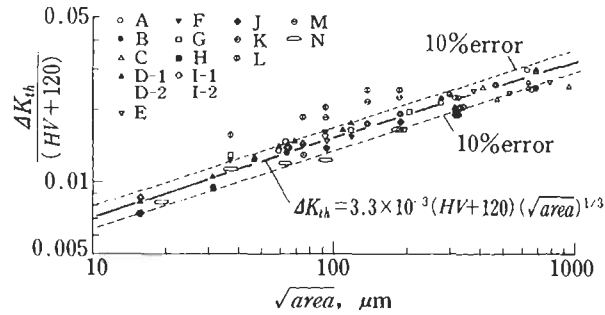


Figure 5.3 Relationship between $\Delta K_{th}/(H_V + 120)$ and \sqrt{area} . Rotating bending, letters correspond to those used in Table 5.1.

$$\Delta K_{th} = 3.3 \times 10^{-3} (H_V + 120) (\sqrt{area})^{1/3} \quad (5.4)$$

where ΔK_{th} is in $\text{MPa m}^{1/2}$ and \sqrt{area} is in μm .

Sumita et al. [28] and Araki [29] reported that the work hardening modulus could be a useful material parameter. Their point is consistent with the present analysis, in that fatigue limits and values of ΔK_{th} for materials containing defects and small cracks are not simply proportional to H_V , but are given by Eq. 5.2.

Fig. 5.3 compares the experimental data shown in Fig. 5.1 with the correlation given by Eq. 5.4. It is pleasing to note that various data for H_V ranging from 70 to 720 are well represented by the equation.³

Combining Eqs. 5.4 and 2.8, the fatigue limit, σ_w , of a cracked specimen can be expressed as:

$$\sigma_w = 1.43(H_V + 120) / (\sqrt{area})^{1/6} \quad (5.5)$$

where σ_w is the nominal stress defined using gross area and is in MPa .⁴

Although Eq. 4.1, $\sigma_w^n \sqrt{area} = C$, is very accurate for individual materials, a disadvantage, as pointed out by Kawai and Kasai [30], is that we need fatigue tests for individual materials in order to determine n and C . This disadvantage is overcome by Eq. 5.5.

Table 5.2 compares values, as predicted by Eqs. 5.4 and 5.5, with experimental results. For most materials, except two types of stainless steel, the error is less than 10%.

It should be noted that Figs. 5.3 and 5.4, and Table 5.2, include many results for specimens containing extremely shallow notches (depths ranging from 5 to 20 μm), small cracks, or very small holes (diameters ranging from 40 to 500 μm). Although it can be said that the theory of notch effects has been established for medium and deep notches, conventional theories [22,23,31–36] may not be applicable to extremely

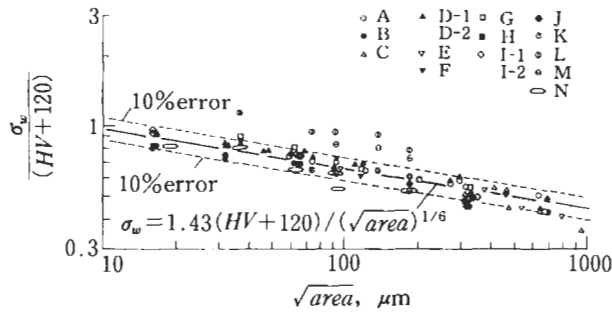
³ The reason why Eq. 5.4 does not predict ΔK_{th} satisfactorily, for the two types of stainless steel [14], is presumably because non-propagating cracks are unlikely to be observed in stainless steels, even at a sharp notch [38–40]. The existence of non-propagating cracks for the stainless steel data [14] was not checked during the present study.

⁴ $\Delta\sigma_w = 2\sigma_w$ should be substituted for σ_0 in Eq. 2.8; \sqrt{area} is in μm in Eq. 5.4 and m in Eq. 2.8.

Table 5.2 Comparison between experimental results and predictions using Eqs. 5.4 and 5.5

Materials	Ref.	Defects	HV	\sqrt{area} μm	ΔK_{th} MPa $\cdot\text{m}^{1/2}$		σ_w MPa		Error %
					Exp.	Cal.	Exp.	Cal.	
A: S10C (A)	15	Notch	120	632	6.1	6.8	105	117	11.8
A: S10C (A)	16	Notch	120	632	6.1	6.8	105	117	11.8
			120	632	6.1	6.8	105	117	11.8
A: S10C (A)	17	Notch	120	316	5.5	5.4	134	132	-1.6
			120	316	5.5	5.4	134	132	-1.6
A: S10C (A)	7, 9	Hole	120	74	3.4	3.3	172	168	-2.5
			120	60	3.2	3.1	181	174	-3.9
			120	93	3.8	3.6	172	162	-6.0
			120	136	4.2	4.1	157	152	-3.5
			120	119	4.0	3.9	157	155	-1.3
			120	185	4.6	4.5	147	144	-2.0
			120	272	5.2	5.1	137	135	-1.5
			120	298	5.7	5.3	142	133	-6.4
			120	463	6.3	6.1	128	124	-3.4
			120	681	7.1	7.0	118	116	-1.8
A: S10C (A)	12	Hole	120	632	7.1	6.8	123	117	-4.6

(A) Annealed, (Q) Queched, (T) Quenched and Tempered

Figure 5.4 Relationship between $\sigma_w/(H_V + 120)$ and \sqrt{area} . Rotating bending, letters correspond to those used in Table 5.1.

shallow notches. However, from the viewpoint of the present study, extremely shallow notches can be placed in the same category as small cracks, and the fatigue limit is easily predicted using either Eq. 5.4 or Eq. 5.5.

5.3 Application of the Prediction Equations

After Eqs. 5.4 and 5.5 were derived, data in further references [26,35,41-53] were investigated. Only a few of the data included hardness values. Therefore, H_V was estimated by using the relationship between H_V and H_B (ASTM E140), and an

Table 5.2 (continued)

Materials	Ref.	Defects	H_V	$\sqrt{\text{area}}$ μm	ΔK_{th} $\text{MPa}\cdot\text{m}^{1/2}$		σ_w MPa		Error %
					Exp.	Cal.	Exp.	Cal.	
B: S30C (A)	18	Notch	153	16	2.0	2.3	220	247	12.3
			153	16	2.1	2.3	225	247	9.9
			153	16	2.1	2.3	225	247	9.9
			153	32	2.6	2.8	199	220	10.7
			153	32	2.6	2.8	204	220	8.0
			153	32	2.7	2.8	208	220	5.5
			153	63	3.6	3.6	196	196	-0.2
			153	63	3.6	3.6	196	196	-0.2
			153	63	3.6	3.6	196	196	-0.2
			153	316	5.7	6.1	140	150	7.3
			153	316	5.7	6.1	140	150	7.3
			153	316	5.9	6.1	144	150	4.0
			C: S35C (A)	19	Notch	160	632	7.0	7.9
160	632	7.1				7.9	122	137	12.4
160	632	7.3				7.9	126	137	8.4
C: S35C (A)	20	Notch	160	316	5.9	6.3	144	154	6.5
			160	474	6.4	7.2	127	144	13.1
			160	949	7.2	9.1	101	128	26.3
C: S35C (A)	55	Hole	160	409	7.1	6.9	152	147	-3.2
			160	681	8.2	8.1	137	135	-1.3
D-1: S45C (A)	21~23	Notch	180	16	2.6	2.5	280	271	-3.1
			180	16	2.5	2.5	275	271	-1.4
			180	16	2.5	2.5	275	271	-1.4
			180	32	3.2	3.1	245	242	-1.4
			180	32	3.2	3.1	250	242	-3.4
			180	32	3.2	3.1	245	242	-1.4
			180	316	6.6	6.7	160	165	2.9
			180	316	6.6	6.7	160	165	2.9
			180	316	6.2	6.7	151	165	8.9
D-2: S45C (A)	7, 9	Hole	170	37	3.3	3.2	235	228	-3.2
			170	46	3.5	3.4	226	219	-3.0
			170	68	4.3	3.9	226	206	-9.1
			170	48	3.7	3.5	230	218	-5.2
			170	74	4.2	4.0	211	203	-3.9
			170	109	4.8	4.6	201	190	-5.5
			170	60	4.0	3.7	226	210	-7.0
			170	60	4.0	3.7	226	210	-7.0
			170	93	4.5	4.3	201	195	-2.8
			170	93	4.3	4.3	196	195	-0.4
			170	136	5.1	4.9	191	183	-4.1
			170	119	5.1	4.7	201	187	-6.9
			170	185	5.7	5.5	181	174	-3.9
			170	272	6.5	6.2	172	163	-5.2
			170	298	7.2	6.4	181	161	-11.2
170	463	7.8	7.4	157	149	-4.9			
170	681	8.8	8.4	147	140	-4.7			

(A) Annealed, (Q) Queched, (T) Quenched and Tempered

Table 5.2 (continued)

Materials	Ref.	Defects	HV	\sqrt{area} μm	ΔK_{th} $\text{MPa}\cdot\text{m}^{1/2}$		σ_w MPa		Error %
					Exp.	Cal.	Exp.	Cal.	
E: S50C (A)	24	Notch	177	316	5.9	6.7	144	163	13.2
			177	316	5.9	6.7	144	163	13.2
E: S50C (A)	26	Crack	177	95	4.4	4.5	196	199	1.5
			177	379	7.2	7.1	160	158	-1.2
			177	538	7.1	8.0	133	149	11.9
			177	791	8.0	9.1	123	140	13.5
F: S45C (Q)	10, 11	Hole	650	37	9.3	8.5	667	604	-9.4
			650	62	10.3	10.1	568	554	-2.5
			650	93	12.4	11.5	559	518	-7.4
			650	117	11.7	12.4	470	499	6.1
G: S45C (T)	10, 11	Hole	520	37	8.0	7.0	568	502	-11.6
			520	62	9.4	8.4	519	460	-11.3
			520	117	10.5	10.3	421	414	-1.6
			520	202	12.5	12.4	382	378	-1.0
H: S50C (T)	24	Notch	319	316	8.6	9.9	209	241	15.3
I-1: S50C (T)	24	Notch	378	316	10.3	11.2	252	273	8.2
I-1: S50C (T)	18	Notch	375	16	4.3	4.1	468	447	-4.4
			375	16	4.4	4.1	478	447	-6.4
			375	63	6.8	6.5	373	355	-4.8
			375	63	6.8	6.5	373	355	-4.8
			375	316	10.3	11.1	252	272	7.6
			375	316	10.3	11.1	252	272	7.6
J: 70/30 Brass	25	Notch	70	316	3.6	4.3	87	104	19.5
			70	316	3.6	4.3	87	104	19.5
J: 70/30 Brass	13	Hole	70	93	2.6	2.8	118	128	8.4
			70	185	3.4	3.6	108	114	5.6
			70	463	4.9	4.8	98	98	-0.3
K: Al alloy (2017-T4)	13	Hole	114	74	3.0	3.2	152	164	7.6
			114	93	3.3	3.5	147	158	7.2
			114	185	3.9	4.4	123	140	14.1
L: Stainless steel (SUS 603)	14	Hole	355	37	7.4	5.2	530	373	-29.7
			355	74	8.7	6.6	441	332	-24.7
			355	93	9.8	7.1	441	320	-27.5
			355	139	11.7	8.1	432	299	-30.8
			355	185	11.7	8.9	373	285	-23.6
M: Stainless steel (YUS 170)	14	Hole	244	93	6.7	5.4	304	245	-19.4
			244	139	8.0	6.2	294	229	-22.1
			244	185	8.3	6.8	265	218	-17.6
N: Maraging steel	8	Vickers indent Hole	720	19	6.9	7.4	686	736	7.3
N: Maraging steel	8		720	37	9.5	9.2	677	659	-2.7
			720	93	11.7	12.5	530	566	6.7
			720	185	13.8	15.8	441	504	14.3
N: Maraging steel	8	Notch	720	63	10.0	11.0	546	603	10.4
			720	95	10.2	12.6	454	563	24.0

(A) Annealed, (Q) Queched, (T) Quenched and Tempered

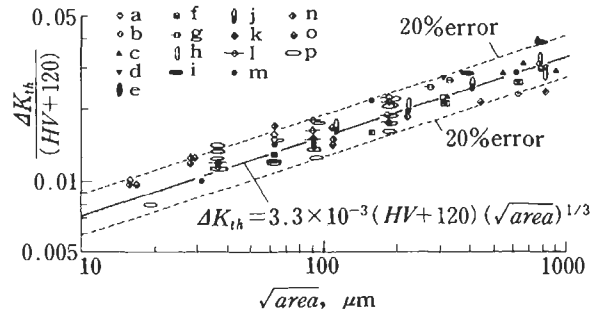


Figure 5.5 Relationship between $\Delta K_{th}/(H_V + 120)$ and \sqrt{area} . (Other researcher's data, letters correspond to those used in Table 5.3.)

empirical equation which is thought to hold between ultimate tensile strength and H_B , that is:

$$\sigma_U \cong 0.36(9.8 \times H_B) \quad (5.6)$$

where σ_U is in MPa and H_B in kgf/mm^2 .

The data investigated included not only rotating bending fatigue test results, but also some tension–compression fatigue test results ($R = -1$) [41,42].

Fig. 5.5 shows details of comparisons between predictions using Eq. 5.4 and the experimental data. Although the references examined lack data for very small values of

Table 5.3 Sources of data in Fig. 5.5

Materials	Defects	Ref.
a : 0.12%C steel	Fatigue crack	Isibasi, Uryu, Sato [43]
b : 0.53%C steel	Fatigue crack	Isibasi, Uryu, Sato[43]
c : SF60	Artificial crack, Hole	Ouchida, Kusumoto [44]
d : Mild steel	Fatigue crack	Frost [42]
e : S10C	Drilled hole	Murakami, Morinaga, Endo[41]
f : S20C	Circumferential notch	Nisitani [35,46]
g : S20C	Drilled hole	Nisitani, Kage [45]
		Hayashi et al [47]
h : S25C	Fatigue crack	Awatani, Matsunami [48]
i : S35C	Fatigue crack	Kobayashi, Nakazawa [49]
j : S45C	Fatigue crack	Murakami, Matsuda [50]
k : Eutectic steel	Circumferential crack	Kobayashi, Nakazawa [26]
l : Eutectic steel	Drilled hole	Harada et al [51]
m : 2.25Cr/1 Mo steel	Circumferential crack	Lukas et al [52]
n : SAE 1552 steel	Electrodischarged hole	Maikuma, Shimizu, Kawasaki [53]
o : SAE 9254 steel	Electrodischarged hole	Maikuma, Shimizu, Kawasaki [53]
p : Maraging steel	Hole, Notch, Vickers indent	Murakami, Abe, Kiyota [8]

\sqrt{area} , it may be concluded that Eq. 5.4 does predict ΔK_{th} very well for cracked or notched specimens provided that \sqrt{area} is less than 1000 μm .

5.4 Limits of Applicability of the Prediction Equations: Eqs. 5.4 and 5.5

As can be seen in Fig. 5.3, Eqs. 5.4 and 5.5 can be applied to small defects or cracks within some range of values of \sqrt{area} . Although the upper limit of \sqrt{area} for these equations is at present uncertain, it appears to be approximately 1000 μm . The lower limit of applicability depends on material properties and microstructures. From experiments, we have a finite value for the fatigue limit, σ_w , for specimens which do not contain defects or cracks. Theoretically, in this case $\sqrt{area} = 0$, and accordingly $\sigma_w = \infty$. However, this never occurs because cracks nucleate along slip bands or grain boundaries as a result of reversed slip in grains. That is, \sqrt{area} is not zero, and accordingly the fatigue limit of defect free specimens, σ_{w0} , is finite. Therefore, as discussed in previous studies [9–11], the lower limit for \sqrt{area} , for which Eqs. 5.4 and 5.5 are applicable, is related to the maximum length of non-propagating cracks, l_0 , which is observed in unnotched (defect free) specimens. It follows that, even if specimens do contain small defects or cracks before fatigue testing, and also if a fatigue limit, σ_w , calculated from values of \sqrt{area} and Eq. 5.5 is greater than σ_{w0} , then a value of σ_w is never measurable because such defects do not lower the fatigue strength of a specimen, and they are virtually harmless [9–11,13]. When we do know the value of σ_{w0} in advance, then the lower limit for \sqrt{area} can be determined using Eq. 5.5. When σ_{w0} is unknown, then its approximate value can be estimated using the empirical equation:

$$\sigma_{w0} \cong 0.5\sigma_U \cong 1.6H_V \quad (5.7)$$

where σ_{w0} and σ_U , the ultimate tensile strength, are in MPa, and H_V is in kgf/mm^2 . Previously, it has been stated that Eq. 5.7 is not necessarily applicable to high strength or hard steels [54]. However, this conclusion was based on experiments in which the original sites of fatigue fractures (slip bands or defects) were not precisely identified. Murakami et al. [10,11] showed, on the basis of careful investigation of fatigue fracture origins, that Eq. 5.7 does apply to hard steels provided that fatigue fracture is not caused by defects. This problem must be discussed carefully, and it is examined in detail in Chapter 6.

5.5 The Importance of the Finding that Specimens with an Identical Value of \sqrt{area} for Small Holes or Small Cracks Have Identical Fatigue Limits: When the Values of \sqrt{area} for a Small Hole and a Small Crack are Identical, are the Fatigue Limits for Specimens Containing these Two Defect Types Really Identical?

According to the earlier discussions, fatigue limits of materials containing small defects and cracks are determined by the microstructure hardness, H_V , and by the characteristic dimension for defects and cracks, \sqrt{area} . The prediction method based on this concept is named the \sqrt{area} parameter model [56,57]. However, previously, many

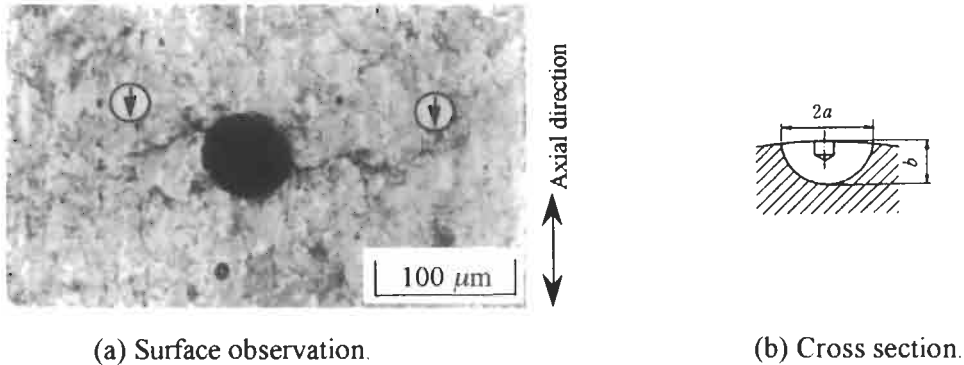


Figure 5.6 Cracks emanating from a small hole. (a) Surface observation. (b) Cross-section.

researchers and engineers did not believe that the fatigue limits for two specimens, one containing a drilled hole with a blunt profile, and the other a semi-elliptical crack, would be identical.

As explained earlier, the fatigue limit for a specimen, containing a small hole or crack, is the threshold condition for non-propagation of a crack emanating from an initial defect or crack, hence the initial value of \sqrt{area} is a more crucial geometrical factor than is the initial 3D defect shape. Nevertheless, there are researchers and engineers who pay much attention to differences in the stress concentrations due to holes and cracks, and vehemently question the validity of the above \sqrt{area} parameter model. The crucial evidence needed to refute this question is shown in the following.

In order to examine the validity of the \sqrt{area} parameter model, fatigue limits were compared for specimens containing either an artificial drilled hole, or an artificial surface crack, both with the same value of \sqrt{area} .

Fig. 5.6 shows the geometries of an artificial crack and the hole from which it was grown. The initial crack was introduced by fatigue testing a specimen containing an artificial hole with a diameter of $40\ \mu\text{m}$. Each specimen was annealed after the preliminary fatigue test to relieve residual stresses due to fatigue. All specimens, containing a hole or a crack, were annealed 0.45% C steel for which $H_V = 170$.

Since the specimens containing an initial crack were re-annealed after cracking, we may assume that the residual stresses due to fatigue were indeed relieved. Figs. 5.7 and 5.8 summarise the fatigue limits obtained by fatigue testing these two types of specimen.

Fig. 5.7 shows the relationship between ΔK_{th} and defect size, defined both as \sqrt{area} and as notch depth, t . Fig. 5.8 is a rearrangement of the linear data shown in Fig. 5.7, in which the fatigue limit, σ_w , is plotted against \sqrt{area} . For both holes and cracks, with \sqrt{area} smaller than $1000\ \mu\text{m}$, ΔK_{th} and σ_w can be correlated very accurately using Eq. 5.4 or Eq. 5.5 as appropriate. Thus, from a fatigue limit viewpoint, holes and cracks are equivalent when they do have the same value of \sqrt{area} .⁵

⁵ It must be noted that if we apply Eqs. 5.4 and 5.5 to defects or cracks with \sqrt{area} larger than $1000\ \mu\text{m}$, then predictions become unconservative. This is because for $\sqrt{area} > 1000\ \mu\text{m}$ ΔK_{th} tends to become constant (see Fig. 5.7).

This experimental fact is of crucial importance when we come to discuss the effects of nonmetallic inclusions on fatigue strength. Problems related to nonmetallic inclusions are discussed in Chapter 6. Although unequivocal experimental evidence demonstrating the equivalence of holes and cracks is presented, there may nevertheless be some researchers who do not believe the fact. They may ask “The influence of holes is exactly the same as cracks?”. As an answer to this question the author can present Table 5.4 and

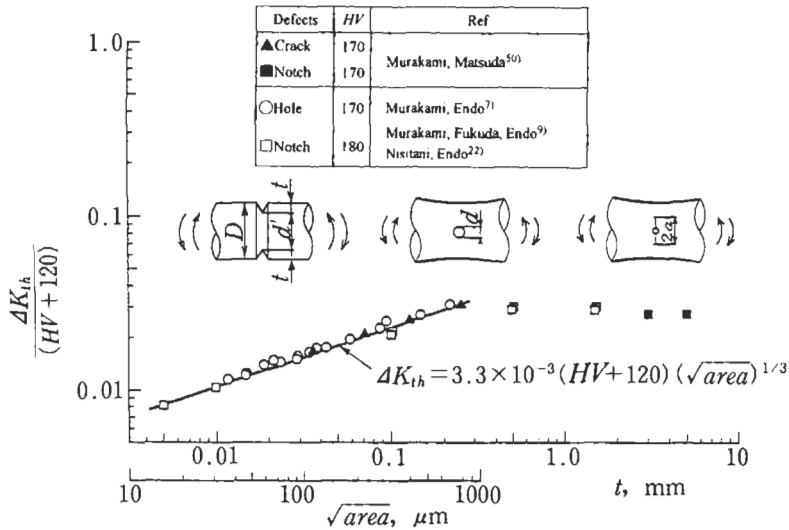


Figure 5.7 Relationship between $\Delta K_{th}/(H_V + 120)$ and \sqrt{area} for medium carbon steel specimens containing a small crack or a small defect.

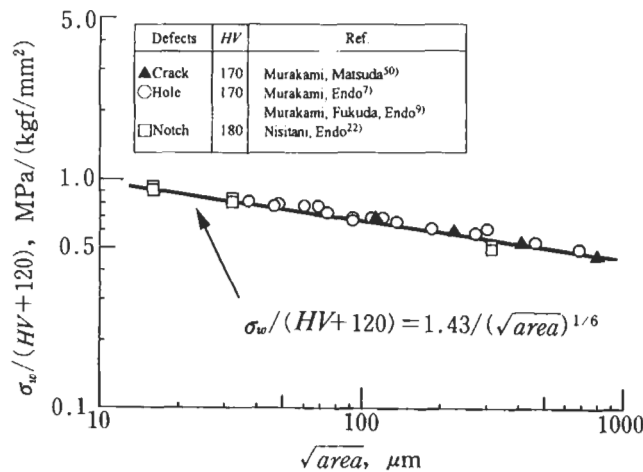
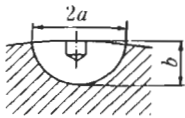
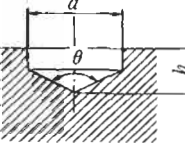


Figure 5.8 Comparison between the relationship of $\sigma_w/(H_V + 120)$ to \sqrt{area} for fatigue cracks and small defects.

Table 5.4 Comparison between the fatigue limits of specimens containing a small crack and a small defect having the same value of \sqrt{area} (medium carbon steel, rotating bending fatigue)

Crack and Hole	\sqrt{area} (μm)	Fatigue limit (MPa)
 <p> $2a = 213\mu\text{m}$ Aspect ratio $b/a = 0.7$ </p>	112	200.9
 <p> $d = 200\mu\text{m}$ $h = 100\mu\text{m}$ $\theta = 120^\circ$ </p>	115	200.9

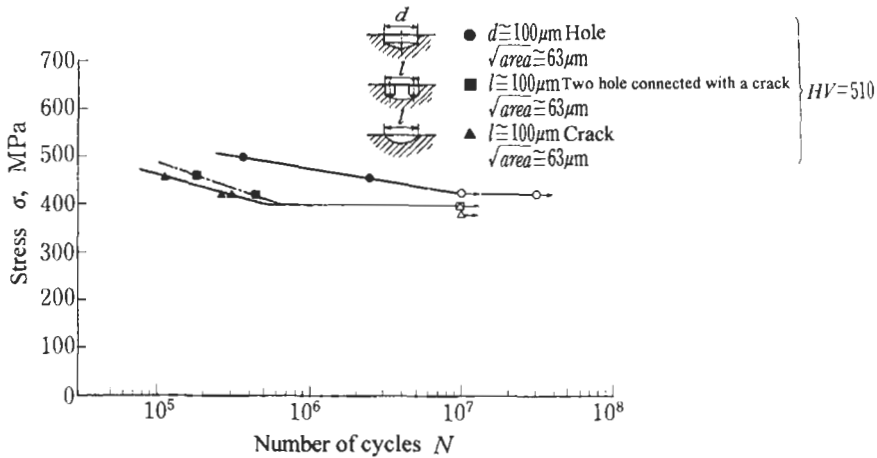


Figure 5.9 S–N curves for maraging steel specimens containing defects with the same value of \sqrt{area} .

Fig. 5.9. In a similar way to Fig. 5.8, Table 5.4 compares the fatigue limits of a specimen containing an initial crack with $\sqrt{area} = 112 \mu\text{m}$ with that for a specimen containing a hole with $\sqrt{area} = 115 \mu\text{m}$. The two fatigue limits are exactly the same: 200.9 MPa. An observation, described in the following, which was made after fatigue testing these two types of specimen, may help the understanding of this strange but rational phenomenon.

After fatigue testing, both types of specimen have new non-propagating cracks emanating either from hole corners, or from the ends of an initial crack. Thus, the final states of both specimen types are mechanically very similar, that is the final defect shapes are both ‘crack’. This explanation is only valid for stress levels close to the fatigue limits of specimens containing small defects. However, if we examine the behaviour of specimens containing small defects and which have a finite life, then

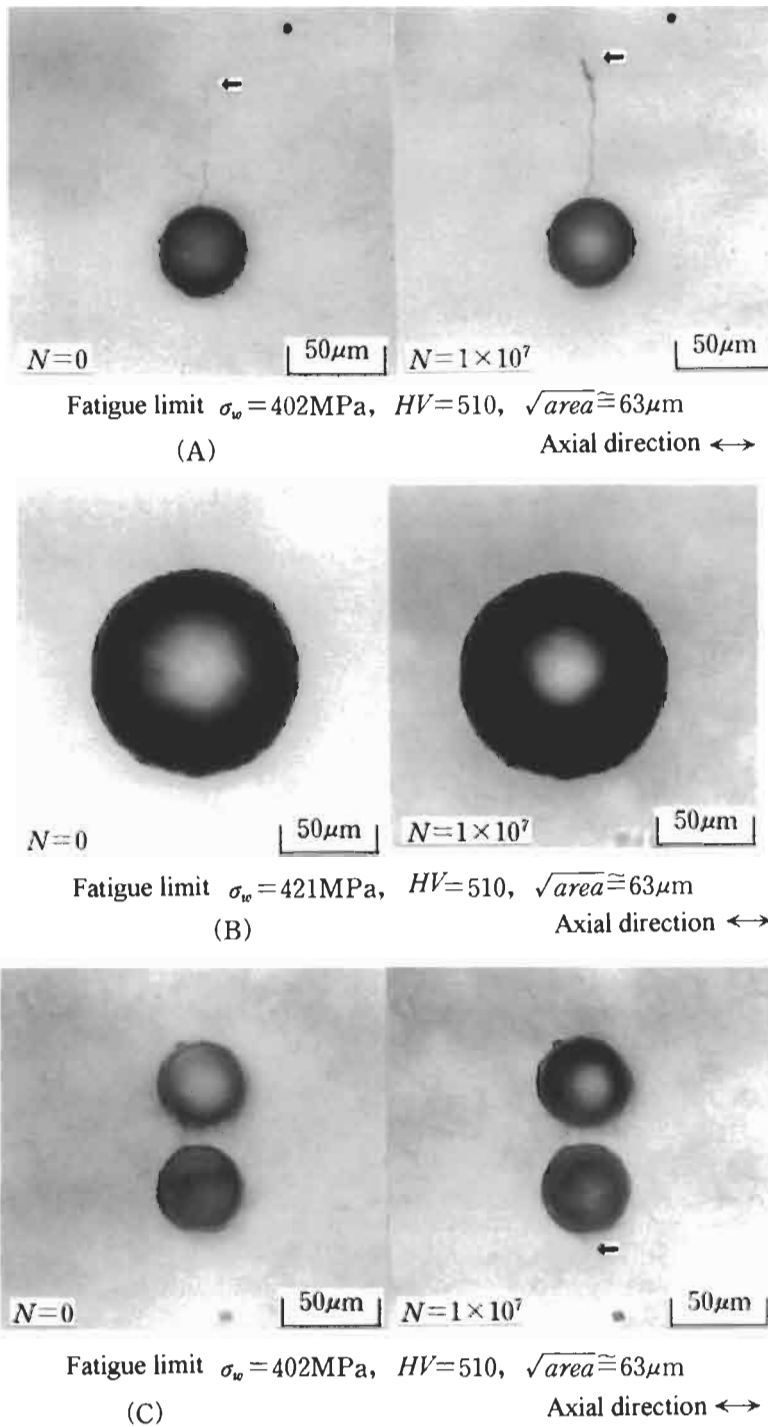


Figure 5.10 Conditions at the fatigue limit for specimens containing a small crack or a small defect with the same value of $\sqrt{\text{area}}$. (A) Specimen containing an initial crack. (B) Specimen containing an artificial hole. (C) Specimen containing two small holes connected by an initial fatigue crack.

differences between holes and cracks are indeed revealed. Namely, for identical values of $\sqrt{\text{area}}$ and at stresses higher than the fatigue limit, the life of a specimen containing a crack is always shorter than that of a specimen containing a hole. This is because the crack initiation life is much shorter for a specimen containing an initial crack. It must be noted that this discussion is only valid for small defects. As defects, such as holes and notches, become larger, the fatigue limit is likely to be higher than that for cracks having the identical value of $\sqrt{\text{area}}$.

Fig. 5.9 shows experimental results [58], for three types of defect introduced into a maraging steel, which help our understanding of fatigue behaviours at both the fatigue limit stress, σ_w , and at stresses higher than σ_w . The three defect types are (A) a crack with $\sqrt{\text{area}} \cong 63.2 \mu\text{m}$ (surface length $\cong 100 \mu\text{m}$), which was grown from an initial hole of $40 \mu\text{m}$ diameter, (B) a drilled hole of $100 \mu\text{m}$ diameter and $\approx 50 \mu\text{m}$ depth ($\sqrt{\text{area}} \cong 62.7 \mu\text{m}$), and (C) two adjacent small holes, of $40 \mu\text{m}$ diameter, which were linked by a crack grown during a preliminary fatigue test ($\sqrt{\text{area}} \cong 62.9 \mu\text{m}$). These defects were introduced before ageing the maraging steel, and $H_V = 290$. The specimens were then aged at 480°C for 5 h in a vacuum, following this treatment the hardness of the microstructure became $H_V = 510$. This material reveals more clearly the notch sensitivity characteristics of hard steels than does 0.46% C steel. Contrary to the commonly accepted prediction, the fatigue limits in tension–compression fatigue, for specimens containing these three defect types are approximately equal. In particular, the fatigue limits for defects (A) and (C) are exactly the same, and the difference between those for (A) (crack) and (B) (hole) is only 4.5%.

As can be seen in Fig. 5.10, the fatigue limits for specimens (A) and (C) are determined by the threshold condition for non-propagating cracks, but it is not clear whether non-propagating cracks determine the fatigue limit for specimen (B). Although there is little difference in the fatigue limits for these three defect types, clear differences appear between the S – N curves. In the finite life region, the lives of initially cracked specimens (A) are the shortest, and those of specimens containing holes (B) are the longest. These characteristics of materials containing defects of various shapes become very important when we discuss the influence of variously shaped nonmetallic inclusions.

5.6 References

1. Y. Murakami and M. Endo: Effects of Hardness and Crack Geometry on ΔK_{th} of Small Cracks, *J. Soc. Mater. Sci., Jpn.*, **35**(395) (1986) 911–917; see also Y. Murakami and M. Endo: Effects of Hardness and Crack Geometries on ΔK_{th} of Small Cracks Emanating from Small Defects. In: K.J. Miller and E.R. de los Rios (Eds): *The Behaviour of Short Fatigue Cracks*, EGF Publ. 1, Mech. Eng. Publ., 1986, pp. 275–293.
2. H. Kitagawa and S. Takahashi: Fracture Mechanical Approach to Very Small Fatigue Crack Growth and to the Threshold Condition, *Trans. Jpn. Soc. Mech. Eng. A*, **45**(399) (1979), 1289–1303.
3. H. Kobayashi and H. Nakazawa: A Stress Criterion for Fatigue Crack Propagation in Metals, *Proc. 1st Int. Conf. Mech. Behav. Mater.*, Kyoto, 11, 1972, pp. 199–208.
4. B.N. Leis, A.T. Hopper, J. Ahmad, D. Broek and M.F. Kanninen: Critical Review of The Fatigue Growth of Short Cracks, *Eng. Fract. Mech.*, **23**(5) (1986), 883–898.
5. Y. Nakai, K. Tanaka and R. Kawashima: Stress-Ratio Effect on Fatigue Crack Growth Threshold in

- Steels, *J. Soc. Mater. Sci., Jpn.*, **33(371)** (1984), 1045–1051.
6. K. Tanaka: Fatigue Crack Growth Property of Steel with particular Reference to Threshold Stress Intensity Range, ΔK_{th} , *Tetsu To Hagane*, **67(2)** (1981), 245–261.
 7. Y. Murakami and M. Endo: A Geometrical Parameter for the Quantitative Estimation of the Effects of Small Defects on Fatigue Strength of Metals, *Trans. Jpn. Soc. Mech. Eng. A*, **49(438)** (1983), 127–136.
 8. Y. Murakami, M. Abe and T. Kiyota: Effects of Small Defects and Inclusions on Fatigue Strength of Maraging Steel, *Trans. Jpn. Soc. Mech. Eng. A*, **53(492)** (1987), 1482–1491.
 9. Y. Murakami, S. Fukuda and T. Endo: Effect of Micro-Hole on Fatigue Strength [1st Report, Effect of Micro-Hole (Dia.: 40, 50, 80, 100 and 200 μm) on the Fatigue Strength of 0.13% and 0.46% Carbon Steels], *Trans. Jpn. Soc. Mech. Eng. Ser. I*, **44(388)** (1978), 4003–4013.
 10. Y. Murakami, H. Kawano and T. Endo: Effect of Micro-Hole on Fatigue Strength (2nd Report, Effect of Micro-Hole of 40–200 μm in Diameter on the Fatigue Strength of Quenched or Quenched and Tempered 0.46% Carbon Steel), *Trans. Jpn. Soc. Mech. Eng. A*, **45(400)** (1979), 1479–1486.
 11. Y. Murakami and T. Endo: The Effects of Small Defects on the Fatigue Strength of Hard Steels, *Proc. Int. Conf. Fatigue '81, Materials Experimentation and Design*, Warwick Univ., 1981, pp. 431–440.
 12. H. Nisitani and M. Kage: Rotating Bending Fatigue of Electropolished Specimens with Transverse Holes — Observation of Slip Bands and Non-Propagating Cracks Near the Holes, *Trans. Jpn. Soc. Mech. Eng. Ser. I*, **39(323)** (1973), 2005–2012.
 13. Y. Murakami, Y. Tazunoki and T. Endo: Existence of Coaxing Effect and Effect of Small Artificial Holes of 40–200 μm Diameter on Fatigue Strength in 2017S-T4 Al Alloy and 7:3 Brass, *Trans. Jpn. Soc. Mech. Eng. A*, **47(424)** (1981), 1293–1300.
 14. S. Nishida: Private communication, 1985.
 15. H. Ohba, Y. Murakami and T. Endo: Effects of Artificial Small Holes on Fatigue Strength of Notched Specimens, *Trans. Jpn. Soc. Mech. Eng. A*, **49(444)** (1983), 901–910.
 16. H. Nisitani and S. Nishida: The Change of Surface States and the Incipient Fatigue Cracks in Electro-Polished Low Carbon Steel (Plain and Notched Specimens) Subjected to Rotating Bending Stress, *Trans. Jpn. Soc. Mech. Eng. Ser. I*, **35(280)** (1969), 2310–2315.
 17. H. Nisitani and Y. Murakami: Torsional Fatigue and Bending Fatigue of Electropolished Low Carbon Steel Specimens, *Trans. Jpn. Soc. Mech. Eng. Ser. I*, **35(275)** (1969), 1389–1396.
 18. H. Nisitani: Correlation between Notch Sensitivity of a Material and Its Non-Propagating Crack, under Rotating Bending Stress, *Proc. 1st Int. Conf. Mech. Behav. Mater.*, Kyoto, I, 1972, pp. 312–322.
 19. H. Nisitani and K. Kawano: Non-Propagating Crack and Crack Strength of Shafts with a Shoulder Fillet Subjected to Rotary Bending, *Proc. 11th Jpn. Congr. Mater. Res.—Metallic Mater.*, 1968, pp. 49–51.
 20. H. Kobayashi and H. Nakazawa: The Effects of Notch Depth on the Initiation Propagation and Non-Propagation of Fatigue Cracks, *Trans. Jpn. Soc. Mech. Eng. Ser. I*, **35(277)** (1969), 1856–1863.
 21. H. Nisitani and M. Endo: Fatigue Strength of Carbon Steel Specimen Having an Extremely Shallow Notch (Discussion Based on Successive Observation), *Trans. Jpn. Soc. Mech. Eng. A*, **51(464)** (1985), 1008–1016.
 22. H. Nisitani and M. Endo: Unifying Treatment of Notch Effects in Fatigue, *Trans. Jpn. Soc. Mech. Eng. A*, **51(463)** (1985), 784–789.
 23. H. Nisitani and M. Endo: Unified Treatment of Deep and Shallow Notches in Rotating Bending Fatigue, *Basic Questions in Fatigue*, ASTM STP, **924** (1988), 136–153.
 24. H. Nisitani and I. Chishiro: Non-Propagating Micro-Cracks of Plain Specimens and Fatigue Notch Sensitivity in Annealed or Heat-Treated 0.5% C Steel, *Trans. Jpn. Soc. Mech. Eng. Ser. I*, **40(329)** (1974), 41–52.
 25. H. Nisitani and K. Okasaka: Effects of Mean Stress on Fatigue Strength, Crack Strength and Notch Radius at Branch Point, under Repeated Axial Stresses, *Trans. Jpn. Soc. Mech. Eng. Ser. I*, **39(317)** (1973), 49–59.
 26. H. Kobayashi and H. Nakazawa: On the Alternating Stress Required to Propagate a Fatigue Crack in Carbon Steels (Continued Report), *Trans. Jpn. Soc. Mech. Eng. Ser. I*, **36(291)** (1970), 1789–1798.
 27. Y. Murakami, H. Kawano and T. Endo: Effect of Artificial Small Defects on Fatigue Strength of Metals, *J. Soc. Mater. Sci., Jpn.*, **29(325)** (1980), 988–992.

28. M. Sumita, I. Uchiyama and T. Araki: A Model Experiment on Relationship between Fatigue Properties of Steel and Size, Shape, and Distribution of Inclusions, *Tetsu To Hagane*, **57(2)** (1971), 335–353.
29. T. Araki: Roles of Inclusions in Steel for the Fatigue Properties and Machinability Problems, Proc. Int. Symp. Inclusions and Their Influence on Material Behavior, Chicago, IL, 1988, pp. 149–155.
30. S. Kawai and K. Kasai: Consideration about Allowable Stress of Corrosion Fatigue, *Trans. Jpn. Soc. Mech. Eng. A*, **51(461)** (1985), 23–30.
31. T. Isibasi: Prevention of Fatigue and Fracture of Metals, Yokendo Ltd., Tokyo, 1967.
32. R.E. Peterson: Stress Concentration Factors, John Wiley, New York, 1953.
33. E. Siebel and M. Stieler: Ungleichformige Spannungsverteilung bei Schwingender Beanspruchung, *VDI Z.*, **97(5)** (1955), 121–126.
34. R.B. Heywood: Designing against Fatigue, Chapman and Hall, London, 1962.
35. H. Nisitani: Size Effects of Branch Point and Fatigue Limit of Carbon Steel in Rotary Bending Tests, *Trans. Jpn. Soc. Mech. Eng.*, **34(259)** (1968), 371–382.
36. R.A. Smith and K.J. Miller: Prediction of Fatigue Regimes in Notched Components, *Int. J. Mech. Sci.*, **20** (1978), 201–206.
37. Y. Kato, N. Hasegawa and M. Hirose: Fatigue Threshold Properties of a Low Carbon Steels, Proc. 19th Fatigue Symp., Soc. Mater. Sci. Jpn., 1988, pp. 228–231.
38. T. Isibasi: Fatigue Strength of Notched Stainless Steel Specimens, Proc. 3rd Jpn. Congr. Test. Mater., 1960, pp. 24–26.
39. H. Ouchida and S. Ando: The Fatigue Strength of Notched Specimens at Low Temperatures, *Trans. Jpn. Soc. Mech. Eng. Ser. I*, **30(209)** (1964), 52–58.
40. K. Ogura, Y. Miyoshi and I. Nishikawa: Fatigue Crack Growth and Closure at Notch Root of SUS304 Stainless Steel, Proc. 26th Jpn. Congr. Mater. Res., Soc. Mater. Sci., Jpn., 1983, pp. 91–96.
41. Y. Murakami, H. Morinaga and T. Endo: Effects of Geometrical Parameter and Mean Stress on ΔK_{th} of Specimens Containing a Small Defect, *J. Soc. Mater. Sci., Jpn.*, **34(385)** (1985), 1153–1159.
42. N.E. Frost: A Relation between the Critical Alternating Propagation Stress and Crack Length for Mild Steel, *Proc. Int. Mech. Eng.*, **173(35)** (1959), 811–827.
43. T. Isibasi, T. Uryu and E. Sato: Fatigue Strength of Carbon Steel Bars with Round-Crack, *Trans. Jpn. Soc. Mech. Eng. Ser. I*, **19(87)** (1953), 34–37.
44. H. Ouchida and S. Kusumoto: Fatigue Strength of Carbon Steel Bars with Artificial Cracks, *Trans. Jpn. Soc. Mech. Eng. Ser. I*, **20(99)** (1954), 739–745.
45. H. Nisitani and M. Kage: Effect of Annealing or Change in Stress Level on the Condition for Propagation of Non-Propagating Fatigue Crack, *Trans. Jpn. Soc. Mech. Eng. Ser. I*, **43(366)** (1977), 398–406.
46. H. Nisitani: Relationship among Stress Distribution, Branch Point and Fatigue Limit of Cylindrical Specimens Having Extremely Shallow Notch (Rotating Bending), Preliminary, Proc. JSME Mtg., No. 198, 1968, pp. 37–40.
47. I. Hayashi, N. Tokuda, T. Suzuki and J. Morita: Mechanism of Non-Propagating Crack of Notched Low Carbon Steel Specimen Near the Stage of Rotating Bending Fatigue Limit, Proc. 25th Jpn. Congr. Mater. Res.–Metallic Mater., 1982, pp. 80–86.
48. J. Awatani and K. Matsunami: On Non-propagating Fatigue Cracks in Specimens with Cracks, *J. Soc. Mater. Sci., Jpn.*, **26(283)** (1977), 343–347.
49. H. Kobayashi and H. Nakazawa: On the Alternating Stress Required to Propagate a Fatigue Crack in Carbon Steels, *Trans. Jpn. Soc. Mech. Eng. Ser. I*, **33(254)** (1967), 1529–1534.
50. Y. Murakami and K. Matsuda: Threshold Stress for Fatigue Crack Initiation from a Small Crack, *Trans. Jpn. Soc. Mech. Eng. A*, **53(489)** (1987), 871–877.
51. S. Harada, S. Nishida, T. Endo, K. Suehiro, Y. Fukushima and H. Yamaguchi: The Rotary Bending Fatigue of a Eutectoid Steel (1st Report, Effects on Surface Finish and Defects on Fatigue Limit), *Trans. Jpn. Soc. Mech. Eng. A*, **53(487)** (1987), 401–409.
52. P. Lukas, L. Kunz, B. Weiss and R. Stickler: Non-Damaging Notches in Fatigue, *Fatigue Fract. Eng. Mater. Struct.*, **9(3)** (1986) 195–204; and private communication.
53. H. Maikuma, M. Shimizu and K. Kawasaki: The Effect of Surface Micropits upon the Fatigue Strength of High Strength Steel, *Trans. Jpn. Soc. Mech. Eng. A*, **53(485)** (1987), 11–16.

54. M.F. Garwood, H.H. Zurburg and M.A. Erickson: Correlation of Laboratory Tests and Service Performance, Interpretation of Tests and Correlation with Service, ASM, 1951, pp. 1–77.
55. H. Nisitani and K. Kawano: Correlation between the Fatigue Limit of a Material with Defects and Its Non-Propagating Crack Some Considerations Based on the Bending or Torsional Fatigue of the Specimen with a Diametrical Hole, Trans. Jpn. Soc. Mech. Eng., Ser. I, **37(300)** (1971), 1492–1496.
56. Y. Murakami and M. Endo: The \sqrt{area} Parameter Model for Small Defects and Nonmetallic Inclusions in Fatigue Strength: Experimental Evidence and Applications, Theoretical Concepts and Numerical Analysis of Fatigue, Eds. A.F. Blom and C.J. Beevers, EMAS Ltd., West Midlands, 1992, pp. 51–71.
57. Y. Murakami and M. Endo: Effects of Defects, Inclusions and Inhomogeneities on Fatigue Strength, Int. J. Fatigue, **16(3)** (1994), 163–182.
58. Y. Murakami and T. Toriyama: Application of the \sqrt{area} Parameter Model to Fatigue Strength Evaluation of Steels Containing Various Artificial Defects (Holes, Cracks and Complex Defects), Proc. 21th Fatigue Symp., Soc. Mater. Sci. Jpn., 1992, pp. 127–130.

Chapter 6

Effects of Nonmetallic Inclusions on Fatigue Strength

The influence of small defects and notches has been investigated over a long period. There are numerous factors which have been assumed to influence the fatigue strength. Existing conclusions, each derived from a limited number of experiments are contradictory. Thus, no reliable quantitative method has been established for evaluation of the effects of nonmetallic inclusions. However, recent advances in the application of fracture mechanics to small crack problems [1] has given us the key to a solution of this complicated problem. The solution to the relationship between small defects and small cracks may be thought of as an example of a fracture mechanics application [2–4]. From a historical perspective, the problems of nonmetallic inclusions are not new when compared with those of small cracks. There must be many experienced engineers who understand very well, empirically but qualitatively, the influences of small defects and nonmetallic inclusions. However, it must be noted that the effects of small defects and nonmetallic inclusions are essentially the small crack problem, and that this problem can only be solved in a unified form from the viewpoint of small crack fracture mechanics. This approach has led to quantitative solution of the inclusion problem, an objective that had not been attained by the traditional prediction methods used in material science and engineering.

6.1 Review of Existing Studies and Current Problems

The effect of inclusions is an important topic for both manufacturers and users of steels. However, so many investigations have been carried out that it is rather difficult to conduct an exact and impartial survey. There are a number of reviews on this subject [5–15], but a further thorough and careful literature review is still worthwhile.

6.1.1 Correlation of Material Cleanliness and Inclusion Rating with Fatigue Strength

Various inclusion rating methods have been proposed in several countries [16], for example the ASTM method, a Russian method (GOST), and a British method (FOX inclusion count). A Japanese Industrial Standard (JIS, see Table 6.1) classifies types

Table 6.1 Comparison between JIS point counting method and ASTM method for rating inclusions

	JIS method	ASTM A method			
Test section	Longitudinal section parallel to rolling direction	Longitudinal section parallel to rolling direction			
Test area	300mm ²	160mm ²			
Classification of inclusions	Type A: Sulfide (deformable) Type B: Row of oxide (Alumina) Type C: Silicate (deformable)	Type A: Sulfide (deformable) Type B: Row of oxide (Alumina) Type C: Silicate (deformable) Type D: Globular oxide All types are classified in to Thin and Heavy. Thin: Length in rolling direction <12.7 μm. Heavy: Length in rolling direction ≥12.7 μm.			
Magnification	×400	×100			
Filter	Lattice mode by 20 horizontal and vertical lines	None			
Numbers of inspection fields	Standards > 60 Minimum 30	All data for Type A, B, C, D with Thin and Heavy must be measured.			
Measured values	Numbers of lattice points occupied by inclusions	Classification of types and Thin and Heavy by Plate I, or Summation of the length of all inclusion in rolling direction of Type A, B, C and Thin and Heavy. Numbers of Type D of Thin and Heavy.			
Index of cleanliness	Cleanliness d (%) $d = n/(p \cdot f) \times 100$ p : Total lattice point in one test field f : Numbers of test field n : Numbers of lattice points occupied by inclusions for f fields.	Inclusion Rating Number (0–5) Number defined by Plate I Number defined by TABLE I			
		TABLE I Minimum values for inclusion rating numbers (methods A and D)			
		Inclusion rating number	Minimum total length in one field at 100×, in (mm)		
	Type A	Type B	Type C	Type D	
1/2	0.15 (3.8)	0.15 (3.8)	0.15 (3.8)	1	
1	0.50 (12.7)	0.30 (7.6)	0.30 (7.6)	3	
1 1/2	1.00 (25.4)	0.70 (17.8)	0.70 (17.8)	9	
2	1.70 (43.2)	1.20 (30.5)	1.20 (30.5)	14	
2 1/2	2.50 (63.5)	2.00 (50.8)	2.00 (50.8)	20	
3	3.50 (88.9)	3.20 (81.3)	3.00 (76.2)	26	
3 1/2	4.50 (114.3)	4.60 (116.8)	4.00 (101.6)	35	
4	6.00 (152.4)	6.00 (152.4)	5.00 (127.0)	44	
4 1/2	7.50 (190.5)	8.00 (203.2)	7.00 (177.8)	52	
5	9.00 (228.6)	10.00 (254.0)	8.50 (215.9)	64	

of inclusions in three or four categories, A, B, C and D, on the basis of deformability and distribution morphology [17]. Table 6.1 compares the JIS and ASTM methods. Correlations between cleanliness and fatigue strength were investigated in early reports, but results were not satisfactory [18–22]. For example, Adachi et al. [23] rated the cleanliness of a vacuum-degassed bearing steel, and a vacuum-remelted bearing steel, by the JIS lattice point counting method, and carried out rotating bending fatigue tests. Their conclusions are that, despite good cleanliness grades, they found unusually large nonmetallic inclusions at fatigue fracture origins, and that the size of these inclusions had no correlation with the JIS cleanliness rating. On the other hand, Atkinson [20] introduced Fairey inclusion counts (see Fig. 6.1), which take into account the number, sizes, and stress concentration factors of nonmetallic inclusions. They successfully demonstrated a very good correlation between the counts, and the plane bending and

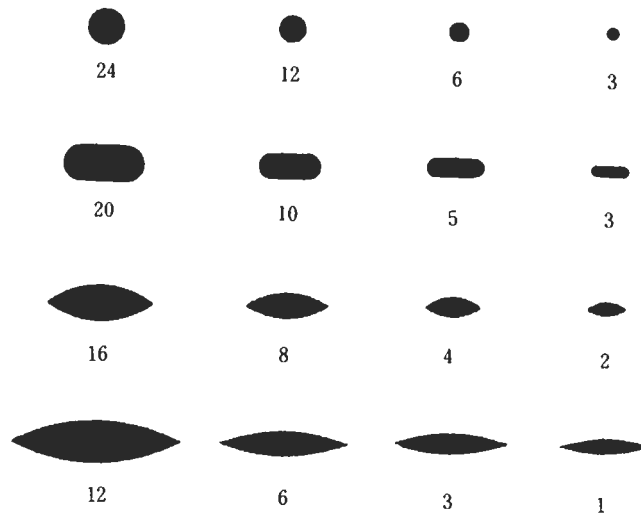


Figure 6.1 Inclusion rating index chart for Fairey inclusion counting method (Atkinson [20]).

rotating bending fatigue strengths of En24 steel, an equivalent to SAE 4340 steel. Nishijima et al. [24] proposed a method in which they evaluated the influence point for individual inclusions and adopted the summation of the points as the inclusion rating. Their cooperative research work on spring steels reported a good correlation between the point and fatigue life.

6.1.2 Size and Location of Inclusions and Fatigue Strength

Correlations between fatigue strength and factors, such as stress concentration factors and numbers of inclusions, as was done by Atkinson, do not lead us to the complete solution. This is because such factors have no direct influence on fatigue strength, including fatigue limits.

Uhrus [21] showed (Fig. 6.2) that only oxide inclusions more than 30 μm in diameter should be counted when evaluating the fatigue life of ball bearings. Duckworth and Ineson [25] showed (Fig. 6.3) that the effect of inclusions of the same size could vary depending on where they were situated in the cross-section of a specimen [11,26]. They also showed that inclusions smaller than a threshold size did not affect the fatigue strength of a material. Similar results were reported by de Kazinczy [22]. In some investigations it was found that inclusions did not influence the fatigue strength of high strength steels [18,19,27–32]. In order to correlate inclusion size with fatigue strength Ramsey and Kedzie [33] used the geometric mean of the length and width of an inclusion, and de Kazinczy [22] used the diameter of the circle circumscribing an inclusion. However, the results of their analyses showed a large amount of scatter.

Fig. 6.4 shows rotating bending fatigue data obtained by Saito and Ito [34] for super clean spring steels and, for comparison, some results for conventional steels. As indicated by Garwood et al. [35] (see Fig. 1.6) the fatigue limit, σ_w , of a conventional

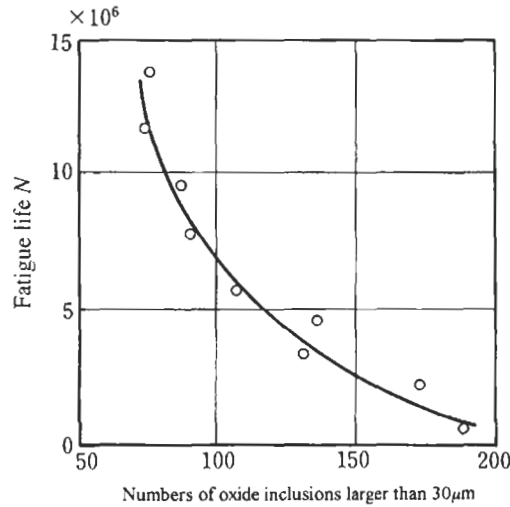


Figure 6.2 Relationship between flaking life of ball bearings and numbers of oxide inclusions larger than 30 μm (Uhrus [21]).

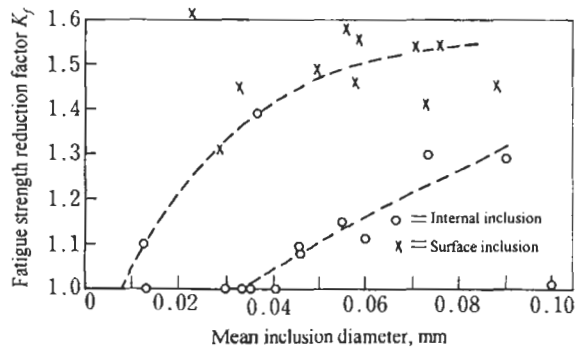


Figure 6.3 Relationship between average inclusion diameter and fatigue strength reduction factor (Duckworth and Ineson [25]).

steel is proportional to H_V for $H_V \leq 400$, but fall below the straight line for steels with $H_V > 400$, despite their high static strength. On the other hand, the fatigue limits of high strength, super clean steels do fall on the straight line extrapolated from the data for low and medium strength steels. Although Saito and Ito did not explicitly control the size of nonmetallic inclusions, they did improve cleanliness by decreasing the oxygen content, and this led to a decrease in the size of nonmetallic inclusions, as shown in Fig. 6.5.

6.1.3 Mechanical Properties of Microstructure and Fatigue Strength

Ineson et al. [18] showed that, for a particular steel containing inclusions, the ratio of fatigue strength to ultimate tensile strength could be decreased from 0.5 to 0.3 by a heat

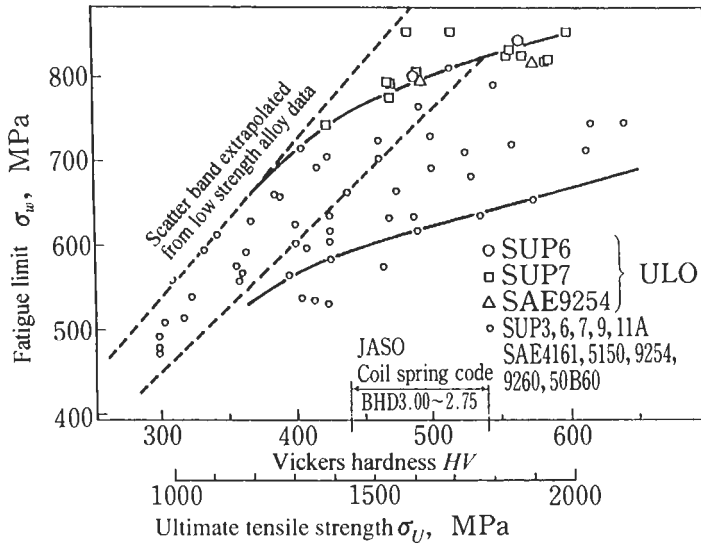


Figure 6.4 Fatigue properties of ultra low oxygen suspension spring steel (Saito and Ito [34]).

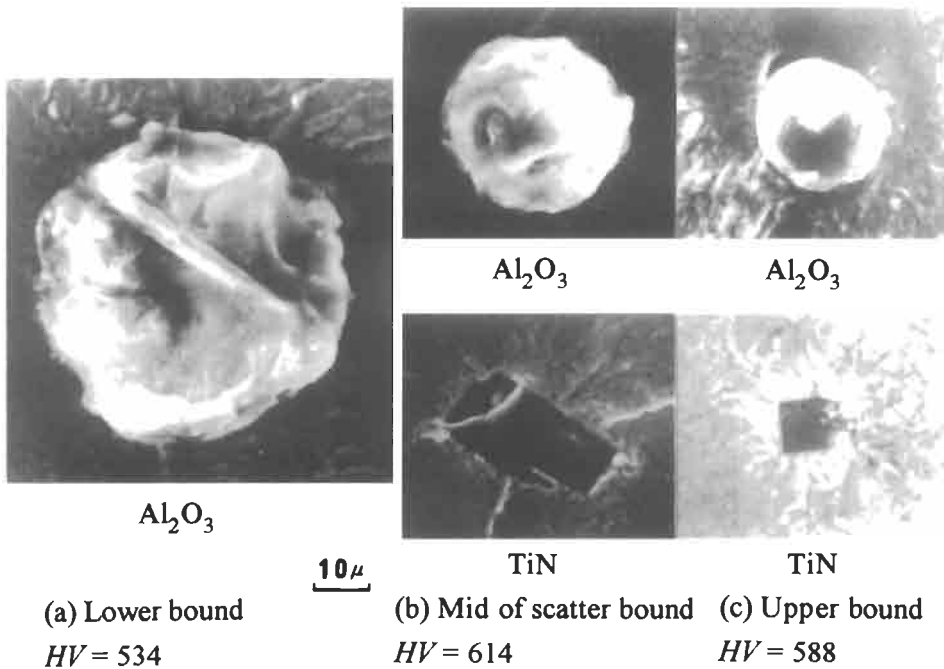


Figure 6.5 Nonmetallic inclusions at fatigue fracture origins (Saito and Ito [34]).

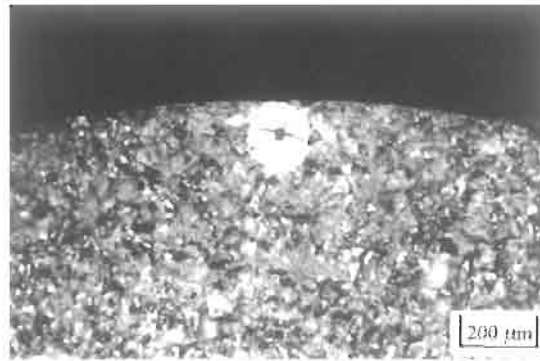


Figure 6.6 Fish eye on fatigue fracture surface (SAE 9254, $H_V = 636$). Distance from surface to fracture origin, $h = 96 \mu\text{m}$. Inclusion size $\sqrt{\text{area}} = 19.3 \mu\text{m}$. Stress at fracture origin $\sigma' = 859 \text{ MPa}$. Estimated fatigue limit $\sigma'_w = 720 \text{ MPa}$. Chemical composition of the inclusion Al–Ca–Mg–O.

treatment which increased the ultimate tensile strength from 85 tonf/in² (1172 MPa) to 125 tonf/in² (1724 MPa). Fig. 1.6 of Chapter 1 shows the well known experimental results, obtained by Garwood et al. [35], which showed for the first time the correlation between fatigue strength and microstructure hardness. As hardness is increased, by heat treatment, the linear relationship between fatigue strength and Vickers hardness, H_V , is lost, and the fatigue strength then shows a large amount of scatter. When the report by Garwood et al. was published in 1951, the fatigue behaviour of steels in the high hardness region was not well understood. The reason for low fatigue strengths at high static strengths, and the accompanying large amount of scatter, had not been identified as due to the influence of nonmetallic inclusions. Nowadays, nonmetallic inclusions are understood to be the cause of the characteristic experimental results obtained by Garwood et al. It seems that the paper of Frith [36], who first found a white spot, now called a fish eye, on a fatigue fracture surface, also identified nonmetallic inclusions as possible fatigue fracture origins in hard steels. When an internal inclusion becomes a fracture origin a white circular area, as in Fig. 6.6, is formed in the vicinity of the inclusion. Frith used the term ‘white area’ for the more recent term ‘fish eye’. These results suggest that the ultimate tensile strength must be higher than a critical value for the effect of inclusions to be exhibited, and in fact there are some papers that report such critical tensile strengths [10,11,25,36–38]. These critical values ought to be affected by inclusion size, but there is no discussion on this point in the literature.

Fig. 6.7 shows a replot of Sumita et al.’s experimental data [6] on the effect of nonmetallic inclusions on steels having various matrix structures. Although using Vickers hardness, H_V , as abscissa means that we cannot make clear the influence of nonmetallic inclusion size, we can identify some indirect and qualitative features of fatigue strength variation. For $H_V < 400$ the vacuum-remelted steel (V), which is assumed to contain very small amounts of nonmetallic inclusions, has almost identical fatigue strengths in the longitudinal (rolling) direction (VL) and in the transverse direction (VT). In contrast, for $H_V > 300$, the open melted steel (A) shows definite differences in fatigue strengths for the longitudinal (AL) and transverse (AT) directions. However, as the fatigue strengths of VL and AL are similar, values of

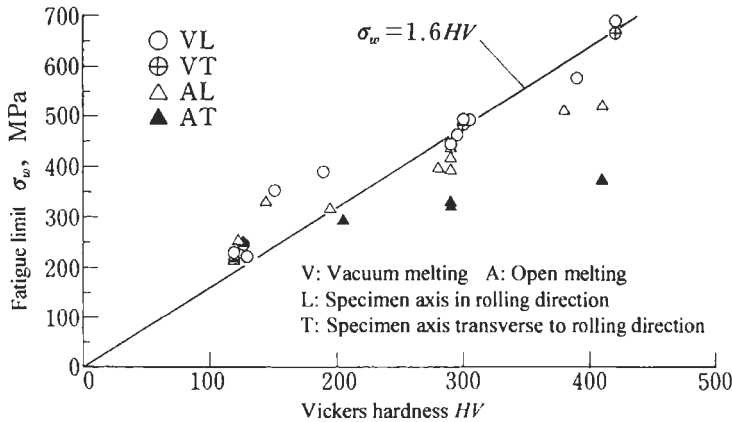


Figure 6.7 Relationship between fatigue limit, melting method, and loading direction [6].

fatigue strength, σ_w , for both can be predicted from H_V by using the empirical Eq. 1.2. Similar experimental results have been reported by other researchers [8,36,39–43]. Although these experimental results imply that the influence of inclusions is related to microstructure properties, and also that there are inclusions which are non-damaging with respect to fatigue strength, quantitative interpretations cannot be derived.

6.1.4 Influence of Nonmetallic Inclusions Related to the Direction and Mode of Loading

The same inclusion can have different effects on fatigue strength depending on the direction of loading [8,36,39–44]. These results indicate that the shape and size of an inclusion are the important factors. Sumita et al.'s experiments (Fig. 6.7) also show this phenomenon, and it is frequently observed in rolled steels. If type A inclusions are present, rolling elongates them in the rolling direction, and they become slender. Thus, different influences of inclusions appear, depending on whether a loading produces a tensile stress in the longitudinal direction, or in the transverse direction.

Similar results, shown in Table 6.2, were obtained in a study on the effect, at constant hardness, of forging ratio on fatigue strength [45]. In this study, the axes of specimens were in the longitudinal (L) direction. It appears from the experimental data that nonmetallic inclusions become increasingly elongated with increasing forging ratio, and at forging ratios of 5–10, $H_V = 220$ –230, nonmetallic inclusions are non-damaging because of the small cross-section areas of elongated inclusions.

Thus, as explained in connection with Fig. 6.7, elongated type A inclusions have little influence on the fatigue strength of a specimen with its axis in the L direction, and much influence on a specimen with its axis in the T direction. However, because the amount of decrease in fatigue strength also depends on microstructure hardness, the forging ratio alone does not determine the decrease. Thus, we cannot evaluate the influence of inclusions if only one parameter is used. Nonmetallic inclusions originally have various shapes, and some of their shapes are altered by plastic deformation. Therefore,

Table 6.2 Influence of forging ratio on fatigue strength [45]

(a) Chemical composition (wt%)					
Specimen	C	Si	Mn	P	S
A	0.64	0.29	0.70	0.020	0.024
B	0.63	0.28	0.72	0.018	0.022

(b) Forging ratio and fatigue strength ($HV = 215\text{--}236$)		
Specimen	Fatigue strength σ_w (MPa)	Forging ratio
A-1-S	274.4	1* (As C. C.)
A-1-C	264.6	
A-2-S	284.2	1.8
A-2-C	294	
A-3-S	333.2	2.8
A-3-C	313.6	
A-4-S	333.2	4.7
A-4-C	323.4	
B-1	303.8	1* (As C. C.)
B-2	313.6	2.0
B-3	323.4	4.3
B-4	333.2	9.7
B-5	323.4	49
B-6	333.2	196

S: Specimens taken from the surface, C: Specimen taken from middle part,

C. C.: Continuous casting

* ϕ 280mm bar, others are ϕ 350mm bar

a very important question is how should we take the three-dimensional shape and size of an inclusion into consideration, that is what geometrical parameter, characterising inclusions, should we define with regard to the loading direction? The influence of inclusions under different types of loading, for example torsional fatigue, has been found to be different to that in rotating bending and in tension–compression fatigue.

The influence of inclusions is not as detrimental in torsional fatigue as it is in rotating bending and in tension–compression fatigue, although there have not been sufficient quantitative studies. This problem is discussed in Chapter 14.

6.1.5 Inclusion Problem Factors

Existing overviews [7–20,46,47] on inclusions usually point out the following factors that should be considered in resolving the effects of inclusions on fatigue strength.

- (a) Inclusion shape.
- (b) Adhesion of inclusions to the matrix.

- (c) Elastic constants of inclusions and matrix.
- (d) Inclusion size.

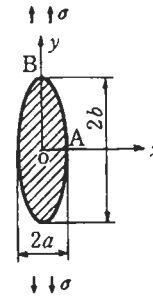
All these factors are related to stress concentration factors, and to the stress distribution around inclusions. Many efforts have been made to evaluate quantitatively stress concentration factors for inclusions by assuming that their shapes are spherical or ellipsoidal, but these assumptions only lead to rough estimates. This is because slight deviations from the assumed geometry can greatly affect stress concentration factors. Using stress concentration factors for the estimation of the fatigue strength of steels is not practical, both because the inclusions found at the centres of fish eyes in high strength steels have various shapes, and also because some of them are far from spherical or ellipsoidal [25,33,34,36,37,48–55]. Another misunderstanding is to assume that a stress concentration factor is less than unity for the case when an inclusion, with Young's modulus higher than that of the matrix, has perfect adhesion to the matrix. As shown in Table 6.3, the assumption is correct at an end of the axis of an inclusion which is perpendicular to the loading direction (point A). However, at a pole in the loading direction (point B) the stress concentration factor is greater than unity [56–58], and a fatigue crack would initiate at that point [53]. Adhesion of inclusions to the matrix is not usually perfect, and there are often some gaps between inclusions and matrix, that is there are intrinsic cracks in the material. In this case stress concentration factors are useless.

It must be noted that, even if exact values for stress concentration factors could be determined, they would not be the crucial factor controlling fatigue strength. This issue was discussed in Chapter 5 with regard to the fatigue strength of specimens containing small artificial holes. Even for small artificial holes with identical stress concentration factors, the fatigue strength varied markedly depending on the sizes of holes. Furthermore, Table 5.4 shows identical fatigue limits for specimens containing a small crack and a small hole, regardless of the difference in stress concentration.

Yokobori et al. [51,59], Masuda et al. [60], Tanaka et al. [61], and Fowler [62] have discussed, using fracture mechanics, the initiation and propagation of fatigue cracks emanating from inclusions. Their application of fracture mechanics to inclusion problems constituted a new approach. However, the crack sizes in inclusion problems are much smaller than those conventionally studied with fracture mechanics. Since the values of ΔK_{th} for small cracks are very different from those measured for long cracks, the estimation of fatigue life, and of fatigue strength based on conventional values for ΔK_{th} , must be reviewed carefully.

One of the best ways of investigating the effect of inclusions on fatigue strength is to prepare test materials in which the shape and size of inclusions is controlled [11,25,34,63], but in practice this is very difficult, as pointed out by many investigators [7–11,64]. Fish eyes on fatigue fracture surfaces are thought to be a useful source of information for the solution of this problem. The relationships between the shape, size, and nature of inclusions at the centres of fish eyes, and the stresses acting at these points, reveal the effect of inclusions or defects on fatigue strengths of high strength materials. This information helps in the understanding of the effect of inclusions and defects on fatigue strength of materials, including low and medium strength steels.

Table 6.3 Stress concentrations around various elliptical inclusions perfectly bonded to the matrix (Donnel [56]). $K = E_I/E_M$ (ratio of Young's modulus of inclusion and matrix)



Aspect ratio a/b	$K=0$ (Hole) Equator A Pole B Stress concentration factor				$K=0.65$ (MnS inclusion) Equator A Pole B Stress concentration factor				$K=0.94$ (Cementite) Equator A Pole B Stress concentration factor				$K=1.82$ (Al_2O_3 inclusion) Equator A Pole B Stress concentration factor			
	σ_x/σ	σ_y/σ	σ_x/σ	σ_y/σ	σ_x/σ	σ_y/σ	σ_x/σ	σ_y/σ	σ_x/σ	σ_y/σ	σ_x/σ	σ_y/σ	σ_x/σ	σ_y/σ	σ_x/σ	σ_y/σ
0.1	0	1.200	-1.000	0	-0.009	1.054	-0.137	0.684	-0.001	1.007	-0.018	0.957	0.018	0.895	0.251	1.615
0.5	0	2.000	-1.000	0	-0.014	1.205	-0.162	0.781	-0.002	1.025	-0.019	0.973	0.024	0.722	0.207	1.301
1.0	0	3.000	-1.000	0	0.000	1.304	-0.152	0.848	0.000	1.035	-0.017	0.983	0.000	0.649	0.175	1.175

From the above discussion, the main questions that must be answered can be summarised as follows.

- Why does fatigue strength lose its linear correlation with hardness beyond a certain hardness value?
- What factors control the critical size of inclusions that affects fatigue strength?
- Why is there a large amount of scatter in the fatigue limits of high strength steels?
- What parameters best represent the shape and size of inclusions?
- Which material characteristic has the strongest correlation with microstructural fatigue strength?

These questions have many points in common with problems concerning defects and microcracks in materials, such as holes and voids. The results for these are useful, in providing basic understanding, for the study of the influence of inclusions.

6.2 Similarity of Effects of Nonmetallic Inclusions and Small Defects and a Unifying Interpretation

It is very difficult to prepare specimens containing nonmetallic inclusions whose shape, size, location, and chemical composition are metallurgically controlled. In order to investigate quantitatively the effects of small defects and cracks, Murakami and Endo [65] conducted rotating bending fatigue tests on quenched ($H_V = 650$), and quenched and tempered ($H_V = 520$), 0.46% C steel. They used specimens which contained a small artificial hole, with diameters ranging from 40 to 200 μm . Fig. 6.8 compares their results with those of Garwood et al. [35]. Although Murakami and Endo's results show the qualitative similarity between the effects of small defects and of nonmetallic

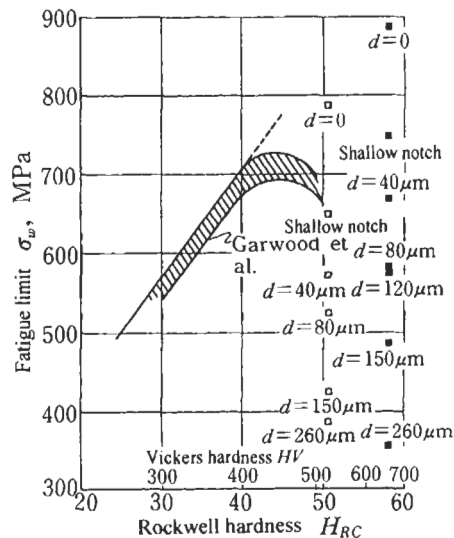


Figure 6.8 Relationship between hardness and fatigue strength in the presence of small defects.

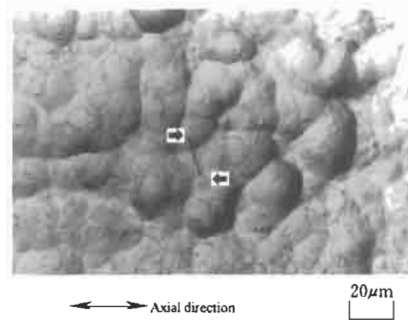


Figure 6.9 Non-propagating crack at the fatigue limit of quenched 0.46% C steel ($H_V = 650$, surface crack length $l_0 \cong 20 \mu\text{m}$).

inclusions, their results do not provide quantitative information on the effects of nonmetallic inclusions. Their results are consistent with those of Saito and Ito [34] on the effect of nonmetallic inclusion size. The general characteristics of this problem may be summarised as follows.

(1) The exact relationship between fatigue limit and hardness cannot be derived from the average hardness of a specimen because it is the hardness of the microstructure in the vicinity of the fracture origin that determines the fatigue limit.

(2) Even a very small hole, $40 \mu\text{m}$ in diameter, causes a distinct decrease in the fatigue limit of steels having $H_V > 500$. This result is related to the tendency of the size of non-propagating cracks at the fatigue limit of an unnotched specimen, l_0 , to decrease with increasing hardness. Fig. 6.9 shows the size of a non-propagating crack, $l_0 \cong 20 \mu\text{m}$, for a microstructure with $H_V = 650$.

(3) When slip bands in the microstructure become the origins of fatigue fracture, the linear empirical equation, $\sigma_w = 1.6H_V$, where the fatigue limit, σ_w , is in MPa and H_V is in kgf/mm^2 , also holds for the case of hard steels.

Even when the detrimental effect of nonmetallic inclusions is evident, it is quite difficult to identify the fatal inclusion which became the fracture origin. For example, the cause of the difference in fatigue strength between AL and AT specimens in Fig. 6.7 may be assumed to be nonmetallic inclusions elongated in the rolling direction, but it is difficult to identify the fatal inclusions which caused this crucial difference. On the other hand, a nonmetallic inclusion at the fracture origin of a hard steel is relatively easy to find because a white spot, a so-called fish eye as shown in Fig. 6.6, almost always appears on the fracture surface. Figs. 6.10 and 6.11 show similar examples, a typical Al_2O_3 inclusion in Fig. 6.10, and a duplex oxide, $(\text{CaO})_x\text{Al}_2\text{O}_3$, in Fig. 6.11. In these cases we can at least know the chemical composition, shape, and size of the inclusion, together with the stress at the fracture origin. Nevertheless, it is not easy to discern the mutual relationships among various influencing factors. Thus, we need to analyse the basic mechanism of fatigue fracture from nonmetallic inclusions.

The fact that a nonmetallic inclusion exists at a fracture origin implies that, after a fatigue crack is nucleated at the interface between the inclusion and the matrix, or the inclusion itself is cracked, the crack then extends into the microstructure, resulting in

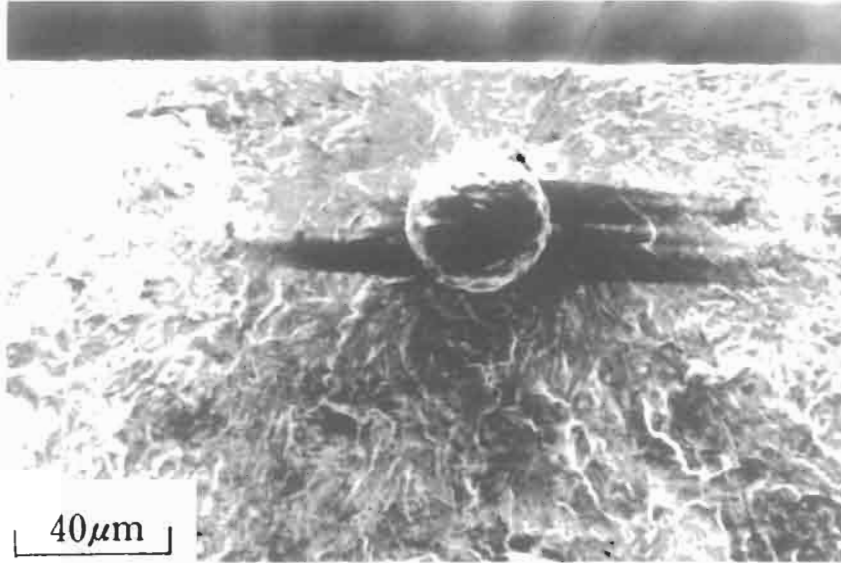


Figure 6.10 Al_2O_3 inclusion at the centre of a fish eye (0.35% C steel, $H_V = 570$, $\sigma = 724$ MPa, $N_f = 4.02 \times 10^6$, distance from surface $h = 42$ μm).

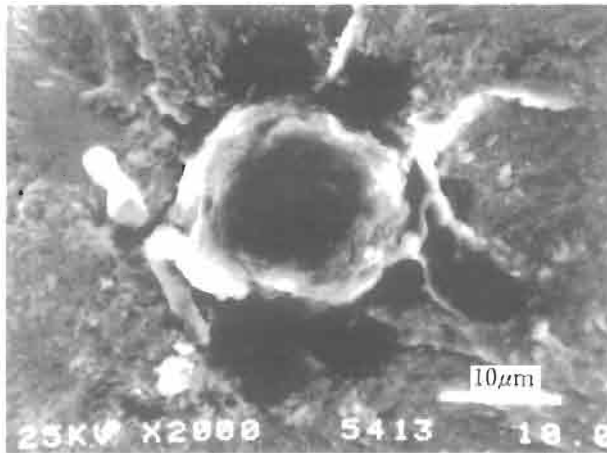


Figure 6.11 $(\text{CaO})_x\text{Al}_2\text{O}_3$ inclusion at the centre of a fish eye (SAE 9254, $H_V = 641$, $\sigma = 980$ MPa, $N_f = 1.69 \times 10^6$, $\sqrt{\text{area}} = 17.9$ μm , nominal stress at inclusion, $\sigma' = 927$ MPa).

final fracture [67]. As previously and repeatedly described, the fatigue limit for a steel is not the critical stress for crack initiation, but is the threshold stress for non-propagation of cracks, regardless of the existence of defects. Therefore, if a nonmetallic inclusion does become a fracture origin, then we should regard the fatigue limit not as the critical stress for crack initiation, but as the threshold stress for a crack which emanates from the nonmetallic inclusion, extends a small distance within the microstructure, and

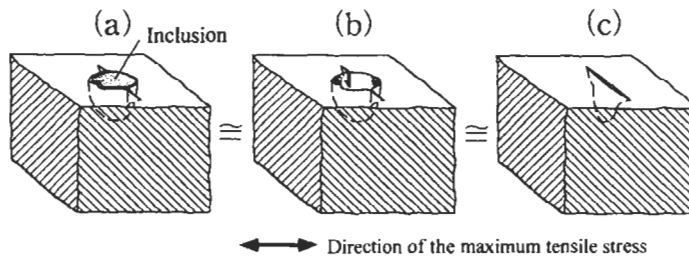


Figure 6.12 Mechanical equivalence of (a) a crack emanating from the inclusion–matrix interface, and (b) a crack emanating from a defect.

eventually stops propagating. When a crack is nucleated at the interface between an inclusion and the matrix (see Fig. 6.12), or a crack originates through cracking of the inclusion, then stresses within the inclusion are relieved, and the inclusion domain may be regarded as mechanically equivalent to a stress-free defect or pore [66–70]. As a matter of fact, Lankford [71–74] reported an example of fatigue crack initiation at the inclusion interface shown in Fig. 6.13. Eid and Thomason [75] observed a crack which nucleated at an inclusion interface (Fig. 6.14) and grew into the matrix. Thus, once an inclusion is debonded at its interface, the interface can no longer sustain the applied stress, and the inclusion becomes mechanically equivalent to a stress-free pore. *This concept is extremely important in the solution of inclusion problems.* The effects of the shape and size of small defects have been resolved quantitatively by using specimens containing small artificial holes, hence it is anticipated that application of this concept will lead us to quantitative solutions of inclusion problems.

It is true that there have been some investigations in which inclusions were regarded as pores. However, existing approaches try only to reach relatively practical conclusions. They are based on simple assumptions, because of ambiguity regarding bonding conditions at inclusion interfaces, together with some observations of interface debonding. These investigations mostly sought to evaluate the influence of inclusions through stress concentration factors for equivalent pores [7,11,76,77]. However, it must be noted that the maximum stress, at some point in the vicinity of an inclusion, is always greater than the remote stress, irrespective of Young's modulus of the inclusion (see page 83) [56–58]. Therefore, even when an inclusion interface is not initially debonded, the interface can always become a candidate site for crack initiation, regardless of inclusion rigidity. Furthermore, since the fatigue limit is determined by the non-propagation of a crack which is initiated at an initial stress concentration of a defect, it should be possible to unify the effect of inclusions by using the model which was used to solve the problem of small defects.

6.3 Quantitative Evaluation of Effects of Nonmetallic Inclusions: Strength Prediction Equations and their Application

The method used to solve the inclusion problem is basically identical with that applied, in Chapter 5, to small cracks and small defects. In other words, nonmetallic

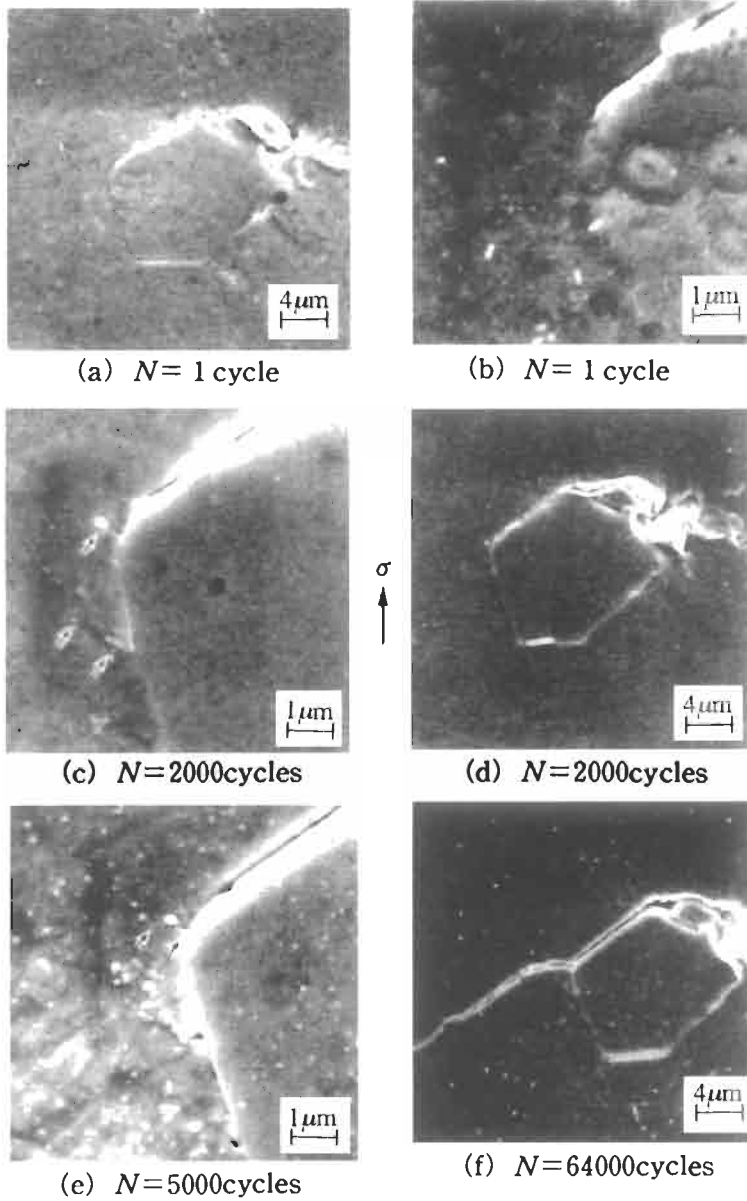


Figure 6.13 Debonding sequence of inclusion–matrix interface, and fatigue crack initiation (4340 steel, Lankford [71]).

inclusions are treated as mechanically equivalent to small defects having the same values of $\sqrt{\text{area}}$.

(a) *Surface Inclusions* (Fig. 6.15a,b): When there is an inclusion at the surface of a material (Fig. 6.15a), ΔK_{th} can be calculated using Eq. 5.4, and the fatigue limit, σ_w ,

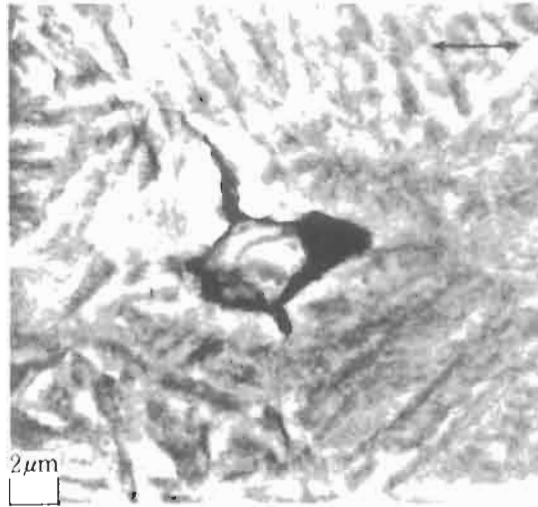


Figure 6.14 Crack initiation and propagation associated with inclusion–matrix interface debonding (Eid and Thomason [75]).

by using Eq. 5.5, where \sqrt{area} is the square root of the projected ‘area’ of an inclusion onto a plane perpendicular to the maximum principal stress. However, when an inclusion is just in contact with a free surface, as shown in Fig. 6.15b, then the definition of \sqrt{area} must be modified to include the weak area between the inclusion and the free surface. The effective value of \sqrt{area} can be estimated by taking a smooth contour line enclosing the inclusion and weak area, as shown by the dashed lines in Fig. 6.15b [2,78]. This modification is justified by a study on the variation of the maximum stress intensity factor, $K_{I_{max}}$, for an irregularly shaped surface crack [79]. By using this modification we have the effective ‘area’ approximately equal to 1.137 times the original ‘area’, that is ‘area*’ = 1.137 ‘area’. Thus, we obtain prediction equations for a surface inclusion, and for an inclusion just in contact with the free surface, as follows [66,68].

[Small surface defects, small surface cracks, and nonmetallic surface inclusions.]

$$\sigma_w = \frac{1.43(H_v + 120)}{(\sqrt{area})^{1/6}} \quad (6.1)$$

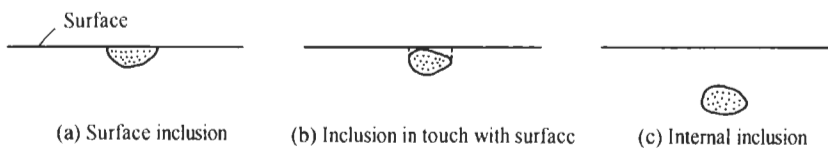


Figure 6.15 Classification of inclusions by location.

[Small surface defects, small cracks, and nonmetallic inclusions in contact with free surface.]

$$\sigma_w = \frac{1.41(H_V + 120)}{(\sqrt{area})^{1/6}} \quad (6.2)$$

where, for both equations, σ_w is in MPa, H_V is in kgf/mm², and \sqrt{area} is in μm .

(b) *Internal Inclusions* (Fig. 6.15c): The maximum value of stress intensity factor along the crack front of a surface crack, $K_{I\max}$, is given by $K_{I\max} \cong 0.65\sigma_0\sqrt{\pi\sqrt{area}}$ (Eq. 2.8). $K_{I\max}$ for an internal crack is given by $K_{I\max} \cong 0.5\sigma_0\sqrt{\pi\sqrt{area}}$ (Eq. 2.7). Therefore, if we consider an inclusion as equivalent to a small crack, then an internal inclusion has a smaller value of $K_{I\max}$ than does a surface inclusion having the same value of \sqrt{area} . This means that for identical values of $K_{I\max}$ the size of a surface crack, $\sqrt{area_s}$, and that of an internal crack, $\sqrt{area_i}$, have the relationship $\sqrt{area_i} = 1.69\sqrt{area_s}$. Thus, the equation for surface defects can be rewritten for internal cracks, defects, and inclusions as in the following.

[Internal cracks, defects, and inclusions.]

$$\sigma_w = \frac{1.56(H_V + 120)}{(\sqrt{area_i})^{1/6}} \quad (6.3)$$

where σ_w is in MPa, H_V is in kgf/mm², and $\sqrt{area_i}$ is in μm .

Eq. 6.3 can be applied, without loss of accuracy, to inclusions close to free surfaces. This is because $K_{I\max} \cong 0.5\sigma_0\sqrt{\pi\sqrt{area}}$ (Eq. 2.7) can be applied approximately to internal cracks very close to the surface [80].

Comparisons between estimates, obtained using Eqs. 6.1–6.3, and rotating bending fatigue test results are given in the following.

Kawada et al. [48] reported the results of rotating bending fatigue tests on bearing steels in considerable detail. Their detailed records on inclusions at fracture origins (inclusions at centres of fish eyes) are very useful in examination of the validity of Eqs. 6.1–6.3.

Table 6.4 compares their data with predictions using Eq. 6.3. The notation σ is the nominal bending stress at a specimen's surface, and σ' is the nominal bending stress at the inclusion at a fracture origin. The notation σ'_w is the estimated fatigue limit at a fracture origin calculated using Eq. 6.3. It should be noted that all the data in Table 6.4 are for specimens fractured from nonmetallic inclusions. Steel N is a conventional Japanese bearing steel. Steel S is a Swedish bearing steel. Steel V is a Japanese vacuum-remelted bearing steel. All these steels were produced in the 1960s so they contain inclusions much larger than those in recent super clean bearing steels.

Values of $area_i$ in Table 6.4 were estimated using the equation $area_i = \pi \times (\text{major axis}) \times (\text{minor axis})/4$ where major and minor axes are those of an ellipse approximating the shape of the inclusion at a fish eye. When the stress amplitude, σ' , at an inclusion location is greater than the predicted fatigue limit, σ'_w , then the inclusion would be expected to become the fracture origin. The values of σ'/σ'_w in Table 6.4 are all greater than 1.0, so the fatigue failure of these specimens is in agreement with predictions.

Table 6.4 Inclusion location, nominal fracture stress, and estimated fatigue limit for individual fracture origins

Materials <i>HV</i>	Nominal stress at surface σ (MPa)	Cycles to failure $N_f \times 10^4$	Inclusion size \sqrt{area} (μm)	Depth from surface (μm)	Inclusion shape	Nominal stress at inclusion σ' (MPa)	Fatigue limit estimated by Eq. (6.3) σ'_w	σ'/σ'_w
Bearing Steel N $HV \approx 734$	981	254.36	31.0	316		907	752	1.21
	981	120.05	36.6	370		895	731	1.22
	932	429.54	34.0	390		846	740	1.14
	883	1280.50	31.0	120		858	752	1.14
	981	192.51	36.6	38		971	731	1.33
	932	296.64	38.7	420		839	724	1.16
	912	134.21	28.4	63		898	763	1.18
	883	277.34	20.4	14		879	806	1.09
883	729.50	29.3	295		821	759	1.08	
Bearing Steel S $HV \approx 758$	1030	125.25	24.0	310		954	806	1.18
	1030	556.77	15.9	140		995	863	1.15
	981	422.95	15.2	28		973	870	1.12
	981	898.01	9.9	74		963	934	1.03
	981	178.51	12.5	10		978	899	1.09
	1030	224.64	18.6	74		1011	841	1.20
	1030	30.52	22.2	24		1023	817	1.25
	1030	26.48	28.4	110		1003	784	1.28
971	735.45	28.9	350		886	782	1.14	
Bearing Steel V $HV \approx 685$	981	50.11	37.5	80		961	686	1.40
	981	39.21	29.3	170		941	715	1.32
	932	683.38	32.5	570		807	703	1.15
	883	138.24	53.5	200		841	647	1.30
	981	75.06	31.0	350		900	708	1.27
	932	160.35	25.6	240		878	732	1.20
	932	11.12	47.0	100		909	661	1.38
	932	23.40	100.7	1030		706	582	1.21
	834	420.00	69.9	600		715	619	1.16

Table 6.5 Inclusion location, nominal fracture stress, and estimated fatigue limit for individual fracture origins (developed from the data of Konuma and Furukawa [55])

Materials	HV	σ	N_f	\sqrt{area}	h	σ'	σ_w'	σ'/σ_w'
S 35 C	570	724	4.02×10^6	33.7	42	716	599	1.20
	610	713	4.40	46.9	200	681	600	1.14
	672	717	3.23	25.3	66	706	721	0.974
	655	735	2.19	32.0	50	727	679	1.07
	638	724	1.08	44.3	70	712	629	1.13
	657	686	1.48	35.4	30	681	669	1.02
S 55 C	782	887	9.35	21.7	250	838	842	0.995
	775	918	2.37	27.7	290	858	802	1.07
	797	897	2.35	27.4	143	868	824	1.05
	801	896	4.40	22.2	110	874	857	1.02
	803	892	7.87	35.5	375	817	803	1.02
	831	910	4.01	35.5	175	874	819	1.05

The units are the same as Table 6.4

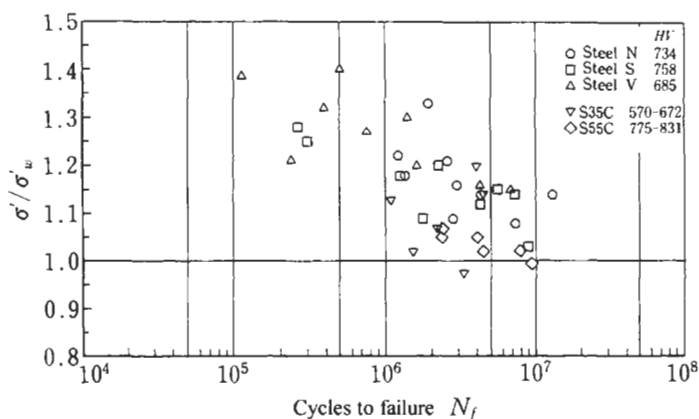


Figure 6.16 Relationship between the ratio of nominal fracture stress, σ' , to estimated fatigue limit at inclusion, σ_w' , and cycles to failure, N_f .

Table 6.5 shows similar comparisons for additional data, on quenched and tempered 0.35% C and 0.55% C steels, obtained by Konuma and Furukawa [55]. In these materials typical fish eyes were observed in most specimens. Values of σ'/σ_w' in Table 6.5 are greater than 1.0, except in two cases where they are very close to 1.0. Therefore, it can again be concluded that predictions are accurate.

In order to examine the expectation that larger values of σ'/σ_w' would result in shorter fatigue lives, the relationships shown in Tables 6.4 and 6.5 between σ'/σ_w' and the number of fatigue cycles to failure, N_f , are plotted in Fig. 6.16. In the following, let us call a curve drawn through data, such as those shown in Fig. 6.16, a modified $S-N$

Table 6.6 Inclusion location, nominal fracture stress, and estimated fatigue limit for individual fracture origins

Materials	H_V	σ	N_f	\sqrt{area}	h	σ'	σ_w'	σ'/σ_w'
S 45 C ⁽⁸¹⁾	803	900	5.27×10^6	26.7	100	864	833	1.04
	641	900	1.19	28.3	59	879	681	1.29
SAE 9254 ⁽²⁴⁾	550	765	10.01	23.8	247	670	616	1.01
	~600						~662	~1.09

The units are the same as Table 6.4

curve. The trend shown in the figure indirectly verifies the accuracy of the prediction method. The same method was applied to data in further references [24,81], and the predictions and experimental results are compared in Table 6.6. The relationships between σ'/σ_w' and N_f in this table all are within the data scatter band in Fig. 6.16.

Fatigue limits, determined by Kawada et al. [48], for the three bearing steels, N, S, and V, were 872, 970 and 843 MPa, respectively. However, these values may not be the correct fatigue limits, because in Table 6.4 there are several examples where values of σ' are lower than the fatigue limits defined by Kawada et al., but actually the specimens fractured. In other words, if the inclusions included in Table 6.4 were at or near the specimen surfaces, then necessarily these specimens would have fractured at a fatigue limit as defined by Kawada et al. Similar discussions are needed for existing data on hard steels.

6.4 Causes of Fatigue Strength Scatter for High Strength Steels and Scatter Band Prediction

Despite the complicated phenomena involved, the discussions in previous sections have made the fatigue problem of hard steels clearer and simpler. The essence of this problem may be described as follows. If inclusions and defects are absent, or they are smaller than a critical size, then fatigue strength depends on the value of the microstructural resistance against fatigue, and this is proportional to the microstructure hardness, as in low and medium strength steels. This value is the upper bound for fatigue strength of the microstructure, σ_{wu} , which may be expressed by:

$$\sigma_{wu} = 1.6H_V \quad (6.4)$$

where σ_{wu} is in MPa and H_V is in kgf/mm².

The conclusions derived in this study give the correct interpretation of fatigue data for various high strength steels reported in the literature [64–68,82–87], and also simplify understanding of the complicated fatigue strength characteristics of high strength steels. An inclusion-free matrix of a high strength steel has its own intrinsic fatigue limit which, as for low and medium carbon steels, is proportional to the hardness (Eq. 6.4). The high intrinsic fatigue limit can be attained if the inclusion size ($\sqrt{area_s}$ or $\sqrt{area_i}$) is smaller than a critical value [2,3,88,89]. In other words, low fatigue limit values

for high strength steels are caused by the presence of inclusions larger than a critical size, which is a function of Vickers hardness. Since the location, as well as the size, of inclusions influences fatigue strength, it may be concluded that specimens of high strength steels each have a different fatigue limit, and it is this characteristic which causes wide scatter bands for experimental data [64–68,82–87]. However, in the cases of low and medium carbon steels the sizes of inclusions and defects, usually formed during production processes, are smaller than a critical value [2,3,88,89], and slip band cracks, or grain boundary cracks, nucleated in a matrix are the usual fatigue fracture origins. Consequently, experimental data scatter becomes negligible. These relationships between fatigue limits, hardness, and inclusions lead to the suggestion that achievement of a high fatigue limit may be expected if the sizes of inclusions and defects are controlled to a size smaller than a critical value, which is a function of hardness. If we look again at Figs. 6.4–6.6 from this point of view, then we are able to deduce many interesting ideas.

In the case of high strength steels, an individual specimen has its own individual fatigue strength because of the presence of inclusions. This characteristic makes the quantitative prediction of fatigue strength difficult. One way to solve this problem would be to inspect non-destructively all inclusions contained in structures, and then to predict the fatigue limits for individual structures. However, this method is not only unrealistic, but would also be unsuccessful because it is extremely difficult to measure accurately the shape, size, and location of nonmetallic inclusions by the use of non-destructive inspection. Another possible approach is at least to predict the upper and lower bounds for fatigue strength by considering the statistics of the distribution of inclusions. The upper bound for fatigue strength is obtained when defects or inclusions do not affect fatigue fracture, and according to earlier experimental results its value can be estimated by using Eq. 6.4.

Although the estimation of the lower bound for fatigue strength is somewhat complicated, the following method is available [66,68,90]. In a tension–compression fatigue test, the inclusion of maximum size, \sqrt{area}_{max} , contained in the test section of the specimen is expected to become the fracture origin.¹ Hence, the lower bound for fatigue strength for N specimens would be predicted by knowing the maximum size of inclusions contained in N specimens. Extreme value statistics [91] can be used to estimate \sqrt{area}_{max} . A practical method of determining \sqrt{area}_{max} is explained in the following, using data on a high speed tool steel, SKH51.

Fig. 6.17 shows the specimen geometry for tension–compression fatigue tests. The Vickers hardness of specimens ranged from $H_v = 616$ to 730, depending on the heat treatment. Microstructures, after quenching and tempering, are martensite plus spheroidal carbide. The chemical composition is, in wt%, 0.81% C, 0.31% Si, 0.29% Mn, 0.018% P, 0.002% S, 3.92% Cr, 6.10% W, 4.85% Mo, 1.81% V, 0.46% Co, 0.07% Cu, 0.004% Ca, 0.035% Al, 0.0005% Mg and 0.018% O.

¹ If the second largest inclusion is just in contact with the specimen surface, then this inclusion, rather than the largest inclusion, may become the fracture origin. Such an inclusion is not considered in prediction of the maximum inclusion size using extreme value statistics.

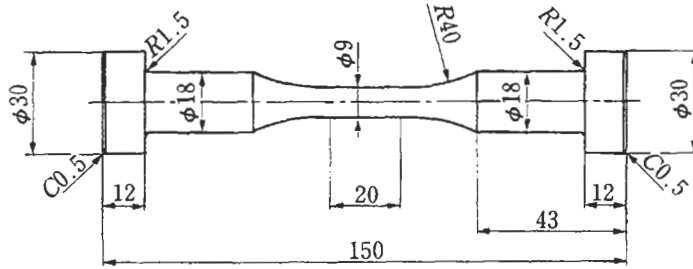


Figure 6.17 Tension–compression fatigue specimen, high speed tool steel SKH51.

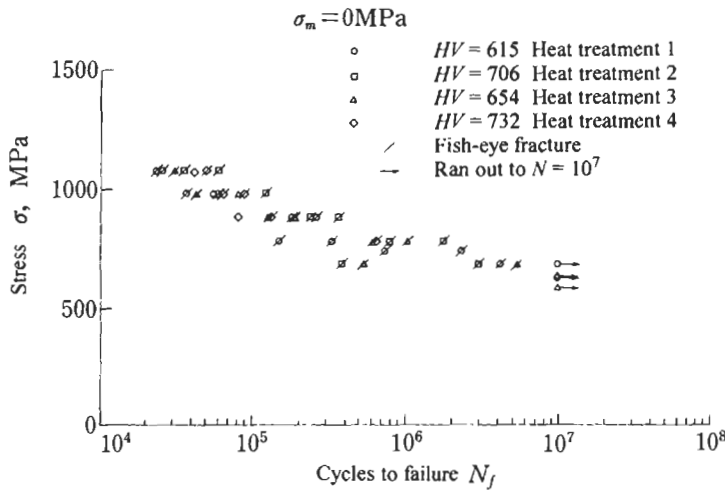


Figure 6.18 Tension–compression fatigue test data for high speed tool steel SKH51.

Fig. 6.18 shows the $S-N$ data obtained. All specimens fractured from inclusions. The scatter of fatigue life and strength is very large, and accordingly it is difficult to define the exact fatigue limit for the material. However, if we construct modified $S-N$ curves, as was described for bearing steels in Section 6.3, we obtain Fig. 6.19. This figure clearly verifies the correlation between applied stress, and the fatigue lives and strengths of individual specimens containing various inclusions. The ordinate, σ'/σ'_w , of Fig. 6.19 is the ratio of the applied stress amplitude at the inclusion at a fracture origin, σ' , to the fatigue limit, σ'_w , estimated using \sqrt{area} and H_V for individual specimens. Fig. 6.20 shows the distribution (distance from specimen surface) of inclusions at fracture origins over the cross-section of specimens. The uniform distribution of the inclusion population over the cross-section confirms that the tension–compression fatigue tests were very carefully conducted under precise alignment. Precise alignment in tension–compression fatigue tests is crucially important if reliable fatigue data are to be obtained. If fatigue test results show mostly surface origins, or a nonuniform distribution of fatigue fracture origins, then it must be suspected either that, due to misalignment, a bending moment

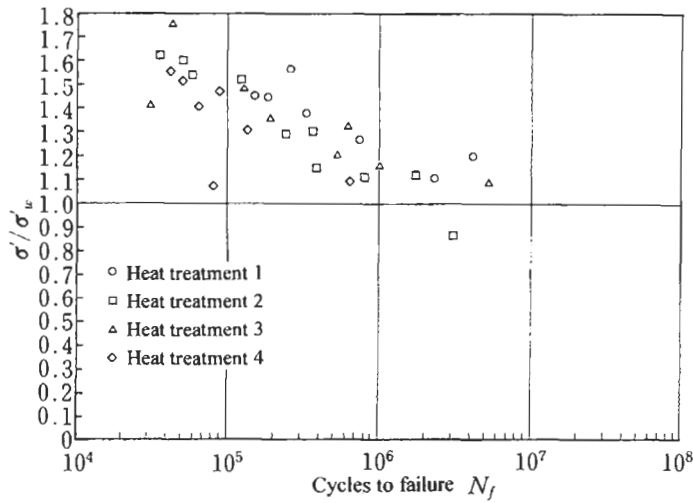


Figure 6.19 Relationship between the ratio of nominal fracture stress, σ' , to estimated fatigue limit at inclusion, σ'_w , and cycles to failure, N_f (in tension-compression $\sigma' = \sigma$).

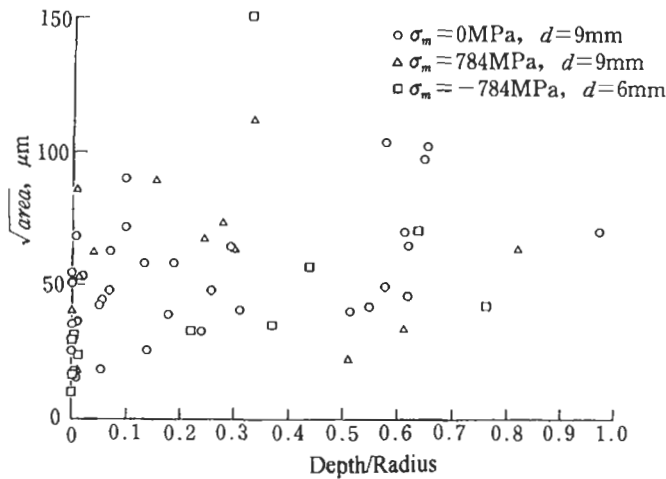


Figure 6.20 Relationship between depth of inclusion at fracture origin and inclusion size, $\sqrt{\text{area}}$, for high speed tool steel SKH51 (d = specimen diameter).

has been superimposed on the tension-compression loading, or that specimens have become bent during heat treatment. In both cases data showing unusually low fatigue strengths are obtained [92,93]. Such unreliable data must not be used when discussing inclusion problems.

The nonmetallic inclusion at a fracture origin may be regarded as the largest inclusion in a specimen, so its size distribution over a number of specimens is expected to obey extreme value statistics. The sizes of nonmetallic inclusions observed at fish eyes on 34

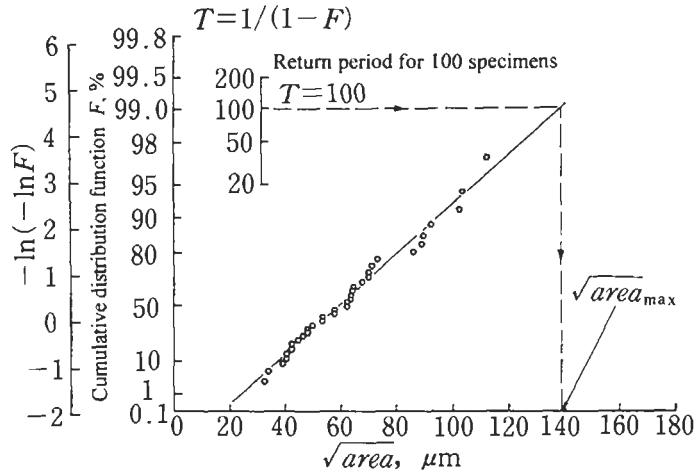


Figure 6.21 Extreme value statistics for inclusion size, $\sqrt{\text{area}}$, for high speed tool steel SKH51 (the fracture origin inclusion at the centre of a fish eye may be taken as the largest inclusion in a specimen).

specimens are plotted in Fig. 6.21.² For details of the extreme value statistics probability paper used see Appendix C. The plotting procedure is as follows. First, arrange the inclusions in ascending order of size: $\sqrt{\text{area}}_{\text{max}1}$, $\sqrt{\text{area}}_{\text{max}2}$, ..., $\sqrt{\text{area}}_{\text{max}i}$, ..., $\sqrt{\text{area}}_{\text{max}34}$. The value of the ordinate, F , for the i -th point is calculated as $F = i/(34 + 1) \times 100\%$, and the abscissa is $\sqrt{\text{area}}_{\text{max}i}$. Fig. 6.21 shows a beautiful straight line which verifies that, if we define inclusion size by $\sqrt{\text{area}}$, then $\sqrt{\text{area}}_{\text{max}}$ obeys extreme value statistics.

Therefore, if we define the test volume of one specimen by V_0 , then the return period, T , for N specimens is defined by $T = N$. For example, we can predict the maximum size of an inclusion contained in 100 specimens to be 138.5 μm by following the arrows in Fig. 6.21.

Once $\sqrt{\text{area}}_{\text{max}}$ is determined, then the lower bound prediction for N specimens can be obtained by substituting $\sqrt{\text{area}}_{\text{max}}$ into the prediction equation. The lowest value of fatigue strength is obtained when the inclusion of maximum size is just below the specimen surface. In this case the effective maximum size is thought to be larger than the actual maximum size, as indicated by the smooth contour line in Fig. 6.15b. Thus, the prediction equation for the lower bound fatigue strength may be written as:

$$\sigma_{wl} = \frac{1.41(H_V + 120)}{(\sqrt{\text{area}}_{\text{max}})^{1/6}} \quad (6.5)$$

Fig. 6.22 compares predictions of σ_{wl} for $N = 10$ and 100 with experimental results. Although this particular prediction procedure is based on data obtained from many

² The reason why a nonmetallic inclusion at a specimen surface was avoided is that it may not be the largest inclusion.

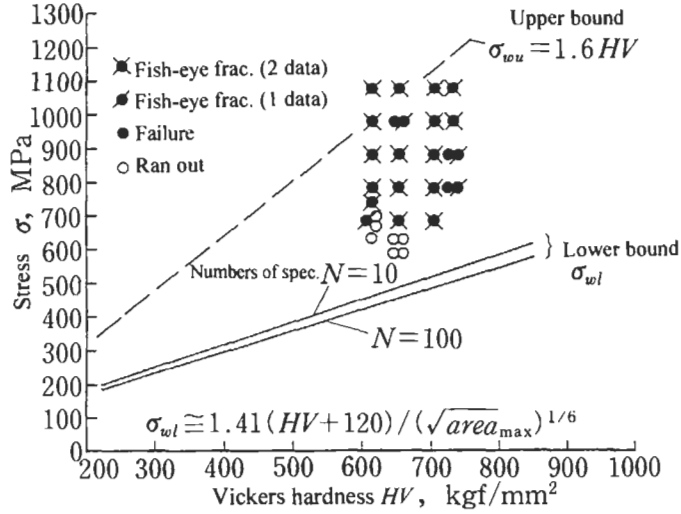


Figure 6.22 Scatter band for tension–compression fatigue strength of high speed tool steel SKH51 (the upper bound, σ_{wu} , is predicted by the empirical equation, the lower, σ_{wl} , is a measure of the scatter).

fatigue tests, it is in fact possible to predict $\sqrt{area_{max}}$ by microscopic examination of inclusions [68,90]. This is explained in Section 6.6.

In the case of rotating bending fatigue tests, the stress distribution is not uniform across a specimen cross-section. The stress has its maximum value at the specimen surface, and the prediction method must be applied in a modified manner, as explained in Section 6.6 and Appendix A.

Fig. 6.22 shows that σ_{wl} is controlled by $\sqrt{area_{max}}$. Thus, control of nonmetallic inclusions during a steel making process controls the fatigue strength scatter band, though optimum process control may be determined by considering the balance between cost and a request for strength.

6.5 Effect of Mean Stress

Under a tensile mean stress, the fatigue strength of a metal containing small defects decreases more than would be expected from consideration of its static strength, and scatter increases. On the other hand, fatigue strength increases under a compressive mean stress, even in the presence of small defects and inclusions. Consequently, heat treatments, shot peening, and other surface treatments, which can produce compressive residual stresses, are used to improve fatigue strength. Since in general, various high strength steels are used under loading conditions for which $R \neq -1$, a method for quantitative evaluation of the effect of small defects and inclusions under a mean stress must be established. If residual stresses exist in machine components, then the effective stress ratio, R , is not identical with that determined only by external loading. Accordingly, as a result of residual stresses, which are equivalent to local mean stresses, the value of R varies from point to point in the material.

There is no previous research which treated this problem systematically and quantitatively for various materials and inclusions. The modified Goodman diagram and the Soderberg diagram are the conventional methods [94,95] used to estimate the influence of mean stress on fatigue strength. With increasing hardness, however, the use of these methods results in large errors and, depending on material, may be unconservative [96]. This is because these conventional methods are not based on the actual fatigue mechanisms of high strength steels. To solve this problem completely, we need first to observe carefully the fatigue fracture mechanisms associated with high strength steels. We then need to elucidate the factors which control a deviation from a monotonic increase in fatigue strength with hardness, and the associated large increase in scatter, together with mean stress effects.

In the following, the method of fatigue strength evaluation established for $R = -1$ (zero mean stress) is extended in order to solve the mean stress problem.

6.5.1 Quantitative Evaluation of the Mean Stress Effect on Fatigue of Materials Containing Small Defects

To establish a fatigue strength prediction equation for small defects under a mean stress, it is more convenient to use specimens containing small artificial defects than those using natural inclusions. This is because we can always identify the shape and size of defects at fracture origins. In order to investigate the effects of microstructures, fatigue tests on materials having different hardness values are also necessary. Research [97] based on these ideas is explained in the following.

Two materials, one soft and the other hard, were used. The soft material is 0.13% C steel ($H_V = 105$), and the hard material a maraging steel ($H_V \cong 740$). Tension-compression fatigue tests, under mean stress, were conducted using specimens containing artificial holes. As the fatigue behaviour of the maraging steel may seem to be more interesting, the data for the grade 2500 MPa maraging steel is described in detail.

Table 6.7 shows the chemical composition of the maraging steel. Fig. 6.23 shows the specimen geometry. Specimen surfaces were first finished using Number 6 emery paper,

Table 6.7 Chemical composition of the maraging steel (wt.%)

C	Si	Mn	P	S	Ni	Mo	Co	Al	Ti
0.007	0.02	0.01	0.003	0.003	17.50	3.79	12.60	0.11	1.86

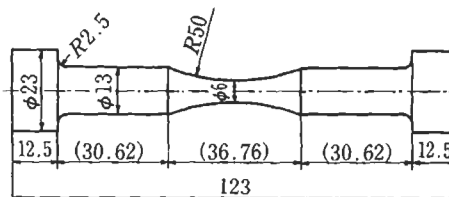


Figure 6.23 Tension-compression fatigue specimen, maraging steel.

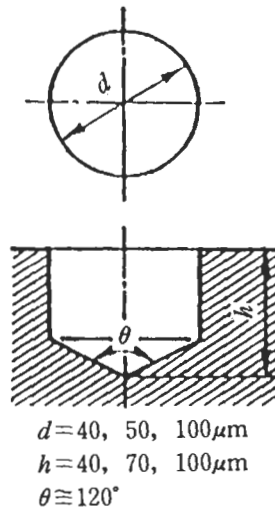


Figure 6.24 Geometry of artificial hole.

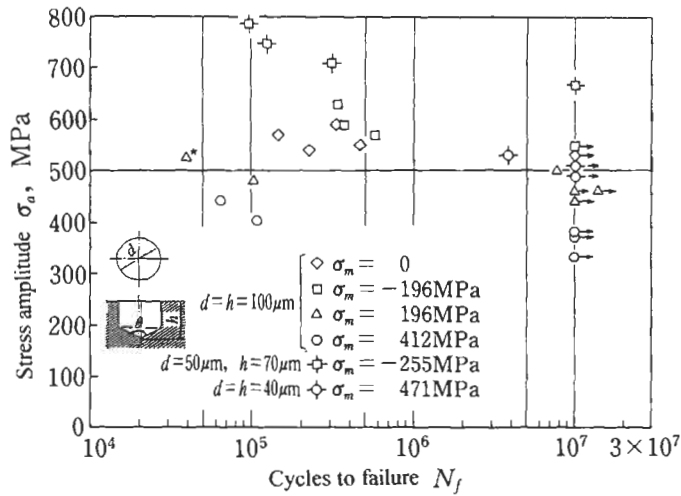


Figure 6.25 $S-N$ data for tension-compression fatigue tests on maraging steel.

and the surface layer was then removed by electropolishing to a depth of approximately $30 \mu\text{m}$. Next an artificial hole, as shown in Fig. 6.24, was introduced into the central part of a specimen. Corresponding fatigue data for zero mean stress ($\sigma_m = 0, R = -1$) are reported in detail in Murakami et al. [98].

Fig. 6.25 shows $S-N$ data for the maraging steel. Numbers of cycles to crack initiation, relative to those for final failure, are large compared with those for low strength steels. Regardless of the presence of an artificial hole, the crack initiation life shows a large amount of scatter, with concomitant large scatter in total lives. Thus, it

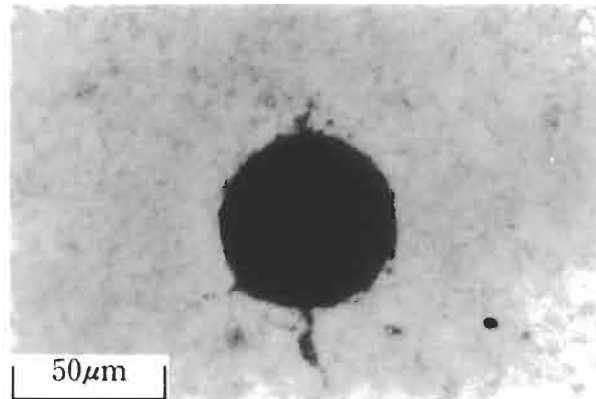


Figure 6.26 Non-propagating crack at fatigue limit of maraging steel ($H_V = 740$, $\sigma_a = 666$ MPa, $\sigma_m = -255$ MPa, hole diameter = $50 \mu\text{m}$, hole depth = $70 \mu\text{m}$).

is not appropriate to draw a single, unique curve through the data for a single series of specimens. The stress steps used for the fatigue tests, either 19.6 MPa (2 kgf/mm^2) or twice this, were larger than for conventional tests. Consequently, non-propagating cracks were not necessarily detected at a stress defined as a fatigue limit, although strictly speaking, the fatigue limit must be determined by the threshold condition for non-propagation of a crack, including steels as hard as maraging steels [98]. However, because fatigue test stresses for high strength steels are relatively very high, a fatigue limit determined by stress steps of 19.6 MPa may be regarded as very close to the exact fatigue limit.

Fig. 6.26 shows an example of non-propagating cracks observed at a fatigue limit. Fig. 6.27 shows endurance data for specimens containing a hole with $d = h = 100 \mu\text{m}$. Data for $R = -1$ were obtained using rotating bending fatigue tests [98]. The modified Goodman diagram prediction, indicated by the dotted line, is unconservative. It may be shown that the Soderberg diagram prediction is also unconservative. This is because then yield stress, σ_Y , is very close to the ultimate tensile strength, σ_B .

Now, a prediction equation which takes into account the effect of mean stress should be based on the equation for $R = -1$ (zero mean stress), that is Eq. 6.1. For $R = -1$ the equation should reduce to Eq. 6.1. Thus, as a possible and relatively simple equation, the following may be assumed.

$$\sigma_w = \frac{1.43(H_V + 120)}{(\sqrt{\text{area}})^{1/6}} \cdot \left[\frac{1 - R}{2} \right]^\alpha \quad (6.6)$$

$$R = \frac{\sigma_{\min}}{\sigma_{\max}} \quad (6.7)$$

In order to determine the value of α in Eq. 6.6, values of the ratios of σ_w to $1.43(H_V + 120)/(\sqrt{\text{area}})^{1/6}$ were plotted against $(1 - R)/2$ on logarithmic scales.

Fig. 6.28 shows the results of this analysis. To investigate the effect of microstructure, data for 0.13% C steel [99] are also plotted on the figure. All the numerical data are summarised in Table 6.8. From Fig. 6.28, we obtain $\alpha = 0.300$ for maraging steel, and

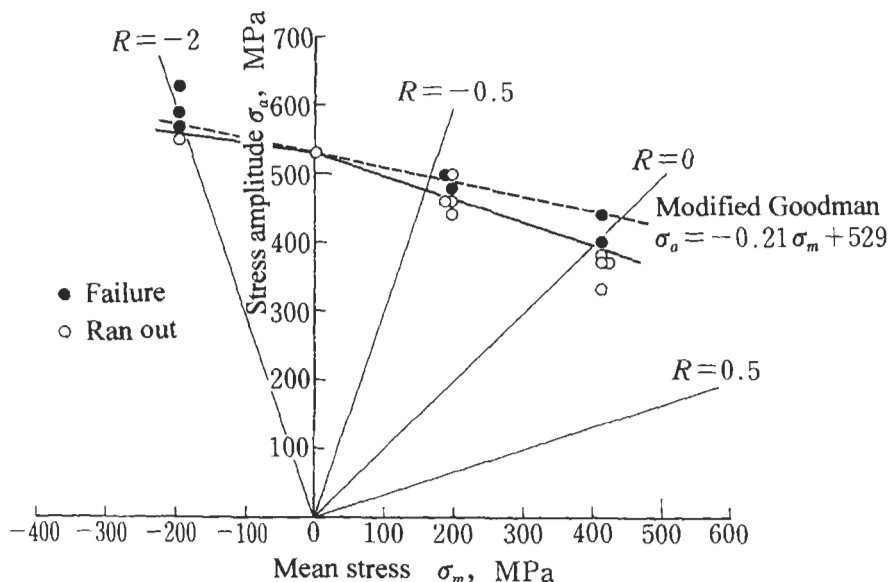


Figure 6.27 Endurance data for specimens containing a hole with $d = h = 100 \mu\text{m}$.

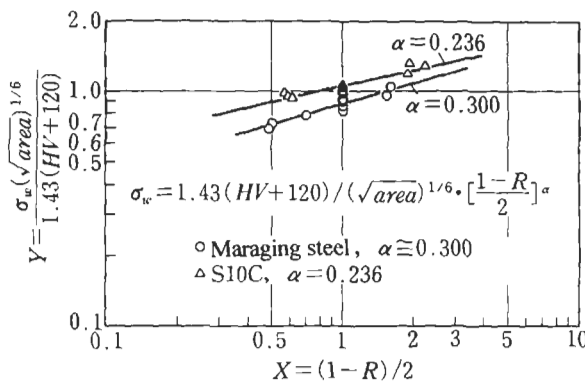


Figure 6.28 Influence of stress ratio, R , on the fatigue limit.

$\alpha = 0.236$ for 0.13% C steel. For $R = -1$ the ordinate and abscissa should both be 1.0, but the data for maraging steel do not obey this rule. This is because, including $R = -1$, there is approximately 10% difference between Eq. 6.1 and experimental data for maraging steel [3]. As can be seen in Fig. 6.28, it seems that the value of α in Eq. 6.6 is only weakly dependent upon microstructure. Since at present we only have data for two materials, we have no definite guide to the choice of the most appropriate material parameter. Despite the large difference in the hardness of the two materials ($H_V = 105$ for 0.13% C steel and $H_V = 740$ for maraging steel), there is only a weak dependency of α on material. We can conclude that it is not wise to introduce a new, additional material

Table 6.8 Experimental results used to derive the fatigue limit prediction equation as a function of R ratio, and evaluation of its accuracy
$$X=(1-R)/2, \quad Y=\sigma_w(\sqrt{area})^{1/6}/[1.43(HV+120)]$$

Maraging steel								
HV	σ_m (MPa)	σ_w (MPa)	R	\sqrt{area} (μm)	X	Y	σ_w' (MPa)	σ_w/σ_w'
740	-255	667	-2.238	56.0	1.62	1.07	727	0.918
730	-196	549	-2.111	92.5	1.56	0.961	652	0.842
744	196	461	-0.402	92.5	0.701	0.785	528	0.873
704	412	383	0.037	92.5	0.482	0.691	446	0.858
780	471	510	-0.040	37.0	0.502	0.723	572	0.892
740	0	686	-1	19.1	1	0.912	752	0.912
740	0	677	-1	37.0	1	1.00	677	1.00
740	0	559	-1	63.2	1	0.907	616	0.907
740	0	530	-1	92.5	1	0.917	578	0.917
740	0	471	-1	94.9	1	0.818	576	0.818
740	0	441	-1	185.0	1	0.856	515	0.856
S 10 C								
105	98	157	-0.231	46.2	0.616	0.925	151	1.04
	98	142	-0.183	92.5	0.592	0.939	134	1.06
	98	132	-0.147	185.0	0.574	0.980	118	1.12
	-98	206	-2.814	46.2	1.91	1.214	198	1.04
	-98	201	-2.902	92.5	1.95	1.330	177	1.14
	-98	176	-3.512	185.0	2.26	1.307	163	1.08
	0	172	-1	46.2	1	1.01	170	1.01
	0	157	-1	92.5	1	1.04	151	1.04
	0	142	-1	185.0	1	1.05	135	1.05

parameter which may make the prediction equation more complicated. Thus, we again adopt H_V as the most appropriate material parameter, as was done in the derivation of Eq. 6.1. By considering values of α in Fig. 6.28, and H_V values for the two materials, we can obtain an equation for α as:

$$\alpha = 0.226 + H_V \times 10^{-4} \quad (6.8)$$

Table 6.8 compares values of the experimental fatigue limit, σ_w , with those for the fatigue limit, σ_w' , calculated using Eqs. 6.6 and 6.8. They agree to within $\pm 15\%$.

6.5.2 Effects of Both Nonmetallic Inclusions and Mean Stress in Hard Steels

The prediction equation obtained in the previous section is applied to the fatigue behaviour of a high speed tool steel, SKH51.

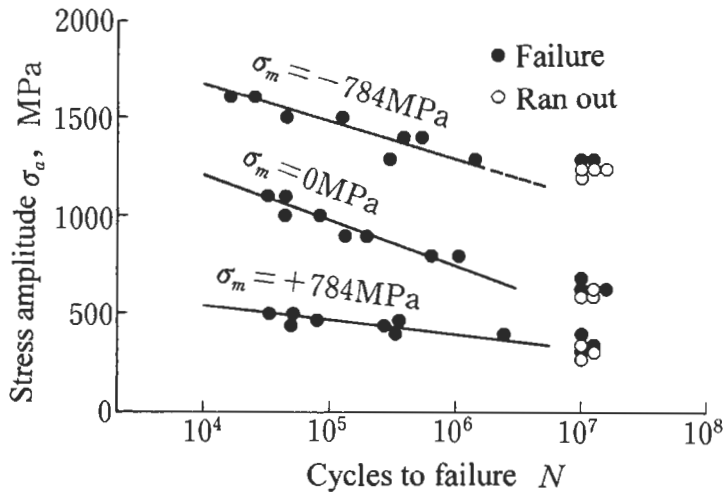


Figure 6.29 $S-N$ curves for high speed tool steel SKH51 ($H_V = 654$).

Tool steels are commonly used, not only for cutting tools, but also for dies. When we use tool steels for cutting tools, their small size means that the effects of nonmetallic inclusions are relatively insignificant. However, when we use tool steels for dies fatigue fracture from nonmetallic inclusions cannot be ignored, because the sizes of dies are in general much larger than those of cutting tools [90,96]. Although the appearance of nonmetallic inclusions is different from those of artificial holes and notches, and of other natural defects, as previously discussed their effect on fatigue limits is mechanically equivalent to those of small defects.

Fig. 6.29 shows $S-N$ curves for the tool steel, $H_V = 654$. The tensile mean stress data show much scatter, and the slope of the $S-N$ curve is much less than for $R = -1$ ($\sigma_m = 0$), resulting in difficulty in determining the exact fatigue strength, and also the fatigue life for a given stress level. Fatigue tests were conducted for up to 10^7 cycles, but for $\sigma_m = 784$ MPa we cannot define the fatigue limit as the maximum stress for an endurance of 10^7 cycles. Emura and Asami [100–102] reported that some heat-treated high strength steels do not have a clearly defined fatigue limit even at $N = 10^8$. These phenomena may be caused by compressive residual stresses which reduce crack growth rates, especially when a crack is small. Fatigue failures after very large numbers of cycles, up to $N = 10^8$ to 10^9 , observed not only in tool steels, but also in other high strength steels, has recently attracted the attention of engineers. In the following, data for SKH51 are discussed from the viewpoint of this phenomenon. An influencing factor is revealed, and this leads to a method for the quantitative evaluation of fatigue limits.

Fig. 6.30 shows a fish eye, and the nonmetallic inclusion at the centre of this fish eye. For this specimen $H_V = 654$, and it failed at $N_f = 29.2 \times 10^4$ under a stress amplitude $\sigma_a = 1275$ MPa, and mean stress $\sigma_m = -784$ MPa. The fatigue limit for this specimen can be calculated from these data. For internal inclusions, modifying Eq. 6.3, which is for $R = -1$, the prediction equation for $R \neq -1$ becomes as follows.

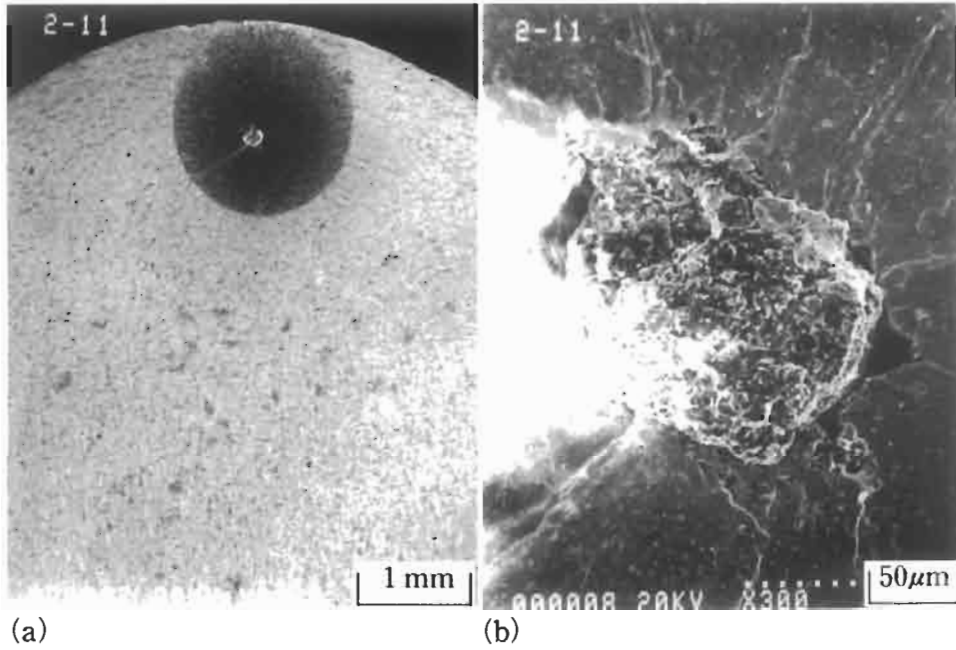


Figure 6.30 Fatigue fracture surface with inclusion at fracture origin ($H_V = 654$, $\sigma_m = -784$ MPa, $\sigma_a = 1275$ MPa, $N_f = 29.2 \times 10^4$). (a) Fish eye. (b) Inclusion at centre of fish eye.

[Fatigue limit prediction equation for internal inclusions, $R \neq -1$.]

$$\sigma_w = \frac{1.56(H_V + 120)}{(\sqrt{\text{area}})^{1/6}} \cdot \left[\frac{1 - R}{2} \right]^\alpha \quad (6.9)$$

where $\alpha = 0.226 + H_V \times 10^{-4}$.

Now, because the fatigue limit, σ_w , is unknown, R is also unknown. Therefore, we take the test stress, σ_a , as the first approximation to σ_w , and take the corresponding value of the stress ratio, R , as given by:

$$R = \frac{\sigma_m - \sigma_w}{\sigma_m + \sigma_w} \quad (6.10)$$

Inserting this value of R into Eq. 6.9 we obtain a new value for σ_w which differs from the first approximation. Thus, we take the next approximation as the average of these two values, and calculate a new value of R using Eq. 6.10. Inserting this new value of R into Eq. 6.9 we obtain a new value for σ_w . We can obtain a final value for σ_w by continuing the iteration until it converges. This converged value is denoted by σ'_w , as the estimated fatigue limit. (The iterative calculation may easily be modified, depending on whether the value of the mean stress, σ_m , is compressive or tensile.)

In the case shown in Fig. 6.30, we have $\sigma_a/\sigma'_w = 1.39$, this means $\sigma_a > \sigma'_w$ which is in agreement with the fact that this specimen actually did fail from the nonmetallic inclusion.

Table 6.9 Inclusion location and size, stress at fracture origin, and estimated fatigue limit (SKH51)

H_V	d (mm)	Mean stress σ_m (MPa)	Stress amp. σ_a (MPa)	Cycles to failure $N_f \times 10^4$	Inclusion size $\sqrt{\text{area}}$ (μm)	Depth h (μm)	Shape	Estimated fatigue limit σ_w'	σ_a/σ_w'	
615	9	784	461	33.2	57.8	73		433	1.06	
			431	289.2	42.4	2766		462	0.94	
			461	163.4	73.0	3719		443	1.11	
			402	150.1	89.0	1125		397	1.01	
			402	242.3	69.3	1360		418	0.96	
	6	-784	1324	20.1	31.4	21		1000	1.32	
			1226	86.5	23.9	43		1024	1.20	
			1177	959.2	56.9	1329		956	1.23	
			1226	389.4	35.1	1116		993	1.24	
	654	9	784	402	340.5	64.8	196		449	0.90
				373	49.4	150.7	1532		377	0.99
				490	5.0	89.6	704		420	1.17
461				34.9	73.5	1282		437	1.05	
6		-784	1373	53.8	33.0	672		1026	1.34	
			1373	37.6	42.4	2297		1005	1.37	
			1275	29.2	150.7	1047		918	1.39	
			1275	140.5	70.4	1938		967	1.32	

Table 6.9 compares the stress amplitude, σ_a , and the estimated fatigue limit, σ_w' , for the tool steel SKH51, for two levels of H_V , under compressive and tensile mean stress, σ_m . The values of σ_a/σ_w' are mostly higher than 1.0, verifying the validity of the prediction method. The table shows that values of σ_w' vary from specimen to specimen. This scatter is due to variations in the size of nonmetallic inclusions. Scatter in fatigue strength of this nature must be carefully considered in fatigue design. In particular, under a tensile mean stress the slope of an $S-N$ curve becomes very small, so that a slight difference in stress amplitude causes a big difference in fatigue life, and possibly the difference between failure and survival. This indicates that use of an arbitrary safety factor may be very unconservative. Accurate prediction of the lower bound fatigue strength, for a large number of specimens or components, is a promising method of coping with the fatigue behaviour of high strength steels, as explained in Section 6.5.3.

Fig. 6.31 shows modified $S-N$ curves in which the abscissa is the number of cycles

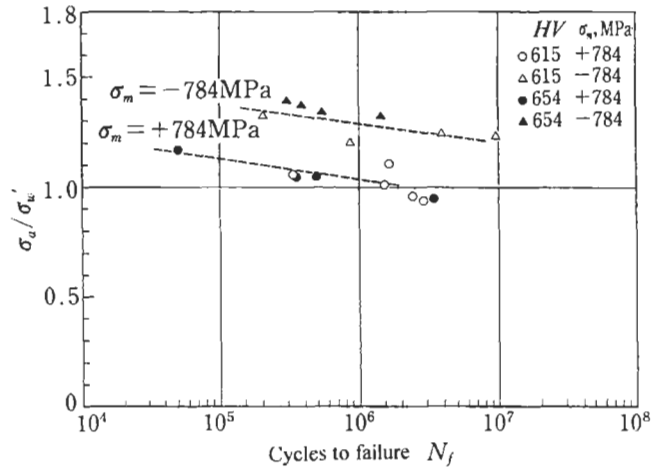


Figure 6.31 Modified $S-N$ curves (relationships between σ_a/σ'_w and N_f).

to failure, N_f , and the ordinate is the ratio, σ_a/σ'_w , of the stress amplitude, σ_a , to the estimated fatigue limit, σ'_w . There is a good correlation between σ_a/σ'_w and N_f . However, values of σ_a/σ'_w for $\sigma_m = -784$ MPa are larger than 1.20 even at $N_f = 10^7$ and accordingly fatigue limit estimates seem too low. This is because only data for $N_f \leq 10^7$ are plotted in Fig. 6.31. As described in the discussion on Fig. 6.29, if we define the fatigue limit by $N_f = 10^8$, then the value of estimated fatigue limit obtained by extrapolating the $S-N$ curve $N = 10^7$ to 10^8 does seem reasonable.

As previously explained, because Eq. 6.9 includes the stress ratio, R , on the right hand side, we need an iterative procedure to calculate σ_w for a known value of σ_m . In order to avoid the iterative procedure, Matsumoto et al. [103] proposed the following equation:

$$\sigma_w = \frac{1.56(H_V + 120)}{(\sqrt{area})^{1/6}} - \frac{1}{2}\sigma_m \tag{6.11}$$

Matsumoto et al. regarded the residual stress, σ_r , produced in a gear steel by shot peening as equivalent to a local mean stress, σ_m . They used Eq. 6.11 to calculate the fatigue limit, σ_w , at local points on specimens which had definite distributions of inclusion size and fracture origin. Differences between values estimated using Eq. 6.9 and Eq. 6.11 were at most 7%, so values estimated using Eq. 6.11 may be used as first approximations.

6.5.3 Prediction of the Lower Bound of Scatter and its Application

Fracture origins in high strength steels, such as tool steels, are mostly at nonmetallic inclusions. This causes fatigue strength scatter, which is a function of inclusion size and location. Thus, prediction of the scatter band lower bound is requested. A method for the case of $R = -1$ was described in Section 6.4. A method for $R \neq -1$ is explained in the following.

In order to predict the lower bound fatigue strength for a series of specimens, the maximum sizes of nonmetallic inclusions must be estimated. Data for extreme value statistics of nonmetallic inclusions at fish-eye centres are available, so it is possible to estimate the maximum inclusion sizes expected to be contained in particular numbers of specimens. The procedure is the same as for $R = -1$, $\sqrt{\text{area}}$ is taken as the representative dimension for nonmetallic inclusions.

Thus, modifying Eq. 6.5 for the prediction of the lower bound fatigue limit, σ_{wl} , we have the following equation.

[Prediction of lower bound fatigue limit, the largest inclusion is in contact with a specimen-free surface.]

$$\sigma_{wl} = \frac{1.41(H_V + 120)}{(\sqrt{\text{area}_{\text{max}}})^{1/6}} \cdot \left[\frac{1 - R}{2} \right]^\alpha \quad (6.12)$$

where $\alpha = 0.226 + H_V \times 10^{-4}$.

Two example predictions are as follows.

(a) Heat treatment 1. ($H_V = 615$), $\sigma_m = 784$ MPa, diameter, $d = 9$ mm, for 100 specimens $\sqrt{\text{area}_{\text{max}}} = 138.5$ μm .

Predicted value of $\sigma_{wl} = 319$ MPa.

(b) Heat treatment 2. ($H_V = 654$), $\sigma_m = -784$ MPa, $d = 6$ mm, 100 specimens.

The value of $\sqrt{\text{area}_{\text{max}}}$ for 100 specimens 6 mm in diameter can be estimated using the return period $T = (6/9)^2 \times 100 = 44.4$, then from Fig. 6.21 $\sqrt{\text{area}_{\text{max}}} = 123.3$ μm .

Thus, we have $\sigma_{wl} = 896$ MPa.

The prediction of σ_{wl} for other values of H_V , produced by different heat treatments, can be performed in the same manner, and we can express σ_{wl} as a function of H_V .

Fig. 6.32 shows the variation of σ_{wl} as a function of H_V for 100 specimens. The experimental data for $H_V = 615$ and $H_V = 654$ are plotted on the figure. The prediction of σ_{wl} for $\sigma_m = 784$ MPa may be considered reasonable in comparison with the experimental results.

Although the prediction of σ_{wl} , for $\sigma_m = -784$ MPa seems too low (too conservative), this, as was discussed for Figs. 6.29 and 6.31, is due to plotting experimental results for $N_f \leq 10^7$. If fatigue tests were carried out up to $N = 10^8$, then with a high degree of probability, there might be specimens which failed at stresses between the curve for σ_{wl} and the experimental results in Fig. 6.32. Fig. 6.33 shows fatigue fracture surfaces for specimens tested with tensile and compressive mean stresses. Fast unstable fracture of a specimen was thought to have taken place after a fatigue crack grew to the size of a fish eye shown in a photograph. The diameter of a fish eye for $\sigma_m = -784$ MPa is much larger than that for $\sigma_m = 784$ MPa. This implies that the fatigue crack growth life is much longer under compressive mean stress. Thus, on the basis of such fatigue crack growth behaviour, the number of cycles used for definition of a fatigue limit should be reconsidered. With understanding of this phenomenon, the prediction of σ_{wl} in Fig. 6.32 for $\sigma_m = -784$ MPa may be considered reasonable.

When specimens containing compressive residual stresses, produced by heat treatment or machining, are tested under rotating bending condition, some specimens may fail at lives longer than $N = 10^8$. This is presumably because the small fatigue crack growth life may be very long under compressive mean stress. In fact, Emura and Asami

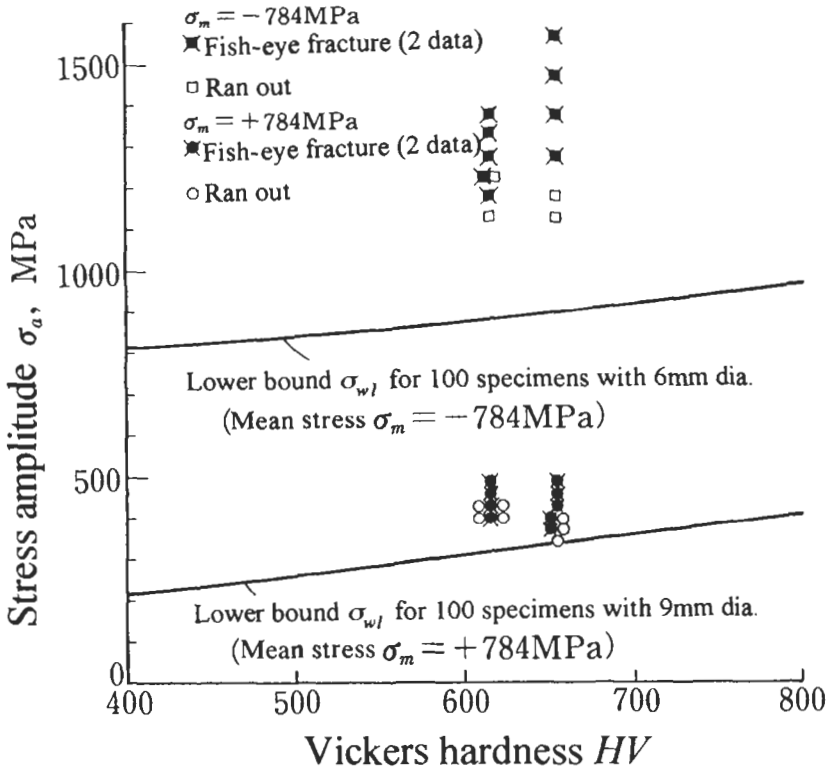


Figure 6.32 Relationship between fatigue strength scatter and estimated lower bound fatigue strength, σ_{wl} .

[101] confirmed that fatigue failure results for $N > 10^7$ could be successfully predicted using Eq. 6.1.

As described, if we can estimate the maximum size of defects or nonmetallic inclusions, \sqrt{area}_{max} , in a material, we can predict the lower bound fatigue strength for particular numbers of machine components, or for a different volume of material. Fatigue design based on lower bound fatigue strength is much more rational than that based on an arbitrary safety factor. Application to the case in which residual stresses are present is explained in Chapter 8.

6.6 Estimation of Maximum Inclusion Size \sqrt{area}_{max} by Microscopic Examination of a Microstructure

Thirty four nonmetallic inclusions found at fish-eye centres on the fracture surfaces of tension-compression specimens, made from high speed tool steel, obeyed extreme value statistics, as was explained in Section 6.4. The maximum inclusion size, \sqrt{area}_{max} , expected to be contained in larger numbers of specimens, was estimated from data

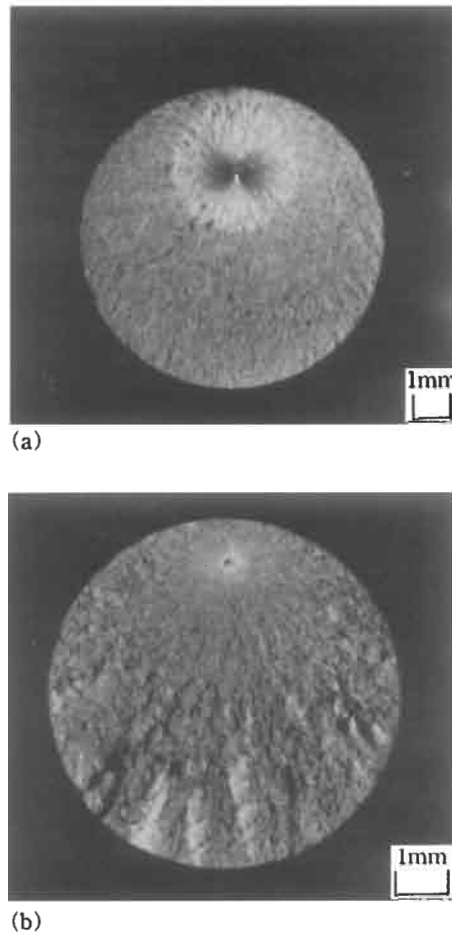


Figure 6.33 Difference in fish-eye size for positive and negative mean stress. (a) $H_V = 654$, $\sigma_m = -784$ MPa, $\sigma_a = 1275$ MPa, fish-eye diameter = 2.51 mm. (b) $H_V = 654$, $\sigma_m = 784$ MPa, $\sigma_a = 461$ MPa, fish-eye diameter = 0.65 mm.

plotted on probability paper. The maximum size, \sqrt{area}_{max} , estimated in this manner is not only useful for the prediction of fatigue strength scatter bands for large numbers of specimens, or mass production products, but also for the quality control of materials at the purchase acceptance stage. However, it is not an easy task to test over 30 specimens in tension-compression fatigue, and then to analyse the inclusion size distribution using extreme value statistics. It may be better to prepare a quicker and more convenient alternative method. Thus, a two-dimensional optical microscope method for the estimation of \sqrt{area}_{max} is explained. Although this method was first proposed by Nishijima et al. [24], they could not obtain a good correlation between the extreme value statistics distribution line and the fatigue life properties of spring steels. They therefore proposed another inclusion rating method called the rating point

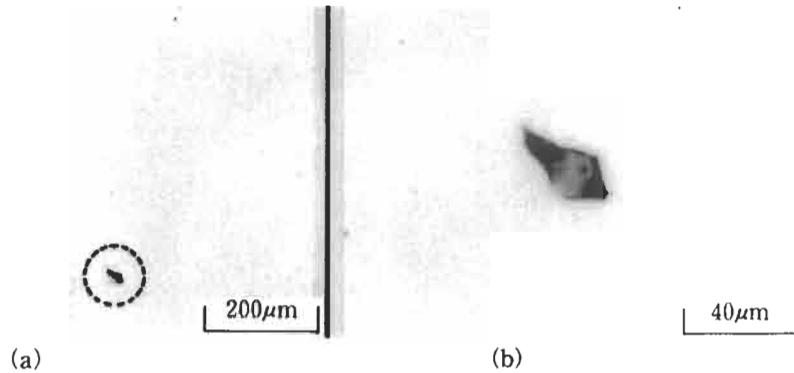


Figure 6.34 Measurement of maximum inclusion size (SAE 10 L 45). (a) Maximum inclusion in a standard inspection area ($S_0 = 0.482 \text{ mm}^2$). (b) Magnification of (a) ($\sqrt{\text{area}}_{\text{max}} = 17.2 \text{ } \mu\text{m}$).

method. Here, it must be noted that fatigue life should not be simply correlated with the extreme value statistics of inclusion data. Considering the background to the derivation of the fatigue limit prediction equations, Eqs. 6.1–6.12, we must pay attention to the contribution of the maximum inclusion size, $\sqrt{\text{area}}_{\text{max}}$. Thus, the estimation of $\sqrt{\text{area}}_{\text{max}}$ for inclusions becomes of great importance.

6.6.1 Measurement of $\sqrt{\text{area}}_{\text{max}}$ for Largest Inclusions by Optical Microscopy

Inspection of the polished surface of a metal using an optical microscope reveals numerous nonmetallic inclusions. The numbers of small inclusions are much larger than those of large inclusions, so the size distribution may be assumed to be close to exponential, as reported by Iwakura et al. [87], Ishikawa and Fujimori [104], Chino et al. [105], and Vander Voort and Wilson [106]. Thus, if we choose the largest inclusions within a sufficiently large number of inspection areas as representative of individual areas, then they are expected to obey extreme value statistics. A practical procedure for inclusion rating, based on this method, is explained for a 0.46% C-free cutting lead steel, SAE 10 L 45 [68]. First, a section perpendicular to the maximum applied stress is polished. (In the present case, a transverse section of a rolled bar.) Forty areas close to the specimen circumference were chosen at random, and inspected using an optical microscope. Each inspection area is of a standard size which is called the ‘Standard inspection area, S_0 ’ In this example the value of S_0 is 0.482 mm^2 . The largest inclusion size ‘ $\sqrt{\text{area}}_{\text{max}}$ ’ in each inspection area is measured, as shown in Fig. 6.34, for $j = 1$ to 40.

Fig. 6.35a shows the inclusion distribution on a transverse section of a rolled bar, and Fig. 6.35b that for a longitudinal section. If the rotating bending test method is used, then the inclusion rating must be done using a transverse section. The present material contains an approximately uniform density, ρ , of inclusions larger than $5 \text{ } \mu\text{m}$ in width, that is $\rho_t = 7.8$ for each standard inspection area, as in Fig. 6.35a, and $\rho_l = 8.2$ for Fig. 6.35b. Fig. 6.36 shows the plot, on extreme value statistics probability paper (Appendix C) of the cumulative frequency (or cumulative function) of $\sqrt{\text{area}}_{\text{max}}$ for a

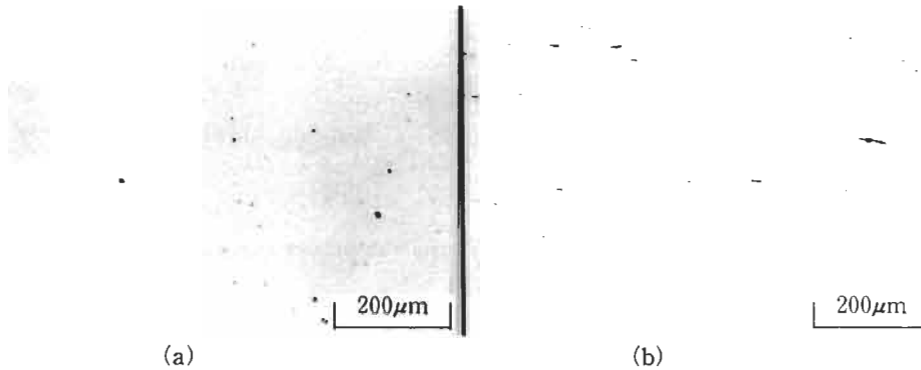


Figure 6.35 Inclusion distribution (SAE 10 L 45). (a) Transverse section. (b) Longitudinal section.

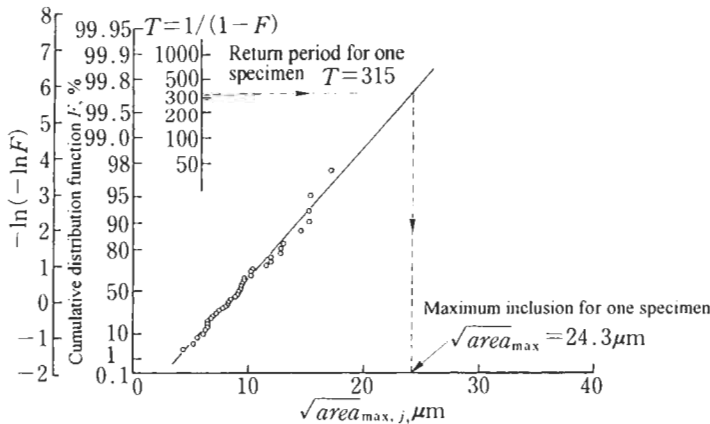


Figure 6.36 Extreme value statistics for inclusion size, $\sqrt{area_{max}}$ (SAE 10 L 45).

transverse section. The value of $\sqrt{area_{max}}$, expected for a larger area, may be predicted from the intersection of the distribution line and the return period, T . As an example, the return period, T , for N rotating bending fatigue specimens, is given by $T = NS/S_0$, where S is the area which is subjected to stresses higher than a critical stress for one specimen.

However, the above procedure is not necessarily precise from the following two viewpoints.

(1) The maximum inclusion size determined, as shown in Figs. 6.34 and 6.36, is not precisely the true maximum size. This is because, as shown in Fig. 6.37, the plane of observation does not necessarily coincide with the plane of the largest section of the largest inclusion [87,107]. However, the error is not expected to be large. This point is discussed in detail in Sections 6.6.2 and 6.6.3.

(2) The value of the return period, T , determined by the above method is not precise. In the above discussion, only the specimen surface, which has an area, was regarded as the region being subjected to fatigue damage, 'The damage area'. This area

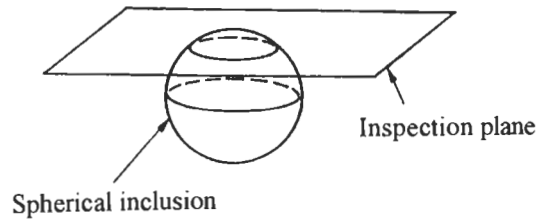


Figure 6.37 Sectioning an inclusion with an inspection plane.

is different from the area of a section perpendicular to the maximum normal stress. The conventional method described does give reasonable results in the case of rotating bending fatigue tests [68]. However, if we are to treat the tension–compression fatigue case, then we must consider the volume under test as the region containing possible fracture origin sites. Accordingly, it follows that accurate prediction of \sqrt{area}_{max} is difficult unless we modify the data, obtained by two-dimensional observation, in order to establish a rational definition of the return period, T . It is obvious that, for rotating bending fatigue, we must define a surface layer as having a finite thickness, and hence a damage volume so that, as for tension–compression fatigue tests, it may be treated as a 3D problem.

Although the extreme value statistics distributions of \sqrt{area}_{max} , as shown in Fig. 6.36, are questionable as indicated above, they are nevertheless important and useful for practical applications, as is explained in later examples. Appendix A explains the procedure for detecting and assessing defect size (in terms of \sqrt{area}) and its applications.

6.6.2 True and Apparent Maximum Sizes of Inclusions

As discussed in the previous section, there are two open questions in the method of determination of \sqrt{area}_{max} for inclusions by optical microscopy. We start by discussing the first of the two questions.

The value of \sqrt{area}_{max} determined by the method described in the previous section, does not coincide with the true maximum inclusion size. This is because the plane of observation does not necessarily coincide with the plane of the largest section of the largest inclusion [87,107]. The distribution line for true values of \sqrt{area}_{max} ($j = 1$ to J) is shown schematically by the dashed line in Fig. 6.38. True maxima are always larger than are corresponding apparent maxima (solid line), so the dashed line is always to the right of the solid line. The two lines are parallel to each other, and meet in the point at infinity, $j = \infty$.

However, because the data we can obtain by optical microscopy are the solid line in Fig. 6.38, and not the dashed line, we need to establish the magnitude of the difference between the two lines. It is very difficult to derive theoretically this difference between true maxima, and apparent maxima, of values obtained from inclusion data for various steel [107]. An experimental method is therefore introduced in which spheroidal graphite nodules in a nodular cast iron are regarded as a model of inclusions [108].

Ideally, in order to elucidate the difference between apparent and true maximum sizes

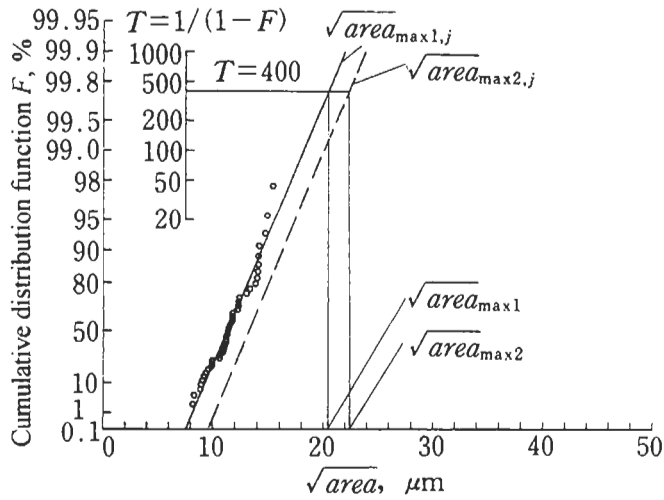


Figure 6.38 Extreme value statistics for apparent maximum and true maximum.

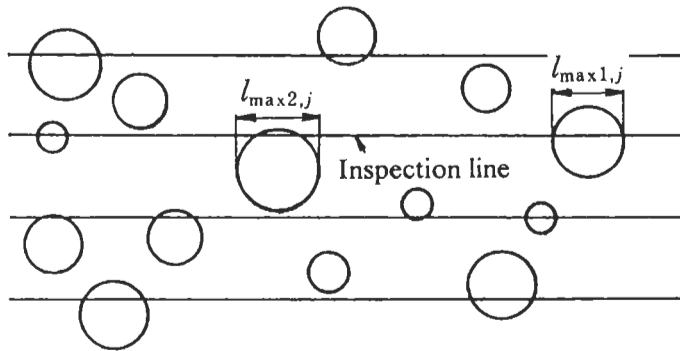


Figure 6.39 Apparent maximum size and true maximum size for nodular cast iron.

of spheroidal graphite nodules, it would be necessary to ascertain the 3D geometries of all the graphite nodules contained within a cast iron sample, but this would be almost impossible. Therefore an alternative problem is considered in which apparent maxima and true maxima are compared on the basis of the information contained within a single observation plane.

Let us prepare photographs of microscopic observations on a spheroidal graphite cast iron and draw equally spaced parallel lines, the inspection lines, as shown in Fig. 6.39. The distance between the lines is chosen such that two adjacent lines do not pass through the same single graphite nodule. We define the apparent largest size, $l_{max1,j}$ ($j = 1$ to J), as the longest line segment cut from an inspection line as it passes through a graphite nodule. The true maximum size, $l_{max2,j}$ ($j = 1$ to J), is defined as the largest measurable diameter of any graphite nodule cut by any line parallel to the inspection line.

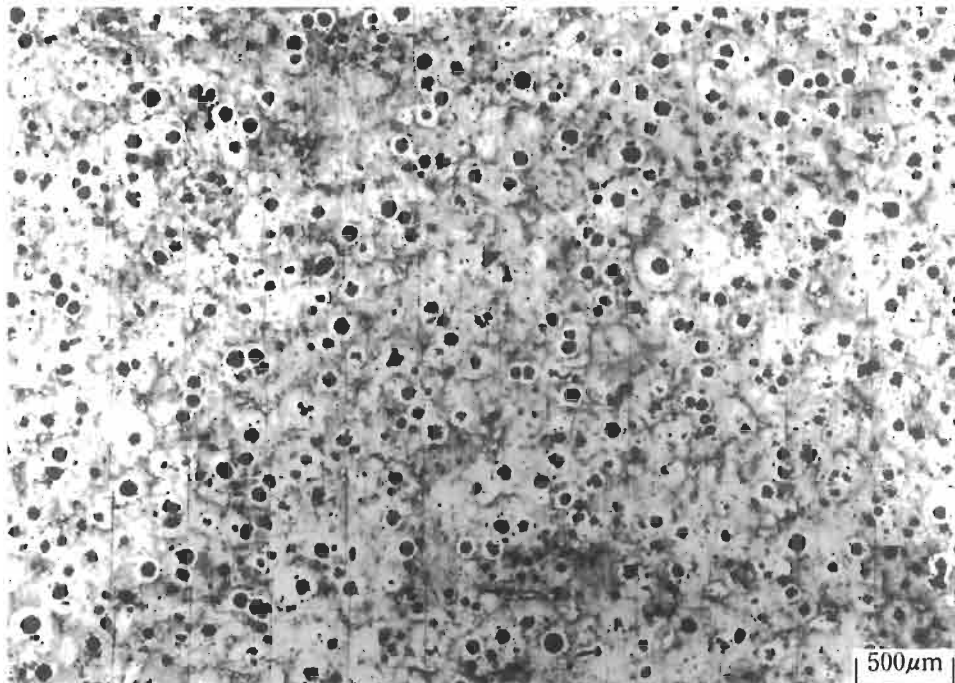


Figure 6.40 Optical micrograph of nodular cast iron microstructure.

The value of $l_{\max 2,j}$ can be measured by moving a scale parallel to the inspection lines and noting the largest reading on the scale cut off by a graphite nodule. If we plot $l_{\max 1,j}$ and $l_{\max 2,j}$ on extreme value statistics probability paper, then the two distribution lines are parallel, as was anticipated in the previous discussion. For a given return period, T , the expected apparent and true maximum graphic nodule sizes, $l_{\max 1,j}$ and $l_{\max 2,j}$, appearing on the inspection plane can be obtained. The value $l_{\max 1,j}$ is the apparent maximum, and the value of $l_{\max 2,j}$ the true maximum, for this value of T . If we could show that differences between $l_{\max 1,j}$ and $l_{\max 2,j}$ are small, then we would confirm the validity of the conventional method, in which observations of a certain plane are used to estimate the true maximum size of graphite nodules contained in a larger field.

Fig. 6.40 shows the micrograph of a nodular cast iron used to test the proposed method of determining $l_{\max 1,j}$ and $l_{\max 2,j}$. The 47 equally spaced inspection lines were drawn 0.1 mm apart, with a standard length, $L_0 = 3.5$ mm, in the vertical direction. This is identical to the vertical size of the photograph.

Fig. 6.41 shows plots of the data obtained. The distribution lines for $l_{\max 1,j}$ and $l_{\max 2,j}$ are both linear and parallel as expected. The return period, $T (= 100/[100 - F(\%)])$, for a line of length 1 cm is $T = 2.9$, and $T = 14.3$ for a line 5 cm long. If we estimate the differences between two return periods of the same order, that is $T = 3$ and 15, they are 8.6% and 7.2%, respectively. As may be seen in Fig. 6.41, the difference between the apparent maximum size and true maximum size is negligibly small for a sufficiently

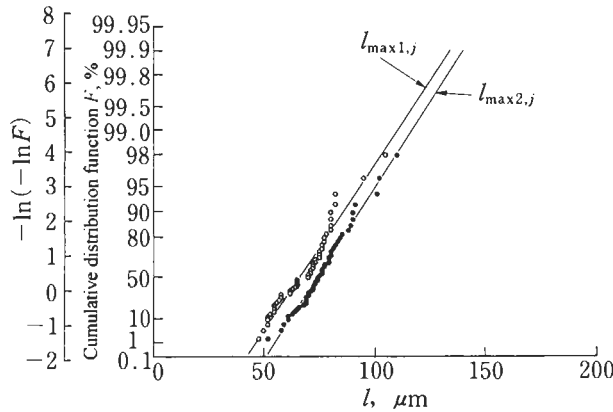


Figure 6.41 Extreme value statistics for graphite nodules, showing the relationship between apparent maximum size, $l_{\max 1, j}$, and true maximum size, $l_{\max 2, j}$.

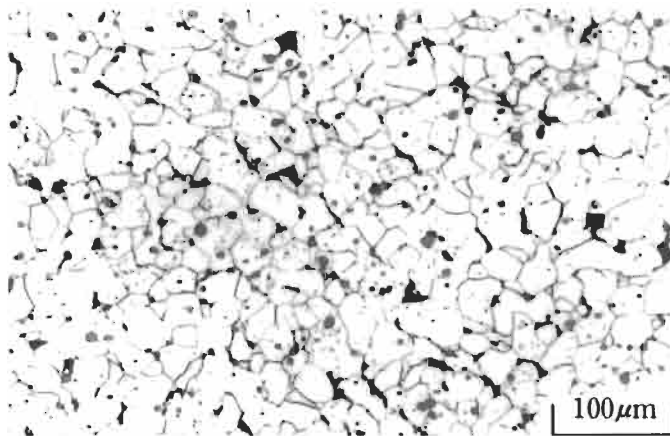


Figure 6.42 Microstructure of SAE 12 L 14.

large value of T . This conclusion is assumed to hold for the case of the maximum size ($\sqrt{\text{area}}$) for nonmetallic inclusions.

Thus, although the solid line in Fig. 6.38 corresponds to apparent maxima, the estimation error through using the solid line, rather than the dashed line, is assumed to be small. In fact, the return period, T , for one specimen in conventional fatigue testing is $T = 100\text{--}300$, and accordingly the error is expected to be much smaller.

In order to verify the validity of the present method of predicting maximum values using extreme value statistics, another example is explained in the following. This second example is the measurement of the grain size of SAE 12 L 14. Fig. 6.42 is a micrograph of the polished microstructure of SAE 12 L 14. Thirty two equally spaced inspection lines (vertical on the micrograph) were drawn 0.079 mm apart, with length, $L_0 = 0.417$ mm.

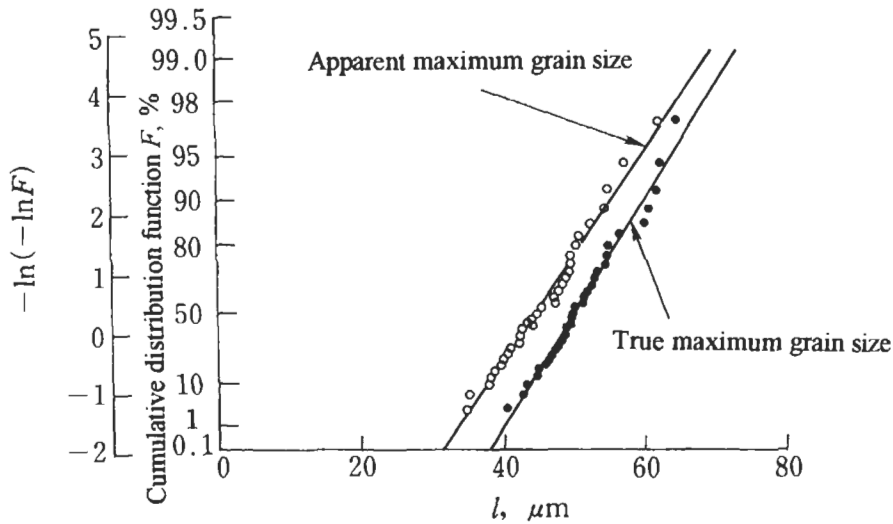


Figure 6.43 Extreme value statistics for grain size of SAE 12 L 14, showing the relationship between apparent maximum size and true maximum size.

Fig. 6.43 shows grain size plots using extreme value statistics. The plots for $l_{\max 1, j}$ and $l_{\max 2, j}$ are both linear, and are almost parallel to each other. Return periods for inspection lines 1 cm and 5 cm long are $T = 24.0$ and $T = 119.9$, respectively. By considering these values, differences for $T = 20$ and 120 are estimated to be 8.5% and 5.4%, respectively. It may be concluded that as the return period, T , increases, differences between apparent and true maximum sizes become negligibly small.

6.6.3 Two-dimensional (2D) Prediction Method for Largest Inclusion Size and Evaluation by Numerical Simulation

The discussion in the previous section was based on the expectation that the relationship between maximum values obtained by 1D and 2D measurements is analogous to the relationship between maximum values obtained by 2D and 3D measurements. Thus, the validity of the prediction method using optical microscopy has not been directly verified. In order to obtain more realistic quantitative information, we investigate the two questions, viewpoints (1) and (2), in Section 6.6.1 by numerical simulation [109]. In the following simulation, the apparent maximum value of $\sqrt{\text{area}}$ is denoted by $\sqrt{\text{area}}_{\max 1, j}$ and the true value by $\sqrt{\text{area}}_{\max 2, j}$. Corresponding predicted maximum values, obtained using these two distributions are denoted by $\sqrt{\text{area}}_{\max 1}$ and $\sqrt{\text{area}}_{\max 2}$.

Question (2) in Section 6.6.1 can be resolved by assigning a finite thickness to the standard area (S_0) as Fig. 6.44. Thus, the largest inclusion observed in the standard area, S_0 , is assumed to be contained within a small plate of thickness h_0 . Based on this idea, the return period, T , for the test volume, V , can be estimated by using $T = V/(S_0 \times h_0)$, and accordingly the predicted value of $\sqrt{\text{area}}_{\max}$ is at the intersection of the distribution line and T . In the following simulation [109], the validity of the method of predicting

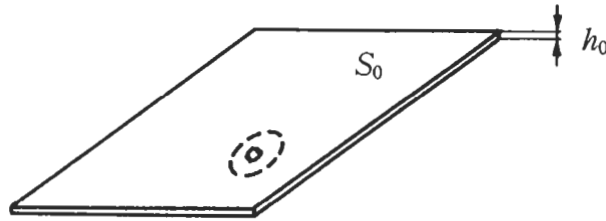


Figure 6.44 Inspection plane, thickness h_0 .

$\sqrt{\text{area}_{\text{max}}}$ is explained, together with the choice of an appropriate value for h_0 . In the simulation inclusions are assumed to be spherical, and their size is defined by diameter, D , rather than by $\sqrt{\text{area}}$. The method can be extended to the case of non-spherical inclusions. The size distribution of inclusions, $\phi(D)$ is assumed to obey the following type of exponential probability density function.

$$\phi(x) = \frac{1}{m} \exp\left(-\frac{x}{m}\right) \quad (6.13)$$

According to data of Iwakura et al. [87], Ishikawa and Fujimori [104], Chino et al. [105], and the author's unpublished data, assuming the exponential probability density function in the above equation seems realistic.

If we assume that the size distribution of inclusions is given by Eq. 6.13, then the mean value is m . In simulations, n inclusions are distributed within a cube, with centres at coordinates selected using random numbers. Fig. 6.45 shows inclusion distributions, obtained by computer simulations, on sections through such a cube. The distributions of apparent maximum size, $D_{\text{max}1,j}$, and true maximum size, $D_{\text{max}2,j}$, on these sections are expected to obey extreme value statistics. The two questions pointed out above are investigated with regard to these extreme value distributions.

In these simulations, nonmetallic inclusions are distributed within a cube with 1 mm sides. Values of m in Eq. 6.13 are taken such that the area fraction of nonmetallic inclusions is equal to that for SKH51 tool steel, and also so that the slopes of extreme value distributions are approximately equal. Accordingly the values $m = 1, 2,$ and $3 \mu\text{m}$ are used.

Fig. 6.45 shows an example of a section for each distribution. Fig. 6.46 shows plots of apparent maxima, $D_{\text{max}1,j}$, and true maxima, $D_{\text{max}2,j}$, on extreme value probability paper. The two previously indicated questions are analysed, referring to Figs. 6.45 and 6.46.

First, the prediction of the largest inclusion, which is expected to be contained within a risk volume, is discussed. We can confirm from Fig. 6.46 that distribution lines for $D_{\text{max}1,j}$ and $D_{\text{max}2,j}$ are parallel to each other. The risk surface on specimens, used for conventional rotating bending fatigue tests, ranges from 100 to 500 mm². Accordingly, the return period, $T = (S/S_0)$, is estimated as 400–2000. The apparent maxima, $D_{\text{max}1,j}$, and true maxima, $D_{\text{max}2,j}$, for $T = 400$ and 2000 are estimated using the distribution lines shown in Fig. 6.46, and the results are shown in Table 6.10. These results confirm the small differences between $D_{\text{max}1}$ and $D_{\text{max}2}$, and therefore guarantee that the distribution of apparent maxima, $D_{\text{max}1}$, is of sufficient accuracy for practical applications.

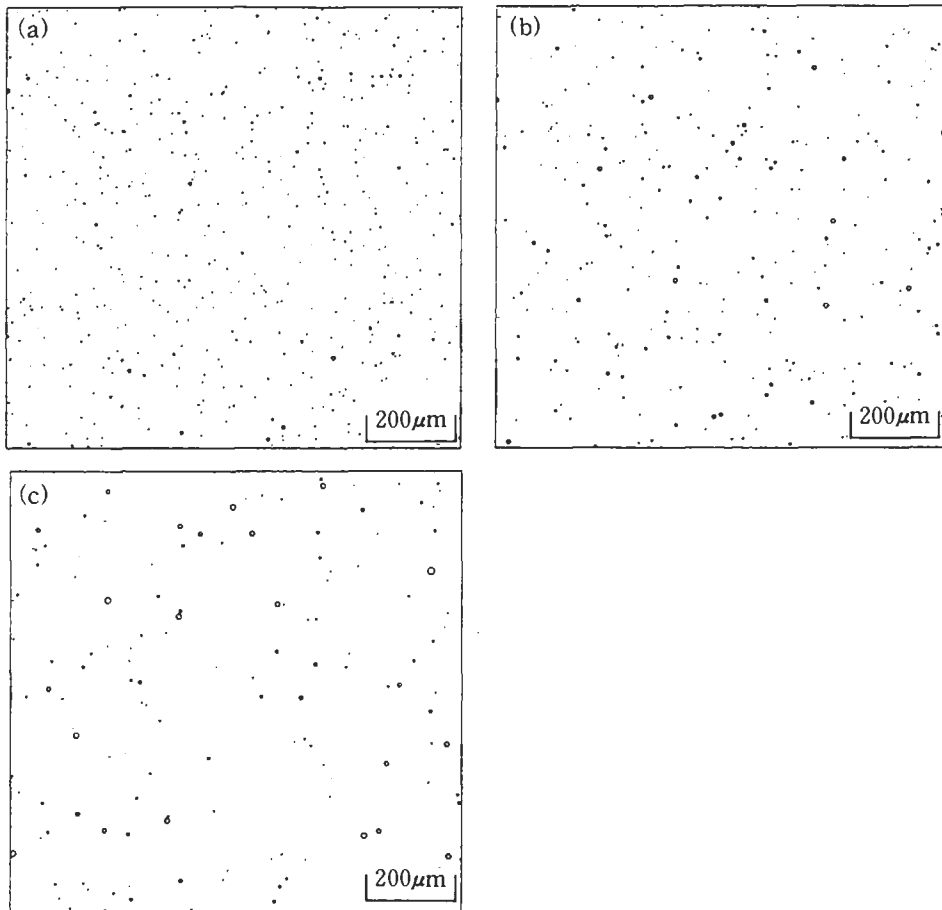


Figure 6.45 Computer simulations of inclusion distributions in a 1 mm^2 inspection area. (a) $m = 1 \text{ } \mu\text{m}$. (b) $m = 2 \text{ } \mu\text{m}$. (c) $m = 3 \text{ } \mu\text{m}$.

The next step is to predict the largest inclusion within a particular volume. For this purpose an appropriate value of h_0 , the plate thickness for a standard inspection area, must be determined. Since the value of h_0 is estimated to be of the order of inclusion size, the mean value of extreme value data for apparent maximum size may be taken as a trial value. Table 6.11 shows predictions of the largest inclusion, contained within a volume of 1 mm^3 , calculated in this manner. Since true maxima, $D_{\text{max}2}$, are known from the numerical simulations, we can calculate the errors for the predicted maxima. In all cases errors are less than 10%. Thus, the assumption for the value of h_0 is reasonable. Therefore, if we use the distributions of extreme values obtained by optical microscopy, then values of h_0 should be of the order of the mean of measured inclusion size data.

Appendix A explains details of the procedure with regard to inclusion rating, loading modes, and specimen geometries.

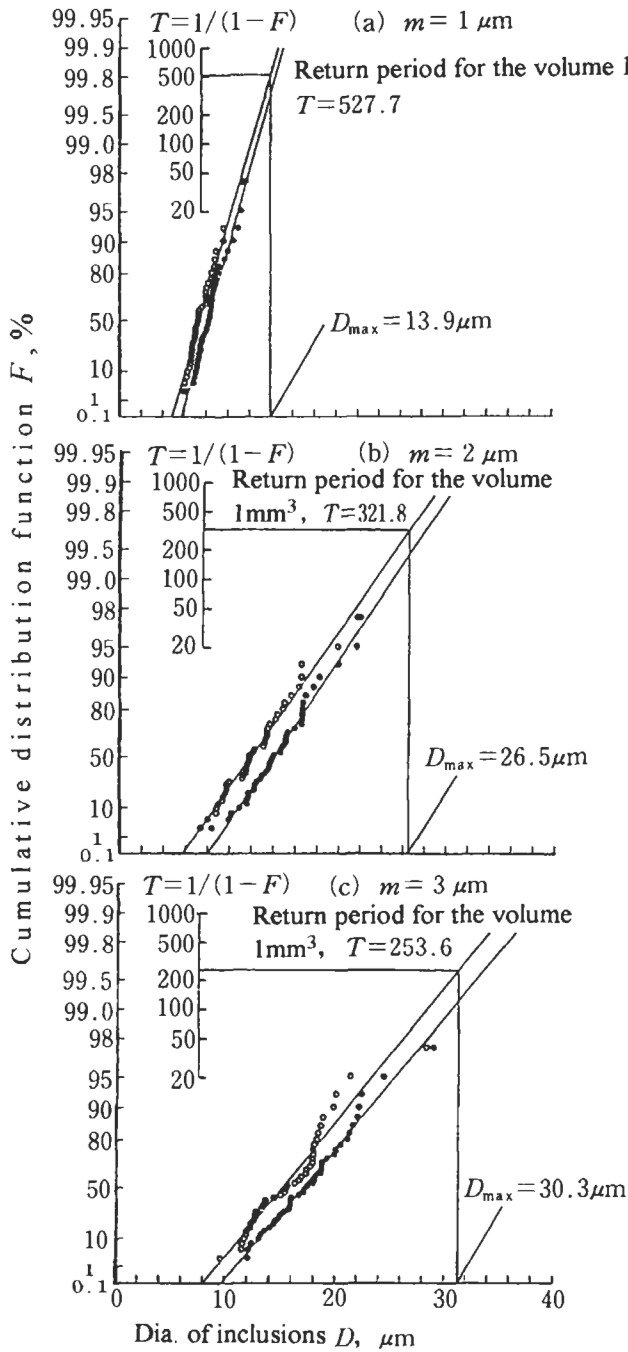


Figure 6.46 Extreme value statistics for inclusion size, showing the relationships between apparent maximum size and true maximum size for all m values used in computer simulations [standard inspection area, $S_0 = 0.25 \text{ mm}^2$, data points (inspection numbers) = 40].

Table 6.10 Difference between apparent maximum size and true maximum size

$m = 1\mu\text{m}$			
	$D_{\text{max}1}, (\mu\text{m})$	$D_{\text{max}2}, (\mu\text{m})$	Error (%)
$T = 400$	13.60	14.14	3.82
$T = 2000$	15.38	15.85	2.97

$m = 2\mu\text{m}$			
	$D_{\text{max}1}, (\mu\text{m})$	$D_{\text{max}2}, (\mu\text{m})$	Error (%)
$T = 400$	27.11	28.59	5.18
$T = 2000$	31.45	32.77	4.03

$m = 3\mu\text{m}$			
	$D_{\text{max}1}, (\mu\text{m})$	$D_{\text{max}2}, (\mu\text{m})$	Error (%)
$T = 400$	32.72	35.11	6.81
$T = 2000$	37.73	40.26	6.28

Table 6.11 Comparison between estimated maximum size and true maximum size

$m (\mu\text{m})$	1	2	3
Average of 40 maximum sizes ($=h_0$) (μm)	7.58	12.43	15.77
Return period T	527.7	321.8	253.6
Prediction (μm)	13.91	26.52	31.30
Maximum size in the volume $1\text{mm}^3 (\mu\text{m})$	15.24	27.83	30.40
Error (%)	- 8.73	- 4.71	+2.96

6.7 References

1. H. Kitagawa and S. Takahashi: Fracture Mechanics Approach to Very Small Fatigue Crack Growth and to the Threshold Condition, *Trans. Jpn. Soc. Mech. Eng. A*, **45(399)** (1979), 1289–1303.
2. Y. Murakami and M. Endo: A Geometrical Parameter for the Quantitative Estimation of the Effects of Small Defects on Fatigue Strength of Metals, *Trans. Jpn. Soc. Mech. Eng. A*, **49(438)** (1983), 127–136.
3. Y. Murakami and M. Endo: Effects of Hardness and Crack Geometry on ΔK_{th} of Small Cracks, *J. Soc. Mater. Sci., Jpn.*, **35(395)** (1986), 911–917.
4. Y. Murakami and K. Matsuda: Dependence of Threshold Stress Intensity Factor Range ΔK_{th} on Crack Size and Geometry, and Material Properties, *Trans. Jpn. Soc. Mech. Eng. A*, **52(478)** (1986), 1492–1499.
5. Report of Fatigue Committee: Special Issue on Material Defects and Fatigue Strength, *J. Jpn. Soc. Testing Mater.*, **6(48)** (1957) 557–636.
6. M. Sumita, I. Uchiyama and T. Araki: The Effect of Inclusions on Fatigue Properties of Steels with Various Matrixes, *Tetsu To Hagane*, **57(2)** (1971), 298–334.
7. K. Nishioka: On the Effect of Inclusion upon the Fatigue Strength, *J. Jpn. Soc. Testing Mater.*, **6(45)** (1957), 382–385.

8. T. Yokobori: General Lecture on Fatigue and Fatigue of Metallic Materials, *Sci. Mach.*, **13(7)** (1961), 973–976.
9. J. Watanabe: How Does Steel Cleanliness Influence on the Mechanical Properties, *Bull. Jpn. Inst. Met.*, **1(2)** (1962), 129–135.
10. K. Narita and K. Ito: Influence of Nonmetallic Inclusions on the Mechanical Properties of Steels II, *Kobe Steel Works Eng. Rep.*, **17(1)** (1967), 53–77.
11. Y. Kawada and S. Kodama: A Review on the Effect of Nonmetallic Inclusions on the Fatigue Strength of Steels, *J. Jpn. Soc. Strength Fract. Mater.*, **6(1)** (1971), 1–17.
12. M. Sumita, I. Uchiyama and T. Araki: Relationship between Various Inclusions and Fatigue of Steels; Fundamental Research on Fatigue Properties and Inclusions of Steels I, *Rep. Natl. Res. Inst. Met.*, **12(2)** (1969), 149–162.
13. M. Sumita, I. Uchiyama and T. Araki: A Model Experiment on Relationship between Fatigue Properties of Steel and Size, Shape, and Distribution of Inclusions, *Tetsu To Hagane*, **57(2)** (1971), 335–353.
14. T. Araki, T. Shih and R. Sagawa: The Effects on Non-metallic Inclusions and Structure on the Fatigue Properties of Deoxidized with Al, Si–Mn and Ca–Si 0.45% Carbon Steels, *Tetsu To Hagane*, **57(13)** (1971), 2042–2056.
15. T. Araki: Roles on Inclusions in Steel for the Fatigue Properties and Machinability Problems, *Proc. Int. Symp. Inclusions and Their Influence on Material Behavior*, Chicago, IL, ASM, 1988, pp. 149–155.
16. For example, Baring Steels: The Rating of Nonmetallic Inclusion, ASTM STP 576, 1975.
17. For example, Iron and Steel Handbook, IV, Iron and Steel Institute of Japan, 1981, p. 432.
18. E. Ineson, J. Clayton-Cave and R.J. Taylor: Variation in Fatigue Properties over Individual Casts of Steel, Part II, *J. Iron Steel Inst.*, **190** (1958), 277–283.
19. M. Ueno, T. Mitsuhashi and Y. Nakano: Studies on Ball Bearing Steels (II) (Effect of Some Metallurgical Factors on Life of Ball Bearing Steels), *Tetsu To Hagane*, **41(10)** (1955), 1102–1107.
20. M.J. Atkinson: The Influence of Nonmetallic Inclusions on the Fatigue Properties of Ultra-High-Tensile Steels, *J. Iron Steel Inst.*, **195** (1960), 64–75.
21. L.O. Uhrus: Through-Hardening Steels for Ball Bearings — Effect of Inclusions on Endurance, *Iron Steel Inst., Spec. Rep.*, **77** (1963), 104–109.
22. F. de Kazinczy: Effect of Small Defects on the Fatigue Properties of Medium-Strength Cast Steel, *J. Iron Steel Inst.*, **208** (1970), 851–855.
23. A. Adachi, H. Shoji, A. Kuwabara and Y. Inoue: Rotating Bending Fatigue Phenomenon of JIS SUJ2 Bearing Steel, *Electr. Furnace Steel*, **46(3)** (1975), 176–182.
24. S. Nishijima, E. Suzuki, Y. Niikura, K. Uchibori, M. Terashita and A. Morii: Interlaboratory Tests on Microscopic Evaluation of Non-Metallic Inclusions in Steels for Spring Use, *Trans. Jpn. Soc. Spring Res.*, **32** (1987), 52–74.
25. W.E. Duckworth and E. Ineson: The Effects of Externally Introduced Alumina Particles on the Fatigue Life of En24 Steel, *Clean Steel*, *Iron Steel Inst. Spec. Rep.*, **77** (1963), 87–103.
26. T. Tanaka and N. Funabashi: Fatigue Strength of 18%-Ni Maraging Steel and the Effect of Distributed Inclusions, *Trans. Jpn. Soc. Mech. Eng.*, **43(366)** (1977), 389–397.
27. E. Ineson, J. Clayton-Cave and R.J. Taylor: Variation in Fatigue Properties over Individual Casts of Steel, Part I, *J. Iron Steel Inst.*, **184** (1956), 178–185.
28. K. Sakabe: The Effect of Slag Inclusion on the Fatigue Strength of Some Alloy Steels, *Tetsu To Hagane*, **42(9)** (1956), 822–823.
29. S. Yasui and H. Yoshida: Influence of Sulphur Ghost on Fatigue Strength, *J. Jpn. Soc. Testing Mater.*, **6(48)** (1957), 619–623.
30. R. Inoue and S. Tsujimoto: On the Effect of Non-Metallic Inclusions upon the Fatigue Strength, *Tetsu To Hagane*, **45(3)** (1959), 322–324.
31. T. Yokobori, I. Maekawa and S. Korekawa: The Influence on Non-metallic Inclusions on the Fatigue Strength and the Statistical Nature of Steel, *J. Soc. Mater. Sci., Jpn.*, **12(117)** (1963), 434–438.
32. M. Sumita, I. Uchiyama and T. Araki: FeO Inclusions and Fatigue of Steel. (Fundamental Research on Relationship between Fatigue Properties of Steel and Inclusions, I), *Tetsu To Hagane*, **52(4)** (1966), 651–654.

33. P.W. Ramsey and D.P. Kedzie: Prot Fatigue Study of an Aircraft Steel in the Ultra High Strength Range, *Trans. AIME J. Met.*, **9(4)** (1957), 401–406.
34. M. Saito and Y. Ito: Some Properties of Ultra Clean Spring Steel, *Trans. Jpn. Soc. Spring Res.*, **30** (1985), 11–19.
35. M.F. Garwood, H.H. Zurburg and M.A. Erickson: Correlation of Laboratory Tests and Service Performance, Interpretation of Tests and Correlation with Service, ASM, Philadelphia, PA, 1951, pp. 1–77.
36. P.H. Frith: Fatigue Tests on Rolled Alloy Steels Made in Electric and Open-Hearth Furnaces, *J. Iron Steel Inst.*, **180** (1955), 26–33.
37. H.N. Cummings, F.B. Stulen and W.C. Schulte: Tentative Fatigue Strength Reduction Factors for Silicate-Type Inclusions in High Strength Steels, *Proc. ASTM*, **58** (1958), 505–514.
38. P.L. Teed: *Fatigue and Fracture of Metals*, Wiley, New York, 1952.
39. P.A. Thornton: The Influence of Nonmetallic Inclusions on the Mechanical Properties of Steel: A Review, *J. Mater. Sci.*, **6** (1971), 347–356.
40. J.T. Ransom: The Effect of Inclusions on the Fatigue Strength of SAE4340 Steels, *Trans. Am. Soc. Met.*, **46** (1954), 1254–1269.
41. T. Takahashi, H. Kishimoto and M. Kojiya: Notch Effect of MnS Inclusion on the Fatigue Strength of Steel, *Toyota Eng.*, **13(3)** (1961), 231–243.
42. K. Ohji and S. Harada: On the Anisotropy of Low-Cycle Fatigue Properties of Rolled Plates, *Trans. Jpn. Soc. Mech. Eng. Ser. I*, **38(313)** (1972), 2193–2200.
43. M. Kage and H. Nisitani: Anisotropy of the Fatigue Limit and of the Crack Propagating Property in a Rolled Steel Plate, *Trans. Jpn. Soc. Mech. Eng. Ser. I*, **41(344)** (1975), 1080–1088.
44. T. Hori, M. Hishiki, H. Kawabe and M. Uemura: Effect of Morphology and Direction of Nonmetallic Inclusions on Fatigue Life, *J. Jpn. Soc. Precision Eng.*, **49(10)** (1983), 1345–1350.
45. Data Sheet: Fatigue Strength of Steels, High Carbon Steels (Material RCC), *Sumitomo Met.*, **35(3)** (1983) 358–361.
46. M.R. Mitchell: Review of the Mechanical Properties of Cast Steels with Emphasis on Fatigue Behavior and the Influence of Microdiscontinuities, *Trans. ASME, J. Eng. Mater. Technol.*, Oct., 1977, pp. 329–343.
47. M.R. Mitchell: A Unified Predictive Technique for the Fatigue Resistance of Cast Ferrous-Based Metals and High Hardness Wrought Steels, *SAE/SP-79/448*, 1979, pp. 31–66.
48. Y. Kawada, H. Nakazawa and S. Kodama: The Effects of the Shapes and the Distributions of Inclusions on the Fatigue Strength of Bearing Steels in Rotary Bending, *Trans. Jpn. Soc. Mech. Eng. Ser. I*, **29(206)** (1963), 1674–1683.
49. T. Yokobori and M. Nanbu: Fatigue Fracture of Vacuum-Melted Ball Bearing Steel, *Proc. 1st Int. Conf. Fract., Sendai*, **2** (1966), 1529–1542.
50. T. Yokobori and M. Nanbu: Fatigue Crack Propagation in the High Hardened Steel, *Rep. Res. Inst. Strength Fract. Mater., Tohoku Univ.*, **2(2)** (1966), 29–44.
51. T. Yokobori, Y. Sawaki, S. Shono and A. Kumagai: Initiation and Propagation of Fatigue Crack in Unnotched Specimens of High Strength Eutectoid Steel, *Rep. Res. Inst. Strength Fract. Mater., Tohoku Univ.*, **12(2)** (1976), 29–44.
52. J.M. Cowling and J.W. Martin: Fatigue of Nitrided En41B Steel: Effect of Internal-Stress Distribution, *Met. Technol.*, Aug., 1981, pp. 289–296.
53. J.M. Hyzak and I.M. Bernstein: The Effect of Defects on the Fatigue Crack Initiation Process in Two P/M Superalloys: Part I, Fatigue Origins, *Met. Trans. A.*, **13** (1982), 33–43.
54. J.M. Hyzak and I.M. Bernstein: The Effect of Defects on the Fatigue Crack Initiation Process in Two P/M Superalloys: Part II, Surface–Subsurface Transition, *Met. Trans. A.*, **13** (1982), 45–52.
55. S. Konuma and T. Furukawa: Relationship between Hardness and Fatigue Strength of High Hardness Steel Having Martensitic Microstructure, *Proc. 18th Fatigue Symp., Soc. Mater. Sci. Jpn.*, 1986, pp. 5–9.
56. L.H. Donnell: In: R.E. Peterson (Ed): *Stress Concentration Factors*, Wiley, New York, 1974, p. 223.
57. R.H. Edwards: Stress Concentrations Around Spheroidal Inclusions and Cavities, *Trans. ASME, J. Appl. Mech.*, **75** (1951), 19–30.

58. M. Yatsuda, Y. Murakami and M. Isida: Interacting Dissimilar Elliptical Inclusions in Plane Problems, *Trans. Jpn. Soc. Mech. Eng. A*, **51(464)** (1985), 1057–1065.
59. T. Yokobori, H. Kuribayashi, M. Kawagishi and N. Takeuchi: Fatigue Crack Initiation and Propagation of a Low Carbon Martensitic High Tensile Steel, *J. Jpn. Inst. Met.*, **35(1)** (1971), 70–77.
60. C. Masuda, S. Nishijima and M. Shimodaira: On Fish Eye Formation in the Fatigue of Carburized Steels, *Trans. Jpn. Soc. Mech. Eng. A*, **49(440)** (1983), 413–423.
61. Y. Tanaka, S. Nishijima and C. Masuda: Fracture Mechanics Evaluation of Fatigue Strength of Spring Steels, Japanese Society of Spring Research, the 1986 Proceedings of the Fall Annual Meeting, pp. 35–38.
62. G.J. Fowler: The Influence of Non-Metallic Inclusions on the Threshold Behavior in Fatigue, *Mater. Sci. Eng.*, **39** (1979), 121–126.
63. T. Yokobori, I. Maekawa and S. Korekawa: The influence on Non-metallic Inclusions on the Fatigue Strength and the Statistical Nature of Steel, *J. Soc. Mater. Sci., Jpn.*, **12(117)** (1963), 434–438.
64. Y. Murakami, H. Kawano and T. Endo: Effect of Micro-Hole on Fatigue Strength (2nd Report, Effect of Micro-Hole of 40 μm –200 μm in Diameter on the Fatigue Strength of Quenched or Quenched and Tempered 0.46% Carbon Steel), *Trans. Jpn. Soc. Mech. Eng. A*, **45(400)** (1979), 1479–1486.
65. Y. Murakami and T. Endo: The Effects of Small Defects on the Fatigue Strength of Hard Steels, In: F. Sherrat and J.B. Sturgeon (Eds.): *Materials, Experimentation and Design in Fatigue*, Proc. Fatigue '81, Westbury House, 1981, pp. 431–440.
66. Y. Murakami, S. Kodama and S. Konuma: Quantitative Evaluation of Effects of Nonmetallic Inclusions on Fatigue Strength of High Strength Steel, *Trans. Jpn. Soc. Mech. Eng. A*, **54(500)** (1988), 688–696.
67. Y. Murakami and M. Shimizu: Effects of Nonmetallic Inclusions, Small Defects and Small Cracks on Fatigue Strength of Metals, *Trans. Jpn. Soc. Mech. Eng. A*, **54(499)** (1988), 413–425.
68. Y. Murakami and H. Usuki: Prediction of Fatigue Strength of High-Strength Steels Based on Statistical Evaluation of Inclusion Size, *Trans. Jpn. Soc. Mech. Eng. A*, **55(510)** (1989), 213–221.
69. Y. Murakami: Quantitative Evaluation of Effects of Defects and Non-metallic Inclusions of Fatigue Strength of Metals, *Tetsu To Hagane*, **75(8)** (1989), 1267–1277.
70. Y. Murakami: Fundamental Aspects of Fatigue Threshold of Metals Containing Small Defects, Small Cracks and Nonmetallic Inclusion — A Unified Quantitative Evaluation and Its Application, In: P. Lukas and J. Polak (Eds): *Basic Mechanisms in Fatigue of Metals*, ACADEMIA, Publishing House of the Czechoslovak Academy of Sciences, 1988, pp. 343–350.
71. J. Lankford: Initiation and Early Growth of Fatigue Cracks in High Strength Steel, *Eng. Fract. Mech.*, **9** (1977), 617–624.
72. J. Lankford: Inclusion–Matrix Debonding and Fatigue Crack Initiation in Low Alloy Steel, *Int. J. Fract.*, **12** (1976), 155–157.
73. J. Lankford and F.N. Kusenberger: Initiation of Fatigue Cracks in 4340 Steel, *Met. Trans. A*, **4** (1973), 553–559.
74. J. Lankford: Effects of Oxide Inclusions on Fatigue Failure, *Int. Met. Rev.*, Sept., 1977, pp. 221–228.
75. N.M.A. Eid and P.F. Thomason: The Nucleation of Fatigue Cracks in A Low-Alloy Steel under High-Cycle Fatigue Conditions and Uniaxial Loading, *Acta Met.*, **27** (1979), 1239–1249.
76. H. Nordberg: The Effect of Notches and Non-Metallic Inclusions on the Fatigue Properties of High Strength Steel, In: H. Nordberg (Ed): *Proc. Swedish Symp. Non-Metallic Inclusions in Steel*, 1981, pp. 395–428.
77. A. Melander: A Finite-Element Study of the Notch Effect at Surface Inclusions, *Int. J. Fatigue*, **12(3)** (1990), 154–164.
78. Y. Murakami and M. Endo: Effects of Hardness and Crack Geometries on ΔK_{th} of Small Cracks Emanating from Small Defects, In: K.J. Miller and E.R. de los Rios (Eds): *The Behaviour of Short Fatigue Cracks*, Mechanical Engineering Publ., London, 1986, pp. 275–293.
79. Y. Murakami and S. Nemat-Nasser: Growth and Stability of Interacting Surface Flaws of Arbitrary Shape, *Eng. Fract. Mech.*, **17(3)** (1983), 193–210.
80. H. Nisitani and Y. Murakami: Stress Intensity Factors of Semi-Elliptical Crack and Elliptical Crack (Tension), *Trans. Jpn. Soc. Mech. Eng.*, **40(329)** (1974), 31–40.
81. H. Nisitani, T. Ogata and M. Endo: Differences of the Fatigue Processes of 0.45% C Steel Quenched

- and Tempered at Various Tempering Temperatures, *Trans. Jpn. Soc. Mech. Eng. A*, **50(453)** (1984), 1104–1109.
82. K. Kimura, K. Yamada, M. Shimizu and T. Kunio: Observations on the Mode of Fatigue Crack Initiation in Induction Hardened S35C Steel at High Hardness Level, *Trans. Jpn. Soc. Mech. Eng. Ser. I*, **35(279)** (1969), 2146–2153.
 83. K. Kimura, K. Yamada, M. Shimizu and T. Kunio: Some Basic Aspects of the Fatigue Behavior of High-Hardened Steel, *Trans. Jpn. Soc. Mech. Eng. Ser. I*, **37(300)** (1971), 1475–1482.
 84. C. Masuda, S. Nishijima and Y. Tanaka: Relationship between Fatigue Strength and Hardness of High Strength Steels, *Trans. Jpn. Soc. Mech. Eng. A*, **52(476)** (1986), 847–852.
 85. H. Maikuma, M. Shimizu and K. Kawasaki: The Effect of Surface Micropits upon the Fatigue Strength of High Strength Steel, *Trans. Jpn. Soc. Mech. Eng. A*, **53(485)** (1987), 11–16.
 86. J. Su, M. Shimizu and K. Kawasaki: Defect Sensitivity of Fatigue Strength in High Strength Steel, *Trans. Jpn. Soc. Mech. Eng. A*, **54(506)** (1988), 1821–1825.
 87. S. Iwakura, M. Shimizu and K. Kawasaki: Effect of Toughness and Inclusion on Fatigue Strength of High Strength Steel, *Trans. Jpn. Soc. Mech. Eng. A*, **54(506)** (1988), 1826–1830.
 88. Y. Murakami, S. Fukuda and T. Endo: Effect of Micro-hole on Fatigue Strength [1st Report, Effect of Micro-hole (Dia.: 40, 50, 80, 100 and 200 μm) on the Fatigue Strength of 0.13% and 0.46% Carbon Steels], *Trans. Jpn. Soc. Mech. Eng. Ser. I*, **44(388)** (1978), 4003–4013.
 89. Y. Murakami, Y. Tazunoki and T. Endo: Existence of Coaxing Effect and Effect of Small Artificial Holes of 40–200 μm Diameter on Fatigue Strength in 2017S-T4 Al Alloy and 7:3 Brass, *Trans. Jpn. Soc. Mech. Eng. A*, **47(424)** (1981), 1293–1300.
 90. Y. Natsume, S. Miyakawa, Y. Uemura and Y. Murakami: Prediction of Fatigue Strength of High-Speed Steel Based on Estimation of the Maximum Size of Inclusions, *J. Soc. Mater. Sci., Jpn.*, **38(433)** (1989), 1133–1138.
 91. E.J. Gumbel: *Statistics of Extremes*, Columbia University Press, New York, 1958.
 92. A. Melander, R. Rolfson, A. Nordgon, B. Jansson, H. Hedberg and T. Land: Influence of Inclusion Contents on Fatigue Properties of SAE52100 Bearing Steels, Swedish Institute of Metals Research, IM-2589, 1990, pp. 1–31.
 93. U. Muralidharan, J.C. Stover and P. Kavadas: Effect of Residual Titanium on Fatigue Resistance of Bearing Steels, *Proc. Fatigue '93*, 1993, pp. 1483–1489.
 94. *Fatigue Design Handbook of Metallic Materials*, Edited by Soc. Material Science, Japan, Yokendo Ltd., Tokyo, 1978, p. 6.
 95. *Handbook of Mechanical Engineering*, Vol. 4, *Strength of Materials*, Japan Society of Mechanical Engineers, 1984, p. 121.
 96. Y. Natsume, S. Miyakawa and T. Muramatsu: Effect of Mean Stress on the Tensile and Compressive Fatigue Strength of High-Speed Steel, *J. Soc. Mater. Sci., Jpn.*, **37(417)** (1988), 606–611.
 97. Y. Murakami, Y. Uemura, Y. Natsume and S. Miyakawa: Effect of Mean Stress on the Fatigue Strength of High-Strength Steels Containing Small Defects or Nonmetallic Inclusions, *Trans. Jpn. Soc. Mech. Eng. A*, **56(525)** (1990), 1074–1081.
 98. Y. Murakami, M. Abe and T. Kiyota: Effects of Small Defects and Inclusions on Fatigue Strength of Maraging Steel, *Trans. Jpn. Soc. Mech. Eng. A*, **53(492)** (1987), 1482–1491.
 99. Y. Murakami, H. Morinaga and T. Endo: Effects of Geometrical Parameter and Mean Stress on ΔK_{th} of Specimens Containing a Small Defect, *J. Soc. Mater. Sci., Jpn.*, **34(385)** (1985), 1153–1159.
 100. H. Emura, K. Asami and Y. Nakazawa: High Cycle Fatigue Properties of High Strength Steels, *Prelim. Proc. of the 25th Japan Heat Treatment Society*, 1987, pp. 21–22.
 101. H. Emura and K. Asami: Fatigue Strength Characteristics of High Strength Steel, *Trans. Jpn. Soc. Mech. Eng. A*, **55(509)** (1989), 45–50.
 102. K. Asami: Long Life Fatigue Strength of Gas-Carburized Steel, *Proc. 6th Int. Conf. Mech. Behav. Mater.*, Kyoto, **2** (1991), 499–504.
 103. K. Matsumoto, T. Sampei, T. Toyoda and T. Kanazawa: Effect of Inclusion on Rotating Bending Fatigue Strength of Carburized and Shot-Peened Steels for Gear Use, *Proc. JSME Meet.*, **900(86)** (1990), 275–277.
 104. N. Ishikawa and T. Fujimori: Size Estimation of Sulfide Inclusions in Hot Rolled Steels Detected by Ultrasonic Testing, *Tetsu To Hagane*, **71(7)** (1985), 893–900.

105. A. Chino, H. Iwata and M. Ihida: The measurement of Particle Size Distribution of Al_2O_3 Inclusion in Ultra Low Oxygen Steel, *Tetsu To Hagane*, **77(12)** (1991), 2163–2170.
106. G.F. Vander Voort and R.K. Wilson: Nonmetallic Inclusions and ASTM Committee E-4, *ASTM Standardization News*, 1991, pp. 28–37.
107. R.T. DeHoff and F.N. Rhines: *Quantitative Microscopy*, McGraw-Hill, New York, 1968.
108. Y. Murakami, Y. Uemura and K. Kawakami: Some Problems in the Application of Statistics of Extreme Values to Estimation of the Maximum Size of Nonmetallic Inclusions in Metals, *Trans. Jpn. Soc. Mech. Eng. A*, **55(509)** (1989), 58–62.
109. Y. Uemura and Y. Murakami: A Numerical Simulation of Evaluating the Maximum Size of Inclusions to Examine the Validity of the Metallographic Determination of the Maximum Size of Inclusions, *Trans. Jpn. Soc. Mech. Eng. A*, **56(521)** (1990), 162–167.

Chapter 7

Bearing Steels

In this and following chapters, practical applications of the fatigue strength evaluation method, explained in earlier chapters, are introduced together with inclusion problems.

In bearing steels, tool steels and spring steels, nonmetallic inclusions have a strong influence on fatigue strength. Investigations have been carried out worldwide on the relationships between steel making processes and the chemical composition, shape, and size of nonmetallic inclusions [1–24]. This shows that the inclusion problem is of great concern to the steel-making industries and bearing-steel manufacturing industries.

Since stress states in ball bearing are mostly produced by contact loading, conventional fatigue strengths, such as are obtained from rotating bending and tension–compression tests, may not be directly related to the strengths of bearings. Some reports support this view [25,26]. However, many test results have been reported which show good correlations between conventional fatigue and contact fatigue [8,17]. The reason for the conflicting reports may be due to insufficient investigation of the causes of fatigue failure in the two cases. While many papers have reported in considerable detail the observation and analysis of nonmetallic inclusions at fracture origins, some papers give almost no description of microstructural features. There are many papers in which it is concluded that one type of nonmetallic inclusion is more detrimental than others simply because it was found more frequently at fracture origins. A typical, and incorrect, conclusion is that “MnS is not detrimental when compared with other types of hard inclusions”.

If the failure of ball or roller bearings is caused by nonmetallic inclusions, then the quality of materials may be evaluated by rotating bending, tension–compression, or ring-compression fatigue tests [20,27]. This is because nonmetallic inclusions have crucial influences on strengths obtained from conventional fatigue tests on materials containing nonmetallic inclusions. Researchers investigating bearing steels have used rotating bending fatigue tests as a standard fatigue test in order to evaluate bearing steels. This is because rotating bending fatigue tests require only a short testing time, are inexpensive, and give reliable information on the nonmetallic inclusions which control the quality of steels. In fact, there are many rotating bending fatigue studies on crack initiation and crack growth from nonmetallic inclusions, and on the fish-eye patterns observed [13,28–30].

The most important problems which strongly concern bearing steel engineers, and

bearing engineers, are the chemical composition of nonmetallic inclusions detrimental to fatigue strength, the relationship between cleanliness and fatigue strength, the correlation of cleanliness with nonmetallic inclusions at fracture origins, and the influence of chemical elements, such as O, S, Ti, Ca and Al, on these factors. The study by Monnot et al. [27] is very interesting from this viewpoint. Their study is reviewed in the following, together with studies by other researchers. Individual problems are described in detail in this chapter. Points discussed are also relevant to problems common to those of spring steels, tool steels, and various other high strength steels.

7.1 Influence of Steel Processing

Frith [31] was the first to indicate the influence of differences in steel-making processes on nonmetallic inclusions, and accordingly on fatigue strength. Although the quality of steels in the 1950s is remarkably different from that of the 1990s, Frith reported that the fatigue strength of British steels produced by vacuum remelting was inferior to that of Swedish steels produced by the open hearth process. The same result, on the influence of steel-making processes, was obtained in the experiments of Kawada et al. [29], as shown in Table 6.4.

Monnot et al. [27] investigated the differences between fatigue lives of ball bearing inner races and balls, and of rotating bending fatigue lives, for steels produced by various processes. They reported the order of excellence of processes as VAR, VD, acid HF, and basic arc. Monnot et al. thought that the cause of differences in fatigue lives was differences in the size and distribution of nonmetallic inclusions, although they did not compare these distributions directly.

Thus, the influence of steel-making processes, from the viewpoint of fatigue strength, has not been made altogether clear. One reason for ambiguous evaluation of steel-making processes may be a poor correlation between the state (shape and size) of inclusions in ingots and the state after plastic forming, such as rolling and forging. Although a decrease in the total oxygen (O) content usually results in fewer and smaller inclusions, control of inclusion size by controlling total oxygen content is not always satisfactory. Even if the total oxygen content is high, the final size of inclusions can be reduced by plastic forming provided that inclusions are made soft. Making inclusions soft is a useful method, available in practical steel-making processes, without decreasing the oxygen content [32]. These problems are of practical importance from the perspective of improving the quality of bearing steels. However, improvement of the quality of steels should always be assessed by correlating steel-making processes with fatigue test results.

7.2 Inclusions at Fatigue Fracture Origins

Fig. 7.1 [27] shows the influence of inclusions by correlating the chemical composition and size of inclusions at fatigue fracture origins with the applied nominal stress at fracture origins. One unit of the scale on the ordinate of Fig. 7.1 corresponds to a de-

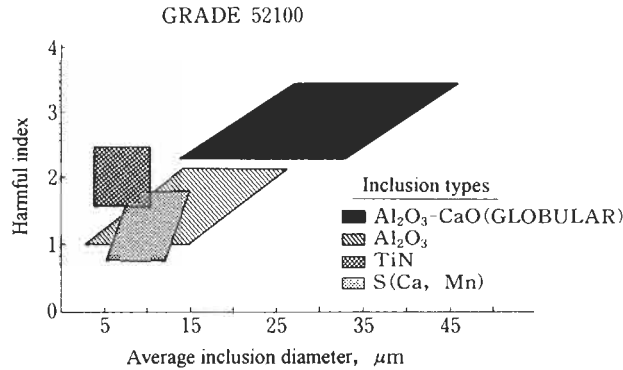


Figure 7.1 Harmful index of various inclusions (the ordinate scale unit is a decrease in fatigue strength of 125 MPa at $N = 10^8$) (after J. Monnot, B. Heritier and J.Y. Cogne [27]).

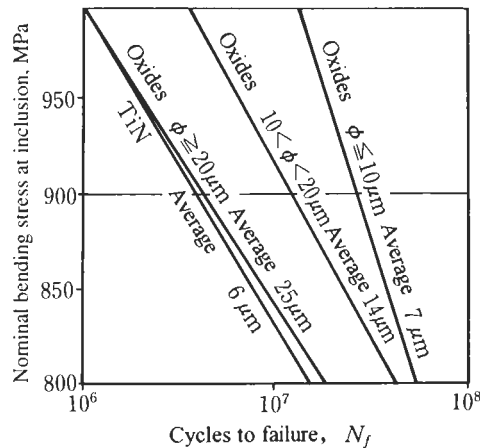


Figure 7.2 Relationship between fatigue life, N_f , and the nominal stress at a fracture origin for oxide and TiN inclusions. (After J. Monnot, B. Heritier and J.Y. Cogne [27].)

crease of 125 MPa in the fatigue strength at $N = 10^8$. Fatigue strengths at $N = 10^8$ were estimated by extrapolating the $S-N$ curves shown in Fig. 7.2. Nevertheless, Fig. 7.1 illustrates the influence of chemical composition and size of inclusions very clearly.

Fig. 7.1 indicates that in general large inclusions are harmful, but TiN is exceptionally detrimental and has an influence almost equivalent to oxide inclusions, such as Al_2O_3 , several times larger. Although the detrimental nature of TiN has been indicated by many researchers, this problem should be treated carefully. This is because the reason for the detrimental effect is guessed to be the high stress concentration factor due to the sharp angular shape of TiN. As previously described in Section 5.5, two different specimens having an identical size ($\sqrt{\text{area}}$) of a hole and a crack, have the identical fatigue strength regardless of the big difference in stress concentration factors. From this viewpoint, high

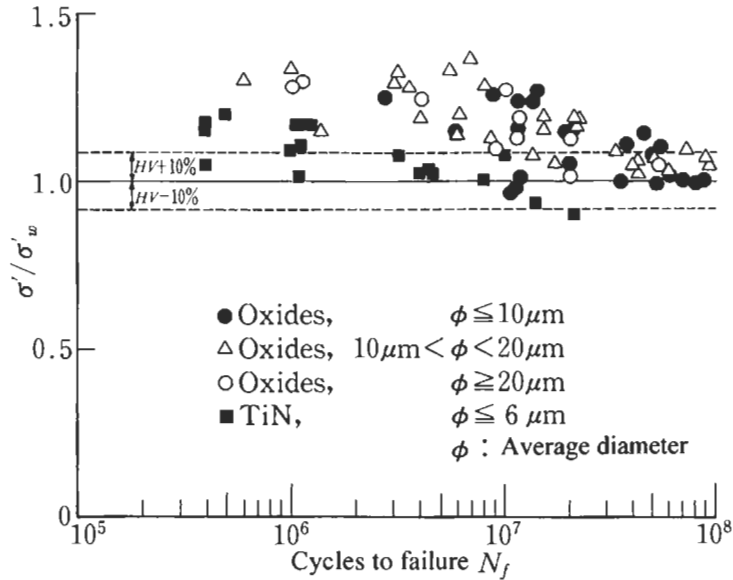


Figure 7.3 Modified $S-N$ data obtained by rearranging Fig. 7.2 (the ordinate scale is normalised by the estimated fatigue limit).

stress concentration factors associated with TiN cannot be the main reason for a low fatigue limit.

In discussing this problem, the extrapolation of the $S-N$ curve in Fig. 7.2 from $N = 10^7$ to $N = 10^8$ must be reconsidered. It must be also noted that when TiN becomes a fracture origin, the total size and shape do not appear on the fatigue fracture surface, and the measured size is likely to be less than the actual size. Since there are many misunderstandings on the influence of the shapes of inclusions, the influence of shape is discussed separately in detail in Chapter 10. The influence of carbides in tool steels, which is described in Chapter 9, also provides useful knowledge towards the understanding of the problem of inclusion shape.

Thus, let us reconsider Fig. 7.2, which was used to construct Fig. 7.1. Fig. 7.3 is a rearrangement of Fig. 7.2, constructed by using the original data taken from Monnot et al. Since the locations of inclusions at fracture origin are not identified, we use Eq. 6.5 to obtain a lower bound, that is the lowest value of fatigue strength. At the ordinate are dimensionless relative values obtained by normalising the applied stress at fracture origin by the estimated fatigue limit, that is the modified $S-N$ data. From this figure it is indeed evident that fatigue life is shorter for the case of fracture from TiN. However, we cannot necessarily say that the fatigue limit is lower than for other cases (fractures from other inclusions). It is not fair to define the fatigue limit by extrapolating the $S-N$ curve for fracture originating from TiN to $N = 10^8$. It may be appropriate, not only for TiN, but also for other inclusions, to interpret the trend of data, with $N_f = 10^7$ to 10^8 at $\sigma'/\sigma'_w \cong 1.0$, as being very close to the fatigue limit. This trend of $S-N$ curves is similar to the difference in $S-N$ curves for specimens containing cracks and holes, which was

described in Chapter 5. In other words, at an applied stress higher than the fatigue limit, in specimens containing a crack, with the same value of $\sqrt{\text{area}}$ as a hole, due to the high stress concentration factor fatigue cracks initiate earlier than in specimens containing a hole, and specimens fail earlier. However, as the applied stress approaches the fatigue limit, the difference in fatigue lives for specimens containing cracks and holes becomes small. Likewise, TiN causes earlier crack initiation than other globular inclusions, resulting in lower fatigue life at a stress higher than the fatigue limit. On the other hand, in terms of fatigue limit, behaviour is determined by the non-propagating condition for cracks initiated at inclusions, and accordingly the value of fatigue limit for a TiN fracture origin is approximately equal to those for other cases.¹

The Harmful Index in Fig. 7.1 is obtained by extrapolating $S-N$ curves to $N = 10^8$, where actually no data points exist. Thus, the Harmful Index exaggerates the influence of TiN. However, if we use the Harmful Index in Fig. 7.1 as an index for fatigue life, it may be useful.

Another interesting point in Fig. 7.1 is that the sizes of duplex inclusions containing CaO are remarkably larger than those of other inclusions.

7.3 Cleanliness and Fatigue Properties

Various inclusion rating methods have been proposed in many countries, such as the JIS (Japanese Industrial Standard) lattice point method [33], the ASTM method (E45), and the GOST-801-60 method (from the former Soviet Union).

According to Koyanagi and Kinoshi [34], the results of inclusion rating by the JIS method are independent of inspectors, it is easier than other methods, and the results obtained by the method are consistent with both the ASTM method and the GOST method. However, the correlation between the rating of cleanliness by these methods and fatigue strengths has not been made clear.

Rotating bending fatigue tests carried out by Adachi et al. [13] showed the unexpected presence of large inclusions in the so-called clean bearing steels tested, which had a high grade in the JIS lattice point method. Table 7.1 shows the results of observations of inclusions in the tests. Adachi et al.'s conclusion emphasises the importance of developing a new method to find this kind of extremely large inclusion, which cannot be predicted by conventional inclusion rating methods. The problem is still unsolved although it is more than 20 years² since it was pointed out by Adachi et al., and regardless of the worldwide remarkable improvement of bearing steels. Monnot et al. [27] reached a stronger conclusion on the absence of correlation between the cleanliness, evaluated by existing inclusion rating methods, and rotating bending fatigue strength.

¹ There is an additional reason why TiN appears more detrimental than do other inclusions, having the same size, in Fig. 7.1. Usually, TiN at a fatigue fracture origin does not show its total size on a fracture surface, and so looks smaller than the actual size (see Fig. 6.5).

² The paper by Adachi et al. was published in 1975 and the cleanliness of the steels they tested was high for the time, though it was lower than the cleanliness of recent bearing steels.

Table 7.1 Size of nonmetallic inclusions at fracture origins [13]

Diameter of inclusions (μm)	Percentage (%)
0~10	9
11~20	24
21~30	27
31~40	18
41~50	11
51~60	7
61~70	4

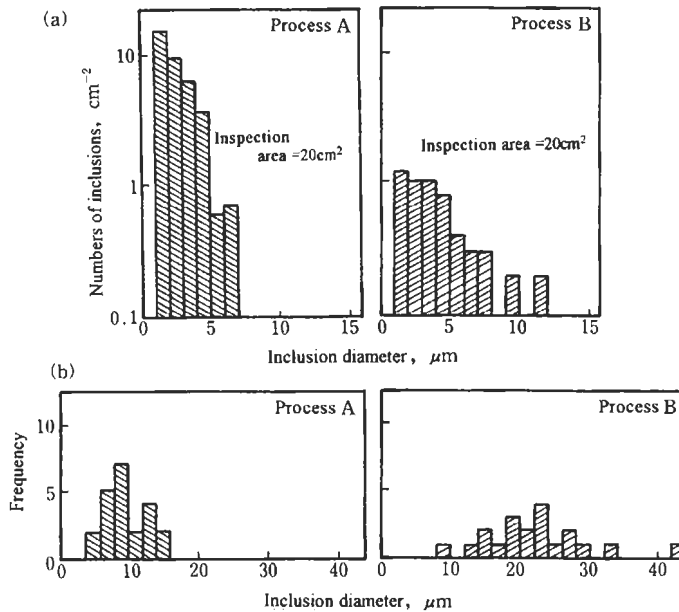


Figure 7.4 Comparison between the inclusion size distributions obtained by optical microscopy of sections, and those obtained by observation of fracture surfaces in rotating bending fatigue tests [27]. (a) Inclusion size distributions obtained by optical microscopy of sections. (b) Size distributions obtained by observation of fracture surfaces in rotating bending fatigue tests.

Fig. 7.4 [27] compares the size distribution of inclusions for bearing steels, produced by processes A and B, with the diameters of inclusions (oxides) appearing at fatigue fracture origins. The scale of size distribution in Fig. 7.4 is logarithmic, hence steel A contains more small inclusions than steel B. The inclusion rating by the ASTM B scale, which is 2.5 for steel A and 1.0 for steel B, indicates that the cleanliness of steel B is expected to be higher than that of A. However, the sizes of inclusions appearing at fracture origins of steel B are larger than those of steel A, and the fatigue limit is 830

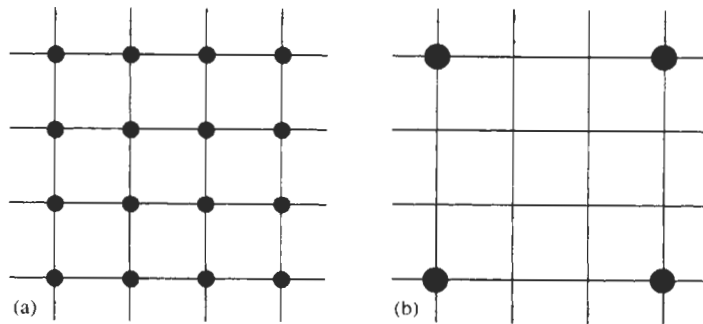


Figure 7.5 (a) 16 small inclusions. (b) 4 large inclusions, whose total volume is identical to (a).

MPa for steel A and 750 MPa for steel B.³ Thus, Fig. 7.4 indicates that steels containing larger inclusions have lower fatigue strength, regardless of high cleanliness measured by conventional inclusion rating methods.

Thus, conventional cleanliness ratings are not necessarily rational criteria for clean steels. Monnot et al. pointed out that conventional cleanliness ratings have no scientific or engineering rationale as scales relating to fatigue strength. Since the crucial inclusion, which causes fatigue fracture of a specimen, is the one present at the centre of a fish eye, it is most important to predict the size of such an inclusion.

Based on the fatigue mechanism described in Chapter 6, such a crucial inclusion should be the one which has the maximum projected area on a plane perpendicular to the stress axis.

Fig. 7.5 illustrates schematically two different inclusion distributions, in which the total volumes of spherical inclusions are kept identical, and all inclusions are at lattice points. Fig. 7.5a contains many, but small, inclusions. On the other hand, Fig. 7.5b contains fewer, but larger, inclusions. According to the JIS lattice point counting method, Fig. 7.5b indicates a higher cleanliness than Fig. 7.5a, even though Fig. 7.5b results in a lower fatigue strength. Fig. 7.4 is consistent with this viewpoint. Thus, the definition of cleanliness, based on conventional inclusion rating methods, such as the ASTM method and others, is not necessarily based on rational parameters for correlation with various material properties. More rational and quantitative inclusion rating methods must be proposed in the near future [16,17,27].

Although there are relatively few major chemical elements, which control shape, size and density of inclusions, and the role of these elements is being made clear, it is not physically meaningful from the viewpoint of fatigue strength to correlate these elements directly with the cleanliness of materials. In order to solve inclusion problems it is rather appropriate to view so-called conventional cleanliness from the viewpoint of why

³ This class of material does not have a unique fatigue limit for each material, because the fatigue limit is dependent on the size and location of the total inclusions contained in an individual specimen (see Chapter 6). Therefore, it must be noted that the definition of fatigue limit used by Monnot et al. is not necessarily clear.

conventional inclusion rating methods have no good correlation with fatigue strength. Chemical elements in inclusions are discussed from this viewpoint in the following.

7.3.1 Total Oxygen (O) Content

Oxygen content indicates the level of total oxides in steels, and it is specified in chemical composition requirements for steels used in the manufacture of bearings. According to Monnot et al.'s experiments, there is no general rule which relates O content to fatigue limits. This is consistent with the fact that there is no good correlation between cleanliness and fatigue limit. Although an oxide inclusion of 40 μm diameter is big, one hundred inclusions of this size in 1 cm^3 contribute a content of only 1 ppm of O. Therefore, decreasing O content, without decreasing the size of oxides, does not achieve a high fatigue limit. If decrease in O content does eventually bring a decrease in inclusion size, as shown in the experiments on ULO steel (Ultra-Low-Oxygen steel, O content less than 10 ppm), by Saito and co-workers [35,36], we can then naturally expect high fatigue strength.

7.3.2 Ti Content

The retained Ti content is an indicator of steel quality. TiN can easily exist independently from oxides. TiN is likely to be fragmented by hot rolling. As TiN content increases, TiN inclusions are observed more frequently at fatigue fracture origins, although as with O content there is no one-to-one correspondence between TiN content and fatigue strength. For example, the steel produced by a remelting process containing 50 ppm Ti has a higher fatigue limit than an ordinary steel containing less Ti [27]. Thus, we must pay attention to the size of TiN inclusions, rather than to their numbers. These facts may require reconsideration of the opinion that TiN is detrimental because of high stress concentration due to its cubic shape [11,37,38]. The same issue was previously described in Section 7.2.

7.3.3 Ca Content

It has been recognised that Ca duplex inclusions, such as $\text{CaO}\cdot\text{Al}_2\text{O}_3$ and $\text{CaO}\cdot\text{Al}_2\text{O}_3\cdot 2\text{SiO}_2$, are most detrimental to fatigue strength. The reason for the detrimental influence of Ca duplex inclusions is that they are larger than other oxide inclusions. Lund and Akesson [39] indicate that Ca duplex inclusions are much more detrimental than inclusions of the Al_2O_3 and Ti families. However, they do not discuss the size of inclusions, even though the size of Ca duplex inclusions in their report is larger than the size of other inclusions. This is because they may be interested only in the chemical composition of inclusions. Ca duplex inclusions, unlike other inclusions, are usually globular, and neither deform nor are fractured by hot rolling. Consequently, deformed triangular vacant spaces are often produced [13,31] at the interface with the microstructure of steels, and hence the effective inclusion size ($\sqrt{\text{area}}$) is likely to become larger than the original size. Since Ca duplex oxide inclusions are not fractured by the VAR and ESR processes, the quality of steel is determined by the condition of Ca du-

plex inclusions in the initial melting process. This problem has become well known, not only in bearing steels, but also in other steels. The difficult problems are that the size and numbers of Ca duplex inclusions have no evident correlation with O content, and that the detection of these inclusions is difficult due to the difficulty of micrographic inspection.

Ca is usually added as a deoxidising element (CaSi), for improving deformability, and also for controlling the shape (spheroidisation) and distribution of inclusions. The last point is thought to be useful for improving the B scale of the ASTM inclusion rating and, accordingly, for addressing the requirements of users. However, adding Ca for the purpose of the last point is rather dangerous, because there is no correlation between the ASTM-B scale and fatigue strength, as already pointed out. Furthermore, it must be noted that Mn in MnS is likely to be replaced by Ca, producing Ca-S inclusions, which are undeformable.

The above discussion has been based on the effect of artificially adding Ca during processing. An additional detrimental influence of Ca is due to Ca originating in refractories. This class of inclusions, which are introduced by the contact of molten metal with refractory walls, are much larger than the usual inclusions, and it is hard to prevent them becoming mixed into molten metal. In order to improve steel quality from the viewpoint of inclusions, this problem must be solved in the near future. According to the author's experience, the size ($\sqrt{\text{area}}$) of these inclusions, of external origin, does not obey the extreme value statistics described in Chapter 6. Therefore, if such an externally originated very large inclusion of Ca oxide does happen to exist at a high stress location, the fatigue strength decreases remarkably. Although there is at present no effective technique to solve this problem, it is indispensable to develop a quality control technique in order to avoid very large inclusions originating from refractories.

Takamura and co-workers [40–43] proposed a new method for improving steel properties by controlling the precipitation of various oxides (oxide metallurgy). Although the size of inclusions detrimental to fatigue strength is one or two orders larger in size than those studied by Takamura and co-workers, the mechanism of nucleation of these oxides is considered to be identical. In this respect, TiN and other inclusions are thought to contain different oxides in the kernels of the inclusions.

7.3.4 Sulphur (S) Content

Although it is commonly acknowledged that the influence of MnS on fatigue strength is small, this idea is not necessarily correct. MnS is deformed and elongated by plastic forming. When stress is applied in the rolling (longitudinal) direction, the projected area ('area') of MnS inclusions becomes small and not detrimental, as compared with other inclusions. However, if stress is applied in the transverse direction, the projected area, as a defect, becomes very large and the phenomenon of anisotropy of fatigue strength properties is experienced [44]. Thus, MnS, being a typical soft inclusion, lowers fatigue strength if the value of $\sqrt{\text{area}}$ is sufficiently large. The influence of MnS should be discussed from the viewpoint of the above properties.

As a matter of fact, Toyama and Yamamoto [20] report the influence of MnS on fatigue tests, using ring-shaped specimens, on a bearing steel containing a few ppm O content. This bearing steel has a very low O content, so contains very small oxide

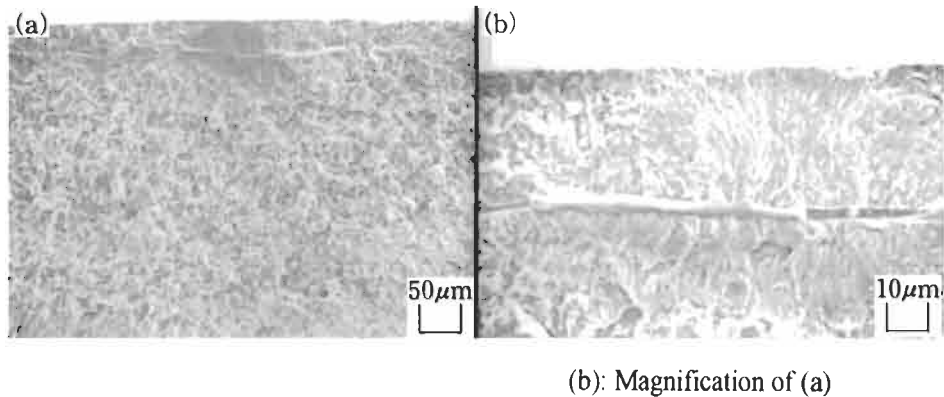


Figure 7.6 MnS inclusion at a fracture origin of a bearing steel (Toyama and Yamamoto [20]).

inclusions. These do not become fatigue fracture origins, because the size of elongated slender MnS (such the one in Fig. 7.6) is rather larger than the oxide inclusions. Murakami and Usuki [45] also show that the fatigue fracture origins of a Pb-free cutting steel, SAE10L45, are mostly MnS inclusions. Thus, if the size of other inclusions is relatively smaller than MnS, then fatigue fracture origins are always MnS inclusions. If we recognise that the extreme case of a soft inclusion is a hole or cavity, then we can understand that the conventional explanation in terms of high stress concentrations around hard inclusions is not correct.

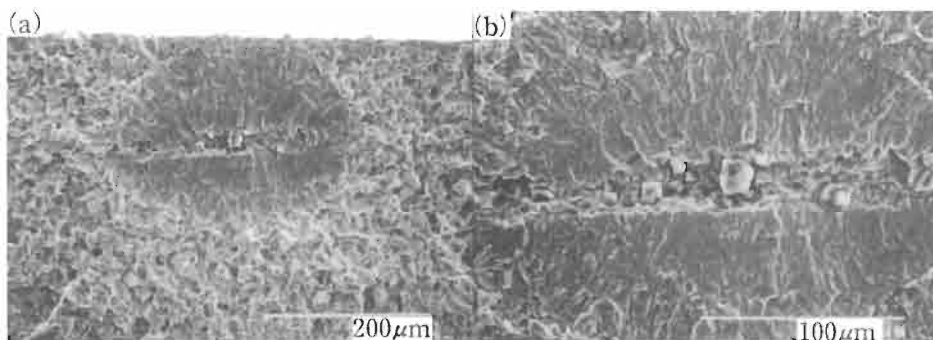
Kinoshi and Koyanagi [46] conducted thrust-type rolling contact fatigue tests on bearing steels containing controlled contents of S and O. Although they did not identify the types of inclusions at fracture origins, they classified inclusions at fracture origins into Al oxides or S + Ca oxides, based on the JIS lattice point method. According to their conclusions, Al oxides are very detrimental to fatigue life. On the contrary, sulphur inclusions are not only harmless but actually useful for improving fatigue life quality. However, in these tests circular plate specimens having a contact surface perpendicular to the rolling direction were used, hence the cross-sections of elongated slender MnS inclusions appear on the contact surface, and the effective size of MnS inclusions is smaller than that of other oxide inclusions. In the tests by Kinoshi and Koyanagi, the influences of the VAR and ESR processes differ with regard to MnS, in that the bearing steel produced by ESR, which has a lower S content, has a longer fatigue life than that produced by VAR. In discussing their results, Kinoshi and Koyanagi noticed the complexity of the effects of inclusions, and pointed out the need for a more rational inclusion rating method. However, we can understand the influence of inclusions, without inconsistencies, if we interpret the influence as due to the competition (mainly the competition in size) between the family of Al_2O_3 inclusions and that of S inclusions. In both cases, the experimental facts confirm that there is no rational correlation between fatigue life, or fatigue strength, and the conventional inclusion ratings such as the JIS method and ASTM method.

Thus, the phenomena related to inclusions seem much more complicated than would appear from a conventional viewpoint. Monnot et al. [27] were pessimistic with regard

to the establishment of a unifying theory. However, this may be because they examined the influence of inclusions on fatigue strength only from a metallurgical viewpoint. By combining metallurgical knowledge with mechanical approaches, the establishment of a unifying theory should become possible. One reason which makes the inclusion problems in bearing steel complex may be the different loading modes in bearings, and in rotating bending or tension–compression fatigue tests. However, in discussing the influence of inclusions on fatigue strength, we should first of all make clear the role of inclusions in rotating bending fatigue, and in tension–compression fatigue. From this point of view, the inclusions which are present at fatigue fracture origins are the most important source of information. This may offer us a unified solution, using the approach described in Chapter 6, not only for bearing steels, but also for other high strength steels.

7.4 Fatigue Strength of Super Clean Bearing Steels and the Role of Nonmetallic Inclusions

Toyama and Yamamoto [20] carried out both repeated compression fatigue tests on ring-shaped specimens, and thrust-type contact fatigue tests, using clean and super clean bearing steels, and showed that all types of inclusions caused decreases in fatigue life (Figs. 7.6 and 7.7). In the repeated compression fatigue tests on ring specimens, a repeated tensile stress appears in the direction perpendicular to the rolling direction of the original steel bar. Fig. 7.8 shows the relationship between the life in the repeated compression fatigue tests and the stress intensity factor range, ΔK , which was calculated assuming inclusions at fracture origin to be cracks and using the stress at fracture origins. The objective of using ΔK might be the evaluation of ΔK_{th} for the microstructure. However, as explained in Chapter 5 the values of ΔK_{th} for small cracks are not an intrinsic material property, but depend on the sizes of cracks, and decrease with decreasing crack size. Therefore, careful interpretation is necessary with regard to the data in Fig. 7.8. This figure shows the values of ΔK for the broken specimens, and



(b): Magnification of (a)

Figure 7.7 Al_2O_3 inclusion at a fracture origin of a bearing steel (Toyama and Yamamoto [20]).

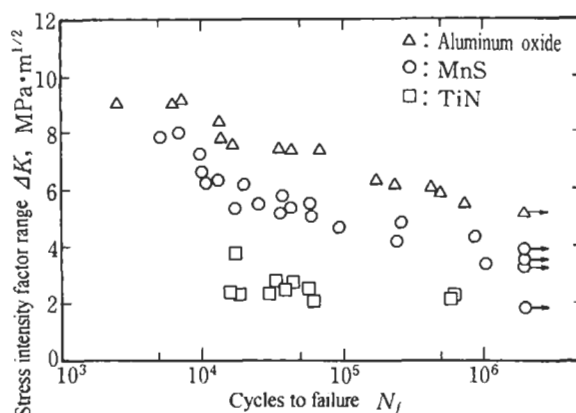


Figure 7.8 Relationship between fatigue life, N_f , of ring-shaped specimens of a bearing steel, and the stress intensity factor, ΔK , for inclusions at fracture origins [20].

not the value of ΔK for the fatigue limit (namely, ΔK_{th}), because the sizes of inclusions at the fatigue limit cannot be identified. Estimating from the data in Fig. 7.8, the values of ΔK_{th} are largest for oxide, decrease to MnS, and then to TiN. This does not mean that ΔK_{th} for aluminum oxides is always larger than values for other inclusions. Since the bearing steels tested by Toyama and Yamamoto contain aluminum oxide inclusions larger than those of MnS and TiN, the values of ΔK_{th} for aluminum oxides are the largest. As described in Chapter 5, the value of ΔK_{th} is proportional to the one third power (1/3) of crack size, or $(\sqrt{area})^{1/3}$. The dependence of ΔK_{th} on crack size also obeys this rule in Fig. 7.8. The characteristics of the data in Fig. 7.8 are consistent with those in Fig. 7.2 obtained by Monnot et al. [27]. In particular, fatigue crack initiation from TiN is relatively early due to its cubic shape, and accordingly fatigue life is shorter. However, it must be noted that fatigue limits of Fig. 7.8 appear to be dependent on the size of inclusion, based on the rule explained in Chapter 5.

Analysis of the results of rotating bending fatigue tests on clean bearing steels are discussed in the following from the viewpoints of Chapters 4–6.

The materials used are almost identical to those used by Toyama and Yamamoto. The specimen axis is in the rolling direction of the original material. Table 7.2 shows chemical compositions. It should be noted that both normal clean and super clean bearing steels have low O and S contents. The inclusion rating by the JIS lattice point method is 0.021–0.033% for the normal clean grade, and 0.017–0.021% for the super clean grade. Most of the 60 areas observed in the optical microscope inspections do not

Table 7.2 Chemical composition of bearing steel (Japanese Standard SUJ2, equivalent to SAE 52100)

	C	Si	Mn	P	S	Cu	Ni	Cr	Ti	Al	N (ppm)	O (ppm)	$d_{60 \times 400}$ (%)
Clean steel	0.99	0.23	0.34	0.014	0.014	0.01	0.02	1.45	0.001	0.025	45	8	0.021–0.033
Super clean steel	0.98	0.23	0.37	0.010	0.005	0.01	0.02	1.43	0.002	0.021	55	5	0.017–0.021

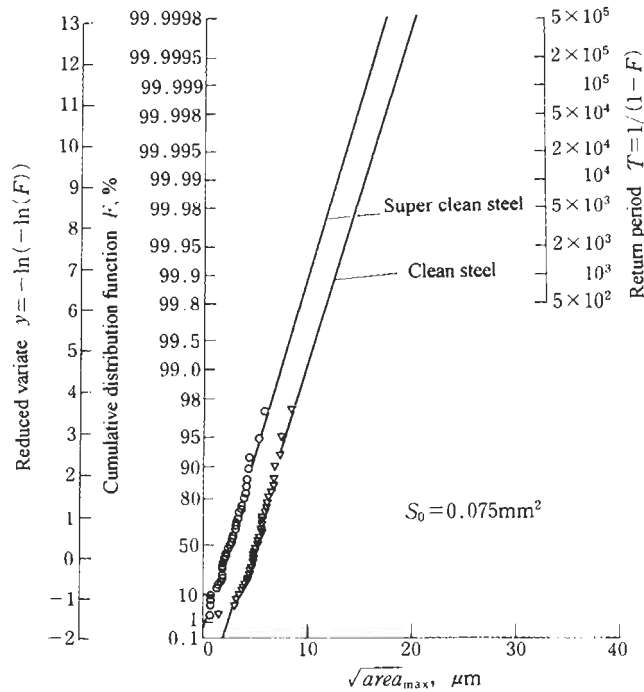


Figure 7.9 Inclusion rating of SUJ2 steel using extreme value statistics.

have inclusions at lattice points, as defined by the JIS lattice point counting method, and it is very difficult to discern the difference between the two materials by the JIS method. Thus, the JIS lattice point method is no longer useful for the examination of recently produced very clean materials. If we apply the method of extreme value statistics, introduced in Chapter 6, to these two materials, we obtain Fig. 7.9. Although both materials are extremely clean, the difference is quantitatively clear in Fig. 7.9. It is important to note that the new inclusion rating method not only clarifies the difference between materials, but it can also be applied to the prediction of fatigue strength.

Figs. 7.10 and 7.11 show the relationship between fatigue strength and hardness. Estimates of the lower bound fatigue limit by the method introduced in Chapter 6 are also shown in the figures.

Fig. 7.12 shows photographs of inclusions at fatigue fracture origins.

Fig. 7.13 shows the relationship between σ'/σ'_w , the stress at the fatal inclusion, σ' , normalised by the estimated fatigue limit, σ'_w , and the number cycles to failure, N_f , that is the modified $S-N$ curve. Thus, in these figures we can see the utility of the method introduced in Chapter 6.

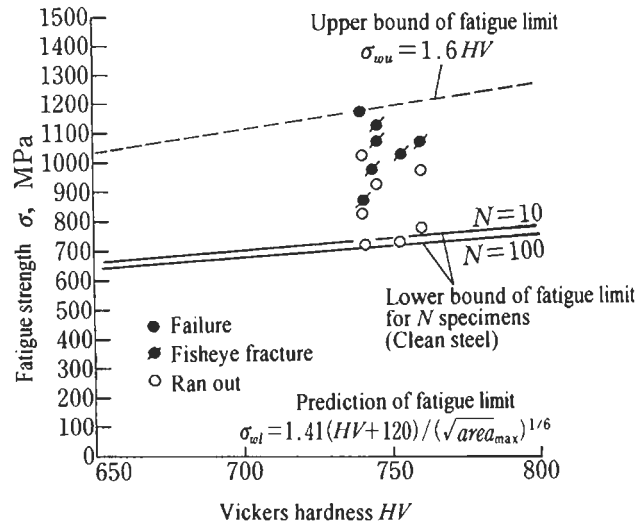


Figure 7.10 Scatter in rotating bending fatigue strength of a clean SUJ2 steel (normal grade) and prediction of the lower bound fatigue strength.

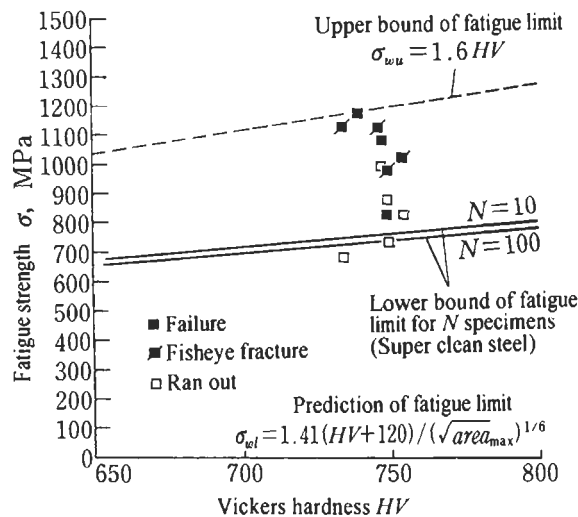
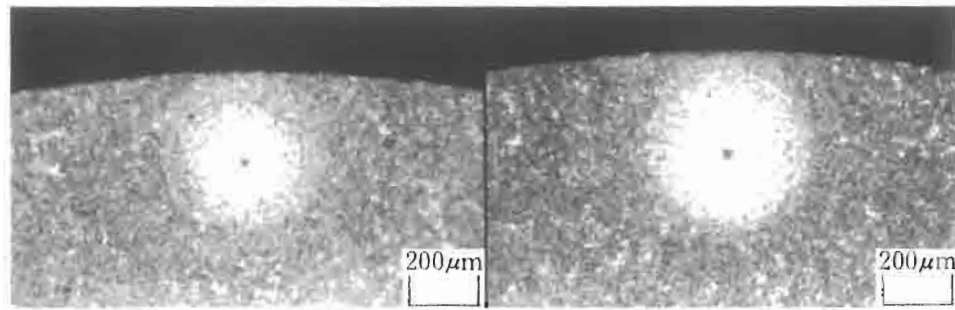


Figure 7.11 Scatter in rotating bending fatigue strength of a super clean SUJ2 steel (super clean grade) and prediction of the lower bound fatigue strength.

7.5 Tessellated Stresses Associated with Inclusions: Thermal Residual Stresses around Inclusions

The residual stresses around inclusions, which are induced during the solidification process of molten metal because of the differences in coefficients of thermal expansion



$HV = 754, \sigma = 1029\text{MPa}, N_f = 6.85 \times 10^7, \sqrt{\text{area}} = 7.75\mu\text{m},$ $HV = 741 \sigma = 882\text{MPa}, N_f = 3.84 \times 10^7, \sqrt{\text{area}} = 17.2\mu\text{m},$
 Distance from surface $h = 250\mu\text{m}$ Distance from surface $h = 275\mu\text{m}$
 (a) Super clean steel (b) Clean steel

Figure 7.12 Inclusions observed at fracture origin. (a) Super clean bearing steel. (b) Clean bearing steel.

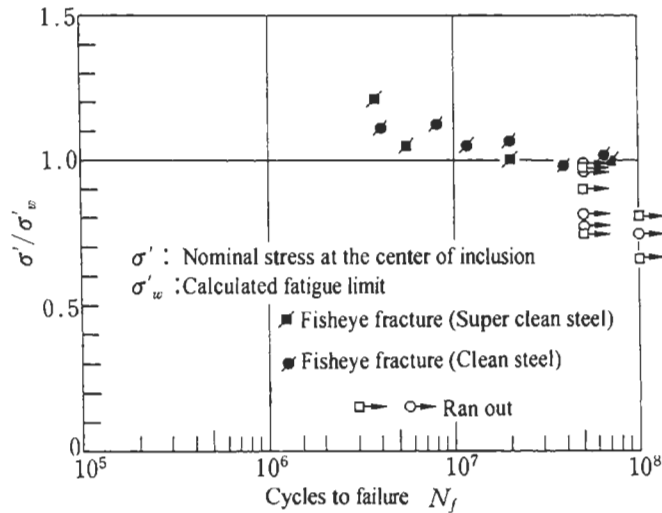


Figure 7.13 Modified S-N data for SUJ2 steel.

between matrix and inclusions, must also be considered in discussing the influence of inclusions on fatigue strength. Discussions on this problem are inconsistent [38,47,48]. A generally accepted view is that oxide inclusions are detrimental because they cause tensile residual stresses, and MnS is not detrimental, or is perhaps useful. However, it must be noted that tensile residual stresses are always induced somewhere around an inclusion regardless of the coefficients of thermal expansion of the matrix α_M and of inclusions α_I .

As shown in Fig. 7.14, if we assume an inclusion to be spherical, then for the case $\alpha_I < \alpha_M$ we have tensile stresses (σ_θ, σ_z) at the matrix in contact with the equator of the inclusion. For the case $\alpha_I > \alpha_M$ (right hand side of Fig. 7.4b), we have a tensile stress (σ_r) at the pole of the inclusion. Therefore, in both of the above cases, the stress around an inclusion is always higher, at some point, than the remote applied stress. This results in crack initiation at an inclusion, regardless of the type of inclusion.

Fig. 7.15 shows the residual stresses around an inclusion [52]. For the case $\alpha_I < \alpha_M$, a crack is expected to initiate at the matrix in contact with the equator of an inclusion, and the crack will propagate along the interface between the inclusion and matrix, resulting in either debonding of the interface, or crack penetration into the inclusion. In both cases, the inclusion eventually becomes equivalent to a stress-free cavity. This hypothesis is consistent with the frequently observed experimental fact that, at the centre of a fish eye, one side of the fracture surface retains a complete inclusion and the other side has a vacant cavity with the shape of the inclusion. A question is how do residual stresses around an inclusion influence crack growth after initiation?

Fig. 7.16 shows the influence of residual stress on stress intensity factors for the cases $\alpha_I > \alpha_M$ (MnS) and $\alpha_I < \alpha_M$ (Al_2O_3) [52]. According to the analytical results shown in Fig. 7.16, in both cases the influence of residual stresses on stress intensity factors

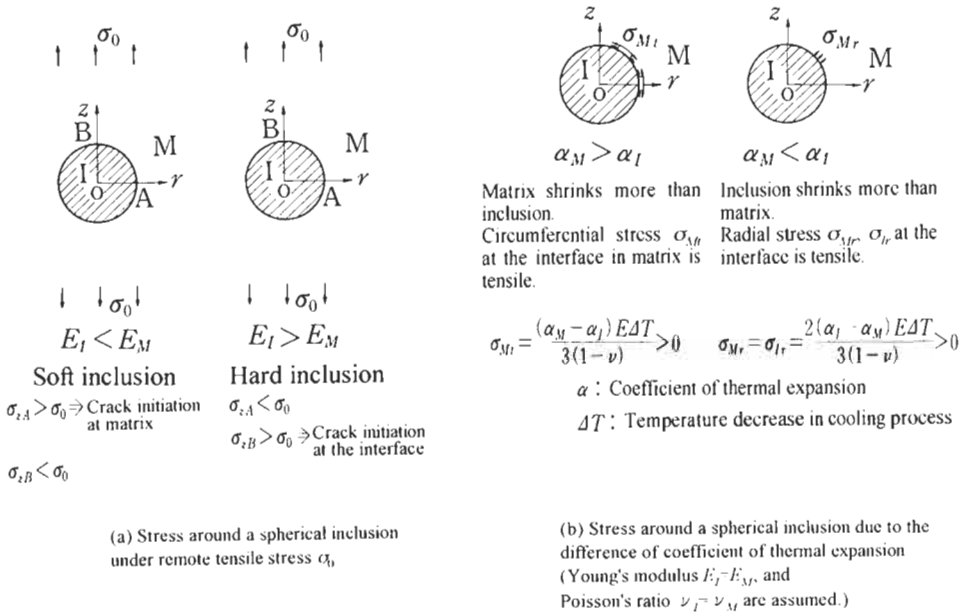


Figure 7.14 Stresses around a spherical inclusion (I = inclusion, M = matrix).

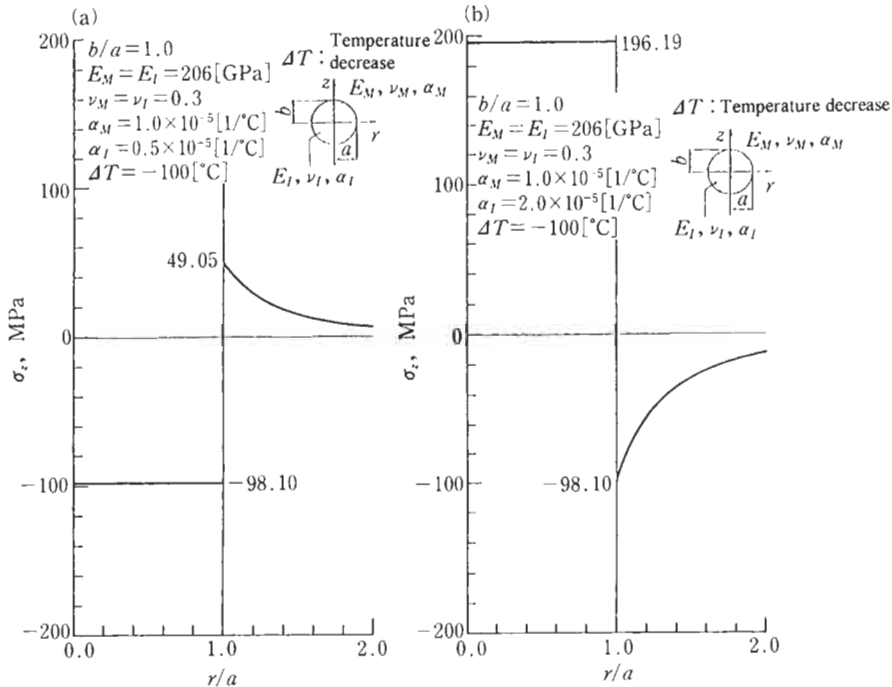


Figure 7.15 Stresses around a spherical inclusion produced by a temperature decrease of 100°C, σ_z is the normal stress in the z direction at the plane $z = 0$. (a) $\alpha_I = 0.5 \times 10^{-5}$, $\alpha_M = 1.0 \times 10^{-5}$. (b) $\alpha_I = 2.0 \times 10^{-5}$, $\alpha_M = 1.0 \times 10^{-5}$.

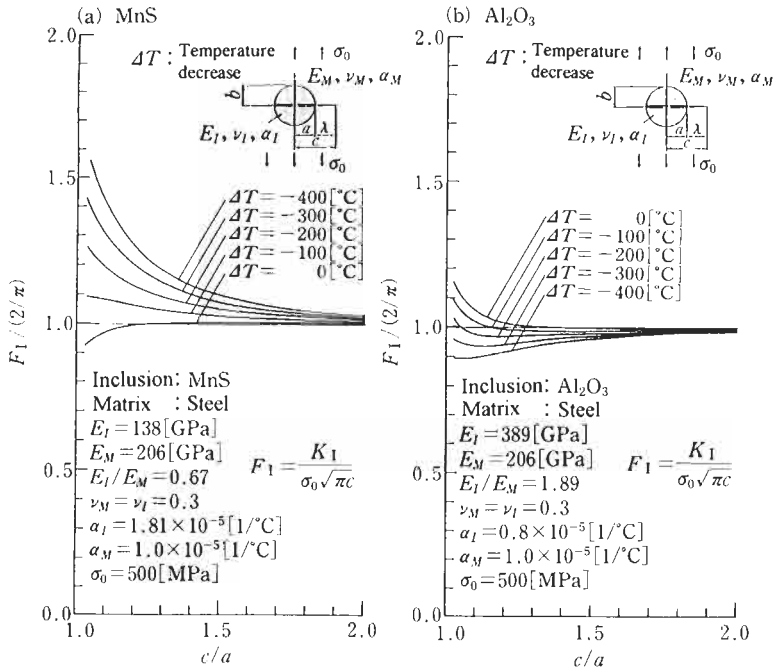


Figure 7.16 Effect of residual stress on stress intensity factors for a crack emanating from a spiracle inclusion, σ_0 is the remote normal stress, $\sigma_0 = 500$ MPa. (a) MnS: in the absence of a crack the normal stress at the interface, $\sigma_r = 133.8$ MPa for $\Delta T = -100^\circ\text{C}$. (b) Al₂O₃: in the absence of a crack the normal stress at the interface, $\sigma_r = -47.8$ MPa for $\Delta T = -100^\circ\text{C}$.

decays rapidly with crack propagation from an inclusion edge.⁴ Table 7.3 shows that the average value α_M for steels is $\alpha_M \cong 10 \times 10^{-6}/^\circ\text{C}$, and $\alpha_I = 8.0 \times 10^{-6}/^\circ\text{C}$ for Al₂O₃ ($\alpha_I < \alpha_M$) and $\alpha_I = 18.1 \times 10^{-6}/^\circ\text{C}$ for MnS ($\alpha_I > \alpha_M$) [38]. In the cases of both Al₂O₃ and MnS the inclusion interface becomes debonded, as shown in Fig. 6.10 and Fig. 7.6. Thus, debonding of an inclusion always occurs regardless of the presence of tensile or compressive residual stresses.

Thus, since the effective influence of residual stresses induced by differences in thermal expansion coefficients may be considered small, making efforts to change steel-making processes so as to control thermal expansion coefficients is of no value. Conventional knowledge of the beneficial influence of MnS is related to its ductility, and its coefficient of thermal expansion, which is larger than that of a steel matrix. However, relationships among inclusion sizes, stress direction, and fatigue strength anisotropy

⁴ Although in the case of MnS (Fig. 7.16a) the detrimental influence of residual stresses appears to be large, it should be noted that the normal stress, σ_r , at the inclusion interface, before debonding, is approximately 400 MPa for $\Delta T = -300^\circ\text{C}$ (decrease in temperature from 300 to 0°C). A stress of 400 MPa is high enough for debonding at the interface. Therefore, the values of stress intensity factor for $|\Delta T| > 300^\circ\text{C}$ are unrealistic. However, the values for $|\Delta T| \cong 200^\circ\text{C}$ may be realistic, and we can understand that the influence of residual stresses will be small.

Table 7.3 Values of coefficient of thermal expansion, Young's modulus, E , and Poisson's ratio, ν [38,49–51]

Inclusions	Chemical composition	Average value of coeff. of thermal expansion $\alpha \times 10^{-6}/^{\circ}\text{C}$ (0 ~ 800°C)	Young's modulus E (GPa)	Poisson's ratio ν
Sulphides	MnS	18.1	(69~138)	(-0.3)
	CaS	14.7		
Calcium Aluminates	CaS · 6Al ₂ O ₃	8.8	(113)	(0.234)
	CaS · 2Al ₂ O ₃	5.0		
	CaO · Al ₂ O ₃	6.5		
	12CaO · 7Al ₂ O ₃	7.6		
	3CaO · Al ₂ O ₃	10.0		
Spinel	MgO · Al ₂ O ₃	8.4	271	0.260
	MnO · Al ₂ O ₃	8.0		
	FeO · Al ₂ O ₃	8.6		
Alumina	Al ₂ O ₃	8.0	389	0.250
	Cr ₂ O ₃	7.9		
Nitrides	TiN	9.4	(317)	(0.192)
Oxides (Reference values)	MnO	14.1	(178)	(0.306)
	MgO	13.5	306	0.178
	CaO	13.5	183	0.21
	FeO	14.2		
Microstructure (Matrix) 1% C, 1.5% Cr steel	Austenite (γ) (850°C → Ms)	(23.0)		
	Martensite (α') (M_f → R. T.)	(10.0)		
Average	$\gamma \rightarrow \alpha'$ (850°C → R. T.)	12.5	206	0.290

were not investigated comprehensively in establishing this conventional viewpoint. If the size of MnS inclusions is relatively larger than the size of other inclusions, then detrimental influence is always due to MnS, as previously described.

Apart from the effects of nonmetallic inclusions, the influence of surface defects, foreign particles [53] and carbides cannot be ignored in bearing steels.

In particular, carbides exist in the matrix of bearing steels, and it must be noted that the extreme value statistics distribution of carbide size differs from that of inclusions. Inclusions and carbides have Young's moduli different from that of a matrix and, accordingly, if large inclusions and carbides are present at or close to a surface, they cause irregular stress distributions, with a spike in Hertzian contact stresses [54]. Thus

large inclusions at or close to a surface will cause shorter fatigue lives in bearings and gears. Although the influence of surface roughness on fatigue life in contact fatigue has been investigated in considerable detail, the effect of inclusions has been largely ignored regardless of the fact that they are one to two orders of magnitude larger in size than surface roughness. It must be noted that a mirror-like surface produced by modern precision grinding equipment always has a thin deformed surface layer which covers and hides inclusions near a surface. Comprehensive studies on this problem are needed.

7.6 What Happens to the Fatigue Limit of Bearing Steels without Nonmetallic Inclusions? — Fatigue Strength of Electron Beam Remelted Super Clean Bearing Steel

Improvements in steel-making technology over the last 20 years have led to continual reduction of inclusion size in bearing steels. The fatigue limit of bearing steels tends to increase year by year, corresponding to the reduction in inclusion size (see Fig. 7.17 [8,13,19,28–31,55–59] and Fig. 7.18). Nevertheless, it is known that inclusions still cause fatigue fracture and decrease the fatigue limit. As inclusions contained in recent super clean bearing steels are fewer in number and very small in size, conventional inclusion rating methods, such as the ASTM and JIS methods, do not reflect the level of cleanliness either qualitatively or quantitatively [16,17,60]. The fatal disadvantage of conventional inclusion rating methods is that there is no definite correlation between the fatigue limit and the measured inclusion rating [16,17]. It is necessary to develop a new inclusion rating method, which can overcome the disadvantages of conventional methods, for both material quality control purposes and for fatigue limit prediction. The method of extreme value statistics, which was introduced in Chapter 6, is a potentially promising rating method. If we could find a quantitative correlation between fatigue limit and inclusion size, it would automatically be reflected in the improvement of steel-making processes.

On the other hand, from the viewpoint of steel-making costs, we need to know the critical inclusion size which is detrimental to fatigue strength. In other words, we want to know what happens as we decrease inclusion size to an extreme limit.

In order to investigate the critical lower bound inclusion size which affects the fatigue limit, Murakami et al. [61] prepared and tested an electron beam remelted super clean bearing steel (EB–CHR: Electron Beam–Cold Hearth Remelted). It is shown that small inhomogeneities in the microstructure, rather than inclusions, have the greater effect on the fatigue limit of this super clean steel. The reason for this is explained below.

7.6.1 Material and Experimental Procedure

The steel-making process for EB–CHR results in a unique material which is very different from commercial bearing steels. The electron beam remelting process is repeated twice to reduce the inclusion content. Fig. 7.19 shows the flow diagram for the EB–CHR steel-making process and for the specimen preparation procedure.

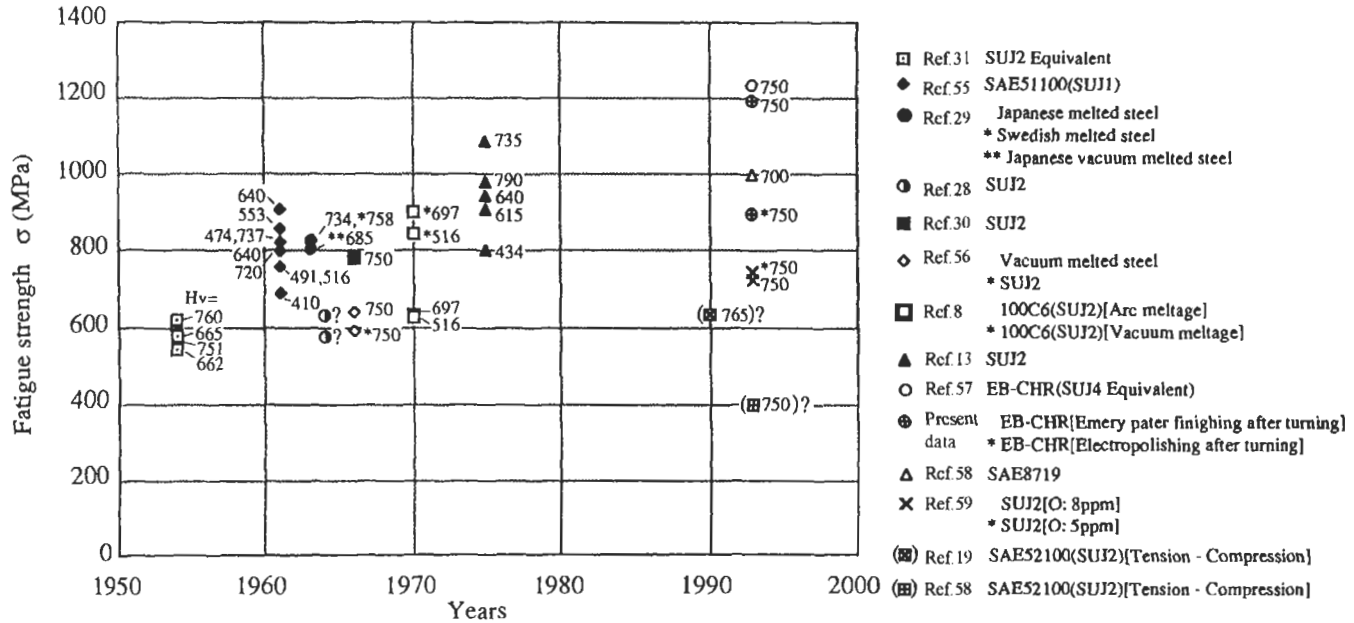
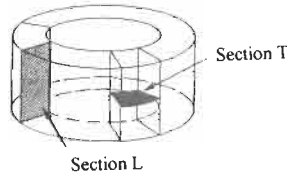


Figure 7.17 Changes in the rotating bending fatigue strength of bearing steels since 1955, numbers beside symbols indicate the Vickers hardness of specimens [8,13,19,28–31,55–59].



The definition of inspection planes in bearing

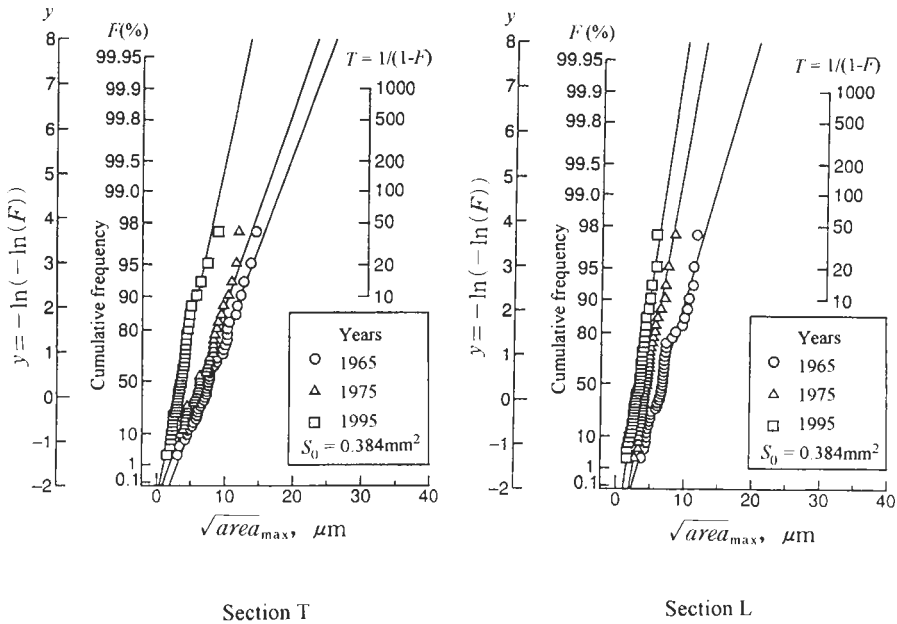


Figure 7.18 Changes in inclusion size in bearing steels since 1965 (cumulative frequency of the maximum size of inclusions, inclusion size is defined by the square root of the projected area, \sqrt{area}).

Table 7.4 shows the chemical composition of EB-CHR. Mo is added in place of Mn, because Mn is lost during electron beam remelting, decreasing hardenability.

The material is first turned to 17 mm diameter bar. After oil quenching and tempering the specimens are ground to final dimensions. Fig. 7.20 shows the specimen geometry. The Vickers hardness, H_V , of the specimens is approximately 770 (kgf/mm^2). Two

Table 7.4 Chemical composition of EB-CHR steel (wt%)

Material	C	Si	Mn	P	S	Ni	Cr	Mo	O (ppm)
EB-CHR	1.18	0.27	Tr	0.013	0.001	0.09	1.10	0.20	4

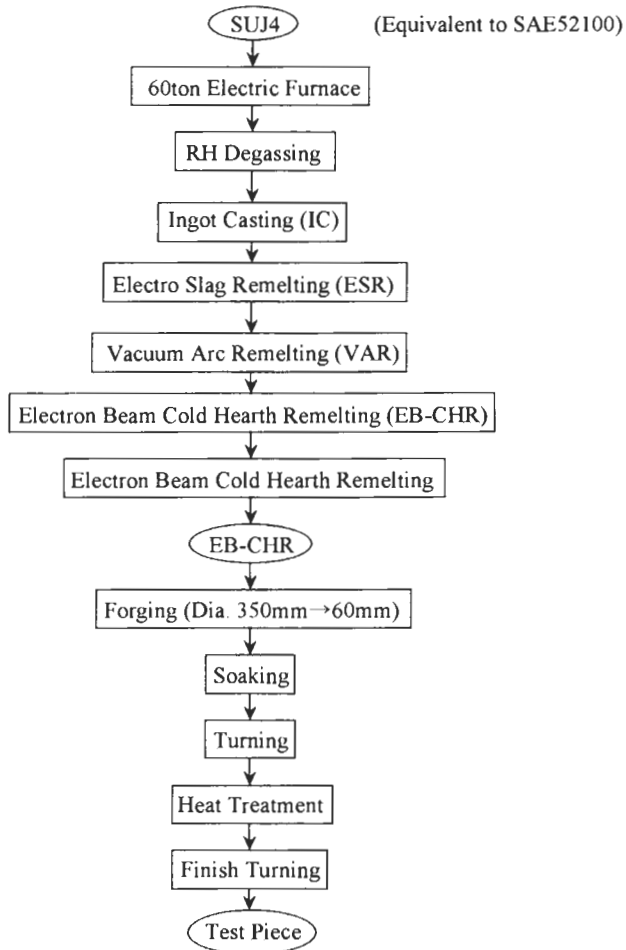


Figure 7.19 Flow diagram for the EB-CHR steel-making process and for the specimen preparation procedure.

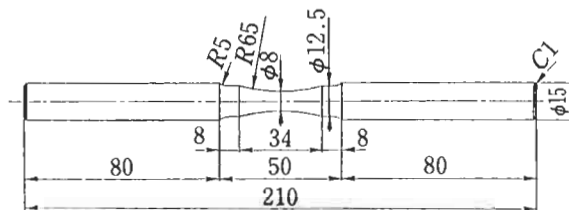


Figure 7.20 Rotating bending specimen geometry.

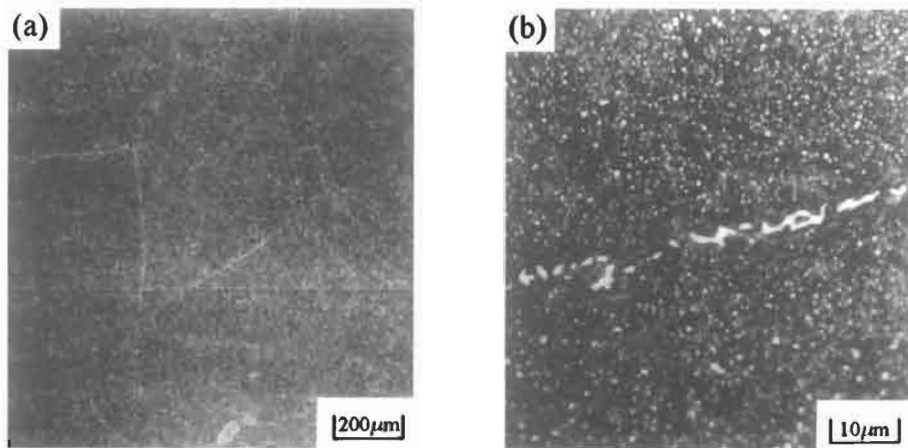


Figure 7.21 Pre-austenite grains (a) and grain boundaries (b) (grain boundaries are revealed on a mirror finished surface by etching with 3% nital, carbides precipitate along grain boundaries).

types of surface finish are used to investigate the effect of surface residual stresses on fatigue strength. The surfaces of specimens type RS are finished with #2000 emery paper and $1/4 \mu\text{m}$ diamond paste. The surfaces of specimens type EP are finished by electropolishing; approximately $40 \mu\text{m}$ of surface layer is removed.

The matrix of EB–CHR is martensite. The pre-austenite grain size is very large; the maximum grain size in an inspection area of 176.7 mm^2 is approximately 1 mm. Fig. 7.21 shows the pre-austenite grains and grain boundaries. Carbides precipitate along the grain boundaries.

X-ray stress measurement indicated the existence of residual stresses of approximately -640 MPa at the surface of type RS specimens. However, these residual stresses vanished after electropolishing a surface layer approximately $40 \mu\text{m}$ deep from the surface. The residual stress (σ_r) is assumed to be a mean stress (σ_m) in the evaluation of fatigue strength.

Rotating bending fatigue testing machines of the uniform moment type (capacity 98 Nm, 2400 rpm) were used.

7.6.2 Inclusion Rating Based on the Statistics of Extremes

Fig. 7.22 shows the inclusion rating of EB–CHR using extreme value statistics. Results for two commercial super clean steels, SUJ2(N) and SUJ2(H) [61] (Fig. 7.9), are included for comparison. The inclusion size of EB–CHR is extremely small in comparison with the commercial super clean steels. The expected inclusion size, $\sqrt{\text{area}}_{\text{max}}$, in the test volume, V , of N rotating bending fatigue test specimens can be determined from the return period, T , shown in Fig. 7.22. The return period is defined by the number of unit volumes contained in the test volume, V , for N specimens, that is by $T = NV/V_0$. The unit volume, V_0 , is calculated by multiplying the standard inspection area, S_0 (0.075 mm^2), by the mean values (h) of all measured values of

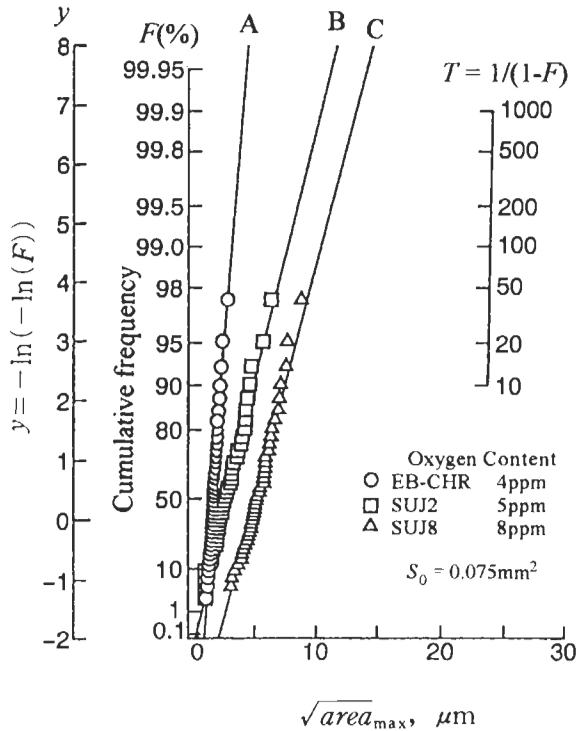


Figure 7.22 Cumulative frequency distribution of $\sqrt{area_{max}}$ of inclusions in EB-CHR steel (A) compared with commercial super clean steel SUJ2 (B and C).

$\sqrt{area_{max,j}}$ for n standard inspection areas [62,63] (see Appendix A), where $j = 1 - n$, that is $V_0 = S_0 \times h$ where $h = (\sum_{j=1}^n \sqrt{area_{max,j}})/n$.

The test volume, V , containing the prospective fracture origin, is $V = 89.8 \text{ mm}^3$. Thus $\sqrt{area_{max}} = 6.4 \text{ }\mu\text{m}$ for $N = 10$ ($T = 8.75 \times 10^6$), and $\sqrt{area_{max}} = 7.1 \text{ }\mu\text{m}$ for $N = 100$ ($T = 8.75 \times 10^7$). Therefore, the statistical analysis shows that inclusions larger than $\sqrt{area_{max}} = 7 \text{ }\mu\text{m}$ do not exist in $N = 100$ specimens. Full details of this procedure are given in Appendix A [62,63]. According to X-ray analysis, the composition of inclusions contained in EB-CHR is either Al-O or Ti-C.

7.6.3 Fatigue Test Results

Fig. 7.23 shows $S-N$ diagrams for specimen types EP and RS. Fish-eye fractures were observed in both types of specimen. Fig. 7.24 shows fish-eye fractures, and the small inhomogeneities at the centres of fracture origins. The maximum size (\sqrt{area}) of the small inhomogeneities at fracture origins is $15.7 \text{ }\mu\text{m}$. This value is clearly larger than the value expected from the statistical analysis of inclusion content shown in Fig. 7.22. The true character of the small inhomogeneities and the reason why they, rather than inclusions, cause fatigue fracture are discussed later.

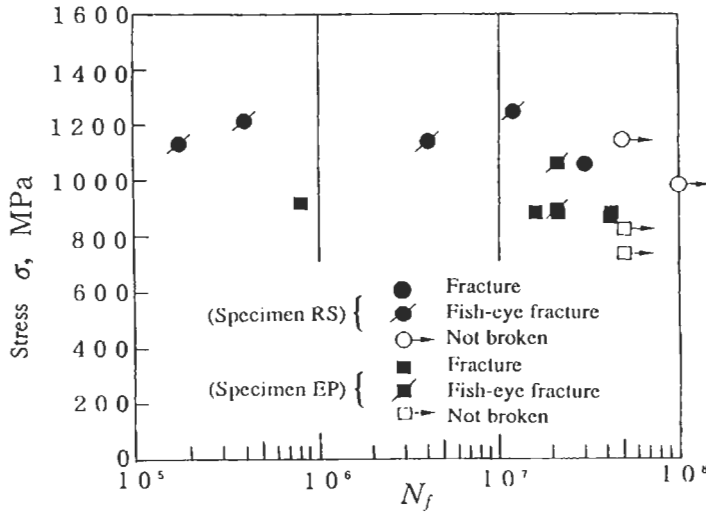


Figure 7.23 S-N diagram for EB-CHR steel.

Table 7.5 compares values of the fatigue limit, σ'_w , calculated using Eq. 6.6 or Eq. 6.9, with the nominal applied stress, σ' , at a fracture origin. The values of σ'/σ'_w for EB-CHR are greater than 1.0 except for one case (EP-14) in which it is close to 1.0. This specimen also has a relatively longer life, that is $N_f = 2.12 \times 10^7$. The data for specimens type RS ($R = -1$) show that for most specimens the fracture origin is relatively deep below the specimen surface, where residual stresses are expected to have vanished. In Table 7.5, the notations $5 \times 10^7 \rightarrow$ and $1 \times 10^8 \rightarrow$ mean that a specimen which endured 5×10^7 or 1×10^8 cycles were retested at a higher stress until failure. The load step was greater than 50 MPa, in order to avoid coxing due to prior loading affecting test results.

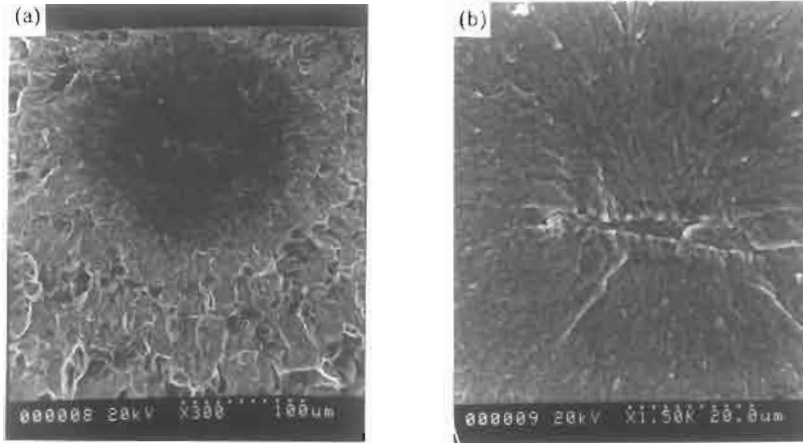
Fig. 7.25 shows the relationship between σ'/σ'_w and the number of cycles to failure, N_f . That is the correlation between the ratio of fracture stress to predicted fatigue limit with N_f . It can be seen that the data in Table 7.5 are better characterised by the \sqrt{area} parameter model than are the more widely scattered data in Fig. 7.23. Thus, we can conclude that the crucial parameters which control the fatigue limit are the maximum size of inclusion or inhomogeneity (\sqrt{area}) and the Vickers hardness, H_V , of the matrix.

7.6.4 The True Character of Small Inhomogeneities at Fracture Origins

Fig. 7.26 shows a small inhomogeneity in the martensitic matrix of EB-CHR. It was revealed in an inclusion inspection plane by etching with 3% nital (nitric acid in alcohol). The true character of this inhomogeneity was investigated as follows.

(1) An X-ray micro-analyser showed no clear difference in chemical composition between the small inhomogeneity and the matrix.

(2) The micro Vickers hardness of the small inhomogeneity ($H_V = 560$) is much lower than that of the matrix ($H_V = 770$).



(Specimen EP)

Vickers hardness: $HV = 766 \text{ kgf/mm}^2$.

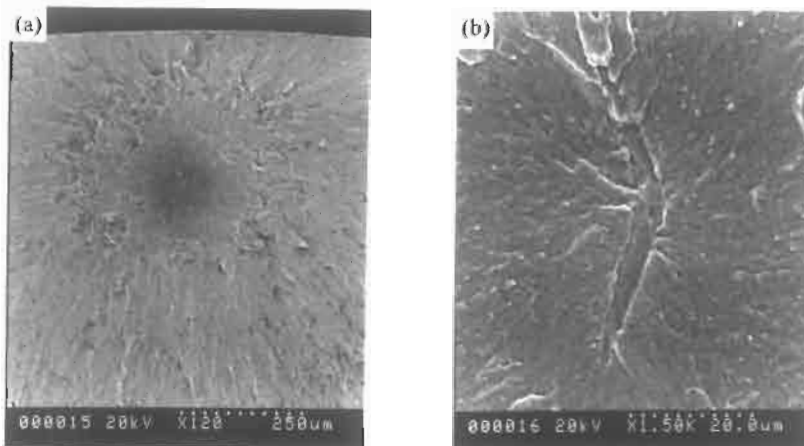
Nominal stress at surface: $\sigma' = 902 \text{ MPa}$.

Number of cycles to failure: $N_f = 8.22 \times 10^5$.

Square root of projection area of inhomogeneity: $\sqrt{\text{area}} = 15.4 \text{ } \mu\text{m}$.

Distance from surface: $h = 90 \text{ } \mu\text{m}$.

Nominal stress at inhomogeneity: $\sigma' = 876 \text{ MPa}$.



(Specimen RS)

Vickers hardness: $HV = 779 \text{ kgf/mm}^2$.

Nominal stress at surface: $\sigma' = 1216 \text{ MPa}$.

Number of cycles to failure: $N_f = 3.95 \times 10^5$.

Square root of projection area of inhomogeneity: $\sqrt{\text{area}} = 11.2 \text{ } \mu\text{m}$.

Distance from surface: $h = 332 \text{ } \mu\text{m}$.

Nominal stress at inhomogeneity: $\sigma' = 1129 \text{ MPa}$.

Figure 7.24 Fish-eye fractures (a) and small inhomogeneities at fracture origins (b).

Table 7.5 Fatigue test results for EB-CHR steel

(a) Specimen EP

Specimen	HV	σ	N_f	\sqrt{area}	h	Shape of inclusion or defect	σ'	$\sigma_w'(R)$	σ'/σ_w'
EP-6	766	922	8.22×10^5	15.4	90		902	876(-1.0)	1.03
EP-14	756	863	2.12×10^7	10.2	0		863	928(-1.0)	0.93
EP-18	780	1078	2.03×10^7	6.3	81		1053	1033(-1.0)	1.02
EP-20	778	764	$5.0 \times 10^7 \rightarrow$	11.5	0		764	855(-1.0)	0.89
		813	$5.0 \times 10^7 \rightarrow$				813		0.95
		863	4.01×10^7				863		1.01

(b) Specimen RS

Specimen	HV	σ	N_f	\sqrt{area}	h	Shape of inclusion or defect	σ'	$\sigma_w'(R)$	σ'/σ_w'
RS-13	770	1177	$5.0 \times 10^7 \rightarrow$	5.5	385		1074	1045(-1.0)	0.99
		1255	1.30×10^7				1145		1.10
RS-15	779	1216	3.95×10^5	11.2	332		1129	938(-1.0)	1.20
RS-16	776	1138	1.78×10^5	15.7	224		1073	883(-1.0)	1.22
RS-17	770	980	$1.0 \times 10^8 \rightarrow$	14.2	0		980	1077(-3.94)	0.91
		1078	3.01×10^7				1078		1.00
RS-19	778	1127	4.04×10^6	4.9	105		1099	1075(-1.0)	1.02

HV : Vickers hardness (kgf/mm²),

σ : Nominal stress at surface (MPa),

N_f : Number of cycles to failure,

\sqrt{area} : Square root of projection area of inclusion or defect (μm),

h : Distance from surface (μm),

σ' : Nominal stress at inclusion or defect (MPa),

σ_w' : Fatigue limit at inclusion or defect predicted by Eqs.(6.6) and (6.9) (MPa).

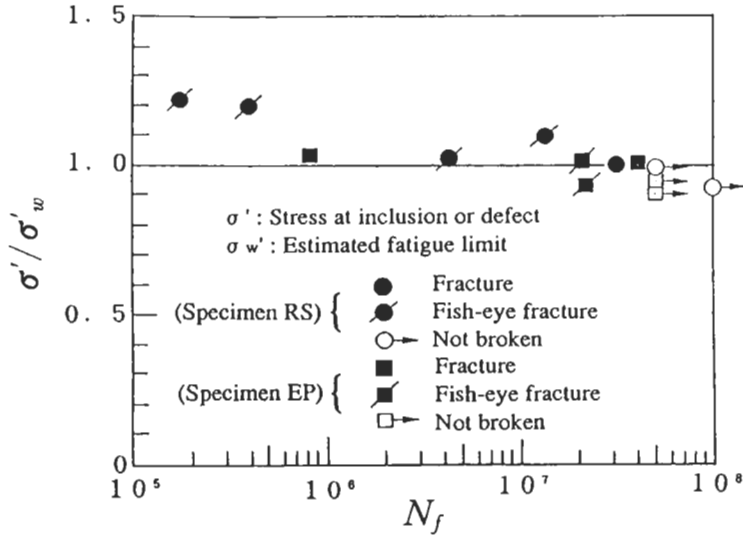


Figure 7.25 Modified *S-N* diagram for EB-CHR steel.

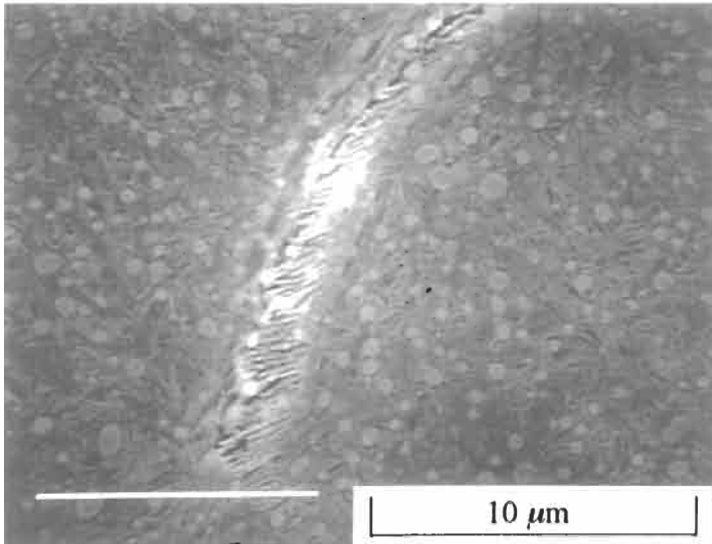


Figure 7.26 Small inhomogeneity observed in martensitic matrix of EB-CHR steel.

(3) The relationships between quenching temperature, hardenability, and the appearance of small inhomogeneities were investigated using bars of 8 mm and 10 mm diameter EB-CHR. Oil quenching was carried from temperatures of 800, 820, 835 and 850°C. Microstructures obtained by oil quenching and by water quenching from 835°C were also compared in order to investigate the effect of quenching method on

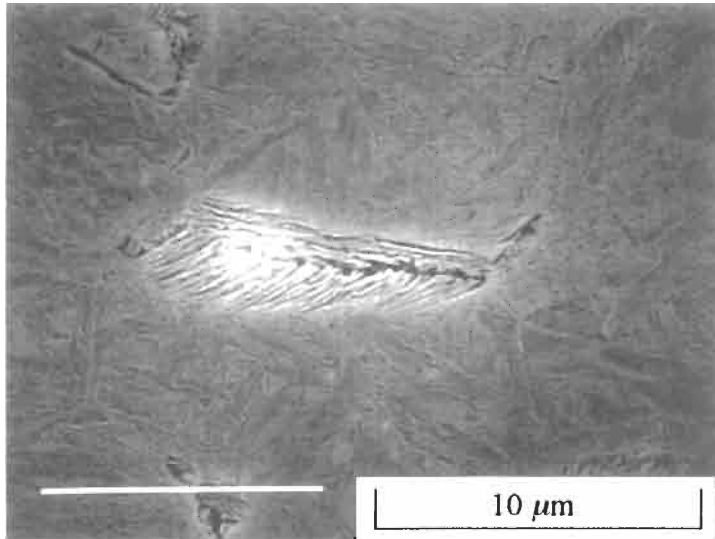


Figure 7.27 Typical bainite structure in martensitic matrix of a commercial bearing steel.

the appearance of small inhomogeneities. The results obtained show that the larger specimen diameter and lower quenching temperatures cause the appearance of small inhomogeneities in the matrix; small inhomogeneities appeared only on oil quenching, and not on water quenching. Thus, there is a strong correlation between hardenability and the appearance of small inhomogeneities.

(4) Fig. 7.27 shows a typical bainite structure in the martensitic matrix of a commercial bearing steel. The structure of the small inhomogeneity in Fig. 7.26 is quite similar to the bainite in Fig. 7.27.

Therefore, it is concluded from (1) to (4) that a small inhomogeneity must be local imperfectly heat-treated microstructure, that is bainite.

Fig. 7.28 compares the distribution of $\sqrt{\text{area}}_{\text{max}}$ for the bainite in EB-CHR with that of inclusions. Fracture origins are mostly at bainite because the bainite size is relatively larger than the inclusion size. The maximum bainite size, $\sqrt{\text{area}}_{\text{max}}$, for N specimens can be determined from the return period, T , shown in Fig. 7.28. Using the same procedure as described in the previous section, $\sqrt{\text{area}}_{\text{max}} = 17.6 \mu\text{m}$ for $N = 10$, and $\sqrt{\text{area}}_{\text{max}} = 19.6 \mu\text{m}$ for $N = 100$. Prediction by statistical analysis is in good agreement with experimental data since the maximum bainite size, $\sqrt{\text{area}}$, for nine fracture origins is $15.7 \mu\text{m}$ (Table 7.5).

Although the fatigue strength of EB-CHR is extremely high in comparison with commercial bearing steels, the fatigue fracture origins of EB-CHR are seldom at inclusions, but are mostly at small inhomogeneities. This is due to the extreme reduction in inclusion size by electron beam remelting. The true character of a small inhomogeneity is a local imperfectly heat-treated structure, bainite. Thus as steels become extremely clean, heat treatment and other processing must be carefully performed so that inhomogeneities, larger in size than inclusions, are not produced in the microstructure.

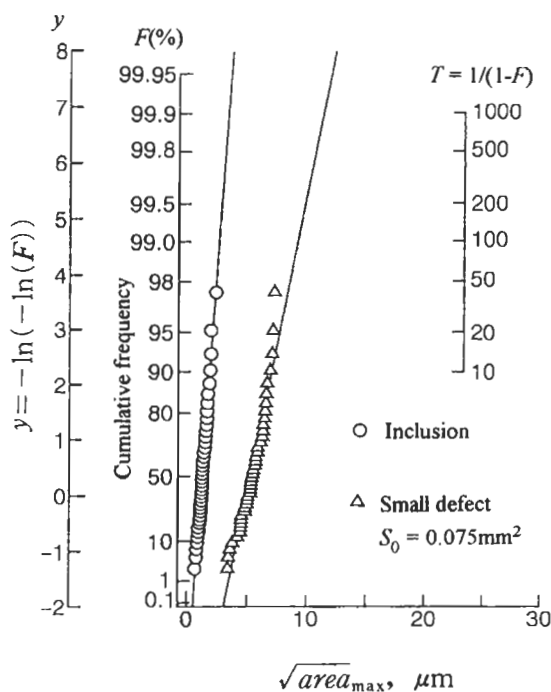


Figure 7.28 Cumulative frequency distributions, of $\sqrt{\text{area}_{\text{max}}}$, of inclusions and bainite in EB-CHR steel.

7.7 References

1. M. Ueno, T. Mitsuhashi and Y. Nakano: Studies on Ball Bearing Steels (II) (Effect of Some Metallurgical Factors on Life of Ball Bearing Steels), *Tetsu To Hagane*, **41**(10) (1955), 1102–1107.
2. K. Narita: Source and Process of Nucleation of Nonmetallic Inclusions in Steels (I), *Bull. Jpn. Inst. Met.*, **1**(2) (1962), 121–128.
3. R.F. Johnson and J.F. Swell: The Bearing Properties of 1% C–Cr Steel as Influenced by Steelmaking Practice, *J. Iron Steel Inst.*, **196** (1960), 414–444.
4. J.A. Martin, S.F. Borgese and A.D. Eberhardt: Microstructural Alterations of Rolling-Bearing Steel Undergoing Cyclic Stressing, *Trans. ASME, J. Basic Eng.*, Sept., 1966, pp. 555–567.
5. J.L. O'Brien and A.H. King: Electron Microscopy of Stress-Induced Structural Alterations Near Inclusions in Bearing Steels, *Trans. ASME, J. Basic Eng.*, Sept., 1966, pp. 568–572.
6. C.M. Lyne and A. Kasak: Effect of Sulfur on the Fatigue Behavior of Bearing Steel, *Trans. ASM*, **61** (1968), 10–13.
7. W.T. Cook: Effect of Sulfur on the Fatigue Properties of 1% C–Cr Bearing Steels, *Iron Steel*, Dec., 1970, pp. 363–366.
8. J. Monnot, R. Tricot and A. Gueussier: Résistance à la Fatigue et Endurance des Aciers Pour Roulements, *Rev. Metall.* Juillet–Août, 1970, pp. 619–638.
9. K. Okamoto and S. Shiyuki: Influence of Nonmetallic Inclusions on Rolling Contact Fatigue Life Bearing Steels, *Seitetsu Kenkyu*, **273** (1971), 108–114.
10. K. Aoki, M. Nagumo and K. Sugino: Microstructural Factors in Rolling Contact Fatigue Life of Bearing Steels, *Seitetsu Kenkyu*, **273** (1971), 115–134.
11. R. Tricot: Nocivité Spécifique des Inclusions sur les Propriétés d'Emploi des Aciers Pour Roulements, *Rev. Metall.*, Oct., 1971, pp. 655–662.

12. K. Kato, H. Yamada and S. Sekiya: Rolling Fatigue Life of High Carbon–Chromium Ball Bearing Steels, *Electr. Furnace Steel*, **45(1)** (1974), 37–43.
13. A. Adachi, H. Shoji, A. Kuwabara and Y. Inoue: Rotating Bending Fatigue Phenomenon of JIS SUJ2 Bearing Steel, *Electr. Furnace Steel*, **46(3)** (1975), 176–182.
14. R. Tricot, J. Monnot and M. Lluansi: How Microstructural Alterations Affect Fatigue Properties of 52100 Steel, *Met. Eng. Q.*, May, 1972, pp. 39–47.
15. H. Yamada and N. Tsushima: Evaluation of Non-Metallic Inclusions of Steels Used for Rolling Bearings from Fracture Surface by Rotating Ring Fatigue Fracture Test, *Wear*, **118** (1987), 305–317.
16. J.J.C. Hoo, P.T. Kilhefner and J.J. Donze (Eds): Bearing Steels; The Rating of Nonmetallic Inclusion, ASTM STP 575, American Society for Testing Materials, Philadelphia, PA, 1975.
17. J.J.C. Hoo (Ed): Effect of Steel Manufacturing Processes on the Quality of Bearing Steels, ASTM STP 987, American Society for Testing Materials, Philadelphia, PA, 1988.
18. K. Narita, T. Onoye and K. Yamamoto: Effect of Non-Metallic Inclusions on the Rolling Fatigue Life of 1% C–Cr Bearing Steel, *Proc. 100th ISIJ Mtg.*, Lecture No. S1135, Oct., 1980, p. B-196.
19. A. Melander, M. Rolfson, A. Nordgren, B. Jansson, H. Hedberg and T. Lund: Influence of Inclusion Contents on Fatigue Properties of SAE 52100 Bearing Steels, *Rep. Swedish Inst. Met. Res.*, IM-2589, 1990, pp. 1–71.
20. K. Toyama and M. Yamamoto: Relationship between Fatigue Properties and Inclusion Content of Bearing Steel, *Proc. Fatigue '90*, **1** (1990) 343–348.
21. H. Narai, T. Abe and K. Furumura: Application of Several New Methods to Evaluation of Oxide Type Inclusions in Bearing Steels, *Proc. ISIJ Mtg.*, *Curr. Adv. Mater. Process.*, **4(4)** (1991), 1178–1181.
22. K. Ogawa, T. Inoue, S. Koyama, Y. Fukusaki, M. Kawasaki and M. Shimosa: Removal of Inclusions of High Carbon Steel, *Proc. ISIJ Mtg.*, *Curr. Adv. Mater. Process.*, **4(4)** (1991), 1206–1209.
23. I. Ibuki, S. Kuwano, S. Okimoto, Y. Kawai, Y. Kikuchi and H. Matsuno: Technology to Reduce Nonmetallic Inclusions for Clean Steel, *Proc. ISIJ Mtg.*, *Curr. Adv. Mater. Process.*, **4(4)** (1991), 1210–1213.
24. Y. Shirota, K. Masame, K. Takatani, Y. Hitomi, M. Toyota and H. Nakashima: Development of Production Process of Highly Clean Steel, *Proc. ISIJ Mtg.*, *Curr. Adv. Mater. Process.*, **4(4)** (1991), 1214–1217.
25. G. Sachs, R. Sell and W.F. Baum Jr.: Tension, Compression, and Fatigue Properties of Several Steels for Aircraft Bearing Applications, *Trans. ASTM*, **59** (1959), 635–657.
26. E.V. Zaretsky and W.J. Anderson: Relation between Rolling-Contact Fatigue and Mechanical Properties for Several Aircraft Bearing Steels, *Trans. ASTM*, **60** (1960), 627–649.
27. J. Monnot, B. Heritier and J.Y. Cogne: Relationship of Melting Practice, Inclusion Type, and Size with Fatigue Resistance of Bearing Steels, ASTM STP 987, American Society for Testing Materials, Philadelphia, PA, 1988, pp. 149–165; and private communication.
28. T. Fujiwara and S. Fukui: The Effect on Non-metallic Inclusions on the Fatigue Life of Ball-Bearing Steel, *Electr. Furnace Steel*, **35(4)** (1964), 170–172.
29. Y. Kawada, H. Nakazawa and S. Kodama: The Effects of the Shape and the Distributions of Inclusions on the Fatigue Strength of Bearing Steels in Rotary Bending, *Trans. Jpn. Soc. Mech. Eng.*, **29(206)** (1963), 1674–1683.
30. T. Yokobori and M. Nanbu: Fatigue Fracture of Vacuum-Melted Ball Bearing Steel, *Proc. 1st Int. Conf. Fract.*, Sendai, **2** (1966), 1529–1542.
31. P.H. Frith: Fatigue Tests on Rolled Alloy Steels Made in Electric and Open-Hearth Furnaces, *J. Iron Steel Inst.*, **180** (1955), 26–33.
32. H. Sato, S. Mogami, Y. Noguchi and M. Murakami: High Tensile Steel Cord, *Seitetsu Kenkyu*, **320** (1986), 35–43.
33. Japanese Industrial Standard, G0555: Lattice Points Counting Method, Optical Method of Nonmetallic Inclusion Rating for Steels, 1977; or *Iron and Steel Handbook*, IV, Materials Testing and Analysis, edited by Iron and Steel Institute of Japan (ISIJ), revised edition 3, 1981, p. 432.
34. A. Koyanagi and M. Kinoshi: Several Rating Methods of Nonmetallic Inclusions in Bearing Steels in Japan, ASTM STP 575, American Society for Testing Materials, Philadelphia, PA, 1975, pp. 22–37.
35. M. Saito and K. Morii: Properties of Ultra-Low Oxygen Structural Steels, *Electr. Furnace Steel*, **51** (1980), 4–12.

36. M. Saito and Y. Ito: Some Properties of Ultra Clean Spring Steel, *Trans. Jpn. Soc. Spring Res.*, **30** (1985), 11–19.
37. L.O. Uhrus: Through-Hardening Steels for Ball Bearings — Effect of Inclusions on Endurance, in *Clean Steel, Spec. Rep. 77*, Iron Steel Inst., 1963, pp. 104–109.
38. D. Brooksbank and K.W. Andrews: Stress Fields around Inclusions and Their Relation to Mechanical Properties, *J. Iron Steel Inst.*, **210** (1972), 246–255.
39. T. Lund and J. Akeson: Oxygen Content, Oxidic Microinclusions, and Fatigue Properties of Rolling Bearing Steels, *ASTM STP 987*, American Society for Testing Materials, Philadelphia, PA, 1988, pp. 308–330.
40. J. Takamura and S. Mizoguchi: Roles of Oxides in Steels Performance — Metallurgy of Oxides in Steels, 1, *Proc. 6th Int. Iron Steel Congr.*, **1** (1990), 591–597.
41. S. Mizoguchi and J. Takamura: Control of Oxides as Inoculants — Metallurgy of Oxides in Steels, 2, *Proc. 6th Int. Iron Steel Congr.*, **1** (1990), 598–604.
42. T. Sawai, M. Wakoh, Y. Ueshima and S. Mizoguchi: Effect of Zr on the Precipitation of MnS in Low Carbon Steels — Metallurgy of Oxides in Steels, 3, *Proc. 6th Int. Iron Steel Congr.*, **1** (1990), 605–611.
43. S. Ogibayashi, K. Yamaguchi, H. Hirai, H. Goto, H. Yamaguchi and K. Takana: The Features of Oxides in Ti-Deoxidized Steel — Metallurgy of Oxides in Steels, 4, *Proc. 6th Int. Iron Steel Congr.*, **1** (1990), 612–617.
44. M. Sumita, I. Uchiyama and T. Araki: The Effect of Inclusions on Fatigue Properties of Steels with Various Matrixes, *Tetsu To Hagane*, **57**(2) (1971), 298–334.
45. Y. Murakami and H. Usuki: Prediction of Fatigue Strength of High-Strength Steels Based on Statistical Evaluation of Inclusion Size, *Trans. Jpn. Soc. Mech. Eng. A*, **55**(510) (1989), 213–221.
46. M. Kinoshi and A. Koyanagi: Effect of Nonmetallic Inclusions on Rolling-Contact Fatigue Life in Bearing Steels, *ASTM STP 575*, American Society for Testing Materials, Philadelphia, PA, 1975, pp. 138–149.
47. K. Nishioka: On the Effect of Inclusion upon the Fatigue Strength, *J. Jpn. Soc. Testing Mater.*, **6**(45) (1957), 382–385.
48. Y. Kawada and S. Kodama: A Review on the Effect of Nonmetallic Inclusions on the Fatigue Strength of Steels, *J. Jpn. Soc. Strength Fract. Mater.*, **6**(1) (1971), 1–17.
49. D. Brooksbank and K.W. Andrews: Thermal Expansion of Some Inclusions Found in Steels and Relation to Tessellated Stresses, *J. Iron Steel Inst.*, **206** (1968), 595–599.
50. D. Brooksbank and K.W. Andrews: Tessellated Stresses Associated with Some Inclusions in Steel, *J. Iron Steel Inst.*, **207** (1969), 474–483.
51. D. Brooksbank: Thermal Expansion of Calcium–Aluminate Inclusions and Relation to Tessellated Stresses, *J. Iron Steel Inst.*, **208** (1970), 495–499.
52. Y. Murakami and M. Uchida: Effects of Thermal Residual Stress and External Stress on Stress Intensity Factors for A Penny-shaped Crack Emanating from An Ellipsoidal Nonmetallic Inclusion, *Proc. JSME Meeting*, No. 920-78, Vol. B, 1992, pp. 239–241.
53. A. Tanaka, K. Furumura and T. Ohkuma: Highly Extended Life of Transmission Bearings of ‘Sealed-Clean’ Concept, *SAE Tech. Pap. Ser.*, 830570, 1983, pp. 1–12.
54. Y. Murakami: Unpublished data.
55. F. Borik and R.D. Chapman: The Effect of Microstructure on the Fatigue Strength of a High Carbon Steel, *Trans. ASM*, **53** (1961), 447–465.
56. T. Yokobori and M. Nanbu: Fatigue Crack Propagation in the High Hardened Stee, *Rep. Res. Inst. Strength Fract. Mater. Tohoku Univ.*, **2**(2) (1966), 29–44.
57. T. Abe, K. Furumura, F. Shimizu, Y. Yukawa, H. Nishimori, R. Hayashi, K. Kobayashi and T. Tubota: Fatigue Property of Extremely Super Clean Bearing Steel, *Rep. ISIJ Mtg.*, **6** (1993), 801.
58. U. Muralidharan, J.C. Stover and P. Kavadas: Effect of Residual Titanium on Fatigue Resistance of Bearing Steels, *Proc. Fatigue '93*, **3** (1993) 1483–1489.
59. T. Toriyama and Y. Murakami: Effects of Inclusions on Fatigue Strength of Super Clean Bearing Steels, *Proc. Fatigue '96*, **2** (1996) 905–910.
60. G.F. Vander Voort and R.K. Wilson: *ASTM Standardization New*, May 1991, p. 28.
61. Y. Murakami, T. Toriyama, K. Tsubota and K. Furumura: What Happens to the Fatigue Limit of Bearing Steel without Nonmetallic Inclusions? Fatigue Strength of Electron Beam Remelted Super

- Clean Bearing Steel, Into the 21st Century, ASTM STP 1327. American Society for Testing Materials, Philadelphia, PA, 1998, pp. 87–105.
62. Y. Murakami, T. Toriyama and E.M. Coudert: Instructions for a New Method of Inclusion Rating and Correlation with the Fatigue Limit, *J. Testing Evaluation*, **22** (1994), 318–326.
 63. Y. Murakami: Inclusion Rating by Statistics of Extreme Values and Its Application to Fatigue Strength Prediction and Quality Control of Materials, *J. Res. Natl. Inst. Stand. Technol.*, **99(345)** (1994), 345–351.

Chapter 8

Spring Steels

8.1 Spring Steels (SUP12) for Automotive Components

Spring steels for automotive use are usually shot peened before use. The effects of shot peening are complicated. In order to simplify analysis of results, fatigue test results on specimens, which were electropolished without shot peening, are discussed first in this section [1].

Table 8.1 shows the chemical composition of the steel, SUP12 (Japanese Industrial Standard), which is used for suspension coil springs. As supplied, the diameter of the material was 17 mm and the length 210 mm. The heat treatment, before machining specimens, is oil quenching from 845°C after soaking for 1 h and tempering in oil at 350°C for 1 h. Fig. 8.1 shows the specimen geometry. The specimen surfaces were polished using emery papers to #2000 grit, and then about 15 μm of the surface layer was removed by electropolishing. During machining, 4.5 mm of the surface layer was removed after heat treatment of the original material, so the difference in hardness between the surface and interior is small.

Fatigue tests were conducted in rotating bending at ambient temperature. In order to investigate the influence of atmospheric corrosion during a long test period (23 days for

Table 8.1 Chemical composition of spring steel SUP12

Materials	C	Si	Mn	P	S	Cr
SUP 12	0.53	1.31	0.75	0.004	0.004	0.63

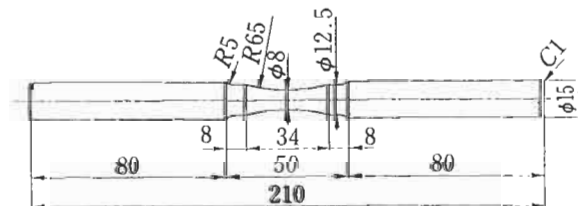


Figure 8.1 Specimen geometry.

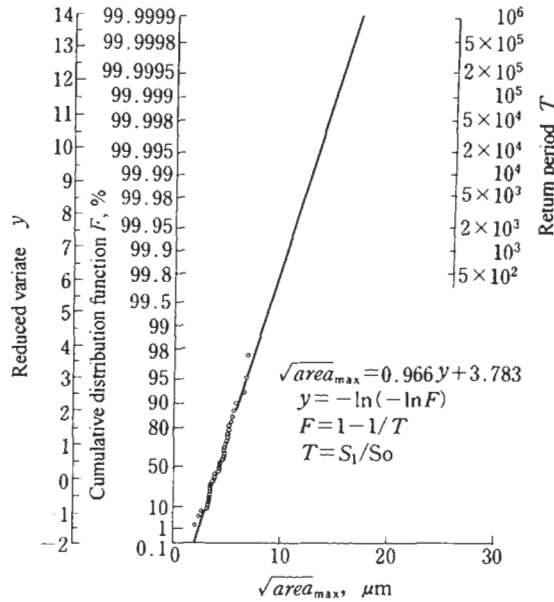


Figure 8.2 Cumulative frequency distribution of \sqrt{area}_{max} for inclusions in steel SUP12. Standard inspection area $S_0 = 0.0309 \text{ mm}^2$.

$N = 10^8$), some fatigue tests were carried out using specimens oiled, with a machine oil, every 3×10^7 cycles. The nominal stress, σ_0 , was calculated for the minimum section of the hourglass specimen (Fig. 8.1). The Vickers hardness, H_v , was measured, before fatigue testing, at 8 surface points using a force of 1.96 N, and the mean value was taken as the representative value. The hardness after fatigue testing was taken as the average value measured at three points near a fatigue fracture origin using a force of 9.8 N.

Fig. 8.2 is the extreme value statistics plot (see Appendix C) of the maximum inclusion size, \sqrt{area} , present in a standard inspection area $S_0 = 0.0309 \text{ mm}^2$. The distribution of \sqrt{area}_{max} in Fig. 8.2 shows good linearity, and may be regarded as obeying the distribution of extremes. There is no inclusion having $\sqrt{area}_{max} > 10 \text{ }\mu\text{m}$ in 40 inspection areas, indicating that this material is a very clean spring steel. However, it does not follow that the maximum inclusion contained in one specimen is smaller than $10 \text{ }\mu\text{m}$. It implies, rather, that there is the possibility of the presence of quite large inclusions in the total volume of one specimen, or of many specimens.

The stress, σ' , at the fracture origins of all the fractured specimens obeyed the relationship $\sigma' \geq 0.95\sigma_0$. Therefore the control volume, which may be regarded as containing the fracture origin, was calculated as the part subjected to a stress greater than 95% of the applied nominal stress, σ_0 , at the minimum section. Thus, the control volume calculated by considering the specimen curvature is 30.6 mm^3 . Table 8.2 shows the control surface S_1 (mm^2), return period $T = S_1/S_0$, the estimated maximum value of \sqrt{area}_{max} for the numbers of specimens $N = 1, 10$ and 100 . These were calculated by assuming that a specimen consists of a set of thin sliced disks, as shown in Fig. 8.3,

Table 8.2 Prediction of \sqrt{area}_{max} for steel SUP12

Thickness of annular plate h_0 (μm)	Control area per unit volume (mm^2/mm^3)	Control area per one specimen S_1 (μm^2)	Return period for one specimen T	\sqrt{area}_{max} for N specimens (μm)		
				$N = 1$	$N = 10$	$N = 100$
0.1	1.0×10^4	3.06×10^5	9.90×10^6	19.34	21.58	23.80
1	1.0×10^3	3.06×10^4	9.90×10^5	17.12	19.34	21.58
2	5.0×10^2	1.53×10^4	4.95×10^5	16.45	18.67	20.90
5	2.0×10^2	6.12×10^3	1.98×10^5	15.55	17.79	16.80
10	1.0×10^2	3.06×10^3	9.90×10^4	14.89	17.12	19.34

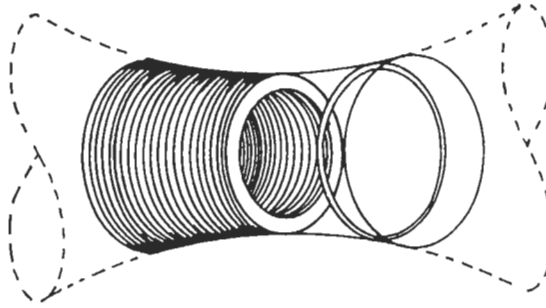


Figure 8.3 Definition of control volume for inclusion calculations.

having thickness, h_0 , of 0.1, 1, 2, 5 and 10 μm . From Table 8.2, assuming the thickness of the sliced disks to be 1/10 smaller leads to only 2.2 μm larger inclusion size, and only 3% difference in fatigue limit estimation using Eq. 6.5.

Fig. 8.4, shows the results of the fatigue tests. The symbols \circ and $\circ \rightarrow$ show data for oiled specimens, and Δ and $\Delta \rightarrow$ data for conventional specimens. \circ^n indicates the n -th test for a specimen which was tested repeatedly, at higher stress, after being unbroken at $N = 10^7$ or 10^8 . Data scatter is too large to draw conventional $S-N$ curves. A test to $N = 10^8$ takes 23 days. Such long period tests may be the reason for the failure of several conventional specimens (without oil) due to corrosion of the surface layer. The spring steel SUP12 has a low probability of containing large inclusions, and few specimens fractured from internal inclusions. Electropolishing specimen surfaces created large pits, which were originally inclusions present at a specimen surface. Two specimens fractured from this kind of pit.

Fig. 8.5 shows a photograph of an inclusion at a fatigue fracture origin. Table 8.3 shows various data on specimens whose fracture origins were identified as an inclusion or a surface pit. H'_V is Vickers hardness after fatigue testing, N_f is number of cycles to failure, \sqrt{area} is the inclusion or pit size, h is the distance from the surface to the centre

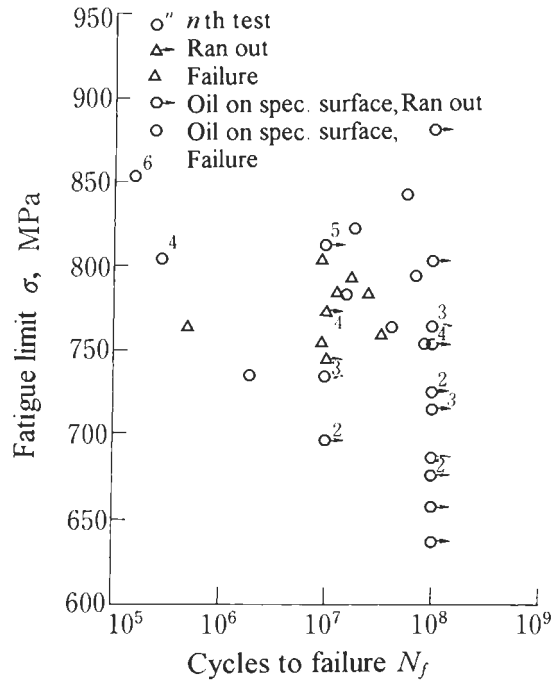


Figure 8.4 Rotating bending fatigue $S-N$ data for steel SUP12.

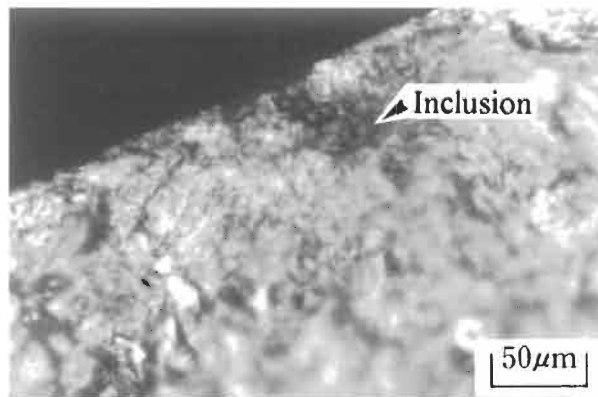


Figure 8.5 Inclusion at fracture origin in steel SUP12. $H_V = 614$, $\sigma = 785$ MPa, $N_f = 2.6 \times 10^7$, $\sqrt{area} = 20.0 \mu\text{m}$, distance from surface = $40 \mu\text{m}$.

of an inclusion, and σ' is the nominal stress applied at a fracture origin. The estimated fatigue limits, σ'_w , in Table 8.3 are calculated by substituting \sqrt{area} and H'_V into Eq. 6.1 or Eq. 6.3. The ratios, σ'/σ'_w , are all larger than 1.0, and the results are consistent with the fact that all these specimens actually fractured. The difference between H_V (before test) and H'_V (after test) was approximately 8%, which we could not conclude to be

Table 8.3 Location, size of inclusion, stress at fracture origin, and estimated fatigue limit

HV'	Cycles to failure N_f	Size of inclusion \sqrt{area} (μm)	Distance from surface h (μm)	Shape	Nominal stress at inclusion σ' (MPa)	Fatigue limit estimated by Eq. (6.1) or (6.3) σ_w'	σ'/σ_w'
636	1.8×10^7	7.7	3		818	753	1.09
614	2.6×10^7	20.0	40		744	695	1.07
622	3.4×10^7	11.6	9		757	690	1.10
644	4.3×10^7	11.0	3		741	717	1.03
609	8.6×10^7	13.2	5		742	664	1.12

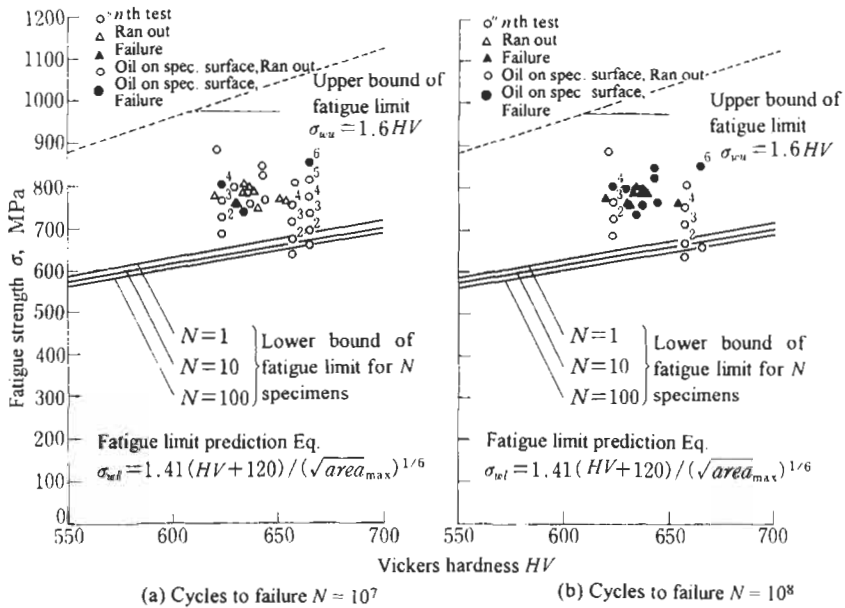


Figure 8.6 Broken and unbroken specimens at $N = 10^7$ and 10^8 , and estimation of lower bound fatigue limit, σ_{wl} . (a) $N = 10^7$. (b) $N = 10^8$.

caused by fatigue testing, or by microstructural variation. Although there is much scatter in the size of inclusions at fracture origins, none of them exceeds the maximum values, $\sqrt{area_{max}}$, predicted using Fig. 8.2. The fracture origins of further specimens, not listed in Table 8.3, could not be identified.

Figs. 8.6a and b summarise the results of all fatigue tests where the fatigue limit is defined by specimens which were unbroken at $N = 10^7$ and $N = 10^8$. The solid lines in Figs. 8.6a and b show the lower bounds of fatigue strength, σ_{wl} , for numbers of specimens $N_s = 1, 10$ and 100 , which were predicted by substituting $\sqrt{area_{max}}$ into

Eq. 6.5. The values of \sqrt{area}_{max} were calculated by assuming the plate thickness h_0 of the standard area for inclusion rating to be $h_0 = 1 \mu\text{m}$. The upper bounds σ_{wu} were calculated by the empirical formula, $\sigma_{wu} = 1.6 H_V$ [2–4].

The data points for broken specimens are all above the prediction lines for the lower bound, σ_{wl} , which may be considered to be predicted very successfully.

The production of automobile engine valve spring in Japan is estimated to be 4–5 million items per month. It is almost impossible to evaluate the fatigue strength of such huge number of components by conventional fatigue testing. Naturally, the fatigue strength of these components varies. If we do not take scatter into consideration, incidental fatigue failure accidents may be reported with unhelpful comments such as ‘an unexpected accident’ or ‘a very rare accident’. Since it is impossible to inspect all individual parts, we need to introduce a rational statistical method into the fatigue design of mass production parts. In this sense, the approach shown in Fig. 8.6 is a promising method.

8.2 Explicit Analysis of Nonmetallic Inclusions, Shot Peening, Decarburised Layers, Surface Roughness, and Corrosion Pits in Automobile Suspension Spring Steels

In components, such as leaf springs, which undergo machining, heat treatment and surface treatment (shot peening) [5–18], and also are exposed to repeated bending loads, several complex factors influence the fatigue strength, making it very difficult to evaluate their individual effects [6–18]. This is why there is difficulty in setting quantitative guidelines for design stress, evaluation of the material quality, and various treatments.

To address this problem, the effects of three basic factors: (1) nonmetallic inclusions [11,19,20]; (2) matrix structure; and (3) mean stress should be resolved individually. In particular, a quantitative evaluation of the effects of nonmetallic inclusions is important. It is impossible, however, to completely solve the complicated problem of springs unless all three factors are considered together.

With respect to the combined influence of the factors (1)–(3), we must consider the variation of both hardness and residual stress from specimen surface to interior. This causes variation of fatigue strength from surface to interior. In this case, the prediction method developed in Chapters 5 and 6 can be applied to determine the fatigue strength at the weakest point. In order to demonstrate a practical procedure, a systematic study [21] on the rotating bending fatigue strength characteristics of leaf spring steels, SUP9 and SUP10M (Japanese Industrial Standards) is described. Specifically, the relationships between such factors as nonmetallic inclusions, shot-peening, decarburised layers, and extremely small surface pits caused by corrosion, all of which affect actual products, are examined quantitatively in order to predict fatigue strength. The effects of shot peening bring in the problems of residual stress, work hardening, and changes in surface properties. Therefore, the study is not limited to the assessment of SUP9 and SUP10M, but can be readily applied to fatigue problems of other materials and components, which also have complex relationships between similar factors.

Table 8.4 Chemical composition of spring steels SUP9 and SUP10M

Materials	C	Si	Mn	P	S	Cr	Cu	V	Nb
SUP 9	0.53	0.31	0.71	0.023	0.012	0.67	0.14	—	—
SUP 10M	0.51	0.23	0.85	0.017	0.001	0.95	0.04	0.16	0.043

Table 8.5 Mechanical properties of spring steels SUP9 and SUP10M

Materials	0.2% proof stress (MPa)	Tensile strength (MPa)	Elongation (%)	Reduction of area (%)
SUP 9	1330	1440	11.2	36.3
SUP 10M	1670	1750	10.7	39.0

Table 8.6 Types of specimen tested

Materials	Spec. types	Surface finishes
SUP 9	T-Em	Turning, Emery paper finish
	T-Em-Pit	Turning, Emery paper finish and small surface pit
	Dec-Shot	Shot peening on decarburized layer
SUP 10M	T-Em	Same as SUP 9 T-Em
	T-Em-Pit	Same as SUP 9 T-Em-Pit
	T-Em-Shot	Turning, Emery paper finish and shot peening
	Dec	As heat treated with decarburized layer
	Dec-Shot	Same as SUP 9 Dec-Shot

8.2.1 Materials and Experimental Procedure

Table 8.4 shows the chemical composition of SUP9 and SUP10M steels, and Table 8.5 their mechanical properties after heat treatment.

SUP10M has been developed recently, by the addition V and Nb, in order to provide a spring steel, not only with high strength, but also with improved toughness.

Both steels were melted in a 60-ton electric furnace, hot rolled to a thickness of 18 mm for softening and annealing, and rough machined. The steels were oil-quenched after soaking for 15 min at 900°C. They were air cooled after tempering for 90 min at 480°C for SUP9, and at 400°C for SUP10M. After heat treatment, the specimens were machined to the geometry shown in Fig. 8.1.

The specimens were finished as shown in Table 8.6. SUP9 (T-Em) and SUP10M (T-Em) are specimens which were turned and finished using emery paper. SUP9 (T-

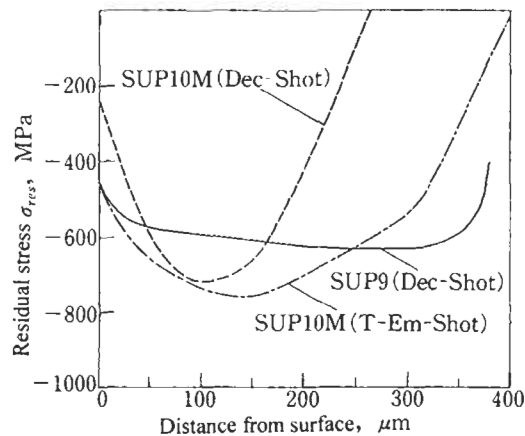


Figure 8.7 Residual stress distribution for specimens SUP9 (Dec-Shot), SUP10M (Dec-Shot), and SUP10M (T-Em-Shot).

Em-Pit) and SUP10M (T-Em-Pit) are specimens in which a pit was introduced by electropolishing after turning and emery paper finishing. SUP9 (Dec-Shot), SUP10M (Dec-Shot) and SUP10M (T-Em-Shot) are shot-peened specimens, where Dec indicates specimens which had a decarburised layer, T denotes turning, and Em denotes emery paper finish.

Corrosion pits were introduced deliberately on the minimum sections of specimens SUP9 (T-Em-Pit) and SUP10M (T-Em-Pit) by electropolishing in 5% NaCl solution. For SUP9 (Dec-Shot) and SUP10M (Dec-Shot) specimens, shot peening was applied directly to the mill scale surface, including the surface decarburised layer. For SUP10M (T-Em-Shot) specimens, shot peening was applied after turning in the same manner as SUP10M (T-Em) specimens. In SUP10M (Dec) specimens, the surface decarburised layer was left intact. The shot-peening conditions are as follows: cut wire, 0.6% C steel of 0.8 mm diameter; arc height 0.48 mm A [7], and coverage 100%. Fig. 8.7 shows the residual stress distribution for shot-peened specimens measured by the X-ray diffraction method. The measured values were obtained by measurements made after successive removal of layers by electropolishing. The surface values are considered accurate and reliable; however, the accuracy of the subsurface values is not as good because of the material removal.

The compressive residual stress on the surface of the turned specimens was measured as about 420 MPa for SUP9 (T-Em) specimens and about 500 MPa for SUP10M (T-Em) specimens. The residual stress became zero when the surface layer was electropolished to 20 μm , so the subsurface distribution of the residual stress was assumed to be linear from the surface to the depth of 20 μm . The fatigue strength was predicted assuming that residual stress is equivalent to a local mean stress. This concept, in which a portion of a specimen is regarded as a small specimen, is shown in Fig. 8.8. Thus, in this study, a method is described for predicting a value for stress amplitude, σ_a , which the specimen is capable of withstanding under a given residual stress, σ_{res} .

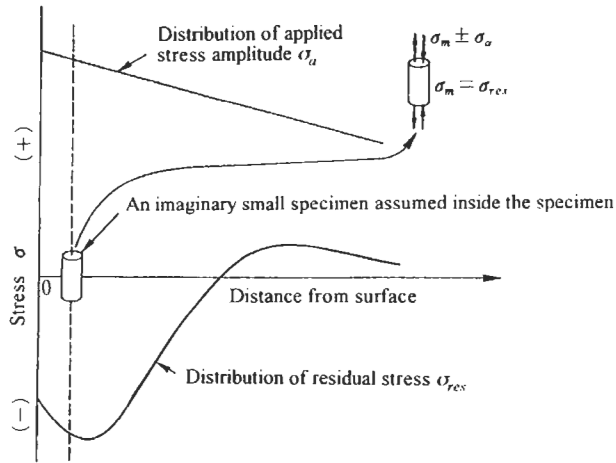


Figure 8.8 Distribution of residual stress and of stress amplitude.

Rotating bending fatigue testing machines (capacity 98 Nm, 2400 rpm) were used.

Fig. 8.9 shows the extreme value statistics of inclusions in steels SUP9 and SUP10M. The figure was prepared using the procedure described in Appendix A. In this case, the standard inspection area, S_0 , is 0.0309 mm^2 . Inclusions with $\sqrt{\text{area}}$ of more than $10 \mu\text{m}$ were not observed in either SUP9 or SUP10M, because both are extremely clean steels. However, this does not mean that $\sqrt{\text{area}}_{\text{max}}$ of inclusions contained in a specimen is less than $10 \mu\text{m}$. On the contrary, it suggests that rather large inclusions would exist in further specimens. Since the critical volume, V , of the specimen shown in Fig. 8.1 is calculated as $V = 89.8 \text{ mm}^3$ and, accordingly $T = 9.0 \times 10^5$, the value of $\sqrt{\text{area}}_{\text{max}}$, which is predicted to exist in one specimen, can be estimated using the procedure indicated by using the arrow shown in Fig. 8.9. Table 8.7 shows return period, T , and the predicted maximum inclusion size, $\sqrt{\text{area}}_{\text{max}}$, for 1, 10 and 100 specimens of both steel types.

Thus, the lower bound of fatigue limit, σ_{wl} , can be determined by substituting $\sqrt{\text{area}}_{\text{max}}$ for $\sqrt{\text{area}}$ in Eq. 6.12. The upper bound value, σ_{wu} , is determined from an

Table 8.7 Prediction of $\sqrt{\text{area}}_{\text{max}}$ for steels SUP9 and SUP10M

Materials	Control volume $V(\text{mm}^3)$	Numbers of spec.	Return period T	$\sqrt{\text{area}}_{\text{max}}$ (μm)
SUP 9	89.8	1	9.0×10^5	21.46
		10	9.0×10^6	23.70
		100	9.0×10^7	27.49
SUP 10 M	89.8	1	9.0×10^5	24.48
		10	9.0×10^6	27.13
		100	9.0×10^7	30.55

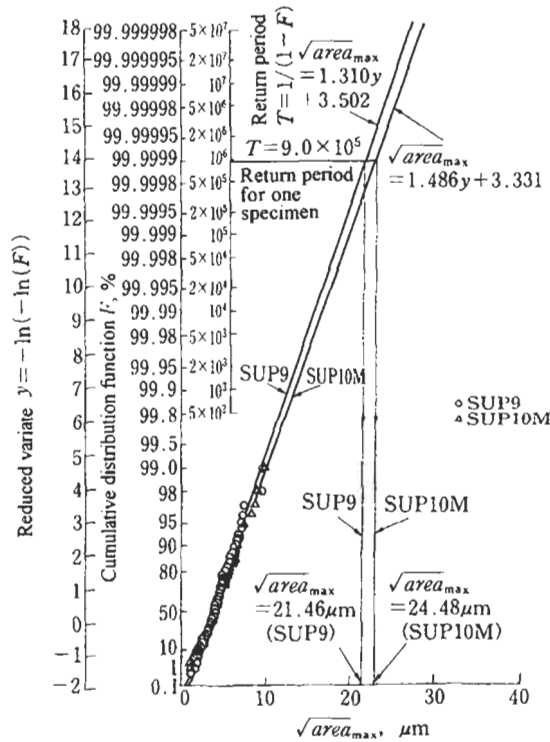


Figure 8.9 Cumulative frequency distribution of $\sqrt{area_{max}}$ of inclusions for steels SUP9 and SUP10M. Standard inspection area $S_0 = 0.0309 \text{ mm}^2$, number of inspections = 100.

empirical formula, which is repeated here for convenience:

$$\sigma_{wu} \cong 0.5 \sigma_U \cong 1.6 H_V \tag{5.7}$$

where σ_{wu} and σ_U , the ultimate tensile strength, are in MPa, and H_V is in kgf/mm^2 .

8.2.2 Interaction of Factors Influencing Fatigue Strength

Figs. 8.10 and 8.11 show $S-N$ data for steels SUP9 and SUP10M, respectively. Since there are significant variations in fatigue life and strength, it is difficult to draw a trend line through a group of experimental results. From observation of the fatigue fracture surfaces, it can be seen that the fatigue fracture origins for both SUP9 (T-Em) and SUP10M (T-Em) specimens are nearly all at nonmetallic inclusions. Origins for SUP9 (T-Em-Pit) and SUP10M (T-Em-Pit) specimens are all at corrosion pits. For SUP9 (Dec-Shot), SUP10M (Dec-Shot) and SUP10M (Dec) specimens, the origins are all at the surface. SUP10M (T-Em-Shot) specimens exhibited two types of fatigue fracture origins, one at internal inclusions, and one at the surface. These complicated fatigue fracture behaviours, and fracture origins, are caused by complicated factors, such as stress gradient, residual stress, inclusions, surface roughness, and hardness distribution.

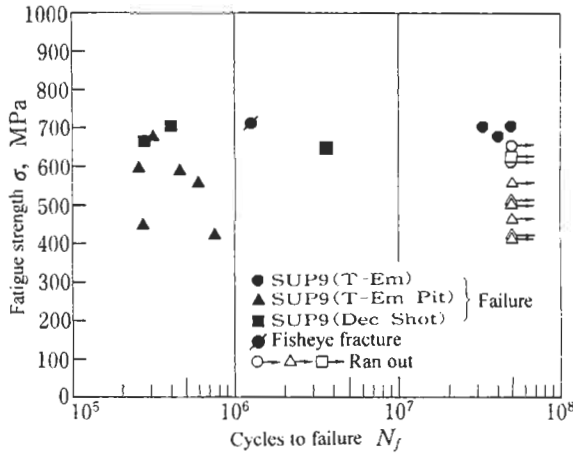


Figure 8.10 *S-N* data for specimens SUP9 (T-Em), (T-Em-Pit) and (Dec-Shot).

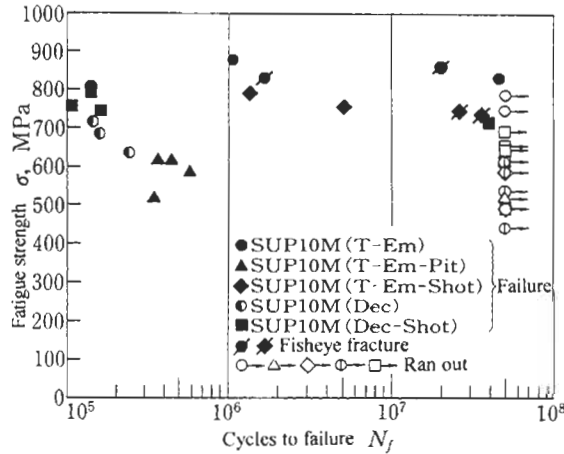


Figure 8.11 *S-N* data for specimens SUP10M (T-Em), (T-Em-Pit), (T-Em-Shot), (Dec) and (Dec-Shot).

8.2.2.1 Effect of Shot Peening

Shot peening generates a residual stress distribution, as shown in Fig. 8.7, and it usually increases the bending fatigue strength. However, since it also roughens the material surface, it can have the effect of reducing fatigue strength [7,9,13,15]. Fig. 8.12 shows the distribution of internal hardness, to a depth of about 400 μm from the surface, for SUP9 (Dec-Shot), SUP10M (Dec-Shot), and SUP10M (Dec) specimens. For all specimens, the hardness rapidly decreases from a depth of about 100 μm towards the surface. This is because a decarburised layer, caused by heat treatment, remains near the surface of the specimen [7,9]. It can be seen that the hardness of the microstructure hardly changed, even though shot-peening produced significant deformation.

Taking into consideration these conditions which are peculiar to springs, we should

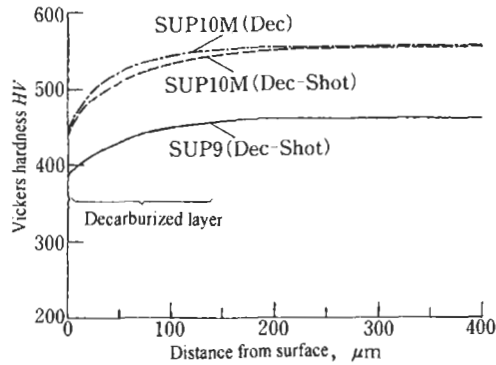


Figure 8.12 Distribution of hardness near surface for specimens SUP9 (Dec-Shot), SUP10M (Dec-Shot) and SUP10M (Dec).

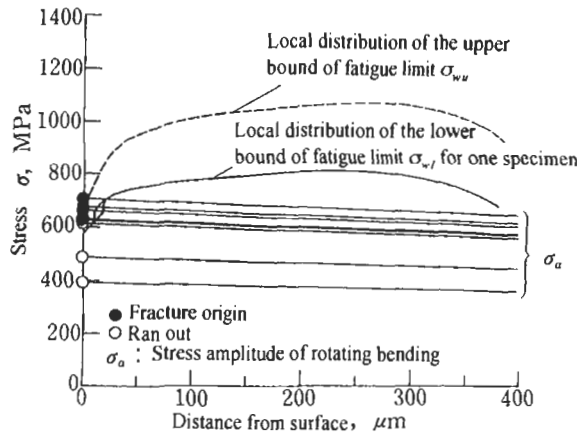


Figure 8.13 Comparison for specimen SUP9 (Dec-Shot) between the predicted fatigue limit at local surface points and the applied stress distribution.

note the mutual interaction of the following five factors for quantitative evaluation of the fatigue strength of shot-peened material: (1) existence of nonmetallic inclusions; (2) hardness of microstructure; (3) distribution of residual stress (mean stress); (4) a decarburised layer; and (5) the irregularity of the surface.

The fatigue limit is determined by H_v , \sqrt{area} , and R , as previously explained. We view factors 1 and 5 as related to \sqrt{area} , factors 2 and 4 to H_v , and factor 3 to stress ratio, R . If we consider the contribution of these factors, and that the applied stress changes with distance from the surface, the possibility of a site becoming a fatigue origin differs according to its position in the specimen. Thus, the changes in the upper and lower bounds for local fatigue strength (*the endurance value for σ_a in Fig. 8.8*) at each position from the surface are as shown in Figs. 8.13–8.15. These figures also show the stress amplitude at the fracture origin. The lower bound of local fatigue strength, σ_{wl} , was obtained by substituting the H_v distribution shown in Fig. 8.12, the distribution

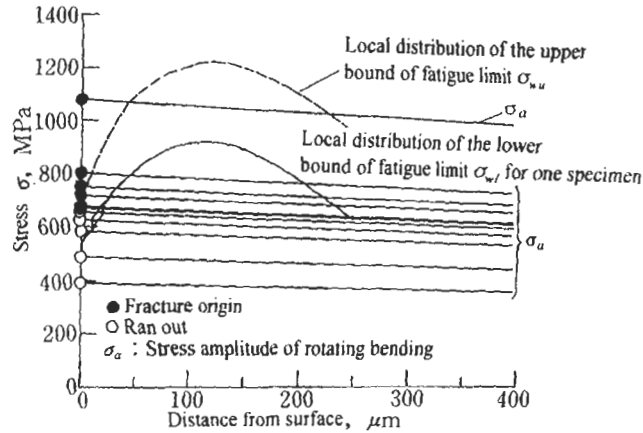


Figure 8.14 Comparison for specimens SUP10M (Dec-Shot) between the predicted fatigue limit at local surface points and the applied stress distribution.

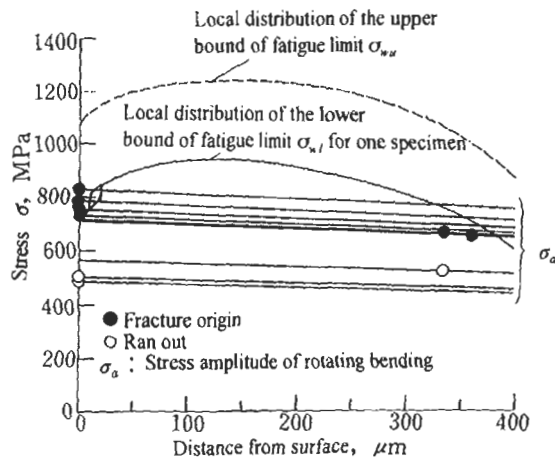
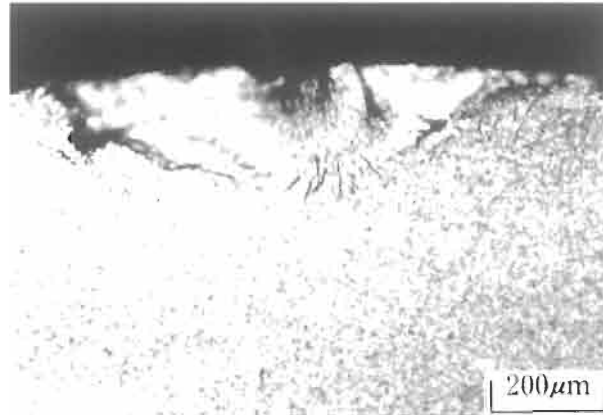


Figure 8.15 Comparison for specimens SUP10M (T-Em-Shot) between the predicted fatigue limit at local surface points and the applied stress distribution.

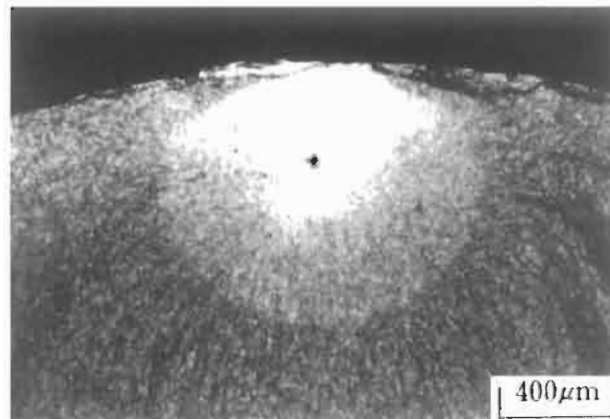
of residual stress shown in Fig. 8.7, and the maximum size of inclusion, \sqrt{area}_{max} , for each specimen in Fig. 8.9, into Eq. 6.12. The upper bound, σ_{wu} , is the value where it is assumed that it is not affected by the inclusion, and is actually calculated by Eq. 5.7, together with a Goodman diagram.

The fracture origins for SUP9 (Dec-Shot) and SUP10M (Dec-Shot) specimens, whose data are shown in Figs. 8.13 and 8.14, were all at, or very near, the surface. The fracture origins for SUP10M (T-Em-Shot) specimens (Fig. 8.15) were near the surface, or at a subsurface nonmetallic inclusion. Figs. 8.16 and 8.17 show examples of these fatigue fractures. Fig. 8.17 shows a typical fish eye fracture. It is not circular, but is very deformed near the surface because growth of the fatigue crack was affected by residual stress.



$$HV = 466, \sigma = 755 \text{ MPa}, N_f = 1.06 \times 10^5$$

Figure 8.16 Example of fatigue fracture origin at surface, SUP10M (Dec-Shot) specimen, shot peening on decarburised layer.



$$HV = 540, \sigma = 735 \text{ MPa}, N_f = 3.54 \times 10^7$$

$$\sqrt{\text{area}} = 29.8 \text{ } \mu\text{m}, R = -2.0, \sigma'/\sigma_w' = 0.984$$

Figure 8.17 Example of fish eye fatigue fracture, SUP10M (T-Em-Shot) specimen, shot peened after machining.

To predict the fatigue strength of shot-peened specimens, we compared the predicted lower bound of the local fatigue strength with the nominal stress amplitude (σ_a in Fig. 8.8). In Figs. 8.13–8.15 note the lowest region of predicted fatigue strength in comparison with σ_a . In SUP9 (Dec-Shot) specimens (Fig. 8.13) and SUP10M (Dec-Shot) specimens (Fig. 8.14), the fatigue strength of the entire specimen is determined by the competition between the lower bound of fatigue strength at the surface, and the stress amplitude σ_a . In SUP10M (T-Em-Shot) specimens (Fig. 8.15), the fatigue strength

of an entire specimen is determined by the competition between the lower bound of fatigue strength at the surface, or at the interior (about 350 μm deep), and the stress amplitude, σ_a .

In the shot-peened specimens, fatigue fracture origins exist both near the surface and subsurface. Competition between the stress amplitude, and the upper and lower bounds of fatigue strength can explain this. For example, in SUP9 (Dec-Shot) specimens (Fig. 8.13), the fatigue fracture origin is at the surface because the upper and lower bounds of fatigue strength near the surface are noticeably lower than those subsurface. Thus the lower bound is not reached subsurface, even if the stress amplitude reaches the upper bound of fatigue strength near the surface.

In SUP10M (T-Em-Shot) specimens (Fig. 8.15), the stress amplitude is approximately the lower bound, in a region about 400 μm below the surface, before it reaches the lower bound of fatigue strength near the surface. For this reason, when the stress amplitude near the surface reaches the lower bound of the fatigue strength, two types of fracture origins, subsurface and surface, occur depending on surface roughness, *surface inclusion size*, and internal inclusion size.

For the internal fracture origin shown in Fig. 8.15, however, the fracture stress amplitude is somewhat lower than the predicted lower bound of local fatigue strength. This margin of error can be explained by taking into consideration both the precision of the prediction equation, and also the reliability of the measured values for subsurface residual stress.

Thus, by taking into consideration all the factors in shot-peened specimen (hardness, inclusions, residual stress, and applied stress), it is possible to explain why the surface, and a region 300–400 μm below the surface, both have a higher possibility of containing a fatigue origin than does the intermediate region 50–300 μm below the surface.

Shot peening produces surface irregularities, and these influence fatigue strength. Comparing the results for SUP10M (T-Em-Shot) specimens in Fig. 8.15 with those for SUP10M (Dec-Shot) specimens in Fig. 8.14, indicates that there is very little difference in fatigue strength between these two specimen types. SUP10M (T-Em-Shot) specimens were produced by removing the mill scale from SUP10M (Dec) specimens before shot peening. SUP10M (T-Em-Shot) specimens have a harder surface microstructure than do SUP10M (Dec-Shot) specimens because they were shot peened after removing the decarburised layer. However, while the fatigue strength was not affected by surface irregularities in SUP10M (Dec-Shot) specimens, surface irregularities have a detrimental effect on SUP10M (T-Em-Shot) specimens because of their high surface hardness. This causes significant variations in fatigue strength. As a result, the fatigue strength of SUP10M (T-Em-Shot) specimens was not increased significantly.

For example, a rough shot-peened surface has an average irregularity of about 20 μm , and when this is assumed to be a small semi-circular defect [15], $\sqrt{\text{area}}$ is about 25 μm . Since the maximum size of an inclusion in a specimen, which provides the lower bound of local fatigue strength shown in Table 8.7, is $\sqrt{\text{area}_{\text{max}}} = 24.5 \mu\text{m}$ in SUP10M, the surface irregularity is equivalent to a defect corresponding in size to such an inclusion. This result is consistent with the fatigue limit for a failed SUP10M (T-Em-Shot) specimen, with a surface fracture origin, as shown later in Fig. 8.21. Its fatigue limit is nearly equal to the predicted lower bound. Since the prediction method proposed

Table 8.8 Comparison between estimated fatigue limits and experimental results for steel SUP9

(a) SUP 9 (T-Em)

Specimens	HV	σ	N_f	\sqrt{area}	h	Shape of inclusion	σ'	$\sigma'_w (R)$	σ'/σ'_w
TM3	436	686	1.51×10^6	6.71	5.3		657	675 (-2.54)	0.973
TM7	454	657	$5 \times 10^7 \rightarrow$	9.49	3.9		666	675 (-2.87)	0.987
		706	5.13×10^7				716		

(b) SUP 9 (T-Em-Pit)

Specimens	HV	σ	N_f	\sqrt{area}	t	Shape of pit	σ'	$\sigma'_w (R)$	σ'/σ'_w
TM1	445	588	4.50×10^5	60.1	31		583	408 (-1)	1.43
TM8	456	441	2.67×10^5	344	160		418	311 (-1)	1.34
TM9	463	421	$5 \times 10^7 \rightarrow$	73.2	43		419	408 (-1)	1.03
		500	$5 \times 10^7 \rightarrow$				497		1.22
		598	2.53×10^5				595		1.45
TM10	388	421	7.58×10^5	58.0	43		417	369 (-1)	1.13
TM11	443	461	$5 \times 10^7 \rightarrow$	61.8	33		459	405 (-1)	1.13
		559	6.03×10^5				556		1.37

HV: Vickers hardness, σ : Nominal stress at surface (MPa),

\sqrt{area} : Size of inclusion or pit (μm),

t : Depth of pit (μm), h : Distance from surface (μm),

N_f : Cycles to failure, σ' : Nominal stress at fracture origin (MPa),

σ'_w : Fatigue limit estimated by Eq. (6.6) or (6.9) (MPa), R : Stress ratio,

\rightarrow Continued test at higher stress

in this study is applicable in the presence of several complex factors, the technique can be utilised to find the optimum shot-peening condition for the achievement of high fatigue strength.

8.2.2.2 Effects of Nonmetallic Inclusions and Corrosion Pits

Tables 8.8 and 8.9 show comparisons between the predicted value for the fatigue strength determined from Eqs. 6.6 and 6.9, and experimental result for specimens fractured due to nonmetallic inclusions and corrosion pits. The effectiveness of the prediction equation will be shown by comparing the stress amplitude, σ' , applied to the fracture origin with the local fatigue limit, σ'_w , determined from the H_V on the surface near the origin and \sqrt{area} .

If the prediction is correct, then for a fractured specimen the values of σ'/σ'_w in the tables should be larger than 1.0. Most values are indeed larger than 1.0, but in a few cases values are less than 1.0. However, since the lowest value is 0.864, the

Table 8.9 Comparison between estimated fatigue limits and experimental results for steel SUP10M

(a) SUP 10M (T-Em)

Specimens	HV	σ	N_f	\sqrt{area}	h	Shape of inclusion	σ'	$\sigma_w'(R)$	σ'/σ_w'
10 M 3	550	862	2.00×10^7	14.1	26		845	673 (-1)	1.26
10 M 6	554	833	1.63×10^6	28.9	251		781	589 (-1)	1.32
10 M 9	558	882	1.05×10^6	16.9	17		866	599 (-1.06)	1.45
10 M 21	536	441	$5 \times 10^7 \rightarrow$	7.93	3.0		444	804 (-3.12)	0.552
		794	1.59×10^7				799		0.993

(b) SUP 10M (T-Em-Pit)

Specimens	HV	σ	N_f	\sqrt{area}	t	Shape of pit	σ'	$\sigma_w'(R)$	σ'/σ_w'
10 M 4	549	588	5.86×10^5	90.6	51		580	451 (-1)	1.29
10 M 7	581	519	3.41×10^5	250	74		461	399 (-1)	1.15
10 M 8	543	323	$5 \times 10^7 \rightarrow$	69.8	39		320	468 (-1)	0.692
		519	$5 \times 10^7 \rightarrow$				514		1.10
		617	4.44×10^5				611		1.31
10 M 10	551	617	3.64×10^5	71.6	42		611	471 (-1)	1.30

(c) SUP 10 M (T-Em-Shot)

Specimens	HV	σ	N_f	\sqrt{area}	h	Shape of inclusion	σ'	$\sigma_w'(R)$	σ'/σ_w'
OMS 13	540	735	3.54×10^7	29.8	360		648	658 (-2.04)	0.984
OMS 15	545	588	$5 \times 10^7 \rightarrow$	23.4	333		520	762 (-3.33)	0.683
		745	2.58×10^7				659		0.864

HV: Vickers hardness, σ : Nominal stress at surface (MPa),

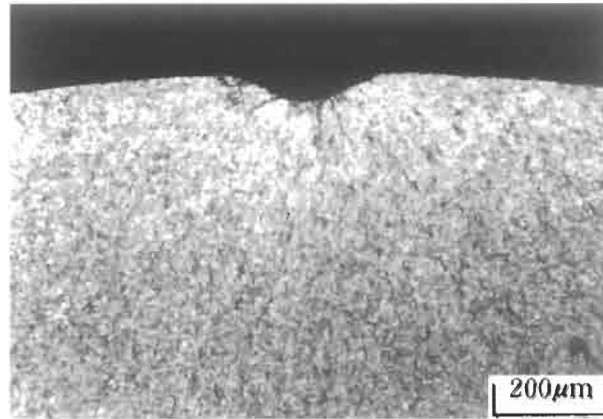
\sqrt{area} : Size of inclusion or pit (μm),

t : Depth of pit (μm), h : Distance from surface (μm),

N_f : Cycles to failure, σ' : Nominal stress at fracture origin (MPa),

σ_w' : Fatigue limit estimated by Eq. (6.6) or (6.9) (MPa), R : Stress ratio,

\rightarrow Continued test at higher stress



$$HV = 549, \sigma = 588 \text{ MPa}, N_f = 5.86 \times 10^5$$

$$\sqrt{\overline{area}} = 90.6 \text{ } \mu\text{m}, R = -1, \sigma'/\sigma_w' = 1.29$$

Figure 8.18 Fatigue fracture origin at corrosion pit, SUP10M (T-Em-Pit), corrosion pit introduced after machining.

prediction accuracy for practical use is satisfactory, when the reliability of subsurface residual stress measurement is considered.¹ The tables show sketches of the shapes of nonmetallic inclusions and corrosion pits which became fracture origins. Fig. 8.18 shows a fracture from a corrosion pit.

Fig. 8.19 shows a modified $S-N$ curve, which is the relationship between σ'/σ_w' and the fatigue life, N_f , for all specimens fractured due to nonmetallic inclusions or to small defects. The plotted fracture points show a trend toward a larger value of σ'/σ_w' for a shorter value of N_f .

N_f is shorter when the pits on the surface become fracture origins. This agrees with Duckworth et al.'s report [22] that a fracture due to a surface nonmetallic inclusion has a shorter life than one due to an internal nonmetallic inclusion.

8.2.2.3 Prediction of Scatter in Fatigue Strength using the Statistics of Extreme

Figs. 8.20 and 8.21 show comparisons between the lower bound of fatigue strength, σ_{wl} , (that is the nominal stress amplitude of the specimen) predicted from the $\sqrt{\overline{area}}_{\max}$ of the largest inclusion which is expected to exist in 10 specimens ($N = 10$), the fatigue upper bound, σ_{wu} , determined from Eq. 6.4 and a modified Goodman diagram, and all the fatigue test results, except for the pitted specimens.

Since the value of residual stress at the fracture origin of each specimen is not always the same, the stress ratio, R , which is a variable affecting predictions using Eqs. 6.6–6.10, does not have a fixed value, but has a range of values, as shown in the figures.

¹ It should be noted that the specimen fractured at $\sigma'/\sigma_w' = 0.864$ endured 2.58×10^7 cycles. If the test had been stopped at 10^7 cycles, this specimen would be judged not to have failed. The problem of fatigue failure at the cycles greater than 10^7 is discussed in Chapter 15.

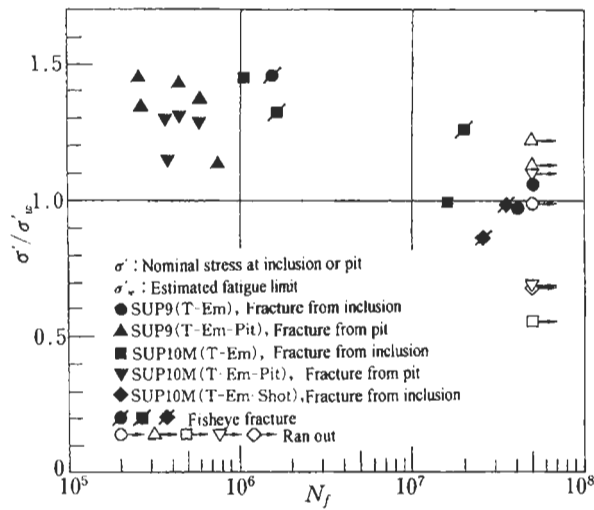


Figure 8.19 Modified $S-N$ data for specimens SUP9 (T-Em) and (T-Em-Pit), and SUP10M (T-Em), (T-Em-Pit) and (T-Em-Shot).

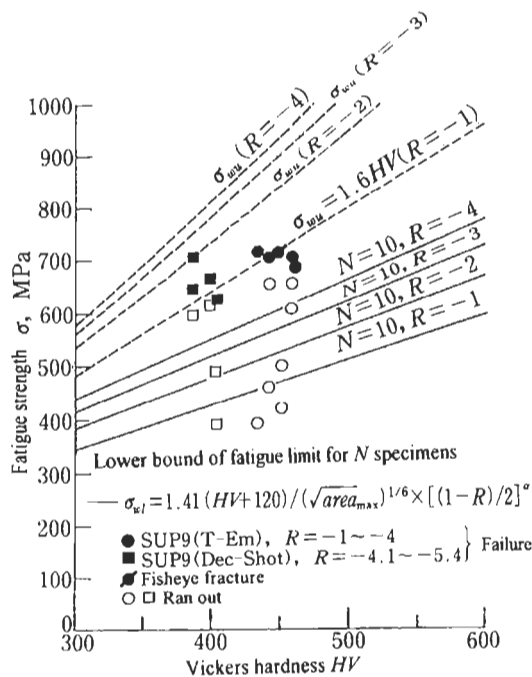


Figure 8.20 Comparison for specimens SUP9 (T-Em) and (Dec-Shot) between the estimated lower bound of fatigue strength and experimental results.

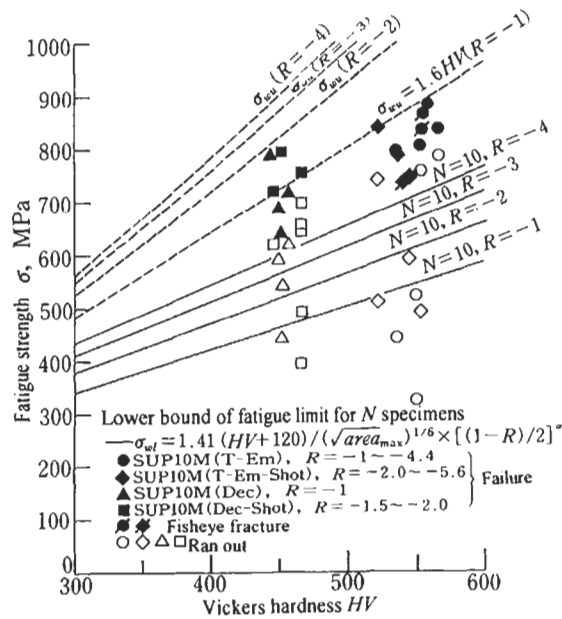


Figure 8.21 Comparison for specimens SUP10M (T-Em), (T-Em-Pit), (Dec-Shot), (T-Em-Shot) and (Dec) between the estimated lower bound of fatigue strength and experimental results.

All experimental points for fractured specimens are above the predicted lower bound of fatigue strength. This indicates that the prediction method in this study is useful. Although there is little difference in apparent fatigue strength between specimens SUP10M (Dec-Shot) and specimens SUP10M (T-Em-Shot), it should be noted that fracture of the former was due to stresses at the upper bound of the fatigue strength while that of the latter was due to stresses near the lower bound, and also that they differ in fatigue origin mechanism.

Actual springs are shot peened onto a decarburised layer. On this point, steel SUP10M is advantageous because its decarburised layer has a higher value of H_V than does that in steel SUP9. This is because a lower tempering temperature is used. Moreover, Figs. 8.20 and 8.21 indicate a remarkable increase in fatigue stress due to shot peening, by which the lower bound of fatigue strength was very much improved compared to the case of $R = -1$.

8.3 References

1. Y. Murakami, K. Kawakami and M. Saito: Effects of inclusions on fatigue strength of a suspension spring steel, *Trans. Jpn. Soc. Spring Res.*, **35** (1990), 1-7.
2. M.F. Garwood, H.H. Zurburg and M.A. Erickson: Correlation of Laboratory Tests and Service Performance, *Interpretation of Tests and Correlation with Service*, ASM, 1951, pp. 1-77.
3. S. Nishijima: Statistical analysis of fatigue test data, *J. Soc. Mater. Sci. Jpn.*, **29(316)** (1980), 24-29.
4. S. Aoyama: Strength of hardened and tempered steels for machine structural use (Part 1), *Review of*

- Toyota Rd Center, 5(2) (1968) 1–30, (Part 2), *ibid*, 5(4) (1968) 1–35.
5. K. Chisima and M. Ohara: Surface residual stress and fatigue life of shot-peened spring steel plate. *Jpn. Soc. Spring Res., Proc. Spring Annual Meeting 1974, 1975*, pp. 1–4.
 6. N. Miyagawa, M. Mukoyama and A. Ohno: Effect of liquid honing and shot peening on the rotating bending fatigue strength of piano wires. *Trans. Jpn. Soc. Spring Res.*, **20** (1975), 55–65.
 7. S. Hirose et al: Study on the shot peening small springs — relations between processing condition and improvement of fatigue strength. *Trans. Jpn. Soc. Spring Res.*, **27** (1982), 73–108.
 8. S. Aoyama: Effect of surface residual stress on fatigue strength of coil spring, Paper presented at the 169th Fatigue Committee Meeting, Soc. Materials, Sci. Jpn., 1983, pp. 1–8.
 9. H. Berns and L. Weber: Influence of residual stresses on crack growth, *Proc. 2nd Int. Conf. Impact Treatment Processes*, 22–26 Sept., Cranfield, 1986.
 10. S. Hisamatsu: Shot peening techniques and its application (2), *Sci. Mach.*, **38(12)** (1986), 1342–1346.
 11. Y. Yamada, J. Koarai, Y. Kawaguchi, O. Ishigami and N. Ibaraki: Influence of undeformable non-metallic inclusions on fatigue life. *Trans. Jpn. Soc. Spring Res.*, **31** (1986), 1–8.
 12. H. Toshino, K. Shigeno and N. Takagi: Effect of multistage shot peening on fatigue strength. *Trans. Jpn. Soc. Spring Res.*, **32** (1987), 31–34.
 13. T. Ozone and N. Hijikata: Effect of processes on rotating bending fatigue strength of Si–Cr valve spring wire. *Trans. Jpn. Soc. Spring Res.*, **33** (1988), 53–58.
 14. T. Ozone: Method of improving fatigue properties of spring by surface treatment, *Proc. Symposium on Durability of Spring*, *Jpn. Soc. Spring Res.*, 1989, pp. 9–16.
 15. A. Tange, T. Akutsu and N. Takamura: Relationship between residual stress by shot peening and fatigue growth life of spring steel. *Proc. 1990 Spring Annual Meeting*, *Jpn. Soc. Spring Res.*, 1990 pp. 1–6.
 16. R. Blom, M. Larsson, A. Melander and S. Preston: An experimental and theoretical study of the effect of shot peening on the fatigue properties of the spring steel SS 2090, *Rep. Swedish Inst. Metals Research, IM-2667*, 1990, pp. 1–52.
 17. M. Larsson, A. Melander, R. Blom and S. Preston: Effects of shot peening on bending fatigue strength of spring steel SS 2090, *Mater. Sci. Technol.*, **7** (1991), 998–1004.
 18. *Advanced Spring Technology*, Edited by *Jpn. Soc. Spring Res.*, *Jpn. Soc. Spring Industries*, 1988, pp. 85–99.
 19. M. Saito and Y. Ito: Some properties of ultra clean spring steel. *Trans. Jpn. Soc. Spring Res.*, **30** (1985), 11–19.
 20. S. Nishijima, E. Suzuki, Y. Niikura, K. Uchibori, M. Terashita and A. Morii: Interlaboratory tests on microscopic evaluation of non-metallic inclusions in steels for spring use. *Trans. Jpn. Soc. Spring Res.*, **32** (1987), 52–74.
 21. Y. Murakami, M. Kobayashi, T. Makino, T. Toriyama, Y. Kurihara, S. Takasaki and R. Ebara: Quantitative evaluation of the factors influencing fatigue strength of spring steels (effects of nonmetallic inclusions, shot peening, decarburized layer and small surface pits). *Trans. Jpn. Soc. Mech. Eng. A*, **57(542)** (1991), 2305–2313.
 22. W.E. Duckworth and E. Ineson: The effects of externally introduced alumina particles on the fatigue life of En24 steel. *Clean Steel, Iron Steel Inst. Sp.*, **77** (1963), 87–103.

Chapter 9

Tool Steels: Effect of Carbides

The effects of inclusions on the fatigue strength of a tool steel (SKH51) were described in Sections 6.4 and 6.5. In some cases, not only inclusions, but also carbides have a detrimental influence on the fatigue strength of tool steels [1–3]. It is not necessarily evident whether inclusions or carbides are the more detrimental. Which is detrimental is determined by the competition between the sizes of inclusions and carbides. Natsume et al. [4] conducted a very interesting experiment on the influence of carbides, which is introduced in the following.

Natsume et al. investigated the influence of cracking of carbides during low temperature plastic forming. They studied the original material SKD-11 after three different forming ratios, 0%, 30% and 50%. The study took, as a starting point, the questions arising from studies by Natsume et al. [5] and Murakami et al. [6], which were described in Sections 6.4 and 6.5. Natsume et al. thought that if carbides are mechanically equivalent to inclusions in terms of fatigue limit, then they should be mechanically equivalent to cracks, or small defects, regardless of whether or not carbides were cracked during plastic forming. Therefore, it follows that even if carbides are cracked during low temperature plastic forming, the fatigue limit will not change (will not decrease) at a constant matrix hardness level. Although this prediction is contrary to conventional ideas, Natsume et al. verified the correctness of their prediction by experiments.

9.1 Low Temperature Forging and Microstructure

Tool steels have advantages both in wear properties and in strength at high temperature. Hence they are used not only for tools, but also for rolls and for various machine components. Tool steels are usually forged at high temperature before machining. This is because high temperature forging can avoid cracking of carbides because of the high deformability of the matrix.

High temperature forging has the advantage of ease of forming a material that has high deformation strength. On the other hand, it has the disadvantage that is difficult to forge to precise dimensions and shape, so a large machining allowance is needed. If we turn to low temperature forging, then we can avoid this disadvantage, though there is still the problem of carbide cracking. However, we need not be afraid of

Table 9.1 Chemical composition of SKD-11 tool steel (wt.%)

C	Si	Mn	P	S	Cr	Mo	V
1.44	0.31	0.40	0.021	0.001	11.55	0.86	0.22

Table 9.2 Mechanical properties of annealed SKD-11 tool steel

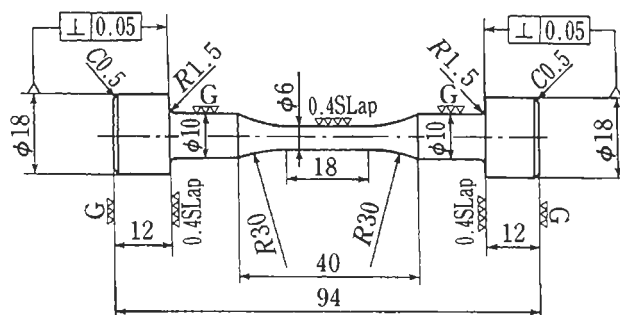
0.2% proof stress (MPa)	Tensile strength (MPa)	Elongation (%)	Reduction of area (%)
353	747	12.1	27.4

carbide cracking during low temperature forging, provided that the influence of cracked carbides on fatigue strength is the same as that of uncracked carbides, as was predicted previously.

The material used by Natsume et al. was a vacuum remelted alloy tool steel, SKD-11, which contains inclusions that are relatively smaller than carbides. Thus, the carbides have a higher possibility of becoming fatigue fracture origin than do the inclusions. Table 9.1 shows the chemical composition of SKD-11, and Table 9.2 its mechanical properties after annealing. Annealed material of 29 mm diameter was formed, by forward forging, to the sizes of 24 and 20.6 mm diameter, so the forging ratios were 30% and 50%, respectively.

Fig. 9.1 shows the specimen geometry. Finishing was by grinding after low temperature forging. After the heat treatment shown in Fig. 9.2, specimen surfaces were finished by lapping to a surface roughness of 0.6–1.4 μm . Fig. 9.3 shows that the microstructure after heat treatment is martensite and carbides.

Thus, the microstructure of the specimens, without low temperature forging, is composed of martensite and carbides. On the other hand, as shown in Fig. 9.4, specimens prepared using low temperature forward forging to 50% forging ratio contain carbides with cracks that are perpendicular to the forging direction. These cracks were produced in carbides larger than 5 μm . In particular, large carbides contain many cracks.

**Figure 9.1 Specimen geometry.**

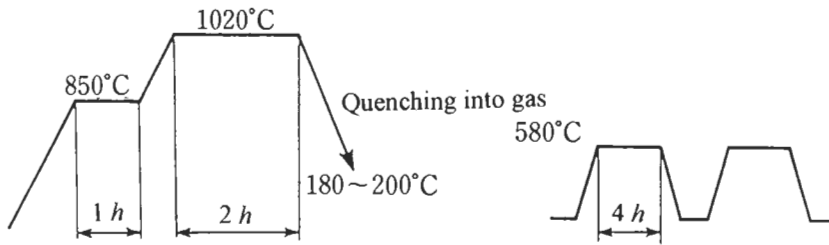


Figure 9.2 Heat treatment.



Figure 9.3 Microstructure of SKD-11 tool steel after heat treatment (Natsume et al. [4]).

9.2 Static Strength and Fatigue Strength

Before investigating the fatigue strength, mechanical properties were obtained. Table 9.3 shows that some mechanical properties, that is ultimate tensile strength, yield strength, and reduction in area, are not influenced by the forging ratio and heat treatment. However, the elongation does tend to decrease with increasing forging ratio.

Fig. 9.5 shows the results of tension compression fatigue tests based on the JSME small sample 14-SN method [7]. It can be seen that there is no significant difference in fatigue strength between the unforged specimens, and those with 50% forging ratio. The forged specimens have slightly larger scatter than do the unforged specimens. However,

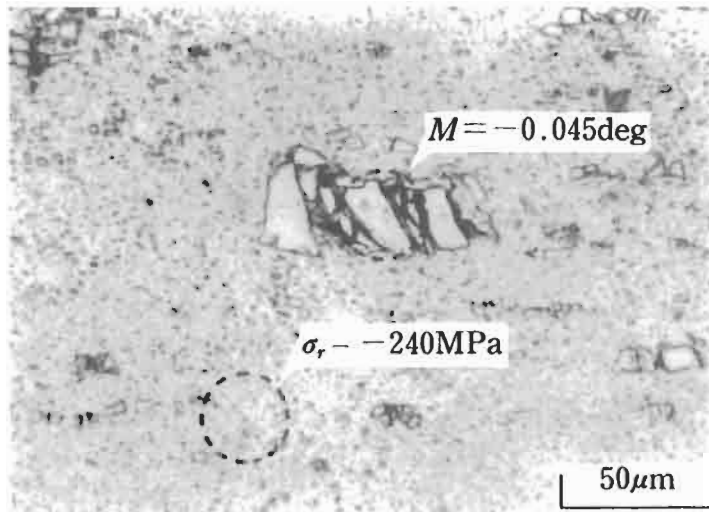


Figure 9.4 Cracking of carbides in SKD-11 tool steel by low temperature forging (Natsume et al. [4]).

Table 9.3 Mechanical properties of SKD-11 tool steel after quenching and tempering

Plastic forming	0.2% proof stress (MPa)	Tensile strength (MPa)	Elongation (%)	Reduction of area (%)	Vickers hardness HV (kgf/mm ²)
0%	1500	1630	2.5	<1.0	725
30%	1450	1690	1.9	<1.0	730
50%	1460	1670	1.0	<1.0	725

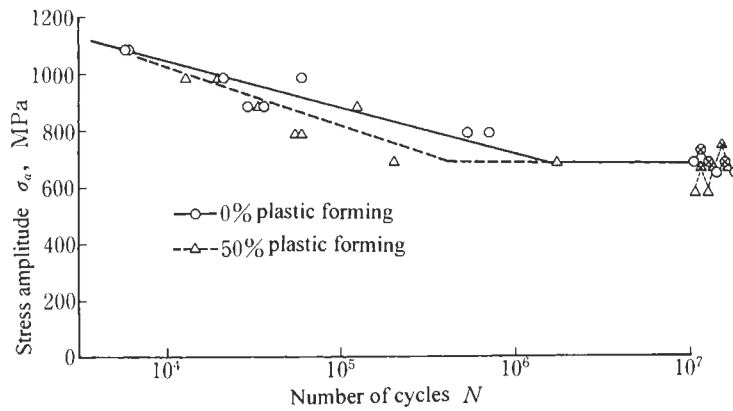


Figure 9.5 S-N curves for SKD-11 tool steel, tension compression fatigue tests.

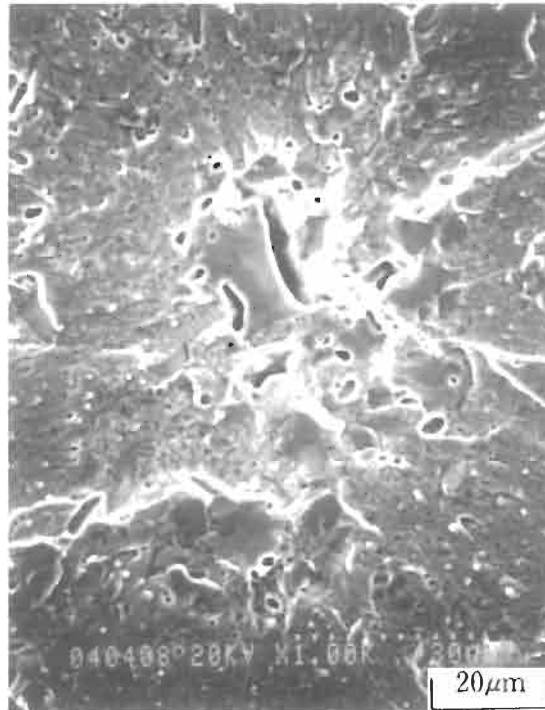


Figure 9.6 Fatigue fracture origin in unforged SKD-11 tool steel (Natsume et al. [4]).

the fatigue limit defined by 50% probability of failure is the same for both types of specimens.

Figs. 9.6 and 9.7 show fractographs of the unforged and 50% forged specimens fractured at the stress ± 800 MPa. The fracture surface of the unforged specimen shows the trace of a carbide cracked at a single section, and also subsequent fatigue crack growth. On the other hand, the fracture surface of the 50% forged specimen looks very rough and complex due to the carbide fragments produced by the low temperature forging.

From these experimental results, a carbide particle can be considered equivalent to a small defect, or small crack, regardless of its original condition, that is cracked or uncracked. This implies that the size of carbides strongly influences the fatigue strength of tool steels. According to discussions in the previous chapters, the maximum carbide size determines the fatigue strength, and accordingly fatigue strength shows much scatter from specimen to specimen, resulting in difficulty in predicting the fatigue strength of individual specimens. However, if we apply the method of Chapter 6, we can predict the lower bound of fatigue strength of specific numbers of specimens. Thus, we need to investigate the extreme value statistics of the size ($\sqrt{\text{area}}$) of carbides.

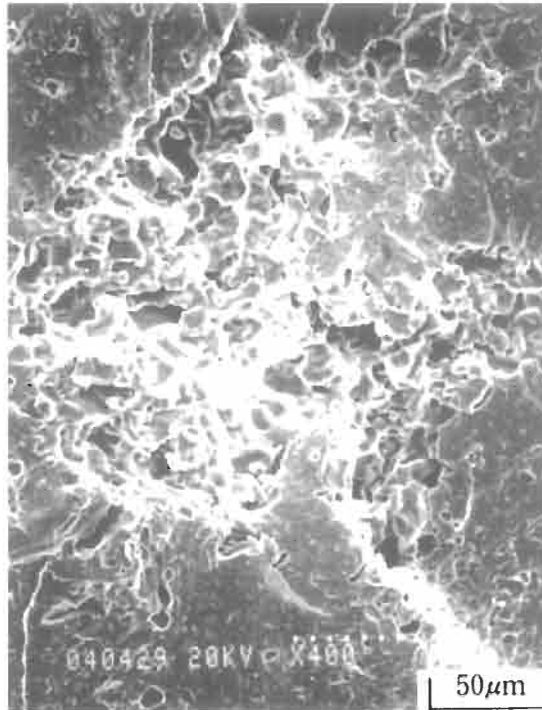


Figure 9.7 Fatigue fracture origin in 50% low temperature forged SKD-11 tool steel (Natsume et al. [4]).

9.3 Relationship Between Carbide Size and Fatigue Strength

Fig. 9.8 shows the extreme value statistics distribution of carbide size. The standard inspection area, $S_0 = 0.043 \text{ mm}^2$, and the numbers of measurements (samples), $n = 44$.

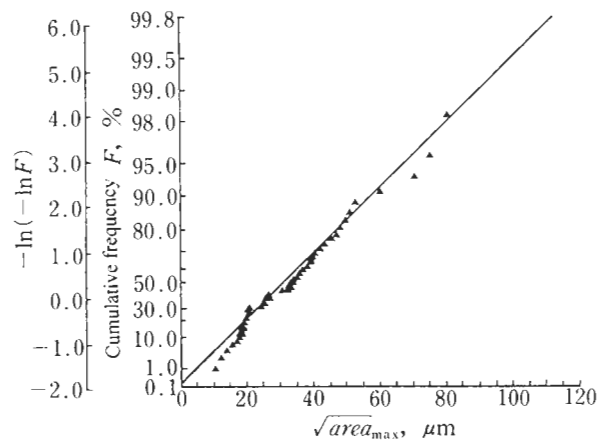


Figure 9.8 Cumulative frequency distribution of $\sqrt{\text{areamax}}$ of carbides.

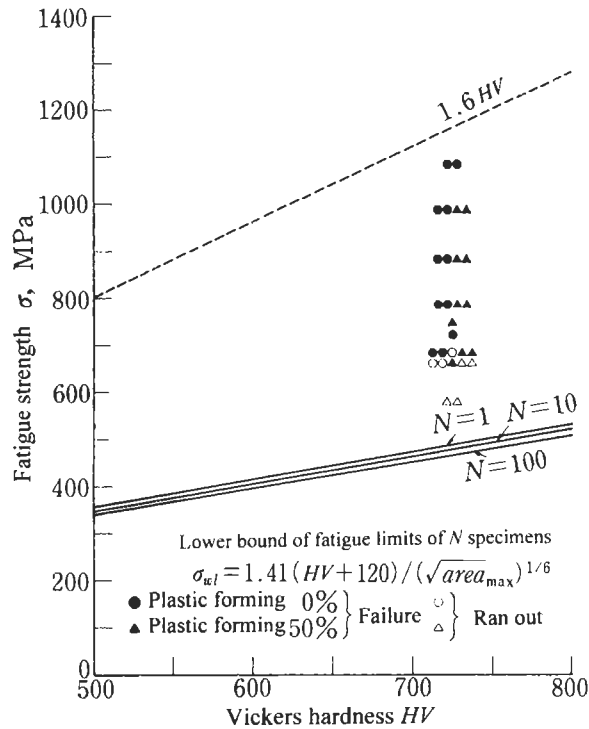


Figure 9.9 Scatter in fatigue strength of SKD-11 tool steel, and estimated upper and lower bounds of the fatigue limit.

If we regard the average value of 44 values of $\sqrt{area_{max}}$ as being the hypothetical thickness of the standard rectangular inspection zone (see pages 118, 119), then $h_0 = 34 \mu\text{m}$, the return period T for one specimen becomes $T = 3.39 \times 10^5$, and it follows that the expected maximum size, $\sqrt{area_{max}}$, to be contained in one specimen can be predicted as $\sqrt{area_{max}} = 205 \mu\text{m}$. Thus, the lower bound of fatigue strength, σ_{wl} , which is caused by the maximum carbide size, can be estimated using Eq. 6.5. Fig. 9.9 shows the comparison between the experimental data and the upper and lower bounds of fatigue strength. The reason why the predicted lower bounds look a little conservative

Table 9.4 Prediction of $\sqrt{area_{max}}$ of carbides and estimated lower bound fatigue limit

N	T	$\sqrt{area_{max}}$ (μm)	σ_{wl} (MPa) ($HV=725$)
1	3.39×10^5	205	491
10	3.39×10^6	237	479
100	3.39×10^7	269	469

may be that the carbide sizes shown in Fig. 9.8 were measured on the longitudinal section of specimens, and these are larger than those on the transverse section.

Table 9.4 shows the lower bound of the fatigue strength, σ_w , calculated from Eq. 6.5 using the maximum carbide size and $H_V = 725$, for $N = 1, 10$ and 100 specimens, which were produced by low temperature forging.

Considering the experimental and calculated results, we may conclude that high temperature forging is not necessary. Improvement of fatigue strength of tool steels can be attained by controlling the carbide size at an appropriate stage of the steel making process, and the direction to be taken in quality control procedures has been clarified.

9.4 References

1. H. Berns and W. Trojahn: Einflub der Warmbehandlung auf das Ermugungsverhalten Ledeburitischer Kaltarbeitsstahle, VDI-Z, **127(22)** (1985), 889–892.
2. H. Berns, J. Lueg, W. Trojahn, R. Wahling and H. Wisell: The fatigue behaviour of conventional and powder metallurgical high speed steels, Powder Metall. Int., **19(4)** (1987), 22–26.
3. H. Berns: Interaction of Microstructure and Fatigue in Tool Steels, Proc. Fatigue '87, Charlottesville, VA, USA, EMAS Ltd., Vol. I, 1987, pp. 527–536.
4. Y. Natsume, T. Muramatsu and T. Miyamoto: Effect of Carbide Crack on Fatigue Strength of Alloy-tool Steel Under Cold Working, Proc. JSME Meeting, No. 900(86) (1990) pp. 323–325 and private communication, 1989.
5. Y. Natsume, S. Miyakawa and T. Muramatsu: Effect of mean stress on the tensile and compressive fatigue strength of high-speed steel, J. Soc. Mater. Sci. Jpn., **37(417)** (1988), 606–611.
6. Y. Murakami, Y. Uemura, Y. Natsume and S. Miyakawa: Effect of mean stress on the fatigue strength of high-strength steels containing small defects or nonmetallic inclusions, Trans. Jpn. Soc. Mech. Eng. A, **56(525)** (1990), 1074–1081.
7. Statistical Fatigue Test Methods, Edited by Jpn. Soc. Mechanical Engineers, S 002, 1981.

Chapter 10

Effects of Shape and Size of Artificially Introduced Alumina Particles on 1.5Ni–Cr–Mo (En24) Steel

From the discussions in previous chapters, we can understand that the shape of defects and inclusions, that is spherical or angular, does not have a crucial influence on the fatigue limit. Comparisons between a hole and a crack (Section 5.5), or cracked and uncracked carbides, are good examples for the understanding of this problem.

As long ago as 1963, Duckworth and Ineson studied the effects of the geometry and size of alumina particles on the fatigue strength of En24 steel [1]. They artificially introduced alumina particles into steels produced in a laboratory furnace, and conducted fatigue tests on specimens prepared from the steels. In their study, all fatigue tests, rotating bending tests and tension compression tests, were conducted at the same nominal stress amplitude. However, the results showed very large scatter in fatigue lives depending on the size and location of the inclusions from which fatigue failure initiated. That is, it was found that individual specimens behaved in different ways under the same stress amplitude. Thus, the existence of non-metallic inclusions causes different fatigue behaviours in individual specimens, and increases the difficulty of quantitative evaluation of fatigue strength.

In this chapter, the study by Duckworth and Ineson [1] is introduced. They tried to clarify directly the effect of inclusion shape, and their large amount of data is reanalysed by the method explained in previous chapters [2]. The reanalysis of their data gives us a unified understanding of their data scatter and clarifies the factors influencing the effects of inclusions. Although Araki and colleagues [3] conducted similar experiments to those of Duckworth and Ineson, the influence of artificially added alumina particles did not appear clearly, probably because of the low hardness of the material they used.

10.1 Artificially Introduced Alumina Particles with Controlled Sizes and Shapes, Specimens, and Test Stress

As the fatigue behaviour of 1.5Ni–Cr–Mo steels is well known En24 steel was adopted as the test material. In some ingots, alumina particles (0.020–0.250 mm size) were added, and for comparison, an ingot with no added alumina particles was also produced.

Table 10.1 Cast numbers and chemical composition

Cast No	Mean size of particles added (μm)	Analysis (wt. %)							
		C	Si	Mn	S	P	Ni	Cr	Mo
Commercial En24 cast JK	None	0.40	0.30	0.56	0.012	0.015	1.46	1.06	0.21
Laboratory En24 cast 1	None	0.42	0.26	0.65	0.022	0.035	1.46	1.16	0.32
Laboratory En24 casts with angular alumina particles added									
55	73	0.45	0.38	0.69	0.022	0.024	1.55	1.28	0.34
56	65	0.45	0.46	0.68	0.022	0.024	1.59	1.42	0.31
61	65	0.47	0.23	0.69	0.021	0.023	1.51	1.30	0.30
63	40	0.47	0.33	0.70	0.022	0.023	1.54	1.11	0.36
78	30	0.41	0.16	0.54	0.011	0.014	1.66	1.02	0.33
76	20	0.44	0.23	0.69	0.017	0.012	1.60	1.06	0.33
77	10	0.46	0.24	0.68	0.011	0.017	1.56	1.02	0.33
84	73	0.43	0.26	0.66	0.014	0.011	1.66	1.19	0.37
119	63	0.41	0.47	0.66	0.013	0.019	1.56	1.13	0.32
118	45	0.43	0.43	0.67	0.011	0.016	1.56	1.16	0.34
117	28	0.43	0.42	0.67	0.015	0.017	1.51	1.17	0.31
116	19	0.41	0.37	0.67	0.017	0.015	1.61	1.20	0.36
115	9	0.39	0.29	0.69	0.011	0.014	1.56	1.23	0.35
Laboratory En24 casts with spherical alumina particles added									
S11	73	0.37	0.31	0.57	0.021	0.033	1.63	1.28	0.30
S2	63	0.39	0.23	0.56	0.012	0.019	1.76	1.27	0.32
S4	45	0.36	0.25	0.54	0.012	0.016	1.74	1.31	0.30
S7	34	0.42	0.35	0.61	0.013	0.015	1.64	1.27	0.33
S6	20	0.35	0.21	0.49	0.012	0.016	1.62	1.25	0.30
S8	10	0.35	0.26	0.53	0.017	0.015	1.53	1.25	0.33

Table 10.1 shows the cast number, the nominal size of the added alumina particles, and the results of chemical analysis of the ingots. Particles of two shapes were added, angular and spherical. Angular particles were added to casts numbers 55, 56, 61, 63, 76–78, 84 and 115–119, and spherical particles to casts numbers S2, S4, S6–S8 and S11. All ingots were forged and rolled to a 19.05-mm diameter bar. All test piece blanks were annealed before machining by heating at 650°C for 4 h. They were then rough machined to 0.76 mm oversize in all dimensions. Subsequent heat treatment was heating at 850°C for 1 h, followed by oil quenching and tempering at 200°C for 8 h. The hardness of each specimen was checked on a Vickers hardness testing machine, and specimens then finally ground to the appropriate final dimensions shown in Fig. 10.1. Therefore, the measured value of hardness may be a little higher ($\approx 10\%$) than that in the final state of the specimens [4].

The purpose of the tests carried out by Duckworth and Ineson was to investigate the effects of the artificially introduced alumina particles on the initiation of fatigue. Therefore, all tests were conducted at a constant stress level, above the fatigue limit, at which the majority of the test pieces would be expected to fail. Thus, a nominal stress of 710 MPa was used. Most of the fatigue tests were performed in two-point loading using Wöhler-type rotating bending fatigue testing machines. Tension compression fatigue tests were carried out at zero mean stress ($R = -1$) in a Losenhausen universal fatigue testing machine, model UHW6, having a maximum capacity of 29.9 kN.

After fatigue testing, all the fractured specimens were examined, using an optical

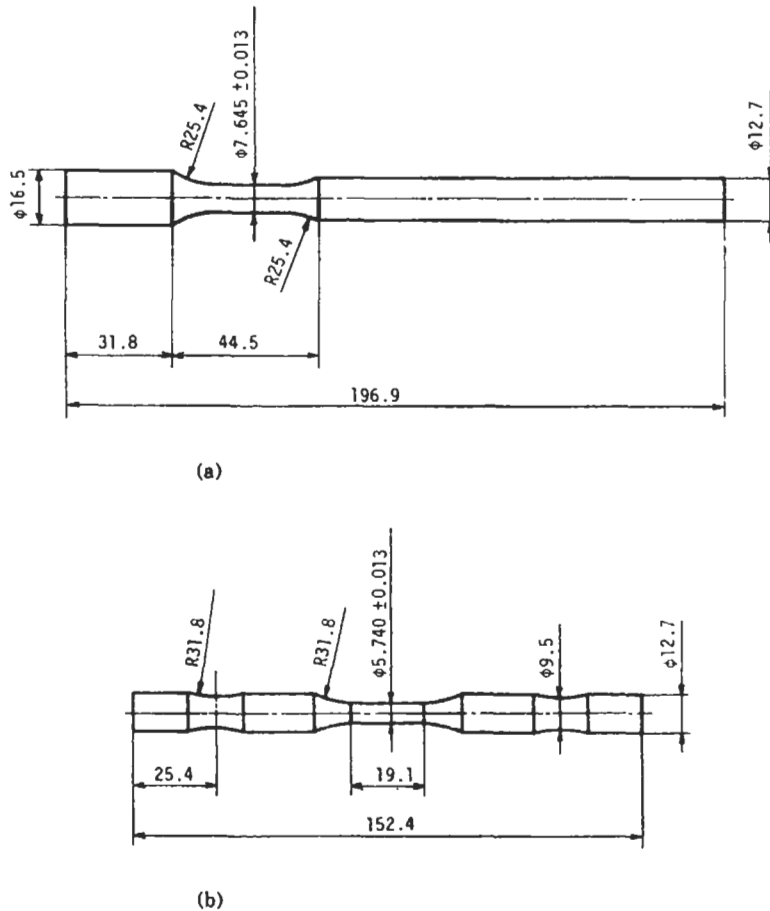


Figure 10.1 Specimen geometry. (a) Rotating bending beam specimen. (b) Tension compression specimen. Dimensions in millimetres.

microscope, at magnifications of $\times 35$ and $\times 100$. In every case, the fracture appearance of the test specimens containing added alumina particles was different from that observed on the specimens without artificial inclusions. In the former, a circular area of lighter colour than the remainder of the fracture surface, the so-called fish eye, was usually observed, and in the centre of this fish eye, an inclusion very often remained in one half of a specimen. In some cases, the inclusion had fractured, leaving part in each half, and in the few remaining situations, the inclusion had completely shattered, leaving a hole in both fracture surfaces.

10.2 Rotating Bending Fatigue Tests without Shot Peening

Table 10.2 shows the fatigue test results.

Table 10.2 Rotating bending fatigue test results, angular particles in specimens not shot peened

Specimen No	Cycles to failure, N_f	Inclusion size, $\sqrt{\text{area}}$ (μm)	Distance from surface, h (μm)	Nominal stress at inclusion, σ' (MPa)	Fatigue limit predicted by equations (6.1), (6.2), (6.3), α_w (MPa)	σ'/α_w
Cast No 55, Hv = 606						
A1	1.05×10^6	77.9	290	656	548 (6.3)	1.20
A3	1.57×10^7	88.8	327	649	536 (6.3)	1.21
A5	4.80×10^4	31.4	0	710	584 (6.1)	1.22
A6	6.56×10^4	30.1	15	707	580 (6.2)	1.22
A9	1.01×10^6	55.5	103	691	580 (6.3)	1.19
A12	2.83×10^6	65.2	122	687	565 (6.3)	1.22
Cast No 56, Hv = 614						
A1	4.33×10^6	47.6	118	688	601 (6.3)	1.14
A4	1.41×10^5	35.9	40	703	630 (6.3)	1.11
A6	7.11×10^4	62.0	0	710	528 (6.1)	1.35
A7	1.96×10^5	51.0	30	704	537 (6.2)	1.31
A9	7.02×10^4	51.7	41	702	593 (6.3)	1.18
A10	8.16×10^4	66.8	71	697	568 (6.3)	1.23
A12	3.58×10^4	53.2	32	704	534 (6.2)	1.32
A13	1.95×10^5	77.7	45	702	501 (6.2)	1.40
A14	9.76×10^4	56.2	50	701	585 (6.3)	1.20
A15	6.47×10^6	51.4	219	669	594 (6.3)	1.13
Cast No 61, Hv = 610						
A9	5.97×10^5	20.4	just breaks free surface	710	623 (6.2)	1.14
A10	1.56×10^5	38.9	just breaks free surface	710	559 (6.2)	1.27
A12	7.84×10^6	38.8	134	685	619 (6.3)	1.11
A13	8.50×10^6	39.6	48	701	617 (6.3)	1.14
A14	3.31×10^5	64.2	59	699	569 (6.3)	1.23
Cast No 63, Hv = 610						
A3	3.11×10^4	15.7	0	710	660 (6.1)	1.08
A4	1.29×10^5	14.7	0	710	667 (6.1)	1.06
A5	2.21×10^6	29.5	20	706	586 (6.2)	1.21
A6	4.57×10^7	30.2	58	699	645 (6.3)	1.08
A7	8.96×10^4	24.1	0	710	614 (6.1)	1.16
A8	4.52×10^7	26.6	58	699	659 (6.3)	1.06
A12	2.81×10^5	28.0	just breaks free surface	710	591 (6.2)	1.20
A15	6.20×10^4	14.6	0	710	668 (6.1)	1.06
A17	5.57×10^4	19.7	0	710	635 (6.1)	1.12
Cast No 78, Hv = 602						
A3	1.64×10^7	17.2	0	710	643 (6.1)	1.10
A5	4.68×10^4	19.7	13	708	619 (6.2)	1.14
A6	4.02×10^5	33.2	58	699	628 (6.3)	1.11
A7	7.21×10^4	19.8	0	710	628 (6.1)	1.13
A9	3.43×10^6	15.6	0	710	653 (6.1)	1.09
A12	4.07×10^4	15.3	0	710	655 (6.1)	1.08
A14	4.39×10^7	29.1	151	682	642 (6.3)	1.06
A15	5.34×10^6	8.86	0	710	718 (6.1)	0.99
A17	2.13×10^7	35.8	115	689	620 (6.3)	1.11
Cast No 76, Hv = 606						
A3	8.34×10^5	25.1	22	706	662 (6.3)	1.07
A7	6.71×10^6	11.5	10	708	754 (6.3)	0.94
A8	1.07×10^4	21.7	0	710	622 (6.1)	1.14
A10	1.42×10^6	15.3	breaks surface	710	650 (6.2)	1.09
Cast No 77, Hv = 610						
A3	7.86×10^6	14.3	break free surface	710	661 (6.2)	1.07
A7	1.57×10^5	12.5	break free surface	710	676 (6.2)	1.05
A8	8.91×10^7	11.5	20	706	758 (6.3)	0.93
A9	7.38×10^6	11.5	15	707	758 (6.3)	0.93

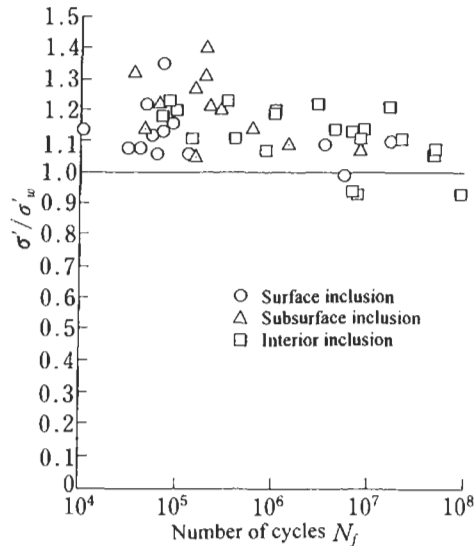


Figure 10.2 Comparison between failure stress and predicted fatigue strength for rotating bending specimens that were not shot peened.

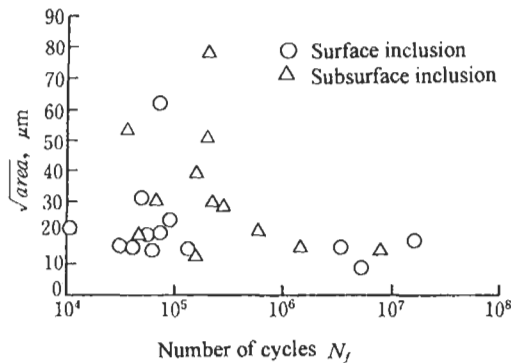


Figure 10.3 Relationship between $\sqrt{\text{area}}$ of inclusions and number of cycles to failure.

Fig. 10.2 shows a comparison between the ratio of the applied stress, σ' , at an inclusion to the calculated fatigue limit, σ'_w , with the number of cycles to failure, N_f . In this figure, the symbols \circ , Δ and \square indicate the location of inclusions. There are no data points located below $\sigma'/\sigma'_w = 0.9$, showing the high accuracy of the evaluation method.

Fig. 10.3 shows the relationship between $\sqrt{\text{area}}$ and the number of cycles to failure for specimens fractured from a surface or a subsurface inclusion. The data trend suggests that the larger the value of $\sqrt{\text{area}}$, the shorter the fatigue life. This figure indirectly verifies the utility of the geometrical parameter, $\sqrt{\text{area}}$. In this figure, the fracture data from internal inclusions were not plotted because the fatigue crack propagation from

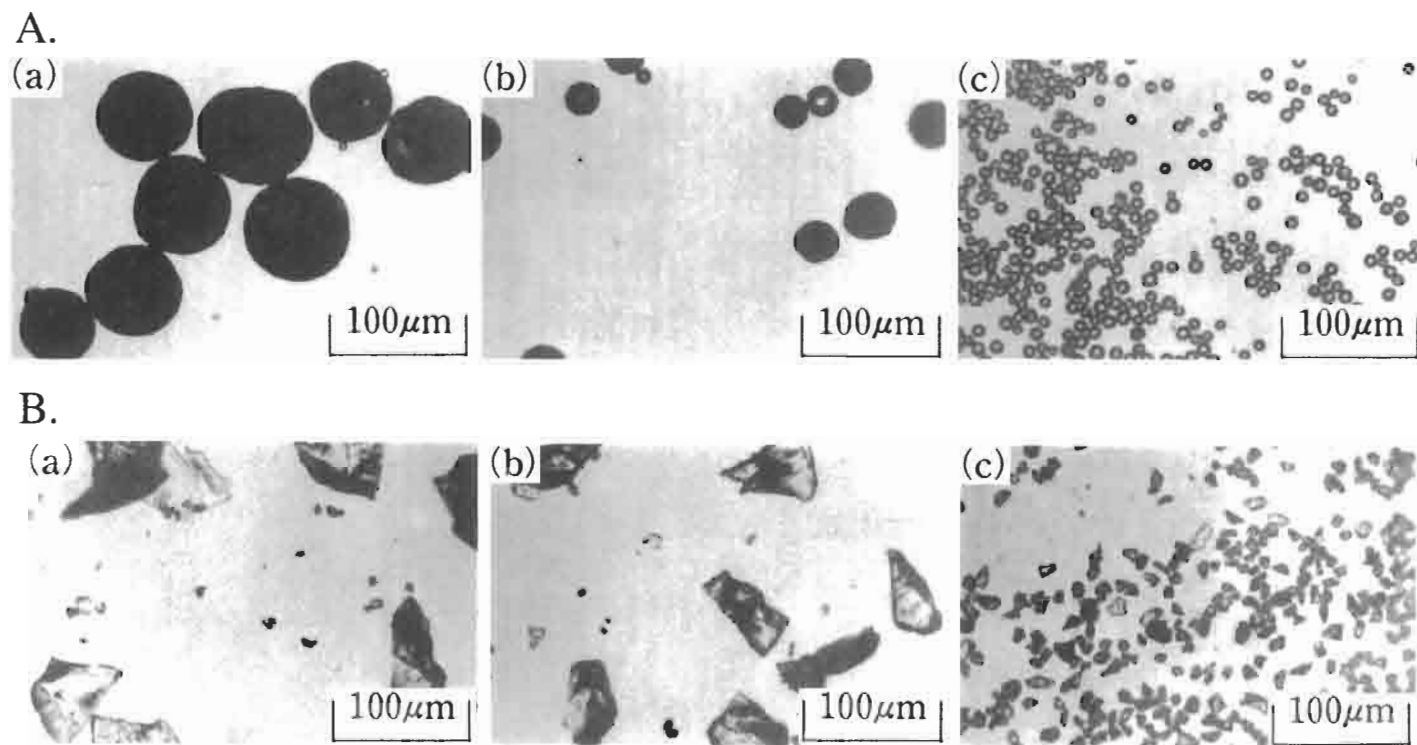


Figure 10.4 Typical alumina particles, as added to ingots. (A) Typical spherical alumina particles. (a) 73 μm nominal size. (b) 40 μm nominal size. (c) 10 μm nominal size. (B) Typical angular alumina particles. (a) 73 μm nominal size. (b) 40 μm nominal size. (c) 10 μm nominal size (Duckworth and Ineson [1]).

an internal inclusion would cause a variation in the $\sqrt{\text{area}}-N_f$ relationship due to the difference in the location of the inclusions.

10.3 Rotating Bending Fatigue Tests on Shot-Peened Specimens

The purpose of these experiments was to examine the effects of the shape of inclusions on fatigue strength. Fig. 10.4 shows typical spherical and angular alumina particles, as added to the ingots. The nominal size does not necessarily indicate the true size of each inclusion, because of variation in the sizes of inclusions of the same nominal size.

After examining Fig. 10.4, a typical common answer to the question "Which is more detrimental, a spherical inclusion or an angular inclusion?" would be "An angular inclusion." However, reality does not correspond to this answer.

Since the sizes of the inclusions found on the fracture surface have large scatter, all the results are classified separately in terms of $\sqrt{\text{area}}$ for spherical and angular inclusions at fracture origins. Fig. 10.5 shows histograms of $\sqrt{\text{area}}$ at the fracture surface for (a) spherical alumina and (b) angular alumina. Although the values of $\sqrt{\text{area}}$ do show a larger scatter, there is no significant difference in the distribution of $\sqrt{\text{area}}$ for spherical and angular inclusions.

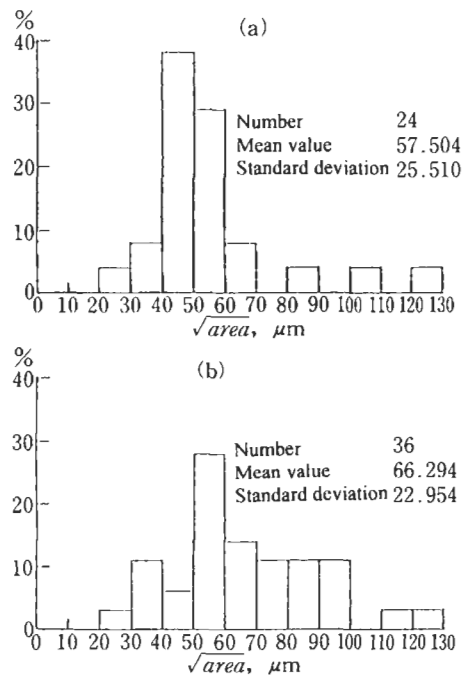


Figure 10.5 Histograms of $\sqrt{\text{area}}$ inclusions at fracture origins. (a) Spherical alumina particles. (b) Angular alumina particles.

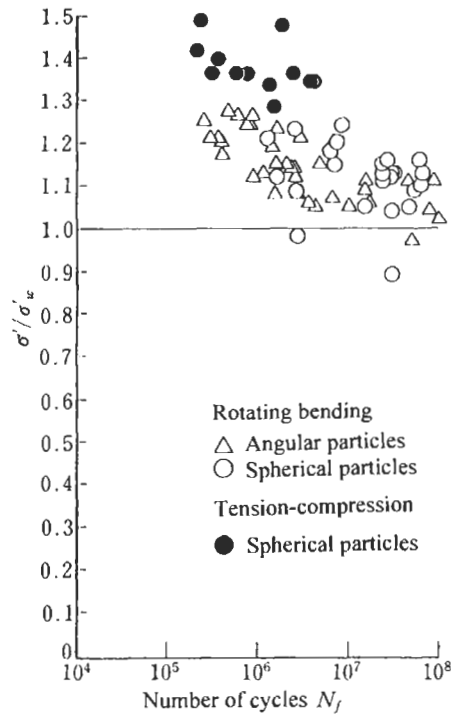


Figure 10.6 Comparison between failure stress and predicted fatigue strength for shot-peened rotating bending specimens and for shot-peened tension compression specimens.

Fig. 10.6 shows the relationship between σ'/σ'_w and N_f in rotating bending fatigue for angular and spherical particles. All data points have values of $\sigma'/\sigma'_w \geq 0.89$. The maximum evaluation error is approximately 10%, which may be caused by a higher estimate for H_V than the actual value, as described above. Thus, the evaluation accuracy is sufficient for practical purposes, regardless of inclusion shape.

If we look at the histograms of Fig. 10.5a and b from the viewpoint of, there is very little difference. This is the reason why the shape of inclusion is not significant at lower stress levels in Fig. 10.6, rather it is \sqrt{area} that is the crucial geometrical factor. Many researchers may find this conclusion difficult to accept if we concentrate our attention on 'stress concentration factors' of small defects and inclusions. If we try to solve a problem of this kind by stress concentration factors, we shall not be able to reach a complete solution. Although the angular shape of TiN inclusions has been thought to be the cause of their detrimental effect, we can understand from the experiments by Duckworth and Ineson that this widely accepted viewpoint is not correct with respect to fatigue limits. However, at higher stress levels the specimens fractured from angular alumina particles do tend to show slightly shorter fatigue lives compared with those fractured from spherical alumina particles, as shown in Fig. 10.6. The most likely reason is that cracks nucleate earlier from angular inclusions than from spherical

Table 10.3 Rotating bending fatigue test results, angular particles in shot-peened specimens

Cycles to failure, N_f	Inclusion size, $\sqrt{\text{area}}$ (μm)	Distance from surface, h (μm)	Nominal stress at inclusion, σ' (MPa)	Fatigue limit predicted by equations (6.1), (6.2) and (6.3), α'_w (MPa)	σ'/α'_w
Cast No 84, Hv = 581					
1.16×10^6	52.0	374	641	566 (6.3)	1.13
1.57×10^6	68.0	686	583	541 (6.3)	1.08
6.97×10^6	56.0	453	626	559 (6.3)	1.20
6.02×10^5	93.0	327	649	514 (6.3)	1.26
1.45×10^6	79.4	449	627	527 (6.3)	1.19
7.67×10^5	74.2	257	662	533 (6.3)	1.24
8.96×10^5	90.8	318	651	516 (6.3)	1.26
2.55×10^6	93.4	375	640	513 (6.3)	1.25
4.12×10^5	69.1	418	632	540 (6.3)	1.17
4.01×10^5	97.0	521	613	510 (6.3)	1.20
3.04×10^5	87.9	445	627	519 (6.3)	1.21
Cast No 119, Hv = 579					
4.92×10^6	52.7	325	650	563 (6.3)	1.15
1.63×10^6	63.8	437	629	546 (6.3)	1.15
1.66×10^6	81.3	361	643	524 (6.3)	1.23
8.31×10^5	83.8	335	648	521 (6.3)	1.24
3.66×10^5	85.6	427	631	519 (6.3)	1.21
2.13×10^6	55.4	364	642	558 (6.3)	1.15
2.98×10^6	63.3	276	659	546 (6.3)	1.21
Cast No 118, Hv = 581					
2.80×10^6	56.7	582	602	558 (6.3)	1.08
6.84×10^6	53.9	575	603	563 (6.3)	1.07
2.43×10^6	63.9	473	622	547 (6.3)	1.14
1.05×10^7	44.2	522	613	582 (6.3)	1.05
3.68×10^6	73.1	766	568	535 (6.3)	1.06
1.56×10^7	57.1	557	607	557 (6.3)	1.09
2.62×10^6	56.7	464	624	558 (6.3)	1.12
Cast No 117, Hv = 581					
8.28×10^7	33.2	402	635	610 (6.3)	1.04
4.68×10^7	51.7	424	631	567 (6.3)	1.11
2.57×10^6	54.5	382	639	562 (6.3)	1.14
1.05×10^8	26.9	367	642	632 (6.3)	1.02
4.43×10^6	72.1	803	561	536 (6.3)	1.05
1.75×10^7	46.6	521	613	576 (6.3)	1.06
Cast No 116, Hv = 574					
9.08×10^7	36.2	277	659	595 (6.3)	1.11
4.78×10^5	125.9	510	615	484 (6.3)	1.27
1.61×10^7	37.6	287	657	591 (6.3)	1.11
9.04×10^5	116.0	860	550	490 (6.3)	1.12
5.24×10^7	33.6	668	586	603 (6.3)	0.97

inclusions, resulting in shorter fatigue lives at higher stress levels, although the fatigue limit is determined by the condition for non-propagation of a crack emanating from an inclusion.

Generally speaking, the compressive stress on the specimen surface produced by shot peening makes the effective distance, h , of the fatal inclusion from the surface deeper, as seen by comparing Tables 10.3 and 10.4 with Table 10.2. In shot-peened specimens, high compressive residual stresses exist on the surface, and tensile residual stresses exist in the interior. Therefore fractures, on the whole, initiate from internal inclusions or defects. The reason why some values of σ'/α'_w in Fig. 10.6 are a little lower than 1.0

Table 10.4 Rotating bending fatigue test results, spherical particles in shot-peened specimens

Cycles to failure, N_f	Inclusion size, $\sqrt{\text{area}}$ (μm)	Distance from surface, h (μm)	Nominal stress at inclusion, σ' (MPa)	Fatigue limit predicted by equations (6.1), (6.2) and (6.3), (MPa)	σ'/σ'_w
Cast No S11, Hv = 556					
1.27×10^6	59.5	341	647	534 (6.3)	1.21
2.64×10^6	137.4	1100	506	464 (6.3)	1.09
7.88×10^6	76.7	515	614	512 (6.3)	1.20
1.60×10^6	93.1	830	556	495 (6.3)	1.12
Cast No S2, Hv = 560					
6.77×10^7	47.8	420	632	557 (6.3)	1.13
6.21×10^7	57.6	460	625	540 (6.3)	1.16
2.85×10^7	49.2	470	623	554 (6.3)	1.12
Cast No S4, Hv = 554					
3.07×10^7	40.8	390	638	567 (6.3)	1.13
2.69×10^6	112.6	1300	469	478 (6.3)	0.98
2.34×10^7	46.1	375	640	555 (6.3)	1.15
7.11×10^6	53.2	470	623	542 (6.3)	1.15
3.34×10^7	46.1	450	626	555 (6.3)	1.13
6.39×10^6	51.4	357	644	545 (6.3)	1.18
1.54×10^7	44.3	675	585	559 (6.3)	1.05
Cast No S7, Hv = 566					
3.06×10^7	55.8	1200	487	547 (6.3)	0.89
3.07×10^7	34.1	500	617	594 (6.3)	1.04
6.58×10^7	33.8	310	652	595 (6.3)	1.10
2.34×10^7	41.7	320	651	575 (6.3)	1.13
Cast No S8, Hv = 550					
5.55×10^7	54.9	680	584	536 (6.3)	1.09
2.37×10^7	58.5	655	588	630 (6.3)	1.11
2.53×10^6	72.5	440	628	512 (6.3)	1.23
8.61×10^6	40.3	56	700	564 (6.3)	1.24
2.73×10^7	46.1	390	638	552 (6.3)	1.16
4.87×10^7	26.6	415	633	605 (6.3)	1.05

may be the result of tensile residual stress in the interior, in addition to an overestimate of the hardness, H_V , at a fracture origin.

The method of evaluating the effects of residual stress on the fatigue strength was explained in Chapter 8. The method is not used in the present chapter because residual stress values are not included in the data of Duckworth and Ineson. If we assume the residual stress at the fracture origin to be $\sigma_r = +200$ MPa, then the fatigue strength, σ'_w , predicted using Eqs. 6.3 and 6.4 is a 7% overestimate, and the ratio of σ'/σ'_w is underestimated by 7%. Thus, if we did consider the effect of residual stresses, then the evaluation error of σ'/σ'_w would be expected to decrease.

10.4 Tension Compression Fatigue Tests

In Fig. 10.6, the values σ'/σ'_w for tension compression fatigue (symbol ●) are evidently larger than those for rotating bending fatigue (symbols Δ and ○). We can easily understand the reason for this if we take into consideration the fact that all the fatigue tests were conducted at the same nominal stress. In tension compression,

a greater volume of a specimen is subjected to high stress than in rotating bending fatigue, with its concomitant stress gradient. Accordingly, the value of \sqrt{area}_{\max} of the maximum inclusion in tension compression is larger than that in rotating bending, reducing the fatigue limit, σ'_w , for tension compression, or increasing the ratio σ'/σ'_w . Prediction of \sqrt{area}_{\max} for inclusions contained in a particular number of specimens can be made by the method based on extreme value statistics, as explained in previous chapters.

According to extreme value statistics, the expected value of \sqrt{area}_{\max} increases with increasing test volume, or number of specimens. For example, the mean values of \sqrt{area}_{\max} of inclusions at the fracture origin are 34.6 μm for non-shot-peened specimens in rotating bending (Fig. 10.2), 62.6 μm for shot-peened specimens in rotating bending (Fig. 10.6), and 76.8 μm for tension compression (Fig. 10.6).

10.5 References

1. W.E. Duckworth and E. Ineson: The effects of externally introduced alumina particles on the fatigue life of En24 steel, Clean Steel, Iron Steel Inst., Sp. Rep., 77 (1963) 87–103.
2. Y. Murakami, K. Kawakami and W.E. Duckworth: Quantitative evaluation of effects of size and shape of artificially introduced alumina inclusions on the fatigue strength of Ni–Cr–Mo steel, Tetsu to Hagane, 77(1) (1991) 163–170. Y. Murakami, K. Kawakami and W.E. Duckworth: Quantitative Evaluation of Effects of Shape and Size of Artificially Introduced Alumina Particles on the Fatigue Strength of 1.5Ni–Cr–Mo (En24) Steel, Int. J. Fatigue, 13(6) (1991) 489–499.
3. M. Sumita, I. Uchiyama and T. Araki: A model experiment on relationship between fatigue properties of steel and size, shape, and distribution of inclusions, Tetsu to Hagane, 57(2) (1971), 335–354.
4. Y. Murakami and H. Usuki: Prediction of fatigue strength of high-strength steels based on statistical evaluation of inclusion size, Trans. Jpn. Soc. Mech. Eng. A, 55(510) (1989), 213–221.

Chapter 11

Nodular Cast Iron

11.1 Introduction

There have been many studies [1–19] on the effects of the shape and size of graphite nodules, and of microstructure, on the fatigue strength of nodular cast iron. In particular, Sofue [7,8] carried out detailed and systematic experiments, and proposed a simple prediction equation for the fatigue limit. This was based on the average nodule diameter, D_g , and the non-propagating crack length, l_{crm} . He applied the equation to other nodular cast irons having different microstructures and graphite nodule sizes. The value of l_{crm} was expressed graphically as a function of the Vickers hardness, H_V , of the microstructure. Microstructures having higher values of H_V are expected to have smaller values of l_{crm} . Therefore, fatigue strength is given as a function of H_V and D_g . This method of prediction is similar to the \sqrt{area} parameter model, explained in Chapters 4–6, which predicts fatigue limit using the two parameters, \sqrt{area} and H_V . However, the value of D_g adopted by Sofue as the representative defect size is the average diameter of nodules, and not their maximum size. Taking into consideration the effects of small defects and nonmetallic inclusions, as described in previous chapters, the fatigue strength of nodular cast irons is thought to be determined by the maximum size of nodules. Thus, it follows that the agreement between Sofue's equation and the experimental results may be attributed to a good correlation between D_g and the maximum size of nodules. In other words, if a nodular cast iron having a nodule size distribution different from those of Sofue (Fig. 11.1) were tested, then the prediction by Sofue's equation may not be good. According to Fig. 11.1, which shows the nodule size distributions of the materials used by Sofue, the maximum size is more than twice D_g . The distributions shown in Fig. 11.1 may change greatly if casting conditions are changed. Furthermore, if the number of specimens is increased, then the maximum size of nodules increases, without changing the value of D_g , and accordingly the lower bound of fatigue strength may have a much lower value than predicted by Sofue's method.

Niimi et al. [2] studied the fatigue strength of nodular cast iron, focusing on the size of graphite nodules. According to their results, metal die cast material has the smallest nodule size and the highest fatigue strength. The microstructures which give high fatigue strength are orderly pearlite, 'bull's eye' and ferrite. The results are qualitatively

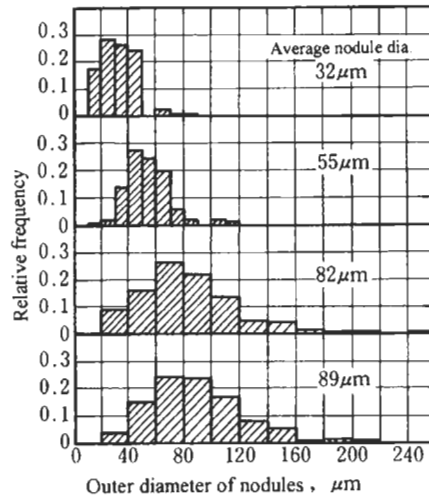


Figure 11.1 Histograms of graphite nodule size distributions and their average size (Sofue [7]).

consistent with the conclusions reached in Chapters 4–6. However, Niimi also adopted the average size of nodules as the representative graphite nodule size.

Previously, the strength of a graphite nodule itself has been thought to be negligibly weak, as compared to that of the microstructure, and therefore mechanically equivalent to a stress free hole or notch [3,14]. However, Yano [15,16] recently reported an elastic effect by which nodules partially support the applied loading. According to Yano, the microstructure compresses nodules, increasing their density, resulting in a 20–24% increase in fatigue strength. Ogawa et al. [17] reported the effect of nodule fragments, getting into a crack, on crack closure behaviour, which eventually influences the threshold stress intensity factor range. These studies insist that nodules cannot be mechanically equivalent to a stress free hole.

However, previous studies do not necessarily evaluate separately the effect of microstructure properties (for example H_V) and that of the size of graphite nodules. With respect to this problem, Endo [18,19] carried out interesting experiments. He compared the fatigue strength of nodular cast iron specimens containing nodules with those which were electropolished to remove nodules at a specimen surface. Thus, the nodules of the latter specimens became stress free vacant pores. Comparison of the fatigue strengths of these two types of specimens reveals the effect of nodules, and is introduced in the following section [18].

11.2 Fatigue Strength Prediction of Nodular Cast Irons by Considering Graphite Nodules to be Equivalent to Small Defects

Endo tested two nodular cast irons, FCD60 and FCD70. Fig. 11.2 shows the specimen used, which contains an array of three notches. Table 11.1 shows the

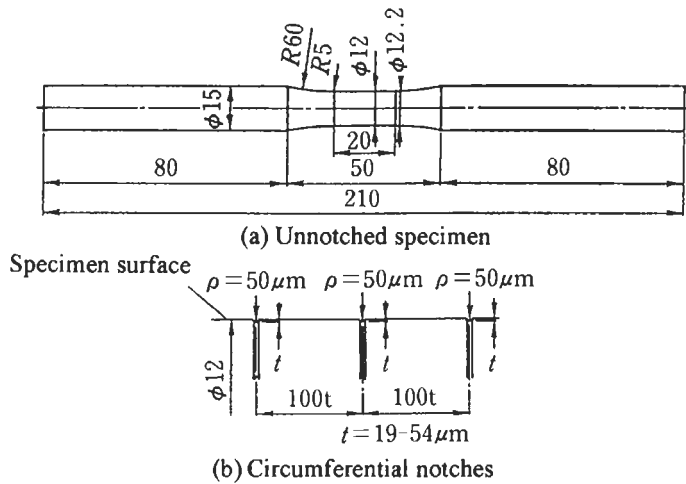


Figure 11.2 Geometry of specimen containing an array of three notches.

chemical composition and mechanical properties, and Fig. 11.3 the microstructures. The spheroidal graphite percentages (nodularity) [20] are 84% for both FCD60 and FCD70, and the area fraction of pearlite is 47% for FCD60 and 72% for FCD70. Endo prepared two series of specimens. One underwent electropolishing, during which 2 μm was removed from the specimen surface; all graphite nodules at a surface were completely removed and became vacant defects. This process is illustrated in Fig. 11.4. These specimens were denoted EP specimens. Another series was not electropolished so that the specimens contained nodules at surfaces. These were denoted N-EP. Fig. 11.5 shows the removal of nodules from a surface. The photographs in the upper row show the condition of the surface during electropolishing, with the microscope focused on the surface. The photographs in the lower row show conditions within a developing

Table 11.1 Chemical composition and mechanical properties of nodular cast irons

Chemical composition (wt %)							
	C	Si	Mn	P	S	Cu	Mg
FCD60	3.76	2.98	0.41	0.023	0.015	0.30	0.052
FCD70	3.77	2.99	0.44	0.023	0.011	0.47	0.058

Mechanical properties		
	FCD60	FCD70
Tensile strength MPa	641	734
Elongation %	14.1	8.0
Vickers hardness (10kgf)	216	241

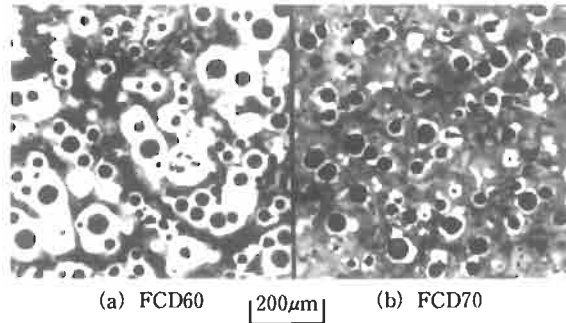


Figure 11.3 Microstructures of nodular cast irons (Endo [18]).

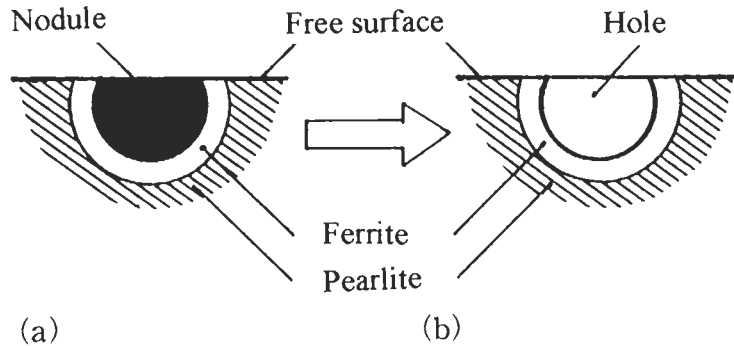


Figure 11.4 Schematic of a graphite nodule at a surface. (a) Without electropolishing (N-EP specimen). (b) After electropolishing (EP specimen).

nodule hole during electropolishing. During electropolishing, the depth of the nodule hole increases, but with almost no change in the shape of the hole at the surface. It could be confirmed that after an entire nodule was removed, a ferrite structure appeared at the bottom of the hole, and that afterwards the depth of the hole did not change. Thus, by slight electropolishing of the surface of a specimen, surface nodules can be removed without changing the shape and size of holes (nodule shape).

Fig. 11.6 shows $S-N$ curves obtained by rotating bending fatigue testing. For both FCD60 and FCD70 there are no distinct differences between the fatigue strengths of N-EP specimens, and those of EP specimens. Therefore, as far as the materials used by Endo are concerned, the contribution of graphite nodules to improvement of fatigue strength is negligible, and a nodule can be regarded as equivalent to a hole.

The effect of graphite nodules on fatigue strength needs discussion to establish that the mechanics does not conflict with the problems of carbides in tool steels, and of nonmetallic inclusions in various materials. The effect of nodules on material response to external loading can be easily judged by experiments which compare the fatigue strengths of unnotched specimen with those of specimens containing artificial holes, whose size is approximately equal to those nodules of maximum size, which become fatigue fracture origins in unnotched specimens.

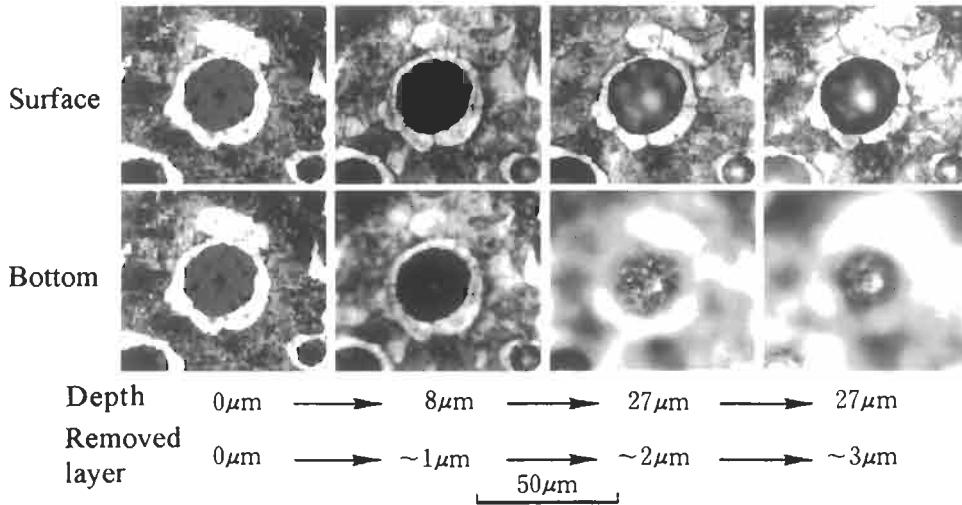


Figure 11.5 Removal of graphite nodules from a surface by successive electropolishing (Endo [18]).

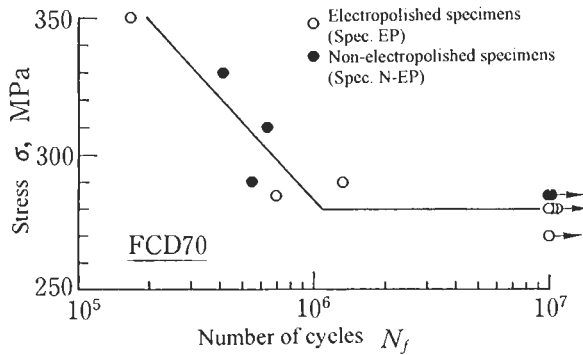
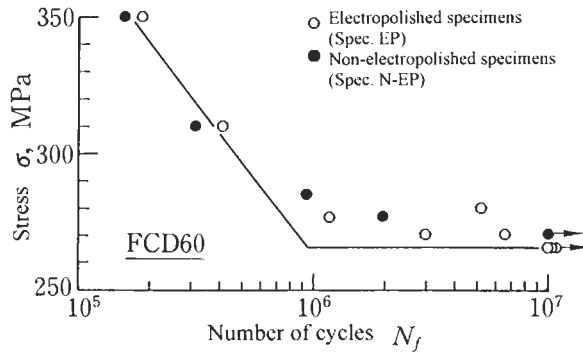


Figure 11.6 S-N curves for nodular cast irons (Endo [18]).

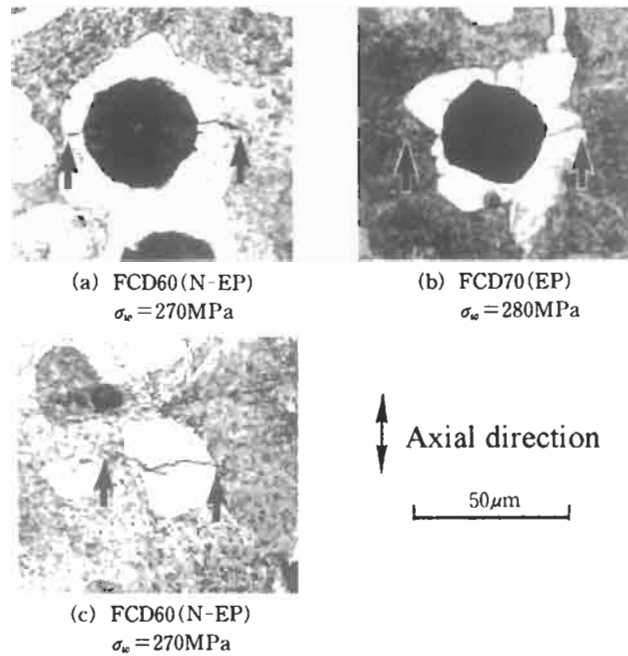


Figure 11.7 Non-propagating cracks observed at the fatigue limit (Endo [18]).

At the fatigue limit of nodular cast iron specimens, non-propagating cracks, as shown in Fig. 11.7, are quite commonly observed. As also pointed out in other studies [3,8,21–24], the fatigue limits of FCD60 and FCD70 are not a critical stress for crack initiation, but are a threshold stress for crack growth and for non-propagation of cracks. However, non-propagating cracks are not necessarily observed at all graphite nodules on specimen surfaces because the crack initiation condition is not satisfied at most nodules. According to detailed observations by Kato and Nakano [21], only 5% of nodules on the surfaces of FCD60 specimens contain non-propagating cracks at the fatigue limit. Moreover, both Endo's experiments and the observations by Hirose et al. [25] verify that the number of non-propagating cracks, which coalesced from one nodule to a neighbouring nodule, is exceptionally small. These facts mean that interaction effects between the nodules, in high quality nodular cast irons, is unexpectedly small at the fatigue limit.

Another interesting fact is that the surface size of graphite nodules, with which non-propagating cracks are associated, is in general smaller than the surface size of nodules without non-propagating cracks. This is because apparently small nodules at a surface mostly have larger dimensions hidden below the surface. Even if the true size of two nodules were identical, the stress intensity factors for cracks emanating from a nodule in contact with the surface are larger than those for cracks emanating from a hemispherical nodule which appears larger at a surface. This mechanism is the same as the case of an inclusion just in contact with a free surface (Chapter 6).

Fig. 11.7c shows a non-propagating crack at a specimen surface, which appears to

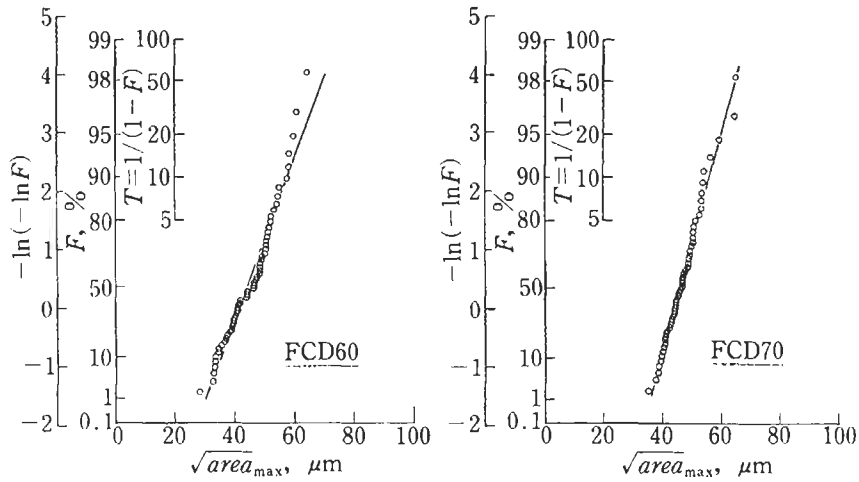


Figure 11.8 Extreme value statistics distributions of graphite nodule size, $\sqrt{area_{max}}$ (Endo [18]).

have initiated independently of a graphite nodule, but undoubtedly emanated from a nodule hidden below the surface. Clement et al. [24] reported two cases of non-propagating cracks which emanated from surface nodules. They established by electropolishing that the centres of these nodules were below the surface. From the above discussion, the domain occupied by nodules can be regarded as equivalent to a hole, or a small defect, without a nodule. Since the fatigue limit is determined by the threshold condition for cracks emanating from such defects, the fatigue problem of nodular cast irons can be treated as a small crack problem.

Fig. 11.8 shows the extreme value statistics distributions (see Chapter 6 and Appendix A) of graphite nodule sizes for FCD60 and FCD70 [18]. Both distributions are sufficiently linear to demonstrate that the maximum size of nodules, $\sqrt{area_{max}}$, obeys extreme value statistics. The size of the largest nodule existing at a specimen surface can be predicted by the intersection of the distribution line and the return period, T , which is dependent on the numbers of specimens. The control surface for one specimen is $S = 754 \text{ mm}^2$ (see Fig. 11.2). The return period, T , is given by $T = NS/S_0$, where S_0 is the standard inspection area, and $S_0 = 0.308 \text{ mm}^2$. Determining the distribution equations for Fig. 11.8 by the least squares method, and substituting the values of T into these equations, we can calculate the values of $\sqrt{area_{max}}$ for $N = 1-10$. Thus, the values of $\sqrt{area_{max}}$ for $N = 1-10$ are 107–124 μm for FCD60 and 92–104 μm for FCD70. If we estimate the maximum equivalent defect size, $\sqrt{area_{max}^*}$, at a surface using Eq. 6.2, then values are 114–132 μm for FCD60, and 98–111 μm for FCD70. It should be noted that these values are much larger than the average nodule sizes.

Although, as described above, we can predict the maximum size, $\sqrt{area_{max}}$, of graphite nodules in the surface control volume of a specimen, it is very difficult to find out directly the true maximum size nodule in a specimen, and to confirm that this particular nodule actually did determine fatigue strength.

However, if this prediction were correct, it would be expected that a specimen,

Table 11.2 Fatigue test results for specimens containing an array of three notches (Endo [18])

Materials (Test stress)	t μm	\sqrt{area} μm	× Failure ○ Ran out	Number of cycles
FCD60 (265MPa)	19	60	○	10^7
	24	76	○	
	21	66	○	
	30	95	○	9.83×10^5
	27	85	×	
	30	95	○	
	38	120	○	7.084×10^5
	46	145	○	
	38	120	×	
FCD70 (280MPa)	33	104	○	10^7
	33	104	○	
	32	101	○	
	42	133	○	9.6×10^5
	42	133	×	
	40	126	○	
	54	171	○	2.685×10^5
	50	158	×	
	54	171	○	

containing an artificial defect whose size, \sqrt{area} , is approximately equal to \sqrt{area}_{\max}^* , should have a fatigue strength almost identical to that of an unnotched specimen of the nodular cast iron. Based on this hypothesis, Endo carried out fatigue tests using electropolished specimens containing notches with the depth, $t = 19\text{--}54$ μm , and root radius, $\rho = 50$ μm . By using rotating bending fatigue tests, the critical value, \sqrt{area}_0 , of the notch which is not detrimental to fatigue strength, was determined as shown in Table 11.2, where \sqrt{area} for a notch is calculated using the equation $\sqrt{area} = \sqrt{10} t = 3.16t$ (see Eq. 2.9).

Table 11.2 shows the results of fatigue tests using a specimen containing an array of three notches. The symbol \times in Table 11.2 means that a notch led to specimen failure, and \circ means that notches were not detrimental. Values of \sqrt{area}_0 are estimated as 76–84 μm for FCD60, and 104–132 μm for FCD70. Table 11.3 compares predicted

Table 11.3 Comparison of predicted values of \sqrt{area}_{\max}^* and experimental values of \sqrt{area}_0 (Endo [18])

Materials	\sqrt{area}_{\max}^* ($N = 1 \sim 10$)	\sqrt{area}_0
FCD 60	114~132 μm	76~84 μm
FCD 70	98~111 μm	104~132 μm

values of $\sqrt{area^*_{max}}$ and the experimental values of $\sqrt{area_0}$. The prediction for FCD70 is in good agreement with the experimental result. However, the prediction for FCD60 is a little smaller than the experimental value. This may be due to the bull's eye structure of FCD60 (see Fig. 11.3a), in which the area fraction of ferrite is approximately equal to that of pearlite. Accordingly, the scatter of microstructure strength and hardness is larger than for FCD70. The Vickers hardness used for prediction was measured at 10 kgf in order to obtain the average hardness of the microstructure. Regardless of some differences between the predictions and experiments, these data indirectly clarify that graphite nodules, of the order of $\sqrt{area^*_{max}}$ on specimen surfaces, do determine the fatigue limit.

In order to predict the fatigue limit of nodular cast irons using Eq. 6.2, we need not only \sqrt{area} ($= \sqrt{area^*_{max}}$) but also the hardness, H_V , of the microstructure close to the fracture origin. If the values of H_V are uniform, then we may measure H_V away from the fracture origin. However, since microstructures of nodular cast irons are usually complex, such as the bull's eye structure, the method of measuring H_V must be reconsidered.

Nodular cast irons produced by recent advanced technology usually contain well separated graphite nodules, and mutual interaction between nodules can be ignored, as demonstrated by Endo. However, if adjacent nodules become coalesced [3], then the equivalent defect size naturally becomes larger than one nodule. In fact, nodular cast irons produced in the 1960s contain many coalesced nodules. The material investigated by Nisitani and Murakami [3] is a typical example of this kind (this material is shown in Fig. 6.40). The extreme value statistics distribution lines for separated nodules and for coalesced nodules are very different, as shown in Fig. 11.9. Table 11.4 compares the experimental fatigue limit, determined using several specimens, and the fatigue limit lower bound predicted by using $\sqrt{area^*_{max}}$ for the largest single nodule and for the largest coalesced nodule. The prediction made by using the size of the largest single nodule is unconservative but, on the other hand, the prediction based on the size of the

Table 11.4 Comparison of the estimated lower bound of fatigue limit and experimental results. Vickers hardness of the microstructure, $H_V = 265$ (load 200 g, average of 8 measurements)

	Control volume of one specimen V (mm ³)	Numbers of specimen N	Return period T	Predicted volume $\sqrt{area^*_{max}}$ (μ m)	Lower bound of fatigue limit σ_{wl} (MPa)	Fatigue limit determined by limited numbers of specimens (MPa)
No interaction of neighboring nodules	34.4	1	595	210.8	223	205.8
		10	5950	246.5	217	
		100	59500	282.2	212	
Interaction of nodules considered	34.4	1	415	456.4	196	
		10	4150	576.0	188	
		100	41500	695.4	182	

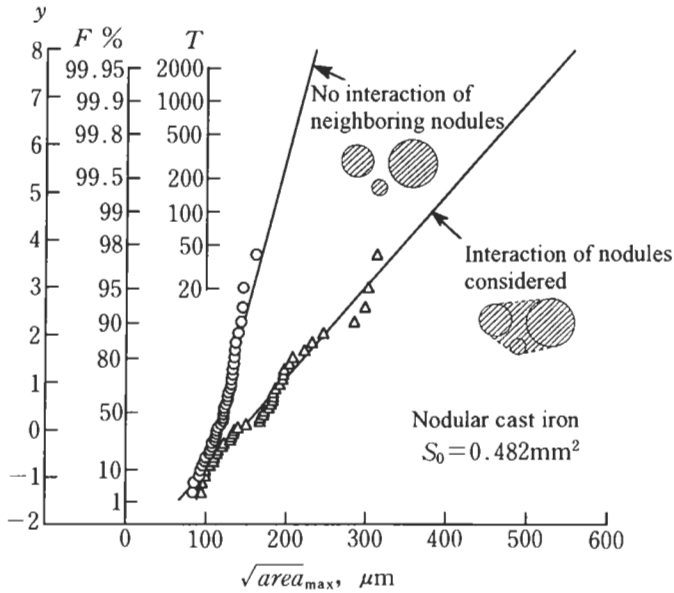


Figure 11.9 Comparison between extreme value statistics distributions of graphite nodule size, $\sqrt{area_{max}}$, for separated nodules and for coalesced nodules.

largest coalesced nodules is conservative. This indicates that the prediction based on the coalescence of nodules is reasonable.

Yano et al. [26] investigated the influence of rolling on the bending fatigue strength at the roots of plane gear teeth made from nodular cast iron. They found that the rolling caused cracking between nodules at the edges of teeth roots, and successfully estimated the amount of decrease in fatigue strength due to cracking by using the idea of Eq. 6.6.

Since in this case, coalescence of graphite nodules was caused by rolling, and not by the initial casting process, not only the evaluation of \sqrt{area} of cracks, but also the increase in Vickers hardness due to plastic forming, was taken into consideration. Thus, the fatigue strengths of nodular cast irons are influenced by many factors, such as interaction between nodules, and presence of both pearlite and ferrite, which makes quantitative evaluation more difficult than for the case of nonmetallic inclusions. It must therefore be noted that discussions which pay attention to only one of these many factors lead us to erroneous conclusions.

The important quantities we have to pay attention to are: (1) the size of the graphite nodule which becomes a fracture origin; (2) the microstructure near the fracture origin (especially the hardness, H_V), and (3) the stress applied at the fracture origin.

With regard to this viewpoint, Sugiyama et al.'s [27] recent study is very interesting. They carried out fatigue tests on 9 nodular cast irons of different chemical composition, different casting size, and different austempered conditions.

They clarified the different effects of small and large casting defects, and proposed a two parameter method for the prediction of fatigue strength. Their method is based on the different behaviour of small casting defects and large casting defects, that is small

cracks and long cracks, and the evaluation of microstructures by their hardness. They then derived a useful practical suggestion in that the optimum heat treatment condition must be decided through consideration of the size of casting defects.

11.3 References

1. M. Ohashi, M. Kuroda, Y. Komatsu and Y. Hibino: Influence of matrix structure on fatigue strength of S.G. cast iron, *IMONO (J. Cast. Inst. Jpn.)*, **42(8)** (1970), 634–638.
2. I. Niimi, M. Ohashi, Y. Komatsu and Y. Hibino: Influence of graphite nodules on the fatigue strength of S.G. cast iron, *IMONO (J. Cast. Inst. Jpn.)*, **43(2)** (1971), 101–107.
3. H. Nisitani and Y. Murakami: Role of nodules on bending and torsional fatigue of nodular cast iron, *Sci. Mach.*, **25(4)** (1973), 543–546.
4. M. Sofue: On the fatigue properties of spheroidal graphite cast irons with various hardness, *IMONO (J. Cast. Inst. Jpn.)*, **48(7)** (1976), 441–447.
5. A.G. Fuller: Effect of graphite form on fatigue properties of pearlitic ductile irons, *AFS Trans.*, **85** (1978), 527–536.
6. T. Shiota and S. Komatsu: Influence of graphite nodule diameter on fatigue strength and crack propagation behavior of ferritic spheroidal graphite cast irons under rotational bending, *IMONO (J. Cast. Inst. Jpn.)*, **54(7)** (1982), 434–439.
7. M. Sofue: Influence of graphite shape on fatigue strength of spheroidal graphite cast iron, *IMONO (J. Cast. Inst. Jpn.)*, **51(5)** (1979), 281–286.
8. M. Sofue: Evaluation of role of graphite nodules in fatigue strength spheroidal graphite cast iron, *IMONO (J. Cast. Inst. Jpn.)*, **51(3)** (1979), 159–163.
9. M. Sofue: Influence of microstructural constituents on the fatigue strength of spheroidal graphite cast iron, *IMONO (J. Cast. Inst. Jpn.)*, **53(11)** (1981), 635–640.
10. Y. Tanaka, K. Kawamura, K. Kato and K. Ikawa: Relation between fatigue properties and microstructure of spheroidal graphite cast iron, *IMONO (J. Cast. Inst. Jpn.)*, **53(9)** (1981), 500–505.
11. H. Suzuki, M. Ouyabu, T. Ueki and T. Kunio: Influence of matrix structure on fatigue strength of nodular iron with high tensile strength, *Trans. Jpn. Soc. Mech. Eng. A*, **51(464)** (1985), 1224–1229.
12. H. Suzuki and T. Kunio: Influences of metallurgical factors on fatigue strength reliability and micro crack distribution of nodular iron casting, *Trans. Jpn. Soc. Mech. Eng. A*, **53(490)** (1987), 1000–1006.
13. M. Buchanan, J.W. Provan and J.E. Gruzleski: An apparatus for four-point bending fatigue testing of materials in a scanning electron microscope and its application to nodular cast iron, *Metallography*, **20** (1987), 125–143.
14. K. Igawa and Y. Tanaka: Microstructure and fatigue strength of cast irons, *Bull. Jpn. Inst. Metals*, **13(9)** (1974), 665–673.
15. M. Yano: Effects of elasticity and compactness of graphites on fatigue strength of malleable iron, *Trans. Jpn. Soc. Mech. Eng. A*, **51(461)** (1985), 132–135.
16. M. Yano: Effects of elasticity and compactness of graphites on the fatigue strength of spheroidal graphite cast iron, *Trans. Jpn. Soc. Mech. Eng. A*, **52(481)** (1986), 2150–2154.
17. T. Ogawa, H. Kobayashi, T. Koide, H. Nakazawa and E. Kometani: Near-threshold characteristics and crack closure in fatigue crack growth for nodular graphite cast iron, *Trans. Jpn. Soc. Mech. Eng. A*, **51(467)** (1985), 1660–1667.
18. M. Endo: Effects of graphite shape, size and distribution on the fatigue strength of spheroidal graphite cast irons, *J. Soc. Mater. Sci. Jpn.*, **38(433)** (1989), 1139–1144.
19. M. Endo: Fatigue Strength Prediction of Nodular Cast Irons containing Small Defects, MD-Vol. 28, Impact of Improved Material Quality on Properties, Product Performance, and Design, ASME, 1991, pp. 125–137.
20. Cast Iron Handbook, 4th revised edn., Japan Soc. Cast Irons, 1986, p. 567.
21. Y. Kato and N. Nakano: Microcrack nucleation and propagation behavior of spheroidal graphite cast iron in rotating bending, *Trans. Jpn. Soc. Mech. Eng. A*, **50(457)** (1984), 1565–1573.

22. Y. Kato and N. Nakano: Microcrack nucleation and propagation behaviors of spheroidal graphite cast iron FCD45 (comparison between rotating bending and reversed torsion), *Trans. Jpn. Soc. Mech. Eng. A*, **51(464)** (1985), 1208–1214.
23. H. Nisitani and S. Tanaka: Initiation and propagation of fatigue crack in cast irons (rotating bending fatigue tests of FC25 and FCD45), *Trans. Jpn. Soc. Mech. Eng. A*, **51(465)** (1985), 1442–1447.
24. P. Clement, J.P. Angeli and A. Pineau: Shot crack behaviour in nodular cast iron fatigue, *Eng Mater. Struct.*, **7(4)** (1984), 251–265.
25. Y. Hirose, T. Kurobe, M. Tsuda, M. Nishimoto and S. Kawai: Nucleation and growth of fatigue crack in spheroidal graphite cast iron, *J. Jpn. Soc. Strength Fract. Mater.*, **16(4)** (1981), 156–166.
26. K. Yano, S. Oda, T. Koide, M. Goka and T. Ozaki: Effect of fillet rolling at the root of the tooth on bending fatigue strength of spur gears (ADI, S45C gears), *Trans. Jpn. Soc. Mech. Eng. C*, **58(551)** (1992), 2212–2218.
27. Y. Sugiyama, K. Asami and S. Matsuoka: The Quantitative evaluation method on fatigue limit of materials with defects by using ductile cast iron and its application to the fatigue limit improvement, *Proc. the 69th JSME Spring Annual Meeting*, No. 920-17, Vol. A, 1992, pp. 476–478.

Chapter 12

Influence of Si-Phase on Fatigue Properties of Aluminium Alloys

In industry, efforts to achieve weight savings in automotive structures mean that aluminium alloys continue to attract attention as substitutes for iron and steel. For durability-related applications, it is important to determine the fatigue characteristics of candidate alloys, and to understand the microstructural basis of performance, in order to optimise material processing. This chapter focuses on the high-cycle (up to $N_f > 10^8$ – 10^9) and low-cycle fatigue behaviour of Al–Si eutectic alloys produced by two different processes: continuous casting and extrusion [1,2].

12.1 Materials, Specimens and Experimental Procedure

Eight types of Al–Si alloys were tested [2]. Fig. 12.1 shows the microstructures of the Al–Si eutectic alloys. Table 12.1 shows the chemical composition and diameter of the materials in their original conditions. Specimens were named using the following scheme. For example, 6B17 denotes original diameter ~ 60 mm, chemical composition category B, and Vickers hardness ~ 170 .

The material series of original diameter 32 and 67 mm were produced by continuous casting, and the others were produced by casting followed by extrusion. Table 12.2 shows heat treatments, and Table 12.3 mechanical properties.

Fig. 12.2 shows the specimen geometry. An artificial hole was introduced into the surface of some specimens by drilling. Four strain gauges were attached to each specimen to check for specimen bending under load.

12.2 Fatigue Mechanism

Fig. 12.3 shows S – N curves obtained by rotating bending and tension compression fatigue tests. The S – N curves show fracture at $>10^8$ cycles, and no definite fatigue limit. Although there are some differences in fatigue life between rotating bending and tension compression, no substantial difference in fatigue mechanism was found in observations of fatigue crack growth processes.

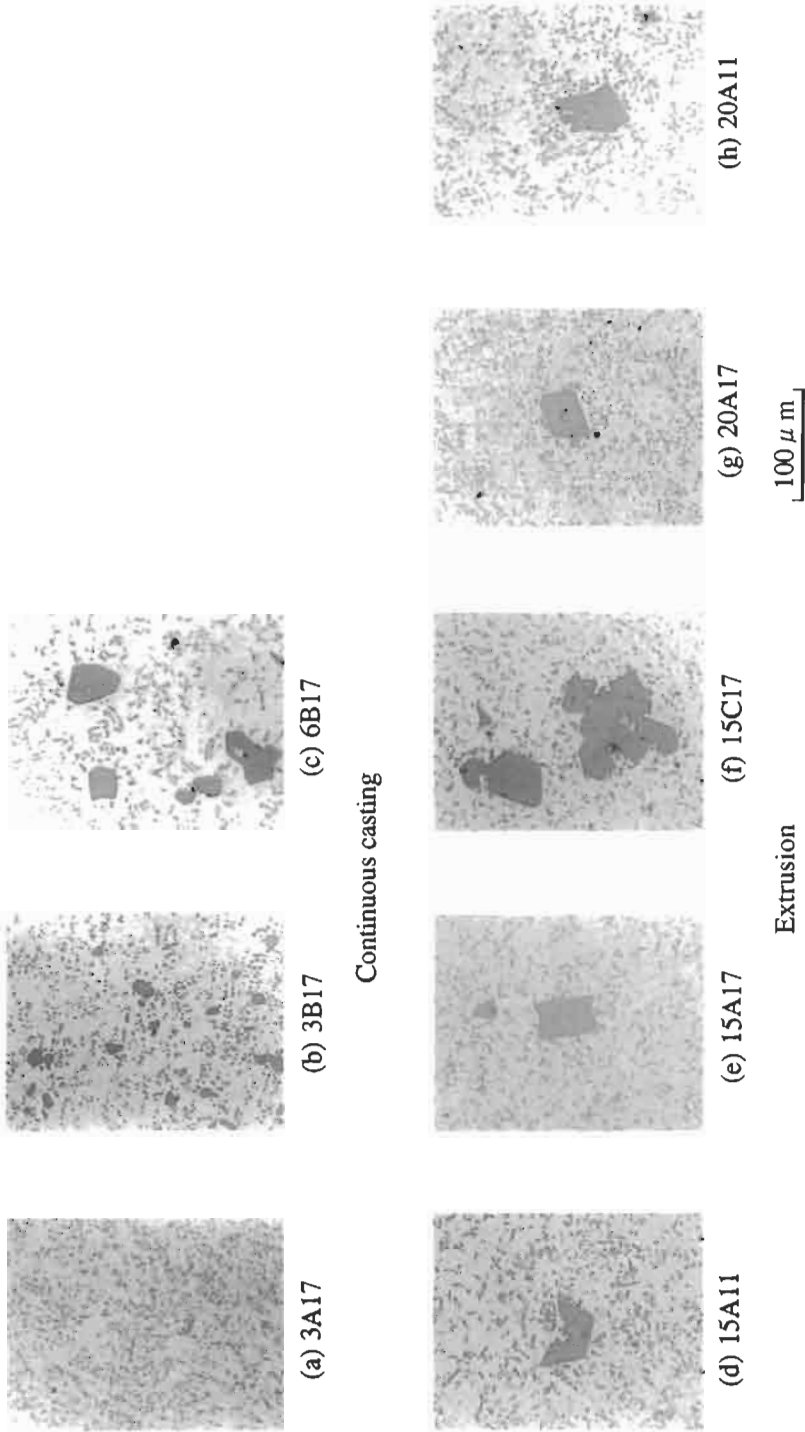


Figure 12.1 Microstructures of Al-Si eutectic alloys.

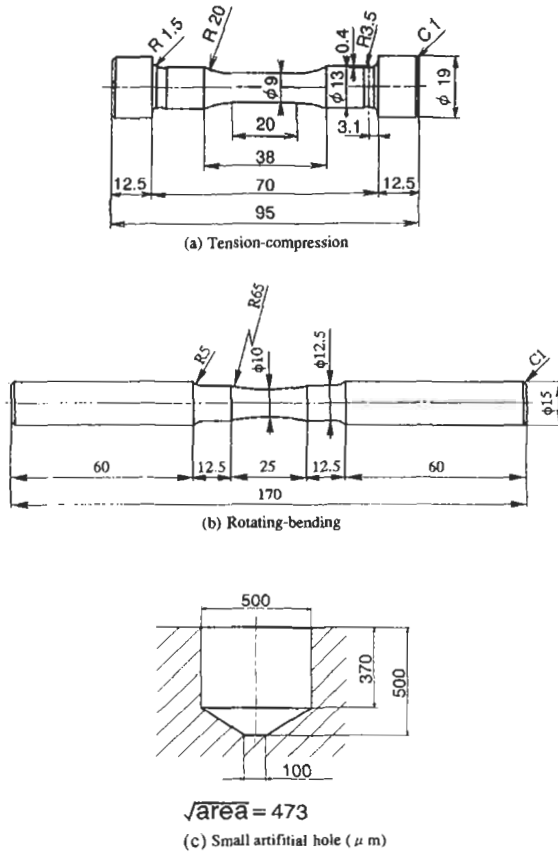


Figure 12.2 Shapes and dimension of specimens in mm and μm . (a) Tension-compression (mm). (b) Rotating-bending (mm). (c) Small artificial hole (μm).

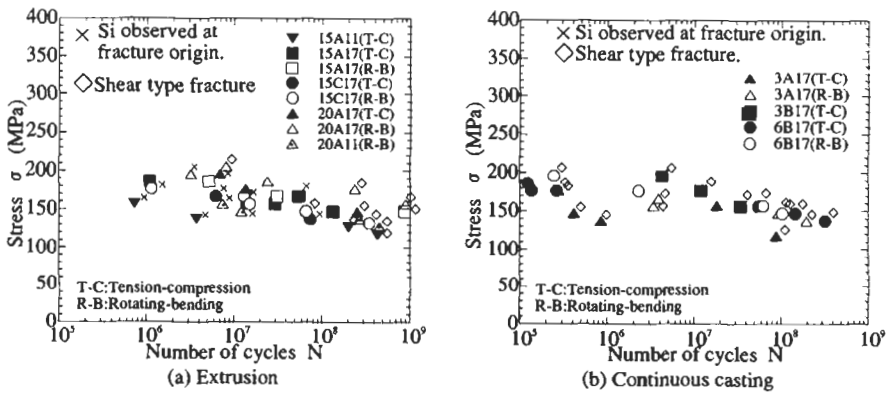


Figure 12.3 $S-N$ curves obtained by rotating bending and tension compression fatigue tests.

Table 12.1 Chemical composition and diameter of cast materials

Process	Sample	Chemical composition (wt%)									<i>d</i> (mm)
		Si	Fe	Cu	Ti	Mn	Mg	Zn	Cr	Ni	
Continuous casting	3A17	10.8	0.19	3.99	0.010	0.007	0.55	0.008		0.005	32
	3B17	11.2	0.19	7.25	0.008	0.012	0.59	0.008		0.003	
	6B17	10.8	0.19	7.33	0.009	0.012	0.58	0.009	0.001	0.007	67
Extrusion	15A11	11.3	0.26	4.1		0.26	0.60				150
	15A17	11.3	0.27	4.2		0.26	0.61				
	15C17	17.0	0.30	4.2		0.23	0.61				
	20A11	11.2	0.24	4.2		0.26	0.61				200
	20A17	11.3	0.23	4.1		0.26	0.61				

d: Diameter of casting piece

Table 12.2 Heat treatment of materials

Sample	Heat treatment	
3A17 3B17 6B17	495°C × 6H → WQ	170°C × 8H
15A11 20A11	495~500°C × 6H → WQ	230°C × 100min
15A17 20A17 15C17	495~500°C × 6H → WQ	170°C × 6H

Extensive observations of fatigued specimens revealed two basic failure mechanisms: (1) fracture origin in the Si phase, or at the interface between Si and the matrix; (2) shear crack initiation and growth in the matrix.

Details of each mechanism, as influenced by material processing, are discussed in the following sections.

12.2.1 Continuously Cast Material

Representative fatigue fracture surfaces for the 3A17, 3B17 and 6B17 materials are shown in Fig. 12.4. Here, a single shear-type crack initiated in the Al matrix and grew to

Table 12.3 Mechanical properties of materials

Sample	$\sigma_{0.2}$	σ_B	σ_T	ϕ	HV (200g.ave.)	HV (3g.ave.)	HV (3g.min.)
3A17	402	479	522	13.1	169	120	80
3B17	407	476	519	8.26	176	128	87
6B17	409	441	453	2.53	175	126	100
20A11	223	332	380	18.1	112	84	68
20A17	396	456	508	15.1	161	119	100
15A11	225	334	378	16.9	115	85	64
15A17	402	459	514	13.8	167	123	90
15C17	378	408	423	3.57	164	118	89

$\sigma_{0.2}$: 0.2% offset yield strength, MPa

σ_B : Ultimate tensile strength, MPa

σ_T : True fracture stress, MPa

ϕ : Reduction of area, %

HV : Vickers hardness number, kgf/mm²

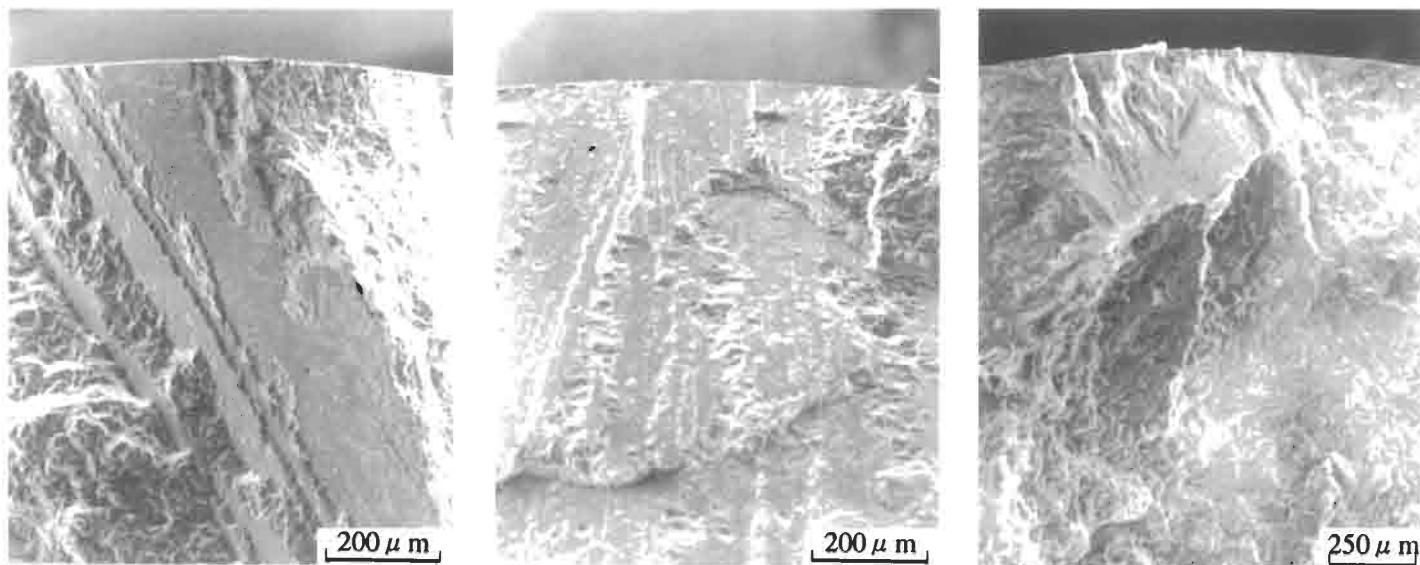
a critical size in a shear mode, that is inclined at $\sim 45^\circ$ to the surface. Fig. 12.5 shows a typical example of shear-type fatigue crack initiation and growth in the 3A17 material. No other cracking was observed. Such shear cracks are found to form before interfacial separation between the Si phase and the matrix.

Fatigue lives of the 3A17 material are shorter than those of the other materials. This is because it has less Si phase, and shear-type cracks easily extend across the specimen section, resulting in higher fatigue crack growth rates because of less crack closure.

12.2.2 Extruded Material

In contrast to the above behaviour, the fatigue mechanisms of the extruded materials are quite different for $N_f \leq \sim 10^7$ and $N_f \geq 10^8$. Fig. 12.6 shows the fracture surface of the 20A11 material, with $N_f = 1.2 \times 10^7$. Fig. 12.7 shows the crack initiation and growth behaviour of the same material. These observations indicate that the fracture origin is either at a cracked Si phase particle, or at the interface of Si phase. Here, it can be seen that cracks form early in the life (see Fig. 12.10), invariably within the Si phase.

On the contrary, the same material (20A11) shows a quite different fracture behaviour for $N_f = 4.5 \times 10^8$. Figs. 12.8 and 12.9 show that shear-type cracks, initiated at Al microstructure, led the specimens to fracture. However, at the same time, many cracks initiated at Si phase in other parts of the same specimen, but stopped propagating. Fig. 12.10 is a typical example of such a non-propagating crack in a specimen (15A11), which fractured at $N_f = 2 \times 10^8$. Under such a low stress level, cracks first initiate at Si phase and behave as non-propagating cracks, and afterward shear-type cracks initiate at Al microstructure, and these continue to grow until specimen fracture.



(a) 3A17 ($\sigma = 176.4 \text{ MPa}, N_f = 7 \times 10^5$) (b) 3B17 ($\sigma = 176.4 \text{ MPa}, N_f = 1.2 \times 10^7$) (c) 6B17 ($\sigma = 137.2 \text{ MPa}, N_f = 3.2 \times 10^8$)

Figure 12.4 Fracture surfaces near the fracture origin, continuous casting, tension compression, $f = 100 \text{ Hz}$.

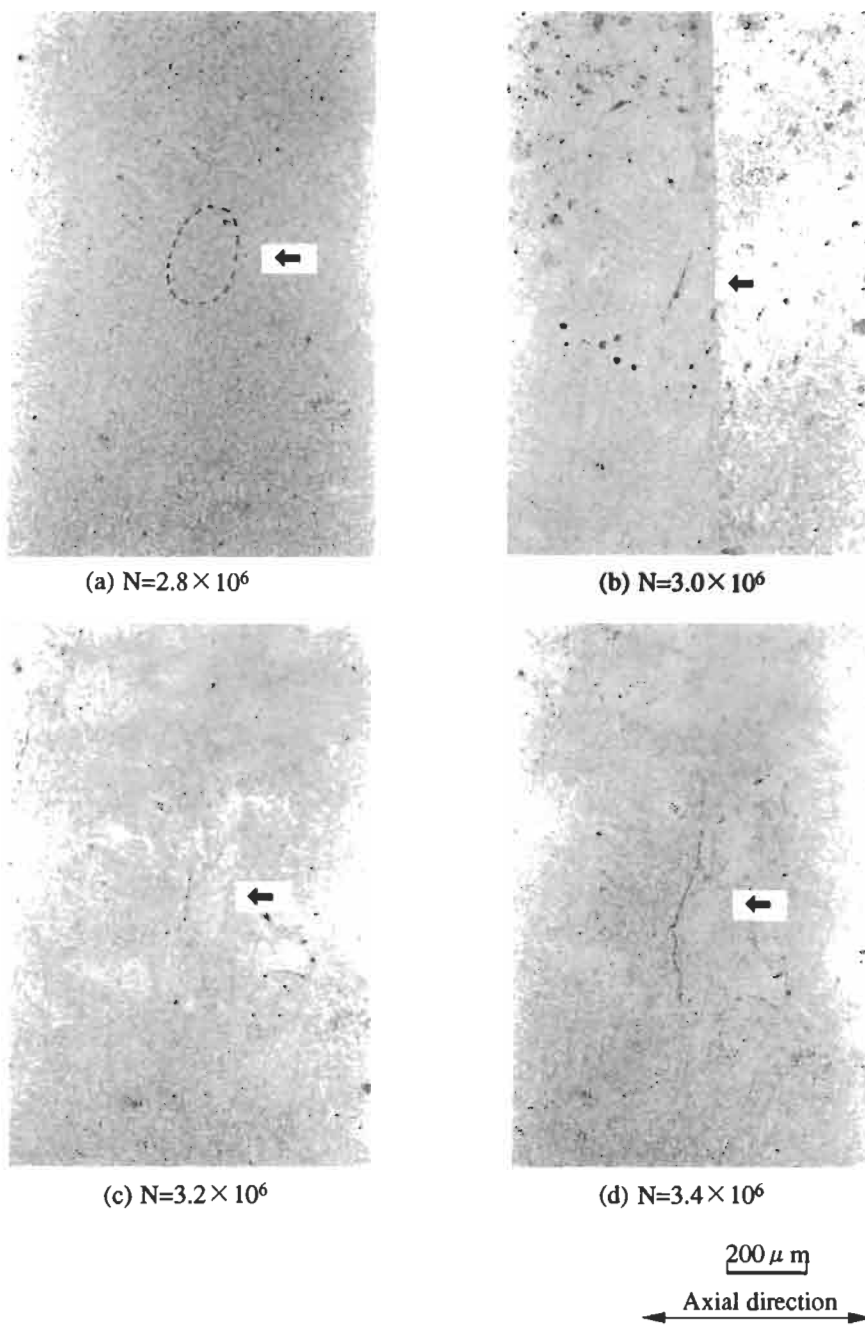
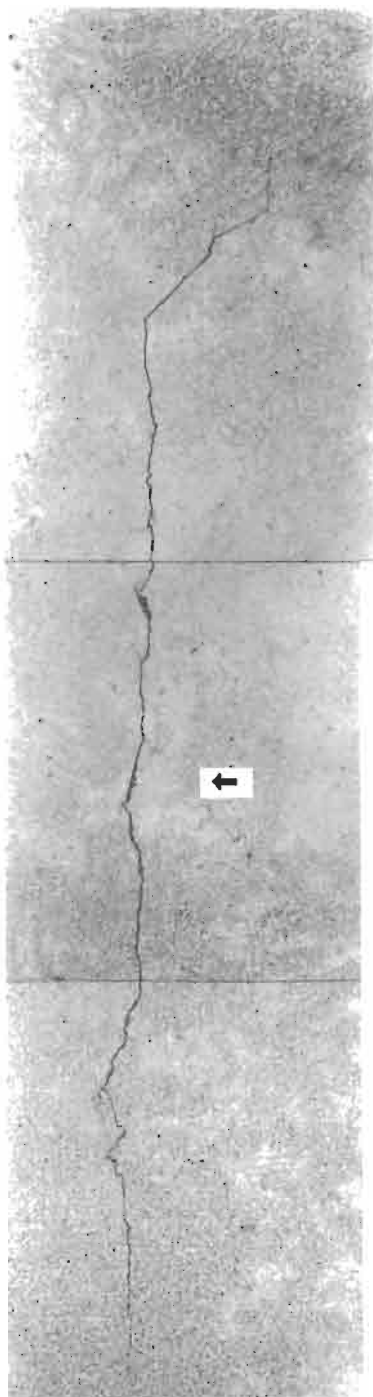


Figure 12.5 Shear type fatigue crack initiation and growth, continuous casting: 3A17, $\sigma = 166.6$ MPa, $N_f = 3.81 \times 10^6$, rotating bending. (Continued on next page.)



(e) $N=3.6 \times 10^6$

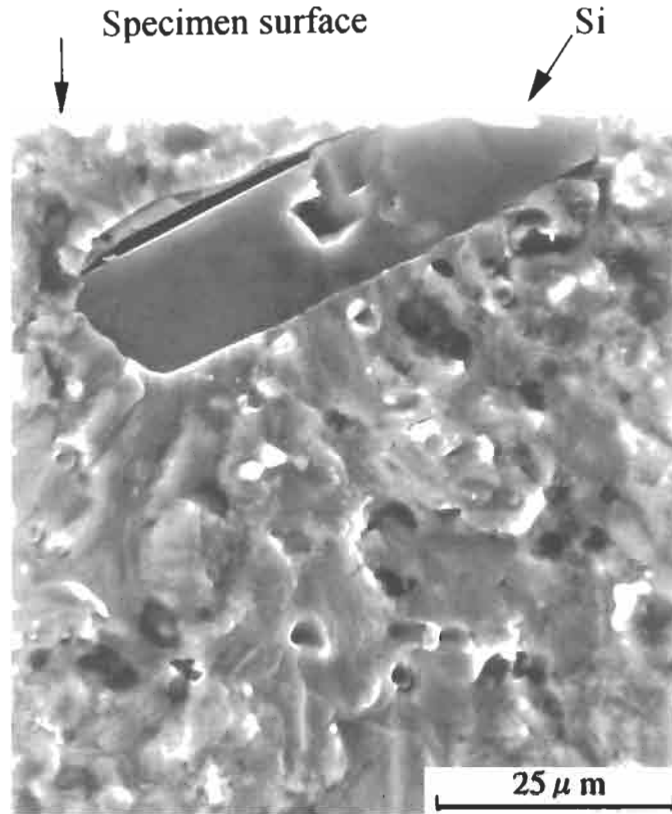


Figure 12.6 Fracture surface near fracture origin which is at Si phase, extrusion: 20A11, $\sigma = 147$ MPa, $N_f = 1.2 \times 10^7$, rotating bending.

Fig. 12.11 shows the fatigue life percentage for crack initiation and propagation. It can be seen that shear-type cracks grow very quickly.

12.2.3 Fatigue Behaviour of Specimens Containing an Artificial Hole

In order to clarify the difference in the fatigue mechanisms for the continuously cast material and for the extruded material, fatigue tests were carried out on specimens containing an artificial hole. Fig. 12.12 shows the $S-N$ curves obtained. Fig. 12.13 shows the crack growth behaviour for a specimen which survived for $N = 10^9$ cycles. $S-N$ curve 3 in Fig. 12.12a shows a fatigue limit with a clear knee point. Fig. 12.13 implies that a plasticity induced crack closure mechanism caused non-propagation (or at least tendency towards non-propagation) of cracks emanating from the artificial hole. Comparing the $S-N$ curves 1, 2 and 3 in Fig. 12.12a, we can interpret the $S-N$ curve for unnotched specimens to be a combination of curves 1 and 2, namely curve 1 which is for failure from Si phase and has a hypothetical clear fatigue limit, and curve 2, which is for failure by shear-type cracking, but has no clear fatigue limit, even at $N \geq 10^8$. The

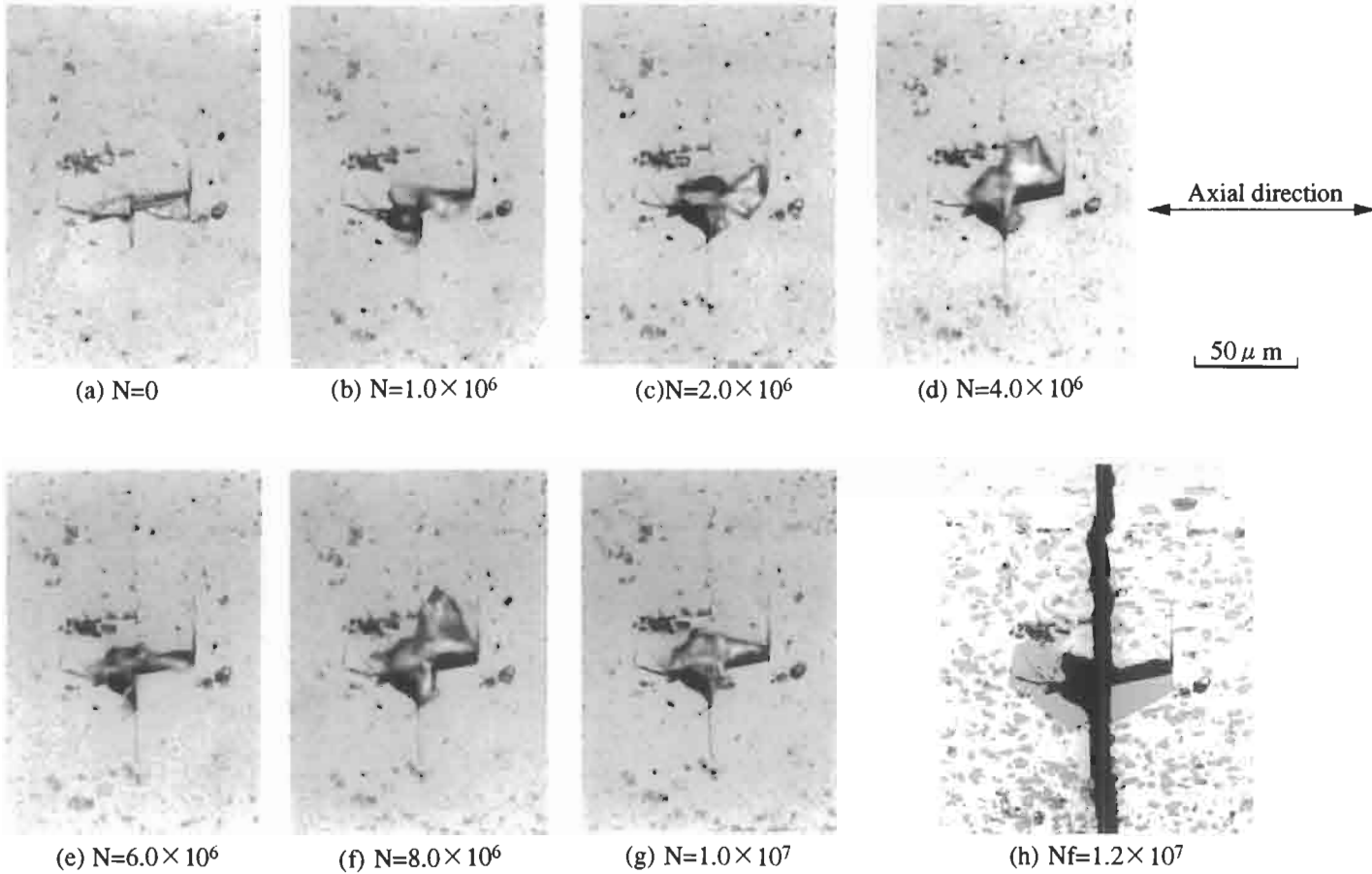


Figure 12.7 Crack propagation from fracture origin, which is at Si phase, extrusion: 20A11, $\sigma = 147$ MPa, $N_f = 1.2 \times 10^7$, rotating bending.

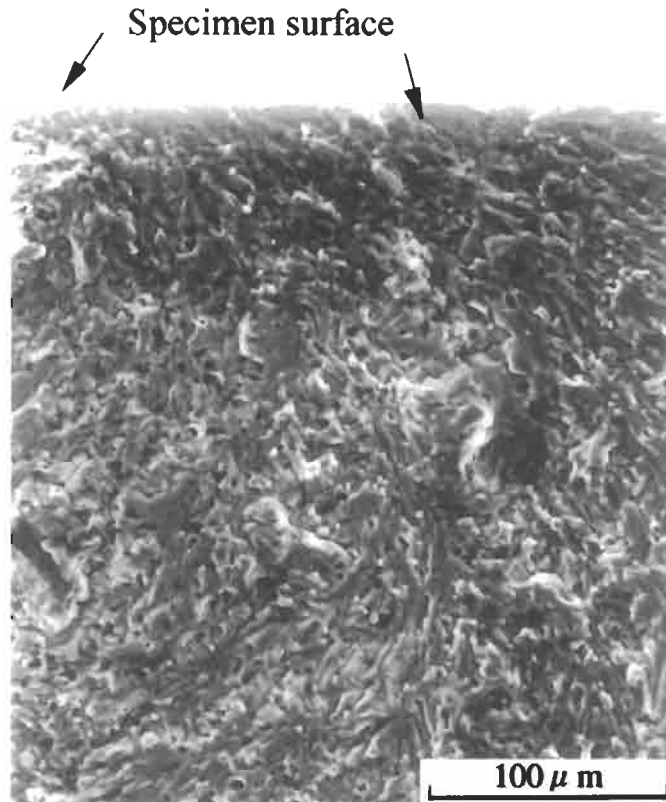


Figure 12.8 Fracture surface near fracture origin showing shear type fracture, extrusion: 20A11, $\sigma = 128$ MPa, $N_f = 4.5 \times 10^8$, rotating bending.

fatigue limit in the curve 3, for specimens containing a small hole, is much lower than the stress which leads unnotched specimens to failure at $N = 10^8$ – 10^9 , and accordingly a curve like curve 2 does not appear explicitly.

On the other hand, the specimens of continuously cast materials containing an artificial hole do not have a clear fatigue limit. This is because shear-type cracks initiate at a hole edge and grow to large size, say ~ 150 μm , so plasticity induced crack closure is unlikely to occur, resulting in fatigue failure at extremely high numbers of cycles.

12.3 Mechanisms of Ultralong Fatigue Life

If we compare the fatigue mechanisms of steels (see Chapter 6) and aluminium alloys in ultralong fatigue life, it seems there are both common and different mechanisms. The common mechanism is fatigue crack growth in Mode I, which occurs in crack growth from inclusions or Si phase. In this case, more or less plasticity-induced crack closure should be present, though oxide-induced crack closure would be absent in crack growth from internal inclusions. However, we cannot determine the relative degrees of influence

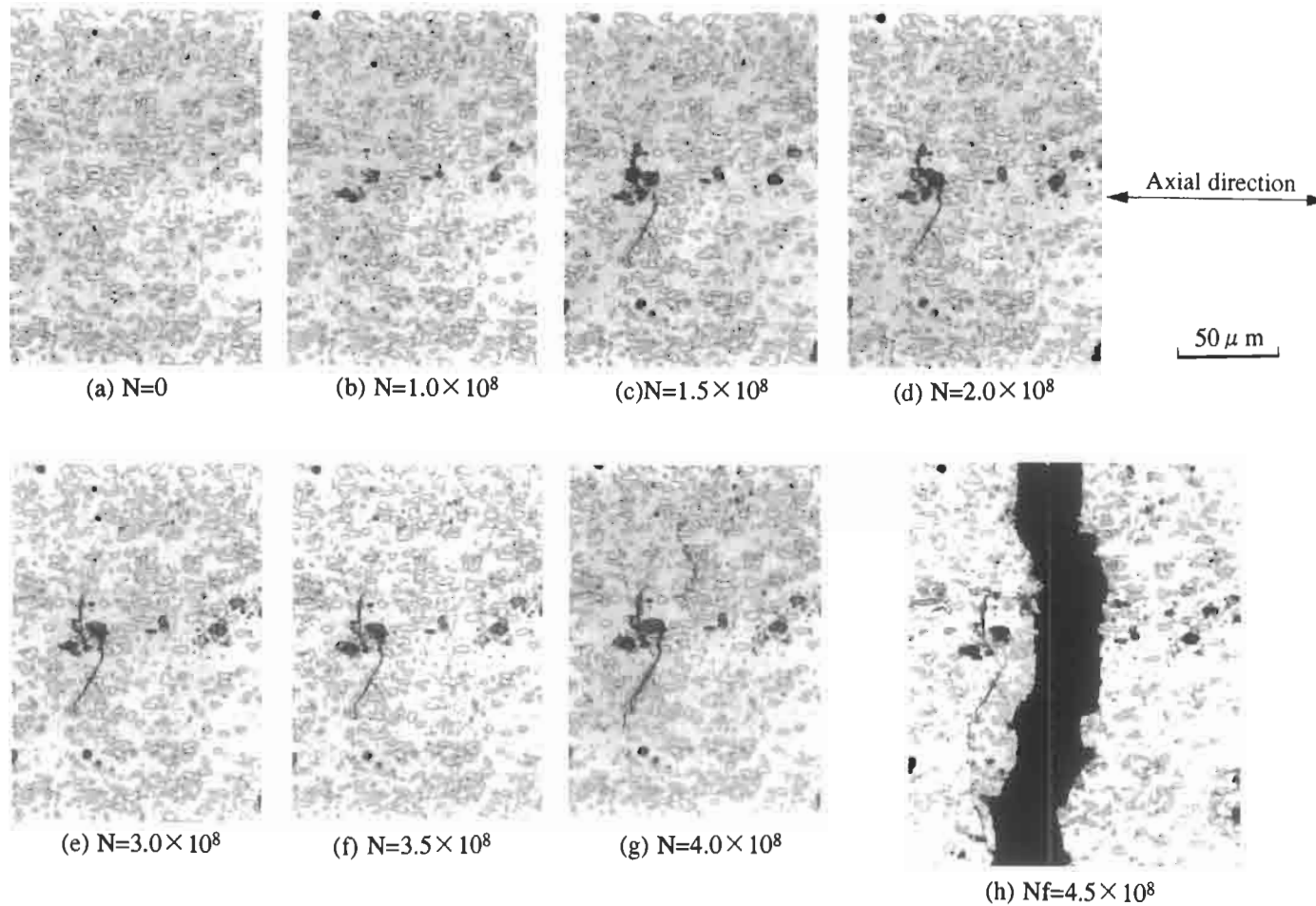


Figure 12.9 Crack initiation and growth, extrusion: 20A11, $\sigma = 128$ MPa, $N_f = 4.5 \times 10^8$, rotating bending. Note that the crack initiates at beyond 10^8 cycles.

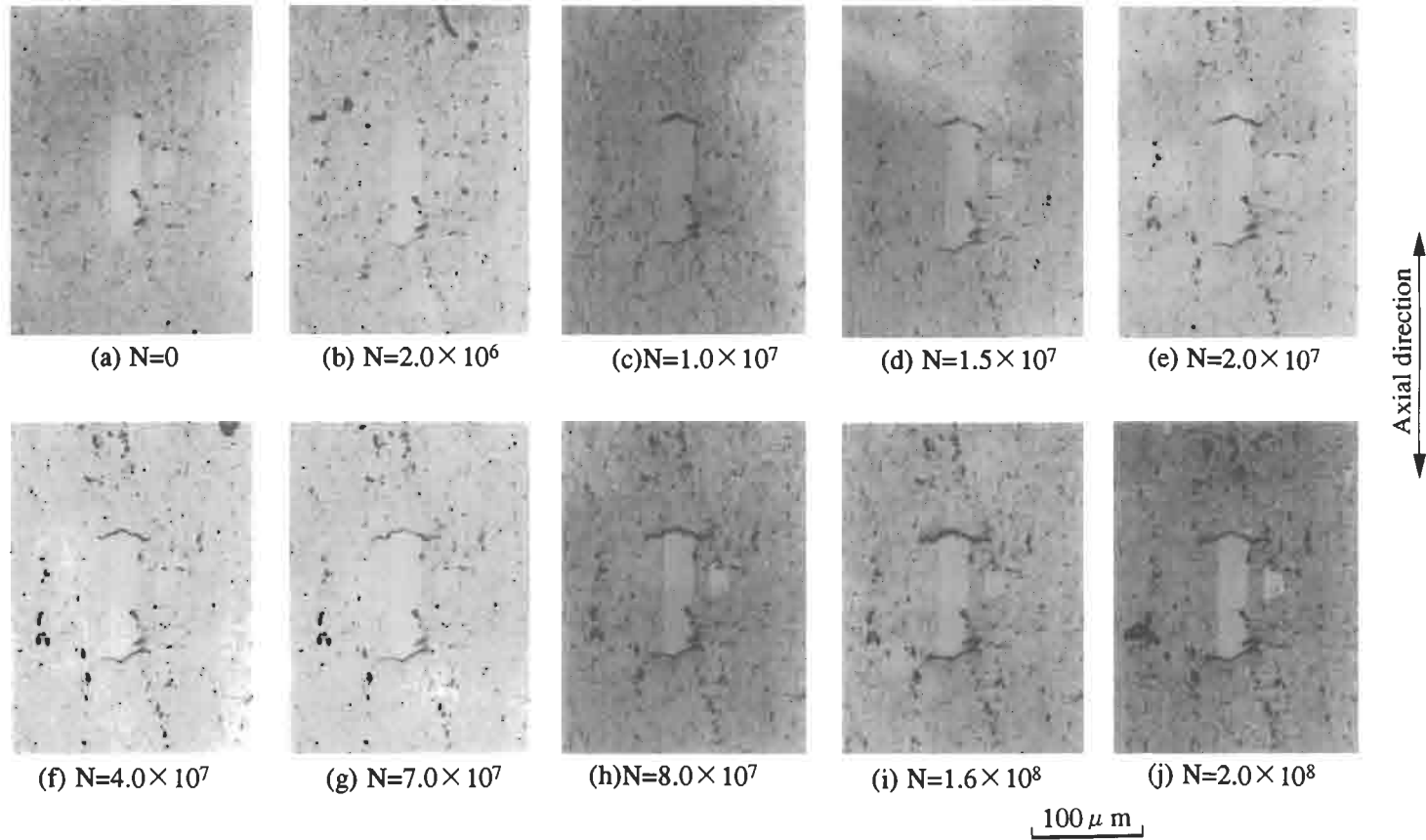


Figure 12.10 Crack initiation at interface between Si phase and matrix, and non-propagation behaviour at superlong endurance, extrusion: 15A11, $\sigma = 127.4$ MPa, $N_f = 2 \times 10^8$, tension compression.

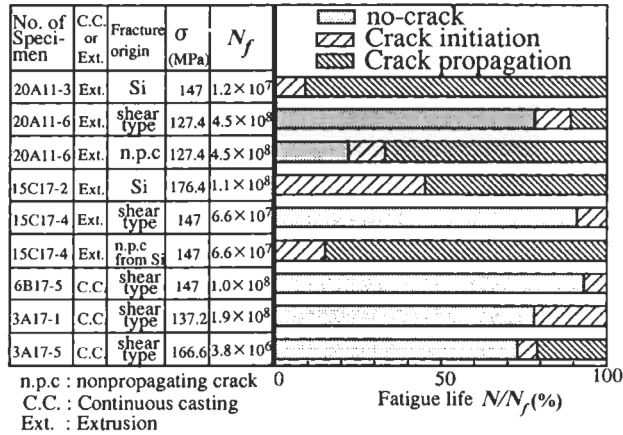


Figure 12.11 Fatigue life percentages, rotating bending, $f = 110\text{--}150$ Hz.

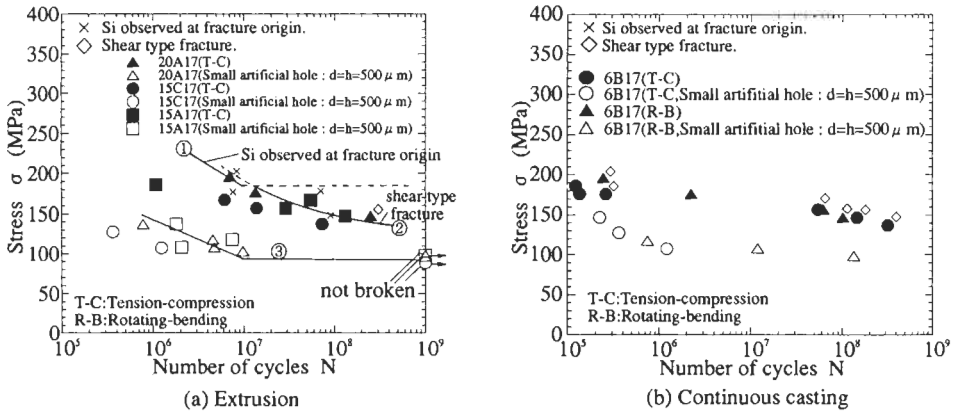


Figure 12.12 $S\text{--}N$ curves for specimens containing a small artificial hole, tension compression, $f = 100$ Hz, rotating bending, $f = 110\text{--}150$ Hz.

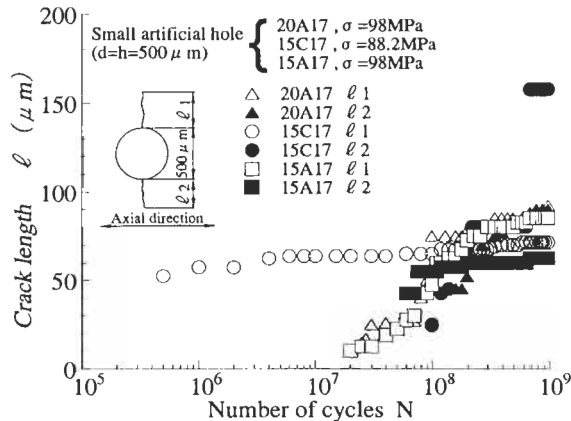


Figure 12.13 Crack growth behaviour from a small artificial hole, tension compression, $f = 100$ Hz.

of plasticity induced crack closure and oxide induced crack closure. This problem still remains unsolved. In the case of fatigue, failure from inclusions in steels in the gigacycle regime, the effect of hydrogen must be considered, as described in Chapter 15.

The different mechanism in Al alloys is shear-type crack initiation and growth beyond $N = 10^8$. Since cracks emanating from Si phase tend to show non-propagating behaviour for $N \simeq 10^8$, the initiation and growth of shear-type crack may be regarded as a main cause of fatigue failure at $N \geq 10^8$.

Thus, the fatigue failure mechanisms of Al alloys in superlong high-cycle fatigue are different from those of steels. Shear-type cracks initiate in aluminium microstructure at $N \geq 10^8$, and continue to grow, without crack closure mechanisms, until specimen failure. However, cracks emanating from inhomogeneities, such as Si phase, or small defects, behave like a non-propagating cracks in steels, in which crack closure mechanisms are thought to prevail.

12.4 Low-Cycle Fatigue (see also ref. [3])

The specimen geometry used is shown in Fig. 12.14. Specimen preparation entailed polishing with #2000 emery paper, buff finishing, and $2 \mu\text{m}$ chemical etching (600 ml phosphoric acid, 10 ml H_2SO_4 , 1400 ml distilled water) followed by neutralisation in a 5% NaOH solution. Fatigue tests were performed in a servo-hydraulic system, under strain control, at cyclic frequencies between 0.1 and 0.5 Hz. Crack development was monitored by means of plastic surface replicas, and fracture surfaces were examined using scanning electron microscopy in order to ascertain the details of operative fatigue mechanisms.

12.4.1 Fatigue Mechanism

Extensive observations of specimens revealed two basic fatigue failure mechanisms: (1) fracture origin in the Si phase, or at the interface between Si and the matrix; and (2) shear crack initiation and growth in the matrix. Details of each mechanism, as influenced by material processing, are discussed in the following sections.

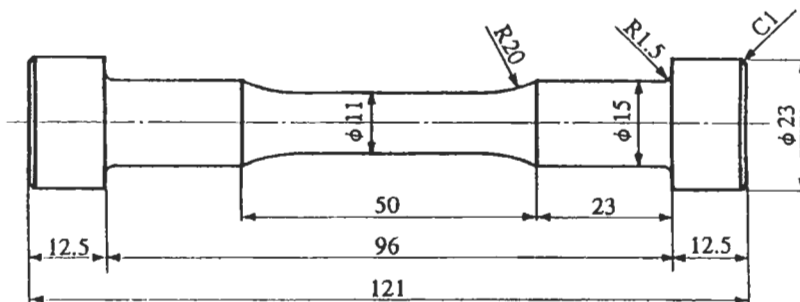


Figure 12.14 Low-cycle fatigue specimen geometry, dimensions in mm.

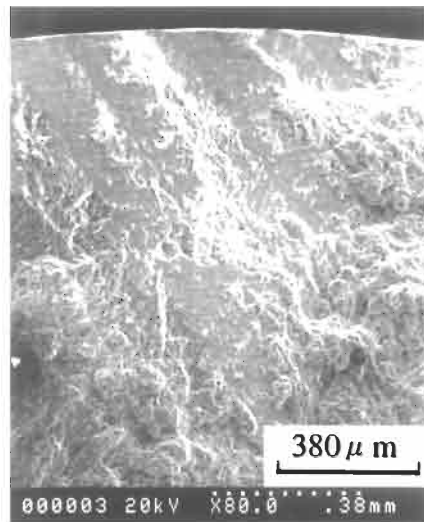


Figure 12.15 Fracture surface near fracture origin, continuous casting: 3A17, $\Delta\epsilon/2 = 0.01$, $N_f = 52$.

12.4.2 Continuously Cast Material

A representative fatigue fracture surface for the 3A17 material is shown in Fig. 12.15. Here a single shear-type crack initiated in the Al matrix, and propagated to a critical size in a shear mode, that is inclined at $\sim 45^\circ$ to the surface. No other cracking was observed. Such shear cracks are found to form before interfacial separation between the Si phase and the matrix.

12.4.3 Extruded Material

In contrast to the above behaviour, the fracture surface for the 20A17 material is shown in Fig. 12.16, along with surface observations of crack growth in Fig. 12.17. Here it can be seen that cracks form early in the life, invariably in the Si phase, and the low-cycle fatigue process is essentially one of crack growth. This behaviour is similar to that observed in medium carbon steel (0.46 C) where cracks form in the pearlite phase in the early stages of low-cycle fatigue, leading to final fracture [4].

12.4.4 Comparison with High-Cycle Fatigue

Stress life plots, incorporating results from this study, and from the previous high-cycle fatigue study, are shown in Fig. 12.18. The low-cycle data represent the steady-state stress response at the half life. As indicated, the continuously cast material exhibits a shear-type failure mechanism throughout the life regimes; the fracture process is essentially the same for low-cycle and high-cycle tests. Fracture topography for a high-cycle test is shown in Fig. 12.4a; the similarities with Fig. 12.15 are noteworthy.

By way of comparison, cracks for the two extruded conditions, shown in Fig. 12.18,

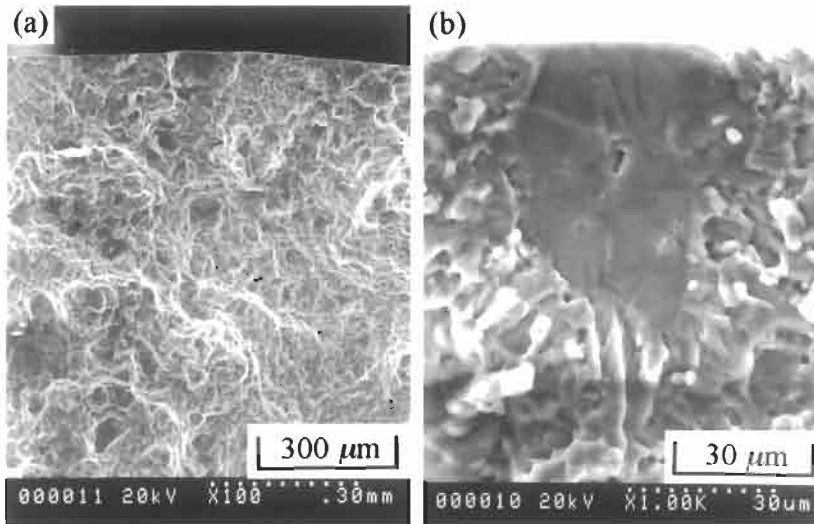


Figure 12.16 Fracture surface near fracture origin which is at Si phase, extrusion: 20A17, $\Delta\epsilon/2 = 0.0075$, $N_f = 421$.

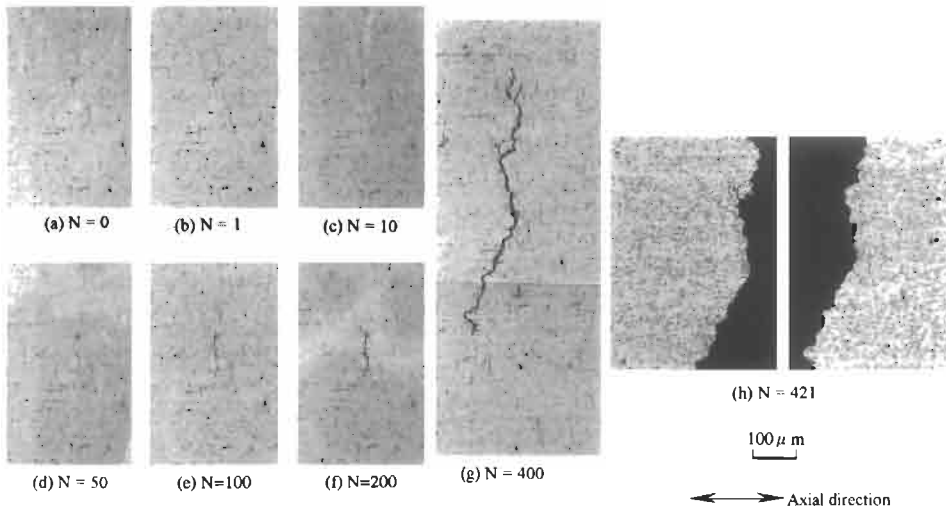


Figure 12.17 Crack initiation and growth, fracture origin at Si phase, extrusion: 20A17, $\Delta\epsilon/2 = 0.0075$, $N_f = 421$.

tend to initiate in the silicon phase, as evidenced by the presence of silicon at the fracture origins. A typical fracture surface for this condition, shown in Fig. 12.19, exhibits features very much like those found in the low-cycle regime (Fig. 12.16). Again, similar mechanisms appear to be operative in both the low- and high-cycle regimes, except at extremely long lives where shear-type failure, similar to the continuously cast material, may be observed.

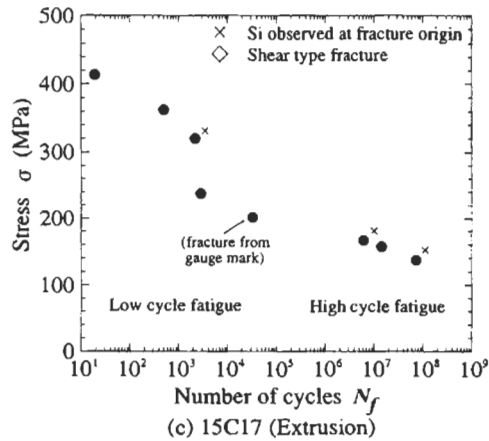
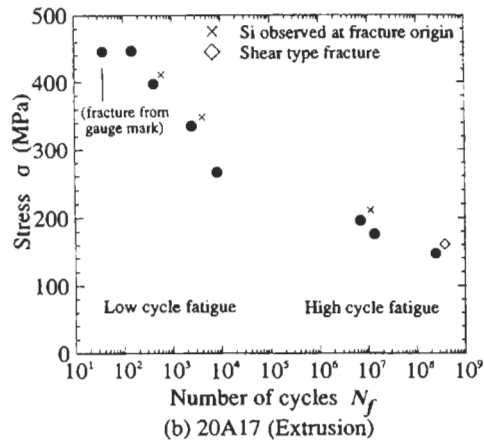
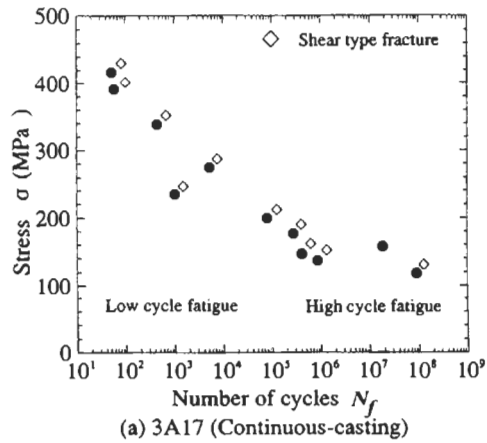


Figure 12.18 Stress life plots for three conditions.

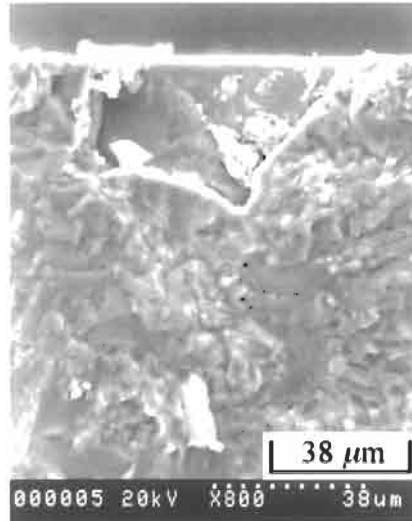


Figure 12.19 Fracture surface with origin at Si phase, extrusion: 20A17, $\sigma = 196$ MPa, $N_f = 7 \times 10^6$.

These observations are of particular relevance when making life predictions for complex service histories that contain events in both the low- and high-cycle regimes. Cumulative damage methods must account for the operative fatigue mechanisms, including the relative contributions of crack initiation and growth.

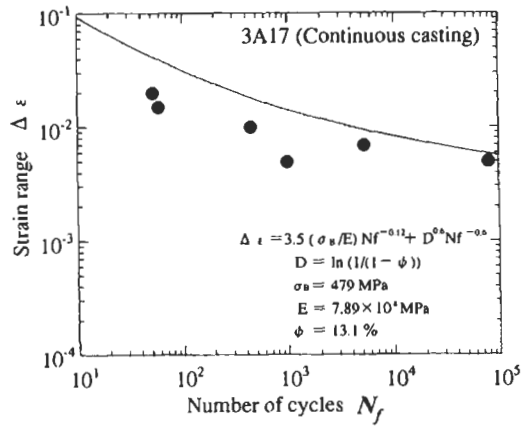
12.4.5 Cyclic Property Characterisation

Fatigue life prediction methods, based on a material's strain cycling resistance are finding increased application in automotive design because of their ability to handle both low- and high-cycle fatigue problems, and to account for material plasticity during high-level service events [5,6]. Central to these procedures is a relationship between strain amplitude, $\Delta\varepsilon/2$, and fatigue life in reversals, $2N_f$, of the following form:

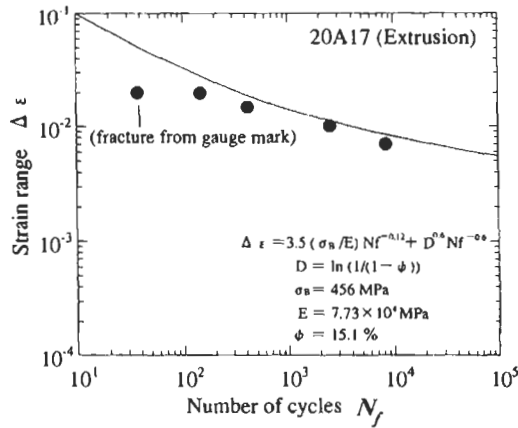
$$\frac{\Delta\varepsilon}{2} = \frac{\sigma'_f}{E}(2N_f)^b + \varepsilon'_f(2N_f)^c \quad (12.1)$$

where E is Young's modulus and σ'_f , b , ε'_f , and c are cyclic material properties. Strain life curves for the three alloy conditions are shown in Fig. 12.20, together with the associated cyclic properties. These were obtained by regression analyses of experimental data summarised as in Table 12.4. The high correlation coefficients indicate an excellent fit.

The intercept values at one reversal, σ'_f and ε'_f , can be related to the true fracture strength and ductility, as determined from a monotonic tension test. The data points for one reversal in Figs. 12.18 and 12.20, obtained from Table 12.5, are seen to agree reasonably well with the fatigue data. Correlations of this type provide useful guidelines for material and process selection based on considerations of a material's relative strength and ductility: strength dominates at long lives, ductility at short lives.



(a) 3A17(Continuous casting)

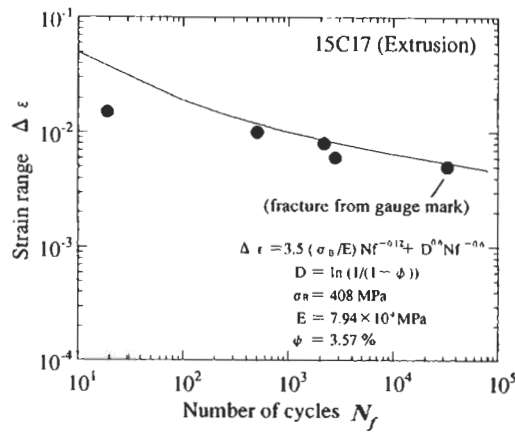


(b) 20A17(Extrusion)

Figure 12.20 (continued on next page.)

Table 12.4 Cyclic material properties

Property	3A17	20A17	15C17
E , GPa	78.9	77.3	79.4
σ'_f , MPa	560	570	475
b	-0.084	-0.067	-0.066
correl. coeff.	0.94	0.96	0.92
ϵ'_f	0.115	0.173	0.027
c	-0.77	-0.73	-0.63
correl. coeff.	0.98	0.99	0.97



(c) 15C17(Extrusion)

Figure 12.20 Strain life curves for three conditions.

Table 12.5 Mechanical properties of materials

Code	$\sigma_{0.2}$	σ_u	σ_f	%RA	HV 200g	HV 3g
3A17	402	479	522	13.1	169	120
20A17	396	456	508	15.1	161	119
15C17	378	408	423	3.6	164	118

$\sigma_{0.2}$: 0.2% offset yield strength, MPa
 σ_u : Ultimate tensile strength, MPa
 σ_f : True fracture stress, MPa
 %RA : Percent reduction in area
 HV : Vicker's hardness number, kgf/mm²

A comparison of the strain cycling resistance of the three materials in Fig. 12.20 reveals that the 20A17 extruded material, by virtue of a favourable balance of strength and ductility, provides the best overall fatigue performance. At short lives, the continuously cast material, 3A17, is comparable, while the low ductility 15C17 condition is inferior. A lower ductility material is also generally more sensitive to notches and other geometric defects.

Manson [7] has proposed an alternative scheme for predicting a material's strain life curve in the following form:

$$\Delta \epsilon = 3.5 \left(\frac{\sigma_u}{E} \right) N_f^{-0.12} + D^{0.6} N_f^{-0.6} \tag{12.2}$$

where D is the fracture ductility given by $\ln\{100/(100 - \%RA)\}$. When applied to the current data sets, reasonable agreement was found for the extruded conditions at

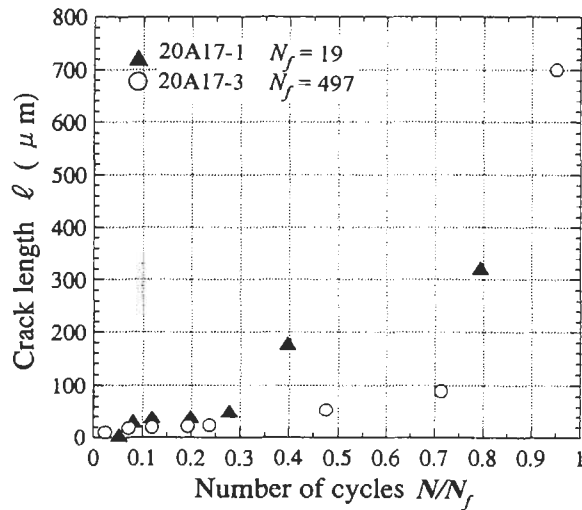


Figure 12.21 Crack growth curves for 20A17 extruded material.

long lives; however, predictions for the continuously cast condition were uniformly unconservative. Part of this disparity can be attributed to the use of constant exponents in the life relation; a ‘ b ’ value of -0.12 is much higher in absolute magnitude than the experimental values in Table 12.4.

Furthermore, Murakami et al. [4] have demonstrated that for many materials the low-cycle fatigue process is dominated by crack growth, hence the Manson–Coffin law, the second term in Eq. 12.2, can be considered to be a crack growth law. In this study, the extruded conditions tended to be dominated by crack growth, thus resulting in better agreement with Eq. 12.2. Crack growth data for the 20A17 extruded condition, shown in Fig. 12.21, confirm that a large fraction of the life is spent in propagating a fatigue crack.

The continuously cast material, however, exhibited a shear mode process, in which crack initiation is the more dominant event. These issues must be considered when formulating damage assessment models for irregular loading histories.

12.5 Summary

Understanding the microstructural aspects of fatigue is crucially important for the application of Al–Si eutectic alloys.

(1) For the continuously cast material, cracks initiate in the matrix and growth is by a shear mode; crack growth is rapid, initiation is a major fraction of life.

(2) In extruded material, crack initiation occurs in the Si-phase, or at the Si-matrix interface; cracks initiate early in the life, followed by Mode I growth. An exception is noted at very long lives, $>10^8$, where shear mode crack initiation is observed in the matrix.

(3) Strain life data for all conditions can be accurately described by a two-term relationship (Eq. 12.1) incorporating material strength and ductility parameters.

(4) Based on a favourable combination of strength and ductility, the 20A17 extruded material provides the best overall fatigue resistance.

(5) Manson's predictive model provides reasonable approximations at long lives for the extruded material, but tends to be unconservative for the continuously cast material, and for the low-cycle region, for all conditions.

(6) A detailed understanding of such damage mechanisms is important when developing cumulative damage models for predicting fatigue performance under irregular service histories that contain both low- and high-cycle events.

12.6 References

1. Y. Murakami, T. Takafuji, H. Ikeda and E. Coudert: Influence of Si phase on mechanical properties of Al-Si eutectic alloys, APCFS '93, Asian Pacific Conf. on Fracture and Strength, **37** (1993) 37–42.
2. H. Kobayashi, H. Ikeda and Y. Murakami: Extra-long life fatigue properties of Al-Si eutectic alloy by rotating-bending and tension-compression fatigue tests, *Trans. Jpn. Soc. Mech. Eng. Ser. A*, **62**(594) (1996), 347–355.
3. Y. Murakami, H. Kobayashi, H. Ikeda and R.W. Landgraf: SAE Paper No. 970704, Low Cycle Fatigue Properties of Al-Si Eutectic Alloys, 1997, pp. 1–6.
4. Y. Murakami, S. Harada, T. Endo, H. Tani-Ishi and Y. Fukushima: Correlations among growth law of small cracks, low-cycle fatigue law and applicability of Miner's rule, *Eng. Fract. Mech.*, **18**(5) (1983), 909–924.
5. *Fatigue Design Handbook*, AE-10, Soc. Auto. Eng., Warrendale, PA, 1988.
6. *Durability by Design: Integrated Approaches to Mechanical Durability Assurance*, SP 730, Soc. Auto. Eng., Warrendale, PA, 1987.
7. S.S. Manson: Fatigue: A Complex Subject-Some Simple Approximations, *Exp. Mech.* **5–7** (1965) 193–226.

Chapter 13

Ti Alloys

Ti alloys have high specific strength, high temperature resistance, and corrosion resistant properties. The commonest application is to aircraft components, such as turbine fan disks. More extended applications are anticipated to structures at high temperature, ultra low temperature, corrosive environments, strong magnetic fields, and radioactive environments.

Typical commercial materials of Ti alloys are Ti–6Al–4V, Ti–5Al–2.5Sn ELI (extra-low-interstitial) and Ti–6Al–2Sn–4Zn–2Mo–0.1Si (Ti–6242S). Although some fatigue behaviours of Ti alloys are similar to those of steels, the particular crystallographic structure does cause some strange fatigue behaviours quite different from steels. Fig. 13.1 shows the relationship between fatigue limit and Vickers hardness, H_V , which Minakawa [1] obtained by analysing data from the literature. The line showing the empirical formula $\sigma_w = 1.6 H_V$ for steels was added by the author. Since it is known that the empirical relationship between UTS and Brinell hardness, H_B , for steels also holds for Ti alloys [2], the value of UTS was converted into H_B and accordingly into the abscissa, H_V , of Fig. 13.1. The scatter of fatigue strength in steels, with respect to the relationship $\sigma_w = 1.6 H_V$, is small up to $H_V = 400$ (see Figs. 1.6 and 1.7). However, the scatter of fatigue strength in Ti alloys is very large, even at $H_V = 300$ –400. If we take the experiences and discussions in the previous chapters into consideration, we should first of all pay attention to defects or inclusions as the cause of the scatter. However, in most studies on Ti alloys, no defects and inclusions were observed at subsurface fracture origins [3–8].

Nagai and Ishikawa [7], Nagai et al. [9], and Umezawa et al. [6,8] investigated in detail the fatigue behaviour at ultra low temperature, and reported that no inherent defects or inclusions were observed, at the subsurface fracture origins, of specimens which failed in the high cycle fatigue regime. A common morphology in all specimens is a facet, which has a size of several μm , and is oriented at a constant angle to the tensile axis. These facets always appear in Ti–6Al–4V regardless of test temperature. Thus, the cause of the subsurface fracture is thought to be cracking by deformation incompatibility, which is produced by the limited active slip planes between the interfaces of α and β phases.

However, the above results do not necessarily exclude the possibility of fatigue fracture from defects and inclusions. If defects and inclusions, relatively larger than

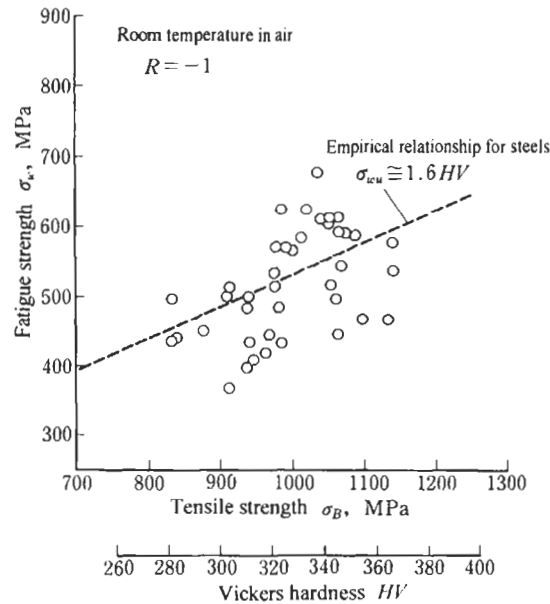


Figure 13.1 Relationship between fatigue strength and ultimate tensile strength, or Vickers hardness, for Ti alloys.

a phase, are present in the microstructure, then such defects and inclusions may have priority as fatigue fracture origins. In fact, Nagai et al. [9] showed that a blow hole 100 μm in size in a welded component became the fatigue fracture origin. Estimating the value of $\sqrt{\text{area}}$ of the blow hole and the Vickers hardness, the fatigue limit, σ_w , was calculated by applying the $\sqrt{\text{area}}$ parameter model described in Chapter 5. The value of σ_w obtained was much lower than the applied stress at which the specimen failed in the experiments of Nagai et al. [9]. Although this estimate does not necessarily completely guarantee the validity of the $\sqrt{\text{area}}$ parameter model for Ti alloys, we at least need to conduct quantitative analysis on many data with respect to the size and shape of defects and facets at fracture origins, and on the hardness of the microstructures.

The reason why nonmetallic inclusions do not become fatigue fracture origins may be that the sizes of inclusions are much smaller than blow holes at welds and the grain size of α phase, which causes incompatibility between β phase regions.

Since at present there are almost no clear and detailed observations on the micromechanisms of fatigue behaviour of Ti alloys at the fatigue limit, the above discussion is only the analogy, or presumption, based on experience with steels. Takao and Kusukawa [10] reported that the behaviour of a fatigue crack emanating from a notch in pure Ti is quite different from that of cracks in steels, and also that cracks in pure Ti, even in the case of a sharp notch, do not show the non-propagating behaviour which is very common in steels. The concept of ΔK_{th} , and its application, which has been developed in previous chapters is essentially based on the non-propagating behaviour of fatigue cracks emanating from small defects. If we apply the same concept to Ti alloys,

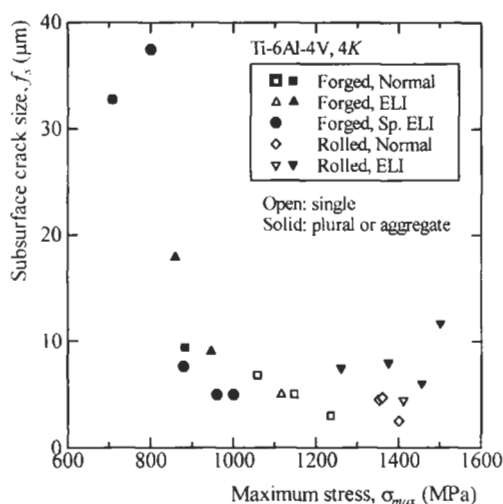


Figure 13.2 Relationship between maximum stress σ_{max} and facet size f_s for Ti-6Al-4V alloys under $R = 0.01$ (Umezawa et al. [8]).

then we have to examine the threshold behaviours of fatigue cracks in Ti alloys. In this sense, the study of Kobayashi et al. [11] is very suggestive, because they reported quite early the dependence of ΔK_{th} on crack size in Ti alloys.

From this viewpoint, we review again the data reported by Umezawa et al. [8]. As shown in Fig. 13.2, Umezawa et al. plotted the relationship between the applied stress range, $\Delta\sigma_{max}$, and $\Delta\sigma_{max}\sqrt{f_s}$ where f_s is the size of a facet at a fracture origin. They regarded the values of $\Delta\sigma_{max}\sqrt{f_s}$ to be equivalent to the stress intensity factor range ΔK , and concluded that the relationship $\Delta K_{th} = \text{constant}$ holds for subsurface fatigue fracture. The definition of facet size, f_s , is ambiguous for the calculation of stress intensity factors, and values of ΔK_{th} in their paper show much scatter, ranging from 2 to 5 $\text{MPa m}^{1/2}$. This large scatter means that the stress at the fatigue limit is scattered by a factor of 2.5, and the size of facets by a factor of magnitude of $2.5^2 (\cong 6.25)$. Thus, the conclusion that $\Delta K_{th} = \text{constant}$ is very rough. Since the data they plotted are not those of fatigue limits, but are those of fractured specimens, we should treat these data with caution in the discussion of ΔK_{th} .

In any case, since the work of Kitagawa and Takahashi [12], it has been an established concept that ΔK_{th} has a crack size dependency; it has smaller values as crack sizes become smaller. We cannot ignore this important concept in the interpretation of fatigue data. Thus, Umezawa et al.'s [8] data (Fig. 13.2) are replotted in Fig. 13.3 to show the relationship between $\Delta\sigma_{max}\sqrt{f_s}$ (equivalent to ΔK_{th}) and f_s . The figure reveals a clear crack size dependency of ΔK_{th} as $\Delta K_{th} \propto (f_s)^{1/3}$, which is essentially the same as for other materials (see Fig. 5.1). Therefore, Fig. 13.3 implies that the facets of a phase at fatigue fracture origins in Ti alloys may have the role which is identical to defects and inclusions in steels. Many hypotheses have been presented in response to this question, though there is no established consensus.

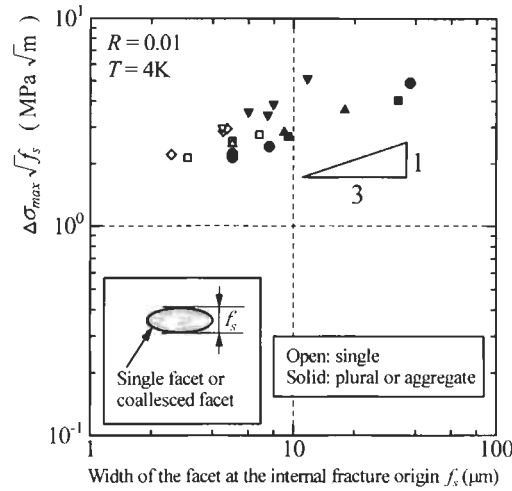


Figure 13.3 Relationship between $\Delta\sigma_{\max}\sqrt{f_s}$ and facet size, f_s , at subsurface fracture origins.

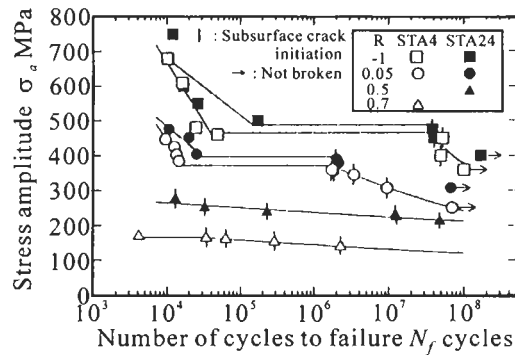


Figure 13.4 $S-N$ curves in air at room temperature for Ti alloys aged for 4 h (STA4) and 24 h (STA24) (Shiozawa et al. [13]).

On the other hand, there are some studies reporting that if Ti alloys are tested up to the regime of $N \geq 10^7$ cycles, fatigue fracture origins are mostly subsurface [13,14]. Fig. 13.4 shows an example of such data, obtained by Shiozawa et al. [13]. The problem of superlong fatigue of steels is treated in Chapter 15. The solution of the problems of steels may also lead to the solution of the fatigue mechanism at a phase in Ti alloys.

13.1 References

1. K. Minakawa: Fatigue of titanium alloys, *Tetsu to Hagan*, **75**(7) (1989), 1104–1111.
2. M. Okada: Private Communication (1992).
3. D.F. Neal and P.A. Blenkinsop: Internal fatigue origins in α - β titanium alloys, *Acta Met.*, **24** (1976), 59–63.

4. D. Eylon and J.A. Hall: Fatigue behavior of beta processed titanium alloy IMI 685, *Met. Trans. A*, **8** (1977), 981–990.
5. R. Chait and T.S. DeSisto: The influence of grain size on the high cycle fatigue crack initiation of a metastable beta Ti alloy, *Met. Trans. A*, **8** (1977), 1017–1020.
6. O. Umezawa, K. Nagai and K. Ishikawa: Internal crack initiation in high cycle fatigue for Ti-5 Al-2.5 Sn ELI alloy at cryogenic temperatures, *Tetsu to Hagane*, **75**(1) (1989), 159–166.
7. K. Nagai and K. Ishikawa: Deformation and fracture characteristics of titanium alloys at low temperatures, *Tetsu to Hagane*, **75**(5) (1989), 707–715.
8. O. Umezawa, K. Nagai and K. Ishikawa: Subsurface crack initiation in high cycle fatigue of Ti-6Al-4V alloys at cryogenic temperatures, *Tetsu to Hagane*, **76**(6) (1990), 924–931.
9. K. Nagai, T. Ogata, T. Yuri, K. Ishikawa, T. Nishimura, T. Mizoguchi and Y. Ito: Fatigue fracture of Ti-5Al-2.5Sn ELI alloy at liquid helium temperature, *Tetsu to Hagane*, **72**(6) (1986), 641–648.
10. K. Takao and K. Kusukawa: Fatigue crack initiation behavior in notched member of commercially pure titanium, *J. Soc. Mater. Sci. Jpn.*, **40**(458) (1991), 1422–1427.
11. H. Kobayashi, Y. Kawada and H. Nakazawa: Initial stage of fatigue cracking in pure titanium under bending and torsion, *J. Soc. Mater. Sci. Jpn.*, **27**(300) (1978), 859–864.
12. H. Kitagawa and S. Takahashi: Fracture mechanics approach to very small fatigue crack growth and to the threshold condition, *Trans. Jpn. Soc. Mech. Eng. A*, **45**(399) (1979), 1289–1303.
13. K. Shiozawa, Y. Kuroda and S. Nishino: Effects of stress ratio on subsurface fatigue crack initiation behavior of beta-type titanium alloy, *Trans. Jpn. Soc. Mech. Eng. Ser. A*, **64**(626) (1998), 2528–2535.
14. T. Nakamura, M. Kaneko, T. Noguchi and T. Teraguchi, *Proc. JSME 1999 Annual Meeting*, Vol. III, 1999, pp. 79–80.

Chapter 14

Torsional Fatigue

14.1 Introduction

So-called classical studies on biaxial (combined stress) fatigue ranging from tension–compression to pure torsion under constant amplitude are well known. However, due to a lack of attention to the behaviour of small cracks, the effects of mechanical and microstructural factors on the fatigue strength of materials, containing small cracks and defects under biaxial or multiaxial stresses, have not been made clear. The behaviour of small fatigue cracks under multiaxial stress has been investigated by several workers [1–6]. Carbonell and Brown [3] investigated short crack growth under torsional low cycle fatigue in a medium carbon steel. They showed that short crack growth in torsional low cycle fatigue is similar to that in tension–compression low cycle fatigue. Socie et al. [4] investigated the behaviour of small semi-elliptical cracks under cyclic torsion and cyclic tension–torsion. They showed that strain-based intensity factors are useful correlating parameters for mixed mode small crack growth. Wang and Miller [5] studied the effect of mean shear stress on short crack growth under cyclic torsion. They showed that a mean shear stress promotes Stage I (Mode II) crack growth, and proposed a model to account for the effect of mean shear stress on fatigue life under torsional loading. Zhang and Akid [6] studied short crack growth in two steels under reversed cyclic torsion with an axial tensile or compressive mean stress. They pointed out that a compressive mean stress was beneficial to the life of both steels.

Murakami and Endo [7] studied the effects of small defects and cracks in rotating bending and tension–compression fatigue, and proposed a prediction model based on the $\sqrt{\text{area}}$ parameter model (Chapter 5). Investigating the behaviour of small cracks using this model is useful in deciding whether the effect of small cracks on multiaxial fatigue is controlled by the Mode I threshold or that for the shear mode.

The effects of small defects and small cracks on torsional fatigue strength are discussed in this chapter.

The effects of artificial small defects on torsional fatigue strength have been studied in various materials using specimens which contain a small drilled hole as an initial defect [8–11,13]. The effects of an initial small crack on torsional fatigue have been studied by Murakami et al. [12]. The results of their experiment are useful in the understanding of crack branching and threshold phenomena under multiaxial fatigue.

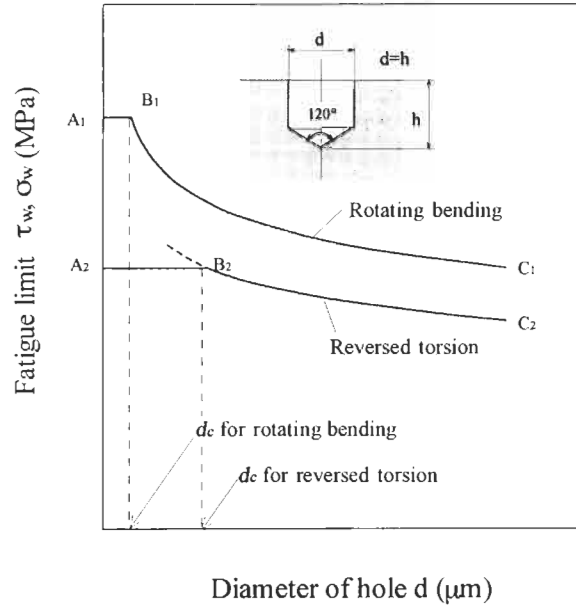


Figure 14.1 Relationship between fatigue limit and hole diameter in rotating bending and in reversed torsion.

14.2 Effect of Small Artificial Defects on Torsional Fatigue Strength

14.2.1 Ratio of Torsional Fatigue Strength to Bending Fatigue Strength

Several studies have been performed in order to investigate the effect of small artificial defects on torsional fatigue strength [8–11,13]. Endo and Murakami [9] conducted both rotating bending and torsional fatigue tests on annealed 0.46% C steel (S45C) specimens, which contained small artificial holes with diameters ranging from $d = 40$ to $500 \mu\text{m}$. Fig. 14.1 illustrates the test results schematically. The value of d_c in Fig. 14.1 is the critical hole diameter which does not affect fatigue strength. The value of d_c in torsional fatigue is much larger than d_c in rotating bending fatigue [9–13]. Later, similar rotating bending and torsional fatigue tests were carried out on a high carbon bearing steel, SUJ2 (equivalent to SAE 52100, $H_V = 740$) by Nose et al. [10], on a nodular cast iron ($H_V = 190$) by Endo [11], and on a maraging steel ($H_V = 740$) by Murakami et al. [13]. The results of the fatigue tests on these four materials, where the depth of a hole is equal to its diameter, indicated that d_c in rotating bending fatigue shows a clear dependence on the hardness of materials. In contrast, d_c in torsional fatigue is approximately constant at $150 \mu\text{m}$, irrespective of the material, that is of hardness [13].

The line B_2C_2 is located at approximately 80% of the line B_1C_1 . This is primarily due to the difference in stress concentration factors (K_t), at the hole, between tension ($K_t = 3$) and torsion ($K_t = 4$) (Fig. 14.2a,b).

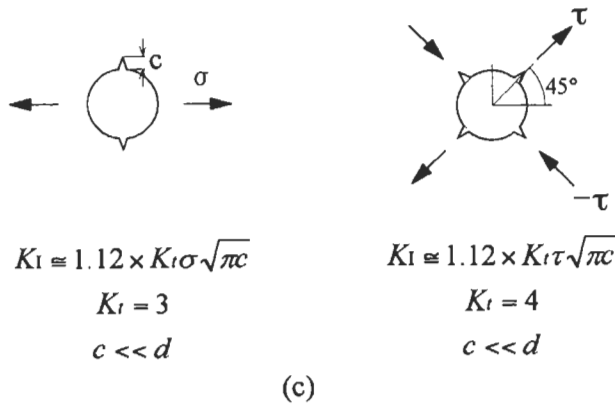
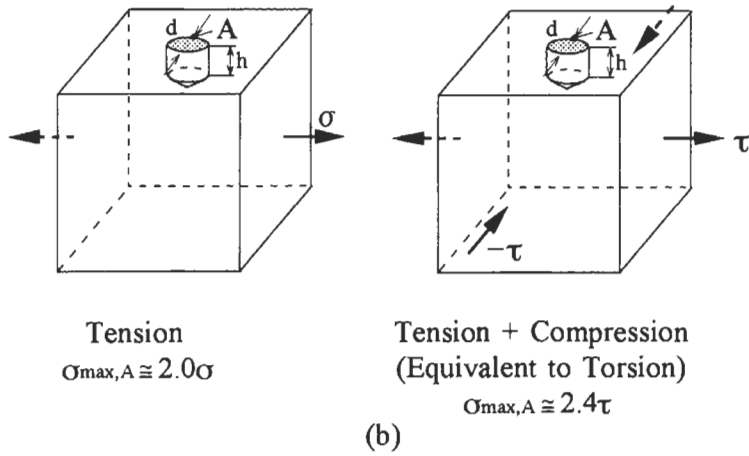
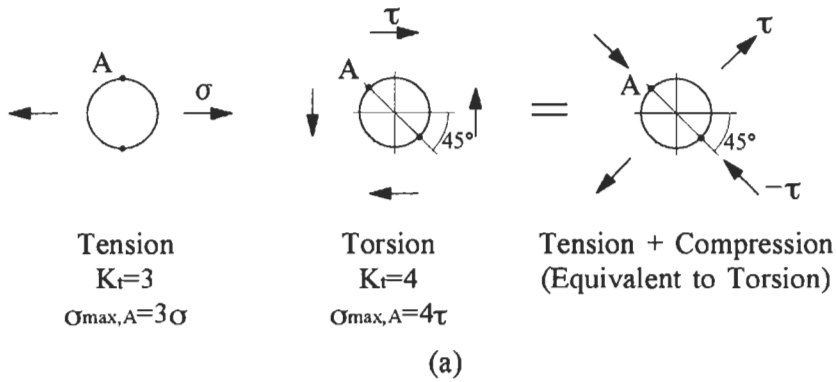


Figure 14.2 Stress analysis of a hole and of a drilled hole. (a) Stress concentration factor for a hole (2D analysis). (b) Stress concentration factor for a drilled hole (3D analysis). (c) Stress intensity factors for cracks emanating from a hole (2D analysis).

Table 14.1 Stress intensity factors for cracks emanating from a circular hole (Fig. 14.3)

λ/a	$F_I = K_I / \sigma_0 \sqrt{\pi\lambda}$	
	Bending Nisitani and Isida, Murakami	Torsion Murakami
0.1	2.78	3.57
0.2	2.41	2.99
0.4	1.97	2.31
0.6	1.73	1.94
0.8	1.57	1.72
1.0	1.47	1.58

$$F_{I0} = 1.1215K_I (\lambda = 0)$$

K_I : Stress concentration factor, Bending, $K_I = 3$, Torsion: $K_I = 4$

Non-propagation of cracks at a hole is the threshold condition for the fatigue limit under both rotating bending and reversed torsion [8–11,13]. Therefore, strictly speaking, the ratio (τ_w/σ_w) of the torsional fatigue limit (τ_w) to the rotating bending fatigue limit (σ_w) for a specimen containing a hole must be treated as a crack problem. If the crack length is relatively short compared to the hole diameter (Fig. 14.2c), then stress intensity factors (K_I) are strongly dependent on the stress concentration factor (K_t) at the hole. Thus, the ratio of K_I for very short cracks for the defects in bending and torsion is approximately equal to the ratio of K_t for the defects in bending and torsion.

According to Nisitani and Kawano's experiments [14] on 0.35% C steel specimens containing an artificial hole of 0.3 mm diameter, the ratio of the torsional fatigue limit, τ_w , to the rotating bending fatigue limit, σ_w , is $\tau_w/\sigma_w \approx 0.75$, which is equal to the ratio of stress concentration factors in torsion and bending: 3/4. This result follows from the fact that the maximum stress at a hole edge is $3\sigma_w$ for rotating bending and $4\tau_w$ for torsion, and that the condition at the fatigue limit is identical for both torsion and bending, that is $3\sigma_w = 4\tau_w$, so that $\tau_w/\sigma_w = 0.75$. However, since in some cases non-propagating cracks at a hole have a size of the order of the hole diameter, strictly speaking we need to compare the stress intensity factors for cracks emanating from a hole in torsion and in bending.

Table 14.1 and Fig. 14.3 show the results of 2D analysis of stress intensity factors for cracks emanating from a circular hole [15,16]. In Fig. 14.3 stress intensity factors are compared for the same maximum stress at the hole. As the crack length increases the stress intensity for bending becomes a little larger than that for torsion. It follows that τ_w/σ_w for specimens containing a small circular hole should be a little larger than 0.75.

Thus, taking a reasonable value of $\tau_w/\sigma_w \approx 0.8$, the fatigue strength curve for torsion becomes B_2C_2 in Fig. 14.1, which is equivalent to B_1C_1 for bending. Since the fatigue strength of unnotched specimens in torsion can be estimated empirically as 0.57–0.58 times those in tension, we can determine the critical size of hole as B_2 in Fig. 14.1.

Table 14.2 shows the fatigue limits of 0.46% C steel ($H_V = 170$), under torsion and

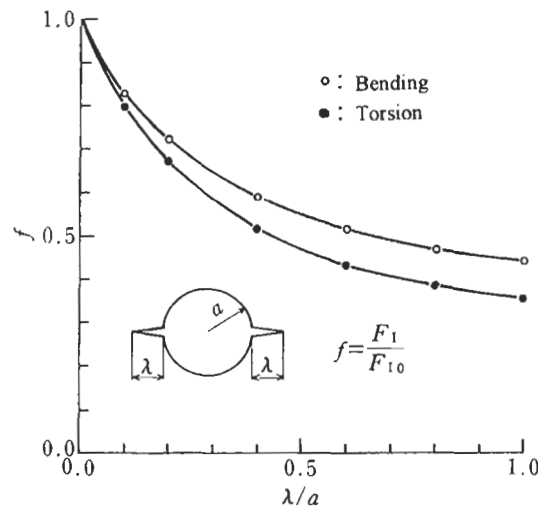
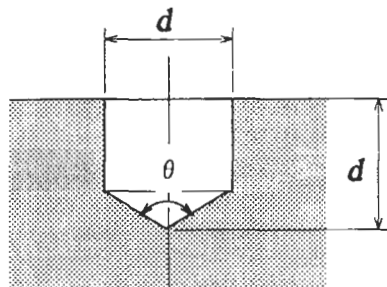


Figure 14.3 Comparison between stress intensity factors for cracks in bending (uniaxial tension) and in torsion.



$\theta = 90 \sim 120^\circ$
 $d = 40, 50, 80, 100,$
 $200, 500 \mu\text{m}$

Figure 14.4 Drilled hole.

bending, for specimens containing artificial drilled holes of two diameters, as shown in Fig. 14.4 [9]. Since three of six unnotched specimens failed at $\tau = 149 \text{ MPa}$ ($= 15.0 \text{ kgf/mm}^2$), $\tau = 142 \text{ MPa}$ ($= 14.5 \text{ kgf/mm}^2$) is taken as the fatigue limit. As expected, $\tau_w/\sigma_w = 0.58\text{--}0.59$ is obtained, and the values of τ_w/σ_w increase with increasing diameter of the artificial hole. The different values of τ_w/σ_w for specimen diameters, $D = 6$ and 10 mm show the size effect due to the stress gradient. Nisitani et al. [14,17] obtained similar values of τ_w/σ_w : 0.59 for 0.13% C steel [17] and 0.58 for 0.35% C steel [14].

Table 14.2 Fatigue limits of specimens containing holes of various diameters

	Diameter of hole $d \mu\text{m}$	Fatigue limit kgf/mm^2		$\frac{\tau_{wD=10}}{\sigma_{wD=10}}$	Fatigue limit kgf/mm^2		$\frac{\tau_{wD=10}}{\sigma_{wD=6}}$
		Torsion $\tau_{wD=10}$	Bending $\sigma_{wD=10}$		Bending $\sigma_{wD=6}$		
Plain specimen	—	14.5	24.5	0.59	25.0		0.58
Specimens containing a small hole	40	14.5	24.0	0.60	24.5		0.59
	50	14.5	23.0	0.63	24.5		0.59
	80	14.5	21.5	0.67	22.0		0.66
	100	14.5	20.5	0.71	21.0		0.69
	200	13.5	18.5	0.73	19.5		0.69
	500	12.0	16.0	0.75	—		—

$\sigma_{wD=10}, \tau_{wD=10}$: Fatigue limit of specimen with diameter of 10 mm.

$\sigma_{wD=6}$: Fatigue limit of specimen with diameter of 6 mm.

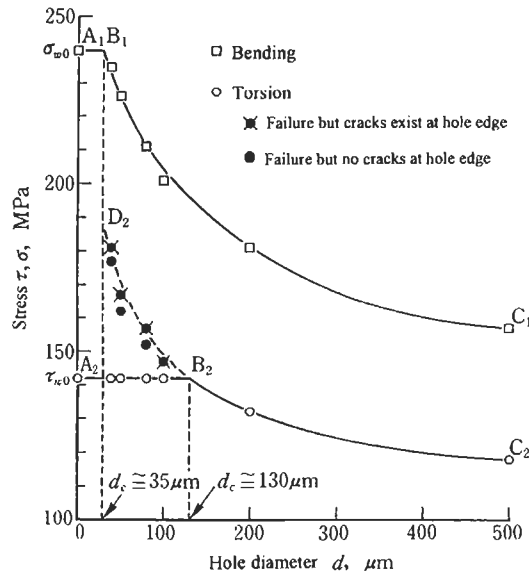


Figure 14.5 Fatigue limit of specimens containing a hole with various diameters: rotating bending and reversed torsion (for explanation of symbols, see text) [9].

Table 14.2 shows that the fatigue limit ratio in torsion and bending τ_w/σ_w ranges from 0.60 to 0.75 for $d = 40\text{--}500 \mu\text{m}$ for specimen with $D = 10 \text{ mm}$. However, the torsional fatigue limit is constant at 142 MPa for $d = 40\text{--}100 \mu\text{m}$, which is identical to the fatigue limit of unnotched specimens. Fig. 14.5 summarises all the data [9]. The symbols \square and \circ indicate data defining the fatigue limits for rotating bending and reversed torsion respectively. The symbols \blacktriangleright and \bullet are specimens broken in torsional fatigue, in particular \blacktriangleright shows specimens which have cracks at holes.

As previously described, the curve for torsion is defined by the horizontal line A_2B_2 and the curve B_2C_2 . Although along the curve B_2C_2 $\tau_w/\sigma_w \approx 0.73\text{--}0.75$, and the value is a little lower than the value ~ 0.8 , which was predicted above, the curve B_2C_2 can be predicted approximately from the data for rotating bending fatigue, that is line B_1C_1 .

14.2.2 The State of Non-Propagating Cracks at the Torsional Fatigue Limit

The state of non-propagating cracks at the fatigue limit determines the threshold condition for the torsional fatigue limit. In particular, we need to check by microscopic observation whether von Mises' yield criterion can explain the reason why the fatigue limit ratio τ_w/σ_w of unnotched specimen in torsion and bending (or tension–compression) has the value ~ 0.58 .

Fig. 14.6 shows a non-propagating crack which was observed at the torsional fatigue limit of an unnotched specimen [9]. The crack length is $\sim 480 \mu\text{m}$. The crack grew along the ferrite layer which elongated during rolling of the original material. Such a long crack was not observed in the circumferential direction with the same value of

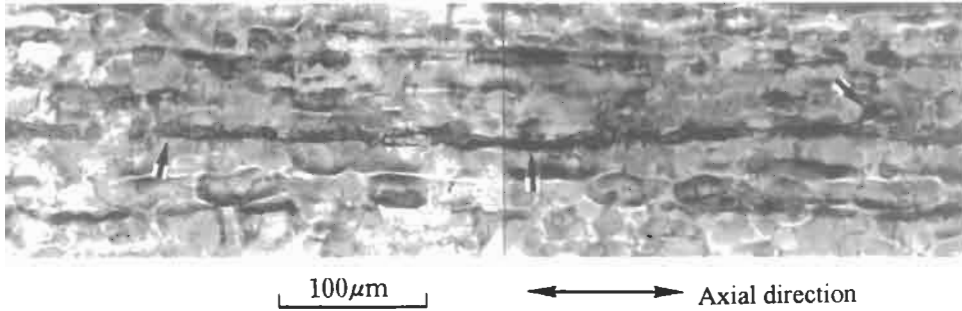


Figure 14.6 Non-propagating crack in an unnotched specimen (length $\cong 480 \mu\text{m}$) [9].

Table 14.3 Size of the largest non-propagating cracks observed in unnotched specimens in rotating bending and in reversed torsion

Loading \ Material	S45C	S10C
Rotating bending	$\sim 50 \mu\text{m}$	$\sim 100 \mu\text{m}$
Cyclic torsion	$\sim 500 \mu\text{m}$	$\sim 1000 \mu\text{m}$

shear stress. Thus, the existence of such long cracks in unnotched specimen is related to the rolled microstructure which consists of ferrite and pearlite layers.

Table 14.3 shows the maximum lengths of non-propagating cracks in unnotched specimens of 0.13% C and 0.46% C steels at the fatigue limit for rotating bending [17,19] and reversed torsion [9,18]. Considering that both the 0.13% C and 0.46% C steel are produced by rolling, the correspondence between the maximum non-propagating crack sizes in torsion and rotating bending in both steels may be for the same reason. The maximum non-propagating crack sizes in torsion are too large to consider that the fatigue limit is determined by von Mises' yield criterion, and it is reasonable to regard the fatigue limit as the threshold condition for crack propagation. There has been some discussion on these points [20]. Recent detailed observations by Murakami and Takahashi [12] shows that, even in torsion fatigue of unnotched specimen, the fatigue limit is determined by the threshold condition of the cracks branching from axial cracks, as in Fig. 14.6 [9]. This means that the fatigue limit in torsional fatigue is essentially determined by non-propagating cracks of the same mode (Mode I), as in rotating bending or tension-compression.

Figs. 14.7–14.9 [9] show the state of artificial holes at the fatigue limit under reversed torsion. Since shear stress in torsion is equivalent to tension at 45° and compression at -45° , non-propagating cracks are observed to emanate from the hole edge at $\pm 45^\circ$ for $d = 500 \mu\text{m}$ and $200 \mu\text{m}$. However, there is no non-propagating crack at the hole for $d = 50 \mu\text{m}$. This is because the stress condition for this case is between A_2 and B_2 on Fig. 14.5.

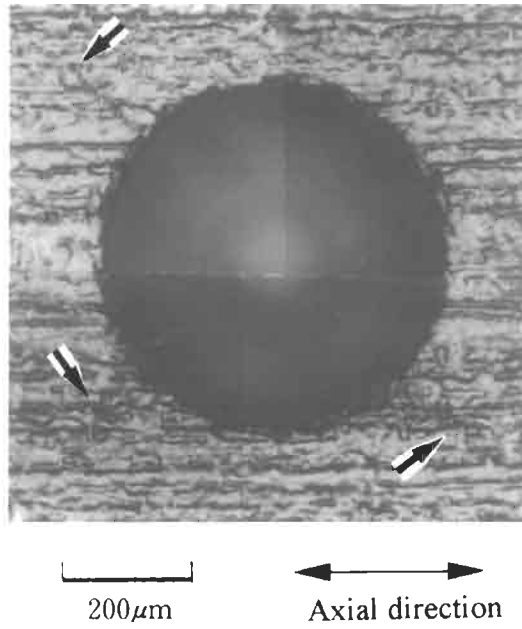


Figure 14.7 Non-propagating cracks at a hole of diameter 500 μm in reversed torsion. $\tau_w = 12.0$ kgf/mm^2 (118 MPa) [9].

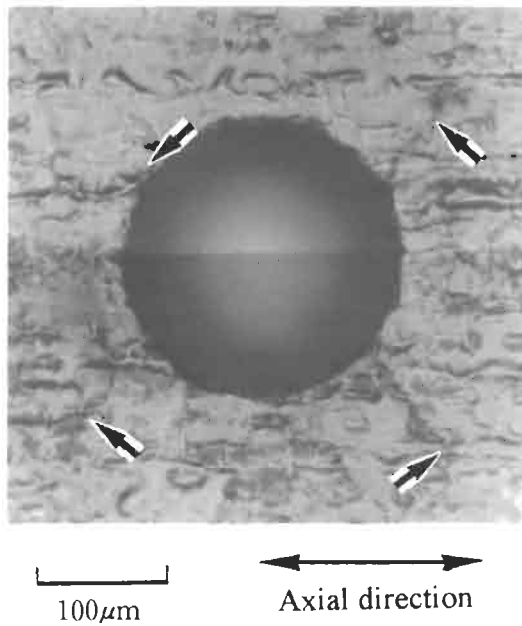


Figure 14.8 Non-propagating cracks at a hole of diameter 200 μm in reversed torsion. $\tau_w = 13.5$ kgf/mm^2 (132 MPa) [9].

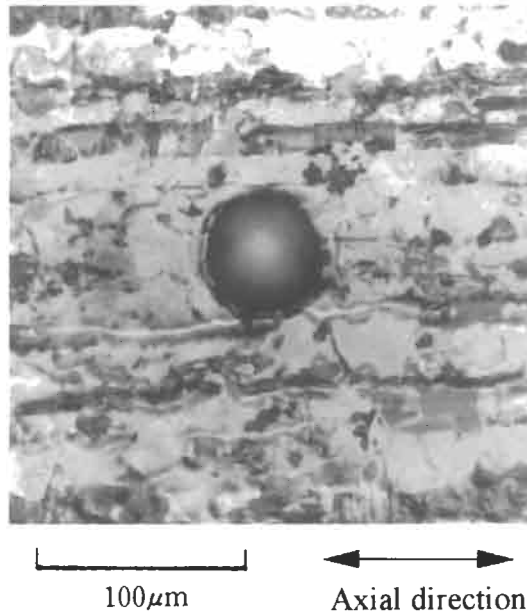


Figure 14.9 Absence of cracks at a hole of diameter $50\ \mu\text{m}$ in reversed torsion. $\tau_w = 14.5\ \text{kgf}/\text{mm}^2$ (142 MPa) [9].

That is, the applied stress is the same as the fatigue limit of unnotched specimens, $\tau_w = 142\ \text{MPa}$, and we can find non-propagating cracks, as in Fig. 14.6, at other places on the same specimen.

However, the stress state at the hole does not satisfy the condition for crack initiation (and non-propagation) as on the curve B_2C_2 . This is because the line A_2B_2 is below the curve D_2B_2 , which is an extrapolation of the curve B_2C_2 .

The existence of the curve D_2B_2 can be confirmed by testing specimens containing an artificial hole of $d < 100\ \mu\text{m}$ at a stress higher than the fatigue limit (line A_2B_2). In such tests all specimens fail away from the hole, but we can observe cracks at the artificial hole. The symbol \blacktriangle in Fig. 14.5 indicates specimens which contained cracks at a hole after specimen failure away from the hole, and the symbol \bullet indicates specimens containing a hole without a crack.

14.2.3 Torsional Fatigue of High Carbon Cr Bearing Steel

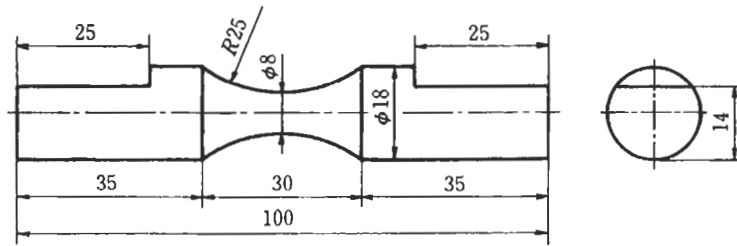
Nose et al. [10] carried out fatigue tests similar to those on 0.46% C steel described in the previous section [9].

Tables 14.4–14.6 show the chemical composition of the material, its inclusion rating by the JIS point counting method, and the mechanical properties.

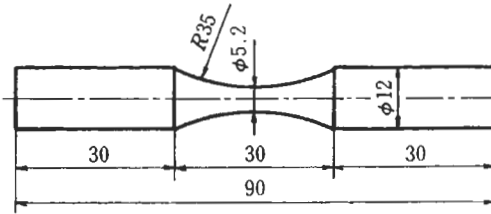
Fig. 14.10 shows the specimen and artificial hole geometries [10]. Fig. 14.11 shows fatigue data for rotating bending and reversed torsion. The results are similar to those for the 0.46% C steel given in the previous section. In rotating bending fatigue, unnotched

Table 14.4 Chemical composition of high carbon Cr bearing steel SAE 52100 (wt.%)

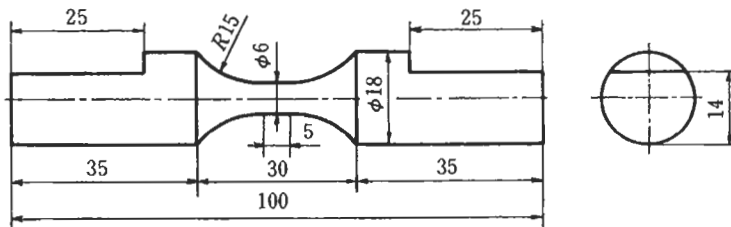
C	Si	Mn	P	S	Cr	Mo	O (ppm)
1.01	0.31	0.31	0.012	0.006	1.54	0.02	7~8



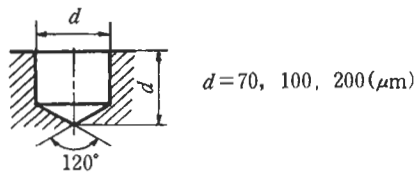
(a)



(b)



(c)



(d)

Figure 14.10 Specimen and hole geometries. (a) Reversed torsion specimen. (b) Rotating bending specimen. (c) Specimen containing a small hole. (d) Geometry of a small hole [10].

Table 14.5 Cleanliness rated by the JIS point counting method

A type	B + C type	Total
0.012	0.004	0.016

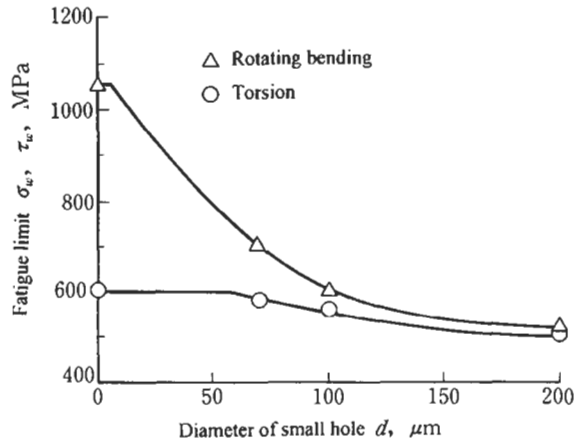


Figure 14.11 Fatigue limit vs diameter of a small hole [10].

specimens failed from nonmetallic inclusions, but specimens containing an artificial hole with $d = 70, 100$ and $200 \mu\text{m}$ failed from these holes. The fatigue limit of unnotched specimens cannot be plotted as one point in Fig. 14.11 but it should be interpreted as a scatter band, which depends on the number of specimens, and on the distribution of nonmetallic inclusions.

In torsional fatigue, one specimen containing an artificial hole of $d = 70 \mu\text{m}$ failed away from the hole (and not from an inclusion). Three of several specimens with artificial holes with $d = 100 \mu\text{m}$ failed away from the hole. These results imply that the effect of nonmetallic inclusion is less detrimental in torsional fatigue. It follows that rotating bending, or tension–compression, fatigue testing is more effective than torsional fatigue testing in evaluating the quality of materials in respect of nonmetallic inclusions.

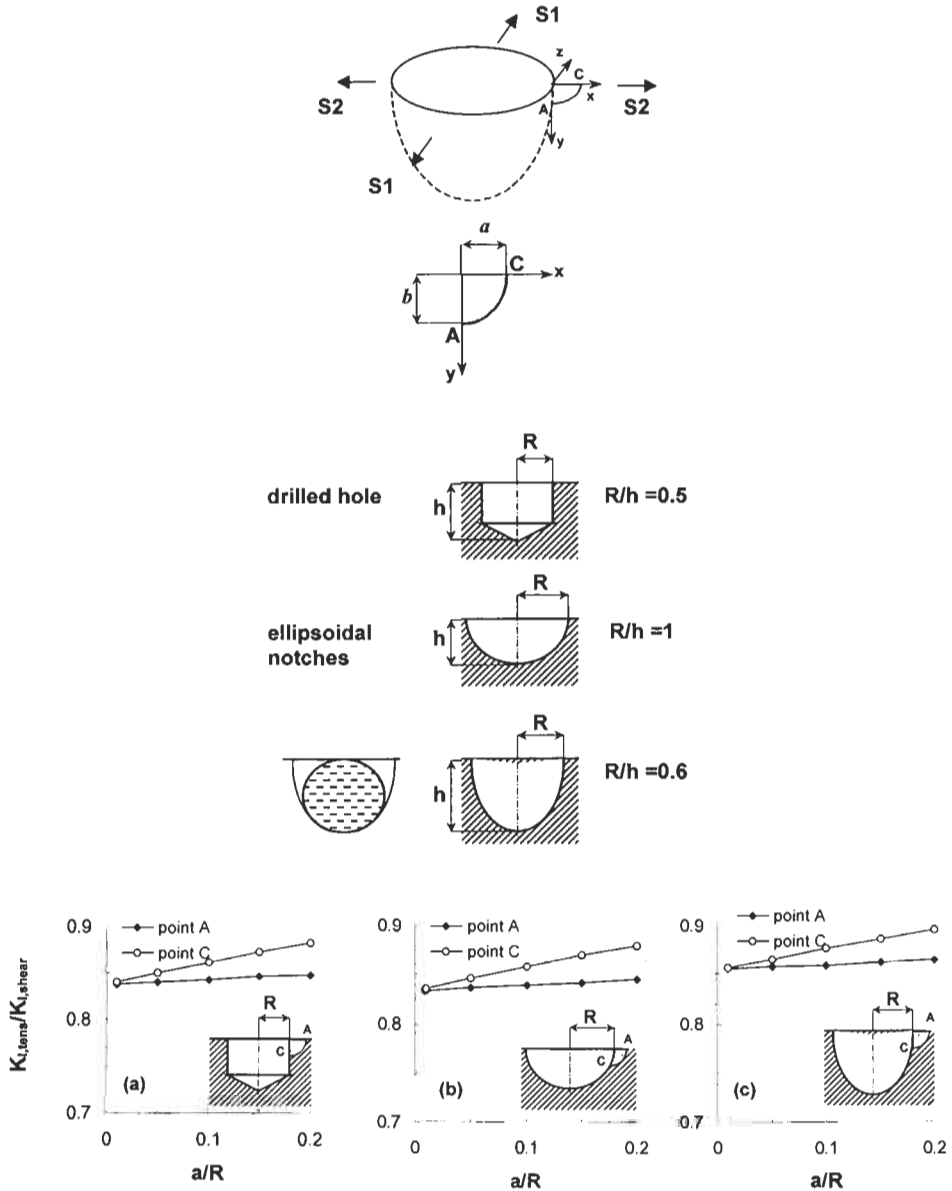
A more accurate approach to the effect of round defects has been taken in the study by Beretta and Murakami [21]. The stress intensity factors for 3D cracks emanating from defects (Fig. 14.12) were analysed and used to predict the ratio of torsional fatigue strength to bending (or tension–compression) fatigue strength.

14.3 Effects of Small Cracks

If an initial defect is a crack, then we must consider directly the value of stress intensity factors (K_I) rather than stress concentration factors (K_t). In rotating bending or tension–compression fatigue, small defects can be considered to be virtually equivalent

Table 14.6 Heat treatment and mechanical properties

Heat treatment		Tensile strength σ_B (MPa)	0.2% proof strength $\sigma_{0.2}$ (MPa)	Elongation δ (%)	Reduction of area ϕ (%)	Hardness <i>HV</i>
Quenching	Tempering					
835°C 40 min Oil quenching (70°C)	180°C 2h., Air cooling	2461	1667	1.0	2.3	740
	250°C 2h., Air cooling	2275	2167	1.0	2.0	660
	300°C 2h., Air cooling	2265	1981	4.0	9.0	620



to small cracks, from the view point of fatigue limits, if both crack and defect have identical values of \sqrt{area} [7]. The geometrical parameter, \sqrt{area}_p , is defined as the square root of the area of a defect or crack projected onto a plane perpendicular to the maximum tensile stress. However, in torsional fatigue, a small defect with short cracks cannot be considered to be equivalent to a crack, even if both the defect and

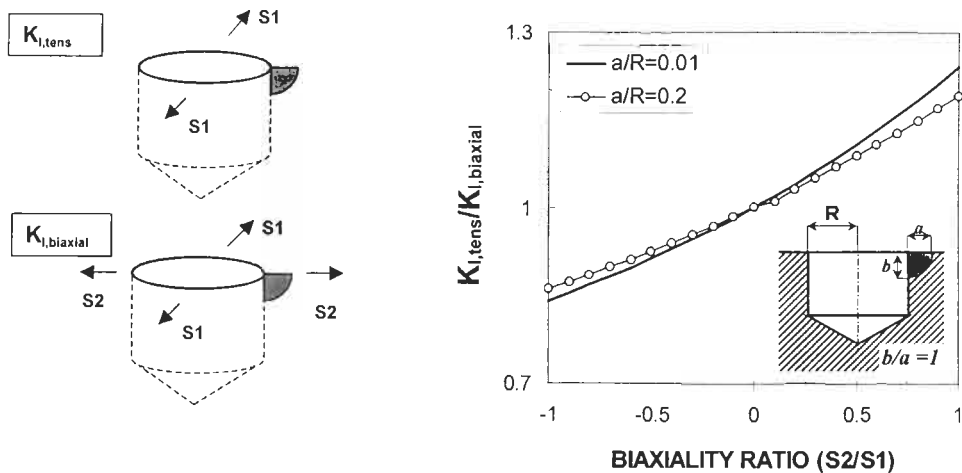


Figure 14.12 Stress intensity factors for a corner crack at the edge of a hole (3D analysis). $S2 = 0$ for tension and $S2 = -S1$ for torsion [21].

the crack have an identical value of the square root of projected area, $\sqrt{area_p}$. This is because K_I for the hole is affected by both the two principal stresses of a biaxial stress. Thus, when a crack emanates from a defect under a biaxial stress, K_I is affected by the corresponding K_I , and hence by the shape of the defect.

14.3.1 Material and Test Procedures

The material used was a rolled bar of 0.47% C steel (S45C) with a diameter of 25 mm. The chemical composition of the material is (wt%) 0.47 C, 0.21 Si, 0.82 Mn, 0.018 P, 0.018 S, 0.01 Cu, 0.018 Ni and 0.064 Cr. The mechanical properties of the material are: 620 MPa tensile strength, 339 MPa lower yield strength, 1105 MPa true fracture strength, and 53.8% reduction of area. Specimens were turned to shape after annealing at 844°C for 1 h. Fig. 14.13a shows the microstructure of the material. Fig. 14.13b shows the specimen geometry. After surface finishing with an emery paper, about 25 μm of surface layer was removed by electropolishing. After electropolishing, a hole was introduced onto the surface of each specimen. Fig. 14.13c shows the dimensions of the hole. The diameter of the hole is equal to its depth. After introducing a small hole, the specimens were annealed in a vacuum at 600°C for 1 h to relieve residual stress introduced by drilling. The Vickers hardness after vacuum annealing is $H_V = 174$. This is a mean value measured at four points on each specimen using a load of 0.98 N. The scatter of H_V is within 5%.

A servo-hydraulic biaxial testing machine was used both for introduction of the precracks by tension–compression loading, and for the torsional fatigue tests. Tension–compression fatigue tests were conducted at $\sigma = 230$ MPa, in order to introduce precracks of 200 μm , 400 μm and 1000 μm in surface length. These tests were conducted under load control, at a frequency of 20 Hz, with zero mean stress ($R = -1$).

The length of a precrack was defined as the surface length including the hole. In

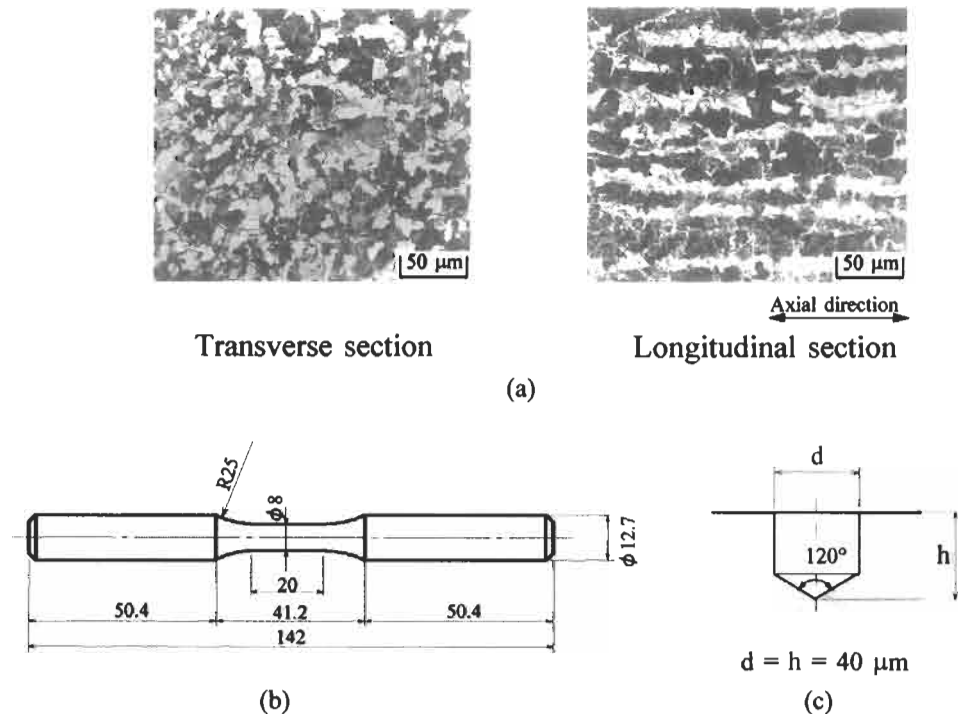


Figure 14.13 Material and specimen. (a) Microstructure. (b) Specimen geometry; dimensions in mm. (c) Small artificial hole.

the subsequent discussion, these three types of specimens are denoted by 200 μm precracked specimen, 400 μm precracked specimen and 1000 μm precracked specimen. The specimens were again annealed in a vacuum at 600°C for 1 h to relieve residual stresses due to the prior tension–compression fatigue loading. Torsional fatigue tests were then conducted under load control at a frequency of 12 Hz with zero mean stress ($R = -1$). The fatigue limit was defined as the maximum nominal stress under which specimens endured 10^7 cycles. The smallest stress level step was 4.9 MPa. Plastic replicas were taken during the tests to monitor crack growth.

14.3.2 Fatigue Test Results

Table 14.7 shows the fatigue tests results. New cracks grew from the tips of the precracks. SEM observation of fracture surfaces showed that the precracks had a semi-elliptical shape. Mean values of the aspect ratio (b/a) are listed in Table 14.7. A geometric parameter, $\sqrt{\text{area}_p}$, is defined as the square root of the area of a precrack projected onto a plane perpendicular to the maximum tensile stress, that is at $\pm 45^\circ$ to the axial direction. As mentioned previously, the critical hole diameter, d_c , is 150 μm . The value of $\sqrt{\text{area}_p}$ for holes of 150 μm in diameter and depth is 139 μm . The value of $\sqrt{\text{area}_p}$ for the 200 μm precracked specimens is 99 μm (Table 14.7). Although the

Table 14.7 Fatigue test results

Surface crack length $2a$ (μm)	Aspect ratio b/a	Torsional fatigue limit τ_w (MPa)	$\sqrt{\text{area}}_p$ (μm)
Plain specimen	—	167	—
200	0.88	152	99
400	0.87	147	197
1000	0.90	127	500

effect of a small hole on fatigue limits in rotating bending and tension–compression fatigue is equivalent to small cracks having identical values of $\sqrt{\text{area}}$, the same rule cannot be applied directly to torsional fatigue. Thus, we must seek a new analysis based on crack branching and non-propagation behaviour.

14.3.3 Crack Initiation and Propagation from Precracks

Fig. 14.14a–d shows cracks emanating from the initial crack tip under a stress level which is higher than the fatigue limit. Both Mode I (branch cracks) and Mode II cracks started from the initial crack tip under reversed torsion (Fig. 14.14b). Mode II cracks stopped propagating after 10 μm growth. However, Mode I cracks continued propagating (Fig. 14.14c,d), and led to specimen failure.

Fig. 14.14e–g illustrate the patterns of crack branching at a crack tip. The crack branching pattern of Fig. 14.14a–d corresponds to the illustration in Fig. 14.14e. Fig. 14.14b shows the initiation of both Mode I and Mode II cracks at the precrack tip. However, as Mode I branch cracks propagate, the value of ΔK_{II} at the Mode II crack tip decreases so that the Mode II crack stops propagating.

The branching behaviour illustrated in Fig. 14.14e was the most frequently observed. Branching of Mode I cracks, as shown in Fig. 14.14f, after Mode II crack growth from the initial crack, was also observed. In some cases, only branching to Mode I, as shown in Fig. 14.14g, was observed.

Fig. 14.15 shows the shapes and directions of the branch cracks in broken specimens. The branch cracks which grew from the initial crack tips are illustrated separately, for the 200 μm , 400 μm and 1000 μm precracked specimens. The branch cracks eventually propagated in directions perpendicular to the principal stresses, that is at $\pm 45^\circ$ to the axial direction, although the initial branching angle obviously differs from $\pm 45^\circ$. The initial angles of crack branching were not necessarily the same, probably due to the scatter of the crystallographic orientations of grains ahead of crack tips. The line at $\pm 70.5^\circ$ is the direction of $\sigma_{\theta_{\max}}$ at a crack tip, where $\sigma_{\theta_{\max}}$ is the maximum normal stress in the tangential direction in the polar coordinate system (r, θ) at the crack tip.

Crack branching at a precrack tip was also observed at a stress below the fatigue limit, although these branch cracks stopped propagating. Fig. 14.16 shows a non-propagating crack emanating from an initial precrack at the fatigue limit. Thus, the fatigue limit under torsion is the threshold condition for non-propagation of Mode I branch cracks.

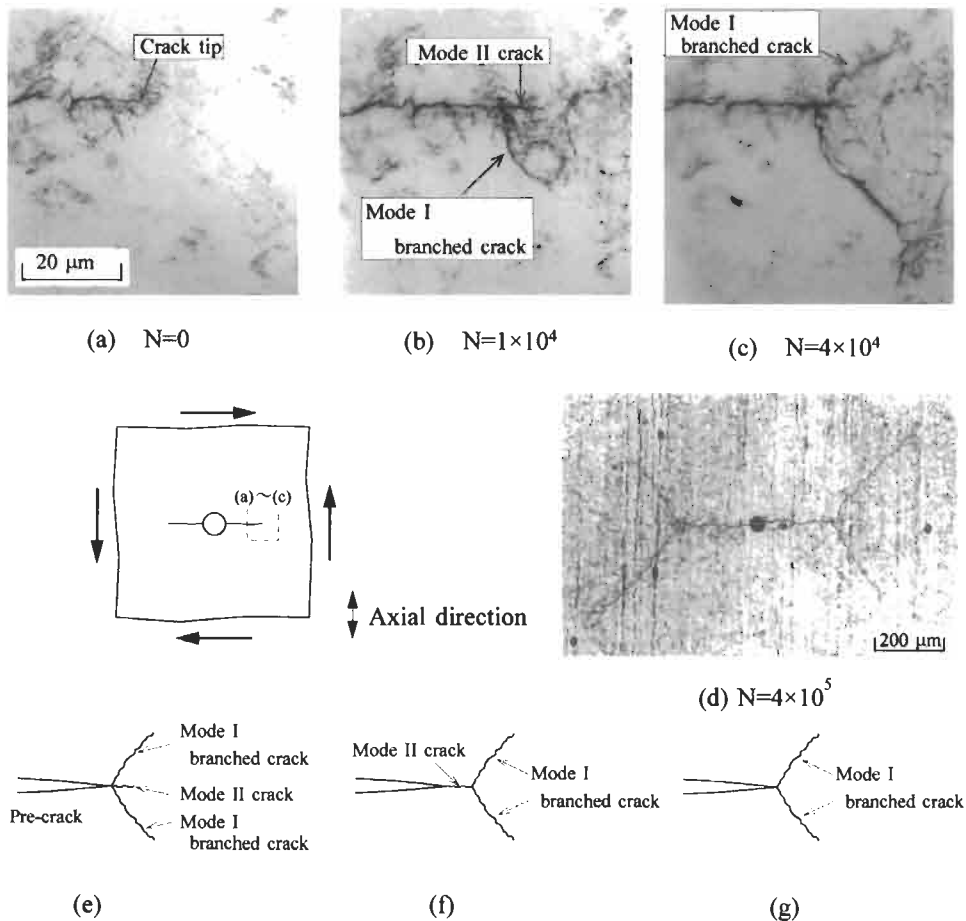


Figure 14.14 Initiation and propagation of branch cracks ($400\ \mu\text{m}$ precracked specimen, $\tau_a = 152\ \text{MPa}$, $N_f = 7.9 \times 10^5$). (a) Zero cycles. (b) 1×10^4 cycles. (c) 4×10^4 cycles. (d) 4×10^5 cycles. (e)–(g) Patterns of crack branching.

Fig. 14.16b illustrates the internal shape of a non-propagating crack. The stress condition is pure Mode III at the deepest point of the surface crack, point A in Fig. 14.16b and Fig. 14.17. Crack initiation and subsequent non-propagation at the deepest point is presumed to be controlled by Mode III, although the detailed mechanism is still unclear at present.

As illustrated in Fig. 14.16b, the size of a non-propagating crack is larger at the surface than in the interior. Therefore, considering crack branching behaviour, as shown in Figs. 14.15 and 14.16, it can be said that the fatigue limit is the condition for non-propagation of Mode I branch cracks at the surface. Mode I crack growth was also confirmed by SEM observation of the fracture surface of a branch crack. This was quite different from that of a Mode II crack surface, which showed a fibrous morphology in the direction of crack growth [22]. Further investigation of the fracture surface near the

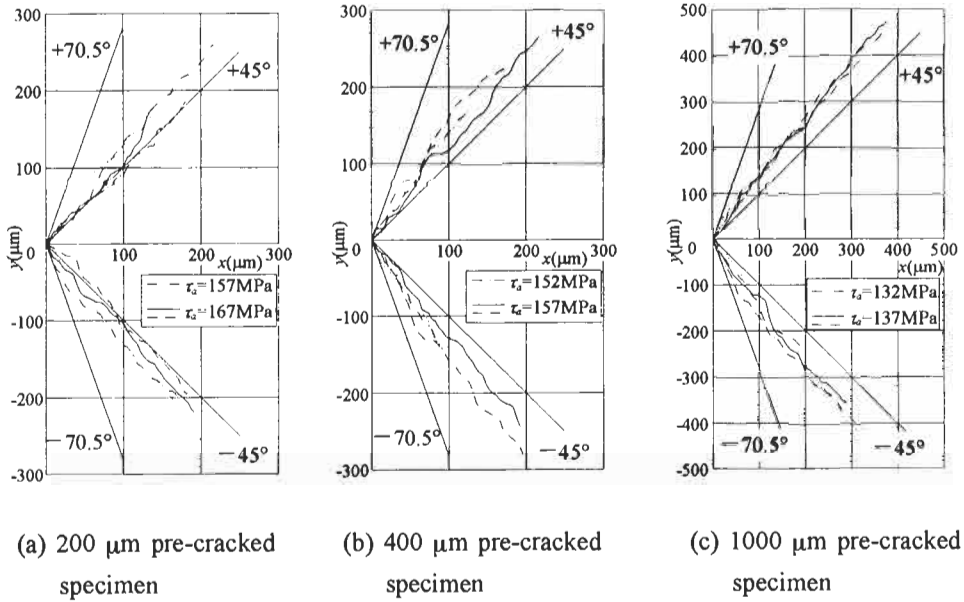


Figure 14.15 Shapes and angles of branched cracks. The origin of the coordinates is the tip of the initial crack. (a) Pre-cracked specimens, 200 μm . (b) Pre-cracked specimens, 400 μm . (c) Pre-cracked specimen, 1000 μm .

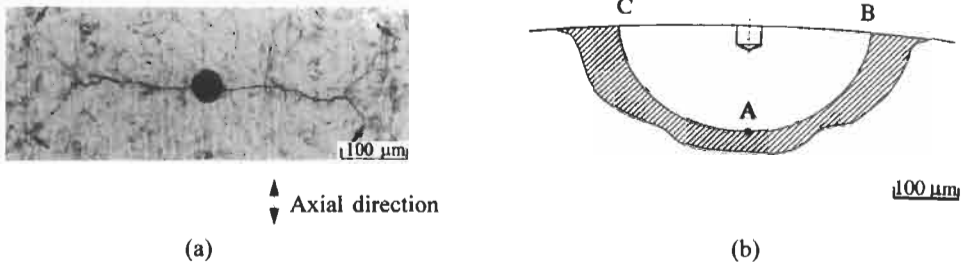


Figure 14.16 Non-propagating crack emanating from a precrack (400 μm pre-cracked specimen, $\tau_a = 147 \text{ MPa}$). (a) Surface appearance. (b) Internal shape.

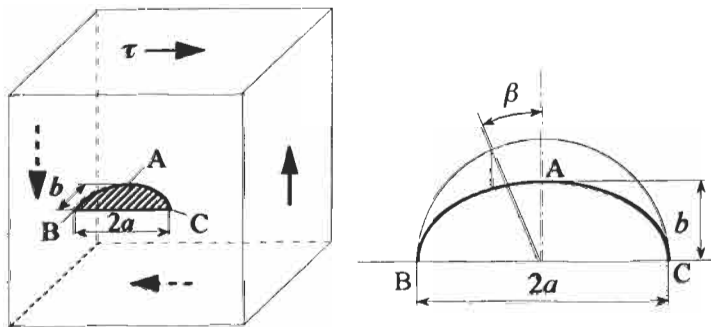


Figure 14.17 Semi-elliptical surface crack under shear.

deepest point of a semi-elliptical crack is needed to investigate the mechanism of Mode III fatigue crack growth [23–25].

14.3.4 Fracture Mechanics Evaluation of the Effect of Small Cracks on Torsional Fatigue

As mentioned above, the fatigue limit is determined by the non-propagation condition of Mode I branch cracks at the initial crack. Therefore, an evaluation based on the threshold stress intensity factor range (ΔK_{th}) for small Mode I cracks is appropriate.

Fig. 14.17 illustrates the semi-elliptical surface crack analysed. Kassir and Sih [26] obtained the solution of the stress intensity factor for an elliptical crack in an infinite body under a remote uniform shear stress.

For the elliptical crack with aspect ratio $b/a < 1$, K_{II} is given by:

$$\begin{aligned}
 K_{II} &= \left(\frac{\pi b^3}{a} \right)^{1/2} \frac{k^2 \tau \sin \beta}{F(k, \nu)(b^2 \sin^2 \beta + a^2 \cos^2 \beta)^{1/4}} \\
 F(k, \nu) &= [(k^2 - \nu)E(k) + \nu k^{*2} K(k)] \\
 k &= \left(1 - \frac{b^2}{a^2} \right)^{1/2}, \quad k^* = \frac{b}{a} \\
 E(k) &= \int_0^{\pi/2} (1 - k^2 \sin^2 \phi)^{1/2} d\phi \\
 K(k) &= \int_0^{\pi/2} \frac{1}{(1 - k^2 \sin^2 \phi)^{1/2}} d\phi
 \end{aligned} \tag{14.1}$$

This solution is applied to a semi-elliptical surface crack in the present study. The condition at the free surface, points B and C in Fig. 14.17, is pure Mode II, that is $K_I = K_{III} = 0$.

To predict the direction of crack propagation, the $\sigma_{\theta_{max}}$ criterion proposed by Erdogan and Sih [27] is used. The tensile stress (σ_{θ}) and shear stress ($\tau_{r\theta}$) in the vicinity of the crack tip are as follows:

$$\sigma_{\theta} = \frac{1}{\sqrt{2\pi r}} \cos \frac{\theta}{2} \left(K_I \cos^2 \frac{\theta}{2} - \frac{3}{2} K_{II} \sin \theta \right) \tag{14.2}$$

$$\tau_{r\theta} = \frac{1}{2\sqrt{2\pi r}} \cos \frac{\theta}{2} [K_I \sin \theta + K_{II}(3 \cos \theta - 1)] \tag{14.3}$$

The direction (θ_0) where σ_{θ} has its maximum value is given by:

$$K_I \sin \theta_0 + K_{II}(3 \cos \theta_0 - 1) = 0 \tag{14.4}$$

This equation gives $\theta_0 = \pm 70.5^\circ$ for pure Mode II ($K_I = 0$) [27].

The stress intensity factor associated with σ_{θ} is defined as follows:

$$\begin{aligned}
 K_{\theta_{max}} &= \sigma_{\theta} \sqrt{2\pi r} \\
 &= \cos \frac{\theta_0}{2} \left(K_I \cos^2 \frac{\theta_0}{2} - \frac{3}{2} K_{II} \sin \theta_0 \right)
 \end{aligned} \tag{14.5}$$

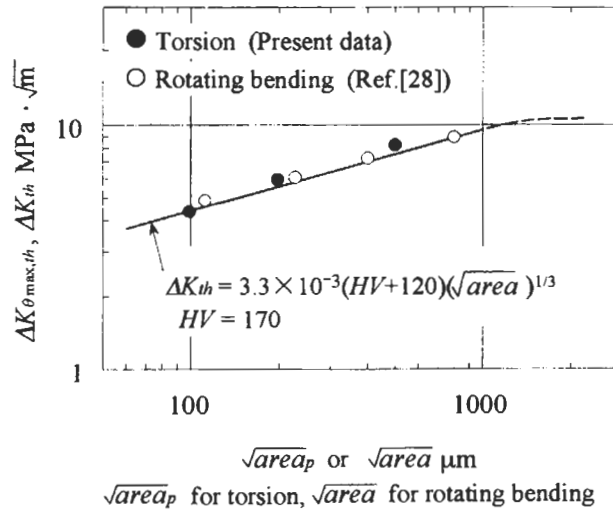


Figure 14.18 Relationship between $\Delta K_{\theta_{max,th}}$ and \sqrt{area}_p . Material: annealed 0.46–0.47% C steel.

The maximum value ($K_{\theta_{max}}$) of K_{θ} for pure Mode II is derived by substituting $\theta_0 = \pm 70.5^\circ$ into Eq. 14.5. Thus, we have:

$$K_{\theta_{max}} = 1.155 K_{II} \tag{14.6}$$

The exact angles of crack branching very close to the tip of the initial crack were not $\pm 45^\circ$, but in some cases were approximately $\pm 70.5^\circ$. However, the branching angles of individual specimens are not identical due to the microstructural scatter of the material ahead of the crack tip.

In order to express the threshold condition at the fatigue limit using stress intensity factors, ΔK_{II} was calculated by substituting the crack shape parameter (a, b), $\beta = 90^\circ$, Poisson’s ratio, $\nu = 0.3$, and the stress at the fatigue limit (τ_w) into Eq. 14.1. Then, the threshold value ($\Delta K_{\theta_{max,th}}$) of $\Delta K_{\theta_{max}}$ was determined by substituting ΔK_{II} into Eq. 14.6. It was assumed that $\Delta K_{\theta_{max,th}}$ should be equal to ΔK_{th} obtained from rotating bending or tension–compression fatigue tests, and is dependent on crack size [28].

Fig. 14.18 shows the relationship between $\Delta K_{\theta_{max,th}}$ and \sqrt{area}_p . Values of ΔK_{th} obtained from rotating bending fatigue tests [28] on annealed 0.46% C steel (S45C) are also plotted in the figure. The straight line in Fig. 14.18 is the prediction equation for ΔK_{th} proposed by the \sqrt{area} parameter model as:

$$\Delta K_{th} = 3.3 \times 10^{-3} (H_V + 120) (\sqrt{area})^{1/3} \tag{14.7}$$

where ΔK_{th} is the threshold stress intensity factor range for $R = -1$ ($\text{MPa m}^{1/2}$), H_V is Vickers hardness number (kgf/mm^2) and \sqrt{area} is in μm . The upper limit of the valid size of \sqrt{area} for this equation is approximately 1000 μm , and the lower limit is dependent on the material [7].

Fig. 14.18 indicates that the values of $\Delta K_{\theta_{max,th}}$ obtained by torsional fatigue tests are equal to the values of ΔK_{th} obtained from rotating bending fatigue tests. The torsional

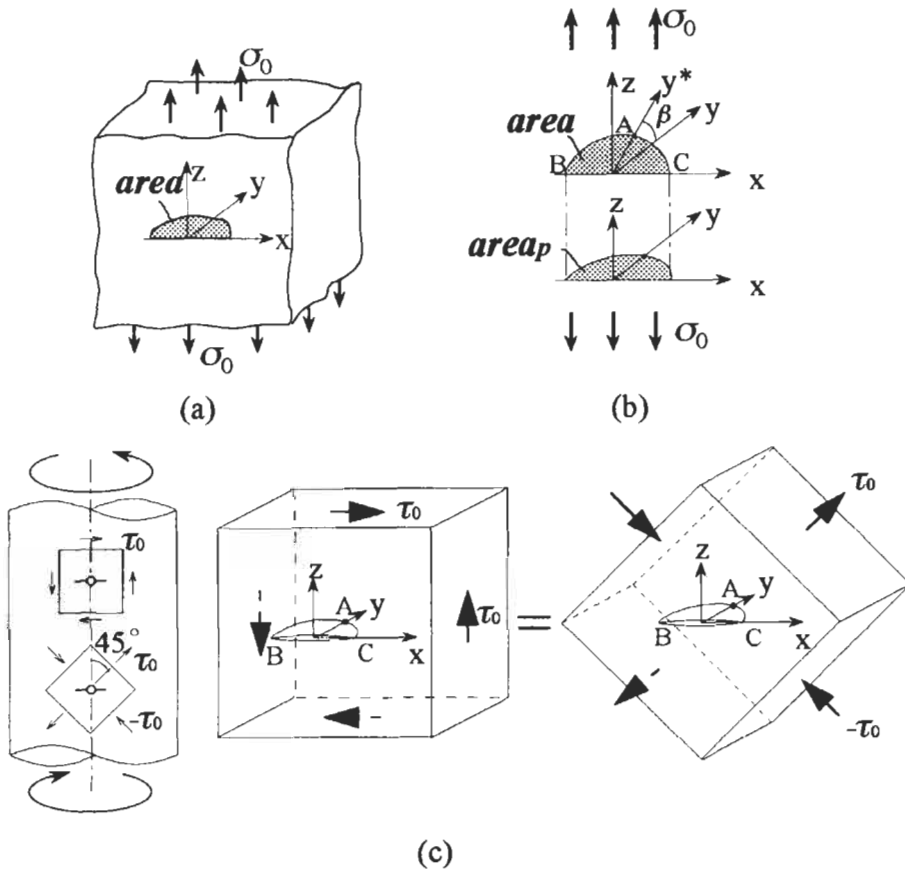


Figure 14.19 Crack orientation with respect to stress state. (a) Arbitrarily shaped surface crack subjected to tension. (b) Inclined surface crack subjected to tension. (c) A semi-elliptical surface crack subjected to torsion.

fatigue limit (τ_w) of precracked specimens can be predicted either from $\Delta K_{\theta_{max,th}}$ (Eq. 14.7) or by the method explained in the next section.

14.3.5 Prediction of Torsional Fatigue Limit by the \sqrt{area} Parameter Model

Before derivation of the prediction equation for τ_w , that for σ_w is explained briefly. The maximum value of the stress intensity factor ($K_{I_{max}}$) along the front of a surface crack of arbitrary shape, as shown in Fig. 14.19a is given by [29]:

$$K_{I_{max}} \cong 0.65\sigma_0\sqrt{\pi\sqrt{area}} \quad (\text{same as Eq. 2.8}) \quad (14.8)$$

where σ_0 is the remote tensile stress.

$K_{\theta_{max}}$ for an inclined surface crack is given, using $\sqrt{area_p}$, by [30]:

$$K_{\theta_{max}} \cong 0.65\sigma_0\sqrt{\pi\sqrt{area_p}} \tag{14.9}$$

Eq. 14.9 includes Eq. 14.8 as a special case. Combining Eqs. 14.7 and 14.8, and substituting $\sigma_0 = \Delta\sigma_w = 2\sigma_w$ into Eq. 14.8, the prediction equation for σ_w is obtained as:

$$\sigma_w = 1.43(H_V + 120) / (\sqrt{area_p})^{1/6} \tag{14.10}$$

This equation has been used widely for predicting the fatigue limit of materials containing surface defects and surface cracks in the region of $\sqrt{area_p} < 1000 \mu\text{m}$ for values of H_V ranging from 70 to 720 [7] (see Chapter 6).

The torsional fatigue limit of materials containing a semi-elliptical surface crack subjected to torsion or shear can be predicted in a similar manner. $K_{\theta_{max}}$ for the semi-elliptical crack in Fig. 14.19c is given by:

$$K_{\theta_{max}} \cong F\tau_0\sqrt{\pi\sqrt{area_p}} \tag{14.11}$$

The value of $K_{\theta_{max}}$ for the crack in Fig. 14.19c cannot be expressed by Eq. 14.9, because the crack in Fig. 14.19c is not in the same condition as that in Fig. 14.19b. We must pay attention to the points B and C, rather than the deepest point A, because $K_{\theta_{max}}$ is attained at the points B and C. The coefficient F in Eq. 14.11 is a function of the aspect ratio (b/a). It follows that values of F for two cracks having the same value of $\sqrt{area_p}$ but different values of b/a are not the same. In other words, F for cracks under a shear stress is not a simple function of ' $area_p$ ' alone but is also a function of the aspect ratio (b/a). F can be obtained by substituting both $K_{\theta_{max}}$ obtained using Eq.

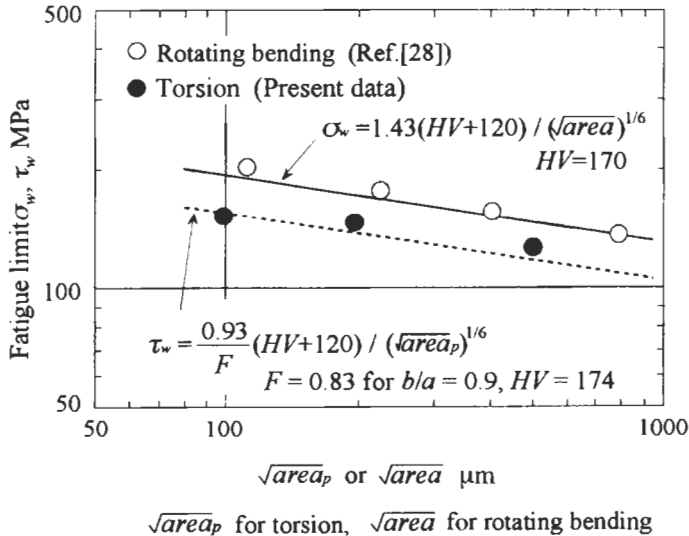


Figure 14.20 Relationship between τ_w and $\sqrt{area_p}$. Material: annealed 0.46–0.47% C steel.

14.6, together with Eq. 14.1, and ' $area_p$ ' ($= \pi abc \cos 45^\circ / 2$) into Eq. 14.11. Thus, the approximate polynomial equation for F is:

$$F(b/a) = 0.0957 + 2.11(b/a) - 2.26(b/a)^2 + 1.09(b/a)^3 - 0.196(b/a)^4 \quad (14.12)$$

where $0.1 < b/a < 2.0$.

Combining Eq. 14.7 with Eq. 14.11, we have the prediction equation for τ_w as:

$$\tau_w = \frac{0.93}{F(b/a)} (H_v + 120) / (\sqrt{area_p})^{1/6} \quad (14.13)$$

Fig. 14.20 shows results for both torsional and rotating bending fatigue tests on annealed 0.46–0.47% C steel (S45C) analysed using the above procedures. As previously reported in Ref. [28], rotating bending fatigue limits (solid line) can be predicted using Eq. 14.10. The dotted line in Fig. 14.20 is the prediction for τ_w , where the aspect ratio (b/a) is 0.9, and accordingly F from Eq. 14.12 is 0.83. Thus, the torsional fatigue limit of specimens containing an initial crack can be successfully predicted. The upper limit of $\sqrt{area_p}$ for Eq. 14.13 is at present uncertain, though from previous studies [7] it may be considered to be approximately 1000 μm .

14.4 References

1. M.W. Brown and K.J. Miller: Biaxial and Multiaxial Fatigue, EGF Publ. 3, Mech. Eng Publ. Ltd., London, 1989.
2. D.F. Socie and G.B. Marquis: Multiaxial Fatigue, Society of Automotive Engineers, Warrendale, PA, 2000 and G.E. Leese and D.F. Socie: Multiaxial Fatigue: Analysis and Experiments, Society of Automotive Engineers, Warrendale, PA, 1989.
3. E. Perez Carbonell and M.W. Brown: A Study of Short Crack Growth in Torsional Low Cycle Fatigue for a Medium Carbon Steel, *Fatigue Fract. Eng. Mater. Struct.*, **9** (1986), 15–33.
4. D.F. Socie, C.T. Hua and D.W. Worthem: Mixed Mode Small Crack Growth, *Fatigue Fract. Eng. Mater. Struct.*, **10** (1987), 1–16.
5. C.H. Wang and K.J. Miller: The Effect of Mean Shear Stress on Torsional Fatigue Behaviour, *Fatigue Fract. Eng. Mater. Struct.*, **14** (1991), 293–307.
6. W. Zhang and R. Akid: Mechanics and Fatigue Performance of Two Steels in Cyclic Torsion with Axial Static Tension/Compression, *Fatigue Fract. Eng. Mater. Struct.*, **20** (1997), 547–557.
7. Y. Murakami and M. Endo: Effects of Hardness and Crack Geometries on ΔK_{Ib} of Small Cracks Emanating from Small Defects, In: *The Behaviour of Short Fatigue Cracks*, EGF Publ. 1, Mech. Eng. Publ. Ltd., London, 1986, pp. 275–293.
8. Y. Murakami and M. Endo: Effects of Defects, Inclusions and Inhomogeneities on Fatigue Strength, *Int. J. Fatigue*, **16** (1994), 163–182.
9. M. Endo and Y. Murakami: Effects of an Artificial Small Defect on Torsional Fatigue Strength of Steels, *J. Eng. Mater. Tech., Trans. ASME*, **109** (1987), 124–129.
10. H. Nose, I. Sakamoto, H. Nakayama, M. Shibata, M. Yamashita and H. Gao: Strength Behaviour in Impact Torsional Fatigue of High Strength Bearing Steel and the Effect of a Small Hole Notch on the Fatigue Strength, In: *Proc. 20th Symp. Fatigue, Soc. Mater. Sci. Japan*, 1990, pp. 199–203.
11. M. Endo: Effects of Artificial Small Defect and Graphite on Torsional Fatigue Strength of Ductile Cast Iron, *J. Soc. Mater. Sci., Jpn.*, **45** (1996), 16–20.
12. Y. Murakami and K. Takahashi: Torsional Fatigue of a Medium Carbon Steel Containing an Initial Small Surface Crack Introduced by Tension–Compression Fatigue: Crack Branching, Non-Propagation and Fatigue Limit, *Fatigue Fract. Eng. Mater. Struct.*, **21**(12) (1998), 1473–1484.
13. Y. Murakami, K. Takahashi, M. Takada and T. Toriyama: Quantitative Evaluation of Effect of Artificial Small Defects on Torsional Fatigue Strength, *Trans. Jpn. Soc. Mech. Eng. A*, **64**(618) (1998), 271–277.

14. H. Nisitani and K. Kawano: Correlation between the Fatigue Limit of a Material with Defects and Its Non-Propagating Crack Some Considerations Based on the Bending or Torsional Fatigue of the Specimen with a Diametrical Hole, *Trans. Jpn. Soc. Mech. Eng. Ser. I*, **37(300)** (1971), 1492–1496.
15. Y. Murakami: A Method of Stress Intensity Factor Calculation for the Crack Emanating from an Arbitrarily Shaped Hole or the Crack in the Vicinity of an Arbitrarily Shaped Hole, *Trans. Jpn. Soc. Mech. Eng. Ser. I*, **44(378)** (1978), 423–432.
16. H. Nisitani and M. Isida: Stress Intensity Factor of the Tension of an Infinite Plate Containing an Elliptical Hole with Two Symmetrical Edge Cracks, *Trans. Jpn. Soc. Mech. Eng. Ser. I*, **39(317)** (1973), 7–14.
17. H. Nisitani and Y. Murakami: Torsional Fatigue and Bending Fatigue of Electropolished Low Carbon Steel Specimens, *Trans. Jpn. Soc. Mech. Eng. Ser. I*, **35(275)** (1969), 1389–1396.
18. Y. Murakami, S. Fukuda and T. Endo: Effect of Micro-Hole on Fatigue Strength [1st Report, Effect of Micro-hole (Dia.: 40, 50, 80, 100 and 200 μm) on the Fatigue Strength of 0.13% and 0.46% Carbon Steels], *Trans. Jpn. Soc. Mech. Eng. Ser. I*, **44(388)** (1978), 4003–4013.
19. H. Nisitani and K. Takao: Successive Observations of Fatigue Process in Carbon Steel, 7:3 Brass and Al-Alloy by Electron, *Trans. Jpn. Soc. Mech. Eng. Ser. I*, **40(340)** (1974), 3254–3266.
20. K. Tanaka, S. Matsuoka and S. Nishijima: Fatigue Strength of SNCM8 Steel under Combined Axial Loading and Torsion (1st Report, Experimental Methods and Results), *Trans. Jpn. Soc. Mech. Eng. Ser. A*, **45(391)** (1979), 195–203.
21. S. Beretta and Y. Murakami: The Stress Intensity Factor For Small Cracks at Micro-Notches under Torsion, Proceedings of the 12th Biennial Conference on Fracture-ECF12-held in Sheffield, Vol. I, 1998, pp. 55–60.
22. Y. Murakami and S. Hamada: A New Method for the Measurement of Mode II Fatigue Threshold Stress Intensity Factor Range ΔK_{th} , *Fatigue Fract. Eng. Mater. Struct.*, **20** (1997), 863–870.
23. R.O. Ritchie, F.A. McClintock, H. Nayeb-Hashemi and M.A. Ritter: Mode III Fatigue Crack Propagation in Low Alloy Steel, *Metall. Trans.*, **13A** (1982), 101–110.
24. E.K. Tschegg: Mode III and Mode I Fatigue Crack Propagation Behaviour under Torsional Loading, *J. Mater. Sci.*, **18** (1983), 1604–1614.
25. K. Tanaka, Y. Akiniwa and H. Nakamura: J-Integral Approach to Mode III Fatigue Crack Propagation in Steel under Torsional Loading, *Fatigue Fract. Eng. Mater. Struct.*, **19** (1996), 571–579.
26. M.K. Kassir and G.C. Sih: Three Dimensional Stress Distribution around an Elliptical Crack under Arbitrary Loading, *J. Appl. Mech.*, *Trans. ASME*, **33** (1966) 601–611. In: Y. Murakami et al. (Eds): *Stress Intensity Factors Handbook 2*, Pergamon Press, Oxford, 1987, pp. 686–689.
27. F. Erdogan and G.C. Sih: On the Crack Extension in Plates under Plane Loading and Transverse Shear, *J. Basic Eng. Trans. ASME*, **85** (1963), 519–527.
28. Y. Murakami and K. Matsuda: Dependence of Threshold Stress Intensity Factor Range ΔK_{th} on Crack Size and Geometry, and Material Properties, *Trans. Jpn. Soc. Mech. Eng. A*, **52(478)** (1986), 1492–1499.
29. Y. Murakami and M. Ishida: Analysis of An Arbitrarily Shaped Surface Crack and Stress Field at Crack Front Near Surface, *Trans. Jpn. Soc. Mech. Eng. A*, **51(464)** (1985), 1050–1056.
30. Y. Murakami: Analysis of Stress Intensity Factors of Mode I, II and III for Inclined Surface Crack of Arbitrary Shape, *Eng. Fract. Mech.*, **22** (1985), 101–114.

Chapter 15

The Mechanism of Fatigue Failure of Steels in the Ultralong Life Regime of $N > 10^7$ Cycles

15.1 Mechanism of Elimination of Conventional Fatigue Limit: Influence of Hydrogen Trapped by Inclusions

Since Wöhler [1] started fatigue testing in the 1850s, the fatigue limit stress for steels has been defined as the highest stress at which specimens do not fail after testing to 10^7 cycles. However, recent studies by Naito et al. [2] and Asami and Sugiyama [3] have added to existing knowledge a warning that fatigue failure does occur at lives longer than $N = 10^7$, that is at $N = 10^8$ to 10^9 , at stress levels lower than the conventional fatigue limit. More recently, similar studies [4–8] followed those of Naito et al., and the mechanism leading to the stepwise S – N curve from low cycle fatigue to extremely high cycle fatigue has been discussed by many researchers. A symposium on this special topic was held in Paris in June 1998 and special issues of a journal on this topic were published in July and August 1999 [9,10]. A gigacycle ($N = 10^9$) corresponds to the number of cycles which a high speed Japanese Shinkansen Train experiences during 10 years service. It is also very common that, due to vibration, turbine blades experience more than $N = 10^7$ stress cycles. Fatigue testing up to $N > 10^7$ cycles using conventional fatigue testing machines is very time-consuming. In the Paris Symposium, data obtained by high speed testing machines were presented by Stanzl-Tschegg [11] and Bathias [12] using ultrasonic fatigue testing machines capable of a frequency of 20 kHz, by Ritchie et al. [13] using a 1 kHz closed loop servo-hydraulic testing machine, and by Davidson [13] using a 1.5 kHz magneto-strictive loading machine.

If we consider the many possible factors which may influence fatigue strength during such a long period of use, it is not easy to identify the crucial mechanism. Miller and O'Donnell [14] and Murakami et al. [15] discussed several possible factors which may cause fatigue failure in the region of $N > 10^7$ cycles. Miller and O'Donnell [14] gave a very thorough overview on the possible factors for the elimination of the classical (or conventional) fatigue limit. They discussed the effects of coxing and rest periods, fluctuating stress, environmental and other transitional effects, and vibrations, in terms of practical problems. Among several possible factors for eliminating the classical fatigue limit, Murakami et al. [15] pointed out the importance of the influence

of hydrogen trapped by nonmetallic inclusions. The influence of hydrogen on static fracture, such as by hydrogen embrittlement and corrosion cracking, is well known. However, the influence of the hydrogen trapped by nonmetallic inclusions on fatigue failure in air has not been reported. This chapter focuses on this particular problem through the use of specimens which contain different levels of hydrogen. It is shown that the fatigue fracture surfaces of specimens containing different levels of hydrogen show very different fracture surface morphologies, and that the influence of hydrogen is crucial for the elimination of the fatigue limit in a cycle region which is longer than in conventional fatigue testing, that is $N > 10^7$.

15.1.1 Method of Data Analysis

Fatigue fracture origins in extremely high cycle fatigue are mostly at nonmetallic inclusions. Therefore, this problem should be discussed from the viewpoint of small fatigue cracks. It is well known that the threshold stress intensity factor ranges, ΔK_{th} , for small cracks are a function of crack size, and are lower than those for long cracks [16].

As explained in Chapters 5 and 6, ΔK_{th} for small cracks and defects can be evaluated by the \sqrt{area} parameter model:

$$\Delta K_{th} = 3.3 \times 10^{-3} (H_V + 120) (\sqrt{area})^{1/3} \quad (5.4)$$

$$\sigma_w = \frac{1.43(H_V + 120)}{(\sqrt{area})^{1/6}} \quad (5.5 \text{ and } 6.1)$$

where the units in the equations are ΔK_{th} (in MPa m^{1/2}), fatigue limit, σ_w (in MPa), H_V (in kgf/mm²), and the square root of the projected area of a defect \sqrt{area} (in μm).

More general expressions for Eqs. 5.4, 5.5 and 6.1 for the stress ratio, $R \neq -1$, are:
Surface defects:

$$\sigma_w = \frac{1.43(H_V + 120)}{(\sqrt{area})^{1/6}} \cdot \left[\frac{1 - R}{2} \right]^\alpha \quad (6.6)$$

Internal defects:

$$\sigma_w = \frac{1.56(H_V + 120)}{(\sqrt{area})^{1/6}} \cdot \left[\frac{1 - R}{2} \right]^\alpha \quad (6.9)$$

where

$$R = \frac{\sigma_{min}}{\sigma_{max}} \quad (6.7)$$

and

$$\alpha = 0.226 + H_V \times 10^{-4} \quad (6.8)$$

If we compare the threshold values, ΔK_{th} , estimated by the \sqrt{area} parameter model for results with $N_f > 10^7$ cycles with values of ΔK at which test specimens failed, we might be able to find the factors which may influence fatigue strength in the region of $N_f > 10^7$ cycles.

Table 15.1 Chemical composition (SCM435)

										(wt %) (ppm)	
C	Si	Mn	P	S	Ni	Cr	Mo	Cu	O ₂		
0.36	0.19	0.77	0.014	0.006	0.08	1.00	0.15	0.13	8		

15.1.2 Material, Specimens and Experimental Method

The material used is a Cr–Mo Steel SCM435. Table 15.1 shows the chemical composition (wt%). The loading is tension–compression with ratio $R = -1$. Three series of specimens were prepared. Table 15.2 summarises the specimen nomenclature and the heat treatment conditions. The first series of specimens were quenched at 850°C and tempered at 170°C after carburising and nitriding. These specimens are termed Specimen QT (Quenched and Tempered). The hardness of a core region of Specimen QT is approximately $H_V = 560$.

The second and third series of specimens were prepared to investigate the influence of hydrogen trapped in specimens. The second series of specimens are those which were annealed at 300°C in a vacuum. The specimens which were annealed for 1 h at 300°C in a vacuum are termed Specimen VA1, and those which were annealed for 2 h at 300°C in a vacuum are termed Specimen VA2. The hardness of a core region of Specimen VA is approximately $H_V = 500$.

The third series of specimens are those which were heated in a vacuum and quenched under the same condition as Specimen QT. These specimens are termed Specimen VQ. The hardness distribution of Specimen VQ is almost the same as for Specimen QT.

Before the fatigue tests, the hydrogen contents in Specimen QT and Specimen VQ were measured. The hydrogen content was 0.7–0.9 ppm in Specimen QT and 0.01 ppm in Specimen VQ.

Table 15.2 Heat treatment and specimen nomenclature

Name of specimens	Heat treatment
QT	Quenched at 850 °C Tempered at 170 °C Carburizing and Nitriding
VA1	Annealing specimen QT at 300 °C for 1h
VA2	Annealing specimen QT at 300 °C for 2h
VQ	Heat treated in a vacuum at 850 °C followed by Quenching Tempered at 170 °C and Carburizing and Nitriding

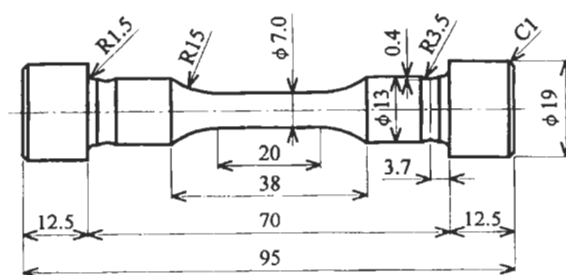


Figure 15.1 Specimen geometry, dimensions in mm.

Fig. 15.1 shows the geometry of the tension–compression fatigue specimens. Four strain gauges were attached to each specimen in order to check the bending of the specimen under load. These specimens were not electropolished in order to leave the hardened surface layer intact. Thus a specimen surface is much harder than the interior. The compressive residual stress at the surface is about 500 MPa.

A servo-hydraulic closed-loop tension–compression fatigue testing machine, operating at a frequency of 30 to 100 Hz, was used.

15.1.3 Distribution of Residual Stress and Hardness

Compressive residual stresses of approximately 500 MPa were present at a specimen surface. Fig. 15.2 shows an example of hardness distribution across the section of a Specimen QT. Fig. 15.3 shows the distribution of fatigue fracture origins on sections

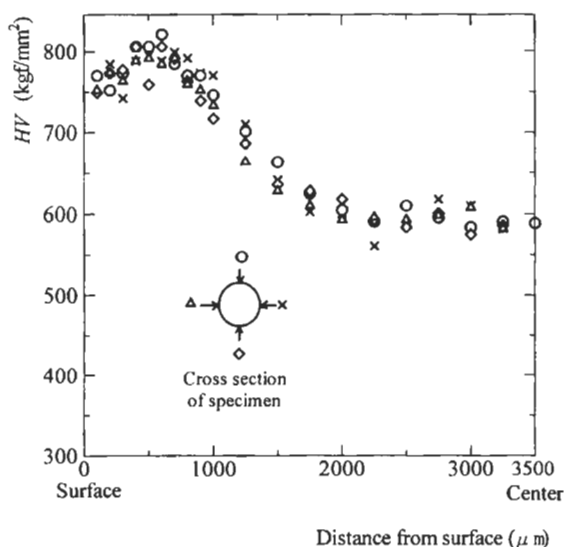


Figure 15.2 Hardness distribution across the section for specimens quenched and tempered after carburising and nitriding (Specimen QT).

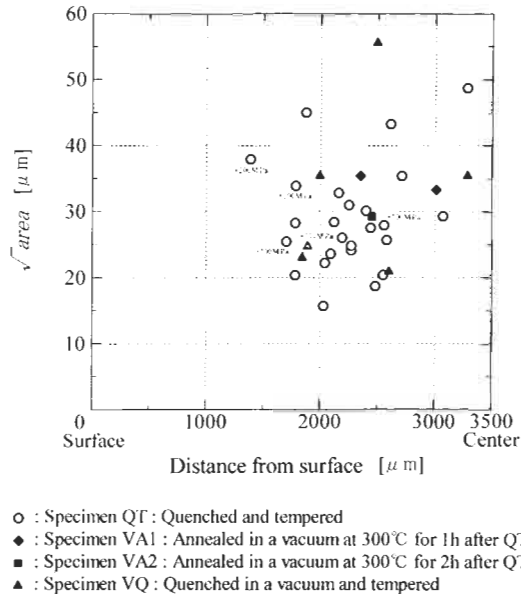


Figure 15.3 Size and radial distribution of the inclusions at fracture origins. The symbols ● annotated +300 MPa indicate specimens tested under a mean stress of +300 MPa.

of specimens. These are mostly distributed in the core region of specimens due to the lower hardness.

15.1.4 Fracture Origins

All fractures occurred from internal inclusions. The locations of these inclusions are at depths from the surface greater than 1700 μm . This is because the core of a specimen is softer than the surface, and also because the residual stress at the surface is compressive.

Fig. 15.4(A) shows an example of a fish-eye fracture and of the inclusion at the centre of the fish eye of a Specimen QT, and Fig. 15.4(B) shows an example for a Specimen VQ. The inclusions were identified using X-ray analysis of the chemical composition to be $\text{Al}_2\text{O}_3 \cdot (\text{CaO})_x$ globular duplex inclusions.

15.1.5 S-N Curves

Fig. 15.5 shows the S-N curve obtained. The scatter of the S-N data is due to the large scatter in the size of inclusions contained in the specimen, the non-uniformity of hardness at the test section, the variation of residual stress from compression at the surface to tension in the interior, and the difference in heat treatments. The fracture origins of all specimens plotted in Fig. 15.5 are at internal inclusions and not at the surface.

In order to evaluate the influence of inclusions, the fatigue limit, σ_w , of each

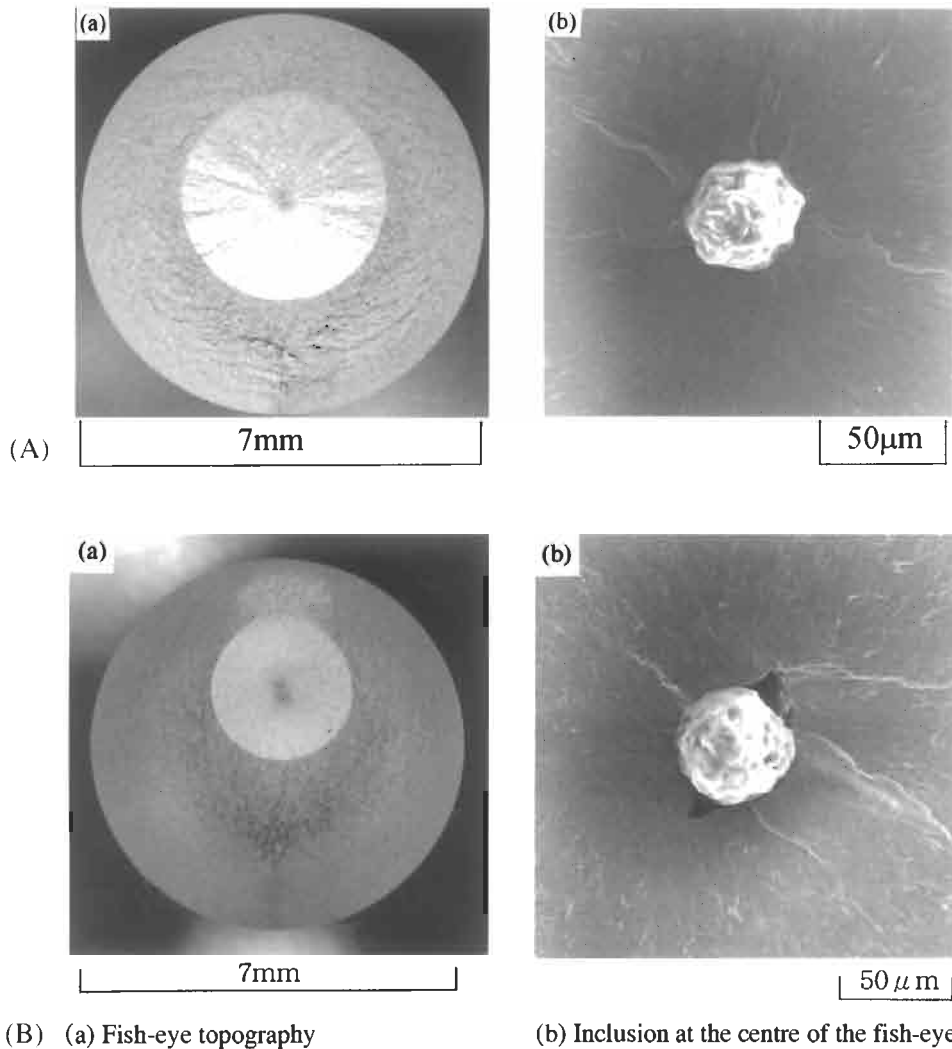
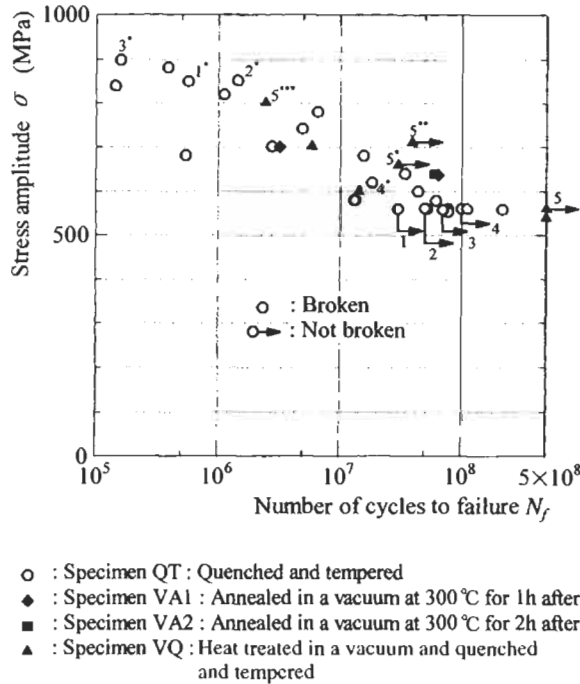


Figure 15.4 (A) Fish-eye topography and the inclusion at the centre of the fish eye for a Specimen QT. $\sigma = 682$ MPa, $N_f = 5.40 \times 10^5$, $\sqrt{area} = 47.8$ μm . (a) Fish-eye topography. (b) Inclusion at the centre of the fish eye. (B) Fish-eye topography and the inclusion at the centre of the fish eye for a Specimen VQ. The specimen was heat treated in a vacuum and the hydrogen content is very low, 0.01 ppm. $\sigma = 600$ MPa, $N_f = 1.43 \times 10^7$, $\sqrt{area} = 55.6$ μm . (a) Fish-eye topography. (b) Inclusion at the centre of the fish eye.

specimen was estimated by the \sqrt{area} parameter model, that is by Eq. 6.9, assuming that a nonmetallic inclusion is equivalent to a small crack. Although the residual stress at the fracture origin inclusion is unknown, for a tentative calculation we assumed that the stress ratio, R , is -1 because the residual stress in the core region of a specimen is thought to be very small.



(The mark * indicates the specimen which ran out and was tested at higher stress levels.)

Figure 15.5 $S-N$ data for Cr-Mo steel, SCM435. Fracture origins are all at nonmetallic inclusions. (The symbols *, ** and *** indicate an unbroken specimen which was retested repeatedly at successively higher stress levels.)

The minimum value of hardness, $H_V = 561$ (see Fig. 15.2), was used for our calculations.

Fig. 15.6 shows a modified $S-N$ curve; this is the relationship between the ratio of the applied stress to the estimated fatigue limit, σ/σ_w , and the number of cycles to failure, N_f . Some specimens failed at $\sigma/\sigma_w < 1.0$ and at $N \geq 10^7$. These results show that evaluations using the \sqrt{area} parameter model are approximately 10% unconservative in predicting the fatigue limit for a fatigue life of $N_f = 10^8$ (approximately).

15.1.6 Details of Fracture Surface Morphology and Influence of Hydrogen

Fig. 15.7 shows optical micrographs of fracture surfaces near fracture origins for Specimen QT. If we carefully observe the centre of a fish eye with an optical microscope, we can find in most cases a dark area in the vicinity of the inclusion at the fracture origin [15]. We call the dark area an ODA (Optically Dark Area). The sizes of ODAs increase with increase in fatigue life. It is interesting that ODAs are not found on the fracture surfaces of specimens which fail at a small number of cycles (see Fig. 15.7a). According to Scanning Electron Microscopy (SEM) observations, ODAs have fracture surfaces

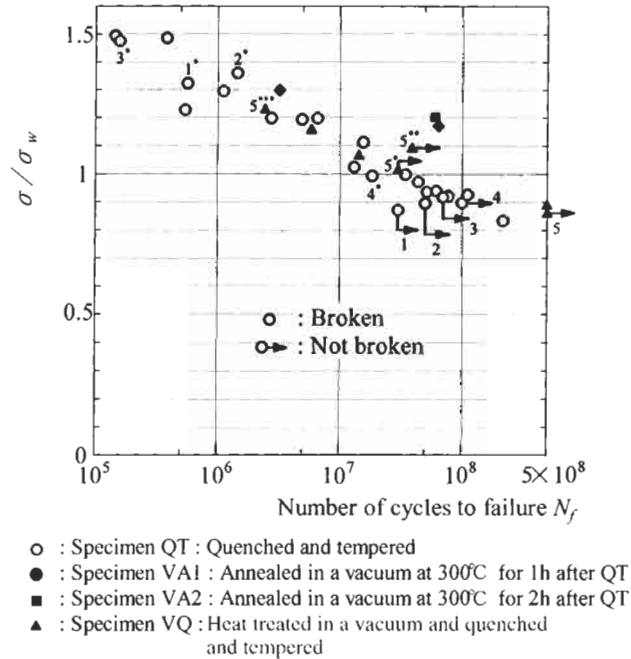


Figure 15.6 Type I modified $S-N$ data. σ = stress amplitude. σ_w = fatigue limit calculated using the $\sqrt{\text{area}}$ parameter model. The value of $\sqrt{\text{area}}$ is calculated from the projected area of the inclusion at a fracture origin. (The symbols *, ** and *** indicate an unbroken specimen which was tested repeatedly at successively higher stress levels.)

quite different from those of the white areas, which show fatigue fracture surfaces typical of the structure of a martensite lath. Fig. 15.8 shows a very rough morphology seen in SEM observation [15] within an ODA. Observations of ODAs by Atomic Force Microscopy (AFM) also reveal a morphology (Fig. 15.9) that is very different from a typical fatigue fracture surface [15].

Fig. 15.10a shows the relationship between the size of ODA and the number of cycles to failure. It is surprising that specimens having a longer life have a larger ODA relative to the original inclusion size as incorporated in the parameter $\sqrt{\text{area}}$ [15]. This implies that fatigue failure after superlong high cycle fatigue beyond $N = 10^7$ cycles may be influenced by environmental conditions such as are induced by hydrogen.

Recently, Takai et al. [17,18], by Secondary Ion Mass Spectrometry (SIMS), verified directly the presence of hydrogen trapped at the interface of inclusions. Figs. 15.11 and 15.12 show the results of Takai et al.'s measurements of desorption of hydrogen from the nonmetallic inclusions by heating steel samples from room temperature to 473 K and 573 K. Takai et al. showed that nonmetallic inclusions trapped hydrogen more strongly than other sites such as dislocations, grain boundaries and microstructural textures, and the hydrogen trapped by nonmetallic inclusions could be desorbed only by heating the sample to more than ~ 573 K. In the present material (Cr-Mo steel, SCM435), the total hydrogen content was found to be 0.3 to 0.4 ppm before heat treatment and 0.7

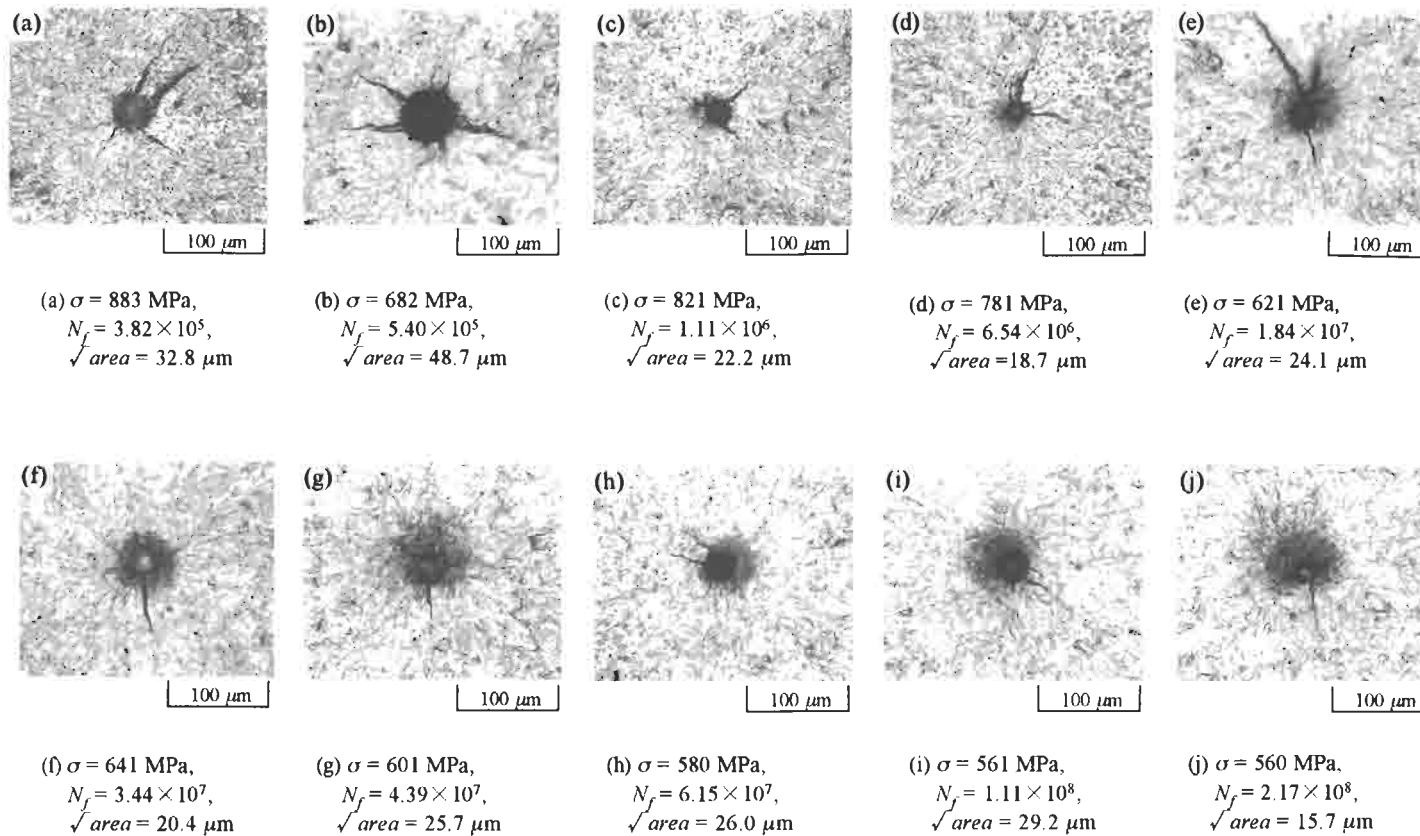


Figure 15.7 Optical micrographs of fracture surfaces near fracture origins for the life region 10^5 cycles to 2×10^8 cycles. The size of dark areas (Optically Dark Area, ODA) in the vicinity of an inclusion at a fracture origin increases with increase in fatigue life.

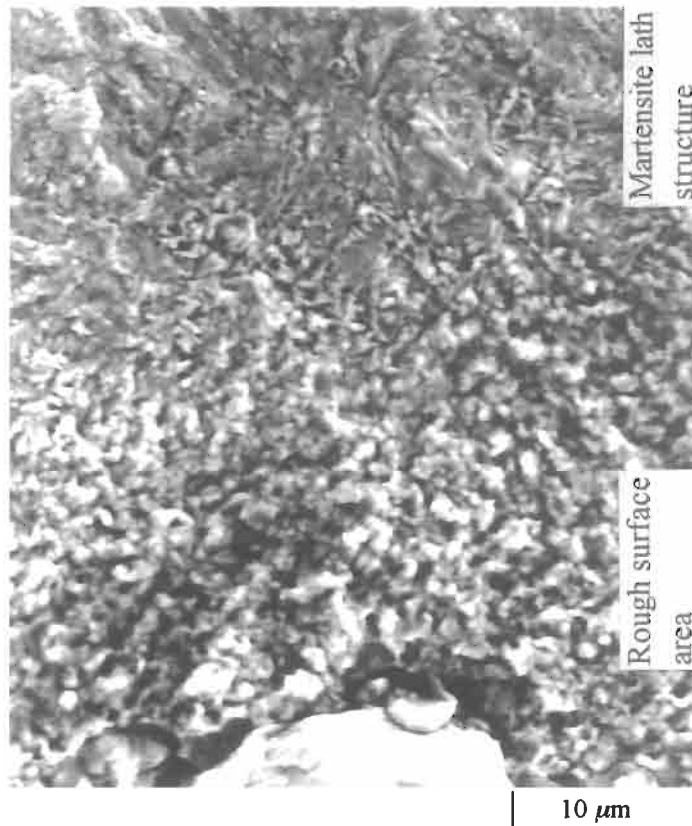


Figure 15.8 The dark area in the vicinity of an inclusion at a fracture origin. Observation by SEM of the ODA shown in Fig. 15.7j. $\sigma = 560$ MPa, $N_f = 2.17 \times 10^8$.

to 0.9 ppm after the conventional quenching and tempering heat treatment of SCM435 (Specimen QT).

If we evaluate the effective size of an inclusion by adding the size of the dark area to the original size of the inclusion, then we can draw another type of modified $S-N$ diagram [15] as indicated in Fig. 15.13. Fig. 15.13 implies a hypothesis that, after very slow fatigue crack growth inside the ODA adjacent to an inclusion, the size of the crack exceeds the critical size for the mechanical threshold value estimated by the $\sqrt{\text{area}}$ parameter model. The fatigue crack then grows, without the assistance of hydrogen, and the resulting fatigue fracture surface is a typical martensite lath structure.

In order to verify this hypothesis, fatigue tests were carried out using Specimens VA1, VA2 and VQ, all of which contain less hydrogen (~ 0.01 ppm) than Specimen QT (0.7–0.9 ppm). Specimens VA1 and VA2 were prepared by annealing Specimen QT at 300°C, in a vacuum, for 1 h and 2 h, respectively. Heating at 300°C is necessary in order to desorb the hydrogen trapped by inclusions. Specimens VQ were prepared by vacuum quenching.

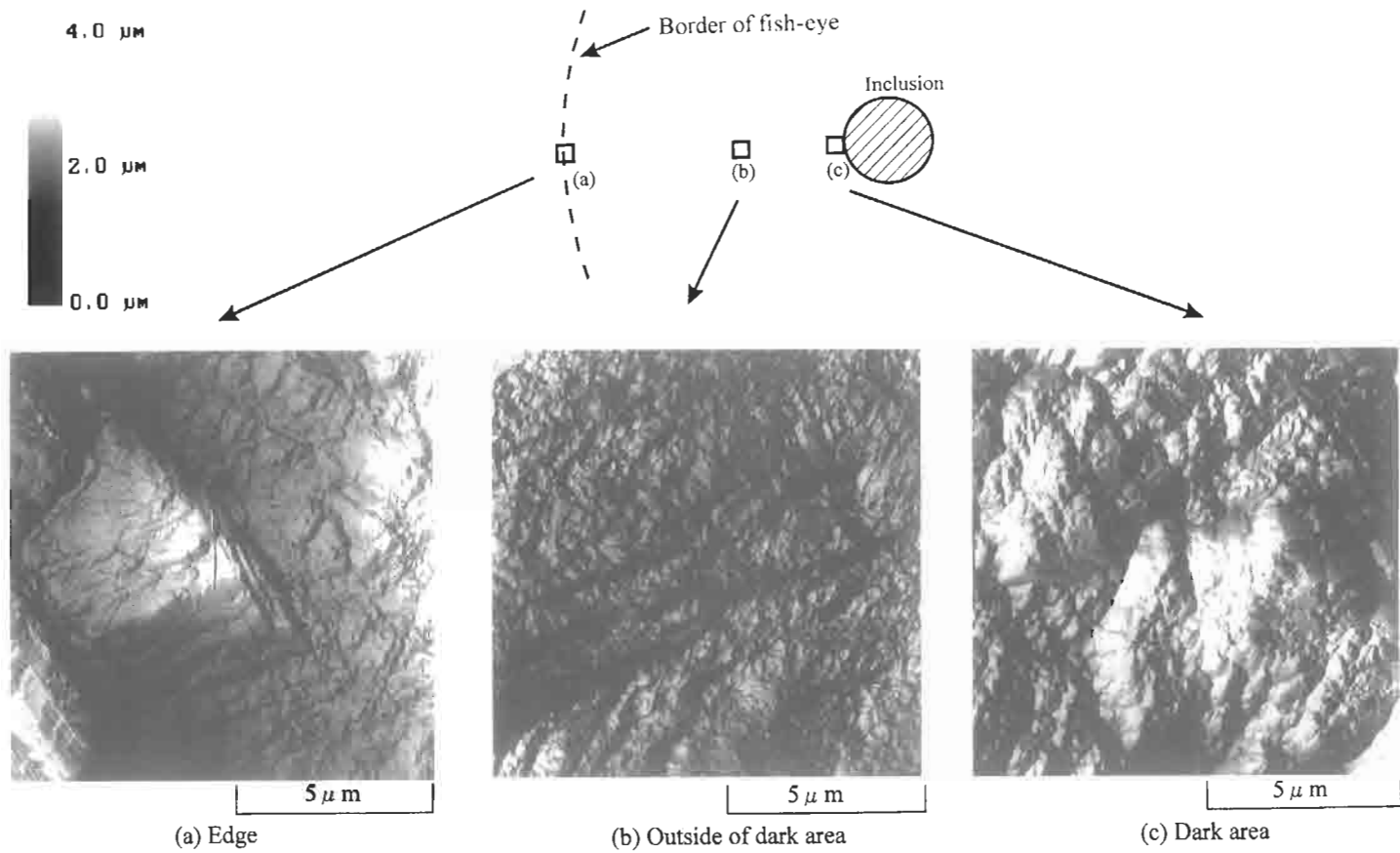


Figure 15.9 AFM observation of the fracture surface of the same specimen as in Fig. 15.8. $\sigma = 560$ MPa, $N_f = 2.17 \times 10^8$.

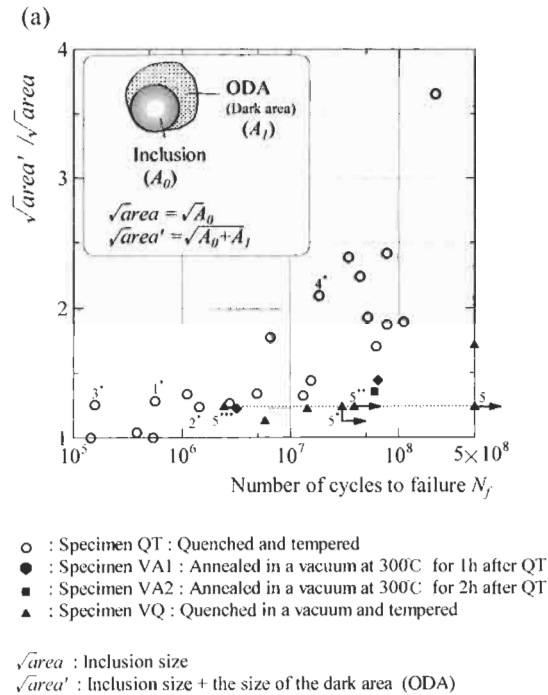
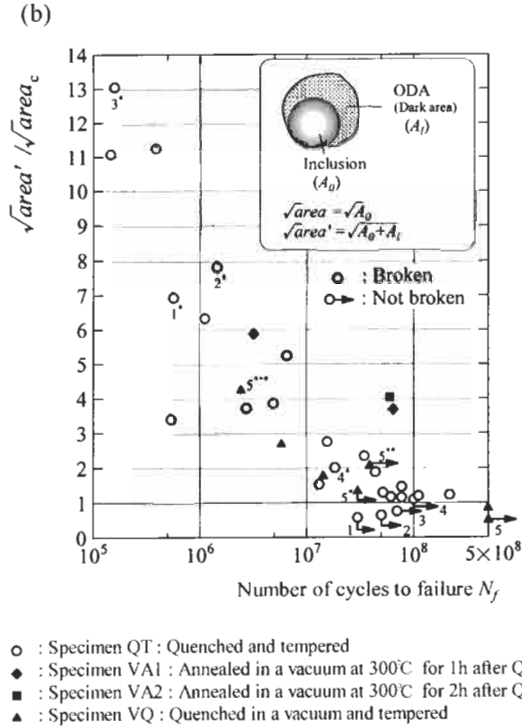


Figure 15.10 The importance of the Optically Dark Area (ODA) in ultralong life fatigue failure. (For symbols *, ** and ***, see caption of Fig. 15.5 or 15.6.) (a) Relationship between ODA size and cycles to failure. Open symbols show ODAs in Specimen QT. The symbols ◆ and ■ show ODAs in Specimen VA1 and Specimen VA2, respectively. The symbol ▲ shows ODAs in Specimen VQ. The ODAs in Specimens VA1 and VA2 are smaller than those for Specimen QT. The ODAs in Specimen VQ are much smaller than in other specimens.

The symbols ◆ and ■ in Fig. 15.10a show the ODAs in Specimens VA1 and VA2 respectively. The symbol ▲ shows the ODAs in Specimen VQ. The ODAs in Specimens VA1 and VA2 are smaller than those for Specimen QT. The ODAs in Specimen VQ are much smaller than in other specimens. Thus, we may conclude that the hydrogen trapped by an inclusion crucially influences the formation of an ODA: the particular fracture morphology around the inclusions at fracture origins. Although the mechanism of the interaction of hydrogen and stress is still not clear, a possible mechanism may be [19–28] that hydrogen enhances the mobility of screw and edge dislocations, and reduces internal friction. In this context, we may regard the influence of hydrogen on superlong fatigue as an internal environmental factor contained within a material.

Examples of fish eyes that were formed at origins other than inclusions may support this hypothesis. Murakami et al. [29] conducted rotating bending fatigue tests on a bearing steel produced by a special melting method (the same material as presented in Chapter 7 (page 148)). In this particular case no ODAs were observed adjacent to fracture origins except for very rare examples in which nonmetallic inclusions did become fracture origins. The bearing steel was processed using a double electron beam



(The mark * indicates the specimen which ran out and was tested at higher stress levels.)

Figure 15.10 (b) \sqrt{area}_c is the critical size of an ODA for crack growth, without the assistance of hydrogen, evaluated using $\sqrt{area}_c = [1.56(H_V + 120)/\sigma]^6$ for an applied stress amplitude, σ . Note that all the values of $\sqrt{area}(\text{ODA}+\text{inclusion})$ exceed the critical size, \sqrt{area}_c , that is $\sqrt{area}' / \sqrt{area}_c > 1.0$, except for just one case.

remelting method and contained extremely small nonmetallic inclusions. In this bearing steel the size of the bainitic structure produced by locally imperfect quenching was larger than the size of the nonmetallic inclusions. Therefore, the fracture origins were mostly at the bainitic structure, which is much softer than the martensite matrix. In this case, hydrogen is not concentrated around the bainitic structure. Fig. 15.14 shows clearly the difference in the morphology of fracture from bainite and from inclusions.

Very recently (beginning of 2000) Murakami et al. [30], using SIMS, found direct evidence of hydrogen present at nonmetallic inclusions which were fatigue fracture origins in Specimen QT (SCM435). Fig. 15.15a shows the hydrogen H^- and aluminum $^{27}Al^-$ concentration found at the inclusion at the fracture origin in a Specimen QT. Fig. 15.15b shows that the Specimen VQ contains almost no hydrogen at the inclusion at the fracture origin.

If we re-examine Fig. 15.10a and compare the size of ODAs for Specimens QT and VQ, we can understand that the longer life for Specimen VQ than for Specimen

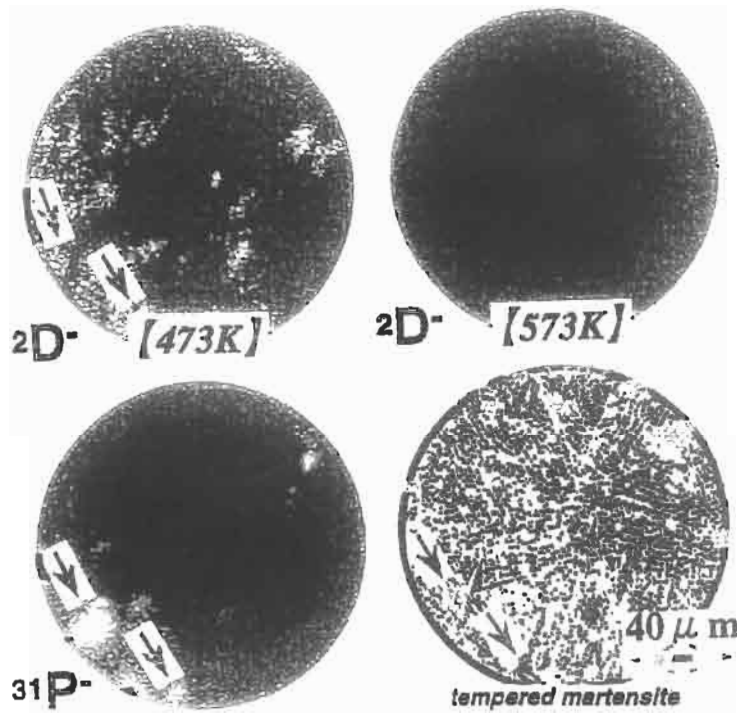


Figure 15.11 Evidence of hydrogen trapped by nonmetallic inclusions. Secondary ion images of $^2\text{D}^-$, and $^{31}\text{P}^-$ after heating at 473 K and 573 K obtained by TDS (Thermal Desorption Spectrometry), and optical microstructure of the PC bar [17].

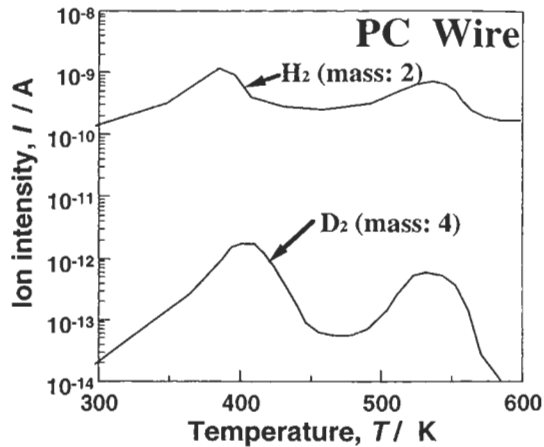


Figure 15.12 Hydrogen and deuterium evolution curves during continuous heating of PC wire measured by FIP test using TDS. FIP: Fédération Internationale de la Précontrainte. It is to be noted that heating over 300°C is necessary to desorb the hydrogen trapped by nonmetallic inclusions [17].

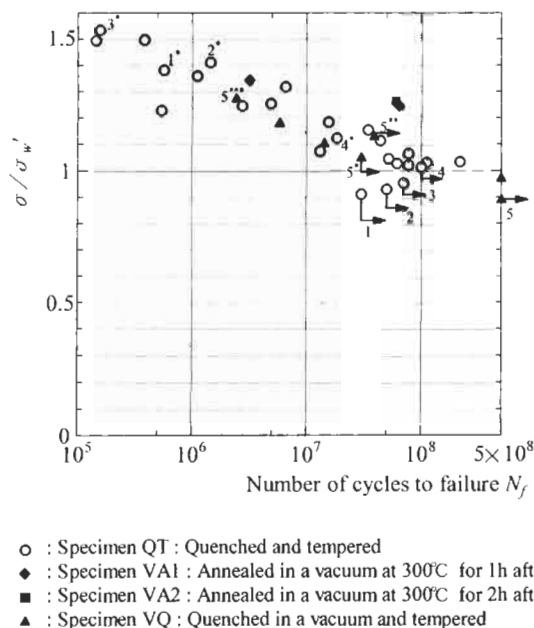


Figure 15.13 A type 2 modified $S-N$ curve. (For the symbols *, ** and ***, see the caption of Fig. 15.5 or 15.6. We assumed that an ODA was produced during the final fatigue test.) σ = stress amplitude. σ_w' = fatigue limit calculated using the \sqrt{area} parameter model taking ODAs into account. The value of \sqrt{area} is evaluated so as to be equivalent to $\sqrt{area(ODA+inclusion)}$. It is noted that ODAs have a crucial role in the elimination the fatigue limit. It can be said that, even if the original size of the inclusion does not exceed the critical size for the fatigue limit stress, $\sqrt{area(ODA+inclusion)}$ for a failed specimen does exceed the critical size.

QT, for the same value of ODA, is due to the lower hydrogen content in Specimen VQ. This retards the fatigue crack growth up to the critical size for the mechanical fatigue threshold. The critical size of an ODA for crack growth without the assistance of hydrogen can be evaluated by using Eq. 6.9 as:

$$\sqrt{area}_c = [1.56(H_V + 120)/\sigma]^6 \tag{15.1}$$

where \sqrt{area}_c is the critical size of (ODA + inclusion) for the applied stress amplitude σ .

Fig. 15.10b shows the relationship between the relative values of the size of $\sqrt{area(ODA+inclusion)}$ observed on the fracture surface to the critical size \sqrt{area}_c and the number of cycles to failure. All specimens having $\sqrt{area(ODA+inclusion)}/\sqrt{area}_c > 1.0$ failed. Specimens having $\sqrt{area(ODA+inclusion)}/\sqrt{area}_c < 1.0$ did not fail up to the number of cycles at the first stress level (the number without the symbol *), except for one specimen which failed at $N_f = 5 \times 10^8$.

Thus, we may conclude that the horizontal step in the $S-N$ diagram that corresponds to the conventional or classical fatigue limit, is caused by the so-called mechanically determined threshold mechanism based on crack closure or on microstructural barriers,

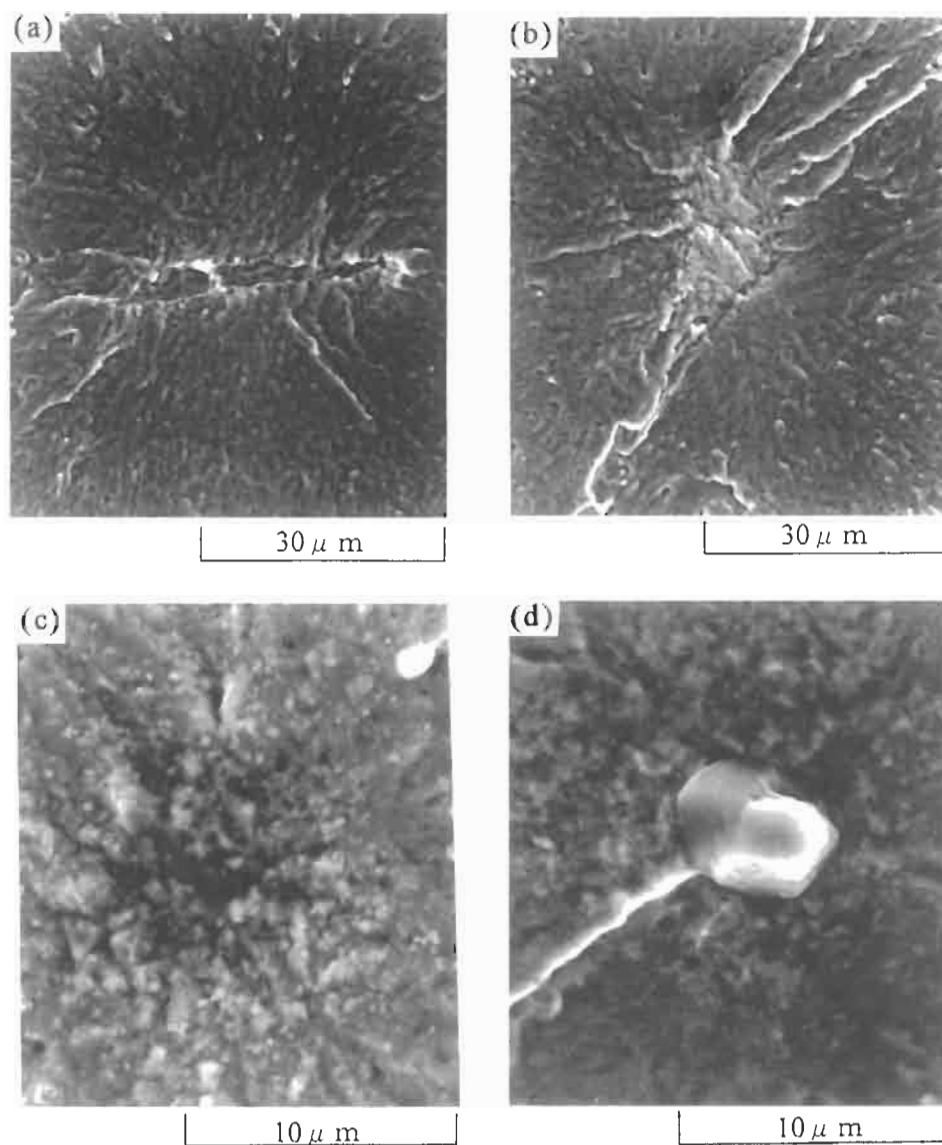
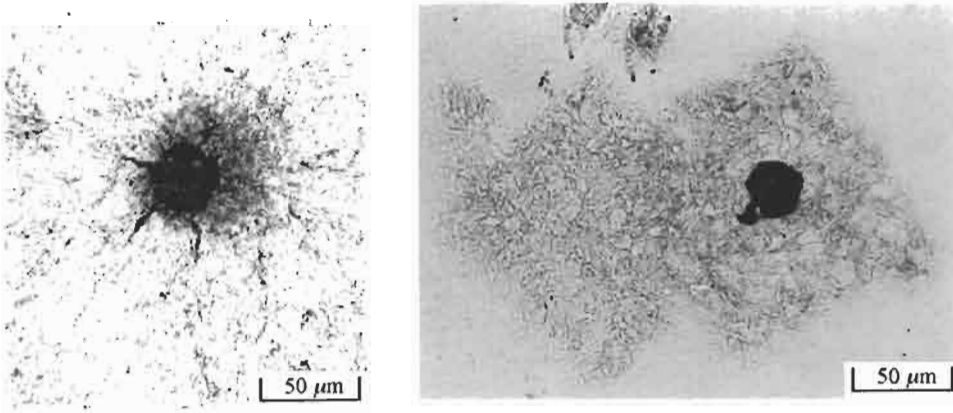
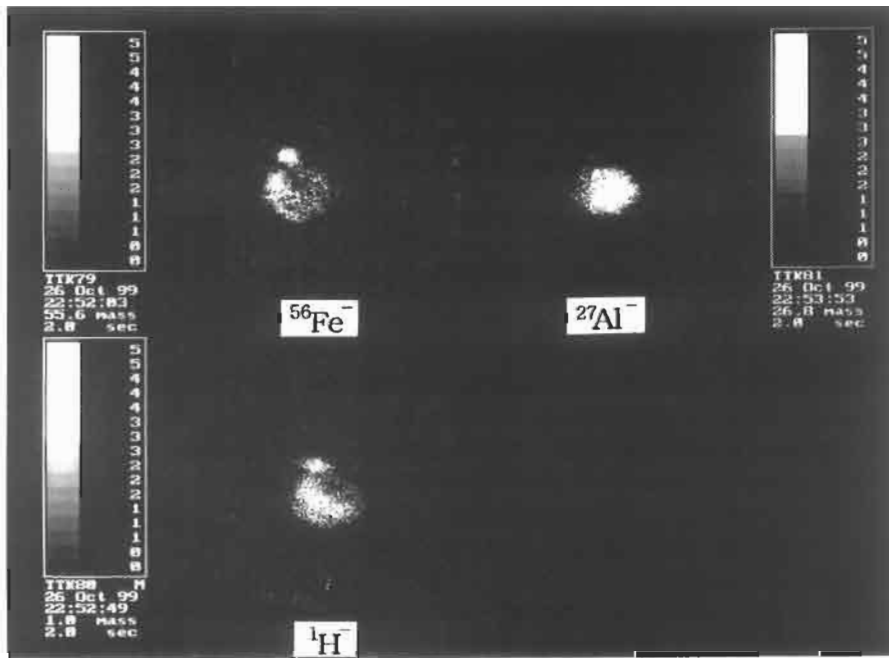


Figure 15.14 Existence of ODA, which looks rough by SEM observation, adjacent to a nonmetallic inclusion at a fracture origin but absence of ODA (rough area) at fracture origins from softer bainites within harder martensitic matrix (rotating bending fatigue of electron-beam remelted super clean bearing steel [29]). (a) Fracture surface of specimen originating at bainite $\sigma = 902$ MPa, $N_f = 8.22 \times 10^5$. (b) Fracture surface of specimen originating at bainite. $\sigma = 1074$ MPa, $N = 5.0 \times 10^7 \rightarrow \sigma = 1145$ MPa, $N_f = 1.3 \times 10^7$. (c) Fracture surface of specimen originating at an inclusion (MnS) $\sigma = 1099$ MPa, $N_f = 4.04 \times 10^6$. (d) Fracture surface of specimen originating at an inclusion (Al_2O_3). $\sigma = 1053$ MPa, $N_f = 2.03 \times 10^7$.



(a-1) Inclusion at fracture origin

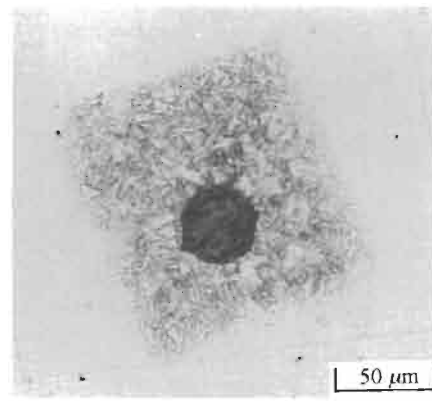
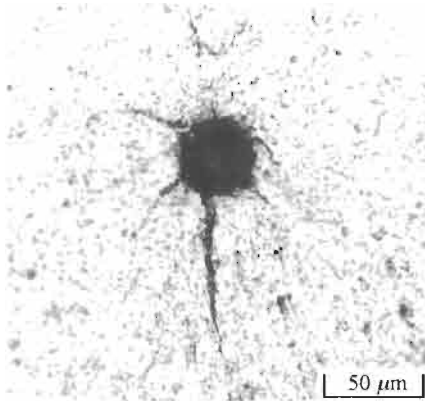
(a-2) Ion beam scanned area by SIMS measurement



(a-3) Secondary ion image by SIMS measurement

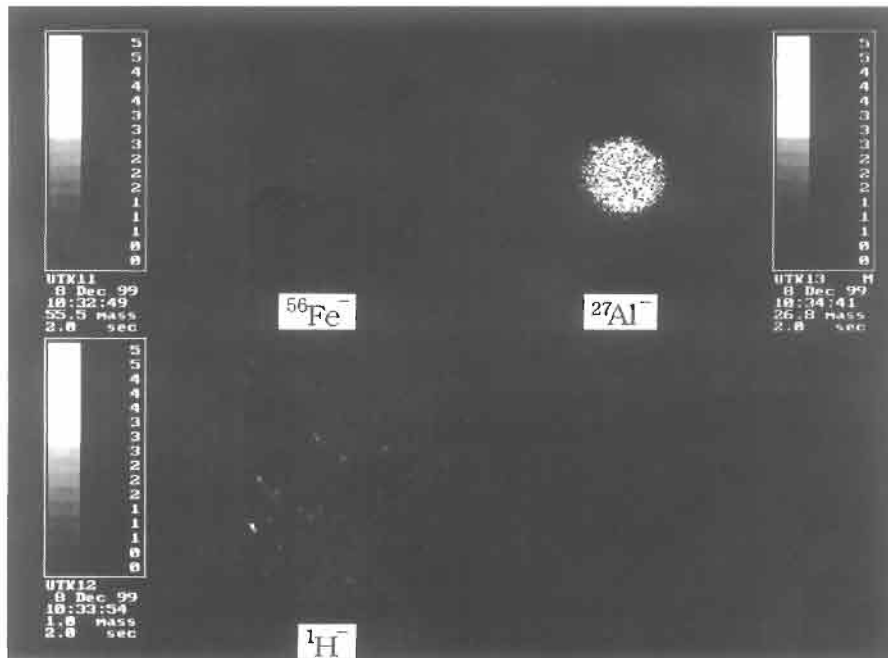
$\sigma = 561 \text{ MPa}$, $N_f = 5.17 \times 10^7$, $\sqrt{\text{area}} = 31 \text{ }\mu\text{m}$.

Figure 15.15 (a) Secondary ion image of hydrogen trapped by the inclusion at fatigue fracture origin for quenched and tempered specimen (Specimen QT, SCM 435) [30]. (a-1) Inclusion at fracture origin. (a-2) Ion beam scanned area by SIMS measurement. (a-3) Secondary ion image by SIMS measurement. $\sigma = 561 \text{ MPa}$, $N_f = 5.17 \times 10^7$, $\sqrt{\text{area}} = 31 \text{ }\mu\text{m}$.



(b-1) Inclusion at fracture origin

(b-2) Ion beam scanned area by SIMS measurement



(b-3) Secondary ion image by SIMS measurement

$$\sigma = 702 \text{ MPa}, N_f = 5.83 \times 10^6, \sqrt{\text{area}} = 35.4 \text{ } \mu\text{m}.$$

Figure 15.15 (b) Secondary ion image of hydrogen trapped by the inclusion at fatigue fracture origin for the specimen heated in a vacuum (Specimen VQ, SCM 435) [30]. (b-1) Inclusion at fracture origin. (b-2) Ion beam scanned area by SIMS measurement. (b-3) Secondary ion image by SIMS measurement. $\sigma = 702 \text{ MPa}$, $N_f = 5.83 \times 10^6$, $\sqrt{\text{area}} = 35.4 \text{ } \mu\text{m}$.

and that the $S-N$ data below the step in the region of $N > 10^7$ cycles are the result of fatigue coupled with environmental conditions such as hydrogen embrittlement.

High strength steels are sensitive to delayed fracture due to hydrogen embrittlement. It is known that heat-treated steels tend to contain a high hydrogen content around inclusions. We need to consider this particular but important practical problem of fatigue failure in the regime of $N > 10^7$ cycles in structural design of components made from high strength steels. The need to revise existing design codes in terms of this problem is suggested by Miller and O'Donnell [14].

15.2 Fractographic Investigation

In the fracture mechanics analysis of superlong fatigue lives described in the previous section, it was shown that fatigue crack growth without the assistance of hydrogen trapped by nonmetallic inclusions starts after the size of the fracture area, \sqrt{area} , exceeds the critical value, $\sqrt{area_c}$ (shown schematically in Fig. 15.16). $\sqrt{area_c}$ includes: (1) the area of the nonmetallic inclusion at a fracture origin, and (2) the area having a particular morphology, ODA (Optically Dark Area) surrounding the inclusion at the fracture origin, within which fatigue crack propagation is aided by hydrogen. In the previous section it was hypothesised that the cause of fatigue failure in the

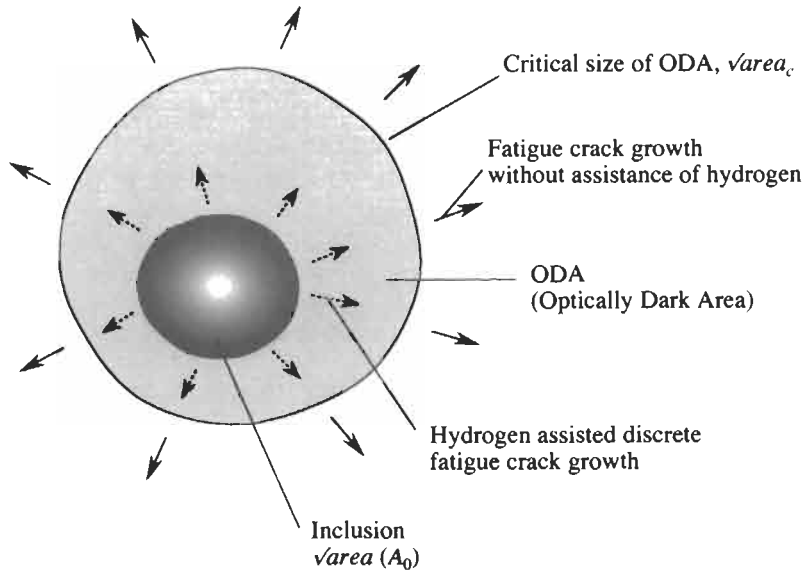


Figure 15.16 Schematic illustration of fatigue crack growth from a nonmetallic inclusion. Hydrogen is trapped by the inclusion. In the first stage, the crack initiates and grows intermittently, and accordingly at a very slow rate, with the assistance of hydrogen trapped by the inclusion. This stage of crack growth under cyclic stress produces a rough fracture surface (ODA). When the size of $\sqrt{area(ODA+inclusion)}$ reaches the critical value, $\sqrt{area_c}$, crack growth without the assistance of hydrogen starts. The value of $\sqrt{area_c}$ is determined by the \sqrt{area} parameter model: $\sqrt{area_c} = [1.56(H_V + 120)/\sigma]^6$ (see Eq. 15.1).

superlong life regime ($N > 10^7$) was that the mechanical fatigue threshold for a small crack emanating from a nonmetallic inclusion was reduced by an environmental effect associated with hydrogen trapped by nonmetallic inclusions. In this section, in order to further verify this hypothesis, the fatigue fracture surface outside an ODA is investigated fractographically using an Atomic Force Microscope (AFM). The number of cycles consumed in crack propagation from the edge of an ODA to the boundary of the fish eye is estimated on the basis of a detailed examination of the fatigue fracture surface.

15.2.1 Measurement of Surface Roughness

The surface roughness, R_a , of fractured fatigue specimens was measured in the radial direction of the circular cross-section (x -coordinate of Eq. 15.2) by AFM. R_a is the mean surface roughness, defined in a square area, $l \times l$ by:

$$R_a = \frac{1}{l} \int_0^l |f(x)| dx \quad (15.2)$$

where $f(x)$ is the surface roughness function in a square area, $l \times l$, which appears on one section cutting the square area by a plane perpendicular to the square area. The value l was set at 10 μm . The plane of $f(x) = 0$ is defined such that the integral area above $f(x) = 0$ is equal to that below $f(x) = 0$. This procedure can be carried out automatically by the AFM software. A crack which initiates at an inclusion quickly tends to a penny shape regardless of the shape of the inclusion. Therefore, the stress intensity factor range for a penny-shaped crack of radius r can be determined using:

$$\Delta K_I = \frac{2}{\pi} \Delta \sigma \sqrt{\pi r} \quad (15.3)$$

Eq. 15.3 is of high accuracy even for a penny-shaped crack which is not concentric with the axis of the cylindrical specimen and also having a radius of up to one-half of the radius of the specimen [31].

Fig. 15.17 shows the results of surface roughness measurements for the Cr–Mo steel, SCM435. At the same value of ΔK_I profiles are very similar, regardless of the values of applied stress. As shown in Fig. 15.18, R_a increases monotonically with increasing ΔK_I . Despite the large scatter in the data, the following equation is considered to hold:

$$R_a = C \Delta K_I^2 \quad (15.4)$$

where C is a material constant.

Fig. 15.19 shows a similar relationship between ΔK_I and R_a for the 0.46% C steel (S45C) [8], that is $R_a \propto \Delta K_I^2$.

15.2.2 The Outer Border of a Fish Eye

The inside of a fish eye looks white to the naked eye or under the optical microscope, whereas the region outside the fish eye looks grey. This difference in colour is presumed to be caused by different fracture mechanisms, although this has not previously been established. The matter is resolved herein by detailed AFM and SEM observations.

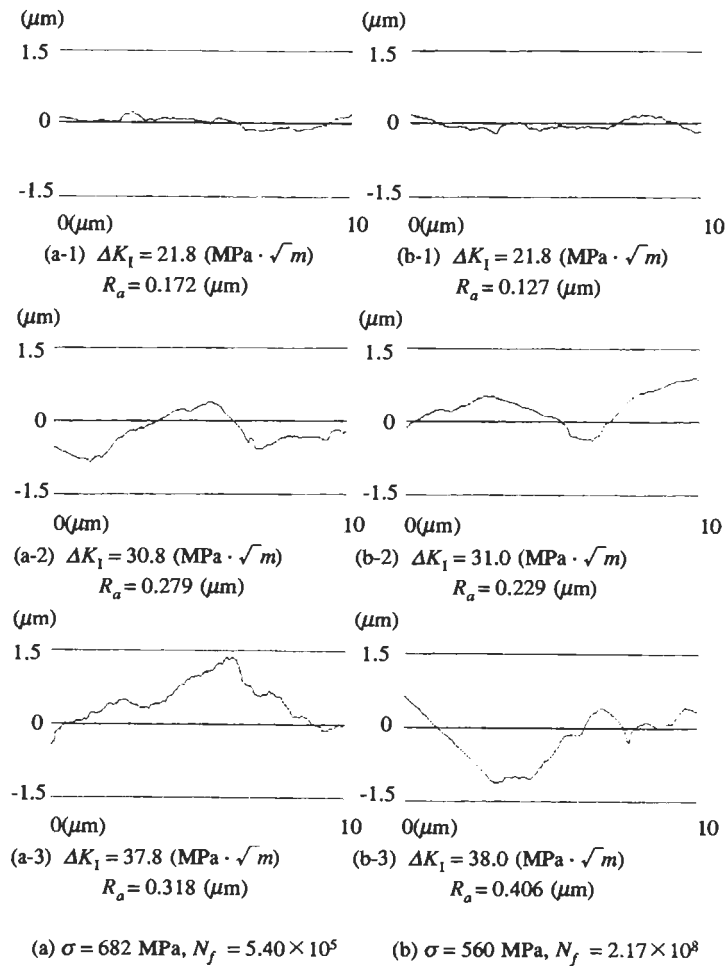


Figure 15.17 Profiles of roughness of the fracture surface R_a (SCM435).

Figs. 15.20 and 15.21 show AFM micrographs at the border of a fish eye, together with roughness curves, for the SCM435 steel and for the 0.46% C heat-treated medium carbon steel. These figures reveal that there is a cliff at the border of a fish eye, with the outside being higher than the inside. This morphology was observed around the entire border of a fish eye. It was also observed that the morphology of the mating fracture surface is similar. Thus, it can be concluded that the border of a fish eye has the characteristics of a stretched zone.

Fig. 15.22 shows the relationship between fatigue life, N_f , and the cliff height, H , at a fish-eye border. Three measurements were made at each symbol \square in Fig. 15.22, and the average value was plotted in the figure. The values of H for SCM435 are approximately $2.0 \mu\text{m}$ regardless of N_f and fish-eye size. The values of H for 0.46% C

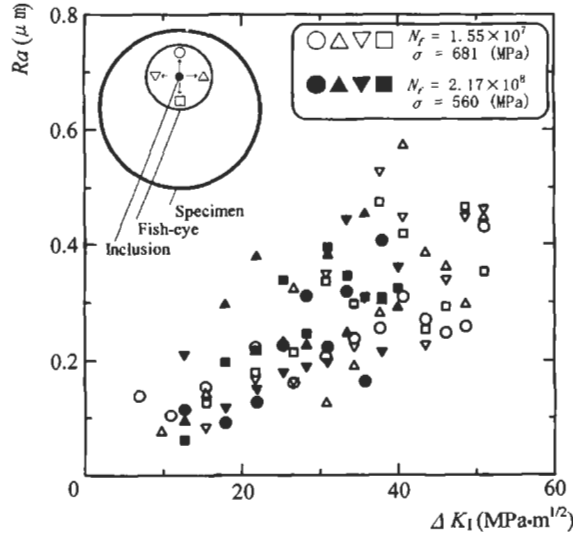


Figure 15.18 ΔK_I vs. fracture surface roughness, R_a (SCM435).

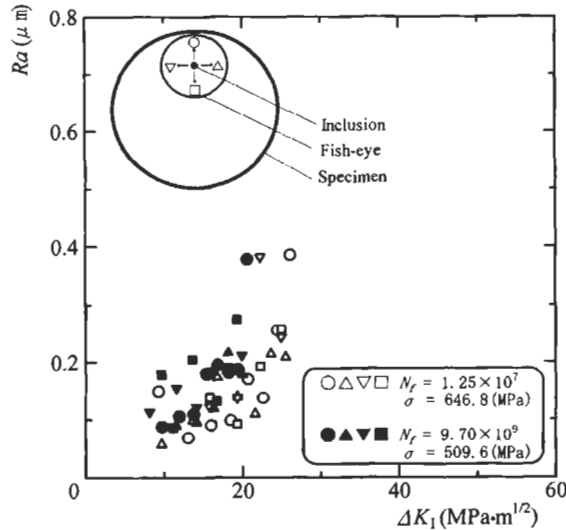
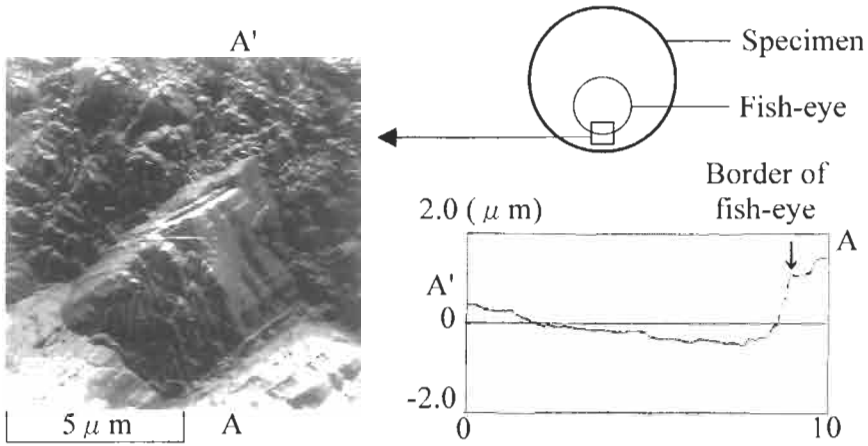


Figure 15.19 ΔK_I vs. fracture surface roughness, R_a (S45C).

steel are approximately $1.4\text{--}1.8\ \mu\text{m}$ also regardless of N_f and fish-eye size. This implies that when the crack tip opening displacement (CTOD) reached a critical constant value, the fracture mechanism changed from fatigue to static fracture.

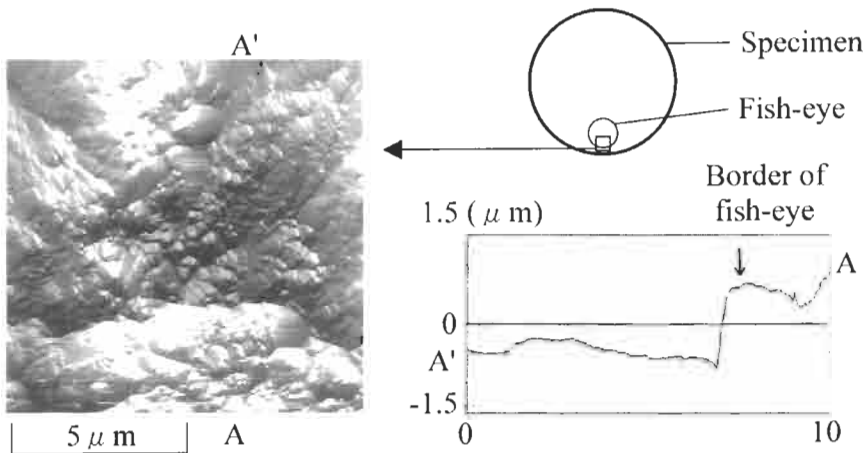
Fig. 15.23 shows the fracture surface morphology at and outside the border of a fish eye. The presence of ductile dimples in portions of Fig. 15.23a–c provides evidence of microscopic ductile fracture. Fig. 15.23d shows intergranular fracture (but partially



(a) Border of fish-eye

(b) Roughness curve (μm)

Figure 15.20 AFM observation at the border of a fish eye (SCM435). $\sigma = 560\text{ MPa}$, $N_f = 2.17 \times 10^8$.



(a) Border of fish-eye

(b) Roughness curve (μm)

Figure 15.21 AFM observation at the border of a fish eye (S45C). $\sigma = 509.6\text{ MPa}$, $N_f = 9.70 \times 10^7$.

transgranular) near the specimen surface where the hardness is higher than the core of a specimen.

The fracture surface morphology of 0.46% C steel was essentially the same as that of SCM435 steel, with the fracture surface outside a fish eye containing evidence of separation by both intergranular and transgranular fracture modes, but with less evidence of ductile dimples.

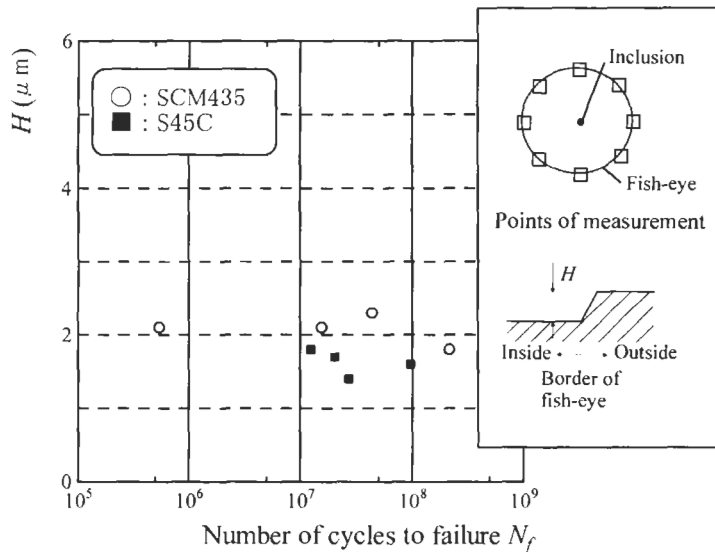
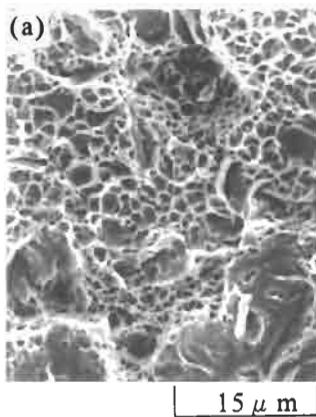
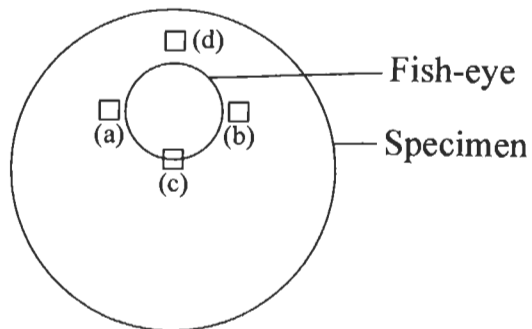


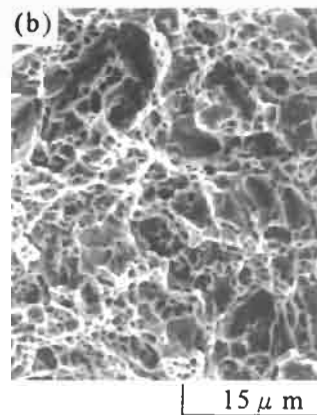
Figure 15.22 Relationship between N_f and cliff height at a fish-eye border, H .

Therefore, it can be concluded from the AFM and SEM observations for tension–compression fatigue that the fatigue fracture surface is limited to the inside of a fish eye, and that the fracture surface outside a fish eye is produced by static fracture. However, we limit this conclusion to tension–compression fatigue, because the situation in rotating bending fatigue is somewhat different, as is discussed in the following.

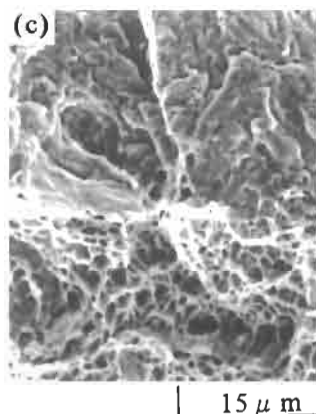
It is quite common for fish eyes to develop in rotating bending fatigue tests on hard steels, with the fracture origin being located at a subsurface, nonmetallic inclusion. However, the contours of fish eyes are not complete circles as in the case of axial loading, but are mostly partial circles because of the interaction of a fish eye with the specimen surface, as shown in Fig. 15.24 [32]. In such cases, the crack usually continues to grow by fatigue even after the fish eye has reached the specimen surface. In this type of crack growth, the stress intensity factor at the crack front near the specimen surface increases drastically once the fish eye has reached the specimen surface and, as a consequence, the fatigue crack growth rate increases rapidly near the specimen surface. As a result, the crack shape quickly changes from a circle to a semicircle or to a semi-ellipse. When the size of the semi-elliptical crack reaches a critical value, the fracture surface changes from a fatigue fracture surface to a static fracture surface. Thus, in rotating bending we have two kinds of fatigue fracture surface. One is within the fish eye and the other is outside. The fatigued region within the fish eye appears white under the optical microscopic, whereas the fatigue zone outside the fish eye appears grey. The difference in the colours of the two types of fatigue fracture surface is caused by cyclic contact of the fracture surfaces in the absence of atmospheric effects within the fish eye, and by cyclic contact of the fracture surfaces in the presence of atmospheric effects outside the fish eye.



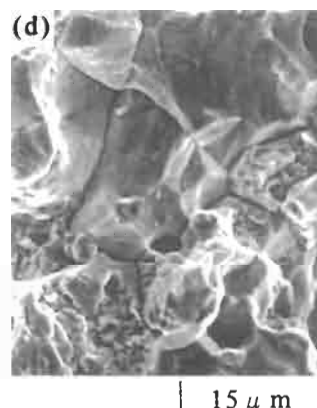
(a) $HV = 560\sim 650$ (kgf/mm²)



(b) $HV = 560\sim 650$ (kgf/mm²)



(c) $HV = 560\sim 650$ (kgf/mm²)



(d) $HV = 700\sim 780$ (kgf/mm²)

Figure 15.23 SEM observation outside fish eyes (SCM435). $\sigma = 560$ MPa, $N_f = 2.17 \times 10^8$.

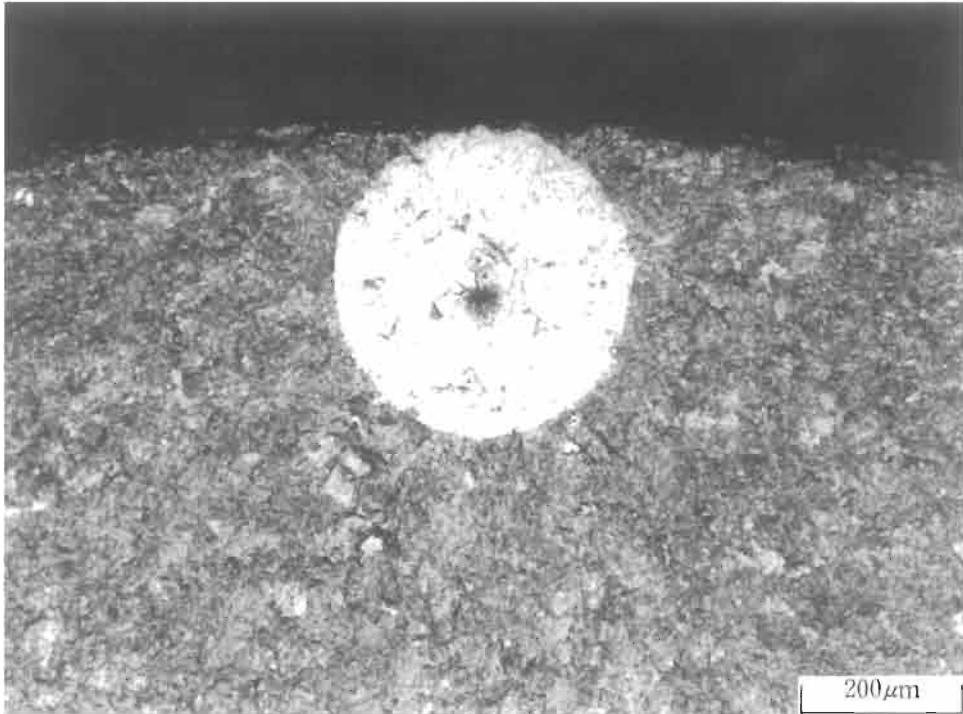


Figure 15.24 Fish eye observed in rotating bending fatigue. Backup roll steel $H_v = 561$, nominal stress $\sigma = 843$ MPa, $N_f = 1.03 \times 10^7$, inclusion size $\sqrt{\text{area}} = 16.7$ μm , depth from surface $h = 212$ μm , nominal stress at the inclusion 772 MPa.

15.2.3 Crack Growth Rate and Fatigue Life

In the fatigue fracture region beyond an ODA, fatigue crack growth is assumed to occur under a mechanical driving force without the assistance of hydrogen. In this region we assume the Paris fatigue crack growth law [33] to hold, that is:

$$\frac{da}{dN} = C \Delta K_I^m \quad (15.5)$$

where C and m are material constants. Those specimens which failed at a small number of cycles did not have an ODA, and we assume that a crack grew cycle by cycle from the edge of an inclusion to the border of the fish eye. Therefore, the material constants C and m were determined by using data from two specimens which did not develop an ODA. These specimens failed at $N_f = 5.40 \times 10^5$ and $N_f = 3.82 \times 10^5$, respectively. To determine C and m , Eq. 15.5 was integrated using the data shown in Table 15.3, that is assuming $a = a_{\text{inc}}$ (radius of inclusion) $\rightarrow a_f$ (radius of fish eye) and $N = N_0 (= 0) \rightarrow N$. The resulting simultaneous equations were then solved to determine C and m .

The value of m obtained in this way was 2.18. On the basis of the Dugdale model, both the plastic zone size and CTOD at a crack tip in the linear elastic fracture mechanics range are proportional to ΔK_I^2 . Hence, Figs. 15.18 and 15.19 should show

Table 15.3 Data for determining C and m in Eq. 15.5

σ (MPa)	N_f	a_{inc} (μm)	a_f (μm)
682	5.40×10^5	27.5	1800
883	3.82×10^5	19.2	930

σ : Stress amplitude. N_f : Cycles to failure.

a_{inc} : Radius of inclusion. a_f : Radius of fish-eye.

the relationship $R_a \propto \Delta K_1^2$. If we assume that the surface roughness, R_a , and crack growth rate da/dN are both proportional to ΔK_1^2 , then m in Eq. 15.5 should be 2. Since the calculated value of m was close to 2, and taking into account experimental scatter we assume $m = 2$. The value of C was taken to be the average of the two values $C = 3.27 \times 10^{-12}$ and 2.56×10^{-12} which were calculated using the data listed in Table 15.3. Thus we have:

$$\frac{da}{dN} = 2.92 \times 10^{-12} \Delta K_1^2 \quad (15.6)$$

From the above discussion, Eq. 15.6 expresses the crack growth rate outside an ODA. Integrating Eq. 15.6, we can obtain the number of cycles, N_{p2} for the crack to grow from the edge of an ODA to the border of the fish eye, that is:

$$N_{p2} = \int_{a_{(ODA)}}^{a_f} \frac{1}{2.92 \times 10^{-12} (\Delta K_1)^2} da \quad (15.7)$$

Fig. 15.25 shows the resulting S - N_{p2} diagram. If we accept the assumptions concerning crack growth discussed above, then we have the result that N_{p2} only ranges at most from 3.0×10^5 to 1.0×10^6 cycles, which is but a small fraction of the total fatigue life in the ultrahigh fatigue life range where the ODA is formed. The result of this calculation indicates that an ultralong fatigue life is mostly consumed in crack initiation and growth within the ODA. Since the size of the ODA increases with decrease in stress amplitude, those specimens having the longest fatigue lifetimes spend the largest portion of the fatigue lifetime propagating cracks within the ODA.

Further, since from Fig. 15.18 we have obtained a relationship between ΔK_1 and R_a , and have also established a relationship between ΔK_1 and da/dN , we can also obtain a relationship between da/dN and R_a , as shown in Fig. 15.26. Fig. 15.26 indicates that the surface roughness, R_a , of the fatigue fracture surface increases with increasing da/dN , and therefore the surface roughness of a fatigue fracture surface reflects the crack growth rate. Fig. 15.26 can therefore be used to estimate fatigue crack growth rates.

15.3 Current Conclusions

The topic treated in this chapter is relatively new. A consensus on the mechanism of disappearance of the conventional (or classical) fatigue limit for $N = 10^7$ has yet to

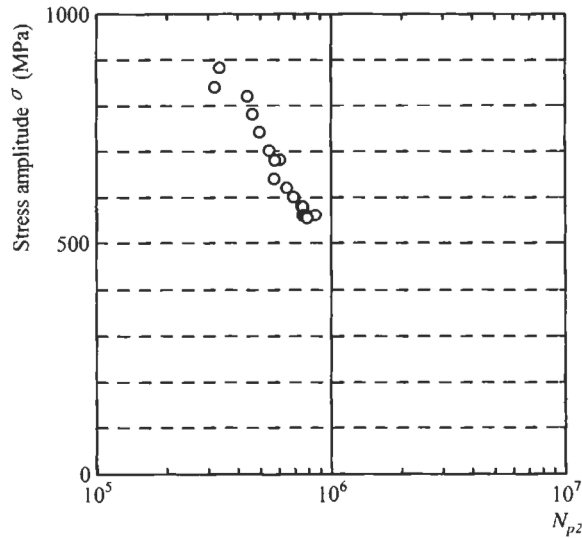


Figure 15.25 $S-N_{p2}$ data (SCM435). N_{p2} : cycles for crack growth from the edge of an ODA to the border of the fish eye.

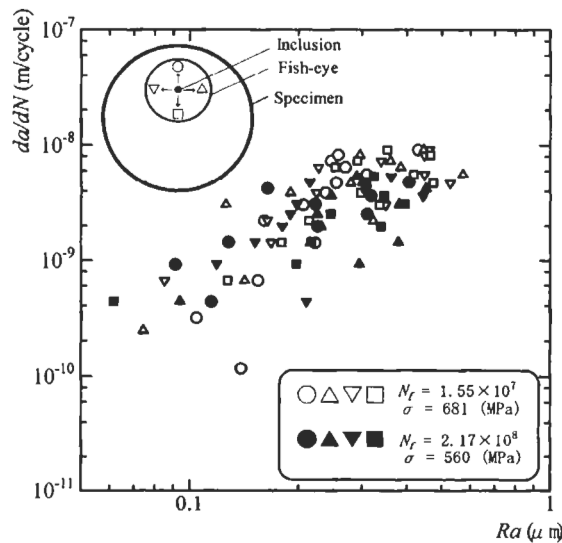


Figure 15.26 Fracture surface roughness R_a vs. estimated da/dN (SCM435).

be achieved. Therefore, more detailed studies must be done in the future. However, at present the following conclusions can be drawn based on fatigue tests up to 5×10^8 cycles on specimens of a heat-treated Cr-Mo steel, SCM435, which contain different amounts of hydrogen.

(1) Three series of specimens were prepared to investigate the influence of hydrogen content on fatigue fracture morphology. The first series of specimens was prepared by a conventional heat treatment (quenched and tempered after carburising and nitriding, Specimens QT), and contained 0.7–0.9 ppm of hydrogen. The second series (Specimen VA) was prepared by annealing Specimens QT in a vacuum at 300°C in order to desorb hydrogen by heating. The third series (Specimens VQ) was prepared by heating in a vacuum followed by quenching, and contained 0.01 ppm of hydrogen. All specimens had a particular fracture surface morphology adjacent to the nonmetallic inclusion at a fracture origin. This looked dark under optical microscopic observation. The dark area was called ODA (Optically Dark Area).

(2) The size of an ODA for Specimen QT increased monotonically with increasing fatigue life. Specimens that failed in the region of $N_f = 10^5$ cycles had almost no ODA, although specimens which failed in the region of $N_f \geq 10^8$ cycles had ODAs larger than twice the size of the inclusions at fracture origins.

(3) Specimens VA had smaller ODAs than Specimens QT (0.7–0.9 ppm hydrogen content). Specimens VQ (0.01 ppm hydrogen content) had much smaller ODAs than Specimens QT and VA.

(4) Concentration of hydrogen at inclusions was detected directly at fracture origins in Specimens QT but not in Specimens VQ.

(5) The fatigue fracture surface of an electron beam remelted bearing steel, which contains very small inclusions relative to microstructural inhomogeneities, showed the same type of fracture surface morphology (ODA) when the specimens failed from nonmetallic inclusions, but not when they failed from a bainitic structure larger in size than inclusions and softer than the martensitic matrix.

(6) The mechanism of formation of ODAs is presumed to be micro-scale fatigue fracture caused by cyclic stress coupled with internal hydrogen trapped by nonmetallic inclusions. Accordingly, it is presumed that when the size of an ODA exceeds the critical size for the intrinsic material fatigue limit in the absence of hydrogen, the fatigue crack grows without the assistance of hydrogen, and the crack cannot become non-propagating. The critical size of an ODA can be determined as the mechanical fatigue threshold by the $\sqrt{\text{area}}$ parameter model. Thus, the influence of hydrogen is a crucial factor for fatigue failure in the cycle region longer than in a conventional (or classical) fatigue test, that is $N > 10^7$.

(7) The fatigue fracture surface roughness, R_a , increases with the radial distance from a fracture origin (inclusion) under constant amplitude tension–compression fatigue. The following approximate relationship holds:

$$R_a = C \Delta K_I^2$$

where C is a material constant.

(8) There is a stretched zone at the border of a fish eye which has been formed in tension–compression cycling. Ductile dimples and intergranular fracture morphologies are present outside the border of the fish eye. The height of the stretch zone is an approximately constant value around the periphery of a fish eye, an indication that when the fatigue crack reaches a critical value of CTOD at the border of a fish eye, unstable static fracture is initiated.

(9) If we assume that a fatigue crack grows cycle by cycle from the edge of an ODA (the optically dark area outside the inclusion at a fracture origin) to the border of the fish eye, then for SCM435 steel we can correlate the crack growth rate, da/dN , stress intensity factor range, ΔK_I , and R_a as follows:

$$\frac{da}{dN} = 2.92 \times 10^{-12} \Delta K_I^2$$

and da/dN is proportional to R_a .

(10) Integrating the crack growth rate equation, the crack propagation period, N_{p2} , for specimens which failed at $N_f > 10^7$ can be estimated. N_{p2} was estimated to be $\sim 1.0 \times 10^6$ for specimens which failed at $N_f \cong 5 \times 10^8$. It follows that the fatigue life in the region of $N_f > 10^7$ is mostly occupied by fatigue crack initiation and intermittent crack growth within an ODA.

15.4 References

1. A. Wöhler: *Z. Bauwes.*, **8** (1858) 642–652; *ibid.*, **10** (1860) 584–616; *ibid.*, **13** (1863) 234–258; *ibid.*, **16** (1866) 68–84; *ibid.*, **20** (1870) 74–106.
2. T. Naito, H. Ueda and M. Kikuchi: Fatigue Behavior of Carburized Steel with Internal Oxides and Nonmartensitic Microstructure near the Surface, *Metall. Trans.*, **15A** (1984), 1431–1436.
3. K. Asami and Y. Sugiyama: Fatigue Strength of Various Surface Hardened Steels, *J. Heat Treatment Technol. Assoc.*, **25(3)** (1985), 147–150.
4. Y. Kuroshima, M. Shimizu and K. Kawasaki: Fracture Mode Transition in High Cycle Fatigue of High Strength Steel, *Trans. JSME A*, **59(560)** (1993), 1001–1006.
5. T. Abe and K. Kanazawa: Influence of Non-Metallic Inclusion and Carbide on High-Cycle Fatigue Strength of Tool Steels, *J. Soc. Mater. Sci., Jpn.*, **45(1)** (1996), 9–15.
6. K. Kanazawa and S. Nishijima: Fatigue Fracture of Low Alloy Steel at Ultra High Cycle Region under Elevated Temperature Conditions, *J. Soc. Mater. Sci., Jpn.*, **46(12)** (1997), 1396–1401.
7. T. Nakamura, M. Kaneko, T. Noguchi and K. Jinbo: Relation between High Cycle Fatigue Characteristics and Fracture Origins in Low-Temperature-Tempered Cr–Mo Steel, *Trans. JSME A*, **64(623)** (1998), 1820–1825.
8. Y. Murakami, M. Takada and T. Toriyama: Super-Long Life Tension–Compression Fatigue Properties of Quenched and Tempered 0.46% Carbon Steel, *Int. J. Fatigue*, **20(9)** (1998), 661–667.
9. *Fatigue Fract. Eng. Mater. Struct.*, **22(7)** (1999) 545–641.
10. *Fatigue Fract. Eng. Mater. Struct.*, **22(8)** (1999) 647–728.
11. S.E. Stanzl-Tschegg: Fracture Mechanisms and Fracture Mechanics at Ultrasonic Frequencies, *Fatigue Fract. Eng. Mater. Struct.*, **22(7)** (1999), 567–579.
12. C. Bathias: There Is No Infinite Fatigue Life in Metallic Materials, *Fatigue Fract. Eng. Mater. Struct.*, **22(7)** (1999), 559–565.
13. R.O. Ritchie, D.L. Davidson, B. L. Boyce, J.P. Campbell and O. Roder: High-Cycle Fatigue of Ti-6Al-4V, *Fatigue Fract. Eng. Mater. Struct.*, **22(7)** (1999), 621–631.
14. K.J. Miller and W.J. O'Donnell: The Fatigue Limit and Its Elimination, *Fatigue Fract. Eng. Mater. Struct.*, **22(7)** (1999), 545–557.
15. Y. Murakami, T. Nomoto and T. Ueda: Factors Influencing the Mechanism of Superlong Fatigue Failure in Steels, *Fatigue Fract. Eng. Mater. Struct.*, **22(7)** (1999), 581–590.
16. H. Kitagawa and S. Takahashi: Applicability of Fracture Mechanics to Very Small Cracks or the Cracks in the Early Stage, *Proc. 2nd Int. Conf. Mech. Behav. Mater.*, Boston, 1976, pp. 627–631.
17. K. Takai, Y. Honma, K. Izutsu and M. Nagumo: Identification of Trapping Sites in High-Strength Steels by Secondary Ion Mass Spectrometry for Thermally Desorbed Hydrogen, *J. Jpn. Inst. Met.*, **60(12)** (1996), 1155–1162.

18. K. Takai, J. Seki, G. Yamauchi and Y. Honma: Observation of Trapping Sites of Hydrogen and Deuterium in High-Strength Steels with Secondary Ion Mass Spectrometry, *J. Jpn. Inst. Met.*, **58**(12) (1994), 1380–1385.
19. W.R. Heller: Quantum Effects in Diffusion: Internal Friction Due to Hydrogen and Deuterium Dissolved in α -Iron, *Acta Metall.*, **9** (1961), 600–613.
20. J.J. Au and H.K. Birnbaum: Magnetic Relaxation Studies of Hydrogen in Iron: Relaxation Spectra, *Scr. Metall.*, **7** (1973), 595–604.
21. J.A. Clum: The Role of Hydrogen in Dislocation Generation in Iron Alloys, *Scr. Metall.*, **9** (1975), 51–58.
22. J.F. Dufrense, A. Seeger, P. Groh and M. Moser: Hydrogen Relaxation in α -Iron, *Phys. Status Solid.*, **36-a** (1976) 579–589.
23. H. Hagi, Y. Hayashi and N. Ohtani: Effect of Dissolved Hydrogen and Its Precipitation on Flow Stress of Electrolytic Iron, *J. Jpn. Inst. Met.*, **42**(2) (1978), 124–130.
24. H. Matsui and H. Kimura: The Effect of Hydrogen on the Mechanical Properties of High Purity Iron, I. Softening and Hardening of High Purity Iron by Hydrogen Charging During Tensile Deformation, *Mater. Sci. Eng.*, **40** (1979), 207–216.
25. J.P. Hirth: Effects of Hydrogen on the Properties of Iron and Steel, *Metall. Trans. A.*, **11** (1980), 861–890.
26. T. Tabata and H.K. Birnbaum: Direct Observation of the Hydrogen on the Behavior of Dislocations in Iron, *Scr. Metall.*, **17** (1983), 974.
27. T. Tabata: Recent study: Influence of Hydrogen on the Mechanical Properties of Irons — Studies on In-Situ Observations by High Voltage TEM (Translation from the Japanese title), *Bull. Jpn. Inst. Met.*, **24**(6) (1985), 485–493.
28. Yu. Jagodzinski, H. Hanninen, O. Tarasenko and S. Smuk: Interaction of Hydrogen with Dislocation Pile-Ups and Vacancy Generation at Plastic Deformation, presented at Int. Conf. Environmental Degradation of Engineering Materials, 19–23 Sept. 1999, Gdansk–Jurata.
29. Y. Murakami, T. Toriyama, K. Tsubota and K. Furumura: What Happens to the Fatigue Limit of Bearing Steel without Nonmetallic Inclusions? Fatigue Strength of Electron Beam Remelted Super Clean Bearing Steel, *Bearing Steels: Into the 21st Century*, ASTM STP 1327, American Society for Testing Materials, Philadelphia, PA, 1998, pp. 87–105.
30. Y. Murakami, H. Konishi and K. Takai: Acceleration of Superlong Fatigue Failure by Hydrogen Trapped by Inclusions and Elimination of Conventional Fatigue Limit, *Tetsu To Hagane*, **86**(11) (2000), 777–783.
31. D. Chen, H. Nisitani and K. Mori: Stress Intensity Factors for a Fish-Eye in a Shaft, *Trans. Jpn. Soc. Mech. Eng.*, **57**(540) (1991) 1768–1774; also see Y. Murakami (Editor-in-chief): *Stress Intensity Factors Handbook*, Vol. 3, Soc. Materials Sci., Japan, and Pergamon Press, London, 1993, pp. 661–662.
32. Y. Murakami, K. Matsuda, Y. Ohkomori, I. Kitagawa and K. Shinozuka: Effects of Nonmetallic Inclusions and Corrosion Pits on the Fatigue Strength of a High Strength Steel, *Proc. Int. Conf. Evaluation of Materials Performance in Severe Environments*, 1989, pp. 143–150.
33. P. Paris and F. Erdogan: A Critical Analysis of Crack Propagation Laws, *Trans. ASME, Ser. D*, **85** (1963), 528–534.

Chapter 16

Effect of Surface Roughness on Fatigue Strength

16.1 Introduction

As fatigue cracks mostly initiate at a free surface, surface condition has a considerable influence on fatigue strength. Therefore, the following four factors must be taken into consideration in the evaluation of fatigue strength: (1) surface roughness as a stress raiser; (2) residual stresses in a surface layer induced by machining; (3) work hardening or softening in a surface layer due to plastic deformation; (4) change or transformation of the microstructure due to plastic deformation.

In practical machine components, these four factors act together, and affect fatigue strength in a complex manner. This causes difficulty in evaluating the effect of surface finish on fatigue strength. Thus, it is essential to evaluate the influence of each factor separately, and then to seek a method of integrating these influences.

The effect of surface finish has been studied by many researchers [1–8]. Siebel and Gaier [6] investigated the relationship between fatigue strength and the maximum depth of a surface groove (R). They found a critical depth (R_0) at which the fatigue strength began to decrease; shallower grooves did not reduce the strength. For grooves deeper than R_0 , the fatigue strength decreased linearly with $\log R$. Suhr [7] considered the relationship between fatigue strength and depth of defects at crack initiation sites using the fracture mechanics of short fatigue cracks. He pointed out that the depth of a crack initiation site could not be predicted because the observed fatigue crack initiation sites were all greater in depth than the value measured prior to the fatigue tests. Cina [8] compared the fatigue strength of specimens of eight alloy steels, mostly stainless steels. The surface worked layers of specimens had been eliminated either by electro-polishing or by annealing. He pointed out that the fatigue strengths of these steels were affected more by the presence of a worked surface layer than by surface roughness.

However, few studies have separated the effects of these four factors clearly. Takahashi and Murakami [9] have conducted studies in order to solve these problems, and to investigate quantitatively the effect of surface finish on fatigue strength. In order to separate out the effect of surface roughness, Murakami, Tsutsumi and Fujishima [10] carried out tension and compression fatigue tests using maraging steel ($H_v \cong 715$). Extremely shallow periodic notches with a constant pitch and depth were introduced onto the surface of the specimens. It was shown that the $\sqrt{\text{area}}$ parameter model, introduced in Chapters 5 and 6, was applicable to the case of surface roughness.

However, the geometric profile of surface roughness produced by normal machining practice is somewhat irregular. In order to investigate the effect of roughness irregularities, extremely shallow periodic surface notches with a constant pitch but irregular depth were introduced onto the surface of specimens by an NC (numerically controlled) machine. Rotating bending fatigue tests were carried out on a medium carbon steel (0.46% C). Some specimens were annealed and hence free of residual stress ($H_V \cong 170$), others were quenched and tempered ($H_V \cong 650$). It was shown that the fatigue strength of a specimen with surface roughness can be evaluated quantitatively by the $\sqrt{\text{area}}$ parameter model.

16.2 Material and Experimental Procedure

16.2.1 Material

The material used for fatigue testing was a 0.46% medium carbon steel (JIS S45C) in the form of rolled cylindrical bars of 26 mm diameter. The specimens were turned to shape after annealing for 1 h at a temperature of 844°C. Table 16.1 shows the chemical composition of the material and Fig. 16.1 the experimental procedure. The heat treatment procedures employed are denoted by A (annealing) and QT (quenching and tempering). Fig. 16.2 shows the geometry of annealed specimens, and Fig. 16.3 the central part of quenched and tempered specimens. Each annealed specimen was turned to the shape shown in Fig. 16.2. These specimens are called material-A. The quenched and tempered specimens were first turned to cylindrical bars of 17 mm diameter and 212 mm in length. After water quenching from 845°C after 1 h and tempering at 200°C for 1 h, these bars were then turned to the shape shown in Fig. 16.3. These specimens are called material-QT.

16.2.2 Introduction of Artificial Surface Roughness and of a Single Notch

Four types of artificial surface roughness were introduced into the test zone of some specimens using an NC machine at various feed rates. The cutting tool used was a throwaway chip, made from cermet and cemented carbide, with nose radius $\rho = 100 \mu\text{m}$ for material-A and $\rho = 200 \mu\text{m}$ for material-QT. The depth of cut for all specimens was $100 \mu\text{m}$, and the cutting speed was 31 m/min for material-A and 25 m/min for material-QT. A new cutting tool was used for each specimen. Fig. 16.4 shows longitudinal sections at the test zone of specimens. Fig. 16.5 shows the surface of a specimen. The notch pitch is constant because turning was carried out at a constant feed rate. However, the depth of notches is not constant; the main reason for this irregularity

Table 16.1 Chemical composition (wt%)

C	Si	Mn	P	S	Ni	Cu	Cr
0.46	0.22	0.74	0.024	0.026	0.02	0.01	0.15

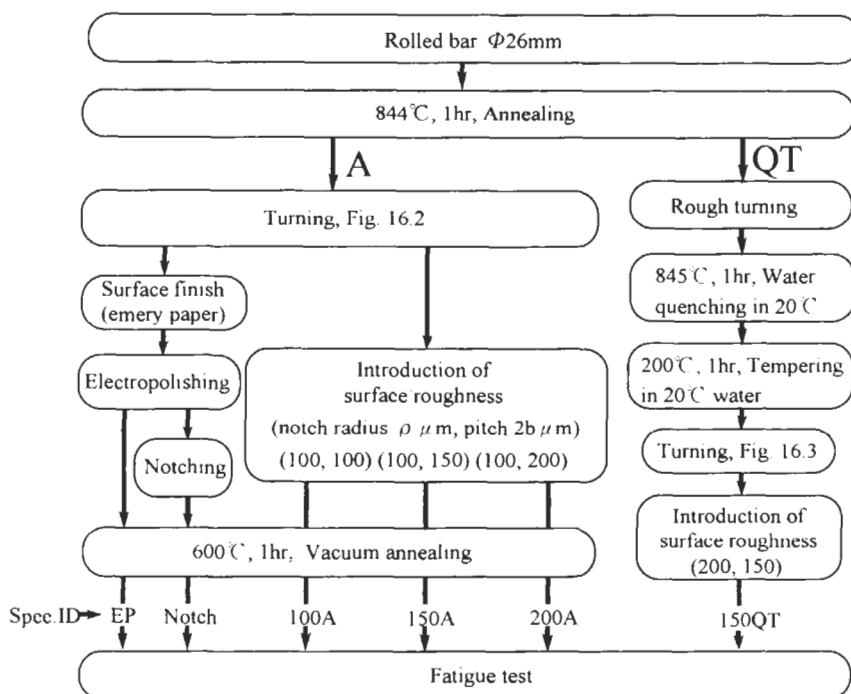


Figure 16.1 Experimental procedure.

in depth is the existence of defects gouged out at the roots of notches by a built up edge. A built up edge is produced when part of a chip is deposited on the rake face of the cutting tool during turning. Therefore, the shape of surface roughness produced by normal machining practice is naturally irregular. Thus, results obtained in this study do give a basis for evaluation of surface roughness produced by normal machining. There were gouged out scratches with a depth of about $3\ \mu\text{m}$ at roots of notches. Fatigue tests were carried out leaving these scratches in place, that is without electro-polishing. In later discussion, the four types of rough specimen are called 100A, 150A, 200A, 150QT. The numbers represent the notch pitch in μm , and the letters the heat treatment condition.

For comparison fatigue tests were also carried out on electro-polished specimens without machined on roughness, and on specimens with a single notch. After machining 'electro-polished' specimens were first polished with emery paper. These specimens were then electro-polished to a depth of about $50\ \mu\text{m}$ per diameter. In the specimens containing a single notch, a circumferential notch with a depth of about $30\ \mu\text{m}$ and a notch root radius of $200\ \mu\text{m}$ was introduced onto the electro-polished surface.

Material-A was annealed at 600°C in a vacuum after all these procedures. This procedure relieved residual stress induced by machining, and the material was of uniform hardness. In contrast, material-QT contained residual stresses induced by heat treatment and by machining. The exact values of these residual stresses could not be

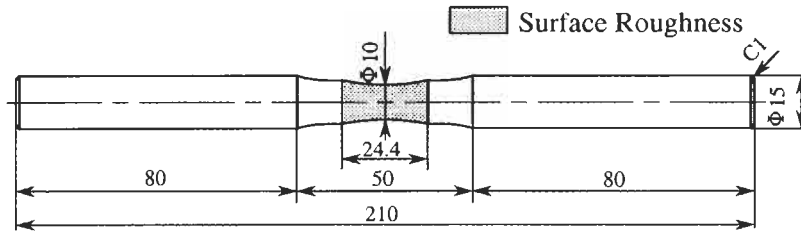


Figure 16.2 Geometry of annealed specimens. Dimensions in mm.

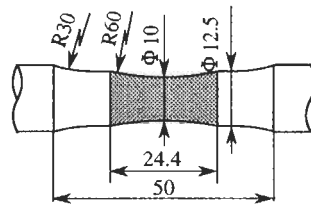
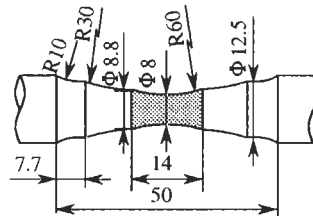


Figure 16.3 Geometry of the central part of quenched and tempered specimens. Dimensions in mm.



obtained due to the deep surface roughness. The values of residual stresses in the longitudinal direction on the surface of an electro-polished specimen of 8 mm diameter, which had received a very similar heat treatment (quenching and tempering), were investigated. The values of residual stress at 12 points on the surface of the specimen were in the range 0 to +150 MPa [11].

16.2.3 Measurement of Hardness and Surface Roughness

Measurement of Vickers hardness was carried out at four points on a smooth part of a specimen. The load used was 1.96 N. The average value of Vickers hardness was $H_V \cong 170$ for material-A and $H_V \cong 650$ for material-QT. The scatter of the hardness is within 5%. Fig. 16.6 shows the microstructure of material-A at a cross-section within the test zone. A surface worked layer with a depth of about 20 μm was observed. The average Vickers hardness of this surface layer measured at four points using a 0.49 N load is $H_V \cong 180$. This indicates that hardness in the vicinity of the surface is a little different from that of the bulk material.

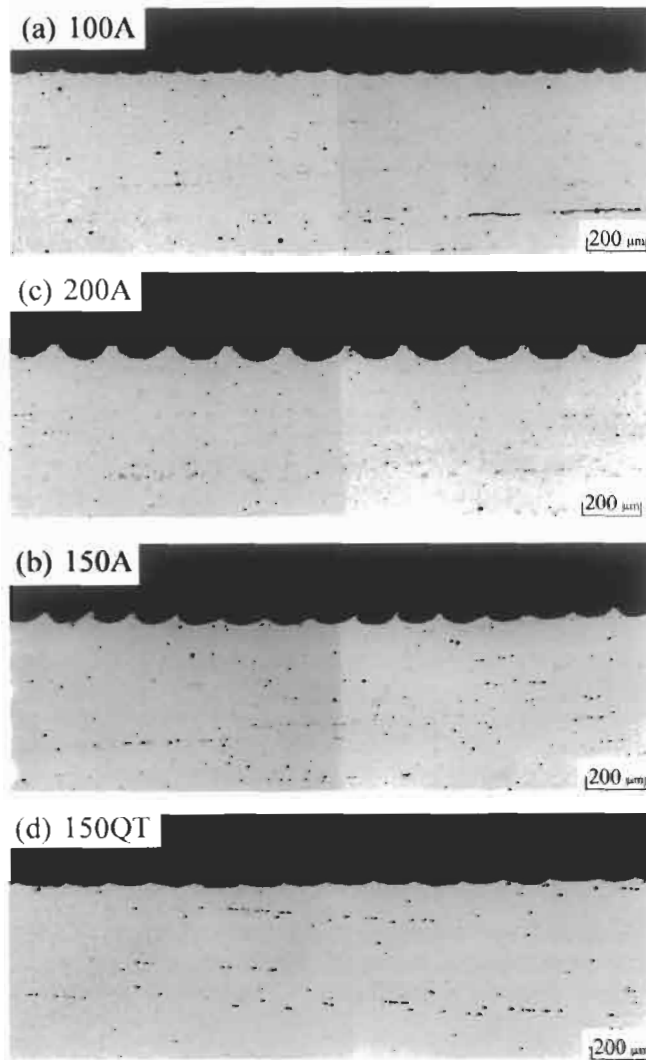


Figure 16.4 Periodic surface notches as artificial surface roughness; longitudinal sections.

Measurement of artificial surface roughness, using the stylus method, was carried out in the longitudinal direction. Fig. 16.7 shows the roughness curves for four nominal levels of roughness. Roughness measurements were made over an 8 mm length on five specimens of each type of specimen. Each 8 mm length was subdivided into eight intervals of 1 mm each, so that 40 sets of data were obtained for each type of specimen. The maximum roughness height, R_y , that is the maximum difference in height in any 1 mm interval, was obtained. The values of the maximum height, R_y , in Table 16.2 are the maximum value among the 40 values obtained. a_{mean} represents the mean value of the depth of the periodic notches as measured in all the roughness curves obtained (depth

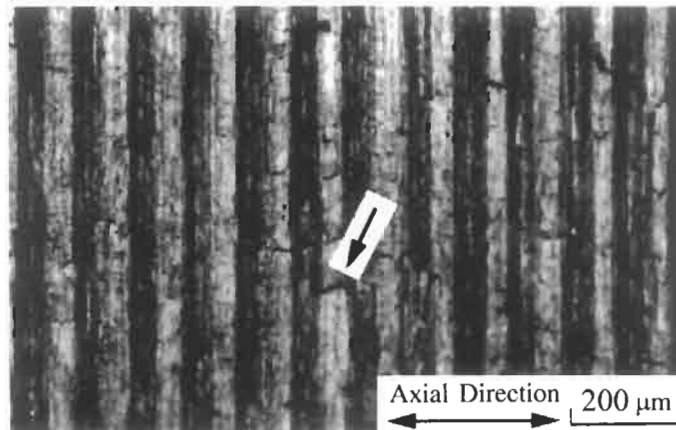


Figure 16.5 Periodic surface notches as artificial surface roughness, 100A. (↓ indicates a defect gouged out by a built-up edge).

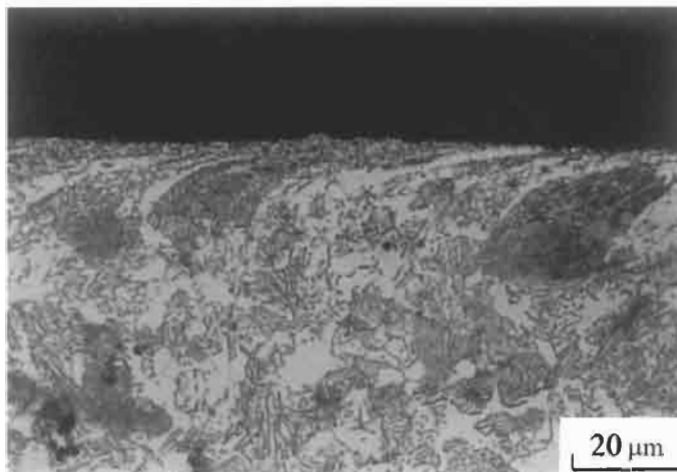


Figure 16.6 Surface worked layer of annealed specimen with artificial surface roughness.

being defined as the vertical distance from the notch root to the nearest higher peak), while the term $2b$ represents the pitch of the periodic notches.

A rotating bending fatigue testing machine of the uniform bending moment type was used. The capacity is 98 N m operating at 2400 rpm. The fatigue limit is defined as the nominal bending stress under which a specimen endured 10^7 cycles. The surfaces of some unbroken specimens, which had been tested at stress levels near the fatigue limit, were microscopically examined in order to observe non-propagating cracks. In order to distinguish non-propagating cracks from scratches, the surface layer was removed to a depth of 6–7 μm by electro-polishing.

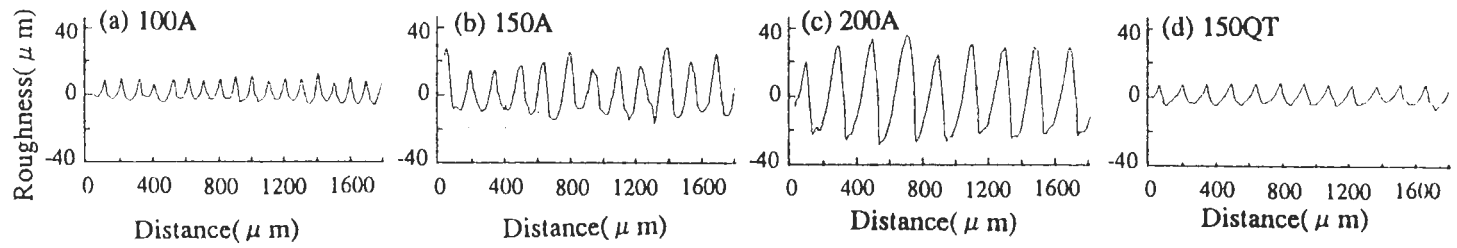


Figure 16.7 Measurement of artificial surface roughness.

Table 16.2 Measurement of artificial surface roughness

Specimen	Maximum height of roughness $R_y \mu\text{m}$	Mean depth of notches $a_{mean} \mu\text{m}$	Pitch of notches $2b \mu\text{m}$
100A	27.3	14.5	100
150A	66.4	37.5	150
200A	74.0	53.3	200
150QT	20.5	13.0	150

16.3 Results and Discussion

16.3.1 Results of Fatigue Tests

The crack initiation site of all specimens with artificial surface roughness was the root of a notch simulating roughness. Fig. 16.8 shows the crack initiation site of a specimen with artificial surface roughness. There is a defect gouged out by a built-up edge as shown by the arrow. At this point, the notch undergoes a sudden change in depth from $8 \mu\text{m}$ to $18 \mu\text{m}$. The crack initiated at the point with the depth of $18 \mu\text{m}$. It is clear that this notch is particularly deep since the depth is approximately equal to the maximum height ($R_y = 20.5 \mu\text{m}$) for this type of specimen, 150QT. This type of defect was also observed at the fracture origins of other specimens, so it is necessary to consider the effect of such defects when evaluating the fatigue strength of components which undergo normal machining.

Fig. 16.9 shows a non-propagating crack observed at a valley within the rough area, that is at a roughness notch root. Thus, the threshold condition at the fatigue limit of a specimen with surface roughness is determined by non-propagation of a crack emanating from a notch root.

Fig. 16.10 shows the $S-N$ curve for material-A. Although the mean depth of notches of the specimen 150A is $37.5 \mu\text{m}$, which is of the same order as the depth of a notch, $30 \mu\text{m}$, in singly notched specimens, the fatigue limit for specimen 150A is 29.8% higher than that for the singly notched specimen. This is because the fatigue notch effect for specimen 150A is reduced because of interference between notches. The fatigue limit of a singly notched specimen is always lower than that of a specimen with surface roughness. When there is no other information this fact may be useful for conservative design.

16.3.2 Quantitative Evaluation by the $\sqrt{\text{area}}$ Parameter Model

16.3.2.1 Geometrical Parameter to Evaluate the Effect of Surface Roughness on Fatigue Strength

In order to evaluate quantitatively the effect of surface roughness on fatigue strength, it is necessary to seek the crucial parameters which control fatigue strength. From the results of the fatigue tests, it is clear that the effect of pitch, that is the interference effect

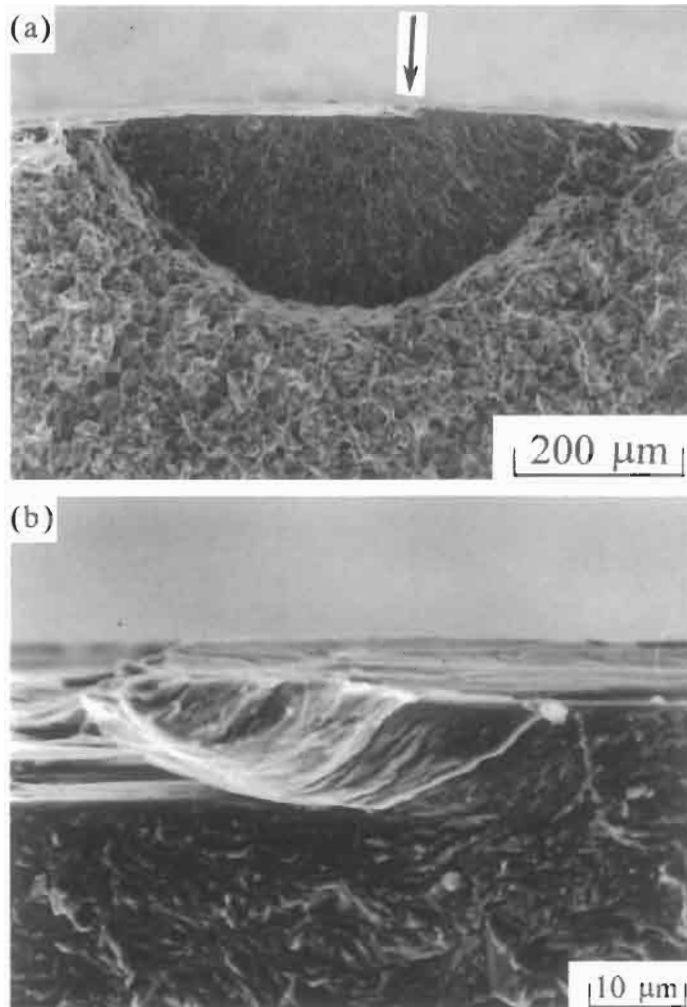


Figure 16.8 (a) Fracture origin of a quenched and tempered specimen 150QT. (b) The same origin as in (a) at higher magnification. $\sigma_{ii} = 608$ MPa, $N_f = 6.55 \times 10^4$ (\downarrow indicates defect gouged out by a built-up edge).

between notches, must be considered. Existing studies, however, consider only the effect of notch depth [6,7,12]. The difficulty here is that it is not convenient to evaluate fatigue strength using two parameters, depth and pitch, as controlling parameters because no simple relationship between fatigue strength and these surface roughness parameters can be obtained. To overcome this difficulty, a method for unifying these two parameters into one representative parameter, $\sqrt{\text{area}_R}$, is used in this chapter.

The fatigue limit of specimens with surface roughness is determined by the threshold condition for non-propagation of a crack emanating from a notch root, as shown in Fig. 16.9. From this viewpoint, the problem of surface roughness must be considered

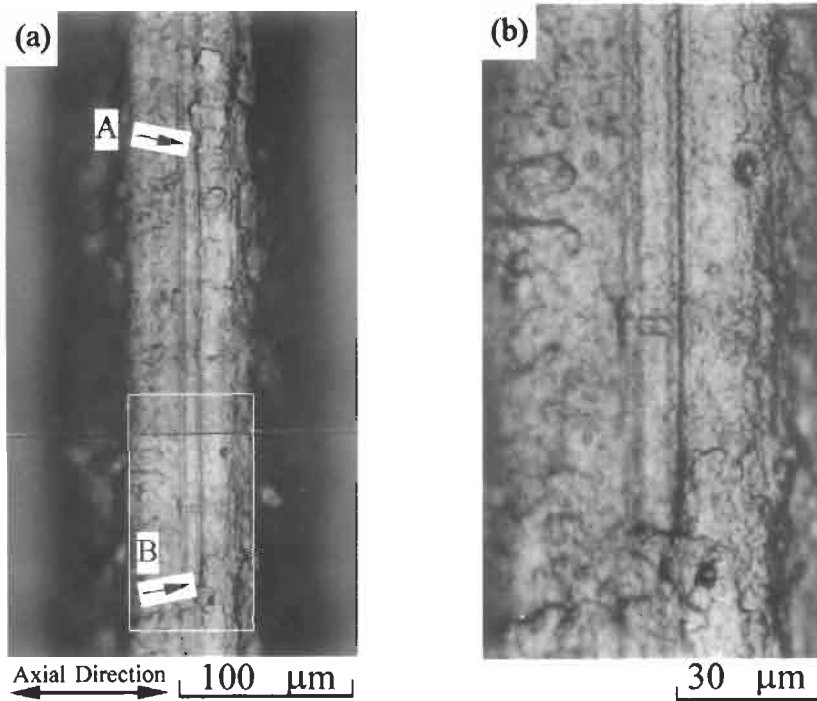


Figure 16.9 (a) Non-propagating crack observed at the notch root of a specimen with artificial surface roughness, 200A. $\sigma_a = 226$ MPa. (b) A higher magnification view of the area indicated by arrow B in (a).

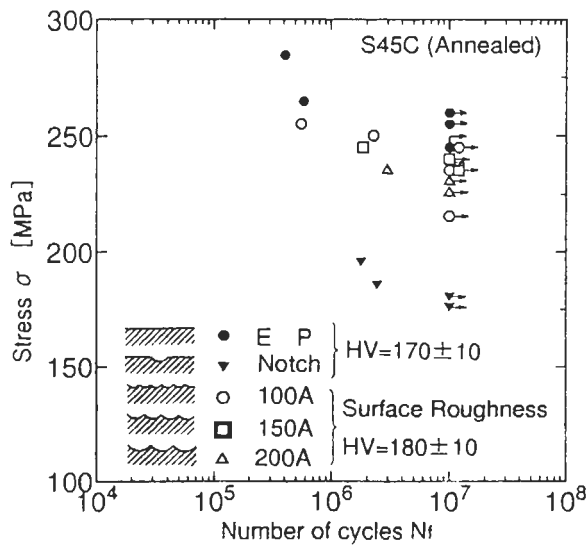


Figure 16.10 S-N curve: annealed specimens.

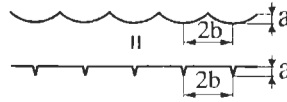


Figure 16.11 Notches and their equivalent cracks.

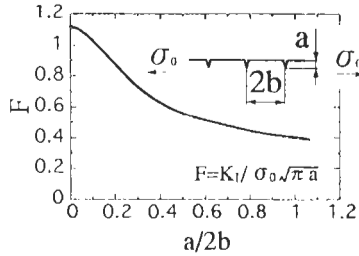


Figure 16.12 Stress intensity factor for periodic surface cracks.

as a crack problem rather than as a notch problem. Murakami et al. [10] applied the \sqrt{area} parameter model to the problem of periodic surface notches simulating surface roughness. In this chapter, the same evaluation method (Eq. 6.6) is applied to surface roughness with irregular depth.

16.3.2.2 Evaluation of Equivalent Defect Size for Roughness \sqrt{area}_R

The initial value of \sqrt{area}_R of a defect is the crucial geometrical parameter that controls the fatigue limit. For a single shallow circumferential notch, \sqrt{area} is given by the following equation:

$$\sqrt{area} \cong \sqrt{10} \times a \tag{2.9}$$

where a = depth of notch (μm). Murakami et al. [10] proposed an evaluation method for the value of \sqrt{area} for periodic notches on the assumption that a periodic roughness notch is equivalent to periodic cracks, as shown in Fig. 16.11. The method of evaluation of \sqrt{area} for periodic notches follows.

Fig. 16.12 shows the stress intensity factor, K_I , for periodic surface cracks in a semi-infinite body [13]. The term F in Fig. 16.12 is a geometric correction factor which depends upon the depth and pitch of cracks, and is defined by the following equation:

$$K_I = F \sigma_0 \sqrt{\pi a} \tag{16.1}$$

When the depth (a) is kept constant and the pitch ($2b$) is decreased, K_I decreases due to the effect of interference between cracks. The maximum value of stress intensity factor, $K_{I_{max}}$, along a surface crack front of arbitrary shape (Fig. 2.9) is given by the following equation:

$$K_{I_{max}} = 0.65 \sigma_0 \sqrt{\pi \sqrt{area}} \tag{2.8}$$

for a Poisson ratio $\nu = 0.3$.

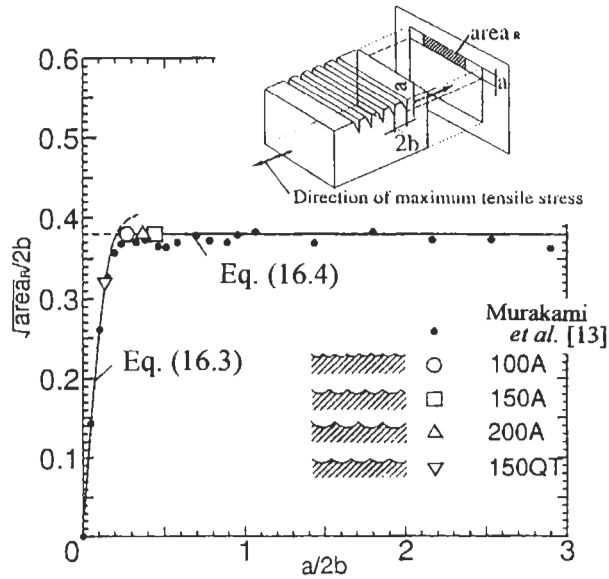


Figure 16.13 Relationship between $\sqrt{area_R}/2b$ and $a/2b$.

Using Eqs. 16.1 and 2.8, the following equation to evaluate the equivalent value of \sqrt{area} for periodic cracks, $\sqrt{area_R}$, can be obtained:

$$\sqrt{area_R} = (F/0.65)^2 \times a \quad (16.2)$$

Fig. 16.13 shows the relationship between $\sqrt{area_R}/2b$ and $a/2b$. If we consider the case when the pitch ($2b$) is kept constant and the depth (a) is increased, then the equivalent defect size $\sqrt{area_R}$ increases as the depth (a) increases. However, the value of $\sqrt{area_R}$ reaches a maximum value at $a/2b = 0.195$; subsequently $\sqrt{area_R}$ is an almost constant value for a wide range of $a/2b$ values.

Numerical analysis indicates that if the ratio $a/2b$ increases further beyond a value of 3, then the value of $\sqrt{area_R}$ gradually decreases. However, because such extreme roughness is seldom observed on the surfaces of real components, this case is not discussed here. Hence, to estimate the equivalent defect size of roughness, the following equations can be derived:

$$\sqrt{area_R}/2b \cong 2.97(a/2b) - 3.51(a/2b)^2 - 9.74(a/2b)^3 \quad \text{for } a/2b < 0.195 \quad (16.3)$$

$$\sqrt{area_R}/2b \cong 0.38 \quad \text{for } a/2b > 0.195 \quad (16.4)$$

The pitch of notches on specimens tested in this study is almost constant, but the depth is not constant. Thus depth, a , must be assigned a certain value for the purpose of evaluating $\sqrt{area_R}$. In this study, the values of maximum height of roughness in Table 16.2 are used as depth (a) for this evaluation. The values of the maximum height, R_y , in Table 16.2 are the maximum values among the 40 data points obtained for each specimen type. The values of $a/2b$ were obtained by assuming $a = R_y$. Results of the estimation of $\sqrt{area_R}$ obtained by substituting $a/2b$ into Eqs. 16.3 and 16.4 are plotted

Table 16.3 Values of \sqrt{area}

Specimen	$R/2b$	$\sqrt{area}_R/2b$	$\sqrt{area}_R \mu m$
100A	0.273	0.38	38
150A	0.443	0.38	57
200A	0.370	0.38	76
150QT	0.137	0.32	47

in Fig. 16.13. Table 16.3 shows the values of \sqrt{area}_R for each type of specimen. For singly notched specimens, the value of \sqrt{area} is evaluated using Eq. 2.9.

Eq. 6.6 for $R = -1$ was used to predict the fatigue limit of the specimens with surface roughness and of those with a single notch. Material-QT contains residual stresses. It must be considered that about 150 MPa of tensile residual stress may exist on the surface, as mentioned previously. Since the residual stress at the fracture origin could not be obtained, the fatigue limit was also predicted using Eq. 6.6. The following empirical equation was used to predict the fatigue limit of electro-polished specimens:

$$\sigma_w = 1.6H_V \quad (H_V \leq 400) \tag{16.5}$$

Table 16.4 and Fig. 16.14 show comparisons between predicted fatigue limits and experimental fatigue limits. There are uncertainties in the value of Vickers hardness for each specimen. There is therefore some scatter in the fatigue limit predictions shown in Table 16.4. The fatigue limit predictions for 100A, 150A, and 200A are in good agreement with the experimental values. The fatigue limits of these specimens are much higher than those of the singly notched specimens. From these results it may be concluded that the evaluation method, which takes into account interference between

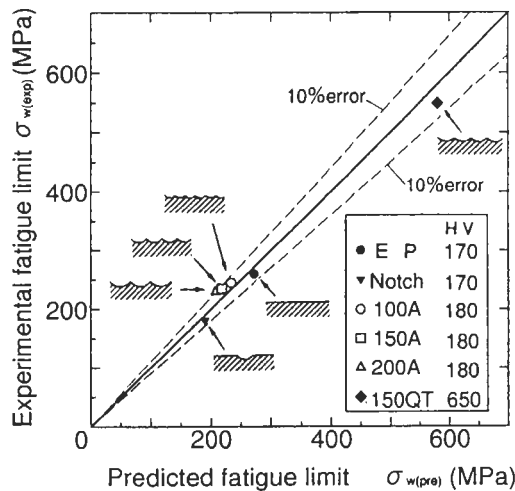


Figure 16.14 Relationship between predicted fatigue limits and experimental results.

Table 16.4 Comparisons between predicted fatigue limits and experimental results: (a) annealed specimens; (b) quenched and tempered specimens

(a) Annealed specimens

Specimen	HV	$\sqrt{area}_R \mu m$	● broken ○ not broken	depth of crack initiation site μm	Experiment σ_a MPa	Prediction σ_w MPa
E P	170 ± 10	—	●	0	284	$272 \pm 16^*$
			●	0	265	
			○	—	260	
			○	—	255	
			○	—	245	
100A	180 ± 10	38	●	17	255	234 ± 8
			●	14	250	
			○	—	245	
			○	—	235	
			○	—	216	
150A	180 ± 10	57	●	32	245	219 ± 7
			○	—	235	
			○	—	216	
200A	180 ± 10	76	●	78	235	208 ± 7
			○	—	230	
			○	—	226	
Single notch	170 ± 10	95**	●	32	196	194 ± 7
			●	31	186	
			○	—	181	
			○	—	177	

* Predicted using equation (16.5). ** Predicted using equation (2.9) for $a = 30 \mu m$

(b) Quenched and tempered specimens

Specimen	HV	$\sqrt{area}_R \mu m$	● broken ○ not broken	depth of crack initiation site μm	Experiment σ_a MPa	Prediction σ_w MPa
150QT	650 ± 30	47	●	17	608	580 ± 22
			●	18	569	
			○	—	549	
			○	—	530	

roughness notches, is valid. The fatigue limit for 150QT might be predicted more precisely if the exact residual stress at a fracture origin was obtained.

The model proposed in this chapter is applicable to other steels and alloys. Different materials can be considered by utilising differences in Vickers hardness.

16.4 Guidance for Fatigue Design Engineers

The following tentative guidance for fatigue design engineers is based on fatigue tests on specimens of a medium carbon steel (0.46% C). Some specimens were annealed and free of residual stress ($H_V \cong 170$), the others were quenched and tempered ($H_V \cong 650$). In the tests to simulate actual surface roughness, as produced by machining, extremely shallow periodic notches were introduced with a constant pitch, but irregular depths.

(1) The fatigue strength of a singly notched specimen is always lower than that of a specimen with surface roughness. The fatigue limit for specimens with artificial surface roughness, specimen 150A (maximum height of roughness $R_v = 66.4 \mu\text{m}$, mean depth of notches is $37.5 \mu\text{m}$, pitch is $150 \mu\text{m}$), is 29.8% higher than that for specimens with a single notch of the same depth. This is because of the interference between notches, which reduces the notch effect. Thus, the effect of the pitch of the roughness has to be considered, in addition to the effect of its depth, when we evaluate the effect of surface roughness on fatigue strength.

(2) Existence of non-propagating cracks at roughness notch roots indicates that the fatigue limit of a specimen with surface roughness is the threshold condition for non-propagation of a crack initiated at a notch root. Thus, surface roughness is mechanically equivalent to periodic surface cracks. To combine two parameters, pitch and depth, into one parameter, and to define an equivalent defect size, $\sqrt{\text{area}_R}$ for roughness, the $\sqrt{\text{area}}$ parameter model introduced in Chapters 5 and 6 can be applied.

(3) The fatigue limit of the annealed specimens with three levels of irregularly shaped roughness can be predicted by invoking the Vickers hardness, H_V , of the matrix and the equivalent defect size $\sqrt{\text{area}_R}$. The fatigue limit of quenched and tempered specimens can also be predicted by the same method. Prediction errors for each specimen type are less than 10%.

16.5 References

1. G.M. Sinclair, H.T. Corten and T.J. Dolan: Effect of Surface Finish on the Fatigue Strength of Titanium Alloys RC130B and Ti 140A, *Trans. ASME*, **79**(1) (1957), 89–96.
2. P.G. Forest: *Fatigue of Metals*, Pergamon Press, Oxford, 1962.
3. *Fatigue of Metals*, JSME Data Book, 1965.
4. T. Isibashi: *Fatigue of Metals and Prevention of Fracture*, Yokendo Ltd., Tokyo, 1977.
5. S. Harada, S. Nishida, T. Endo, K. Suehiro, Y. Fukushima and H. Yamaguchi: The Rotary Bending Fatigue of a Eutectoid Steel (1st Report, Effects of Surface Finish and Defects on Fatigue Limit), *Trans. Jpn. Soc. Mech. Eng. Ser. A*, **53**(487) (1987), 401–409.
6. E. Siebel and M. Gaier: Influence of Surface Roughness on Fatigue Strength of Steels and Non-Ferrous Alloys, *VDI Z.*, **98** (1956), 1715–1723.
7. R.W. Suhr: The Effect of Surface Finish on High Cycle Fatigue of a Low Alloy Steel. In: K.J. Miller

- and E.R. de los Rios (Eds): *The Behavior of Short Fatigue Cracks*, EGF Publ., Mechanical Engineering Publications, London, 1986, pp. 69–86.
8. B. Cina: *The Effect of Surface Finish on Fatigue*, *Metallurgia*, **53** (1957), 11–19.
 9. K. Takahashi and Y. Murakami: *Quantitative Evaluation of Effect of Surface Roughness on Fatigue Strength*, *Eng. Against Fatigue*, Eds. J.H. Beynon, M.W. Braun, T.C. Lindley, R.A. Smith and B. Tomkins, Balkema, Rotterdam, 1999, pp. 693–703.
 10. Y. Murakami, K. Tsutsumi and M. Fujishima: *Quantitative Evaluation of Effect of Surface Roughness on Fatigue Strength*, *Trans. Jpn. Soc. Mech. Eng. Ser. A*, **62(597)** (1996), 1124–1131.
 11. Y. Murakami, M. Takada and T. Toriyama: *Super-Long Life Tension–Compression Fatigue Properties of Quenched and Tempered 0.46% Carbon Steel*, *Proc. 23rd Symp. Fatigue, Soc. Mater. Sci. Jpn.*, 1996, pp. 241–244.
 12. M. Kawamoto, K. Nishioka, T. Inui and F. Tsuchiya: *The Influence of Surface Roughness of Specimens on Fatigue Strength under Rotating-Beam Test*, *J. Soc. Mater. Sci. Jpn.*, **4(19)** (1954), 42–48.
 13. Y. Murakami et al.: *Stress Intensity Factors Handbook*, Pergamon Press, Oxford, 1987, Vol. 1, 116.

Appendix A: Instructions for a New Method of Inclusion Rating and Correlations with the Fatigue Limit

Many inclusion rating methods already exist, some of which have been adopted as the standards for particular countries or industries. However, with the existing methods, it is difficult to evaluate the relationship between the fatigue limit and the type, size, or distribution of the inclusions.

As explained in the main text, inclusions behave as small defects and the quantitative effect on the fatigue strength can be assessed from an evaluation of the square root of the projected area of the largest inclusion, on a plane perpendicular to the maximum principal stress direction. This parameter, designated \sqrt{area}_{max} , contained in a definite volume, can be evaluated using the statistics of extremes of the inclusion distribution.

By the application of the statistics of extremes to inclusions, materials can be classified according to the expected maximum size of the inclusion, namely \sqrt{area}_{max} and accordingly, a prediction of the lower bound of fatigue strength can be made. Furthermore, the results can be used as a relative quality comparison between materials produced at different times or localities.

A1 Background of Extreme Value Theory and Data Analysis

When the cumulative probability F_Z of a given population Z (or parent distribution) is known, the distribution of maximum values Z_n from sets of n individuals has a cumulative function F_{Z_n} , which is related to the previous one with the relationship [1]:

$$F_{Z_n} = (F_Z)^n \quad (\text{A1.1})$$

It could be shown that if the parent distribution is exponentially decreasing [2] then the distribution of extremes $X \equiv Z_n$ is asymptotically ($n \rightarrow \infty$) described by a largest extreme value distribution (also called Gumbel distribution [1]):

$$F_X(x, \lambda, \delta) = \exp \left\{ - \exp \left[- \frac{(x - \lambda)}{\delta} \right] \right\} \quad (\text{A1.2})$$

The parameters λ and δ of this doubly exponential distribution, respectively, are the location and scale parameters: λ is the X value which has a cumulative probability of 0.367 (λ is the 36.7% quantile), while δ is proportional to the scatter of the X variable.

The P th quantile of the distribution is:

$$x(P) = F_X^{-1}(P) = \lambda + \delta \cdot y \quad (\text{A1.3})$$

where $y = -\ln(-\ln(P))$. Eq. A1.3 can be used for producing a probability plot since it is a linearisation of Eq. A1.2 (see Section A2).

The distribution of inclusions in metals is supposed to be nearly exponential or described by Weibull or log-normal distributions. Since these distributions are exponentially decreasing it can be expected that the distribution of extreme defects can be described by the Gumbel distribution.

The key point in the 'statistics of extremes' is measuring extreme inclusions (or defects); this can be done by recording the maximum defects in a given set of control areas (or volumes). The data obtained with this procedure, called *extreme value sampling*, are then analysed with the Gumbel distribution.

The advantages of using LEVD (Largest Extreme Value Distribution) and maximum inclusions instead of using conventional ratings, which analyse the parent distribution, are the easier detection of maximum defects and the fact that this procedure is focused on the upper 'tail' of defect distribution.

The most interesting feature of extreme value inclusion rating — *EVIR* — is the possibility of predicting the size of the maximum inclusion.

Let x be the dimension of extreme inclusions and S_0 be the inspection area used for the sampling. Then the *characteristic largest defect* in an area S (the maximum defect which is expected to be exceeded once in the area S) is the inclusion size corresponding to a return period:

$$T = S/S_0 \quad (\text{A1.4})$$

Since $T = 1/(1 - P)$, from Eq. A1.3 the dimension of the defect with return period T can be calculated as:

$$x(T) = \lambda - \delta \cdot \ln[-\ln(1 - 1/T)] \quad (\text{A1.5})$$

For a given set of extreme defects, the parameters λ and δ can be calculated with different methods whose statistical properties have been discussed by Beretta and Murakami [3]. In the following Sections, A2–A7, the application of *EVIR* by using the least squares method for estimating the lower bound of fatigue strength is shown and the results are compared with fatigue tests. The optimisation of inclusion rating is discussed in Section A8.

A2 Simple Procedure for Extreme Value Inclusion Rating

In this section, a new inclusion rating method based on the statistics of extremes, is explained. The procedure can be divided into the following phases.

(1) A section perpendicular to the maximum principal stress is cut from the specimen. After polishing with a No. 2000 emery paper, the test surface is mirror-finished with buff.

(2) A standard inspection area (or control area) S_0 (mm^2) is fixed. Generally, it is advised to take a microscope picture of an area approximately equivalent to S_0 . In this area S_0 , an inclusion of maximum size is selected. Then, the square root of the projected area, $\sqrt{\text{area}_{\text{max}}}$, of this selected inclusion is calculated. This operation is repeated n times (in n areas S_0) (see Fig. A2.1).

(3) The values of $\sqrt{\text{area}_{\text{max},j}}$ are classified, starting from the smallest, and indexed: (with $j = 1, \dots, n$). We then have the following relation:

$$\sqrt{\text{area}_{\text{max},1}} \leq \sqrt{\text{area}_{\text{max},2}} \leq \dots \leq \sqrt{\text{area}_{\text{max},n}} \tag{A2.1}$$

The cumulative distribution function F_j (%), and the reduced variates y_j are then calculated from the equations:

$$F_j = j \times 100 / (n + 1) \quad (\%) \tag{A2.2}$$

$$y_j = -\ln\{-\ln[j / (n + 1)]\} \tag{A2.3}$$

Examples of F_j and y_j are shown in Table A2.1.

(4) The data of Table A2.1 are then plotted in a probability paper for extreme value distribution (see Appendix C). Point j has an abscissa co-ordinate of $\sqrt{\text{area}_{\text{max},j}}$ while the ordinate axis represents either F_j or y_j . An example is shown in Fig. A2.2.

(5) The reduced variates, y_j plotted against $\sqrt{\text{area}_{\text{max},j}}$ gives a straight line (the practical example procedure is explained in Section A7). The linear distribution of the maximum size of inclusions can be expressed by Eq. A2.4.

$$\sqrt{\text{area}_{\text{max}}} = a \cdot y + b \tag{A2.4}$$

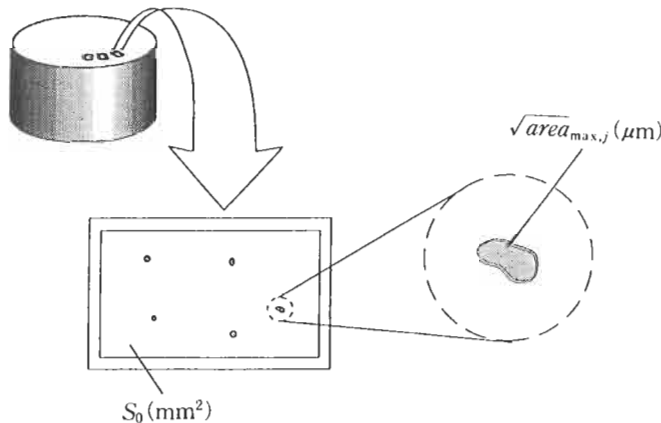
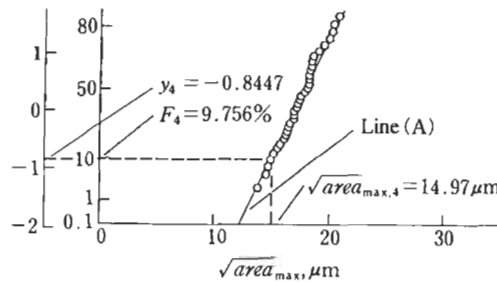


Figure A2.1 Example of inclusion inspection.

Table A2.1 Inclusion inspection data

Material: Control section: Standard inspection area: $S_0 =$ Number of inspections: n		Date: Cum. distr. func. $F_j = j/(n+1) \times 100(\%)$ Reduced variate $y_j = -\ln[-\ln\{j/(n+1)\}]$		
No.	$F_j (\%)$	y_j	$\sqrt{\text{area}}_{\max,j} (\mu\text{m})$	photo No.
1	$1/(n+1) \times 100$	$-\ln[-\ln\{1/(n+1)\}]$	$\sqrt{\text{area}}_{\max,1}$	
2	$2/(n+1) \times 100$	$-\ln[-\ln\{2/(n+1)\}]$	$\sqrt{\text{area}}_{\max,2}$	
3	$3/(n+1) \times 100$	$-\ln[-\ln\{3/(n+1)\}]$	$\sqrt{\text{area}}_{\max,3}$	
:	:	:	:	
:	:	:	:	
j	$j/(n+1) \times 100$	$-\ln[-\ln\{j/(n+1)\}]$	$\sqrt{\text{area}}_{\max,j}$	
:	:	:	:	
:	:	:	:	
n	$n/(n+1) \times 100$	$-\ln[-\ln\{n/(n+1)\}]$	$\sqrt{\text{area}}_{\max,n}$	

Figure A2.2 Graph of statistics of extremes ($n = 40$, $j = 4$, $\sqrt{\text{area}}_{\max,4} = 14.97 \mu\text{m}$).

where

$$y = -\ln[-\ln\{(T-1)/T\}] \quad (\text{A2.5})$$

and

$$T = S/S_0 \quad (\text{A2.6})$$

T represents the return period and S the area of prediction.

(6) If a straight line can be drawn through the graph of Fig. A2.2 then, by implication, this means that the distribution is doubly exponential in form as required

Table A2.2 Inclusion inspection data

Inspection items		
Material:		
Control section:		
Standard inspection area: $S_0 =$		
Number of inspections: n		
Chemical composition		
Maximum inclusion distribution		
$\sqrt{area}_{max} = \text{_____} \times y + \text{_____}$		
Test area:	S (mm ²)	
Return period:	$T = S/S_0$	
Cum. distr. func.	$F = (T - 1) / T \times 100$ (%) or $j/(n+1) \times 100$ (%)	
Reduced variate	$y = -\ln[-\ln\{(T-1)/T\}]$	
Prediction of \sqrt{area}_{max}		
S (mm ²)	T	\sqrt{area}_{max} (μm)
1	_____	_____
100	_____	_____

by the statistical method of extremes. Nonlinearity for $F < 10\%$ or $F > 85\%$ is not significant.¹

(7) Substituting $S = 1$ mm² and 100 mm² into Eqs. A2.4 through A2.6, T and \sqrt{area}_{max} for the two S values are computed. The expected values of \sqrt{area}_{max} for $S = 1$ mm² and 100 mm² can be used to compare material quality with respect to inclusions regardless of the use of different values of S_0 . The data are recorded in Table A2.2. The chemical composition of the material is also recorded together with the data.

¹ The presence of inclusion data which do not fall onto a straight line in the right tail ($F > 85\%$) is in several cases caused by the presence of different types of defects. It can then be worth checking the chemical composition and morphology of the particles which do not follow the line (see Section A8).

The database of this kind for various commercial steels has been accumulated in Kyushu University for the prediction of fatigue strength and the improvement of the steel-making process. Several examples of the database are given in Appendix B.

A3 Prediction of the Maximum Inclusion

Fig. A3.1 shows the statistics of extremes graph of a medium carbon steel obtained by the previously described procedure. The table in Fig. A3.1 indicates the predicted values of \sqrt{area}_{max} included in $S = 1 \text{ mm}^2$ and $S = 100 \text{ mm}^2$. The straight line (A) of the graph shows the relationship between the reduced variate y and \sqrt{area}_{max} . This relation is expressed by the equation of line (A) (also indicated in Table A2.1).

The dotted line in Fig. A3.1 indicates the procedure to determine \sqrt{area}_{max} for $S = 100 \text{ mm}^2$ ($T = S/S_0 = 100/0.482 = 207$). Point A indicates the return period T for $S = 100 \text{ mm}^2$. A horizontal line is drawn from point A. Then, from the intersection point between this horizontal line and line (A), a vertical line is drawn. The value of \sqrt{area}_{max} is read on the abscissa axis (point B). This value of the abscissa is the prediction of \sqrt{area}_{max} expected to be contained in an area $S = 100 \text{ mm}^2$. This graphic method is equivalent to substituting $S = 100 \text{ mm}^2$ into the equation of the straight line (A); i.e., first substitute $S = 100 \text{ mm}^2$ into Eq. A2.6 to find the return period T , then substitute T into Eq. A2.5 to find the reduced variable y and finally substitute y into Eq. A2.4.

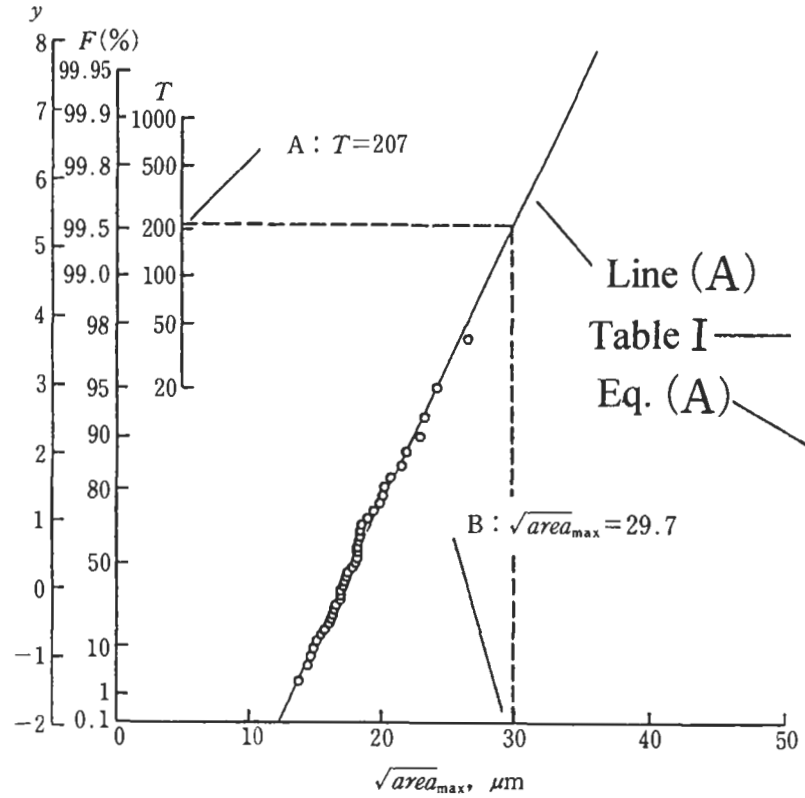
$$\begin{aligned} T &= S/S_0 & (A2.6) \\ &= 100/0.482 \\ &= 207 \end{aligned}$$

$$\begin{aligned} y &= -\ln\{-\ln[(T-1)/T]\} & (A2.5) \\ &= -\ln\{-\ln[(207-1)/207]\} \\ &= 5.330 \end{aligned}$$

$$\begin{aligned} \sqrt{area}_{max} &= a \cdot y + b & (A2.4) \\ &= 2.389 \times 5.330 + 16.96 \\ &= 29.7 \end{aligned}$$

Thus, the predicted value of \sqrt{area}_{max} in $S = 100 \text{ mm}^2$ is $29.7 \mu\text{m}$.

The domain of prediction explained above was a surface. When the domain in question is three-dimensional (3D), the above method cannot be applied directly. When the domain investigated is a volume, the method which is modified from a two-dimensional (2D) procedure will be explained in the following.



Inspection items						
Date: Feb. 14, 1990						
Material: Medium C steel						
Inspection section: Transverse						
Standard inspection area: $S_0 = 0.482 \text{ mm}^2$						
Number of inspections: $n = 40$						
Chemical composition (wt%)						
C	Si	Mn	P	S	Al	
0.28	0.45	1.40	0.028	0.015	0.005	
Cr	Cu	N	Ni	V		
0.05	0.03	0.0135	0.04	0.06		
Maximum inclusion distribution						
$\sqrt{\text{area}}_{\text{max}} = 2.389 \times y + 16.96$						
Test area:	$S \text{ (mm}^2\text{)}$					
Return period:	$T = S/S_0$					
Cum. distr. func.	$F = (T-1)/T \times 100 \text{ (%)}$ or $j/(n+1) \times 100 \text{ (%)}$					
Reduced variate	$y = -\ln[-\ln\{(T-1)/T\}]$					
Prediction of $\sqrt{\text{area}}_{\text{max}}$						
$S \text{ (mm}^2\text{)}$	T	$\sqrt{\text{area}}_{\text{max}} \text{ (}\mu\text{m)}$				
1	3.07	19.2				
100	207	29.7				

Figure A3.1 Prediction of the maximum inclusion from the statistics of extremes graph.

A4 Prediction of $\sqrt{\text{area}}_{\text{max}}$ of Inclusions Expected to be Contained in a Volume

Strictly speaking, the method described in the previous sections can be applied only to 2D problems. Since the volumetric shape of inclusions is not taken into account, the exact value of $\sqrt{\text{area}}_{\text{max}}$ in a volume cannot be directly predicted with this 2D method. In order to predict the value of $\sqrt{\text{area}}_{\text{max}}$ of inclusions contained in a volume, the inspection domain should be 3D instead of 2D; i.e., the statistics of extreme values of inclusion in a standard inspection volume V_0 . However, in practice, the 3D inspection of inclusions is extremely difficult. Therefore, a modified practical method based on 2D data for the prediction of $\sqrt{\text{area}}_{\text{max}}$ of inclusions contained in a volume must be developed.² The method proposed here transforms the inspection area into a volume by attributing a certain thickness to a 2D area [4–6]. For example, Fig. A4.1(a) shows the inclusions contained in a standard inspection area S_0 (mm^2). If a thickness h is added to S_0 , the 3D inspection domain is created as Fig. A4.1(b) and the standard inspection volume is then defined by $V_0 = h \times S_0$ (mm^3). The practical procedure to determine $\sqrt{\text{area}}_{\text{max}}$ is as follows.

(1) The mean value of the $\sqrt{\text{area}}_{\text{max},j}$ previously measured is taken empirically as an appropriate value of the thickness h . In the following it should be noted that units of h are in mm.

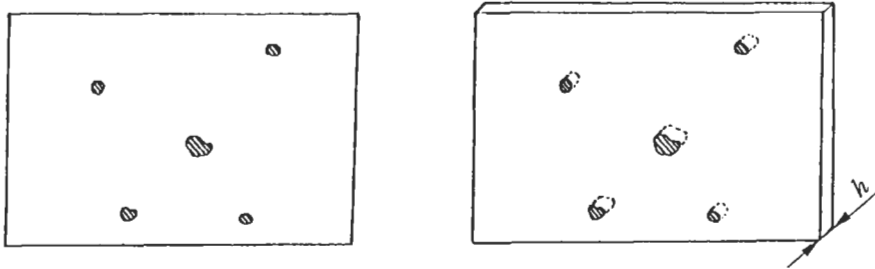
$$h = \left(\sum \sqrt{\text{area}}_{\text{max},j} \right) / n \quad (\text{A4.1})$$

(2) Calculate the standard inspection volume V_0 (mm^3).

$$V_0 = h \cdot S_0 \quad (\text{A4.2})$$

where S_0 is the 2D standard inspection area and h is the thickness.

² The estimation of distribution of 3D spheres from data on 2D sections is a classical problem in stereology and statistics known as the ‘Wicksell problem’ (see also Section A9). S.D. Wicksell: The Corpuscle Problem: a Mathematical Study of a Biometric Problem. *Biometrika*, 17 (1925) 84–99.



(a) Standard inspection area S_0 (mm^2)

(b) Standard inspection volume $V_0 (= h \cdot S_0)$ (mm^3)

Figure A4.1 Basic concept of 3D inspection. (a) Standard inspection area S_0 (mm^2). (b) Standard inspection volume $V_0 (= h \cdot S_0)$ (mm^3).

(3) Calculate the volume of prediction V (mm^3). The method is explained in the next section.

(4) From the prediction volume V (mm^3) and the standard inspection volume V_0 (mm^3), calculate the return period T .

$$T = V/V_0 \quad (\text{A4.3})$$

(5) In the same manner as in Section A3, from the return period T , calculate the corresponding predicted value of $\sqrt{\text{area}}_{\text{max}}$. The value obtained is the predicted $\sqrt{\text{area}}_{\text{max}}$ contained in volume V (mm^3).

A5 Method for Estimating the Prediction Volume (or Control Volume)

The prediction volume is the domain subjected to high stress, i.e., where fatigue crack initiation points might be included. As the stress distribution depends on the type of loading, the estimation of V in the case of bending, rotating bending, and tension–compression will be treated separately.

A5.1 Plate Bending

In the case of bending loading, in addition to the stress gradient, the effect of free surface is strong so that the fatigue crack initiation points tend to be on the surface and in the vicinity of the surface. It was empirically (from a significant number of previous experimental results) considered that the critical part of the specimen is that where $\sigma \geq 0.9\sigma_0$ (σ_0 is the nominal stress).³

Plate specimen (Fig. A5.1):



Figure A5.1 Plate bending.

$$V = 0.1tWl \text{ (mm}^3\text{)} \quad (\text{A5.1})$$

where:

- V = critical volume, mm^3 ;
- t = plate thickness, mm;
- W = plate width, mm;
- l = plate length, mm.

A5.2 Rotating Bending Loading

As for rotating bending loading too, the initiation points are likely to be at the surface and in the vicinity of the surface. It was empirically considered that the critical part of the specimen is that where $\sigma \geq 0.9\sigma_0$ (σ_0 is the nominal stress). Fig. A5.2 shows the histogram of fatigue fracture origin of 117 experimental cases [7–15] which were collected from other sources in addition to the data of the author's laboratory. The abscissa is the dimensionless depth normalised by the specimen section radius. The few hatched data having the deepest fracture origins are collected from the paper by Kawada

³ As long as the lower bound of the fatigue limit is concerned as described in Section A3, the surface area ($2Wl$) subjected to highest stress may be regarded to be the prediction area S (mm^2) for predicting $\sqrt{\text{area}}_{\text{max}}$. This approximation does not create a big error for the prediction of the lower bound of fatigue strength.

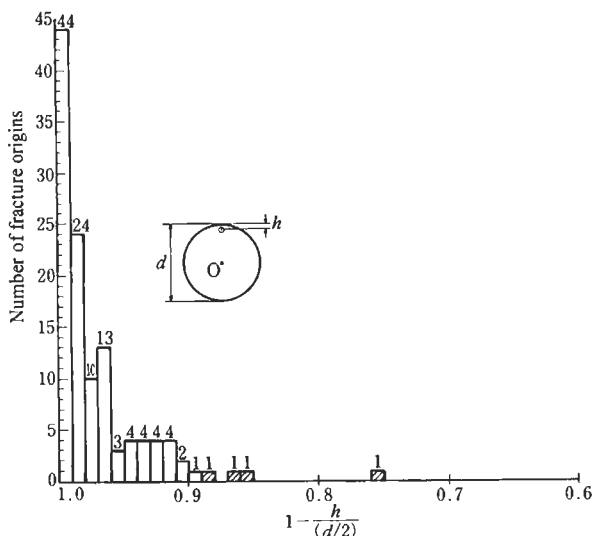


Figure A5.2 Distribution of fatigue fracture origins (rotating bending). (*h*: Distance from surface, *d*: specimen diameter at fracture section).



Figure A5.3 Rotating bending of a round bar.

et al. [7] published in 1963. These fracture origins are all big inclusions, particularly the deepest one is a giant inclusion and has $\sqrt{area} = 100.7 \mu\text{m}$. Recent steels seldom contain these giant inclusions; therefore, estimation of the control volume to be the depth to $\sigma \geq 0.9\sigma_0$ from the surface may be practically reasonable.⁴

(a) Round bar specimen (Fig. A5.3)

$$V = 0.05\pi d^2 l \tag{A5.2}$$

where:

⁴ If we assume the control volume to be the depth to $\sigma \geq 0.8\sigma_0$ or $\sigma \geq 0.7\sigma_0$, which has a larger return period *T*, the estimated value of \sqrt{area}_{max} will increase. However, the lower bound of the fatigue limit (the nominal stress at the specimen surface) for this case shows no big difference compared to the case in which we take the volume to be $\sigma \geq 0.9\sigma_0$ [4]. This is because the lower bound of the fatigue limit is the lower bound of the nominal stress, and even if \sqrt{area}_{max} increases with increasing the control volume by considering a deeper volume, the nominal stress extrapolated from the fatigue limit σ' at a deeper point gives no big difference compared to the one extrapolated from the fatigue limit at a shallow point. As long as the lower bound of the fatigue limit is concerned as described in Section A3, the surface area (πdl) subjected to highest stress may be regarded as the prediction area *S* (mm²) for predicting \sqrt{area}_{max} . This approximation does not create a big error for the prediction of the lower bound of fatigue strength.

- V = control volume, mm^3 ;
- d = diameter of the round bar, mm;
- l = length of the round bar, mm.

(b) *Hourglass-shaped specimen* (Fig. A5.4)

When the radius (R) of the notch of the specimen is at least one order larger than the diameter of the central part (d), the following equations can be applied.

Here, the additional parameters γ ($= \sigma/\sigma_0$), d_1 and z_1 have to be introduced. The domain having a stress larger than $\gamma \sigma_0$ is considered as a control volume. The value of γ is empirically chosen in the range $0.95 \geq \gamma \geq 0.9$.

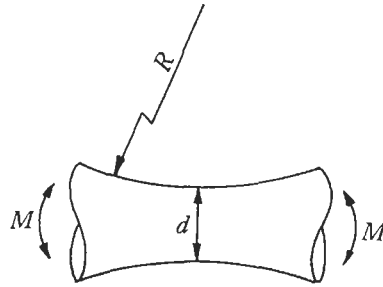


Figure A5.4 Rotating bending of an hourglass-shaped specimen.

$$d_1 = d/\sqrt[3]{\gamma} \tag{A5.3}$$

$$z_1 = \sqrt{R^2 - [R - 0.5(d_1 - d)]^2} \tag{A5.4}$$

$$V = 0.25\pi(1 - \gamma)(d + d_1)^2 z_1 \tag{A5.5}$$

where:

- V = control volume, mm^3 ;
- d = diameter of the central part, mm;
- R = notch radius, mm;
- d_1 = mm;
- z_1 = mm.

A5.3 Tension Compression Loading

Tension–compression specimen (Fig. A5.5)

$$V = 0.25\pi d^2 l \tag{A5.6}$$

where:

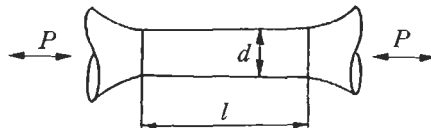


Figure A5.5 Tension compression specimen.

- V = control volume, mm^3 ;
 d = diameter of the specimen, mm;
 l = length of the specimen, mm.

A6 Prediction of the Lower Limit (Lower Bound) of the Fatigue Strength

(1) Surface inclusion (Fig. A6.1):

$$\sigma_w = 1.43(H_V + 120)/(\sqrt{\text{area}})^{1/6} \quad (\text{A6.1})$$

(2) Inclusion just below the surface (Fig. A6.2):

$$\sigma_w = 1.41(H_V + 120)/(\sqrt{\text{area}})^{1/6} \quad (\text{A6.2})$$

(3) Interior inclusion (Fig. A6.3):

$$\sigma_w = 1.56(H_V + 120)/(\sqrt{\text{area}})^{1/6} \quad (\text{A6.3})$$

The units are: σ_w , MPa; H_V , kgf/mm²; $\sqrt{\text{area}}$, μm .

Among these three equations, the lower bound of a scatter of fatigue strength is predicted with Eq. A6.2. Therefore, substituting the value of $\sqrt{\text{area}}_{\text{max}}$ obtained with the statistics of extremes into Eq. A6.2, the lower bound of the fatigue strength of many specimens can be estimated.

The lower limit of the fatigue strength:

$$\sigma_{wl} = 1.41(H_V + 120)/(\sqrt{\text{area}}_{\text{max}})^{1/6} \quad (\text{A6.4})$$

The units are: σ_{wl} , MPa; H_V , kgf/mm²; $\sqrt{\text{area}}_{\text{max}}$, μm .

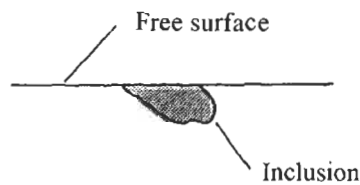


Figure A6.1 Surface inclusion.

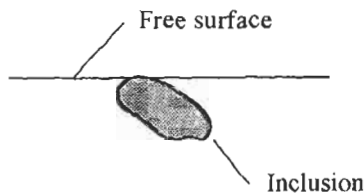


Figure A6.2 Inclusion just below surface.

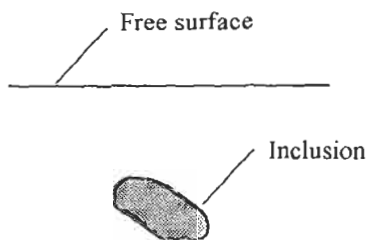


Figure A6.3 Interior inclusion.

A7 The Comparison of Predicted Lower Bound of the Scatter in Fatigue Strength of a Medium Carbon Steel with Rotating Bending Fatigue Test Results

Predictions and experimental results on the scatter in fatigue strength of a medium carbon steel will be shown.

A7.1 Construction of a Graph of the Statistics of Extremes

(a) Inspection parameters are:

- standard inspection (control) area $S_0 = 0.482 \text{ mm}^2$;
- number of inspections $n = 40$.

The authors found the values of $S_0 = 0.482 \text{ mm}^2$ and $n = 40$ adequate for this test. For better accuracy, S_0 and n can be increased.

From Eqs. A2.2 and A2.3, for $j = 1$ to n , calculate the cumulative distribution function F_j and the reduced variate y_j :

$$F_j = j \times 100 / (n + 1) \quad (\%) \quad (\text{A2.2})$$

$$y_j = -\ln\{-\ln[j / (n + 1)]\} \quad (\text{A2.3})$$

Then plot F_j and y_j together with $\sqrt{\text{area}_{\text{max},j}}$ as shown in Table A7.1.

(b) Determination of the distribution of the maximum inclusions by the least squares method.

$$\begin{aligned} \sum \sqrt{\text{area}_{\text{max},j}} &= \sqrt{\text{area}_{\text{max},1}} + \sqrt{\text{area}_{\text{max},2}} + \cdots + \sqrt{\text{area}_{\text{max},40}} \\ &= 13.82 + 14.50 + \cdots + 24.22 + 26.51 \\ &= 730.36 \end{aligned}$$

$$\begin{aligned} \sum y_j &= y_1 + y_2 + \cdots + y_j + \cdots + y_{40} \\ &= (-1.132) + (-1.105) + \cdots + 2.996 + 3.701 \\ &= 21.745 \end{aligned}$$

$$\begin{aligned} \sum (y_j)^2 &= (y_1)^2 + (y_2)^2 + \cdots + (y_j)^2 + \cdots + (y_{40})^2 \\ &= (-1.132)^2 + (-1.105)^2 + \cdots + 2.996^2 + 3.701^2 \\ &= 63.925 \end{aligned}$$

$$\begin{aligned} \sum (y_j \sqrt{\text{area}_{\text{max},j}}) &= (y_1 \sqrt{\text{area}_{\text{max},1}}) + (y_2 \sqrt{\text{area}_{\text{max},2}}) + \cdots + (y_{40} \sqrt{\text{area}_{\text{max},40}}) \\ &= (-1.132 \times 13.82) + (-1.105 \times 14.50) + \cdots + (3.701 \times 26.51) \\ &= 521.54 \end{aligned}$$

Calculation of coefficients a and b of Eq. A2.4:

$$\begin{aligned} a &= \left\{ n \cdot \sum (y_j \sqrt{\text{area}_{\text{max},j}}) - \sum y_j \cdot \sum \sqrt{\text{area}_{\text{max},j}} \right\} / \left\{ n \cdot \sum (y_j)^2 - (\sum y_j)^2 \right\} \\ &= \{40 \times 521.54 - 21.745 \times 730.36\} / \{40 \times 63.925 - (21.745)^2\} \\ &= 2.389 \end{aligned} \quad (\text{A7.1})$$

Table A7.1 Inclusion data

Material: Medium carbon steel Inspection section: Transverse Standard inspection area: $S_0 = 0.482 \text{ mm}^2$ Number of inspections: $n = 40$			Date: Feb. 14, 1990 Cum. distr. func.: $F_j = j/(n+1) \times 100(\%)$ Reduced variate: $y_j = -\ln[-\ln\{j/(n+1)\}]$	
No.	$F_j(\%)$	y_j	$\sqrt{\text{area}_{\text{max},j}}(\mu\text{m})$	photo No.
1	2.439	-1.312	13.82	16
2	4.878	-1.105	14.50	2
3	7.317	-0.9612	14.69	26
4	9.756	-0.8447	14.97	3
5	12.20	-0.7439	15.15	13
6	14.63	-0.6533	15.51	40
7	17.07	-0.5697	15.78	27
8	19.51	-0.4911	16.13	35
9	21.95	-0.4163	16.21	38
10	24.39	-0.3443	16.38	14
11	26.83	-0.2744	16.47	5
12	29.27	-0.2059	16.63	25
13	31.71	-0.1386	16.88	18
14	34.15	-0.07187	16.88	34
15	36.59	-0.0055	16.96	9
16	39.02	0.06083	17.21	39
17	41.46	0.1274	17.29	17
18	43.90	0.1946	17.37	28
19	46.34	0.2625	17.52	30
20	48.78	0.3315	17.84	36
21	51.22	0.4019	18.07	22
22	53.66	0.4740	18.15	21
23	56.10	0.5480	18.15	32
24	58.54	0.6245	18.22	12
25	60.98	0.7038	18.37	7
26	63.41	0.7864	18.45	23
27	65.85	0.8729	18.45	33
28	68.29	0.9640	18.52	37
29	70.73	1.061	18.97	8
30	73.17	1.164	19.47	11
31	75.61	1.274	19.89	4
32	78.05	1.395	20.17	19
33	80.49	1.528	20.24	6
34	82.93	1.676	20.78	24
35	85.37	1.844	21.50	20
36	87.80	2.040	21.88	15
37	90.24	2.276	22.87	10
38	92.68	2.577	23.29	31
39	95.12	2.996	24.22	29
40	97.56	3.701	26.51	1

$$\begin{aligned}
 b &= \left\{ \sum \sqrt{\text{area}_{\max,j}} - a \cdot \sum y_j \right\} / n \\
 &= \{730.6 - 2.389 \times 21.745\} / 40 \\
 &= 16.96
 \end{aligned} \tag{A7.2}$$

Hence, the distribution of the maximum inclusions, the equation of the straight line, is expressed as follows:

$$\sqrt{\text{area}_{\max}} = 2.389y + 16.96 \tag{A7.3}$$

(c) Drawing of the graph, as shown in Fig. A7.1.

A7.2 Prediction of the Lower Bound of the Scatter in Fatigue Strength

(a) Estimation of the thickness h of the standard inspection (control) volume V_0 , as described in Section A4.

$$\begin{aligned}
 h &= \sum \sqrt{\text{area}_{\max,j}} / n \\
 &= 730.36 / 40 \\
 &= 18.26 \text{ } (\mu\text{m}) \\
 &\cong 18.26 \times 10^{-3} \text{ (mm)}
 \end{aligned} \tag{A4.1}$$

(b) Determination of the standard inspection volume V_0 :

$$\begin{aligned}
 V_0 &= h \cdot S_0 \\
 &= 18.26 \times 10^{-3} \times 0.482 \\
 &\cong 8.80 \times 10^{-3} \text{ (mm}^3\text{)}
 \end{aligned} \tag{A4.2}$$

(c) Estimation of the critical volume V .

The specimens in the test are the hourglass-shaped rotating bending specimens shown in Fig. A5.4.

The part of the specimen where $\sigma \geq 0.9\sigma_0$ (σ_0 is the nominal stress) tends to contain the fatigue crack initiation points and hence is considered as the critical part. Thus, substitute $\gamma = 0.9$, $R = 65$ mm, and $d = 8$ mm into Eqs. A5.3 to A5.5:

$$\begin{aligned}
 d_1 &= d / \sqrt[3]{r} \\
 &= 8 / \sqrt[3]{0.9} \\
 &= 8.286 \text{ (mm)}
 \end{aligned} \tag{A5.3}$$

$$\begin{aligned}
 z_1 &= \sqrt{R^2 - \{R - 0.5(d_1 - d)\}^2} \\
 &= \sqrt{65^2 - \{65 - 0.5(8.286 - 8)\}^2} \\
 &= 4.309 \text{ (mm)}
 \end{aligned} \tag{A5.4}$$

$$\begin{aligned}
 V &= 0.25\pi(1 - \gamma)(d + d_1)^2 z_1 \\
 &= 0.25\pi(1 - 0.9)(8 + 8.286)^2 \times 4.309 \\
 &= 89.8 \text{ (mm}^3\text{)}
 \end{aligned} \tag{A5.5}$$

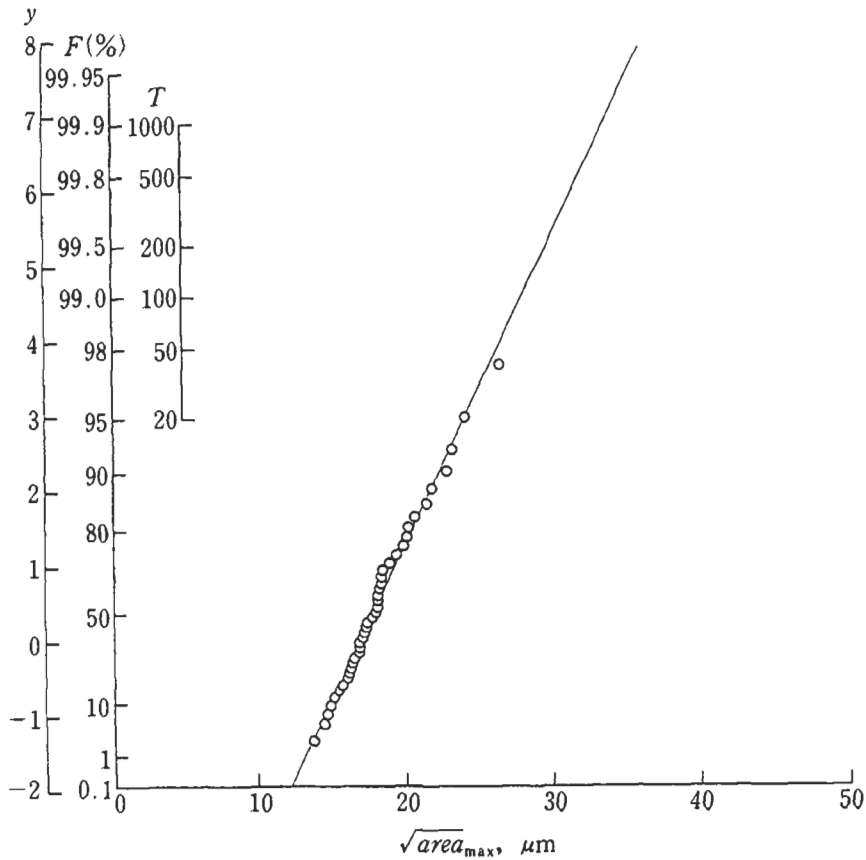


Figure A7.1 Statistics of extremes graph (a medium carbon steel).

Inspection items					
Date: Feb. 14, 1990					
Material: Medium C steel					
Inspection section: Transverse					
Standard inspection area: $S_0 = 0.482 \text{ mm}^2$					
Number of inspections: $n = 40$					
Chemical composition (wt%)					
C	Si	Mn	P	S	Al
0.28	0.45	1.40	0.028	0.015	0.005
Cr	Cu	N	Ni	V	
0.05	0.03	0.0135	0.04	0.06	
Maximum inclusion distribution					
$\sqrt{\text{area}}_{\text{max}} = 2.389 \times y + 16.96$					
Test area:	$S \text{ (mm}^2\text{)}$				
Return period:	$T = S/S_0$				
Cum. distr. func.:	$F = (T-1)/T \times 100 \text{ (}\% \text{)}$ or $j/(n+1) \times 100 \text{ (}\% \text{)}$				
Reduced variate	$y = -\ln \{-\ln[(T-1)/T]\}$				
Prediction of $\sqrt{\text{area}}_{\text{max}}$					
$S \text{ (mm}^2\text{)}$	T	$\sqrt{\text{area}}_{\text{max}} \text{ (}\mu\text{m)}$			
1	3.07	19.2			
100	207	29.7			

(d) For $N = 1, 10$ and 100 , the return periods $T_{(1)}$, $T_{(10)}$ and $T_{(100)}$ are calculated as follows:

$$T = NV/V_0 \quad (\text{A4.3})$$

$$\begin{aligned} T_{(1)} &= V \times 1/V_0 \\ &= 89.8 \times 1/(8.80 \times 10^{-3}) \\ &= 1.02 \times 10^4 \end{aligned}$$

$$\begin{aligned} T_{(10)} &= V \times 10/V_0 \\ &= 89.8 \times 10/(8.80 \times 10^{-3}) \\ &= 1.02 \times 10^5 \end{aligned}$$

$$\begin{aligned} T_{(100)} &= V \times 100/V_0 \\ &= 89.8 \times 100/(8.80 \times 10^{-3}) \\ &= 1.02 \times 10^6 \end{aligned}$$

(e) For $N = 1, 10$ and 100 , the reduced variates $y_{(1)}$, $y_{(10)}$ and $y_{(100)}$ are:

$$y = -\ln\{-\ln[(T-1)/T]\} \quad (\text{A2.5})$$

$$\begin{aligned} y_{(1)} &= -\ln\{-\ln[(T_{(1)}-1)/T_{(1)}]\} \\ &= -\ln\{-\ln[(1.02 \times 10^4 - 1)/1.02 \times 10^4]\} \\ &= 9.23 \end{aligned}$$

$$\begin{aligned} y_{(10)} &= -\ln\{-\ln[(T_{(10)}-1)/T_{(10)}]\} \\ &= -\ln\{-\ln[(1.02 \times 10^5 - 1)/1.02 \times 10^5]\} \\ &= 11.53 \end{aligned}$$

$$\begin{aligned} y_{(100)} &= -\ln\{-\ln[(T_{(100)}-1)/T_{(100)}]\} \\ &= -\ln\{-\ln[(1.02 \times 10^6 - 1)/1.02 \times 10^6]\} \\ &= 13.84 \end{aligned}$$

Substituting each value of y into Eq. A2.4, $\sqrt{\text{area}}_{\text{max}}$ of the maximum size inclusions which are expected to exist in $N = 1, 10$ and 100 specimens are determined as follows:

$$\sqrt{\text{area}}_{\text{max}} = a \cdot y + b \quad (\text{A2.4})$$

$$\begin{aligned} \sqrt{\text{area}}_{\text{max}(1)} &= a \cdot y_{(1)} + b \\ &= 2.389 \times 9.23 + 16.96 \\ &= 39.0 \text{ } (\mu\text{m}) \end{aligned}$$

$$\begin{aligned} \sqrt{\text{area}}_{\text{max}(10)} &= a \cdot y_{(10)} + b \\ &= 2.389 \times 11.53 + 16.96 \\ &= 44.5 \text{ } (\mu\text{m}) \end{aligned}$$

Table A7.2 The estimated value of \sqrt{area}_{max} and the lower bound of fatigue strength σ_{wl}

Number of specimens	1	10	100
\sqrt{area}_{max} (μm)	39.0	44.5	50.0
σ_{wl} (MPa)	475	464	456

$$\begin{aligned}\sqrt{area}_{max(100)} &= a \cdot y_{(100)} + b \\ &= 2.389 \times 13.84 + 16.96 \\ &= 50.0 \text{ } (\mu\text{m})\end{aligned}$$

(f) Substituting each value of \sqrt{area}_{max} into Eq. A6.4, the lower bounds of the fatigue strengths σ_{wl} as a function of the Vickers hardness H_V ($= 500$) are predicted as follows:

$$\sigma_{wl} = 1.41(H_V + 120) / (\sqrt{area}_{max})^{1/6} \quad (\text{A6.4})$$

$$\begin{aligned}\sigma_{wl(1)} &= 1.41(H_V + 120) / (39.0)^{1/6} \\ &= 475 \text{ (MPa)}\end{aligned}$$

$$\begin{aligned}\sigma_{wl(10)} &= 1.41(H_V + 120) / (44.5)^{1/6} \\ &= 464 \text{ (MPa)}\end{aligned}$$

$$\begin{aligned}\sigma_{wl(100)} &= 1.41(H_V + 120) / (50.0)^{1/6} \\ &= 456 \text{ (MPa)}\end{aligned}$$

The units are: σ_{wl} , MPa; H_V , kgf/mm²; \sqrt{area}_{max} , μm .

Table A7.2 shows the values of \sqrt{area}_{max} and σ_{wl} .

A8 Optimisation of Extreme Value Inclusion Rating (EVIR)

From the results shown in the previous sections one could draw the wrong conclusion that the estimation of the maximum inclusion (or defect) in a component is a very simple procedure which can be based on a few measurements on small areas. The key point is to optimise the sampling procedure in order to obtain significant and reliable estimates of extreme defects.

The first problem that has to be addressed is the uncertainty in the $x(T)$ estimation. The value of $x(T)$ can be easily calculated by Eq. A1.5 from the parameters λ and δ of the actual sample. However, these values are only estimates of the true parameters of the population of defects, from which the sample was taken. The parameter estimates are more precise with the increasing number (n) of maximum defect examined and they tend to true values when $n \rightarrow \infty$.

It follows that the number of defects to be collected with extreme value sampling has to be chosen in order to make an $x(T)$ estimate precise enough for fatigue strength calculations. This can be done by obtaining more precise estimates of $x(T)$ with the maximum likelihood method and by choosing the minimum number of defects with the map shown in Fig. A8.1 [3].

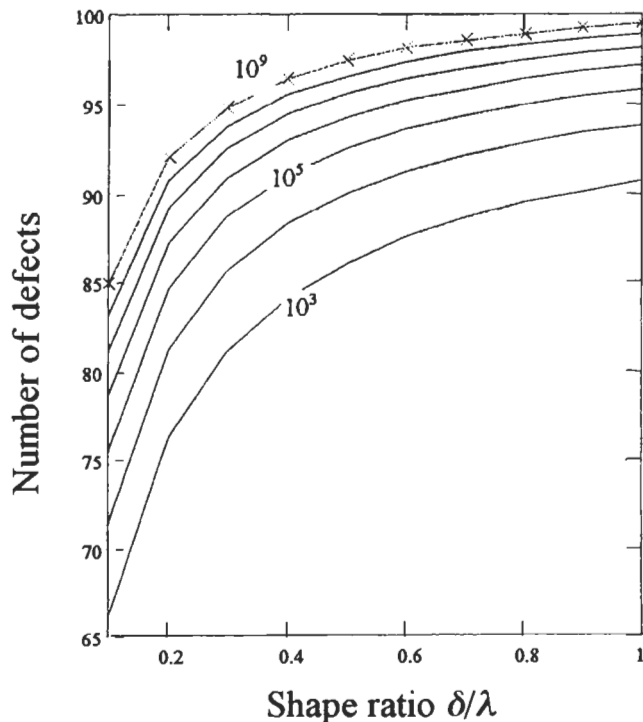


Figure A8.1 Maps for optimising the precision of $x(T)$ estimates for maximum likelihood statistical analysis [3].

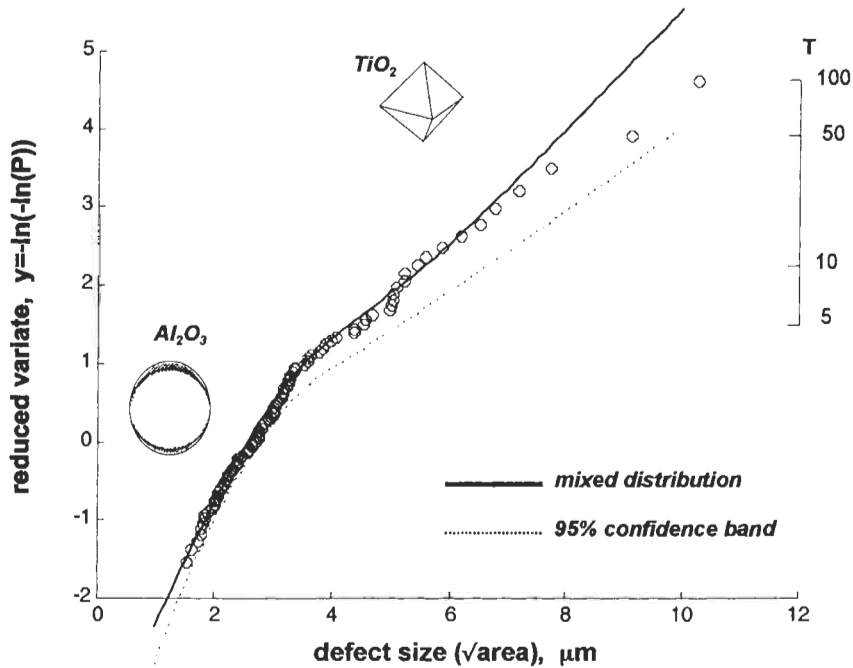


Figure A8.2 Defects sampled with polished sections ($S_0 = 1 \text{ mm}^2$) on an SUJ2 bearing steel equivalent to SAE52100 [16].

The second problem to be addressed is the fact that in a steel there are always many different kinds of defects with different 'density' (see Fig. A8.2) in S_0 . If one carries out the sampling of extreme inclusions on small S_0 areas, then it is possible that he does not include in the analysis some 'rare' big particles that are eventually responsible for fatigue failure [16].

The solution to this problem is analysing the inclusions sampled with two different control areas S_{01} and S_{02} (S_{02} being much larger than S_{01}). If the estimates of extremes inclusions obtained from the two data sets are different, then two different particle types are likely to be present in the steel under examination (at first instance the two control areas can be chosen as: $S_{01} = 0.5\text{--}1 \text{ mm}^2$ and $S_{02} \geq 100 \text{ mm}^2$). In this case the estimation of the maximum inclusion should be simply based on S_{02} data. The correct analysis for the choice of the optimum inspection area and for taking into account the presence of two defect types is discussed in Ref. [16].

Recent results show that the presence of two distributions of extreme defects can be related to a different morphology of particles, even if the chemical composition remains the same [17].

A9 Recent Developments in Statistical Analysis and its Perspectives

The method for estimating the distribution of defects shown in the previous paragraphs is based on measuring the maximum size of defects in randomly chosen areas or volumes (this sampling technique is called 'block maxima' [2]).

An alternative method recently proposed [18,19] for the analysis of extremes inclusions is to observe on polished sections the sizes of particles larger than a chosen size (this technique is called 'peak over threshold'). The inclusion sizes are then analysed with the generalised pareto distribution [2], which was originally applied to estimation of extreme winds, flood levels and wave heights, for estimating the maximum inclusion within a piece of steel [18,19]. This method, if applied under the same hypothesis of the estimation with Gumbel distribution, seems to offer narrower confidence bands [20].

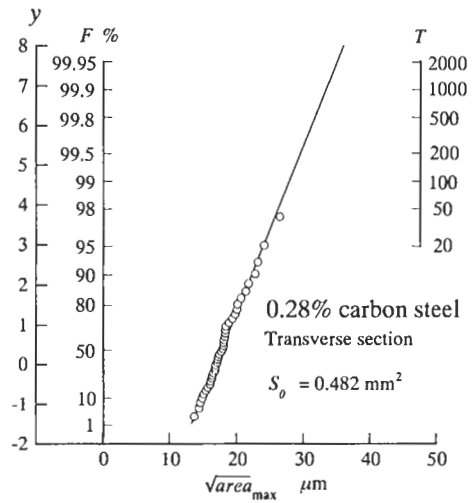
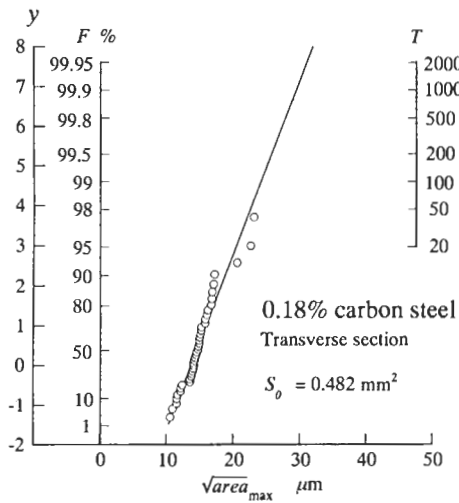
A promising field of research in which very interesting results are being obtained is the statistical estimation about the 3D sizes of large inclusions from 2D data from polished sections analysed with 'peak over threshold' methods [21–26]. In this way the stereological problem is already included in the analysis. However, these complicated analyses, in the case of spherical particles, tend to support the use of the simple rule explained in Section A4.

A10 References

1. E.J. Gumbel: *Statistics of Extremes*, Columbia University Press, New York, 1957.
2. R.D. Reiss and M. Thomas: *Statistical Analysis of Extreme Values*, Birkhauser, Basel, 1997.
3. S. Beretta and Y. Murakami: Statistical Analysis of Defects for Fatigue Strength Prediction and Quality Control of Materials, *Fatigue Fract. Eng. Mater. Struct.*, **21** (1998), 1049–1065.
4. Y. Murakami and H. Usuki: Prediction of Fatigue Strength of High-Strength Steels Based on Statistical Evaluation of Inclusion Size, *Trans. Jpn. Soc. Mech. Eng. A*, **55(510)** (1989), 213–221.
5. Y. Murakami, Y. Uemura and K. Kawakami: Some Problems in the Application of Statistics of Extreme Values to Estimation of the Maximum Size of Nonmetallic Inclusions in Metals, *Trans. Jpn. Soc. Mech. Eng. A*, **55(509)** (1989), 58–62.
6. Y. Uemura and Y. Murakami: A Numerical Simulation of Evaluating the Maximum Size of Inclusions to Examine the Validity of the Metallographic Determination of the Maximum Size of Inclusions, *Trans. Jpn. Soc. Mech. Eng. A*, **56(521)** (1990), 162–167.
7. Y. Kawada, H. Nakazawa and S. Kodama: The Effects of the Shapes and the Distributions of Inclusions on the Fatigue Strength of Bearing Steels in Rotary Bending, *Trans. Jpn. Soc. Mech. Eng. Ser. I*, **29(206)** (1963), 1674–1683.
8. W.E. Duckworth and E. Ineson: The Effects of Externally Introduced Alumina Particles on the Fatigue Life of En24 Steel, *Clean Steel, Iron Steel Inst., Spec. Rep.*, **77** (1963), 87–103.
9. S. Konuma and T. Furukawa: Relationship between Fatigue Strength and Hardness in Hard Martensitic Steels, *Proc. 18th Fatigue Symp., Soc. Mater. Sci., Jpn.*, 1986, pp. 5–9.
10. Y. Murakami, S. Kodama and S. Konuma: Quantitative Evaluation of Effects of Nonmetallic Inclusions on Fatigue Strength of High Strength Steel, *Trans. Jpn. Soc. Mech. Eng. A*, **54(500)** (1988), 688–696.
11. Y. Murakami, K. Mine and H. Usuki: Fatigue Strength of Annealed 0.45 C Pb-Free-Cutting Steel, *Tetsu To Hagane*, **74(6)** (1988), 1113–1118.
12. Y. Murakami, K. Matsuda, Y. Ohkomori, I. Kitagawa and K. Shinozuka: Effects of Nonmetallic Inclusions and Corrosion Pits on the Fatigue Strength of a High Strength Steel, *Proc. Int. Conf. Evaluation of Materials Performance in Severe Environments, EVALMAT 89*, 1, 1989, pp. 143–150.
13. Y. Murakami, M. Kobayashi, T. Makino, T. Toriyama, Y. Kurihara, S. Takasaki and R. Ebara: Quantitative Evaluation of the Factors Influencing Fatigue Strength of Spring Steels (Effects of Nonmetallic Inclusions, Shot Peening, Decarburized Layer and Small Surface Pits), *Trans. Jpn. Soc. Mech. Eng. A*, **57(542)** (1991), 2305–2313.
14. Y. Murakami, K. Kawakami and M. Saito: Effects of Inclusions on Fatigue Strength of a Suspension Spring Steel, *Trans. Jpn. Soc. Spring Res.*, **35** (1990), 1–7.
15. Y. Murakami, T. Toriyama, T. Makino, Y. Koyasu and S. Nishida: Effects of Chemical Composition of Nonmetallic Inclusions on Fatigue Strength of High Strength Steel, *Proc. 69th JSME Fall Annual Meeting*, No. 910(62) A, 1991, pp. 22–24.
16. S. Beretta and Y. Murakami: Largest Extreme Value Distribution Analysis of Multiple Inclusions Types in Determining Steel Cleanliness, *Metallurgical and Materials Transactions B*, **32B** (2001), 517–523.
17. Y. Murakami, S. Zhou, Y. Fukushima and S. Beretta: *Tetsu To Hagane*, Iron and Steel Institute, Japan, **87(12)** (2001), 748–755.
18. G. Shi, H.V. Atkinson, C.M. Sellars and C.W. Anderson: Application of the Generalized Pareto Distribution to the Estimation of the Size of the Maximum Inclusion in Clean Steels, *Acta Mater.* **47** (1999), 1455–1468.
19. G. Shi, H.V. Atkinson, C.M. Sellars and C.W. Anderson: Comparison of Extreme Value Statistics Methods for Predicting Maximum Inclusion Size in Clean Steels, *Ironmaking Steelmaking*, **26** (1999), 239–246.
20. C.W. Anderson, G. Shi, H.V. Atkinson and C.M. Sellars: The Precision of Methods Using the Statistics of Extremes for the Estimation of the Maximum Size of Inclusions in Clean Steels, *Acta Mater.* **48** (2000), 4235–4246.
21. R. Takahashi and M. Sibuya: The Maximum Size of Planar Section of Spheres and its Application to Metallurgy, *Ann. Inst. Stat. Math.*, **48** (1996), 127–144.
22. R. Takahashi and M. Sibuya: Prediction of the Maximum Size in Wicksell's Corpuscle Problem, *Ann. Inst. Stat. Math.*, **50** (1998), 361–377.

23. H. Drees and R.D. Reiss: Tail Behaviour in Wickseil's Corpuscle Problem. In: J. Galambos and I. Katai (Eds): Probability and Applications, Kluwer, Dordrecht, 1992, pp. 205–220.
24. H.V. Atkinson, C.M. Sellars and G. Shi: Statistical Prediction of Inclusion Size in Clean Steels, Mater. Sci. Technol., **16** (2000), 1175–1180.
25. H.V. Atkinson, C.M. Sellars and G. Shi: The Maximum Inclusion Size in Two Clean Steels I: Comparison of the Maximum Size Estimates by the Statistics of Extremes and Generalized Pareto Distribution Methods, Private communication (2001).
26. H.V. Atkinson, C.M. Sellars and G. Shi: The Maximum Inclusion Size in Two Clean Steels II: Use of Data from Cold Crucible Remelted Samples and Polished Optical Cross-Sections, Private communication (2001).

Appendix B: Database of Statistics of Extreme Values of Inclusion Size \sqrt{area}_{max}



Chemical composition of 0.18% C steel, wt.%, Rated in 1989

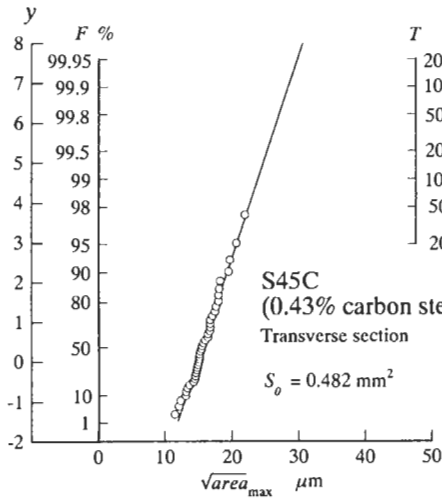
C	Si	Mn	P	S	Ni	Cr	Mo	Cu
0.18	0.26	1.28	0.018	0.028	0.08	0.12	0.05	0.24

Chemical composition of 0.28% C steel, wt.%, Rated in 1989

C	Si	Mn	P	S	Ni	Cr	Mo	Cu
0.28	0.45	1.40	0.028	0.015	0.04	0.05	—	0.03

Fig. B1

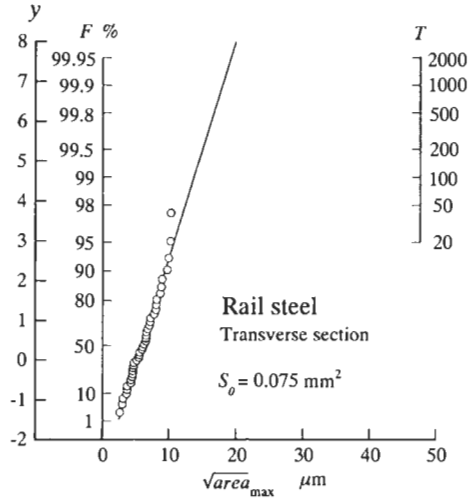
Fig. B2



Chemical composition of S45C, wt.%, Rated in 1989

C	Si	Mn	P	S	Ni	Cr	Mo	Cu
0.43	0.21	0.74	0.027	0.043	0.10	0.57	—	0.27

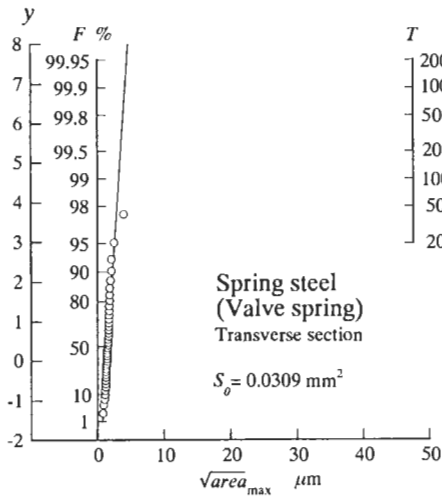
Fig. B3



Chemical composition of rail steel, wt.%, Rated in 1992

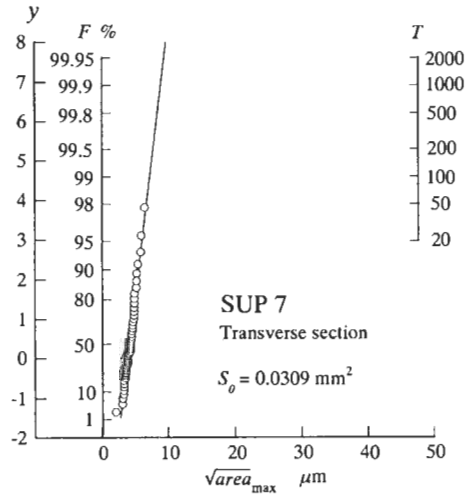
C	Si	Mn	P	S	Ni	Cr	Mo	Cu
0.67	0.23	0.87	0.018	0.009	—	—	—	—

Fig. B4



Rated in 1987

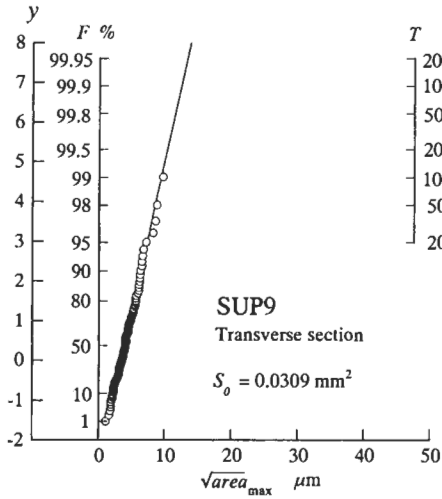
Fig. B5



Chemical composition of SUP7, wt.%, Rated in 1987

C	Si	Mn	P	S	Ni	Cr	Mo	Cu
0.61	2.05	0.86	0.019	0.014	0.16	—	0.01	—

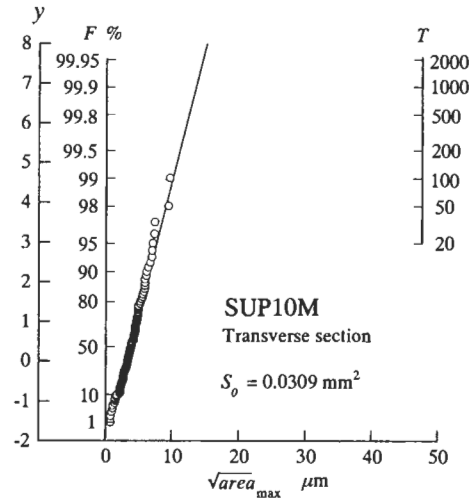
Fig. B6



Chemical composition of SUP9, wt.%, Rated in 1991

C	Si	Mn	P	S	Ni	Cr	Mo	Cu
0.53	0.31	0.71	0.023	0.012	—	0.67	—	0.14

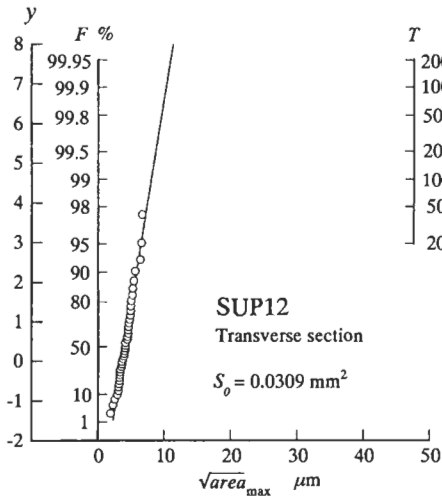
Fig. B7



Chemical composition of SUP10M, wt.%, Rated in 1991

C	Si	Mn	P	S	Ni	Cr	Mo	Cu	V	Nb
0.51	0.23	0.85	0.017	0.001	—	0.95	—	0.04	0.16	0.043

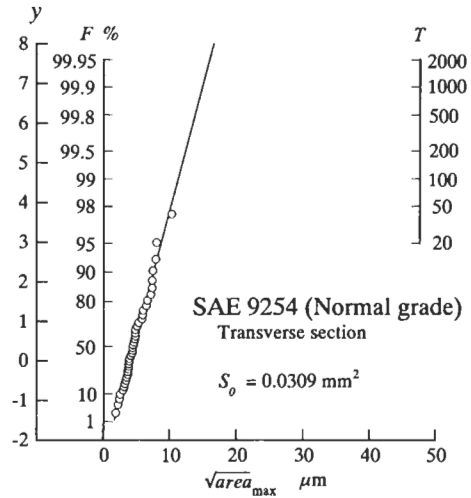
Fig. B8



Chemical composition of SUP12, wt.%, Rated in 1987

C	Si	Mn	P	S	Ni	Cr	Mo	Cu
0.53	1.31	0.75	0.004	0.004	0.04	—	0.01	—

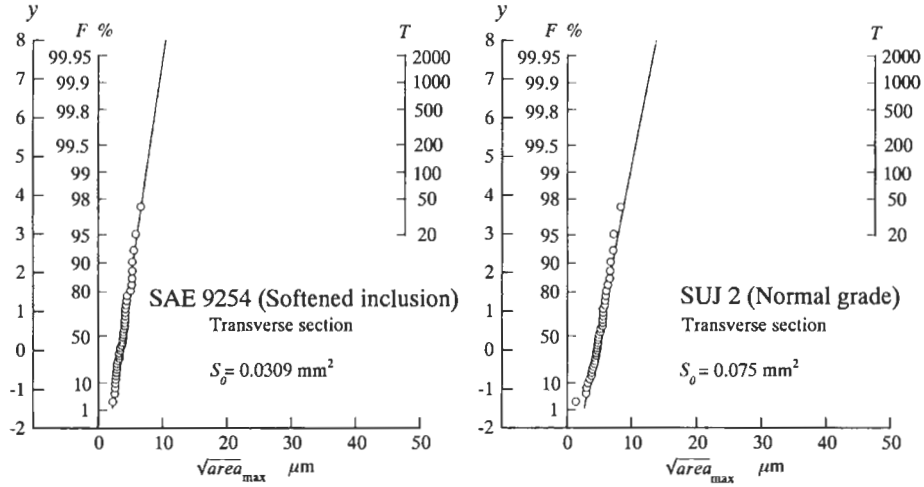
Fig. B9



Chemical composition of SAE9254 (Normal grade) wt.%, Rated in 1991

C	Si	Mn	P	S	Ni	Cr	Mo	Cu	O(ppm)
0.52	1.43	0.71	0.023	0.005	—	0.723	—	—	10

Fig. B10



Chemical composition of SAE9254 (Softened inclusion) wt.%, Rated in 1991

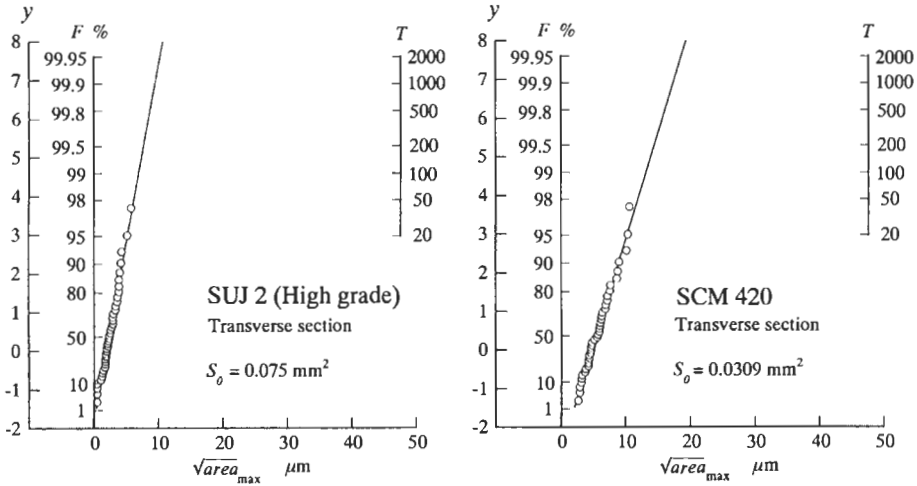
C	Si	Mn	P	S	Ni	Cr	Mo	Cu	O(ppm)
0.58	1.47	0.69	0.014	0.003	—	0.693	—	—	20

Chemical composition of SUJ2 (Normal grade), wt.%, Rated in 1991

C	Si	Mn	P	S	Ni	Cr	Cu	Ti	Al	N (ppm)	O (ppm)
0.99	0.23	0.34	0.014	0.014	0.02	1.45	0.01	0.001	0.025	45	8

Fig. B11

Fig. B12



Chemical composition of SUJ2 (High grade), wt.%, Rated in 1991

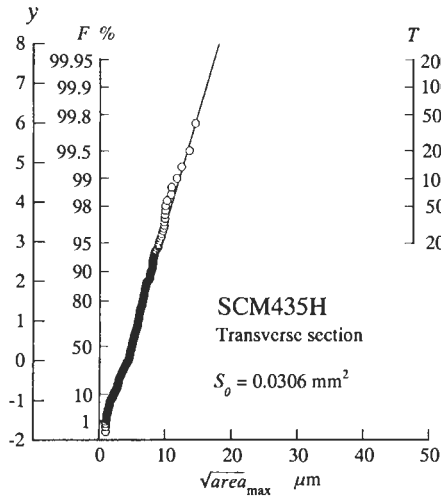
C	Si	Mn	P	S	Ni	Cr	Cu	Ti	Al	N(ppm)	O(ppm)
0.98	0.23	0.37	0.010	0.005	0.02	1.43	0.01	0.002	0.021	55	5

Chemical composition of SCM420, wt.%, Rated in 1991

C	Si	Mn	P	S	Ni	Cr	Mo	Cu
0.22	0.27	0.79	0.018	0.007	—	15.76	0.18	—

Fig. B13

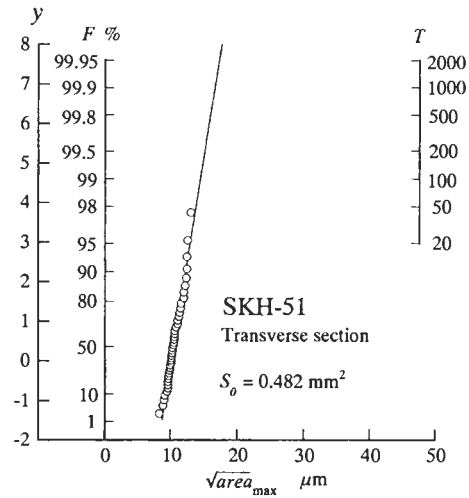
Fig. B14



Chemical composition of SCM435H, wt.%, Rated in 1999

C	Si	Mn	P	S	Ni	Cr	Mo	Cu
0.36	0.30	0.77	0.027	0.015	0.02	1.06	0.18	0.02

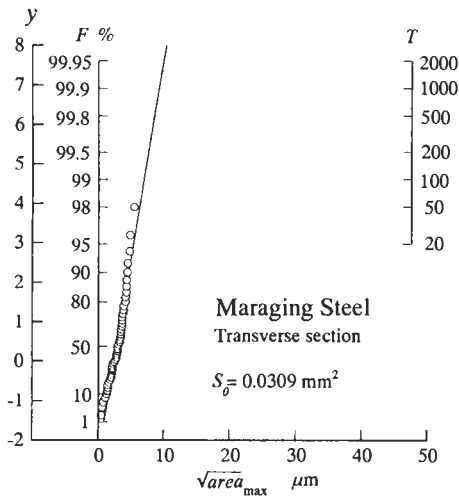
Fig. B15



Chemical composition of SKH-51, wt.%, Rated in 1988

C	Si	Mn	P	S	Ni	Cr	Mo	Cu	W
0.81	0.31	0.29	0.018	0.002	—	3.92	4.85	0.07	6.10

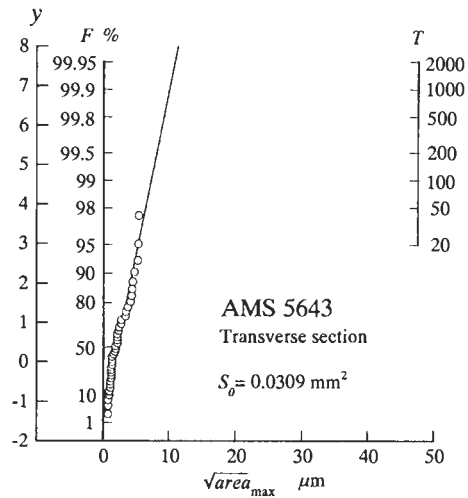
Fig. B16



Chemical composition of maraging steel, wt.%, Rated in 1987

C	Si	Mn	P	S	Ni	Cr	Mo	Cu	Ti	Co
0.007	0.02	0.01	0.003	0.003	17.50	—	3.79	—	1.86	12.50

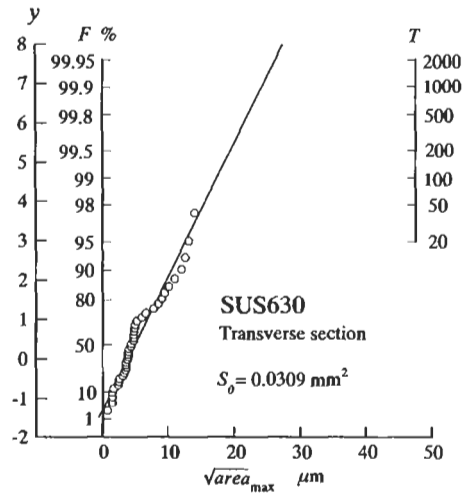
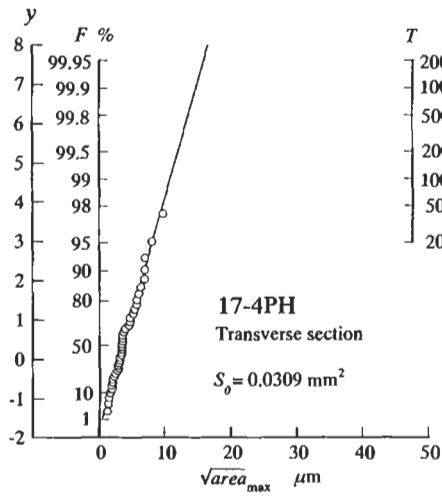
Fig. B17



Chemical composition of AMS5643, wt.%, Rated in 1990

C	Si	Mn	P	S	Ni	Cr	Mo	Cu
0.04	0.015	0.08	0.008	0.003	4.26	15.13	0.01	3.42

Fig. B18



Chemical composition of 17-4PH, wt.%, Rated in 1990

C	Si	Mn	P	S	Ni	Cr	Mo	Cu
0.04	0.18	0.78	0.006	0.002	4.30	15.10	0.07	15.7

Fig. B19

Chemical composition of SUS630, wt.%, Rated in 1990

C	Si	Mn	P	S	Ni	Cr	Mo	Cu
0.03	0.51	0.58	0.35	0.06	4.29	15.97	—	—

Fig. B20

Appendix C: Probability Sheets of Statistics of Extremes

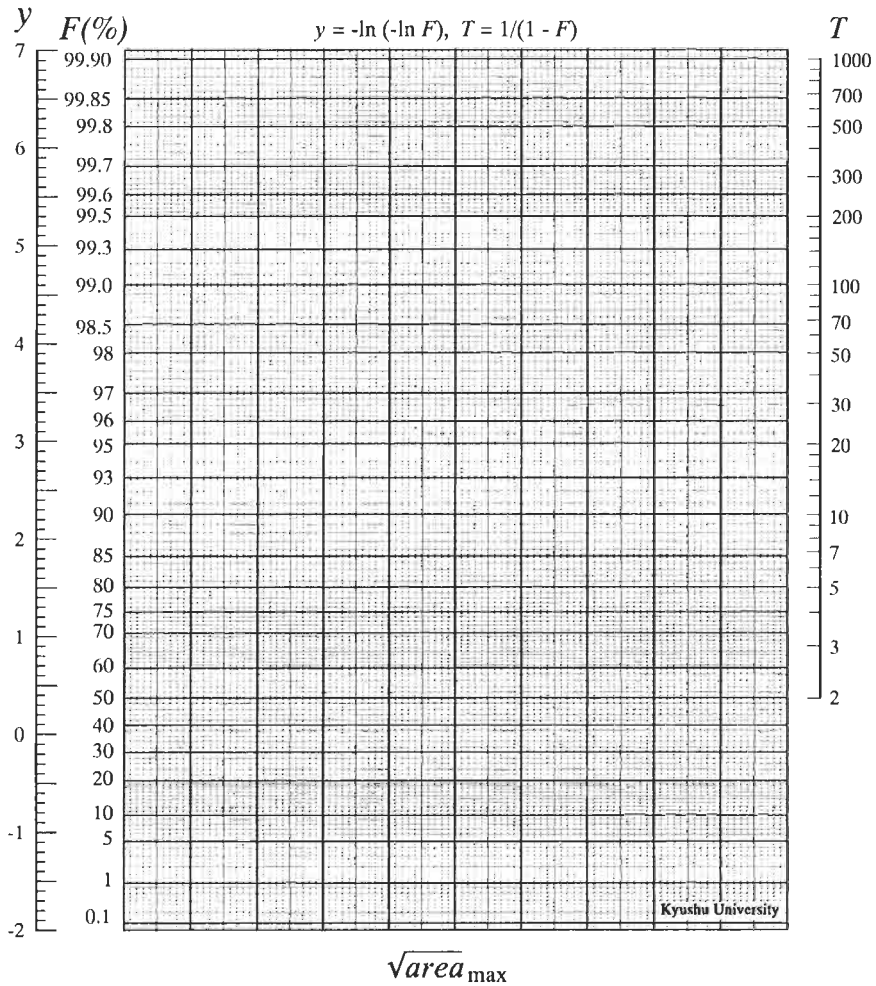


Figure C.1 Probability paper for extreme value distribution (type I).

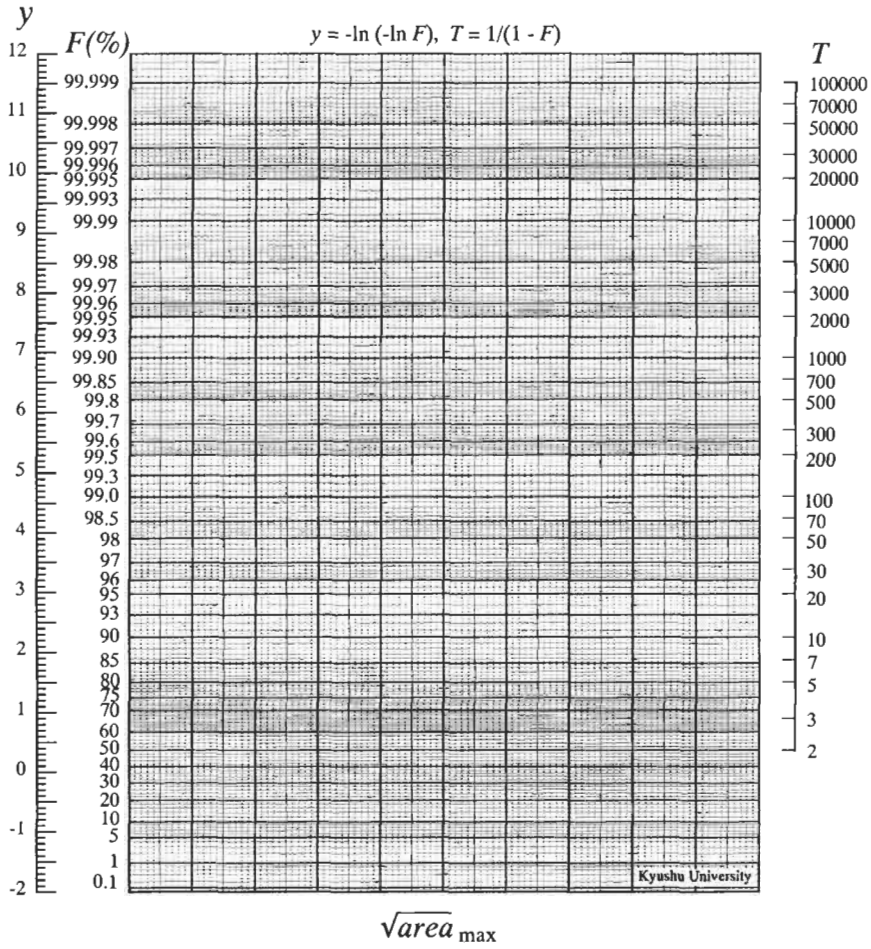


Figure C.2 Probability paper for extreme value distribution (type II).

Index

- 0.13% C steel, annealed 2–3, 37, 38, 43, 44
 mean stress effect 100, 103
 τ_w/σ_w for 251
- 0.35% C steel 93, 250
 τ_w/σ_w for 251
- 0.46–0.47% C steel 37–38, 43, 44, 67, 248, 261, 267, 293, 306
- 0.55% C steel, quenched and tempered 93
- 1.5Ni-Cr-Mo (En24) steel 193
- 2017-T4 aluminum alloy 4–5, 8, 64
- 70/30 brass 4, 5, 8, 64
- A**
- Al oxides 138
- ASTM B scale 134
- ASTM method 75–76, 133, 135
- Acid HF 130
- Al–Si eutectic alloys 217–239
- Al₂O₃
 at centre of fish eye 87
 inclusion 79, 86, 131, 138, 146
- α and β phases in Ti-6Al-4V 241
- Alumina particles on 1.5Ni-Cr-Mo (En24) steel 193
- Aluminum alloys, fatigue properties 217–239
- Aluminum oxides 140
- Angular inclusion 199
- Annealing method, for determination of $\Delta K_{\text{eff, th}}$ 48
- Apparent maximum size of inclusions 114–118
- Artificial surface roughness 306–311
- Aspect ratio (b/a) of surface cracks 262–263, 266, 269
- Atomic Force Microscopy, AFM 280, 292
- B**
- Backup roll steel 298
- Ball bearing 129
- Basic arc, steel-making process 130
- Bearing steels 91–94, 129
 high carbon 248, 255–258
 vacuum-degassed 76
 vacuum-remelted 76, 91
 without nonmetallic inclusions 148
- Beinrite
 distribution of $\sqrt{\text{area}}_{\text{max}}$ for 158
 structure 158, 301
- Biaxial
 fatigue 247
 stress condition 12
- Block maxima 347
- Blunt notch 27–28
- Branch cracks 263, 266
- Built up edge 307, 312
- Bull's eye 205, 213
- C**
- CTOD
 at crack tip 298
 at border of fish eye 301
- Ca content 136
- Ca duplex inclusions 136
- Carbides
 distribution of $\sqrt{\text{area}}_{\text{max}}$ 190
 in bearing steels 147, 152
 in tool steels 185–192
 cracking of 188

Carburising 275, 301
 Casting defects 214
 Clean bearing steels 133
 Cleanliness 32, 78, 130, 133, 135
 and fatigue properties 135–139
 Coaxing effect 4
 Combined stress fatigue 247
 Concept of equivalent ellipse 12
 Continuous casting, Al–Si eutectic alloys 217
 Continuously cast material 220–221, 232, 237
 Control
 (*surface*) *area* 164, 325
 volume 164, 333
 Correction factor for stress intensity factor 21
 Corrosion
 cracking 274
 pits 168, 178–180
 Cr–Mo steel, SCM435 275, 292, 300
 Crack branching under multiaxial fatigue 247
 Crack closure 30, 54
 oxide-induced 29, 48, 231
 plasticity-induced 29, 48, 225, 227, 231
 roughness-induced 29, 48
 Crack initiation 2–4
 at notch root 28
 critical condition for 38
 critical stress for 27
 from small crack 47–54
 Crack opening
 range of 46
 stress 48
 Cracking of carbides in SKD-11 tool steel 188
 Critical hole diameter, d_c 262
 Critical lower bound inclusion size 148
 Critical part of specimen 333
 Critical stress for crack initiation 27
 at notch root 27
 from small crack 47–54

Cumulative distribution function 325
 Cumulative probability 323

D

Damage area 113
 Database of statistics of extreme values of inclusion size $\sqrt{\text{area}_{\text{max}}}$ 351
 Debonding of inclusion 146
 Decarburised layers 168, 170, 174
 Defects 1
 casting 214
 equivalent size for roughness, $\sqrt{\text{area}_R}$ 315
 gouged out by built up edge 312
 small artificial 37–47, 248
 location of 90–91
 Dependence of ΔK_{th} on crack size (defect size) 48, 243
 Desorption of hydrogen from nonmetallic inclusions 280
 Difference between holes and cracks 68
 Dimensionless stress intensity factors 21
 Distance from crack tip, r 15
 Dislocation structure 1
 Distribution
 Gumbel 323, 347
 Weibull 323
 doubly exponential 323
 generalised pareto 347
 log-normal 323
 of internal hardness 173, 276–277
 of residual stress (mean stress) 174, 276–277
 Double electron beam remelting method 284
 Doubly exponential distribution 323
 Drilled hole 58, 67
 Ductile dimples 295, 301
 Dugdale model 36, 53, 298
 Duplex oxide, $(\text{CaO})_x\text{Al}_2\text{O}_3$ 86

E

- EB-CHR 148, 151
 ESR 136, 138, 151
 EVIR 323–328, 345–346
 Effective
 area 17, 90
 stress intensity factor range 54
 threshold stress intensity factor range 46, 48
 Electron beam remelted super clean bearing steel 148–159
 Electron beam-cold hearth remelted super clean steel 148
 En24 steel 77, 193
 Equivalence of holes and cracks 68
 Expected values of $\sqrt{\text{area}}_{\text{max}}$ 327
 Extreme value
 theory 323–324
 distribution 323
 inclusion rating, EVIR 323–328, 345–346
 Extreme value statistics 95, 97, 98, 110, 112, 152
 for graphite nodules 117, 211
 of nonmetallic inclusions at fish eye centres 109
 probability paper 98, 112, 116
 Extremely shallow notch 35–36, 61
 Extremely short cracks 35–36
 Extrusion, Al–Si eutectic alloys 217, 225

F

- FCD60 and FCD70 206–212
 FOX inclusion count 75
 Facet at fracture origin, Ti-6Al-4V alloys 243
 Fairey inclusion counts 76
 Fatigue cracks
 non-propagation behaviour of 4
 emanating from inclusions 83
 Fatigue limit 1–

- 0.13% C steels, rotating bending 2, 44
 0.46% C steel, rotating bending 44
 artificial hole 37–47
 at fracture origin 91
 intrinsic 94
 proportional to H_V 78
 of cracked specimen 61
 of defect free specimens 66
 of notched specimen 26
 of unnotched specimen 26, 29, 36
 prediction equation for internal inclusions 106
 prediction equations 57–74
 small defects 35–55
 steels 1–4
 Fatigue notch effect 15, 25–32
 Fatigue strength
 prediction of lower bound of 337
 scatter for high strength steels 94–99
 scatter band prediction 94–99
 with macroscopic non-propagating cracks 29
 with microscopic non-propagating cracks 29
 Fatigue testing machines
 1 kHz closed loop servo-hydraulic 273
 Losenhausen universal 194
 magneto-strictive loading 273
 rotating bending 152, 171, 194
 servo-hydraulic biaxial 261
 servo-hydraulic closed-loop tension compression 276
 ultrasonic 273
 Fictitious crack length 36
 Fish eye 80, 83, 86–87, 91, 97–98, 105, 135, 278, 284, 292–301
 outer border of 292–298, 300
 Fish-eye fracture 153–155, 175–176
 Forging ratio 81
 Fracture mechanics 31, 83
 of short fatigue cracks 305
 Fracture origin

- at interface between Si and matrix* 231
 - facets in Ti-6Al-4V* 243
 - in Si (silicon) phase* 231
 - nonmetallic inclusion at* 97, 291
 - small inhomogeneities at* 153
- G**
- GOST 75, 133
 - Generalised pareto distribution 347
 - Geometrical parameter, *area*, $\sqrt{\text{area}}$ 16, 47, 57
 - Gigacycle regime 231
 - Globular duplex inclusions, $\text{Al}_2\text{O}_3(\text{CaO})_x$ 277
 - Goodman diagram 175
 - Grain boundary cracks 95
 - Grain size
 - of SAE 12 L 14* 117
 - of α phase* 242
 - Graphite nodules
 - effects of shape and size of* 205
 - equivalent to small defects* 206–215
 - extreme values statistics for* 117
 - spheroidal* 114
 - Gumbel distribution 323, 347
- H**
- Handbook
 - stress concentration factors* 13
 - stress intensity factor solutions* 16
 - Hard inclusions 129
 - Hardenability 158
 - Hardness 5
 - Brinell 241
 - effect on fatigue limit* 57–74, 94
 - measurement of* 308–311
 - of microstructure* 8
 - scatter of* 308
 - Harmfull Index 131, 133
 - Hertzian contact stresses 147
 - High carbon Cr bearing steel 255
 - High speed tool steel, SKH51 95, 104
 - Hole edge radius 13
 - Hole(s)
 - artificial* 42–47, 85, 219, 225–227, 230
 - stress concentration* 11–15
 - Hydrogen
 - content* 301
 - embrittlement* 274
 - trapped by (nonmetallic) inclusions* 273–291, 292, 301
- I**
- Ideal crack 52
 - In-plane shear crack (Mode II crack) 16
 - Inclined crack 19
 - Inclusion rating 75–77, 133, 321–350
 - ASTM method* 75, 133
 - GOST method* 75, 133
 - JIS lattice point counting method* 76, 133
 - based on statistics of extremes* 152
 - by ASTM B scale* 134
 - correlation with fatigue limit* 321–350
 - index chart* 77
 - instruction for* 321–350
 - Inclusion(s) 1
 - ODA surrounding* 291
 - adhesion to matrix* 35, 82
 - angular* 199
 - apparent maximum size of* 114
 - at centre of fish eye* 87, 105, 278
 - at fatigue fracture origins* 130–133, 139, 277
 - bonding condition at* 88
 - chemical composition* 35
 - classification of* 76
 - critical size* 95
 - effects on fatigue strength* 75–127
 - elastic constants of* 35, 83

- elliptical* 84
 - fatigue cracks emanating from* 83
 - globular duplex* 277
 - in touch (contact) with surface* 90–91, 337
 - internal/interior* 90, 91, 105, 177, 337
 - location* 77, 337
 - of maximum size* 95, 98, 325
 - prediction of $\sqrt{\text{area}}_{\text{max}}$ of* 331–332
 - problems* 35, 75
 - rigidity* 88
 - shape* 35, 82, 92, 156, 178, 179
 - size* 35, 77, 83, 92, 94, 98, 177
 - size distribution* 111, 119, 134
 - size distributions by computer simulations* 119
 - spherical* 145, 199
 - stress distribution around* 83
 - surface* 89–90, 177, 337
 - true maximum size of* 114
 - Incompatibility between β phase regions 242
 - Inhomogeneities 153–159
 - Interaction
 - between crack and free surface* 22–24
 - between nodules* 213
 - between two cracks* 21–22
 - Interface debonding 88
 - Intergranular fracture 295, 301
 - Irregularly shaped crack 18
- J**
- JIS cleanliness rating 76
 - JIS lattice point counting method 76, 133, 135, 138, 140, 255
- K**
- Knee-point 1, 3
- L**
- LEVD 323
 - Largest extreme value distribution, LEVD 323
 - Largest inclusion size, prediction method 118–122
 - Leaded free cutting steel, SAE10L45 112, 138
 - Leaf spring steels 168
 - Location parameter, λ 323
 - Losenhausen universal fatigue testing machine 194
 - Lower bound of fatigue strength (fatigue limit) 95, 109, 141, 182, 191, 213, 321, 333–334
 - prediction equation for* 98, 109
- M**
- Magneto-strictive loading machine 273
 - Manson–Coffin law 238
 - Maraging steel 64
 - mean stress effect* 100
 - non-propagating crack at fatigue limit of* 102
 - torsional fatigue tests on* 248
 - Martensite lath structure 282
 - Maximum equivalent defect size, $\sqrt{\text{area}}_{\text{max}}^*$ 211
 - Maximum inclusion size, $\sqrt{\text{area}}_{\text{max}}$ 110–122, 113, 164, 171, 175
 - Maximum likelihood method 345
 - Maximum permissible stress 35
 - Maximum roughness height, R_y 309, 316, 319
 - Maximum stress 25
 - at hole edge* 12
 - Maximum stress intensity factors, K_{Imax} 16–17
 - for internal crack* 17
 - for surface crack* 17
 - for three-dimensional cracks* 16

- Mean stress 99–110
effect on fatigue of materials containing small defects 100–104
in hard steel 104–108
prediction equation 102–108
residual stress 152, 174
- Mill scale 170
- Misalignment in tension–compression fatigue tests 96
- Mixed mode small crack growth 247
- MnS 129, 140, 146
inclusions 137, 147
- Mode I crack 16
branch cracks 266
branching from 263
started from initial crack tip 263
- Mode II crack 16
started from initial crack tip 263
- Mode III crack 16
- Modified Goodman diagram 100, 180
- Modified *S–N* curve 93, 96, 107, 108, 132, 141, 157, 180, 279, 282, 287
- Multiaxial stress 247
- N**
- Nitriding 275, 301
- Nodular cast iron 114–117, 205–216, 248
- Nodularity 207
- Nominal stress 27
- Non-damaging defect 41
- Non-destructive inspection 95
- Nondimensional stress gradient, χ 26
- Nonferrous metals 4–5
- Non-propagating crack(s) 4
at fatigue limit of maraging steel 102
at fatigue limit of nodular cast iron 210
at notch root 28–31
at root of sharp notches 30
at roughness notch root 312, 319
at small artificial holes 38–39
at torsional fatigue limit 253–255
emanating from ends of initial crack 67
for stainless steel 61
in the surface of unnotched specimens 2
macroscopic 29
maximum size in torsion 254
microscopic 29
size (length) at fatigue limit (of unnotched specimens) 40, 66, 86, 205
threshold condition (stress) for 4, 27
- Non-propagation 4
 Al_2O_3 79
of circumferential cracks, sharply notched specimens 30
of crack emanating from notch 27
of cracks at a hole under reversed torsion 248
- Nonmetallic inclusion(s), see *Inclusion(s)* 85–88, 174, 178–180
TiN 79
at fracture origin 97, 291
effects on fatigue strength 75–127
hydrogen trapped by 274
in hard steels 104
strength prediction 88
subsurface 175
- Notch
blunt 27, 28
circumferential 307
root radius 15
sharp 27, 28
- Notch effect 25–31
due to natural defects 35
due to nonmetallic inclusions 35
due to scratches 35
due to surface defects 35
- Notch root
stress distribution 25–28
radius 13, 27, 29
- Notched specimen, fatigue limit of 26
- Notches, stress concentrations at 11–15

O

ODA, Optically Dark Area 279, 292, 299–302
 Oblique surface crack 19
 Open hearth process 130
 Open melted steel 80
 Opening mode crack (Mode I crack) 16
 Out-of-plane shear crack (Mode III crack) 16
 Oxide metallurgy 137
 Oxygen content 78, 130, 136

P

Parent distribution 323
 Paris fatigue crack growth law 298
 Peak over threshold method 347
 Penny-shaped crack 292
 Plane gear teeth made from nodular cast iron 214
 Plastic zone size
 crack tip 36, 298
 Plate bending 333
 Poisson's ratio 13
 Population 323
 Precracked specimens 262
 Probability paper for extreme value distribution 325, 357–358
 Pure Mode III 264, 266
 Pure Ti 242

R

R (ratio) 36, 99, 102, 106, 180
 Reduced variate, y_i 325
 Replica method 50
 Residual stress 99, 108, 152, 168, 305, 317, 319
 due to fatigue 67
 influence on stress intensity factors 144

Return period 98, 113, 152, 158, 164, 171, 323, 329, 332
 Ring-compression fatigue tests 129
 Ring-shaped specimens 138–139
 Roller bearing 129
 Root radius
 notch 15, 27, 29
 crack 15
 Rotating bending
 fatigue 202, 247
 fatigue testing machines 152, 171, 194
 loading 333–335
 R_y 309

S

S + Ca oxides 138
 S inclusions 138
 S–N curve (diagram, data) 1–3, 154, 277–279
 for high speed tool steel SKH51 96, 105
 for maraging steel specimens containing defects 69
 for rotating bending fatigue tests on 0.13 % C and 0.46 % C steels 38
 modified 93, 96, 107, 108, 132, 141, 157, 180–181, 279, 282, 287
 stepwise 273
 S10C 62
 S30C 63
 S35C 63
 S45C 63
 S50C 64
 SAE12 L 14 117
 SAE 4340 steel 77
 SAE 52100 248, 346
 SAE 9254 87
 SAE10L45 112, 138
 SCM435 282, 300, 302
 SKD-11 185
 SKH51 95, 104, 107, 119
 SUJ2 140, 185, 248, 346

- SUJ4 151
 SUJ8 153
 SUP10M 168, 179
 SUP9 168, 178
 SUP12 163
 distribution of $\sqrt{\text{area}}_{\text{max}}$ for inclusions in 164
 SUS 603 (stainless steel) 64
 Scale parameter, δ 323
 Scanning electron microscopy, SEM 231, 279, 297
 Scatter band
 for strength 31
 prediction 94–99
 Scatter in fatigue strength, prediction of 180–182
 Scratches 307
 notch effect due to 35
 Secondary Ion Mass Spectrometry, SIMS 280, 285
 Semi-circular cracks 22
 Semi-elliptical crack(s) 67, 296
 Servo-hydraulic biaxial testing machine 261, 276
 Sharp notch 27, 28
 Sharply notched specimens for nonferrous metals 4
 Shear-type crack 220
 Shinkansen train 273
 Shot peening 168, 173, 195–199
 compressive stress produced by 201
 $\sigma_{\theta\text{max}}$ criterion 266
 Si-phase in aluminum alloys 217–240
 Singular stress distribution in vicinity of crack tip 16
 Singularity of $r^{-1/2}$ 15
 Size effect 25–32
 Slip band 2, 86
 cracks 95
 Small crack problem 75
 Small defects 25, 35, 85
 effects on fatigue limit 35–54
 effects on torsional fatigue strength 247
 Small inhomogeneities 153–159
 Small-scale yielding 54
 Soderberg diagram 100
 Soft inclusions 136
 Solidification process of molten metal 142
 Specimen
 round bar 334
 hourglass-shaped 335
 tension compression 335
 Spherical inclusions 145, 199
 Spring steel 111, 163–184
 for automotive components 163–168
 $\sqrt{\text{area}}$ 16
 effective value of 90
 for small crack 66–71
 for small hole 66–71
 lower limit of 65, 67
 upper limit of 67
 $\sqrt{\text{area}}$ parameter model 67, 154, 242, 247, 274, 278–279, 282, 301, 312–319
 prediction of torsional fatigue limit 267–270
 Stage I (Mode II) crack growth 247
 Stainless steels 64
 Standard inspection
 area, S_0 112, 325
 volume, V_0 331–332
 Statistical scatter 32
 of strength and microstructure 31
 Statistics of extremes 323–324
 Steel(s)
 fatigue limit 1–4
 hard 42
 soft 42
 stainless 61, 64
 of failure in ultralong life regime 273–303
 Stepwise S – N curve 273
 Strain-based intensity factors 247
 Stress concentration factor 12
 Stress concentration(s) 11–24
 ahead of the elliptical hole 15
 around elliptical inclusions 84

- at crack* 15–24
- at elliptical hole* 12
- at holes* 11–15
- at notches* 11–15
- at spherical cavity* 14
- at spherical inclusion* 15
- at structural discontinuities* 25
- for biaxial stress condition* 12
- due to holes and cracks* 67
- elastic* 29
- equivalent ellipse concept* 12–14
- for a hole under tension and torsion* 249
- for defects* 41, 200
- for geometrically similar specimens* 32
- for small inclusions* 200
- handbook* 13
- Stress distribution**
 - at notch root* 25–28
 - near elliptical hole* 26
 - around inclusions* 83
- Stress gradient** 26–28, 32
- Stress intensity factor** 15
 - correction factor for* 21
 - dimensionless* 21
 - for 3D cracks emanating from defects* 258
 - for arbitrary shaped 3D surface crack* 18
 - for cracks emanating from ellipsoidal cavity* 21
 - for cracks emanating from elliptical hole* 21
 - for cracks emanating from hole under tension and torsion* 249
 - for penny-shaped crack* 21
 - for periodic surface cracks* 315
 - for surface roughness* 18
 - for very shallow circumferential crack* 18
 - handbook* 16
 - range, ΔK_{th}* 139
- Stress ratio** 99, 106, 180
- Sulphur**

- content* 137–139
- inclusions* 138
- Super clean spring steels** 77, 139–142
 - electron beam remelted* 148–159
- Surface finish** 305
- Surface pit** 165
- Surface roughness** 148, 168–182, 299
 - artificial* 306–311
 - effect on fatigue strength* 305–320
 - measurement of* 308–312
 - of fractured fatigue specimens* 292
- Suspension spring steel** 79

T

- Tension compression**
 - fatigue* 202, 247
 - loading* 335
 - low cycle fatigue* 247
- Thermal expansion**
 - between matrix and inclusions* 142
 - coefficients* 146
- Threshold condition for non-propagating crack(s)**
 - emanating from initial defect or crack* 67
 - emanating from holes* 39
 - for unnotched specimens* 40
 - of Mode I branch cracks* 263
- Threshold stress**
 - for non-propagation of cracks* 4, 27
 - for crack propagation* 4.27
- Threshold stress intensity factor range, ΔK_{th}** 36
- Thrust-type contact fatigue tests** 139
- Ti alloys** 241–245
- Ti content** 136
- Ti-5Al-2.5Sn ELI (extra-low-interstitial)** 241
- Ti-6Al-2Sn-4Zn-2Mo-0.1Si (Ti-6242S)** 241
- Ti-6Al-4V** 241
- TiN inclusion** 79, 131, 136, 140
- Tool steels, SKD-11** 185–192

- microstructure of* 187
- fatigue fracture origin in* 189–190
- Torsional fatigue 247–271
 - effect of small artificial defects* 248–258
 - prediction of* 268–270
- Transgranular fracture 295
- True maximum size of inclusions 114–118
- Turbine blades 273
- Two parameter method 214

U

- Ultimate tensile strength, UTS 5, 58, 65, 66, 172, 241
- Ultralong (fatigue) life 273–303
- Ultrasonic fatigue testing machines 273
- Unnotched specimens, fatigue limit of 26
- Upper bound for fatigue strength 94–95, 191

V

- VAR 130, 136, 138, 151
- VD 130
- Vacuum quenching 282
- Vacuum-degassed bearing steel 76
- Vacuum-remelted
 - bearing steel* 76, 91
 - steel* 80
- Valve spring 168
- Very deep crack, effective area 17
- Very shallow crack, effective area 17, 58
- Very shallow notch 36, 58
- Very slender crack, effective area 17
- Very small crack 36, 59
- Very small drilled hole 58
- Vickers hardness 6, 58, 59, 80, 85, 95, 150, 154, 164, 205, 217, 308

- indentations* 58
- von Mises' yield criterion* 253

W

- Weibull distribution 323
- White area 80
- Wicksell problem 331
- Work hardening 168, 305
 - modulus* 61
- Work softening 305
- Wöhler-type rotating bending fatigue testing machines 194

X

- X-ray diffraction method 170
- X-ray micro-analyser 154
- X-ray stress measurement 152

Y

- YUS 170 (stainless steel) 64
- Yield stress 5, 58
- Young's modulus
 - inclusion* 13, 83, 88
 - matrix* 13, 83

Symbols

- $2N_f$ 235
- E 13
- F_f 21
- H_B 5
- H_V 5
- H'_V 165
- K_I 15
- K_{II} 266
- $K_{I\max}$ 16
- $K_{\max.th}$ 53
- K_t 12

- $K_{\theta\max}$ 267
 $K_{\theta\max,th}$ 267
 R 102, 106
 R_a 292
 R_y 309
 S_0 112
 T 98, 323
 V_0 152, 331
 $area$ 16
 $area_p$ 18
 d_c 262
 r 15
 y_i 325
 ΔK 139
 ΔK_{II} 263
 ΔK_{eff} 46
 $\Delta K_{eff,th}$ 46, 48
 ΔK_{th} 36
 $\Delta\epsilon$ 235
 α 102, 104
 χ 26
 δ 323
 $\epsilon_0/2$ 26
 ϵ'_f 235
 λ 323
 ν 13
 ρ 15
 ρ_0 28
 σ_U 5
 σ_Y 5
 σ_{in} 101
 σ_{max} 25
 σ_n 27
 σ_r 108
 σ_w 57
 σ_{w0} 26
 σ_{w1} 29
 σ_{w2} 29
 σ_{wi} 47
 σ_{wi} 168
 σ_{wu} 94
 $\sigma_{\theta\max}$ 266
 σ' 91
 σ'/σ'_w or σ_u/σ'_w 91, 106
 σ'_f 235
 σ'_w 91
 τ_w 248
 τ_w/σ_w 248
 \sqrt{area} 90
 \sqrt{area}_{max}^* 211
 \sqrt{area}_0 212
 \sqrt{area}_R 313
 \sqrt{area}_c 291
 \sqrt{area}_i 94
 \sqrt{area}_{max} 95
 \sqrt{area}_p 260
 \sqrt{area}_s 94

ISBN 0 08 044064 9



9 780080 440644